frontiers | Research Topics

The biochemistry of amyloids in neurodegenerative diseases, volume II

Edited by
Cláudio M. Gomes, Jinghui Luo and Wolfgang Hoyer

Published in
Frontiers in Neuroscience
Frontiers in Chemistry
Frontiers in Molecular Biosciences
Frontiers in Molecular Neuroscience

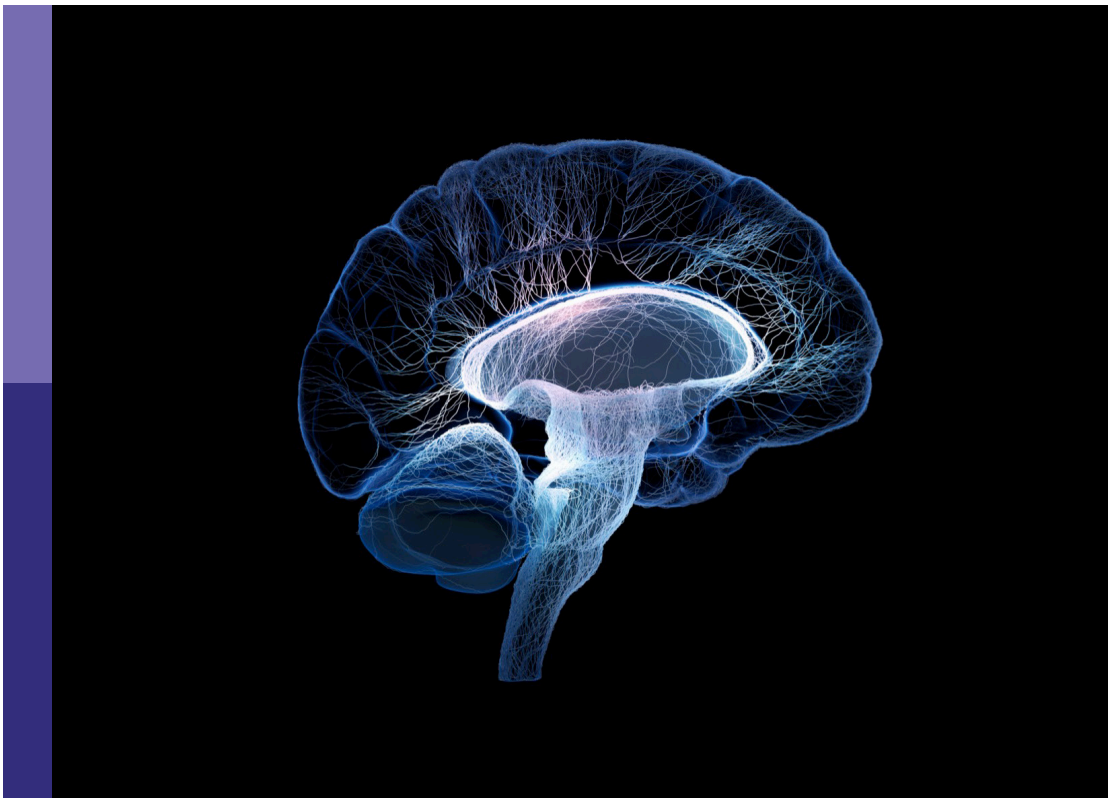

ISSN 1664-8714
ISBN 978-2-8325-2979-9
DOI 10.3389/978-2-8325-2979-9

About Frontiers

Frontiers is more than just an open access publisher of scholarly articles: it is a pioneering approach to the world of academia, radically improving the way scholarly research is managed. The grand vision of Frontiers is a world where all people have an equal opportunity to seek, share and generate knowledge. Frontiers provides immediate and permanent online open access to all its publications, but this alone is not enough to realize our grand goals.

Frontiers journal series

The Frontiers journal series is a multi-tier and interdisciplinary set of open-access, online journals, promising a paradigm shift from the current review, selection and dissemination processes in academic publishing. All Frontiers journals are driven by researchers for researchers; therefore, they constitute a service to the scholarly community. At the same time, the *Frontiers journal series* operates on a revolutionary invention, the tiered publishing system, initially addressing specific communities of scholars, and gradually climbing up to broader public understanding, thus serving the interests of the lay society, too.

Dedication to quality

Each Frontiers article is a landmark of the highest quality, thanks to genuinely collaborative interactions between authors and review editors, who include some of the world's best academicians. Research must be certified by peers before entering a stream of knowledge that may eventually reach the public - and shape society; therefore, Frontiers only applies the most rigorous and unbiased reviews. Frontiers revolutionizes research publishing by freely delivering the most outstanding research, evaluated with no bias from both the academic and social point of view. By applying the most advanced information technologies, Frontiers is catapulting scholarly publishing into a new generation.

What are Frontiers Research Topics?

Frontiers Research Topics are very popular trademarks of the *Frontiers journals series*: they are collections of at least ten articles, all centered on a particular subject. With their unique mix of varied contributions from Original Research to Review Articles, Frontiers Research Topics unify the most influential researchers, the latest key findings and historical advances in a hot research area.

Find out more on how to host your own Frontiers Research Topic or contribute to one as an author by contacting the Frontiers editorial office: frontiersin.org/about/contact

The biochemistry of amyloids in neurodegenerative diseases, volume II

Topic editors

Cláudio M. Gomes — University of Lisbon, Portugal

Jinghui Luo — Paul Scherrer Institut (PSI), Switzerland

Wolfgang Hoyer — Heinrich Heine University of Düsseldorf, Germany

Citation

Gomes, C. M., Luo, J., Hoyer, W., eds. (2023). *The biochemistry of amyloids in neurodegenerative diseases, volume II*. Lausanne: Frontiers Media SA.

doi: 10.3389/978-2-8325-2979-9

Table of contents

frontiers | Frontiers in Neuroscience

TYPE Editorial
PUBLISHED 27 June 2023
DOI 10.3389/fnins.2023.1236518

OPEN ACCESS

EDITED AND REVIEWED BY
Einar M. Sigurdsson,
New York University, United States

*CORRESPONDENCE
Cláudio M. Gomes
✉ cmgomes@fc.ul.pt
Wolfgang Hoyer
✉ wolfgang.hoyer@hhu.de
Jinghui Luo
✉ jinghui.luo@psi.ch

RECEIVED 07 June 2023
ACCEPTED 09 June 2023
PUBLISHED 27 June 2023

CITATION
Gomes CM, Hoyer W and Luo J (2023) Editorial: The biochemistry of amyloids in neurodegenerative diseases, volume II. *Front. Neurosci.* 17:1236518. doi: 10.3389/fnins.2023.1236518

Editorial: The biochemistry of amyloids in neurodegenerative diseases, volume II

Cláudio M. Gomes[1,2]*, Wolfgang Hoyer[3,4]* and Jinghui Luo[5]*

[1]Biosystems & Integrative Sciences Institute, Faculdade de Ciências, Universidade de Lisboa, Lisboa, Portugal, [2]Departamento de Química e Bioquímica, Faculdade de Ciências, Universidade de Lisboa, Lisboa, Portugal, [3]Institute of Physical Biology, Heinrich Heine University Düsseldorf, Düsseldorf, Germany, [4]Institute of Biological Information Processing (IBI-7) and Jülich Center for Structural Biology, Forschungszentrum Jülich, Jülich, Germany, [5]Department of Biology and Chemistry, Paul Scherrer Institute, Villigen, Switzerland

KEYWORDS

protein aggregation, Tau, synuclein, Parkinson's disease, Alzheimer's disease, prion protein, huntingtin (HTT), chaperone

Editorial on the Research Topic
The biochemistry of amyloids in neurodegenerative diseases, volume II

The aggregation of proteins into amyloid fibrils is a key feature of multiple disorders, in particular neurodegenerative diseases such as Alzheimer's disease (AD), Parkinson's disease (PD), Huntington's disease (HD) and prion diseases. The critical role of protein fibrils and oligomeric assemblies for pathogenesis is widely acknowledged, yet many questions remain unanswered, such as the identity and activities of the most relevant aggregate species and the factors that trigger or inhibit their formation. The articles included in this Research Topic and e-book take a close look at the fate of amyloidogenic proteins alon g the pathway from their monomeric states to oligomeric assemblies and seeding-competent amyloid fibrils. A recurring motif is the enormous structural versatility of the involved proteins, which needs to be appreciated in order to elucidate their functions and dysfunctions.

Structural versatility is evident already at the level of protein monomers, which are often intrinsically disordered, ready to structurally adapt to various binding partners. Bisi et al. review experimental and computational studies analyzing the conformations adopted by α-synuclein. They comprehensively describe the effects of various factors on α-synuclein's conformational ensemble, including disease-related mutations, metal ions, lipids, proteins, and small molecules. In order to map the metal binding sites in α-synuclein by NMR, Gonzalez-Garcia et al. combine amide protection factor determination with relaxation and chemical shift perturbation data. Different monovalent and divalent metal ions have variable effects on the different observables, indicating that the binding modes of the metal ions differ, although they all eventually promote α-synuclein aggregation. Further modulators of α-synuclein's properties are posttranslational modifications (PTMs), with N-terminal acetylation as a prominent example. Iyer et al. provide an overview of the effects of N-terminal acetylation on conformation, lipid binding, and amyloid formation of α-synuclein. The authors discuss that N-terminal acetylation might prime the protein for further PTMs which are crucial for α-synuclein function. In the case of protein Tau, an additional layer of versatility is added by the presence of six different protein isoforms, with a connection of certain Tau isoforms to specific tauopathies. Bachmann et al. report how the individual isoforms behave in a cellular context. They find that the isoform affects the extent of axonal sorting as well as cell size and microtubule number, revealing isoform-dependent microtubule dynamics.

Oligomers are candidates for the main pathogenic triggers, with strong evidence in particular for Aβ oligomers in AD. Iliyasu et al. review pathways involved in AD pathogenesis, including oxidative stress, neuroinflammation, and Aβ clearance. Relating to Aβ proteostasis, Figueira et al. report how different multimers of S100B, an extracellular signaling Ca^{2+}-binding protein with holdase-type chaperone activity on Aβ, achieve inhibition of oligomer and fibril formation. Analysis of the chemical kinetics of Aβ aggregation reveals that especially formation of Aβ oligomers by fibril surface-catalyzed secondary nucleation is hampered in presence of S100B multimers. The inhibitory activity depends on the oligomeric state of S100B, with sub-molar potency observed for S100B tetramers. Nazere et al. study the mechanism of cellular uptake of Aβ oligomers. Their data supports a major role of macropinocytosis, depending on lipid rafts and heparan sulfate proteoglycans, and regulated by the GTPase Rac1.

Several articles in this Research Topic address the formation of amyloid fibrils and their potential to act as seeds in the amplification of protein aggregation. Angelli et al. compare the conversion of rabbit and mouse cellular prion protein (PrP^{C}) to the scrapie form (PrP^{Sc}). Rabbits exhibit a comparatively low propensity for prion infection. In line with this, the authors find a reduced propensity of rabbit PrP^{C} to convert to PrP^{Sc} *in vitro*, independent of the nature of the individual cofactors used to trigger conversion. Closing in on the pool of species that drive the pathogenic process in HD, Schindler et al. describe the detection of small (average length of 200 nm) fibrils of mutant huntingtin in the brains of knock-in HD mice. These small, soluble particles are seeding-competent in a sensitive FRET-based protein amplification assay. The authors conclude that not only non-fibrillar oligomers but also fibrillar structures are part of the pool of soluble species and can contribute independently to the pathogenic process. Whether or not the fibril structure of the seed is maintained during seeding is the topic of a review by Alijanvand et al.. The authors point out the necessity to differentiate between seeding through fibril elongation and seeding through secondary nucleation, i.e., through nucleation of new fibrils from monomer that is facilitated by the presence of existing fibrils. While fibril growth by monomer addition has been shown to maintain the structure of the seed fibril, the available data does not support the same for fibril amplification through secondary nucleation, where the structure of the new fibril seems to be determined rather by other factors such as the solution conditions. As amyloid fibrils interact differently with ligands than monomers do, Roldán-Martín et al. elaborate on the interactions of an S-shaped Aβ fibril polymorph with metal ions Cu^{2+} and Al^{3+}. Applying structural prediction of metal binding sites, protein-ligand docking, and molecular dynamics simulations, the authors find the metal ions bind to distinct sites, i.e., the N-terminus vs. residues Glu22 and Asp23, with opposed consequences for fibril stability. Amyloid fibrils can also be modified and stabilized by dityrosine (DiY) formation, however, the consequences of DiY formation for aggregation and toxicity are not fully understood. Maina et al. review the current literature on the effect of DiY formation on Aβ and Tau assembly and (dys)function. They point out the variability of the results obtained thus far, describe the complexity inherent to DiY modification of aggregating proteins, and discuss the experimental hurdles that need to be overcome for future progress. As an approach to reduce the seeding capacity of amyloid fibrils, the green tea polyphenol epigallocatechin gallate (EGCG) has a long history in protein aggregation research, as reviewed by Fernandes et al.. The authors summarize the effects of EGCG on PrP, huntingtin, α-synuclein and Aβ, including inhibition of aggregation, remodeling of fibrils to seeding-incompetent species, along with a reduction in neurotoxicity. Finally, Szegő et al. report the potential of the engineered binding protein β-wrapin AS69 to reduce fibril seeding in a PD mouse model. AS69 binds to the N-terminus of α-synuclein and interferes with fibril nucleation. When co-injected together with preformed fibril seeds (PFFs) into PD mice, AS69 inhibits PFF-induced α-synuclein pathology, suggesting that the α-synuclein N-terminus is a potential site for interference with aggregation and seeding.

Author contributions

All authors listed have made a substantial, direct, and intellectual contribution to the work and approved it for publication.

Acknowledgments

We are extremely grateful to all that made this Research Topic possible and that have contributed to its success. We thank the seventy seven authors that have chosen our Research Topic as the most adequate venue to disseminate their research in fourteen published articles, and the twenty eight reviewers for their valuable time and for contributing to improve quality through constructive comments. We are also grateful to the Frontiers publishing team and editors for their support.

Conflict of interest

The authors declare that the research was conducted in the absence of any commercial or financial relationships that could be construed as a potential conflict of interest.

Publisher's note

frontiers in Molecular Biosciences

MINI REVIEW
published: 16 April 2021
doi: 10.3389/fmolb.2021.669994

Secondary Nucleation and the Conservation of Structural Characteristics of Amyloid Fibril Strains

*Saeid Hadi Alijanvand[1], Alessia Peduzzo[2] and Alexander K. Buell[2]**

[1] Bioprocess Engineering Department, Institute of Industrial and Environmental Biotechnology, National Institute of Genetic Engineering and Biotechnology, Tehran, Iran, [2] Technical University of Denmark, Department of Biotechnology and Biomedicine, Lyngby, Denmark

Amyloid fibrils are ordered protein aggregates and a hallmark of many severe neurodegenerative diseases. Amyloid fibrils form through primary nucleation from monomeric protein, grow through monomer addition and proliferate through fragmentation or through the nucleation of new fibrils on the surface of existing fibrils (secondary nucleation). It is currently still unclear how amyloid fibrils initially form in the brain of affected individuals and how they are amplified. A given amyloid protein can sometimes form fibrils of different structure under different solution conditions *in vitro*, but often fibrils found in patients are highly homogeneous. These findings suggest that the processes that amplify amyloid fibrils *in vivo* can in some cases preserve the structural characteristics of the initial seed fibrils. It has been known for many years that fibril growth by monomer addition maintains the structure of the seed fibril, as the latter acts as a template that imposes its fold on the newly added monomer. However, for fibrils that are formed through secondary nucleation it was, until recently, not clear whether the structure of the seed fibril is preserved. Here we review the experimental evidence on this question that has emerged over the last years. The overall picture is that the fibril strain that forms through secondary nucleation is mostly defined by the solution conditions and intrinsic structural preferences, and not by the seed fibril strain.

Keywords: amyloid, secondary nucleation, α-synuclein, amyloid beta, proliferation

OPEN ACCESS

Edited by:
Louise Charlotte Serpell, University of Sussex, United Kingdom

Reviewed by:
Martin M. Muschol, University of South Florida, United States
Jan Bieschke, University College London, United Kingdom

***Correspondence:**
Alexander K. Buell
alebu@dtu.dk

Specialty section:
This article was submitted to Structural Biology, a section of the journal Frontiers in Molecular Biosciences

Received: *26 February 2021*
Accepted: *30 March 2021*
Published: *16 April 2021*

Citation:
Hadi Alijanvand S, Peduzzo A and Buell AK (2021) Secondary Nucleation and the Conservation of Structural Characteristics of Amyloid Fibril Strains. Front. Mol. Biosci. 8:669994. doi: 10.3389/fmolb.2021.669994

INTRODUCTION

Amyloid fibrils are highly ordered protein polymers and represent a common hallmark of a range of severe human disorders, many of which are neurodegenerative in nature (Knowles et al., 2014). Particularly prominent examples include Alzheimer's disease, Parkinson's disease, amyotrophic lateral sclerosis (ALS) and Creutzfeldt-Jakob disease. The most striking common feature of these diseases is their progressive nature, whereby the amyloid fibril pathology involves ever increasing regions of the central nervous system (CNS), as the disease advances (Braak and Braak, 1991; Brettschneider et al., 2015). It was found that often the pathology originates in a localised area of the nervous system, from which it spreads for up to several decades through a well-defined pathway toward other regions until the overall damage to the nervous system is fatal.

The quantity of fibrillar material inside a patient increases over time, and this increase appears to proceed along a defined, connected trajectory. These observations suggest that processes are at work

that amplify the low quantities of amyloid fibrils that are present in the very early, asymptomatic stages of the disease. The amyloid proteins and peptides (e.g., α-synuclein, Aβ) are often found throughout most of the brain in their monomeric forms, but new fibrils do not seem to form independently in different parts of the brain. Therefore, the presence of fibrils at a given location facilitates the formation of more fibrils, ultimately leading to spreading. Fibril amplification can either proceed through repeated cycles of fragmentation and elongation, or else through secondary nucleation. Combined growth and fragmentation has been shown in many studies to allow efficient amplification of very small quantities of fibrils for diagnostic or analytical purposes *in vitro*, e.g., in prion misfolding cyclic amplification (PMCA; Saá et al., 2006) or in real-time quaking-induced conversion (RT-QuIC; Saijo et al., 2019). Secondary nucleation, on the other hand, corresponds to the nucleation of new fibrils from monomer that is facilitated by the presence of existing fibrils, e.g., through surface-catalysis (heterogeneous nucleation; Buell, 2017)). One of the key questions that remains to be answered in the field of protein aggregation and misfolding diseases is as to which of these, if any, amplification mechanisms plays the dominant role in the spreading of a particular amyloid pathology. Such knowledge would enable a targeted intervention, as there is good theoretical evidence that interference with the amplification mechanism could be the most effective therapeutic strategy (Michaels et al., 2019).

Evidence that secondary nucleation might play a role in fibril amplification *in vivo* comes from *in vitro* experiments, in which secondary nucleation rates can be very high even under completely quiescent conditions (Cohen et al., 2013; Buell et al., 2014). On the other hand, fibril fragmentation rates have been shown to be very strongly increased by mechanical agitation or stirring (Xue and Radford, 2013), conditions which are unlikely to be replicated *in vivo.* Indeed, it is experimentally challenging to detect fibril fragmentation under completely quiescent conditions, and the little available data suggests very low rates (Smith et al., 2006; Fränzl et al., 2019).

In this review, we will focus on another line of available experimental evidence, namely the propagation of structural properties. Amyloid structural biology has experienced a breakthrough in recent years, due to the availability of atomic resolution structures of amyloid fibrils from cryo-electron (cryo-EM) microscopy. This method is applicable both to fibrils formed *in vitro* (Gremer et al., 2017; Guerrero-Ferreira et al., 2018; Röder et al., 2019), as well as to fibrils derived from patients [Aβ (Kollmer et al., 2019), α-synuclein (Schweighauser et al., 2020), tau (Fitzpatrick et al., 2017) and immunoglobulin light chains (Radamaker et al., 2019)].

Lower resolution structural and biochemical information had been available for years and had suggested that a given amino acid sequence is able to form different types of amyloid fibrils, called strains, often under different solution conditions (Toyama et al., 2007). The existence of such fibril strains has now been given a firm structural basis through high resolution cryo-EM structures (Li et al., 2018).

It is found that patient-derived amyloid fibrils are often very homogeneous (Cendrowska et al., 2020) and consist of a small number of polymorphs (Fitzpatrick et al., 2017; Schweighauser et al., 2020). Different patients with the same amyloid disease (Annamalai et al., 2016), as well as patients with different diseases, but involving the same protein (Schweighauser et al., 2020), can display different fibril structures. However, there are also cases where patient-derived fibrils have been found to show a higher degree of polymorphism (Kollmer et al., 2019).

The fact that fibrils extracted from a given patient are of the same, or a small number of, morphologies suggests that the molecular processes at work to amplify the fibrils can at least in some cases preserve the structural information encoded in the initial seed fibrils. An alternative explanation is that the specific physico-chemical environment in the given patient is only conducive to the formation of very specific type(s) of fibrils. An answer to the question whether or not secondary nucleation is able to preserve the structural information of the seed fibril is therefore a pertinent one in this context (Linse, 2017), and we will review here the available evidence. Before reviewing secondary nucleation, we will summarize the available evidence for the preservation of the fibril strain by fibril elongation/growth.

FIBRIL ELONGATION PRESERVES THE STRAIN CHARACTERISTICS

Fibril strain propagation is the capability of preserving the physical and structural properties of the seed fibrils even under conditions that favour the *de novo* nucleation of another fibril structure (**Figure 1A**). In this process, the seed can act as a template and transmit its conformational properties to the incorporating monomer by "conformational memory" (Yamaguchi et al., 2005). Seeding is very efficient in accelerating the aggregation reaction, as the energy barrier for the primary nucleation of new fibrils from monomer is significantly higher than that for the incorporation of monomers at the end of the existing fibril, even if this addition does not lead to the formation of the most stable state under the particular set of solution conditions (Buell, 2019). The reason for which seeding is so effective, as well as the mechanism by which the seed fibril guides the incoming monomer into the template structure, are not known in detail. However, the fact that fibril elongation rates saturate at high monomer concentration (Buell, 2019) indicates that elongation involves more than a single molecular step. It probably involves an initial weak association between the monomer and the seed fibril end, followed by a conformational search for the thermodynamically most stable state (Jia et al., 2020). Sometimes the fibril end can remain in a state in which the last incoming monomer has not yet reached the correct structure for extended periods of time, as suggested by the fibril's inability to grow further during this time period, i.e., stop-and-go-kinetics of fibril growth (Ferkinghoff-Borg et al., 2010). There is also increasing evidence that the transition state for fibril elongation, i.e., the highest free energy state separating the isolated monomer from the fully incorporated one, involves a close contact between the fibril and the monomer (Vettore and Buell, 2019). Overall, there is strong evidence that fibril growth mechanisms correspond to induced fit, rather than

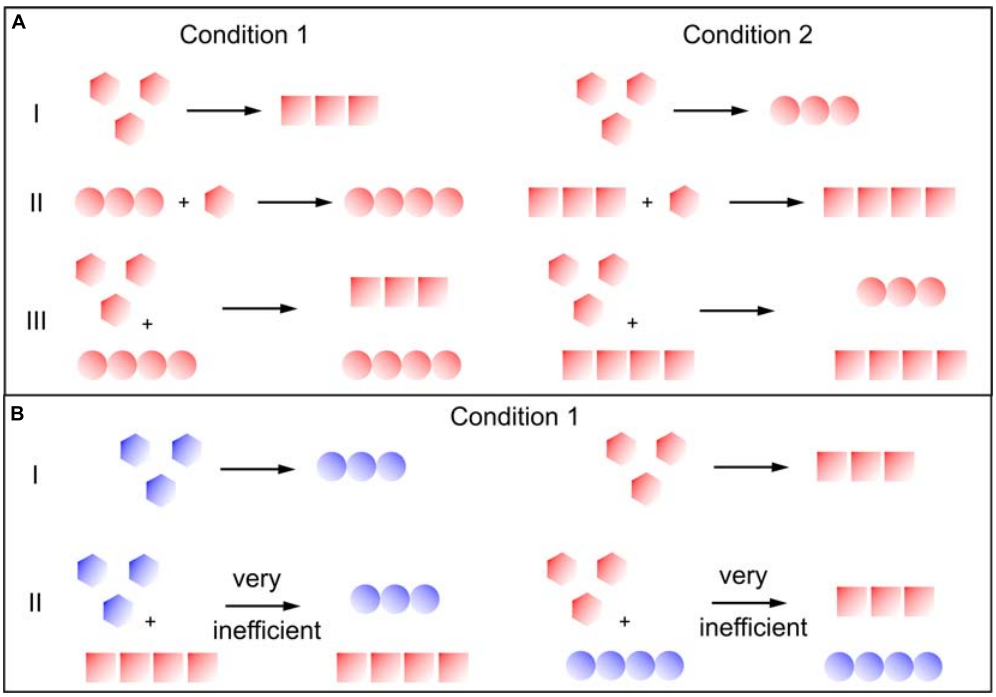

FIGURE 1 | Secondary nucleation and the transmission of structural information. Different colors indicate different sequences and different symbols indicate different structures. **(A)** Proteins where the same sequence can form different strains under different conditions (e.g., insulin, α-synuclein). I: Fibrils formed through primary nucleation from monomer alone form different fibril strains, depending on the solution conditions. II: In fibril elongation, the templating effect of the seed fibrils guides the monomer into a conformation that is not dictated by the solution conditions, but by the seed. III: in secondary nucleation, the newly formed fibril strains are defined by the solution conditions, rather than the seed fibrils. **(B)** Proteins where closely related sequences have different structural preferences (e.g., Aβ 1-40 and Aβ 1-42). I: the related sequences may form different fibrils even under identical solution conditions. II: Cross-surface nucleation can be inefficient if the monomers have a different structural preference from the seed fibrils.

conformational selection (Arai et al., 2015). The latter would correspond to the fibril end "fishing" the appropriate pre-formed monomer conformation out of solution, whereas the former corresponds to the fibril end assisting, through direct interaction, in the "correct misfolding" of the incoming monomer.

Different environmental conditions such as temperature, pH, salt components, shear forces, denaturants, concentration of protein, and co-solvents can lead to the formation of different amyloid strains (**Table 1A** and **Figure 1A**). Many *in vitro* (cross-)seeding experiments performed with a particular fibril strain, under conditions where a different strain would form *de novo,* confirmed the efficient imprinting of the conformational properties of the growing fibrils by the pre-formed fibrils, overcoming the structural preferences induced by the particular set of solution conditions (**Table 1**). The "conformational memory" of fibril strains used as seeds can in some cases be maintained over many generations of seeding (Jones and Surewicz, 2005; Frost et al., 2009).

SECONDARY NUCLEATION AND THE PRESERVATION OF THE FIBRIL STRAIN

Before being able to investigate whether or not secondary nucleation transmits the seed fibril strain, it first has to be established if a given amyloid fibril system is able to proliferate through secondary nucleation. In recent years, a range of amyloid proteins have been investigated in this respect and it has been found that secondary nucleation appears to be relatively widespread (Ruschak and Miranker, 2007; Foderà et al., 2008; Cohen et al., 2013; Buell et al., 2014; Lundqvist et al., 2021). Indeed, secondary nucleation might only be a special case of general surface nucleation (Buell, 2017). It has been shown that fibrils of one protein can nucleate from monomer on the surface of fibrils of another protein, while the same proteins are unable to elongate each others fibrils (Koloteva-Levine et al., 2020; Vaneyck et al., 2021). This difference suggests that cross-surface nucleation has much lower requirements for sequence similarity than cross-elongation.

Secondary nucleation can be either detected through systematic variation of monomer concentration in unseeded experiments, followed by kinetic analysis (Cohen et al., 2013), or else from the comparison of weakly seeded experiments with unseeded experiments under quiescent conditions (Buell et al., 2014). If the seed concentrations are too high (approx. $\geq$1% by mass and more) then the kinetic traces of the aggregation reaction are dominated by the growth of the seed fibrils (Buell, 2019) and any contribution from secondary nucleation can be very difficult to resolve. A systematic decrease in seed concentration

TABLE 1 | Overview over *in vitro* studies investigating the propagation of structural properties through (A) fibril elongation and (B) secondary nucleation.

Protein	Condition varied to produce strains	Conditions of seed production	Observation and [Ref]
(A) Elongation			
Insulin	Protein concentration	LCF (Low concentration fibrils), HCF (high concentration fibrils)	When LCF (HCF) used as seeds in the high (low) insulin concentration, the resulting fibrils have the structural properties of the seeds (Sakalauskas et al., 2019).
	Solvent composition	Ethanol, Water	Structural characteristics of fibrils completely dictated by the parent seed rather than the solvent conditions (Dzwolak et al., 2004, 2005).
	pH	pH 1.6–2	Conformational properties of the template were transferred to growing fibrils in spite of the unfavorable environmental condition (Sneideris et al., 2015a).
	Different sequences	Human insulin analog KR, bovine insulin (BI)	High concentrations of KR seeds revert the superstructural chirality of BI fibrils compared to the absence of KR seeds (Dzwolak et al., 2013).
			Homologous seeds have dominant effect on imprinting their conformational properties in daughter amyloid generations (Surmacz-Chwedoruk et al., 2014).
Glucagon	Solution condition	Salt concentration Protein concentration and different temperature	Some of the characteristics of strains may be propagated by seeding but other characteristics, e.g., thermostabilty, are not inherited upon seeding (Pedersen et al., 2006).
K3 fragment of (β2-microglob.	Different solution	F210, F218	The seeding of f201 monomer with f218 seeds lead to the formation of fibrils with f218 properties, but repeating the seeding reaction leads to gradual disappearance of f218 properties and f218 fibrils are transformed completely into f210 fibrils over several cycles (Yamaguchi et al., 2005).
Aβ	Sequences	Aβ1–40, Aβ1–42	Aβ1–42 can be cross-templated by Aβ1–40 fibril ends, while Aβ1–40 monomers are not efficiently incorporated into the end of Aβ1–42 fibrils (Brännström et al., 2018).
	Solution conditions	Quiescent or agitation condition	The results showed that quiescent and agitated parent fibrils show pronounced structural differences that are transmitted to subsequent generations of fibrils (Petkova et al., 2005).
α - synuclein	Solution conditions	Different buffers	Cross-seeding with α-syn fibril strains showed that these strains imprint their structural properties to soluble α-syn molecules upon their incorporation within fibrils (Bousset et al., 2013; Peduzzo et al., 2020).
PrP	Different sequence	Human PrP, Mouse PrP, Hamster PrP	Cross seeding of these variants leads to the formation of fibril strains that have properties like the parent fibril (Jones and Surewicz, 2005).
	Solution conditions	2M or 4M of GuHCl	Cross seeding by these two different types of seeds showed that conformational stability can be transmitted to the final fibrils in a seed concentration-dependent manner (Sneideris et al., 2015b).
Tau	Sequence	K18, K19	K18 monomers incorporate into K18 seeds but K19 monomers do not, while both K18 and K19 monomers can add onto K19 fibrils (Dinkel et al., 2011).
Sup35	Solution condition	Temperature (4 and 37°C)	Two strains of Sup 35 termed SC4 and SC37 have different division rates and conformational properties. These differences determine the acceptable conformation of SupNM monomers that could be incorporated at the end of these strains (Toyama et al., 2007).
			SC4 strain from *S. cerevisiae Sup35* can seed SupNM polymerization from *C. albicans* and imprints is properties onto the newly formed fibrils (Tanaka et al., 2005).
(B) Secondary nucleation			
Insulin	Protein concentration	0.2–1 mM	As seed concentration is decreased, propagation of seed structural properties decreases, as evaluated by AFM imaging and FTIR spectroscopy (Sakalauskas et al., 2019).
PrP	Denaturant concentration	2 and 4 M GndHCl	As seed concentration is decreased, propagation of seed structural properties decreases, as evaluated by AFM imaging, chemical depolymerisation and FTIR spectroscopy (Sneideris et al., 2015b).
α-synuclein	pH	pH 7 and pH 5	As seed concentration is decreased under conditions conducive for secondary nucleation (pH 5), propagation of seed structural properties decreases, as evaluated by AFM/TEM imaging and protease resistance (Peduzzo et al., 2020).
Aβ	Sequence	Aβ40 vs. Aβ42	Aβ42 fibrils formed through cross-surface nucleation on Aβ40 fibril surfaces display the seeding properties of de novo formed Aβ42 fibrils, as evaluated by SPR experiments (Brännström et al., 2018).
		Various point mutations	Cross-surface nucleation was found to be only efficient if monomer has same structural preference as seed fibril (Thacker et al., 2020).

will eventually reveal the presence, or not, of secondary nucleation (Buell et al., 2014; Sneideris et al., 2015b; Sakalauskas et al., 2019).

So far, compared to fibril elongation, only a small number of studies have addressed the question whether or not secondary nucleation propagates the structural information of the seed

fibril strain. In the case of insulin, it was found that the degree of transmission of the seed strain characteristics decreases with decreasing seed concentration (Sakalauskas et al., 2019). This finding suggests that only in a seed concentration regime dominated by elongation, efficient propagation of structural properties takes place, whereas an increasing proportion of newly generated fibrils from secondary nucleation leads to a loss of strain propagation. Similar findings were made with a fragment of the mouse prion protein (Sneideris et al., 2015b), as well as with human α-synuclein (Peduzzo et al., 2020). In these studies, the different strains were distinguished by spectroscopy (Sneideris et al., 2015b; Sakalauskas et al., 2019), equilibrium depolymerisation (Sneideris et al., 2015b), as well as resistance to proteolytic degradation (Peduzzo et al., 2020) and high resolution imaging (Sakalauskas et al., 2019; Peduzzo et al., 2020). Apart from providing insight into fundamental aspects of secondary nucleation, these types of experiments also establish that secondary nucleation is clearly distinct from elongation (Scheidt et al., 2019; Peduzzo et al., 2020; **Table 1B**) provides a summary of these studies.

Similar experiments have also been performed for cases where two closely related sequences could be shown to form different fibril structures under a given set of solution conditions. In one such study, involving surface plasmon resonance (SPR) experiments with the Aβ 1-40 and Aβ 1-42 peptides the strain characteristics were evaluated based on the cross-seeding ability (Aβ 1-40 fibrils seed both types of monomer, but Aβ 1-42 fibrils are only capable of self-seeding). It was found that the structural characteristics of fibrils formed through cross-surface nucleation (the term secondary nucleation should be reserved to scenarios where the monomer and the seed fibril have the same amino acid sequence) were not defined by the seed structure, in contrast to fibril elongation. In another recent study also involving the Aβ peptide, several sequence variants were investigated. It was shown that surface cross-nucleation was only efficient if the monomer had an innate preference (as judged from the fibrils formed *de novo*) for the structure of the seed fibril (Thacker et al., 2020). While these experiments are suggestive of some degree of specificity of fibril surface nucleation, they do not demonstrate the actual transmission of the template structure.

In summary, therefore, we do not currently have any evidence for the direct transmission of structural properties of amyloid fibrils by secondary nucleation, and secondary nucleation appears merely as a particular example of the general phenomenon of surface-catalysed formation of amyloid fibrils.

POTENTIAL ORIGIN OF THE DIFFERENCES IN THE STRAIN PROPAGATION PROPERTIES BETWEEN FIBRIL ELONGATION AND SECONDARY NUCLEATION

The existence of a multitude of fibril strains for most amyloid proteins, in the form of alternative structures formed by a given amino acid sequence, illustrates presumably the degeneracy of the amyloid free energy landscapes, i.e., the existence of several free energy minima with comparable stability. However, the relative populations of different strains in any given scenario *in vitro* or *in vivo* does not necessarily solely reflect the relative thermodynamic stabilities, as they can also be influenced by differences in nucleation kinetics. For example could different strains nucleate with different efficiencies on surfaces vs. in the bulk, or display different concentration dependencies of their nucleation rates. The nucleation of amyloid fibrils is associated with high free energy barriers (Buell, 2017; Cohen et al., 2018), possibly due to the large loss in entropy associated with the formation of a multimeric nucleus from two or more often disordered monomeric precursor molecules. The addition to a seed fibril enables the often highly flexible monomer to be efficiently templated into the same structure as the seed, even if this structure does not correspond to the most stable one under these conditions. The seeding effect only continues if the last added monomer adopts the correct structure. Otherwise, the incorrectly incorporated monomer will re-arrange or dissociate again. Such a selectivity for correctly added monomers does not seem to operate for monomers adsorbed to the fibril surface, the precursors of secondary nuclei (Šarić et al., 2016). The binding of monomer to fibril surfaces has been measured for the Aβ peptide and was found to be of two orders of magnitude lower affinity than that of correct incorporation into fibril ends (Šarić et al., 2016) and strongly exothermic (Cohen et al., 2018). These characteristics are reminiscent of the generic requirements of interaction between a catalyst and its substrate, which must be neither too strong, nor too weak (Sabatier principle; Kari et al., 2018).

In the case of α-synuclein, it has been shown that the binding of protein to the fibril surface is strongly enhanced at mildly acidic pH, where also secondary nucleation rates are very high. Therefore, secondary nucleation appears to correlate with a generic, non-specific attachment of monomer to the fibril surface. Nucleation is then presumably favored for the same reasons that binding to other types of interfaces accelerate it (Galvagnion et al., 2015; Buell, 2017). While being strongly favored through binding to the surface of the seed fibrils, nucleation on fibril surfaces appears to still be subject to the influence of the solution conditions, as in the case of nucleation on foreign surfaces, such as the polymer-water or air-water interfaces (Bousset et al., 2013; Campioni et al., 2014). The only existing evidence for nucleation on fibril surfaces to be different from generic, non-specific surface nucleation is the data on the Aβ peptide, which suggests that this type of nucleation is inefficient if the monomer has a different structural preference from the seed fibril (Brännström et al., 2018; Thacker et al., 2020).

Based on these existing data, it is too early to draw a final conclusion whether or not secondary nucleation can play a role in the propagation of strain homogeneity and in diseased organisms. Perhaps the physico-chemical environment *in vivo* allows only a limited number of strains to form *de novo*, and hence faithful strain transmission is not required in order to maintain strain homogeneity. There is, however, recent evidence that points toward the possibility that in cases where strain propagation is observed, most notably the mammalian prions,

fragmentation could be the mechanism responsible for this propagation (Meisl et al., 2021). More research is needed to establish the degree of strain homogeneity in additional *in vivo* settings and to investigate the strain propagation of secondary nucleation for additional proteins and solution conditions that mimic *in vivo* conditions as closely as possible. The observation that only a fraction of the oligomers generated by secondary nucleation ultimately converts into fibrils (Michaels et al., 2020) also suggest the possibility that the roles of secondary nucleation in the generation of toxic species and in the overall propagation of the pathology could be de-coupled to some extent.

OUTLOOK

We believe that the future of this line of research lies in the combination of various cross-seeding schemes, between fibrils of the same sequence formed under different conditions, as well as of different sequences under the same conditions, with high resolution cryo-EM. This combination of methods will ultimately reveal exactly how fibril elongation is able to propagate structural information, and whether in secondary nucleation the properties of the newly generated fibrils are solely defined by the solution conditions.

AUTHOR CONTRIBUTIONS

AB conceived the study. AB and SH wrote the manuscript. AP contributed to the initial draft of the manuscript and commented on the final manuscript. All authors contributed to the article and approved the submitted version.

ACKNOWLEDGMENTS

AB thanks the Novo Nordisk Foundation for funding (NNFSA170028392).

REFERENCES

Annamalai, K., Gührs, K.-H., Koehler, R., Schmidt, M., Michel, H., and Loos, C. (2016). Polymorphism of Amyloid Fibrils In Vivo. *Angew. Chem. Int. Ed. Engl.* 55, 4822–5.

Arai, M., Sugase, K., Dyson, H. J., and Wright, P. E. (2015). Conformational propensities of intrinsically disordered proteins influence the mechanism of binding and folding. *Proc. Natl. Acad. Sci. U. S. A.* 112, 9614–9. doi: 10.1073/pnas.1512799112

Bousset, L., Pieri, L., Ruiz-Arlandis, G., Gath, J., Jensen, P. H., Habenstein, B., et al. (2013). Structural and functional characterization of two alpha-synuclein strains. *Nat. Commun.* 4:2575.

Braak, H., and Braak, E. (1991). Neuropathological stageing of Alzheimer-related changes. *Acta Neuropathol.* 82, 239–59. doi: 10.1007/bf00308809

Brännström, K., Islam, T., Gharibyan, A. L., Iakovleva, I., Nilsson, L., Lee, C. C., et al. (2018). The Properties of Amyloid-β Fibrils Are Determined by Their Path of Formation. 430, 1940–1949. doi: 10.1016/j.jmb.2018.05.001

Brettschneider, J., Tredici, K. D., Lee, V. M.-Y., and Trojanowski, J. Q. (2015). spreading of pathology in neurodegenerative diseases: a focus on human studies. *Nat. Rev. Neurosci.* 16, 109–20. doi: 10.1038/nrn3887

Buell, A. K. (2017). The Nucleation of Protein Aggregates - From Crystals to Amyloid Fibrils. *Int. Rev. Cell Mol. Biol.* 329, 187–226. doi: 10.1016/bs.ircmb.2016.08.014

Buell, A. K. (2019). The growth of amyloid fibrils: rates and mechanisms. *Biochem. J.* 476, 2677–2703. doi: 10.1042/bcj20160868

Buell, A. K., Galvagnion, C., Gaspar, R., Sparr, E., Vendruscolo, M., Knowles, T. P. J., et al. (2014). Solution conditions determine the relative importance of nucleation and growth processes in α-synuclein aggregation. *Proc. Natl. Acad. Sci. U. S. A.* 111, 7671–6. doi: 10.1073/pnas.1315346111

Campioni, S., Carret, G., Jordens, S., Nicoud, L., Mezzenga, R., and Riek, R. (2014). The presence of an air-water interface affects formation and elongation of α-synuclein fibrils. *Am. J. Chem. Soc.* 136, 2866–75. doi: 10.1021/ja412105t

Cendrowska, U., Silva, P. J., Ait-Bouziad, N., Müller, M., Guven, Z. P., Vieweg, S., et al. (2020). unraveling the complexity of amyloid polymorphism using gold nanoparticles and cryo-EM. *Proc. Natl. Acad. Sci.U. S. A.* 117, 6866–6874. doi: 10.1073/pnas.1916176117

Cohen, S. I. A., Cukalevski, R., Michaels, T. C. T., Šarić, A., Törnquist, M., Vendruscolo, M., et al. (2018). Distinct thermodynamic signatures of oligomer generation in the aggregation of the amyloid-β peptide. *Nat. Chem.* 10, 523–531. doi: 10.1038/s41557-018-0023-x

Cohen, S. I. A., Linse, S., Luheshi, L. M., Hellstrand, E., White, D. A., Rajah, L., et al. (2013). Proliferation of amyloid-β42 aggregates occurs through a secondary nucleation mechanism. *Proc. Natl. Acad. Sci. U. S. A.* 110, 9758–63. doi: 10.1073/pnas.1218402110

Dinkel, P. D., Siddiqua, A., Huynh, H., Shah, M., and Margittai, M. (2011). Variations in filament conformation dictate seeding barrier between three- and four-repeat tau. *Biochemistry* 50, 4330–6. doi: 10.1021/bi2004685

Dzwolak, W., Jansen, R., Smirnovas, V., Loksztejn, A., Porowski, S., and Winter, R. (2005). Template-Controlled conformational patterns of insulin fibrillar self-assembly reflect history of solvation of the amyloid nuclei. *Phys. Chem. Chem. Phys.* 7, 1349–1351. doi: 10.1039/b502255j

Dzwolak, W., Smirnovas, V., Jansen, R., and Winter, R. (2004). Insulin forms amyloid in a strain-dependent manner: an ft-ir spectroscopic study. *Protein Sci.* 13, 1927–32. doi: 10.1110/ps.03607204

Dzwolak, W., Surmacz-Chwedoruk, W., and Babenko, V. (2013). Conformational memory effect reverses chirality of vortex-induced insulin amyloid superstructures. *Langmuir* 29, 365–70. doi: 10.1021/la304374q

Ferkinghoff-Borg, J., Fonslet, J., Andersen, C. B., Krishna, S., Pigolotti, S., and Yagi, H. (2010). Stop-and-go kinetics in amyloid fibrillation. *Phys. Rev. E Stat. Nonlin. Soft Matter Phys.* 82:010901.

Fitzpatrick, A. W. P., Falcon, B., He, S., Murzin, A. G., Murshudov, G., Garringer, H. J., et al. (2017). Cryo-EM structures of tau filaments from Alzheimer's Disease. *Nature* 547, 185–190.

Foderà, V., Librizzi, F., Groenning, M., van, M., de, Weert, and Leone, M. (2008). Secondary nucleation and accessible surface in insulin amyloid fibril formation. *Phys. J. Chem. B.* 112, 3853–8. doi: 10.1021/jp710131u

Fränzl, M., Thalheim, T., Adler, J., Huster, D., Posseckardt, J., Mertig, M., et al. (2019). Thermophoretic trap for single amyloid fibril and protein aggregation studies. *Nat. Methods* 16, 611–614. doi: 10.1038/s41592-019-0451-6

Frost, B., Ollesch, J., Wille, H., and Diamond, M. I. (2009). Conformational diversity of wild-type tau fibrils specified by templated conformation change. *J. Biol. Chem.* 284, 3546–51. doi: 10.1074/jbc.m805627200

Galvagnion, C., Buell, A. K., Meisl, G., Michaels, T. C. T., Vendruscolo, M., Knowles, T. P. J., et al. (2015). Lipid vesicles trigger α-synuclein aggregation by stimulating primary nucleation. *Nat. Chem. Biol.* 11, 229–34. doi: 10.1038/nchembio.1750

Gremer, L., Schölzel, D., Schenk, C., Reinartz, E., Labahn, J., Ravelli, R. B. G., et al. (2017). Fibril Structure of Amyloid-ß(1-42) by Cryoelectron Microscopy. *Science* 358, 116–119.

Guerrero-Ferreira, R., Taylor, N. M., Mona, D., Ringler, P., Lauer, M. E., Riek, R., et al. (2018). Cryo-EM structure of alpha-synuclein fibrils. *ELife* 7:e36402.

Jia, Z., Schmit, J. D., and Chen, J. (2020). Amyloid assembly is dominated by misregistered kinetic traps on an unbiased energy landscape. *Proc. Natl. Acad. Sci. U. S. A.* 117, 10322–10328. doi: 10.1073/pnas.1911153117

Jones, E. M., and Surewicz, W. K. (2005). Fibril conformation as the basis of species- and strain-dependent seeding specificity of mammalian prion amyloids. *Cell* 121, 63–72. doi: 10.1016/j.cell.2005.01.034

Kari, J., Olsen, J. P., Jensen, K., Badino, S. F., Krogh, K. B. R. M., Borch, K., et al. (2018). Sabatier Principle for Interfacial (Heterogeneous) Enzyme Catalysis. *ACS Catal.* 8, 11966–11972. doi: 10.1021/acscatal.8b03547

Knowles, T. P. J., Vendruscolo, M., and Dobson, C. M. (2014). The amyloid state and its association with protein misfolding diseases. *Nat. Rev. Mol. Cell Biol.* 15, 384–96. doi: 10.1038/nrm3810

Kollmer, M., Close, W., Funk, L., Rasmussen, J., Bsoul, A., Schierhorn, A., et al. (2019). Cryo-EM structure and polymorphism of aβ amyloid fibrils purified from Alzheimer's brain tissue. *Nat. Commun.* 10:4760.

Koloteva-Levine, N., Marchante, R., Purton, T. J., Hiscock, J. R., Tuite, M. F., and Xue, W. F. (2020). Amyloid particles facilitate surface-catalyzed cross-seeding by acting as promiscuous nanoparticles. *BioRxiv* [preprint]. doi: 10.1101/2020.09.01.278481

Li, B., Ge, P., Murray, K. A., Sheth, P., Zhang, M., Nair, G., et al. (2018). Cryo-EM of full-length α-synuclein reveals fibril polymorphs with a common structural kernel. *Nat. Commun.* 9:3609.

Linse, S. (2017). Monomer-dependent secondary nucleation in amyloid formation. *Biophys. Rev.* 9, 329–338. doi: 10.1007/s12551-017-0289-z

Lundqvist, M., Rodriguez, D., Camargo, C., Bernfur, K., Chia, S., and Linse, S. (2021). Expression, purification and characterisation of large quantities of recombinant human IAPP for mechanistic studies. *Biophys. Chem.* 269:106511. doi: 10.1016/j.bpc.2020.106511

Meisl, G., Kurt, T., Condado-Morales, I., Bett, C., Sorce, S., and Nuvolone, M. (2021). Scaling analysis reveals the mechanism and rates of prion replication in vivo. *Nat. Struct. Mol. Biol.* doi: 10.1038/s41594-021-00565-x [Epub ahead of print].

Michaels, T. C. T., Šarić, A., Curk, S., Bernfur, K., Arosio, P., Meisl, G., et al. (2020). Dynamics of oligomer populations formed during the aggregation of Alzheimer's Aβ42 Peptide. *Nat. Chem.* 12, 445–451. doi: 10.1038/s41557-020-0452-1

Michaels, T. C. T., Weber, C. A., and Mahadevan, L. (2019). Optimal Control Strategies for Inhibition of Protein Aggregation. *Proc. Natl. Acad. Sci. U. S. A.* 116, 14593–14598. doi: 10.1073/pnas.1904090116

Pedersen, J. S., Dikov, D., Flink, J. L., Hjuler, H. A., Christiansen, G., and Otzen, D. E. (2006). The changing face of glucagon fibrillation: structural polymorphism and conformational imprinting. *J. Mol. Biol.* 355, 501–23. doi: 10.1016/j.jmb.2005.09.100

Peduzzo, A., Linse, S., and Buell, A. K. (2020). The Properties of α-Synuclein Secondary Nuclei Are Dominated by the Solution Conditions Rather than the Seed Fibril Strain. *ACS Chem. Neurosci.* 11, 909–918. doi: 10.1021/acschemneuro.9b00594

Petkova, A. T., Leapman, R. D., Guo, Z., Yau, W. M., Mattson, M. P., and Tycko, R. (2005). Self-Propagating, Molecular-Level Polymorphism in Alzheimer's ß-Amyloid Fibrils. *Science* 307, 262–5. doi: 10.1126/science.1105850

Radamaker, L., Lin, Y.-H., Annamalai, K., Huhn, S., Hegenbart, U., Schönland, S. O., et al. (2019). Cryo-em structure of a light chain-derived amyloid fibril from a patient with systemic AL amyloidosis. *Nat. Commun.* 10:1103.

Röder, C., Vettore, N., Mangels, L. N., Gremer, L., Ravelli, R. B. G., Willbold, D., et al. (2019). Atomic structure of pi3-kinase sh3 amyloid fibrils by cryo-electron microscopy. *Nat. Commun.* 10:3754.

Ruschak, A. M., and Miranker, A. D. (2007). Fiber-dependent amyloid formation as catalysis of an existing reaction pathway. *Proc. Natl. Acad. Sci. U. S. A.* 104, 12341–12346. doi: 10.1073/pnas.0703306104

Saá, P., Castilla, J., and Soto, C. (2006). Ultra-efficient replication of infectious prions by automated protein misfolding cyclic amplification. *J. Biol. Chem.* 281, 35245–52. doi: 10.1074/jbc.m603964200

Saijo, E., Groveman, B. R., Kraus, A., Metrick, M., Orrù, C. D., Hughson, A. G., et al. (2019). Ultrasensitive RT-QuIC Seed Amplification Assays for Disease-Associated Tau, α-Synuclein, and Prion Aggregates. *Methods Mol. Biol.* 1873, 19–37. doi: 10.1007/978-1-4939-8820-4_2

Sakalauskas, A., Ziaunys, M., and Smirnovas, V. (2019). Concentration-dependent polymorphism of insulin amyloid fibrils. *PeerJ* 7:e8208. doi: 10.7717/peerj.8208

Šarić, A., Buell, A. K., Meisl, G., Michaels, T. C. T., Dobson, C. M., Linse, S., et al. (2016). Physical determinants of the self-replication of protein fibrils. *Nat. Phys.* 12, 874–880. doi: 10.1038/nphys3828

Scheidt, T., Łapińska, U., Kumita, J. R., Whiten, D. R., Klenerman, D., Wilson, M. R., et al. (2019). Secondary nucleation and elongation occur at different sites on Alzheimer's amyloid-β aggregates. *Sci. Adv.* 5:eaau3112. doi: 10.1126/sciadv.aau3112

Schweighauser, M., Shi, Y., Tarutani, A., Kametani, F., Murzin, A. G., Ghetti, B., et al. (2020). Structures of α-synuclein filaments from multiple system atrophy. *Nature* 585, 464–469.

Smith, J. F., Knowles, T. P. J., Dobson, C. M., MacPhee, C. E., and Welland, M. E. (2006). Characterization of the nanoscale properties of individual amyloid fibrils. *Proc. Natl. Acad. Sci. U. S. A.* 103, 15806–15811. doi: 10.1073/pnas.0604035103

Sneideris, T., Darguzis, D., Botyriute, A., Grigaliunas, M., Winter, R., and Smirnovas, V. (2015a). PH-Driven Polymorphism of Insulin Amyloid-Like Fibrils. *PLoS One* 10:e0136602. doi: 10.1371/journal.pone.0136602

Sneideris, T., Milto, K., and Smirnovas, V. (2015b). Polymorphism of amyloid-like fibrils can be defined by the concentration of seeds. *PeerJ* 3:e1207. doi: 10.7717/peerj.1207

Surmacz-Chwedoruk, W., Babenko, V., and Dzwolak, W. (2014). Master and slave relationship between two types of self-propagating insulin amyloid fibrils. *J. Phys. Chem. B* 118, 13582–9. doi: 10.1021/jp510980b

Tanaka, M., Chien, P., Yonekura, K., and Weissman, J. S. (2005). Mechanism of cross-species prion transmission: an infectious conformation compatible with two highly divergent yeast prion proteins. *Cell* 121, 49–62. doi: 10.1016/j.cell.2005.03.008

Thacker, D., Sanagavarapu, K., Frohm, B., Meisl, G., Knowles, T. P. J., and Linse, S. (2020). The role of fibril structure and surface hydrophobicity in secondary nucleation of amyloid fibrils. *Proc. Natl. Acad. Sci. U. S. A.* 117, 25272–25283. doi: 10.1073/pnas.2002956117

Toyama, B. H., Kelly, M. J. S., Gross, J. D., and Weissman, J. S. (2007). The structural basis of yeast prion strain variants. *Nature* 449, 233–7. doi: 10.1038/nature06108

Vaneyck, J., Segers-Nolten, I., Broersen, K., and Claessens, M. M. A. E. (2021). Cross-seeding of alpha-synuclein aggregation by amyloid fibrils of food proteins. *J. Biol. Chem.* 296:100358. doi: 10.1016/j.jbc.2021.100358

Vettore, N., and Buell, A. K. (2019). Thermodynamics of amyloid fibril formation from chemical depolymerization. *Phys. Chem. Chem. Phys.* 21, 26184–26194.

Xue, W.-F., and Radford, S. E. (2013). An imaging and systems modeling approach to fibril breakage enables prediction of amyloid behavior. *Biophys. J.* 105, 2811–9.

Yamaguchi, K. -I, Takahashi, S., Kawai, T., Naiki, H., and Goto, Y. (2005). Seeding-dependent propagation and maturation of amyloid fibril conformation. *J. Mo. Biol.* 352, 952–60.

Conflict of Interest: The authors declare that the research was conducted in the absence of any commercial or financial relationships that could be construed as a potential conflict of interest.

frontiers in Neuroscience

BRIEF RESEARCH REPORT
published: 25 May 2021
doi: 10.3389/fnins.2021.643115

Differential Effects of the Six Human TAU Isoforms: Somatic Retention of 2N-TAU and Increased Microtubule Number Induced by 4R-TAU

Sarah Bachmann[1,2], *Michael Bell*[1,2], *Jennifer Klimek*[1,2] *and Hans Zempel*[1,2]*

[1] *Institute of Human Genetics, Faculty of Medicine and University Hospital Cologne, University of Cologne, Cologne, Germany,* [2] *Center for Molecular Medicine Cologne (CMMC), Faculty of Medicine and University Hospital Cologne, University of Cologne, Cologne, Germany*

In the adult human brain, six isoforms of the microtubule-associated protein TAU are expressed, which result from alternative splicing of exons 2, 3, and 10 of the *MAPT* gene. These isoforms differ in the number of N-terminal inserts (0N, 1N, 2N) and C-terminal repeat domains (3R or 4R) and are differentially expressed depending on the brain region and developmental stage. Although all TAU isoforms can aggregate and form neurofibrillary tangles, some tauopathies, such as Pick's disease and progressive supranuclear palsy, are characterized by the accumulation of specific TAU isoforms. The influence of the individual TAU isoforms in a cellular context, however, is understudied. In this report, we investigated the subcellular localization of the human-specific TAU isoforms in primary mouse neurons and analyzed TAU isoform-specific effects on cell area and microtubule dynamics in human SH-SY5Y neuroblastoma cells. Our results show that 2N-TAU isoforms are particularly retained from axonal sorting and that axonal enrichment is independent of the number of repeat domains, but that the additional repeat domain of 4R-TAU isoforms results in a general reduction of cell size and an increase of microtubule counts in cells expressing these specific isoforms. Our study points out that individual TAU isoforms may influence microtubule dynamics differentially both by different sorting patterns and by direct effects on microtubule dynamics.

Keywords: TAU, MAPT, microtubule-associated proteins, microtubule dynamics, primary neuron cell culture, SH-SY5Y cell line, axonal targeting, somatodendritic localization

OPEN ACCESS

Edited by:
Cláudio M. Gomes, University of Lisbon, Portugal

Reviewed by:
Guy Lippens, Institut Biotechnologique de Toulouse (INSA), France
Ioannis Sotiropoulos, University of Minho, Portugal

***Correspondence:**
Hans Zempel
hans.zempel@uk-koeln.de

Specialty section:
This article was submitted to Neurodegeneration, a section of the journal Frontiers in Neuroscience

Received: *17 December 2020*
Accepted: *16 April 2021*
Published: *25 May 2021*

Citation:
Bachmann S, Bell M, Klimek J and Zempel H (2021) Differential Effects of the Six Human TAU Isoforms: Somatic Retention of 2N-TAU and Increased Microtubule Number Induced by 4R-TAU. Front. Neurosci. 15:643115. doi: 10.3389/fnins.2021.643115

INTRODUCTION

The human microtubule-associated protein TAU is encoded by the *MAPT* gene on chromosome 17. Expression of *MAPT* results in six major TAU isoforms in the adult human central nervous system and two isoforms in the peripheral nervous system (Goedert et al., 1989, 1992; Andreadis et al., 1992; Couchie et al., 1992). The brain-specific isoforms vary in the number of N-terminal inserts (0N, 1N, or 2N) and C-terminal repeat domains (3R or 4R) due to alternative splicing of exons 2, 3, and 10, resulting in sizes between 48 kDa (0N3R) and 67 kDa (2N4R) of the corresponding proteins (Goedert et al., 1989; **Figure 1A**). TAU isoform expression is directly linked to brain development: During neurogenesis, only the shortest TAU isoform, 0N3R, is expressed, whereas in the adult brain, all six isoforms are present with roughly equal amounts of 3R and 4R isoforms

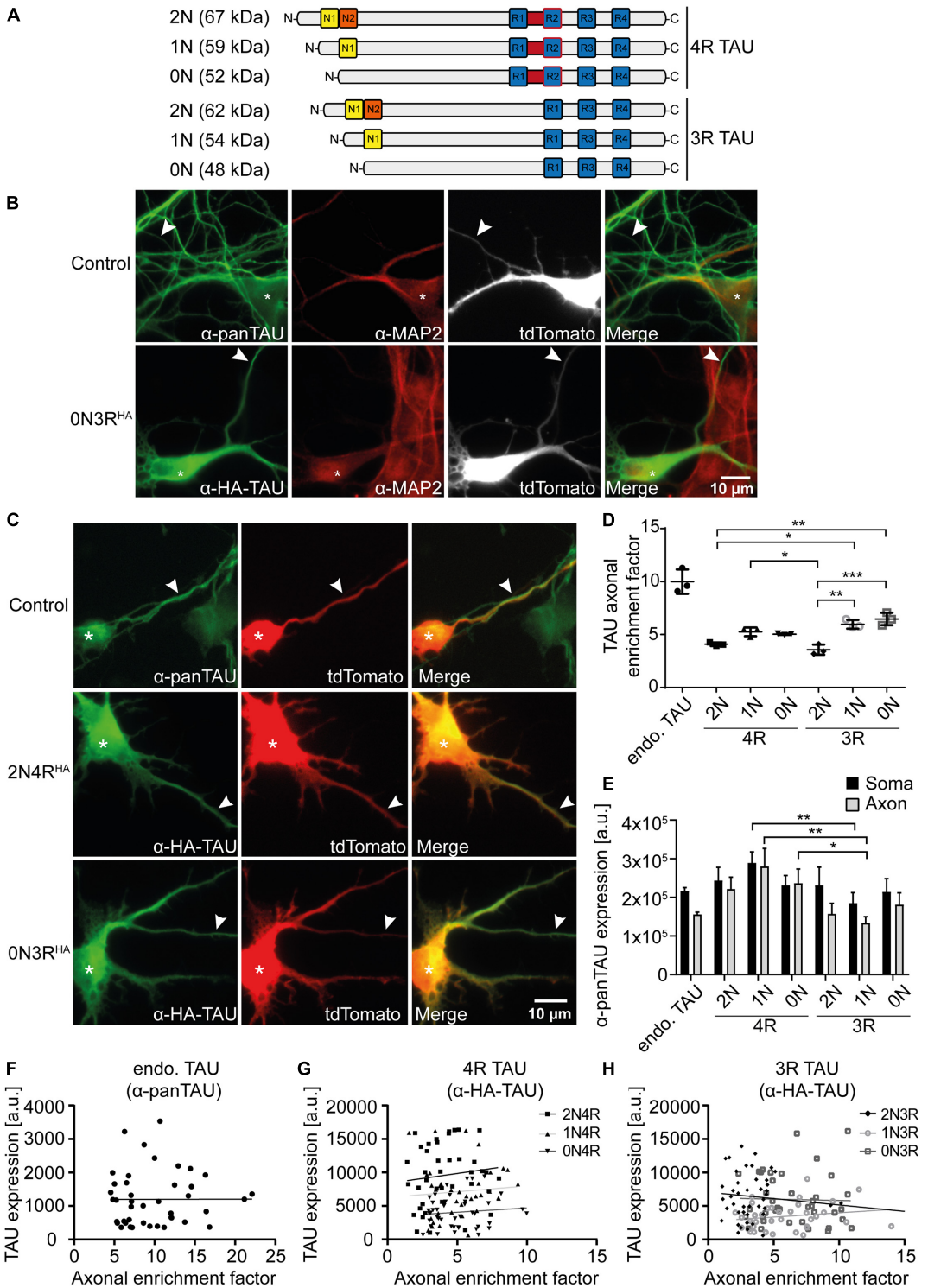

FIGURE 1 | 2N-containing TAU^{HA} isoforms are less efficiently sorted into the axon in mouse primary neurons. HA-tagged TAU isoforms (0N, 1N, 2N, and 3R or 4R) and tdTomato as a volume marker were co-transfected into mouse primary neurons (DIV4) and expressed for two days. **(A)** Schematic overview of the six TAU isoforms expressed in human brains and their estimated sizes in kDa. N1, N2 = N-terminal inserts; R1–R4 = C-terminal repeat domains. **(B)** Representative images of mouse primary neurons (DIV6) transfected with tdTomato (Ctrl.) or co-transfected with tdTomato and 0N3R-TAU, respectively. Neurons were stained with α-pan-TAU (for endogenous TAU in control) or α-HA antibody (for transfected TAU^{HA}) and α-MAP2 to distinguish axons and dendrites. Arrowheads indicate axons, asterisks indicate cell bodies. **(C)** Representative images of mouse primary neurons (DIV6) transfected with tdTomato (Ctrl.) or co-transfected with tdTomato and 2N4R-TAU^{HA} and 0N3R-TAU^{HA}, respectively. Neurons were stained with α-Tau (for control) or α-HA antibody to analyze axonal enrichment of transfected or

(Continued)

FIGURE 1 | Continued
endogenous TAU. Arrowheads indicate axons, asterisks indicate cell bodies. **(D)** Axonal enrichment of TAU was calculated from soma-to-axon ratio of TAU fluorescence intensity and normalized to soma-to-axon ratio of the tdTomato signal. An axonal enrichment of one is considered as a random distribution. $N = 3$, at least 10 cells were analyzed per condition. Error bars represent SEM. Shapiro–Wilk test was performed to test for normal distribution of data; statistical analysis was performed by one-way ANOVA with Tukey's test for correction of multiple comparisons. Statistical significance: $^{*}p \leq 0.05$; $^{**}p \leq 0.01$; $^{***}p \leq 0.001$. **(E)** Comparison of pan-TAU expression in axon and soma of untransfected neurons (endo.TAU) and TAU^{HA} isoform-expressing neurons. Error bars represent SEM. Shapiro–Wilk test was performed to test for normal distribution of data; statistical analysis was performed by Kruskal–Wallis test with Dunn's correction for multiple comparisons. Statistical significance: $^{*}p \leq 0.05$; $^{**}p \leq 0.01$. **(F–H)** Linear regression of somatic TAU expression and axonal enrichment. Linear regression was performed for **(F)** untransfected neurons (endo. TAU), **(G)** 4R isoform-expressing neurons, and **(H)** 3R isoform-expressing neurons. No significant correlation of TAU expression levels and axonal enrichment was observed for all experimental groups.

(Goedert et al., 1989; Trabzuni et al., 2012). Splicing of TAU is also species-dependent, e.g., TAU isoform expression in rodents shifts from 0N3R during brain maturation to only 4R isoforms in adults (McMillan et al., 2008; Bullmann et al., 2009). Accumulation of TAU in neurofibrillary tangles (NFTs) is a hallmark of many neurodegenerative diseases, named tauopathies. All isoforms are potent to form NFTs under pathological conditions; causes can be mutations in *MAPT* affecting splicing or function of TAU, or mislocalization of TAU into the somatodendritic compartment upon cellular stress (reviewed in Arendt et al., 2016). Tauopathies can be classified *via* the isoforms that accumulate in NFTs: While TAU tangles mainly consist of 3R-TAU isoforms, e.g., in Pick's disease (PiD) and 4R-TAU in progressive supranuclear palsy (PSP), both 3R- and 4R-TAU isoforms are present in NFTs of Alzheimer's disease patients (Goedert et al., 1995; Buee and Delacourte, 1999; Arai et al., 2003). During brain development and especially during neuronal polarization, TAU becomes efficiently sorted into the axon (Mandell and Banker, 1995). In the adult human brain, TAU is mainly localized in the axon; however, a small fraction can also be observed in the somatodendritic compartment and in the nucleus (Binder et al., 1985; Rady et al., 1995; Tashiro et al., 1997). The subcellular distribution of TAU seems to be isoform-specific, e.g., 2N isoforms show a higher propensity for a somatodendritic localization than other variants (Zempel et al., 2017a). Axonal targeting of TAU is thought to be mediated by a variety of processes, such as the presence of a TAU diffusion barrier (TDB) at the axon initial segment (AIS), which prevents retrograde diffusion of TAU (Li et al., 2011; Zempel et al., 2017a). Furthermore, microtubule-binding affinity of TAU might be higher in the axon, likely accomplished by the presence or absence of posttranslational modifications (PTMs), such as phosphorylation and acetylation (Evans et al., 2000; Kishi et al., 2005; Tsushima et al., 2015). TAU interactions are also important for proper sorting of TAU., e.g., interaction with the calcium-regulated plasma membrane-binding protein Annexin A2 was shown to link microtubules and the membrane of the growth cone, thereby trapping TAU at the presynaptic membrane (Gauthier-Kemper et al., 2011). Through its interaction with microtubules, TAU supports axonal differentiation, morphogenesis, outgrowth, transport, and neuronal plasticity (Esmaeli-Azad et al., 1994; Kempf et al., 1996; Takei et al., 2000). *In vitro* studies already described a reduced microtubule-binding affinity and assembly for 3R-TAU isoforms (Goedert and Jakes, 1990; Goode et al., 2000; Panda et al., 2003), which is in line with the fact that the C-terminal repeat domains together with the proline-rich linker domain mediate microtubule binding (Goode et al., 1997). If and how the different TAU isoforms alter microtubule dynamics a *in vivo* is still unclear and might also depend on the differential subcellular localization of the isoforms. In this study, we address these questions by using primary mouse neurons and SH-SY5Y human neuroblastoma cells as neuronal model systems. Our results show that human TAU isoforms differ in their subcellular localization and that especially 2N-TAU isoforms are less axonally enriched than shorter isoforms. In addition, we show an isoform-specific effect on cell size and microtubule number: Expression of 4R-TAU isoforms, for example, results in smaller cells and increased microtubule counts. Microtubule dynamics, such as microtubule stability, run length, and growth rate, are not altered upon expression of different TAU isoforms in undifferentiated SH-SY5Y cells. We show here that individual TAU isoforms may influence microtubule dynamics differentially both by different sorting patterns as well as by direct effects on microtubule dynamics in a non-disease background.

METHODS

Cell Culture

SH-SY5Y cells were cultured in DMEM/F12, GlutaMAX [Thermo Fisher Scientific (TFS)] supplemented with 10% fetal bovine serum (FBS, Biochrom AG), and 1 × antibiotic/antimycotic solution (TFS) in a humidified incubator at 37°C, 5% CO_2.

Primary mouse neurons were isolated and cultured as described before (Zempel and Mandelkow, 2017) with slight modifications. In brief, brains of FVB/N mouse embryos were dissected at embryonic day 13.5. Brainstem and meninges were removed and the whole cortex was digested with 1 × trypsin (PAN-Biotech). The cell suspension was diluted in prewarmed (37°C) neuronal plating medium [Neurobasal media (TFS), 1% FBS, 1 × antibiotic/antimycotic solution (TFS), 1 × NS21 (PAN-Biotech)] seeded onto coated plates, and cultivated in a humidified incubator at 37°C, 5% CO_2. Four days after plating, the medium was doubled with neuronal maintenance media [Neurobasal media (TFS), 1 × antibiotic/antimycotic solution (TFS), 1 × NS21 (PAN-Biotech)], and cells were treated with 0.5 μg/ml AraC (Sigma-Aldrich).

Microtubule Dynamics

SH-SY5Y cells were co-transfected with expression plasmids containing Dendra2c-TAU (TAU^{D2}) isoforms and

tdTomato-N1-EB3 by using Lipofectamine2000 (TFS) according to the manufacturer's protocol. Control cells were transfected with tdTomato-N1-EB3 and an empty Dendra2c plasmid. Only cells showing both Dendra2c and tdTomato signal were used for analysis. Two days after transfection, cells were transferred into a live-cell imaging chamber (ALA Scientific) and EB3 comets of a single cell were imaged for 120 s (1 frame per second) with a Leica DMi8 microscope (Leica). The original movie file was processed by ImageJ software (Schindelin et al., 2012; Schneider et al., 2012) as follows: An average minimum projection was calculated from all frames and subsequently subtracted from all. Afterwards, a threshold was set and microtubule dynamics were analyzed by ImageJ plugin TrackMate (Tinevez et al., 2017), using LoG detector with an estimated blob size of 2 px. The following parameters were examined: cell area (μm^2), microtubule number/μm^2, microtubule run length (μm), microtubule stability (s), and microtubule growth rate (μm/s). Data were filtered for quality $\geq$1.5, track start $>$0 s, and track end $<$120 s. All experiments were conducted in three replicates and at least five cells were analyzed per condition. Cell area was measured from at least 30 cells. Shapiro–Wilk test was performed to test for normal distribution of data; afterwards, statistical analysis was performed by either one-way ANOVA with correction for multiple comparisons (Tukey's test) for normally distributed data or Kruskal–Wallis test with Dunn's correction for multiple comparison of non-parametric data using GraphPad Prism software (v8.0.1). The statistical test performed is highlighted in the figure legends for each graph.

Cell Lysis and Western Blot Analysis

SH-SY5Y cells were lysed with RIPA buffer [50 mM HEPES pH 7.6, 150 mM NaCl, 1 mM EDTA, 1% Triton X-100, 0.1% sodium dodecyl sulfate, 0.5% sodium deoxycholate, 1 × cOmplete ULTRA EDTA-free protease inhibitor cocktail (Merck)]. Samples were diluted with SDS buffer and separated on 10% polyacrylamide gels. Proteins were transferred to PVDF membranes and blocked in 5% non-fat dry milk in TBS-T. Membranes were incubated with the primary antibody overnight at 4°C, washed with TBS-T, and incubated with the corresponding secondary HRP-coupled antibody for one hour at room temperature. The used antibodies are listed in **Table 1**. Luminescent signals were detected with ChemiDoc XRS + system (Bio-Rad).

Axonal Enrichment Factor and TAU Expression

To analyze TAU axonal enrichment, primary mouse neurons were transfected as described before with Lipofectamine2000 (TFS) (Zempel et al., 2017b). In brief, neurons were co-transfected with the corresponding N-terminally HA-tagged TAU (TAU^{HA}) isoform and tdTomato. After two days, neurons were fixed and stained for endogenous mouse Tau with a pan-TAU antibody, or HA for exogenous TAU^{HA} and MAP2 as described before (Zempel and Mandelkow, 2017), using antibodies listed in **Table 1**. After imaging on a fluorescence microscope (Axioscope 5, Zeiss), axonal sorting was analyzed by measuring mean fluorescence intensities (MFI) of tdTomato and TAU in the axon and soma. Axons were identified by the absence of MAP2 and the presence of TAU signal, branching pattern of ∼90°, a length of above 300 μm, and constant diameter. Axonal enrichment factor (AEF) was calculated as follows: $AEF = (MFI_{(TAU,Axon)}/MFI_{(TAU,Soma)})/(MFI_{(tdTom,Axon)}/MFI_{(tdTom,Soma)})$. The experiment was performed in three replicates and at least 10 cells were analyzed per condition. For the analysis of TAU expression, neurons were transfected with TAU^{HA} isoforms, fixed, and stained for TAU by using a pan-TAU antibody and HA-tagged TAU by using an anti-HA antibody (see **Table 1** for details). Expression was analyzed by measuring the MFI of pan-TAU in the soma and axon of untransfected and transfected cells.

Shapiro–Wilk test was performed to test for normal distribution of data; afterwards, statistical analysis was performed by either one-way ANOVA with correction for multiple comparisons (Tukey's test) for normally distributed data or Kruskal–Wallis test with Dunn's correction for multiple comparison of non-parametric data using GraphPad Prism software (v8.0.1). The statistical test performed is highlighted in the figure legends for each graph.

TABLE 1 | Antibodies used in this study.

Antibody	Company	Cat. no.	Application	Dilution
Primary antibodies				
Rabbit polyclonal anti-TAU (K9JA)	Dako	A0024	WB / ICC	1:10,000 / 1:1,000
Chicken polyclonal anti-MAP2	Abcam	ab5392	ICC	1:2,000
Mouse monoclonal anti-HA (16B12)	Biolegend	901501	ICC	1:1,000
Mouse monoclonal anti-GAPDH (1D4)	Novus Biologicals	NB300-221	WB	1:2,000
Secondary antibodies				
Donkey anti-mouse IgG, Alexa Fluor 488	Thermo Fisher Scientific	A21202	ICC	1:1,000
Goat anti-chicken IgG, Alexa Fluor 647	Thermo Fisher Scientific	A21449	ICC	1:1,000
Donkey anti-rabbit IgG, Alexa Fluor 488	Thermo Fisher Scientific	A21206	ICC	1:1,000
Phalloidin, Alexa Fluor 568	Thermo Fisher Scientific	A12380	ICC	1:40
Goat anti-mouse IgG (H + L), HRP-linked	Dianova	115-035-003	WB	1:20,000
Goat anti-rabbit IgG, HRP-linked	Cell Signaling Technologies	7074	WB	1:200,000

Antibody List

The antibodies used for this study are listed in **Table 1**.

RESULTS

TAU Axonal Sorting Is Isoform-Specific and Independent of Expression Levels

TAU is considered an axonal protein in mature neurons (Binder et al., 1985). However, previous results indicate a difference in axonal enrichment of the six human TAU isoforms that were overexpressed as Dendra2c-tagged fusion proteins in primary rodent neurons (Zempel et al., 2017a). To further investigate TAU isoform axonal sorting and rule out the influence of a big protein tag (such as Dendra2c with approx. 26 kDa) on cellular localization, all six human TAU isoforms were fused to an HA-tag (TAU^{HA}) and co-transfected for two days with a volume marker (tdTomato) into primary mouse neurons aged for 7–9 days (DIV). One benefit of the HA-tag is the relatively small size, which leads to a size shift of the TAU isoforms of only 1.1 kDa (**Figure 1A**). Control neurons were transfected only with tdTomato as a volume marker, assuming an unbiased axodendritic distribution after two days of expression. To quantify axonal targeting of the different versions of TAU, we normalized the axonal presence of TAU against the unbiased distribution of tdTomato, expressed as the AEF (see *Methods* for details). To distinguish axons and dendrites, neurons were fixed and stained for endogenous mouse TAU or transfected human TAU^{HA} using an anti-HA antibody and the dendritic marker MAP2. Axons were identified by the absence of MAP2, the presence of TAU or HA signal, and further morphological criteria (see *Methods* for details; **Figure 1B**). Differences in axonal sorting of TAU were observed for the different TAU^{HA} isoforms (**Figures 1C,D**). For endogenous TAU, which mostly consists of 0N3R in prenatal rodent brains (McMillan et al., 2008; Bullmann et al., 2009), a strong axonal localization is visible from the immunofluorescence images, indicated by a strong TAU signal in the axon and only low levels in the soma and dendrites (AEF of ∼10, **Figures 1C,D**). Strong axonal enrichment was also observed in neurons expressing 0N3R-TAU^{HA}. In contrast, neurons expressing 2N4R-TAU^{HA} show lower levels of axonal TAU but still strong axonal targeting compared to tdTomato (**Figure 1C**). To compare the different TAU^{HA} isoforms quantitatively, axonal enrichment of TAU was calculated from soma-to-axon ratio of TAU fluorescence intensity and normalized to soma-to-axon ratio of the tdTomato signal (**Figure 1D**). Axonal enrichment of endogenous TAU was approximately 10-fold higher compared with tdTomato, while the human TAU^{HA} isoforms showed approximately 4- to 6-fold enrichment (**Figure 1D**). From all six transfected isoforms, 0N3R-TAU^{HA} showed the strongest axonal enrichment, which reaches approximately 65% of endogenous TAU. A relatively efficient (but still ∼40% less than endogenous TAU) axonal sorting could also be observed for 1N3R-TAU^{HA}. Of note, both 2N-TAU^{HA} isoforms showed the weakest axonal enrichment. Differences in TAU expression levels were assessed by measuring mean fluorescence intensities of the pan-TAU signal in the soma and axon (MFI) of neurons expressing only endogenous TAU (endo. TAU) or neurons co-expressing endogenous TAU with TAU^{HA} (**Figure 1E**). Comparison of expression rates of endogenous TAU with neurons expressing endogenous and TAU^{HA} revealed only slight overexpression rates for the different TAU isoforms (up to 0.5 times), both in the soma and axon, which were not significantly higher than in control cells (**Figure 1E**). This might indicate that either primary neurons downregulate endogenous TAU expression to prevent overexpression of TAU or that the amount of exogenously expressed TAU is small compared with endogenous TAU. To rule out that differential expression and overexpression of TAU isoforms influences cellular sorting mechanisms, we correlated somatic TAU expression levels of endogenous TAU and TAU^{HA} with the axonal enrichment of TAU (**Figures 1F–H**). No significant correlation was observed for any of the experimental groups, indicating that the expression levels likely do not impact TAU sorting. Taken together, our results implicate that the efficiency of axonal sorting of TAU is independent of TAU expression levels. Furthermore, the subcellular distribution of TAU seems to be isoform dependent and is influenced by the number of N-terminal inserts, since 2N4R- and 2N3R-TAU^{HA} showed the lowest axonal enrichment. No significant difference was observed between the other 3R- and 4R-expressing neurons, hinting towards a repeat-independent sorting mechanism of the isoforms.

Differential Effect of TAU Isoforms on Cell Size and Microtubule Number

One main function of TAU is its role in microtubule stability and spacing (Weingarten et al., 1975; Witman et al., 1976). The influence of individual TAU isoforms on microtubule dynamics, however, has not been addressed in living cells. To investigate TAU isoform-specific effects on microtubules, SH-SY5Y neuroblastoma cells were transfected with TAU^{D2} isoforms. The expression levels of TAU^{D2} were confirmed by Western blot analysis (**Figure 2A**). Of note, only low levels of endogenous TAU (∼55 kDa) were observed in control and transfected cells, which most likely corresponds to 0N3R-TAU that is mainly expressed by undifferentiated SH-SY5Y cells (**Figures 1A**, **2A**, long exposure) (reviewed in Bell and Zempel, 2020). Exogenously expressed TAU isoforms show a shift in size of approx. 26 kDa due to the fused D2-tag (**Figure 2A**). TAU^{D2} overexpression rate was assessed by comparing the amount of endogenous and exogenous TAU and considering a transfection efficiency of ∼15–20% in SH-SY5Y cells, which resulted in a ∼50-fold overexpression. Since differentiated SH-SY5Y cells show an increase of about 12-fold of endogenous TAU expression, overexpression of D2-tagged TAU isoforms was normalized to expression in differentiated SH-SY5Y cells, which results in approx. four times higher final expression of exogenously expressed TAU.

Since microtubules are essential components of the cytoskeleton, initial analysis of TAU isoform-specific effects focused on changes in cell size, which may hint at cytoskeletal alterations. Cell area was significantly (∼20%) smaller in cells overexpressing 4R-TAU^{D2} isoforms compared with

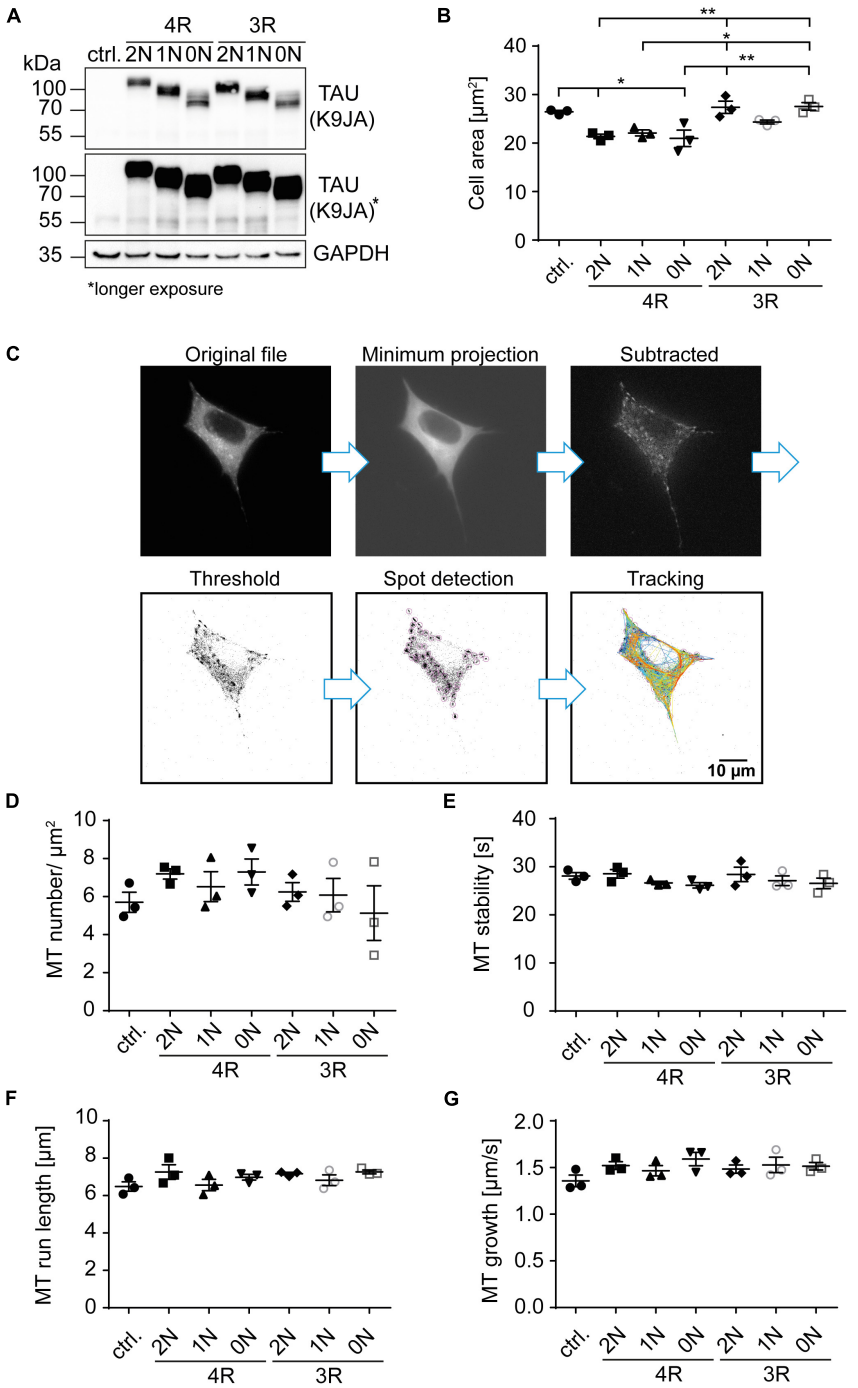

FIGURE 2 | 4R-TAU isoforms decrease cell size and increase microtubule counts in undifferentiated SH-SY5Y neuroblastoma cells. Expression of TAU^{D2} isoforms (0N, 1N, 2N, and 3R or 4R) in undifferentiated SH-SY5Y cells. **(A)** Western blot of SH-SY5Y cells transfected with the corresponding TAU^{D2} isoforms. Longer exposure of TAU signal shows negligible endogenous TAU expression (~55 kDa). GAPDH was used as a loading control. **(B)** Cell area was measured from SH-SY5Y cells, co-transfected with tdTomato-N1-EB3 and TAU^{D2}. Cell area was analyzed from at least 30 cells. Error bars represent SEM. Statistical analysis was performed by one-way ANOVA with Tukey's test for correction of multiple comparisons. Asterisks indicate statistical significance: $^{*}p \leq 0.05$; $^{**}p \leq 0.01$. **(C)** Image processing for input into TrackMate. Minimum projection was calculated from all frames and subtracted from all. Afterward, threshold was set, and microtubule dynamics were analyzed by TrackMate. **(D–G)** Microtubule dynamics of SH-SY5Y cells co-transfected with Dendra2c-tagged TAU isoforms (0N, 1N, 2N, and 3R or 4R) and tdTomato-N1-EB3. Growing microtubule plus-ends were monitored in living cells for 2 min (1 fps). The following parameters were examined: **(D)** microtubule number (MT number/μm^2) (normalized to corresponding cell area), **(E)** microtubule run length (μm), **(F)** microtubule stability (s), and **(G)** microtubule growth rate (μm/s). $N = 3$, at least five cells were analyzed per condition. Error bars represent SEM. Shapiro–Wilk test was performed to test for normal distribution of data; statistical analysis was performed by one-way ANOVA with Tukey's test for correction of multiple comparisons for **(D–F)**. Kruskal–Wallis test with Dunn's correction for multiple comparisons was performed for panel **(G)**.

control cells (**Figure 2B**). In addition, cells expressing 2N3R- and 0N3R-TAU^{D2} had a significantly greater cell area than 4R-expressing cells (∼20%), comparable with untransfected cells, while 1N3R only showed a trend towards increased cell size compared with the 4R-TAU^{D2} isoform-expressing cells (∼15% bigger cell size). To further investigate the role of TAU isoforms in microtubule dynamics, SH-SY5Y cells were co-transfected with the corresponding TAU^{D2} isoform and tdTomato-N1-EB3 (**Figures 2C–G**). EB3 binds the growing microtubule plus-ends and can be used in live-cell imaging to track microtubule assembly (Stepanova et al., 2003). Expression of TAU^{D2} was confirmed *via* the green fluorescence of the D2-tag in live-cell imaging. EB3 comets were recorded for 2 min (1 fps), images were processed as described in **Figure 2C**, and microtubule dynamics were analyzed afterward using TrackMate plugin for ImageJ (Tinevez et al., 2017). The overall number of microtubules was quantified and normalized to the corresponding cell area (**Figure 2D**). Microtubule count was slightly increased compared with the control cells (5.5 MTs/μm^2) in cells expressing 2N4R- and 0N4R-TAU^{D2} (7.2 and 7.3 MTs/μm^2, respectively). In contrast, 3R-TAU^{D2} isoforms showed no difference in microtubule counts compared with control cells, despite a slight trend towards a reduced number of microtubules for 0N3R. Comparing 3R- and 4R-TAU^{D2} isoforms showed that microtubule numbers were significantly decreased for 0N3R compared to 4R-TAU^{D2}-expressing cells (**Figure 2D**). To further investigate how microtubule counts might be affected by TAU^{D2} isoforms, microtubule stability, total microtubule run length, and microtubule growth rate (**Figures 2E–G**) were analyzed. We observed several tendencies that, however, did not reach statistical significance: 1N- and 0N-TAU^{D2} isoforms seem to cause a slight decrease in microtubule stability independent of the presence of the second N-terminal repeat (**Figure 2E**), and 2N4R-TAU^{D2} seems to increase microtubule run length (**Figure 2F**). Microtubule growth rate was slightly, but not significantly, increased for individual TAU isoform-overexpressing cells compared with control cells (**Figure 2G**), but it was significantly increased ($p < 0.0143$, unpaired *t*-test) when we compared all TAU isoform-expressing cells to control cells. All in all, the results indicate that TAU isoforms have a significant impact on cell size and show slight differences in microtubule counts and impact on microtubule growth rate, without significant differential effects on microtubule stability and run length in undifferentiated SH-SY5Y cells.

DISCUSSION

In this study, we show that human TAU isoforms can influence microtubule dynamics in a differential matter, through i) differential compartment-specific cellular distribution and ii) differential effect on cell size and, to lesser extent by influencing microtubule density and microtubule dynamics. Expressed TAU isoforms with an N-terminal HA-tag differ in their subcellular localization in mouse primary neurons already after two days of expression. 2N-TAU isoforms especially showed less axonal enrichment than shorter isoforms, which is in line with previous findings, demonstrating less axonal enrichment for Dendra2c-tagged 2N-TAU isoforms (Zempel et al., 2017a). The shortest human TAU isoform, 0N3R, showed the strongest axonal enrichment compared with the other isoforms. Axonal sorting of endogenous mouse TAU was also highly efficient. During this stage of maturation (E13.5), mouse primary neurons mainly express 0N3R-TAU (McMillan et al., 2008; Bullmann et al., 2009), which supports our results obtained in this study demonstrating efficient sorting of human 0N3R-TAU in primary neurons. In contrast, especially 2N-TAU isoforms poorly localized to the axon. Since 2N3R and 1N4R nearly have the same size, with 410 and 412 aa, respectively, this effect is rather dependent on the N-terminal inserts and is independent of the corresponding isoform size. No significant difference was observed between the other 3R and 4R isoform-expressing neurons, pointing towards a repeat-independent sorting mechanism of the isoforms. Nevertheless, the C-terminal half of TAU is essential for proper axonal sorting, as a TAU construct lacking the repeat domains accumulates in the soma and did not localize to the axon in SH-SY5Y-derived and primary mouse neurons (Bell et al., 2021). These observations indicate that microtubule-binding affinity mediated by the C-terminal repeat domains [which is increased for four-repeat TAU isoforms (Goode et al., 2000)] alone does not mediate axonal sorting. Axonal sorting of TAU isoforms might also be influenced by PTMs, such as phosphorylation and acetylation, which are known to affect microtubule affinity and spacing (Evans et al., 2000; Kishi et al., 2005; Tsushima et al., 2015). In addition, isoform-specific protein interactions might influence axonal targeting (Gauthier-Kemper et al., 2018); however, this has not been addressed in detail for the different isoforms. Of note, axonal sorting of endogenous mouse TAU is more efficient compared to all HA-tagged human TAU isoforms. To rule out a saturation effect of the sorting machinery, we correlated TAU expression levels among our experimental groups with the axonal enrichment and found no significant effect. These results indicate that axonal sorting is independent of TAU expression levels and did not result in saturation of the sorting machinery of primary neurons. Since we could not observe the expected strong overexpression levels for pan-TAU in transfected neurons compared with neurons only expressing endogenous TAU (as reported before, e.g., in Tashiro et al., 1997), exogenous expression of TAU^{HA} likely is rather minor, or results in downregulation of endogenous TAU expression, preventing detrimental effects of overexpression.

The differences observed in axonal sorting of TAU isoforms might also have methodological reasons: i) Expression time was relatively short in our study, and increasing it from two to four days might be beneficial for the axonal enrichment of exogenous TAU. ii) The HA-tag might impair efficient axonal targeting of endogenous TAU, as seen also for Dendra2c-tagged TAU (Zempel et al., 2017a), due to its molecular size or by interfering with critical TAU interactions. iii) Sorting of human TAU might be different from mouse TAU, which could have several reasons: Young primary neurons, aged roughly one week, mainly express 0N3R-TAU; mouse TAU in general is slightly shorter; and the protein lifetime might be different due to tagging

or changed protein interactions (Goedert et al., 1989; Kosik et al., 1989). In addition, the different TAU isoforms could influence each other and their sorting *in vivo*, while in this study, we analyzed the isoforms in an isolated approach. Overall, we show here that in polarized primary neurons, human TAU isoforms differ remarkably in their axonal sorting efficiencies (with 0N3R-TAU sorting ∼1.5 times better than the 2N-TAU isoforms), and that the somatic retention of 2N-TAU isoforms is repeat domain independent.

So far, no studies were conducted to investigate TAU isoform-specific effects on microtubule dynamics in a cellular context. We decided to use the well-established SH-SY5Y neuroblastoma cell line, which expresses only low levels of mainly 0N3R-TAU in the undifferentiated state (reviewed in Bell and Zempel, 2020) to investigate microtubule dynamics in dependence of the six different human TAU isoforms. 4R-TAU isoform-expressing cells showed a significant reduction in cell size (∼30%); however, microtubule numbers were slightly increased in these cells. These results go in line with *in vitro* studies showing an increased binding affinity and assembly of microtubules by 4R-TAU isoforms (Goedert and Jakes, 1990; Goode et al., 2000; Panda et al., 2003). Since cell size is affected in undifferentiated SH-SY5Y cells, there might be also an isoform-specific effect on neurite growth, which needs to be investigated in differentiated neuronal models. Microtubule dynamics were not significantly altered by the expression of individual TAU isoforms in our model system; however, there might be a compartment-specific effect visible in neurons, due to the differential localization of TAU isoforms demonstrated in the first part of this study. Possible compartment-specific effects might be caused by different PTMs, differences in microtubule-binding affinity, and different protein–protein interactions of TAU isoforms (Tashiro et al., 1997; Evans et al., 2000; Kishi et al., 2005; Tsushima et al., 2015). Of note, our results suggest that the N-terminal inserts play a major role in subcellular localization of TAU and, thus, may be important for the development or prevention of pathological processes, such as missorting of TAU into the somatodendritic compartment and subsequent synapse loss. This is in line with the observation that the presence of the H2 haplotype of the *MAPT* locus, resulting in a two times higher expression of exon 3 + transcripts (2N-TAU isoforms, respectively), has neuroprotective effects (Caffrey et al., 2006; Beevers et al., 2017). 2N-TAU isoforms were also shown to differ in their interactome from the other TAU isoforms, suggesting differences in the cellular functions of the TAU isoforms (Liu et al., 2016). While the generation and effects of the 3R- and 4R-TAU isoforms have been studied in detail, the splicing and behavior of the N-terminally different isoforms are understudied. Future studies with polarized cells, such as primary and iPSC-derived neurons, should aim to further characterize TAU isoforms regarding their impact on microtubule dynamics in different subcellular compartments, taking into account the differential sorting, impact on cell size, and microtubule number. In sum, we show that i) the efficiency of human TAU sorting into the axon is isoform dependent, with 2N isoforms being most retained in the somatodendritic compartment, and ii) 4R-TAU isoforms result in a general reduction of cell size and seem to increase microtubule counts. This points to isoform- and compartment-specific functions of TAU in neurons. Follow-up experiments are needed to clarify how the different TAU isoforms might influence cellular functions and if they contribute differentially to the pathological processes underlying AD and related tauopathies.

DATA AVAILABILITY STATEMENT

The original contributions presented in the study are included in the article/supplementary material, further inquiries can be directed to the corresponding author.

ETHICS STATEMENT

Primary mouse neuron culture generation was reviewed and approved by Carolin Debuschewitz, Animal Welfare Officer of the University of Cologne (according to §4 Tierschutzgesetz).

AUTHOR CONTRIBUTIONS

SB: study design, data acquisition, analysis, interpretation, and drafting of the manuscript. MB and JK: assistance in data acquisition and methodology development. MB: manuscript proofreading. HZ: project funding, providing of concept, study design, interpretation of data, and drafting of the manuscript. All authors contributed to the article and approved the submitted version.

FUNDING

This study was funded by Else-Kröner-Fresenius Stiftung, Köln Fortune (grant numbers: 467/2018 and 475/2020) and supported by a doctoral fellowship of the Studienstiftung des deutschen Volkes.

ACKNOWLEDGMENTS

We thank Prof. Dr. Rudolf Wiesner (Institute for Vegetative Physiology, University Hospital Cologne, Cologne, Germany) for providing SH-SY5Y cells. Live-cell imaging experiments were performed at CMMC microscopy facility (Cologne, Germany). Animals were provided by CMMC animal facility and CECAD *in vivo* research facility (both Cologne, Germany). We acknowledge support from Alzheimer Forschung Initiative e.V. for Open Access Publishing.

REFERENCES

Andreadis, A., Brown, W. M., and Kosik, K. S. (1992). Structure and novel exons of the human .tau. gene. *Biochemistry* 31, 10626–10633. doi: 10.1021/bi00158a027

Arai, T., Ikeda, K., Akiyama, H., Tsuchiya, K., Iritani, S., Ishiguro, K., et al. (2003). Different immunoreactivities of the microtubule-binding region of tau and its molecular basis in brains from patients with Alzheimer's disease, Pick's disease, progressive supranuclear palsy and corticobasal degeneration. *Acta Neuropathol.* 105, 489–498. doi: 10.1007/s00401-003-0671-8

Arendt, T., Stieler, J. T., and Holzer, M. (2016). Tau and tauopathies. *Brain Res. Bull.* 126, 238–292. doi: 10.1016/j.brainresbull.2016.08.018

Beevers, J. E., Lai, M. C., Collins, E., Booth, H. D. E., Zambon, F., Parkkinen, L., et al. (2017). MAPT Genetic Variation and Neuronal Maturity Alter Isoform Expression Affecting Axonal Transport in iPSC-Derived Dopamine Neurons. *Stem Cell Rep.* 9, 587–599. doi: 10.1016/j.stemcr.2017.06.005

Bell, M., Bachmann, S., Klimek, J., Langerscheidt, F., and Zempel, H. (2021). Axonal TAU sorting is independent of ANKG and TRIM46 enrichment at the AIS in SH-SY5Y-derived neurons. *Neuroscience* doi: 10.1016/j.neuroscience.2021.01.041

Bell, M., and Zempel, H. (2020). SH-SY5Y-derived Neurons: A Neuronal Model System for Investigating TAU Sorting Mechanisms and Neuronal Subtype-specific TAU Vulnerability. *Preprints* 2020:0203. doi: 10.20944/preprints202006.0203.v1

Binder, L. I., Frankfurter, A., and Rebhun, L. I. (1985). The distribution of tau in the mammalian central nervous system. *J. Cell Biol.* 101, 1371–1378. doi: 10.1083/jcb.101.4.1371

Buee, L., and Delacourte, A. (1999). Comparative biochemistry of tau in progressive supranuclear palsy, corticobasal degeneration, FTDP-17 and Pick's disease. *Brain Pathol.* 9, 681–693. doi: 10.1111/j.1750-3639.1999.tb00550.x

Bullmann, T., Holzer, M., Mori, H., and Arendt, T. (2009). Pattern of tau isoforms expression during development in vivo. *Int. J. Dev. Neurosci.* 2009:001. doi: 10.1016/j.ijdevneu.2009.06.001

Caffrey, T. M., Joachim, C., Paracchini, S., Esiri, M. M., and Wade-Martins, R. (2006). Haplotype-specific expression of exon 10 at the human MAPT locus. *Hum. Mol. Genet.* 15, 3529–3537. doi: 10.1093/hmg/ddl429

Couchie, D., Mavilia, C., Georgieff, I. S., Liem, R. K., Shelanski, M. L., and Nunez, J. (1992). Primary structure of high molecular weight tau present in the peripheral nervous system. *Proc. Natl. Acad. Sci.* 89, 4378–4381. doi: 10.1073/pnas.89.10.4378

Esmaeli-Azad, B., McCarty, J. H., and Feinstein, S. C. (1994). Sense and antisense transfection analysis of tau function: Tau influences net microtubule assembly, neurite outgrowth and neuritic stability. *J. Cell Sci.* 107, 869–79. doi: 10.1242/jcs.107.4.869

Evans, D. B., Rank, K. B., Bhattacharya, K., Thomsen, D. R., Gurney, M. E., and Sharma, S. K. (2000). Tau Phosphorylation at Serine 396 and Serine 404 by Human Recombinant Tau Protein Kinase II Inhibits Tau's Ability to Promote Microtubule Assembly. *J. Biol. Chem.* 275, 24977–24983. doi: 10.1074/jbc.M000808200

Gauthier-Kemper, A., Alonso, M. S., Sündermann, F., Niewidok, B., Fernandez, M. P., Bakota, L., et al. (2018). Annexins A2 and A6 interact with the extreme N terminus of tau and thereby contribute to tau's axonal localization. *J. Biol. Chem.* 2018:000490. doi: 10.1074/jbc.RA117.000490

Gauthier-Kemper, A., Weissmann, C., Golovyashkina, N., Sebö-Lemke, Z., Drewes, G., Gerke, V., et al. (2011). The frontotemporal dementia mutation R406W blocks tau's interaction with the membrane in an annexin A2-dependent manner. *J. Cell Biol.* 2011:201007161. doi: 10.1083/jcb.201007161

Goedert, M., and Jakes, R. (1990). Expression of separate isoforms of human tau protein: correlation with the tau pattern in brain and effects on tubulin polymerization. *EMBO J.* 9, 4225–4230. doi: 10.1002/j.1460-2075.1990.tb07870.x

Goedert, M., Spillantini, M. G., and Crowther, R. A. (1992). Cloning of a big tau microtubule-associated protein characteristic of the peripheral nervous system. *Proc. Natl. Acad. Sci.* 89, 1983–1987. doi: 10.1073/pnas.89.5.1983

Goedert, M., Spillantini, M. G., Jakes, R., Crowther, R. A., Vanmechelen, E., Probst, A., et al. (1995). Molecular dissection of the paired helical filament. *Neurobiol. Aging* 16, 325–334. doi: 10.1016/0197-4580(95)00017-9

Goedert, M., Spillantini, M. G., Jakes, R., Rutherford, D., and Crowther, R. A. (1989). Multiple isoforms of human microtubule-associated protein tau: sequences and localization in neurofibrillary tangles of Alzheimer's disease. *Neuron* 1989:9. doi: 10.1016/0896-6273(89)90210-9

Goode, B. L., Chau, M., Denis, P. E., and Feinstein, S. C. (2000). Structural and functional differences between 3-repeat and 4-repeat tau isoforms. Implications for normal tau function and the onset of neurodegenetative disease. *J. Biol. Chem.* 275, 38182–38189. doi: 10.1074/jbc.M007489200

Goode, B. L., Denis, P. E., Panda, D., Radeke, M. J., Miller, H. P., Wilson, L., et al. (1997). Functional interactions between the proline-rich and repeat regions of tau enhance microtubule binding and assembly. *Mol. Biol. Cell* 8, 353–365. doi: 10.1091/mbc.8.2.353

Kempf, M., Clement, A., Faissner, A., Lee, G., and Brandt, R. (1996). Tau binds to the distal axon early in development of polarity in a microtubule- and microfilament-dependent manner. *J. Neurosci.* 16, 5583–5592 doi: 10.1523/jneurosci.16-18-05583.1996

Kishi, M., Pan, Y. A., Crump, J. G., and Sanes, J. R. (2005). Mammalian SAD kinases are required for neuronal polarization. *Science* 2005:1107403. doi: 10.1126/science.1107403

Kosik, K. S., Orecchio, L. D., Bakalis, S., and Neve, R. L. (1989). Developmentally regulated expression of specific tau sequences. *Neuron* 2, 1389–1397. doi: 10.1016/0896-6273(89)90077-9

Li, X., Kumar, Y., Zempel, H., Mandelkow, E., Biernat, J., and Mandelkow, E. (2011). Novel diffusion barrier for axonal retention of Tau in neurons and its failure in neurodegeneration. *EMBO J.* 30, 4825–4837. doi: 10.1038/emboj.2011.376

Liu, C., Song, X., Nisbet, R., and Götz, J. (2016). Co-immunoprecipitation with Tau Isoform-specific Antibodies Reveals Distinct Protein Interactions and Highlights a Putative Role for 2N Tau in Disease. *J. Biol. Chem.* 291, 8173–8188. doi: 10.1074/jbc.M115.641902

Mandell, J. W., and Banker, G. A. (1995). The microtubule cytoskeleton and the development of neuronal polarity. *Neurobiol. Aging* 1995:00164. doi: 10.1016/0197-4580(94)00164-V

McMillan, P., Korvatska, E., Poorkaj, P., Evstafjeva, Z., Robinson, L., Greenup, L., et al. (2008). Tau isoform regulation is region- and cell-specific in mouse brain. *J. Comp. Neurol.* 2008:21867. doi: 10.1002/cne.21867

Panda, D., Samuel, J. C., Massie, M., Feinstein, S. C., and Wilson, L. (2003). Differential regulation of microtubule dynamics by three- and four-repeat tau: Implications for the onset of neurodegenerative disease. *Proc. Natl. Acad. Sci.* 100, 9548–9553. doi: 10.1073/pnas.1633508100

Rady, R. M., Zinkowski, R. P., and Binder, L. I. (1995). Presence of tau in isolated nuclei from human brain. *Neurobiol. Aging* 16, 479–486. doi: 10.1016/0197-4580(95)00023-8

Schindelin, J., Arganda-Carreras, I., Frise, E., Kaynig, V., Longair, M., Pietzsch, T., et al. (2012). Fiji: an open-source platform for biological-image analysis. *Nat. Methods* 9, 676–682. doi: 10.1038/nmeth.2019

Schneider, C. A., Rasband, W. S., and Eliceiri, K. W. (2012). NIH Image to ImageJ: 25 years of image analysis. *Nat. Methods* 9, 671–675. doi: 10.1038/nmeth.2089

Stepanova, T., Slemmer, J., Hoogenraad, C. C., Lansbergen, G., Dortland, B., De Zeeuw, C. I., et al. (2003). Visualization of Microtubule Growth in Cultured Neurons via the Use of EB3-GFP (End-Binding Protein 3-Green Fluorescent Protein). *J. Neurosci.* 23, 2655–2664. doi: 10.1523/JNEUROSCI.23-07-02655.2003

Takei, Y., Teng, J., Harada, A., and Hirokawa, N. (2000). Defects in axonal elongation and neuronal migration in mice with disrupted tau and map1b genes. *J. Cell Biol.* 150, 989–1000. doi: 10.1083/jcb.150.5.989

Tashiro, K., Hasegawa, M., Ihara, Y., and Iwatsubo, T. (1997). Somatodendritic localization of phosphorylated tau in neonatal and adult rat cerebral cortex. *Neuroreport* 8, 2797–2801. doi: 10.1097/00001756-199708180-00029

Tinevez, J.-Y., Perry, N., Schindelin, J., Hoopes, G. M., Reynolds, G. D., Laplantine, E., et al. (2017). TrackMate: An open and extensible platform for single-particle tracking. *Methods* 115, 80–90. doi: 10.1016/j.ymeth.2016.09.016

Trabzuni, D., Wray, S., Vandrovcova, J., Ramasamy, A., Walker, R., Smith, C., et al. (2012). MAPT expression and splicing is differentially regulated by brain region: relation to genotype and implication for tauopathies. *Hum. Mol. Genet.* 21, 4094–4103. doi: 10.1093/hmg/dds238

Tsushima, H., Emanuele, M., Polenghi, A., Esposito, A., Vassalli, M., Barberis, A., et al. (2015). HDAC6 and RhoA are novel players in Abeta-driven disruption of neuronal polarity. *Nat. Commun.* 6:7781. doi: 10.1038/ncomms8781

Weingarten, M. D., Lockwood, A. H., Hwo, S. Y., and Kirschner, M. W. (1975). A protein factor essential for microtubule assembly. *Proc. Natl. Acad. Sci. U. S. A.* 1975:1858. doi: 10.1073/pnas.72.5.1858

Witman, G. B., Cleveland, D. W., Weingarten, M. D., and Kirschner, M. W. (1976). Tubulin requires tau for growth onto microtubule initiating sites. *Proc. Natl. Acad. Sci. U. S. A.* 73, 4070–4074. doi: 10.1073/pnas.73.11.4070

Zempel, H., Dennissen, F. J. A., Kumar, Y., Luedtke, J., Biernat, J., Mandelkow, E.-M., et al. (2017a). Axodendritic sorting and pathological missorting of Tau are isoform-specific and determined by axon initial segment architecture. *J. Biol. Chem.* 292, 12192–12207. doi: 10.1074/jbc.M117.784702

Zempel, H., Luedtke, J., and Mandelkow, E. M. (2017b). Tracking Tau in neurons: How to transfect and track exogenous tau into primary neurons. *Methods Mole. Biol.* 2017:21. doi: 10.1007/978-1-4939-6598-4_21

Zempel, H., and Mandelkow, E. M. (2017). Tracking Tau in neurons: How to grow, fix, and stain primary neurons for the investigation of Tau in all developmental stages. *Methods Mole. Biol.* 2017:20. doi: 10.1007/978-1-4939-6598-4_20

Conflict of Interest: The authors declare that the research was conducted in the absence of any commercial or financial relationships that could be construed as a potential conflict of interest.

frontiers in Neuroscience

ORIGINAL RESEARCH
published: 18 June 2021
doi: 10.3389/fnins.2021.689315

Rabbit PrP Is Partially Resistant to *in vitro* Aggregation Induced by Different Biological Cofactors

*Juliana N. Angelli[1,2], Yulli M. Passos[3], Julyana M. A. Brito[2], Jerson L. Silva[2], Yraima Cordeiro[3] and Tuane C. R. G. Vieira[1,2]**

[1] Federal Institute of Rio de Janeiro, Rio de Janeiro, Brazil, [2] Institute of Medical Biochemistry Leopoldo de Meis, National Institute of Science and Technology for Structural Biology and Bioimaging, Federal University of Rio de Janeiro, Rio de Janeiro, Brazil, [3] Department of Pharmaceutical Biotechnology, Faculty of Pharmacy, Federal University of Rio de Janeiro, Rio de Janeiro, Brazil

Prion diseases have been described in humans and other mammals, including sheep, goats, cattle, and deer. Since mice, hamsters, and cats are susceptible to prion infection, they are often used to study the mechanisms of prion infection and conversion. Mammals, such as horses and dogs, however, do not naturally contract the disease and are resistant to infection, while others, like rabbits, have exhibited low susceptibility. Infection involves the conversion of the cellular prion protein (PrP^{C}) to the scrapie form (PrP^{Sc}), and several cofactors have already been identified as important adjuvants in this process, such as glycosaminoglycans (GAGs), lipids, and nucleic acids. The molecular mechanisms that determine transmissibility between species remain unclear, as well as the barriers to transmission. In this study, we examine the interaction of recombinant rabbit PrP^{C} (RaPrP) with different biological cofactors such as GAGs (heparin and dermatan sulfate), phosphatidic acid, and DNA oligonucleotides (A1 and D67) to evaluate the importance of these cofactors in modulating the aggregation of rabbit PrP and explain the animal's different degrees of resistance to infection. We used spectroscopic and chromatographic approaches to evaluate the interaction with cofactors and their effect on RaPrP aggregation, which we compared with murine PrP (MuPrP). Our data show that all cofactors induce RaPrP aggregation and exhibit pH dependence. However, RaPrP aggregated to a lesser extent than MuPrP in the presence of any of the cofactors tested. The binding affinity with cofactors does not correlate with these low levels of aggregation, suggesting that the latter are related to the stability of PrP at acidic pH. The absence of the N-terminus affected the interaction with cofactors, influencing the efficiency of aggregation. These findings demonstrate that the interaction with polyanionic cofactors is related to rabbit PrP being less susceptible to aggregation *in vitro* and that the N-terminal domain is important to the efficiency of conversion, increasing the interaction with cofactors. The decreased effect of cofactors in rabbit PrP likely explains its lower propensity to prion conversion.

Keywords: prion, rabbit PrP, resistance, conversion, cofactor, DNA, glycosaminoglycan, lipid

OPEN ACCESS

Edited by:
Cláudio M. Gomes, University of Lisbon, Portugal

Reviewed by:
Pedro Fernandez-Funez, University of Minnesota, United States
Karen Marshall, University of Sussex, United Kingdom

***Correspondence:**
Tuane C. R. G. Vieira
tuane@bioqmed.ufrj.br

Specialty section:
This article was submitted to Neurodegeneration, a section of the journal Frontiers in Neuroscience

Received: *31 March 2021*
Accepted: *14 May 2021*
Published: *18 June 2021*

Citation:
Angelli JN, Passos YM, Brito JMA, Silva JL, Cordeiro Y and Vieira TCRG (2021) Rabbit PrP Is Partially Resistant to in vitro Aggregation Induced by Different Biological Cofactors. Front. Neurosci. 15:689315. doi: 10.3389/fnins.2021.689315

INTRODUCTION

The cellular prion protein (PrP^C) is a constitutive protein that is mostly found attached to the extracellular membrane. PrP^C occurs naturally in the cells of all mammals, primarily in the nervous system (Prusiner, 1991), and is a conserved protein that exhibits a high sequence and structural identity. The protein has an N-terminal unstructured and flexible region formed by residues 23 to 121. It has an octapeptide region known as an octarepeat, which is comprised of a sequence of eight amino acids (PHGGGWGQ) that are repeated five times. The globular C-terminal region is composed of residues 122 to 231, which have three α-helices (H1 to H3), with H2 and H3 connected by a disulfide bridge and one small antiparallel β-sheet (Hornemann et al., 1997). Minor differences have been observed between the globular domain conformation in different species related to specific amino acid substitutions, including surface charge potential and dynamics (Pastore and Zagari, 2007; Wen et al., 2010a; Srivastava and Lapidus, 2017).

The prion protein has been physiologically related to several functions in the central nervous system, including neuronal protection, neuroplasticity, and cell signaling (Chen et al., 2003; Lopes et al., 2005; Linden, 2017; Wulf et al., 2017). However, it is most prominently associated with the development of pathologies known as transmissible spongiform encephalopathies (TSEs) or prion diseases. PrP^C can undergo changes in its native conformation that turn it into its pathogenic isoform, PrP scrapie (PrP^{Sc}), a structure rich in β-sheets (Prusiner, 1982). PrP^{Sc} can arise because of errors in the protein folding process, post-translational conformational changes, and conversion by direct contact between PrP^{Sc} and PrP^C in an autocatalytic process (Castilla and Requena, 2015).

Naturally occurring TSEs have been described in several mammal species. These include scrapie in sheep and goats, bovine spongiform encephalopathy (BSE) in cattle, chronic wasting disease (CWD) in deer, and Creutzfeldt-Jakob disease (CJD) in humans. Scrapie has been experimentally transmitted to rats and cats, although with varying degrees of difficulty (Gibbs and Gajdusek, 1973). The molecular mechanisms that determine transmissibility between species and barriers to transmission remain poorly understood (Sweeting et al., 2010). For example, some species do not develop TSEs at all, such as rabbits, dogs, and horses (Sigurdson and Miller, 2003; Bian et al., 2017). These mammals' PrP^C have been reported as being resistant to conversion by PrP^{Sc} samples from other species (Vorberg et al., 2003; Polymenidou et al., 2008). However, prions have been generated *in vitro* from rabbit material using protein misfolding cyclic amplification (PMCA), and are capable of infecting leporids (Chianini et al., 2012) and transgenic mice expressing rabbit PrP (Vidal et al., 2015). Species previously considered completely resistant to prions have therefore been shown to be slightly susceptible to TSE infections (Castilla et al., 2005; Saá et al., 2006; Chianini et al., 2013; Vidal et al., 2015).

Although human and rabbit PrPs have very similar primary sequences (88%) (Yan et al., 2014), some amino acid residues in the rabbit PrP^C sequence appear to contribute significantly to its inability to convert into PrP^{Sc} and are thus closely associated with rabbits' low susceptibility to TSEs (Loftus and Rogers, 1997; Vorberg et al., 2003; Wen et al., 2010b; Yuan et al., 2013; Eraña et al., 2017). The primary sequence alignment between rabbit and mouse PrP has nine different amino acid residues in the flexible N-terminus and 14 in the structured C-terminus (**Figure 1**). In rabbits, PrP has a larger positively charged surface than it does in mice (Wen et al., 2010a; Silva et al., 2011).

Although the conversion of PrP^C is caused by PrP^{Sc}, several cofactors have been identified as important adjuvants in this process. These include glycosaminoglycans (GAGs), lipids, and nucleic acids (Deleault et al., 2007; Silva and Cordeiro, 2016; Vieira and Silva, 2016).

Several studies have linked GAGs to prion biology. Dermatan sulfate is one of the most commonly found components in amyloid deposits (Hirschfield and Hawkins, 2003). Membrane heparan sulfate plays a crucial role in the development of prion disease as a receptor for PrP^{Sc} (Horonchik et al., 2005; Vieira and Silva, 2016). However, while these molecules have been observed to stimulate conversion in some instances, at other times, they inhibit the conversion, thus showing a paradoxical effect. Low molecular weight heparin interacts with murine PrP, leading to a transient oligomerization/aggregation process (Vieira et al., 2011). The octapeptide region has also been shown to be important for interaction at neutral pH (Vieira et al., 2011; Kim et al., 2020), while a second binding site in the C-terminal region of the protein under acidic conditions has also been suggested (Vieira et al., 2011). In addition, low molecular weight heparin acts as an inhibitor of PrP fibrillation, indicating its therapeutic potential (Vieira et al., 2011, 2014).

Lipids also play a role in the conversion of PrP^C, and some phospholipids have been described as important for conversion and aggregation (Supattapone, 2014). Lipids such as phosphatidylserine (PS), phosphatidic acid (PA), phosphatidylethanolamine (PE), and phosphatidylinositol (PI) lead to the aggregation of PrP^C (Tsiroulnikov et al., 2009), converting it to a protease-resistant form (Wang et al., 2007). Palmitoyloleoyl-phosphatidylglycerol (POPG) vesicles have been shown to induce PrP structural changes, leading to intermediates that, with the addition of RNA, form aggregates with infectious characteristics (Miller et al., 2013).

Besides lipids, GAGs, and proteins (Linden et al., 2008; Satoh et al., 2009), PrP also binds nucleic acids, both DNA and RNA. These interactions have been the subject of research over recent decades. Nucleic acids have been proposed to act as catalysts in the conversion of PrP^C to a PrP^{Sc}-like form (Cordeiro et al., 2001; Cordeiro and Silva, 2005). More recently, DNA-induced prion-like conversion in a physiological process was also observed, with specific DNA aptamers modulating PrP liquid-liquid phase separation (Matos et al., 2020). The binding of nucleic acids can thus influence the unfolding of proteins in both disease-related and physiological situations.

Some regions of murine PrP have already been observed to bind to nucleic acids, such as the lysine-rich regions 23–27 and 101–110 and the C-terminal globular domain (Lima et al., 2006; Cavaliere et al., 2013). DNA can bind to PrP *in vitro*, modulating protein aggregation; this interplay changes the native conformation of PrP and increases the presence of

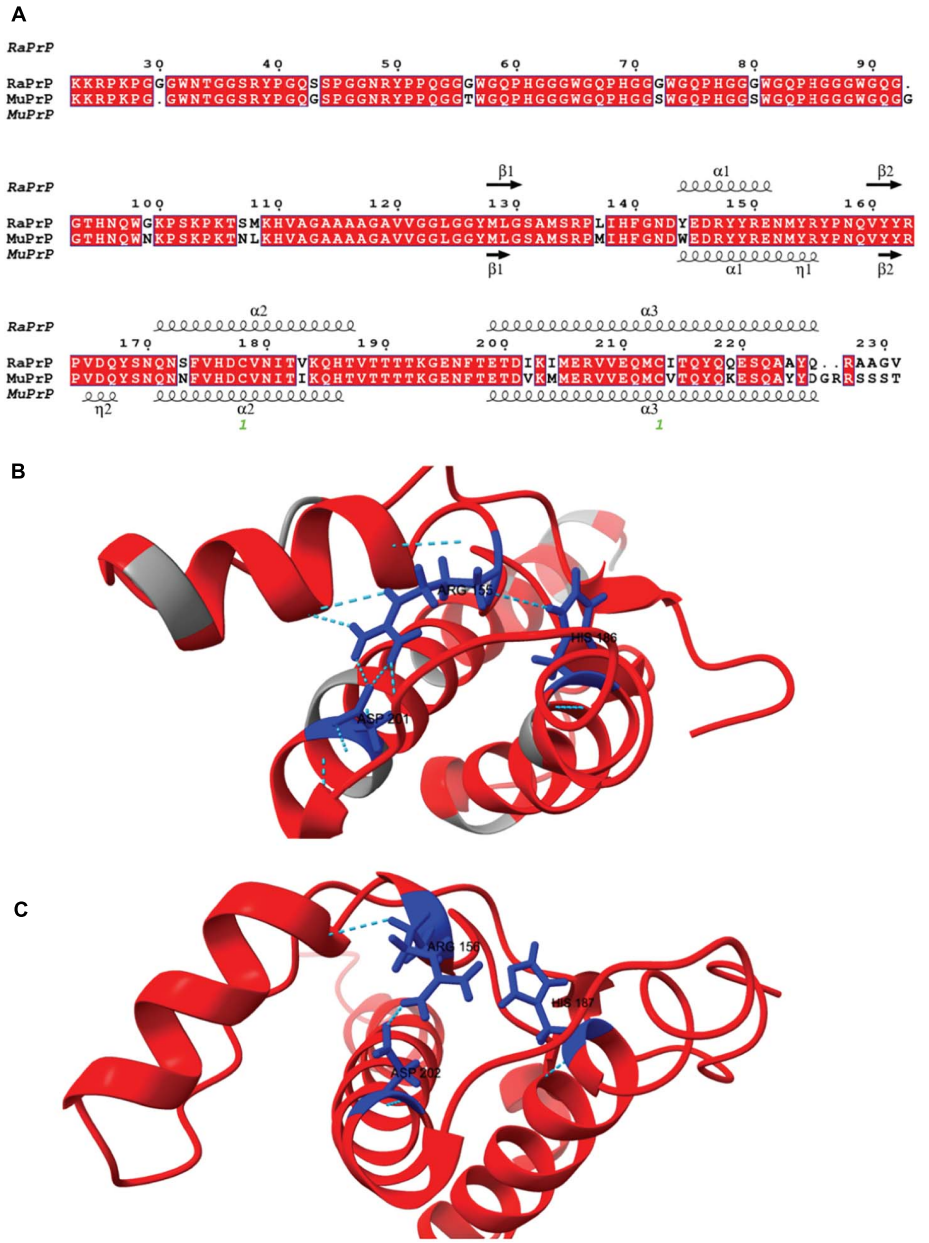

FIGURE 1 | Rabbit and murine PrP structural alignment and comparison. **(A)** RaPrP$^{23-231}$ sequence (UNIPROT Q95211) was aligned with MuPrP$^{23-231}$ sequence (UNIPROT P04925) using the T-Coffee server. The figure was produced with the ESPrip server, using PDB 2FJ3 for RaPrP$^{23-231}$ and PDB 1XYX for MuPrP$^{23-231}$ secondary structure depiction. Aligned amino acid residues are in red boxes to distinguish them from low similarity residues. The secondary structures (alpha-helix and beta-strands) are shown on the top of the alignment for RaPrP$^{23-231}$ and the bottom for MuPrP$^{23-231}$. **(B)** RaPrP$^{23-231}$ 3D structure is shown in red, and non-homologous residues are colored gray. ARG 155, HIS186, and ASP201 (rabbit sequence numbering) are depicted in blue, showing hydrogen bonds and saline bridges between these residues. **(C)** MuPrP$^{23-231}$ 3D structure in red with ARG 156, HIS187, and ASP 202 (mouse sequence numbering) are depicted in blue. No hydrogen bond is observed between ARG 156 and HIS187, and ARG 156-ASP 202 shows one salt bridge. ChimeraX was used for structure visualization and H-bond and salt bridge identification.

β-sheets (Cordeiro et al., 2001; Nandi et al., 2002). A complex formed by the interaction with a GC-rich 21 bp DNA (D67) has been shown to be toxic to a murine neuroblastoma cell line (Macedo et al., 2012). Recently, PrP-DNA interactions were investigated in a more targeted manner, selecting short single-stranded NA sequences that bind with high affinity and specificity to the extended C-terminal domain of the prion protein (PrP$^{90-231}$). A selected 25-mer apatmer (A1) was able to modulate the phase transition of PrP – from LLPS to aggregation (Matos et al., 2020).

Since several cofactors are important in modulating the conversion and aggregation of PrP, the interaction of these

molecules with different PrP sequences may help explain differences in susceptibility between species. In this study, we compare the interactions of rabbit and mouse PrP with different biological cofactors such as GAGs (heparin and dermatan sulfate), phosphatidic acid (PA), and DNA oligonucleotides (A1 and D67), demonstrating that the interaction with these cofactors is related to a lower susceptibility of RaPrP to aggregation *in vitro*.

MATERIALS AND METHODS

Glycosaminoglycans

Dermatan sulfate from porcine intestinal mucosa (code C3788, M.W. 30 kDa avg.) was purchased from Sigma-Aldrich (St. Louis, MO, United States). Unfractionated heparin (code 2608411, M.W. 15 kDa avg.) was purchased from Merck (Darmstadt, Germany).

Preparation of PA Large Unilamellar Vesicles

Phosphatidic acid (L-α-phosphatidic acid, monosodium salt of chicken egg, cod. 840101) was purchased from Avanti Polar Lipids, Inc. (Alabaster, AL, United States). Powdered PA was solubilized in chloroform (code 102445, Merck, Darmstadt, Germany). For the formation of the lipid film, chloroform was evaporated using nitrogen gas. Subsequently, the film was resuspended in PBS buffer. To form large unilamellar vesicles (LUVs), the sample was extruded (code 610000) against polycarbonate membranes with a pore diameter of 0.1 μm (code 610005), all from Avanti Polar Lipids, Inc. (Alabaster, AL, United States).

DNA Oligonucleotides

Two DNA sequences previously studied by the group were chosen, one single-stranded (A1) and one double-stranded (D67). A1 contains 25 nucleotides (5′-CCGCGTACAATCGAGCTCGGGTGTC-3′) and D67 has 21 nucleotides (5′-AAAGGACGCGCGCGCGTTA-3′). The oligonucleotides were synthesized and purified by Integrated DNA Technologies (Coralville, IA, United States). The DNA material was annealed by heating at 95°C for 5 min and subsequently slow cooling overnight before the experiments. The DNA concentration was determined by absorbance at 260 nm using the corresponding molar extinction coefficient of each oligonucleotide.

Prion Protein Expression and Purification

The expression in *E. coli* and purification by high-affinity chromatography of recombinant full length (PrP^{23-231}) and truncated (PrP^{90-231}) murine (Mu) and rabbit (Ra) proteins were performed as described in Vieira and Silva (2019).

Spectroscopic Measurements

Protein intrinsic fluorescence and light scattering spectra were acquired using an FP-8200 spectrofluorometer (Jasco Corp., Tokyo, Japan) or a PC1 spectrofluorometer (ISS, Champaign, IL, United States) in an "L" geometry (at 90° relative to the excitation light). All samples were prepared in one of two solutions at 25°C: 50 mM Tris (pH 7.4) and 100 mM NaCl, or 20 mM sodium acetate buffer (pH 5.5), and 100 mM NaCl. For all PrP constructs, the concentration used was 2 μM for interactions with GAG and PA. To assess the interaction with the DNA sequences, a concentration of 5 μM was used for PrP^{90-231} constructs and 2 μM for PrP^{23-231} due to signal intensities. For light scattering, the samples were illuminated at 450 nm, and data were acquired from 430 to 470 nm (DNA analysis) or else at 320 nm with data acquisition from 300 to 340 nm (GAG and PA analysis). Intrinsic fluorescence measurements were performed by exciting the sample at 290 nm and collecting the fluorescence emissions between 300 and 420 nm (DNA analysis) or exciting the sample at 280 nm and collecting the fluorescence emissions between 300 and 420 nm. The Stern-Volmer constant (K_{SV}) was obtained from the linear regression equation of fluorescence data (F_0/F) from quencher cofactors and can be interpreted as the association constant of the complex (K_a) according to the following equation (Jameson, 2014):

$$F_0/F = 1 + K_a[Q] \quad (1)$$

Where F_0 is the free protein initial fluorescence and F is the fluorescence signal at each quencher concentration, represented by [Q]. PrP interaction with PA data were analyzed as the center of spectral mass and fitted using GraphPad Prism with a one-site binding non-linear regression:

$$\Delta CM = Bmax\,[PA]/K_d + [PA] \quad (2)$$

Where ΔCM is the variation of the center of fluorescence spectral mass, Bmax is the maximum number of binding sites, [PA] is the concentration of PA, and K_d is the equilibrium dissociation constant. K_d was converted to its inverse, K_a.

PrP:GAG fluorescence was measured after protein disaggregation. Samples were prepared at each specified PrP:GAG concentration in Eppendorf Protein LoBind Tubes at 25°C, and measurements were taken after 4 h.

Heparin Affinity Chromatography

A HiTrap Heparin column was used (code 17040701, GE Healthcare, Little Chalfont, United Kingdom). The PrP sample was applied to the column, followed by a washing step with 20 mL of buffer (20 mM sodium acetate solution at pH 5.5, or 50 mM Tris solution at pH 7.4). Protein elution was carried out with 70 mL of 20 mM sodium acetate with 1 M NaCl at pH 5.5, or 50 mM Tris solution with 1 M NaCl at pH 7.4. The flow rate used in all steps was 1 mL/min. The data were normalized by the maximum absorption at 280 nm of each tested condition, and negative absorbance values were considered equal to zero. Retention factor values were calculated to allow comparison of the relative affinities for the immobilized cofactor. It is calculated by the formula (Gjerde et al., 2009):

$$k = (t_r - t_m)/t_m \quad (3)$$

Where t_r is the retention time of the test substance, and t_m is the column dead time.

RESULTS

Aggregation and Interaction of Murine and Rabbit PrP With GAGs

In the cell, GAGs (especially heparan sulfate) and PrP molecules can both be found in the plasma membrane and endocytic compartments (Godsave et al., 2015) and thus are able to experience pH values close to neutral and acid (Silva et al., 2011). We therefore evaluated the PrP:low molecular weight heparin interaction at these two pH values. We found an interaction with a binding site in the N-terminal domain of murine PrP (MuPrP) at pH 7.4 and an interaction with a second site located at the C-terminal domain of MuPrP at pH 5.5 (Vieira et al., 2011). Low molecular weight heparin was also shown to induce transient aggregation in MuPrP (Vieira et al., 2011).

We used light scattering measures to evaluate and compare the effect of GAGs on the aggregation of $MuPrP^{23-231}$ and $RaPrP^{23-231}$. The results showed that increasing heparin concentrations at pH 7.4 and 5.5 were accompanied by an increase in light scattering for $MuPrP^{23-231}$ and $RaPrP^{23-231}$, suggesting the formation of aggregates (**Figures 2A,B**, respectively). However, the effect was 200% greater in $MuPrP^{23-231}$ (**Figure 2A**) than in $RaPrP^{23-231}$ (**Figure 2B**). Meanwhile, dermatan sulfate triggered aggregation only at pH 5.5 in $MuPrP^{23-231}$ and $RaPrP^{23-231}$ (**Figures 2C,D**). The aggregation was 60% greater for MuPrP, further demonstrating the contrasting effect between the two PrPs at an acidic pH. Aggregation was transient in all conditions (**Supplementary Figures 1A,B**), consistent with observations for low molecular weight heparin with MuPrP (Vieira et al., 2011).

We also compared the interaction of GAGs with PrP^{90-231} to explore the importance of the unstructured N-terminal region for the observed effect (**Figure 3**). A robust aggregation was only observed at pH 5.5 for heparin (**Figure 3A**), though the effect was 500% lesser than for PrP^{23-231}, corroborating data obtained for low molecular weight heparin that showed only one binding site at the C-terminal domain at acidic pH (Vieira et al., 2011). The same effect was observed for dermatan sulfate (**Figure 3C**), suggesting that heparin and dermatan sulfate share the same binding regions but with different affinities. $RaPrP^{90-231}$ showed a negligible aggregation for both heparin (**Figure 3B**) and dermatan sulfate (**Figure 3D**).

To evaluate binding and affinities, we performed affinity chromatography with a heparin column (**Figure 4**). The result showed that all PrP^{23-231} types were able to interact with the resin, with a higher concentration of NaCl required to displace this interaction at pH 5.5. A retention factor (k) difference between pH 5.5 and 7.4 was of 12.3 for MuPrP and 13 for RaPrP, reflecting a greater affinity at pH 5.5. We observed that k difference between $MuPrP^{23-231}$ and $RaPrP^{23-231}$ was of 1.4 at pH 7.4 and 0.7 at pH 5.5, suggesting a low difference in the affinities using this methodology (**Figure 4**).

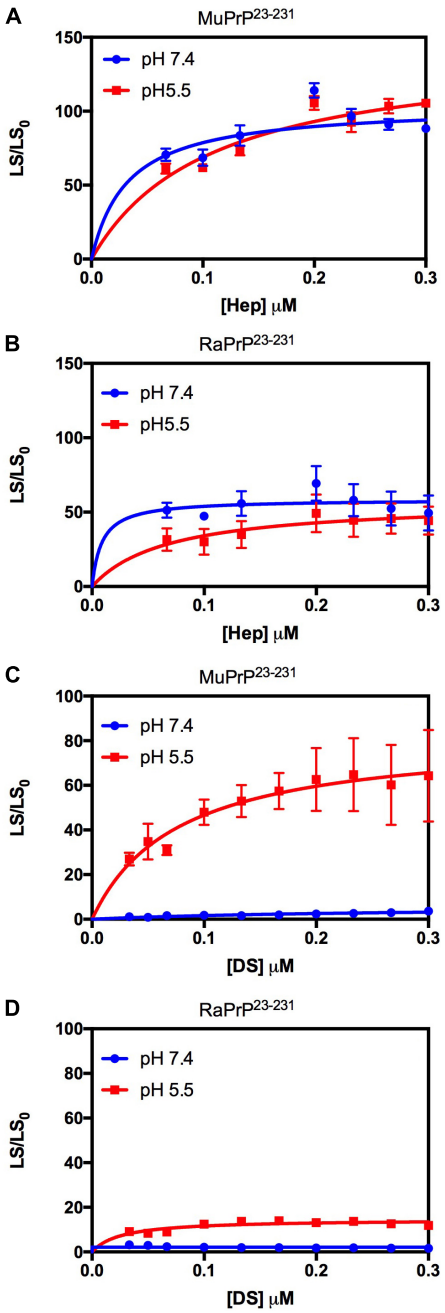

FIGURE 2 | Rabbit PrP^{23-231} aggregates less in the presence of GAGs. Effect of increasing concentrations of Hep **(A,B)** and DS **(C,D)** on the aggregation of $MuPrP^{23-231}$ (2 μM) **(A,C)** and $RaPrP^{23-231}$ (2 μM) **(B,D)** at pH 5.5 (red) and 7.4 (blue). Representative data from three experiments. The experiments were performed in 50 mM Tris buffer containing 100 mM NaCl at pH 7.4 or in 20 mM sodium acetate buffer containing 100 mM NaCl at pH 5.5. All experiments were performed at 25°C. The error bars represent the standard deviation of at least two independent experiments.

To further analyze affinity differences, we also performed protein intrinsic fluorescence measurements (**Figure 5**) after protein disaggregation. The results showed that binding led to a

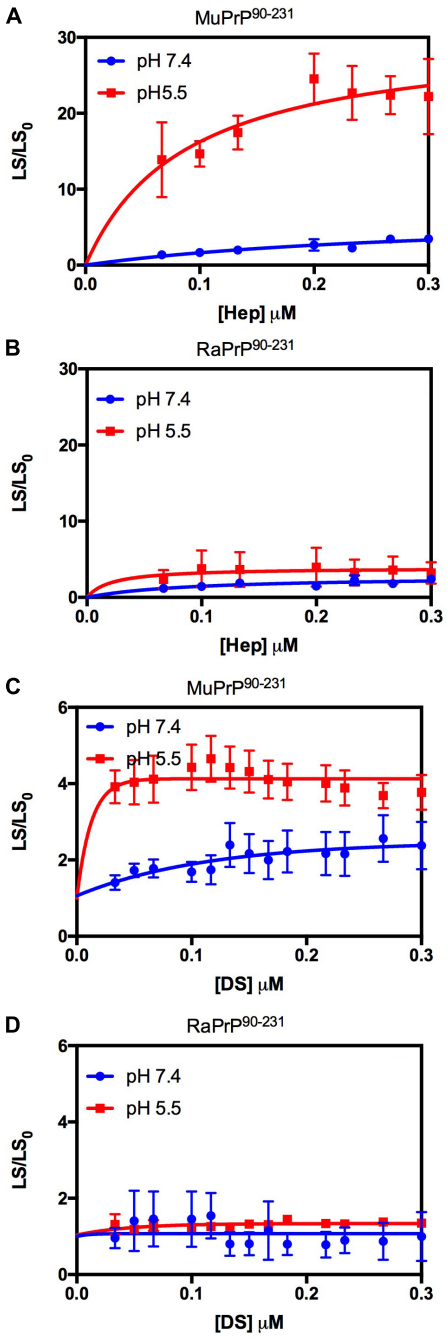

FIGURE 3 | Rabbit PrP^{90-231} aggregates less in the presence of GAGs. Effect of increasing concentrations of Hep **(A,B)** and DS **(C,D)** on the aggregation of $MuPrP^{90-231}$ (2 μM) **(A,C)** and $RaPrP^{90-231}$ (2 μM) **(B,D)** at pH 5.5 (red) and 7.4 (blue). The experiments were performed in 50 mM Tris buffer containing 100 mM NaCl at pH 7.4 or in 20 mM sodium acetate buffer containing 100 mM NaCl at pH 5.5. All experiments were performed at 25°C. The error bars represent the standard deviation of at least two independent experiments.

decrease in fluorescence intensity with increasing concentrations of heparin (**Figures 5A,B**) and dermatan sulfate (**Figures 5C,D**) at pH 7.4 and 5.5. Binding therefore led to fluorescence quenching, probably due to the approximation of glucosamine and galactosamine moieties (by heparin and dermatan sulfate, respectively) to tryptophan residues. **Table 1** shows the results of the Stern-Volmer linear regression to compare affinity. All conditions were analyzed except for the interaction of PrP^{23-231} (murine and rabbit) with heparin at pH 5.5 since disaggregation was not complete under heparin treatment (**Supplementary Figure 1C**), and remaining aggregates can interfere with intensity measurements, promoting an inner filter effect (Jameson, 2014).

We did not observe any significant differences in terms of affinity when comparing the fluorescence data obtained for the interactions of $MuPrP^{23-231}$ and $RaPrP^{23-231}$ with heparin (**Figure 5A**) at pH 7.4. Meanwhile, we observed an eightfold affinity increase for $MuPrP^{90-231}$ at pH 5.5 (**Figure 5B** and **Table 1**). Dermatan sulfate exhibited a low affinity for all PrP constructs (**Figures 5C,D**) except for PrP^{23-231} at pH 5.5 that it was twice as high for MuPrP than for RaPrP (**Table 1**). All GAGs had a greater affinity for PrP^{23-231} than PrP^{90-231}.

Evaluation of PA Interaction With Murine and Rabbit PrP

Lipids have also been identified in several studies as adjuvants of PrP conversion (Shyng et al., 1993; Nishina et al., 2004). To detect any differences in the interactions between RaPrP and a cofactor with different chemical and structural characteristics from GAGs, we also performed intrinsic fluorescence measurements to investigate the interaction with PA (**Supplementary Figure 2**). PA leads to an increase in fluorescence emission in all constructs at pH 7.4 and 5.5 (**Supplementary Figure 2**). This increase was accompanied by a blue shift of the emission spectra, indicating a shift to a more non-polar environment in the chemical environment of tryptophan. This suggests an interaction with the hydrophobic region of the LUVs and/or a reorganization of the structure where these amino acids are located (**Supplementary Figure 2**).

Variation of the center of mass (ΔCM) from intrinsic fluorescence data was obtained and fitted with a one-site binding non-linear curve, obtaining K_a values (**Table 1**) for all PrP constructs. Although ΔCM was greater at pH 5.5, the affinity was higher at pH 7.4 (**Figures 6A–D** and **Table 1**), suggesting that the structural changes observed as a result of the interaction do not depend directly on affinity. ΔCM and K_a were statistically different between pH values except concerning the interaction between PA and $RaPrP^{90-231}$ (**Figure 6C** and **Table 1**). Affinity differences were only observed between MuPrP and RaPrP at pH 5.5, where RaPrP was 1.5-fold greater than MuPrP (**Table 1**). Affinity was also 1.5-fold greater in the presence of the complete N-terminal domain at pH 7.4 (**Table 1**). In PrP^{90-231}, affinity is twice greater for RaPrP at pH 5.5 (**Table 1**).

Light scattering measurements of $MuPrP^{23-231}$ and $RaPrP^{23-231}$ showed that PA was able to induce protein aggregation and that its effect was also pH-dependent (**Figures 7A,B**), with greater aggregation at pH 5.5. The aggregation of MuPrP (**Figures 7A,C**) was higher than RaPrP

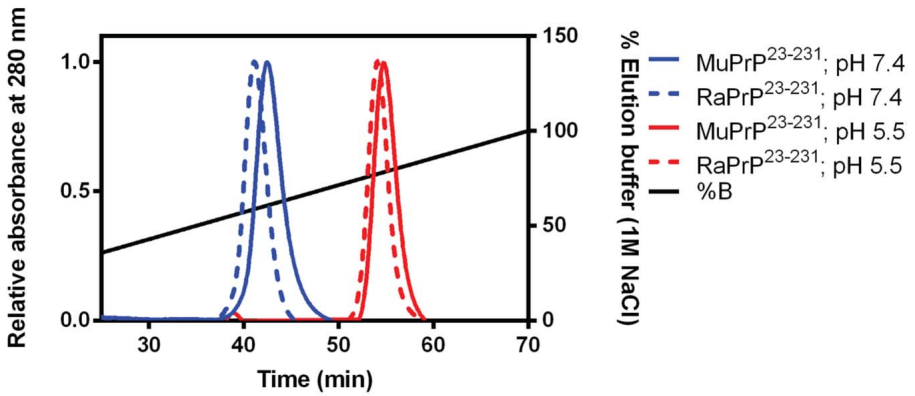

FIGURE 4 | Murine and Rabbit PrP^{23-231} interaction with Heparin. Affinity chromatography of a heparin column of $MuPrP^{23-231}$ (solid) and $RaPrP^{23-231}$ (dotted) at pH 7.4 (in blue) and pH 5.5 (in red). Representative data from three experiments.

(**Figures 7B,D**) (175% for PrP^{23-231} and 900% for PrP^{90-231}) at pH 5.5, despite the higher affinity observed for RaPrP (**Table 1**). This confirms that, in this case, structural changes and aggregation are not directly related to affinity.

Interaction Between PrP C-Terminal Extended and DNA Oligonucleotides

DNA can bind with high affinity to the prion protein *in vitro* and modulate its aggregation (Cordeiro et al., 2001; Macedo et al., 2012). It has also been shown that the DNA structure leads to distinct interactions with $MuPrP^{90-231}$ (Matos et al., 2020). In this study, we analyzed two DNA sequences previously described as high-affinity cofactors of MuPrP and evaluated whether they have different binding profiles in their interactions with MuPrP and RaPrP. We did this by monitoring intrinsic protein fluorescence and light scattering on a titration curve.

We began by evaluating the interaction of PrP^{90-231} and two DNA sequences previously studied by the group, A1 and D67, at two different pH values. There are evident differences when analyzing the light scattering of different combinations of the two proteins ($MuPrP^{90-231}$ and $RaPrP^{90-231}$) with both oligonucleotides (**Figure 8**). These changes are also linked to the pH, with acidic environments leading to four- to twenty-fold increase in light scattering for $MuPrP^{90-231}$ and $RaPrP^{90-231}$ when interacting with the DNA sequences. Aggregation was greater with A1 (**Figures 8A,B**) than with D67 (**Figures 8C,D**). A 20-fold increase was observed for the $MuPrP^{90-231}$:A1 sample (**Figure 8A**) relative to the initial light scattering, while the increase in $RaPrP^{90-231}$ was only sixfold (**Figure 8B**). The effect of D67 was less than A1 (**Figures 8C,D**). The same profile was observed at pH 7.4, though with a lower relative difference than at the lower pH.

The intrinsic fluorescence quenching upon binding with oligonucleotides revealed that $MuPrP^{90-231}$ had a higher affinity than $RaPrP^{90-231}$ for both A1 (1.2 and 1.4 times at pH 7.4 and 5.5, respectively) and D67 (1.8 and 1.9 times at pH 7.4 and 5.5, respectively) (**Figure 9** and **Table 1**). However, in contrast to the light scattering results, the differences between the samples containing A1 were not significant. The association constants show that the MuPrP:D67 interaction has the highest affinity of any treatment (**Table 1**).

To prove that any quenching effect observed was related to the addition of cofactors, the PrP^{90-231} fluorescence was evaluated with the addition of only reaction medium (**Supplementary Figure 3**). The fluorescence was not suppressed in a manner consistent with the observations for cofactors, GAGs or DNA.

Interaction Between Full-Length PrP and DNA Oligonucleotides

In addition to the nucleic acid binding sites also present in PrP^{90-231}, PrP^{23-231} has an additional predicted binding site in the lysine-rich region (residues 23–27) located at the extreme N-terminus (Yin et al., 2008; Cavaliere et al., 2013). We therefore sought to assess whether this region would change the interactions with the two DNA sequences.

Depending on the aptamer used, we observed a 2- to 9-fold increase in the relative light scattering in the lowest stoichiometric ratio (**Figure 10**). In contrast to the results for PrP^{90-231}, the light scattering of $RaPrP^{23-231}$ with both oligonucleotides at pH 5.5 had a slightly higher scattering than the $MuPrP^{23-231}$ samples (**Figure 10**). The profile for the two DNA sequences was similar to the observations for PrP^{90-231}: A1 induced more aggregation than D67. Another difference between PrP^{23-231} and PrP^{90-231} was that the neutral pH treatments showed a higher relative light scattering for MuPrP (**Figures 10A,C**).

Similar to the findings for the PrP^{90-231} C-terminal extended protein, the interaction between DNA and the full-length PrP caused fluorescence suppression in every treatment analyzed (**Figure 11**). As expected, since PrP^{23-231} has

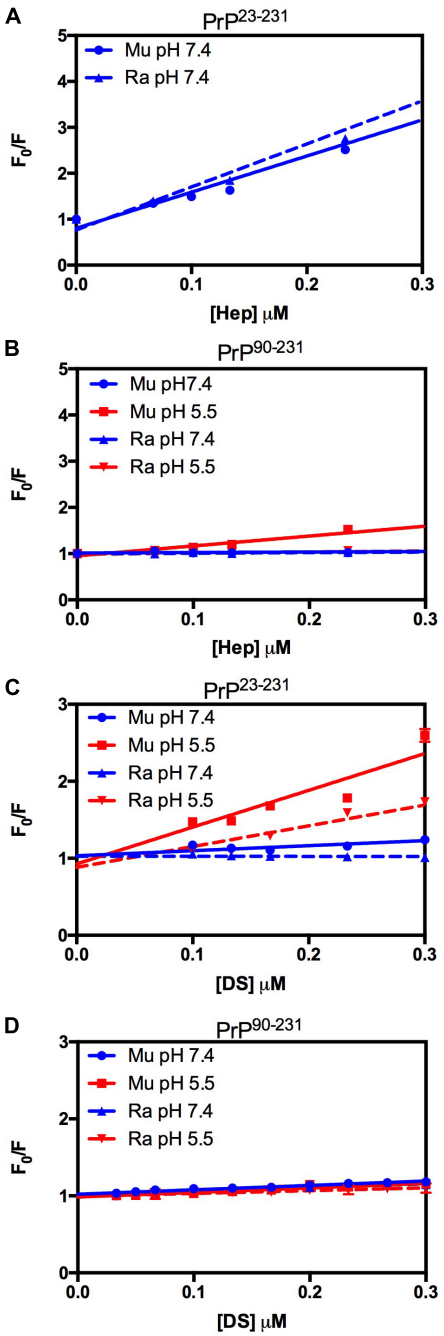

FIGURE 5 | RaPrP$^{23-231}$ interacts less with GAGs than MuPrP at pH 5.5, and the N-terminus is important for this interaction. Effect of increasing concentrations of Hep **(A,B)** and DS **(C,D)** on the fluorescence emission of PrP$^{23-231}$ (2 μM) **(A,C)** and PrP$^{90-231}$ (2 μM) **(B,D)** at pH 5.5 (red) and 7.4 (blue). Representative data from three experiments. The experiments were performed in 50 mM Tris buffer containing 100 mM NaCl at pH 7.4 or in 20 mM sodium acetate buffer containing 100 mM NaCl at pH 5.5. All experiments were performed at 25°C. The error bars represent the standard deviation of at least two independent experiments.

more nucleic acid binding sites, the association constants were higher than those found for PrP$^{90-231}$ (**Table 1**). Surprisingly, the interaction that showed the greatest

TABLE 1 | Observed association constants for all cofactors studied.

Sample	K_a (μM^{-1})			
	PrP$^{23-231}$		PrP$^{90-231}$	
	pH 5.5	pH 7.4	pH 5.5	pH 7.4
MuPrP:Hep	NA	7.9 ± 0.52^{ns}	2.1 ± 0.14**	0.11 ± 0.078
RaPrP:Hep	NA	9.4 ± 0.61^{ns}	0.24 ± 0.048**	0.12 ± 0.028
MuPrP:DS	4.8 ± 0.53*	0.66 ± 0.13	0.59 ± 0.047	0.57 ± 0.026
RaPrP:DS	2.7 ± 0.30*	zero	0.36 ± 0.091	0.46 ± 0.020
MuPrP:PA	0.054 ± 0.009$^{\#}$	0.30 ± 0.006	0.08 ± 0.003$^{\&}$	0.19 ± 0.01
RaPrP:PA	0.086 ± 0.003$^{\#}$	0.48 ± 0.048	0.18 ± 0.04$^{\&}$	0.13 ± 0.01
MuPrP:A1	0.17 ± 0.02	0.22 ± 0.03	0.17 ± 0.03	0.16 ± 0.02
RaPrP:A1	0.18 ± 0.03	0.29 ± 0.007	0.12 ± 0.01	0.13 ± 0.008
MuPrP:D67	0.28 ± 0.015	0.20 ± 0.02	0.21 ± 0.06	0.20 ± 0.05
RaPrP:D67	0.23 ± 0.08	0.41 ± 0.04	0.11 ± 0.009	0.11 ± 0.0007

We used linear regressions to fit fluorescence (F/F_0) data from titration with GAGs and oligonucleotides.
A one-site binding equation was used to fit fluorescence (ΔCM) data from titration with PA.
The values shown are the mean ± SE from three experiments.
Hep, heparin; DS, dermatan sulfate; PA, phosphatidic acid. A1 and D67 are oligonucleotides.
NA, not analyzed; ns, not significant.
**p = 0.0002, **p < 0.0001, $^{\#}$p = 0.03, $^{\&}$p = 0.001.*

association constant was between RaPrP and D67 at pH 7.4 (**Table 1**), which had the lowest light scattering increase (**Figure 10D**).

DISCUSSION

In this study, we compared the interaction of recombinant murine and rabbit PrP with different cofactors that have been identified as adjuvant molecules for conversion and aggregation of PrP, namely heparin, dermatan sulfate, PA, and DNA oligonucleotides (Tsiroulnikov et al., 2009; Silva et al., 2010). We show that RaPrP is less susceptible to aggregation by any of the cofactors tested, suggesting that the limited effect of these molecules may be associated with greater resistance to prion protein conversion observed in rabbits (Fernandez-Funez et al., 2011).

Recombinant rabbit PrP^{c} exhibits different electrostatic potential distribution than MuPrP, which has a larger positively charged surface (Wen et al., 2010a; Silva et al., 2011; Matos et al., 2020). This may affect interactions with negatively charged cofactors and, therefore, likely vary with pH. We found that all tested cofactors induce both MuPrP and RaPrP aggregation, and this effect does not correlate with differences on biding affinity, suggesting that the positive charge area found on RaPrP, covering residues 125–135, 150–160, and 180–190 (Wen et al., 2010a), is not related to RaPrP resistance to cofactor-induced aggregation.

The N-terminus of PrP does not seem to interfere with conversion to PrP^{Sc}-like species, since truncated PrP can be converted, even if with lower efficiency (Lawson et al., 2001). However, this region is markedly different in rabbits (**Figure 1**; Myers et al., 2020), and is the main site for interaction with

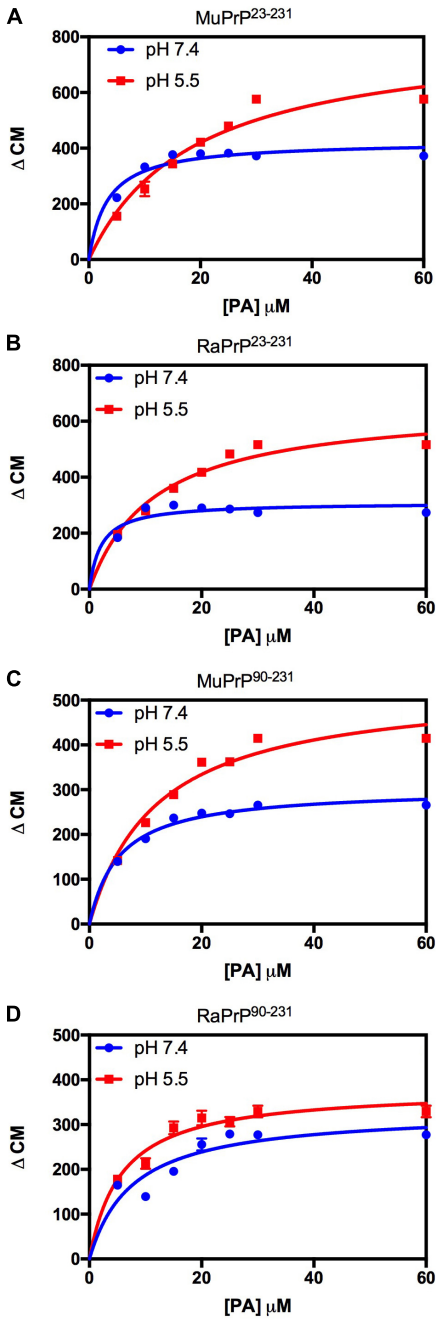

FIGURE 6 | PA-induced structural change is enhanced at acid pH but to a lesser extent for rabbit PrP. Effect of increasing the concentration of PA on the center of mass values obtained from the fluorescence spectra of MuPrP$^{23-231}$ **(A)**, RaPrP$^{23-231}$ **(B)**, MuPrP$^{90-231}$ **(C)**, and RaPrP$^{90-231}$ **(D)** at pH 5.5 (red) and 7.4 (blue). All proteins were analyzed at 2 μM. The experiments were performed in 50 mM Tris buffer containing 100 mM NaCl at pH 7.4 or in 20 mM sodium acetate buffer containing 100 mM NaCl at pH 5.5. All experiments were performed at 25°C. The error bars represent the standard deviation of at least two independent experiments.

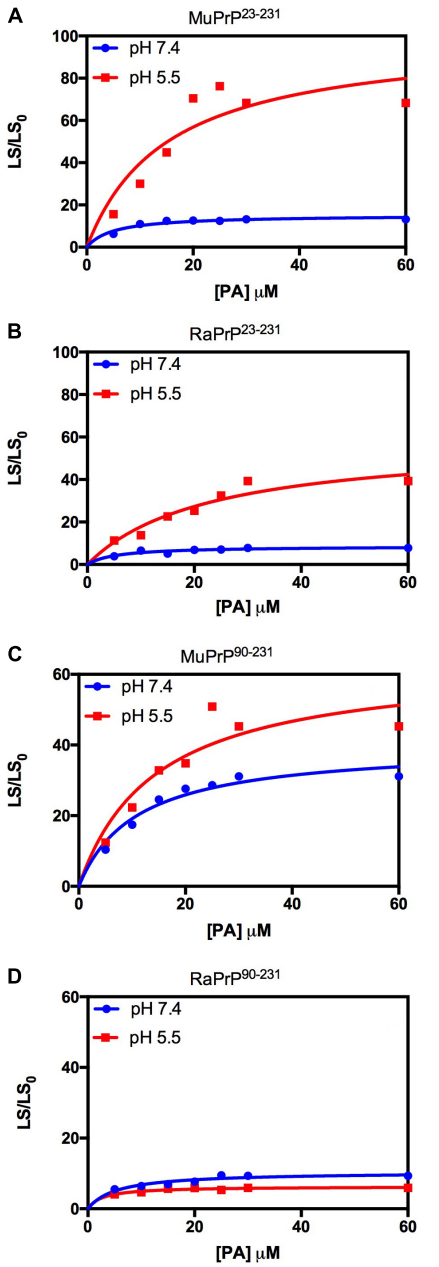

FIGURE 7 | Rabbit PrP$^{90-231}$ aggregates less in the presence of PA. Effect of increasing the concentration of PA on the relative light scattering of MuPrP$^{23-231}$ **(A)**, RaPrP$^{23-231}$ **(B)**, MuPrP$^{90-231}$ **(C)**, and RaPrP$^{90-231}$ **(D)** at pH 5.5 (red) and 7.4 (blue). All proteins were at 2 μM. The experiments were performed in 50 mM Tris buffer containing 100 mM NaCl at pH 7.4 or in 20 mM sodium acetate buffer containing 100 mM NaCl at pH 5.5. All experiments were performed at 25°C. The error bars represent the standard deviation of at least two independent experiments.

many of the studied cofactors (Silva et al., 2011). We observed the same effect for PrP$^{23-231}$ and PrP$^{90-231}$ for both MuPrP and RaPrP, although the overall interaction with cofactors was pronounced in the case of the full-length protein, suggesting that the N-terminal domain is determinant for interaction with cofactors resulting in an increased conversion efficiency, but not related to cofactor-induced aggregation resistance.

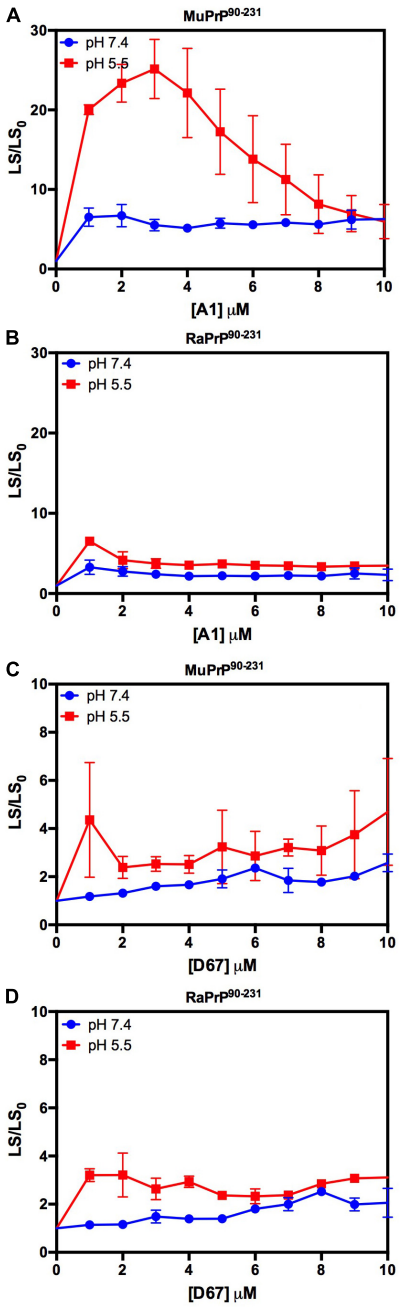

FIGURE 8 | RaPrP$^{90-231}$ aggregates less upon binding to DNA oligonucleotides. Effect of A1 **(A,B)** and D67 **(C,D)** on the relative light scattering of PrP$^{90-231}$. Proteins used are MuPrP **(A,C)** and RaPrP **(B,D)** at pH 5.5 (red) and 7.4 (blue). The curves were performed with 5 μM PrP$^{90-231}$ and increasing concentrations of oligonucleotides (from 1 to 10 μM). The experiments were performed in 50 mM Tris buffer containing 100 mM NaCl at pH 7.4 or 20 mM sodium acetate buffer containing 100 mM NaCl at pH 5.5. All experiments were performed at 25°C. The error bars represent the standard deviation of at least two independent experiments.

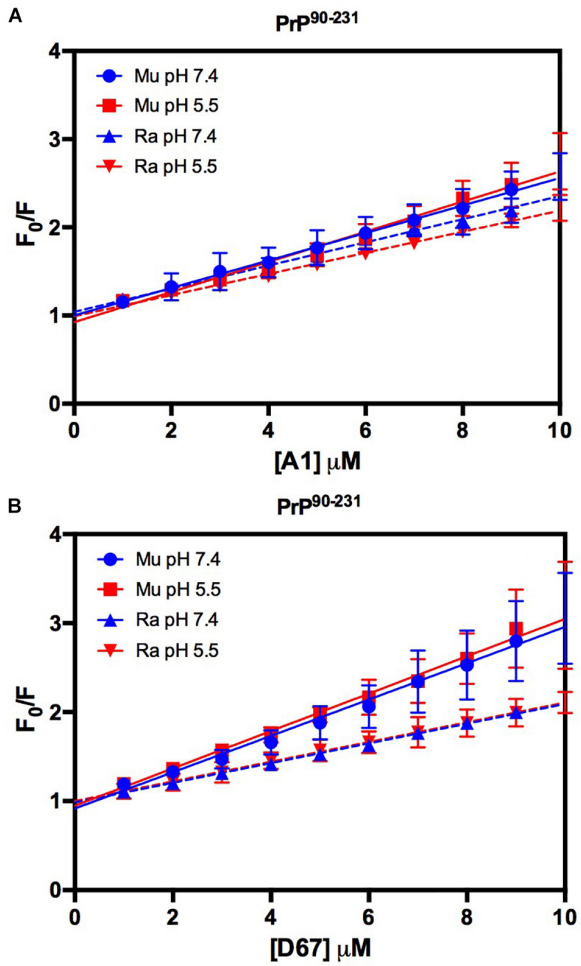

FIGURE 9 | RaPrP$^{90-231}$ interacts less with the DNA oligonucleotides. F_0/F curves for titrations of A1 **(A)** and D67 **(B)** on PrP$^{90-231}$ at pH 5.5 (red) or 7.4 (blue). The curves were performed with 5 μM PrP$^{90-231}$ and increasing concentrations of oligonucleotides (from 1 to 10 μM). The experiments were performed in 50 mM Tris buffer containing 100 mM NaCl at pH 7.4 or 20 mM sodium acetate buffer containing 100 mM NaCl at pH 5.5. All experiments were performed at 25°C. The error bars represent the standard deviation of at least two independent experiments.

Horse PrP has four saline bridges (GLU196 -ARG156-HIS187, ARG156-ASP202, and GLU211-HIS177). RaPrP has a strong ASP177-ARG163 saline bridge, which keeps the β2-α2 loop attached (Zhang, 2011; Zhang and Zhang, 2014). ASP201-ARG155, which connects helices H3 and H1, makes two saline bridges in RaPrP, while MuPrP has only one (**Figure 1**). All these saline bridges contribute to the increased stability in RaPrP, especially at neutral pH, since losing these salt bridges at low pH reduces thermostability (Zhang, 2011; Zhang and Zhang, 2014). This effect of pH was consistent across the cofactors studied. However, even at low pH, aggregation of RaPrP was lower than that of the murine protein, suggesting that other interactions may be important.

Rabbit PrP SER173 forms a double hydrogen bond, forming a helix-capping motif, which decreases the tendency of RaPrP to populate a β-structured state at low pH (Khan et al., 2010). This may also contribute to RaPrP being less prone to

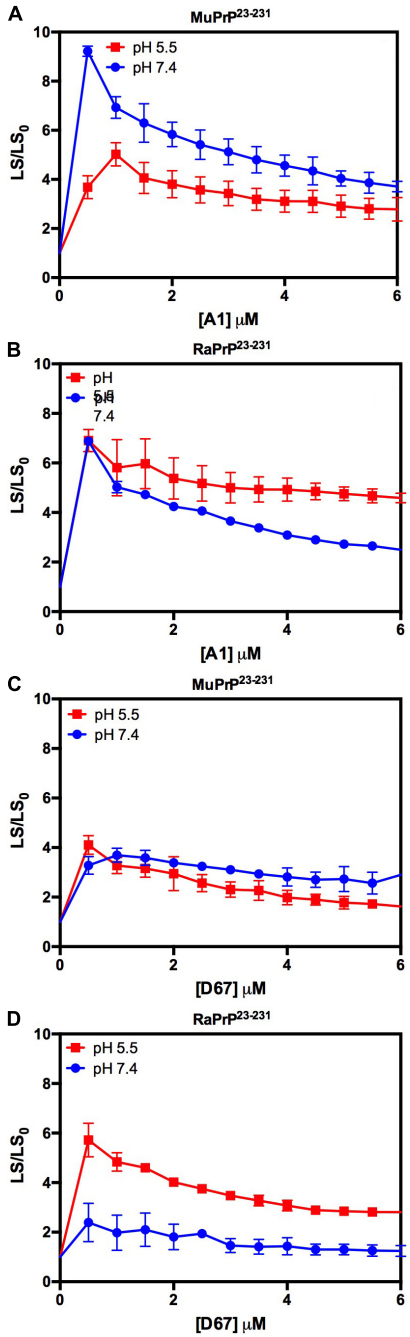

FIGURE 10 | Interaction of PrP^{23-231} with DNA oligonucleotides causes an increase in light scattering. Effect of A1 **(A,B)** and D67 **(C,D)** on the relative light scattering of PrP^{23-231}. Proteins used are MuPrP **(A,C)** and RaPrP **(B,D)** at pH 5.5 (red) and 7.4 (blue). The curves were performed with 2 μM PrP^{23-231} and increasing concentrations of oligonucleotides (from 0.5 to 6 μM). The experiments were performed in 50 mM Tris buffer containing 100 mM NaCl at pH 7.4 or 20 mM sodium acetate buffer containing 100 mM NaCl at pH 5.5. All experiments were performed at 25°C. The error bars represent the standard deviation of at least two independent experiments.

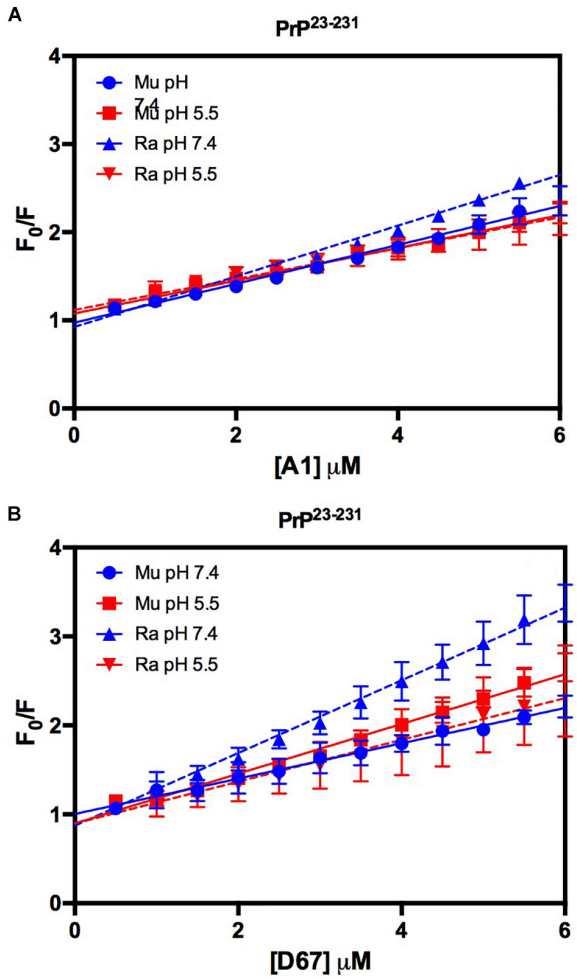

FIGURE 11 | The intrinsic fluorescence of PrP^{23-231} is reduced upon binding to DNA oligonucleotides. F_0/F curves for titrations of A1 **(A)** and D67 **(B)** on PrP^{23-231} at pH 5.5 or 7.4. The curves were performed with 2 μM PrP^{23-231} and increasing concentrations of oligonucleotides (from 0.5 to 6 μM). The experiments were performed in 50 mM Tris buffer containing 100 mM NaCl at pH 7.4 or 20 mM sodium acetate buffer containing 100 mM NaCl at pH 5.5. All experiments were performed at 25°C. The error bars represent the standard deviation of at least two independent experiments.

cofactor-mediated aggregation, as observed here. The interaction site of low molecular weight heparin in the globular region of PrP is close to HIS186 (Vieira et al., 2011). Rabbit PrP shows a less dynamic hydrogen bond between HIS185 and ARG155 than murine PrP at neutral pH (**Figure 1**; Zhang, 2010, 2011). This HIS residue shows reduced pKa (∼5) in different species, and its protonation affects PrP stability. The HIS186ARG mutation, which introduces a positively charged residue, is correlated with familial CJD and destabilizes the murine protein (Singh and Udgaonkar, 2016). This more stable hydrogen bond may hinder the aggregation induced by low molecular weight heparin and other GAGs, although it does not prevent interaction due to residue protonation. The same must be important for the other studied cofactors. The introduction of a positive charge (due to protonation or residue mutation) should favor the interaction with negatively charged cofactors, such as those tested in this study, but

the effect on RaPrP structural conversion and aggregation should be limited.

We observed some differences in the effects of the various cofactors tested. The aggregation profile of PrP in the presence of A1 and D67 was distinct from that in the presence of GAGs or PA. This may be due to differences in the regions of interaction, dissimilar charge and polarity, and/or even in the folding of these molecules. Intriguingly, the overall effect was identical.

We also evaluated the effect of a 21-mer double-stranded and of a 25-mer single-stranded DNA oligonucleotide (D67 and A1, respectively), on PrP aggregation. A1 induced higher aggregation than D67, possibly due to differences in binding affinity and/or DNA conformation (Macedo et al., 2012; M. Passos et al., 2021). Due to secondary structure, length, and sequence, nucleic acids may have different effects on PrP, in the extent of aggregation and toxicity of the aggregated species, as previously shown (Gomes et al., 2008; Macedo et al., 2012).

Interaction with PA induces PrP aggregation, but in a different manner than observed with GAGs and nucleic acids. The changes induced by PA led to a blue shift and increased fluorescence, suggesting more pronounced structural changes. PA interacted with full-length and truncated PrP, with a five-fold higher affinity at pH 7.4, contrasting with observations with phosphatidylserine, another anionic lipid, which actively interacted with human PrP^{20-231} at pH 5.0 but showed no interaction with human PrP^{90-231} (Morillas et al., 1999). The negative head group in PA may interact with positively charged amino acids. The N-terminal domain of PrP has two positively charged clusters, one between residues 23 and 30 and the other between residues 101 and 110, both of which are candidate sites for the interaction with PA, possibly explaining the differences observed with the two PrP constructs (full-length and truncated). Interestingly, dipolar phospholipids have also been shown to interact with and induce PrP aggregation (Kazlauskaite et al., 2003; Tsiroulnikov et al., 2009), indicating that the effect may not be necessarily related to the charge of the polar head group.

The present study is the first report of the direct interaction *in vitro* of dermatan sulfate with PrP. Dermatan sulfate is a GAGs found in the central nervous system, important for brain physiology, but is also involved in diseases that involve deficiency in the degradation of GAGs and consequent accumulation in endocytic vesicles - such as ataxia, intellectual disabilities, spasticity and other neurological symptoms are found in patients with mucopolysaccharidoses (Rauch and Kappler, 2006; Schwartz and Domowicz, 2018). Dermatan sulfate enhances the efficiency of PrP conversion by PMCA (Yokoyama et al., 2011), but there is no information available on its interaction with PrP and on the importance of this interaction for prion replication *in vivo*.

Our data also show that the interaction of PrP with dermatan sulfate leads to a similar effect to that observed with heparin, although with lower affinity and reduced aggregation. The interaction was not observed at pH 7.4, suggesting that structural differences between these GAGs are important at a neutral pH. Low molecular weight heparin binds to the octarepeat region of PrP at pH 7.4, and to helices H2 and H3 at pH 5.5 (Vieira et al., 2011). The fact that interactions with dermatan sulfate only took place at pH 5.5, with a higher affinity for PrP^{23-231}, suggests that N- and C-terminal domains must be available to allow interaction. Interestingly, the differences observed for dermatan sulfate may be related to a relevant role in prion pathology.

CONCLUSION

In summary, our findings demonstrate that most cofactors induce milder effects on RaPrP. Aggregation of RaPrP is weaker than that of MuPrP, specifically at acidic pH, suggesting that the mechanism involved in resistance to cofactors may be linked to RaPrP conformational/structural stability at low pH, and less to the physicochemical characteristics of the cofactors. The decreased effect of cofactors contributes to a better understanding of PrP conversion mechanisms and susceptibility among different mammalian species.

DATA AVAILABILITY STATEMENT

The original contributions presented in the study are included in the article/**Supplementary Material**, further inquiries can be directed to the corresponding author/s.

AUTHOR CONTRIBUTIONS

JA and YP: data collection and analysis and manuscript writing. JB: data collection. JS: data analysis and study design. YC: data analysis, study design, and manuscript writing. TV: data collection and analysis, study design, and manuscript writing. All authors read and approved the final manuscript.

FUNDING

This work is supported by the Coordenação de Aperfeiçoamento de Pessoal de Nível Superior – Brazil (CAPES) (Finance Code 001), Fundação de Amparo à Pesquisa do Estado do Rio de Janeiro (FAPERJ), and the Conselho Nacional de Desenvolvimento Científico e Tecnológico (CNPq).

SUPPLEMENTARY MATERIAL

The Supplementary Material for this article can be found online at: https://www.frontiersin.org/articles/10.3389/fnins.2021.689315/full#supplementary-material

Supplementary Figure 1 | Effect of Hep (1 μM) **(A)** and DS (1 μM) **(B)** on the aggregation of $RaPrP^{23-231}$ (0.5 μM) at pH 5.5 monitored by light scattering (LS) over time. **(C)** Turbidimetry of disaggregated samples acquired on a spectrophotometer at 600 nm, after 18 h of incubation in low binding Eppendorfs. The experiments were performed in 50 mM Tris buffer containing 100 mM NaCl at pH 7.4 or 20 mM sodium acetate buffer containing 100 mM NaCl at pH 5.5. All experiments were performed at 25°C. Representative data from three experiments.

Supplementary Figure 2 | Interaction with PA leads to increased tryptophan fluorescence and spectral shift to lower wavelengths. **(A–D)** Spectra based on the intrinsic tryptophan fluorescence emissions of murine **(A,C)** and rabbit **(B,D)** PrP^{23-231} **(A,B)** and PrP^{90-231} **(C,D)**. Self-normalized spectra of murine **(E,G)** and rabbit **(F,H)** PrP^{23-231} **(E,F)** and PrP^{90-231} **(G,H)**. Solid lines represent PrP alone. Dashed lines represent PrP in the presence of PA. All proteins were at 2 mM and PA at 30 mM. The experiments were performed in 50 mM Tris buffer containing 100 mM NaCl at pH 7.4 or in 20 mM sodium acetate buffer containing 100 mM NaCl at pH 5.5. All experiments were performed at 25°C. Representative data from three experiments.

Supplementary Figure 3 | PrP^{90-231} intrinsic fluorescence reduction effect is caused by DNA oligonucleotides. Percentage curves of the PrP total intrinsic fluorescence intensity for titrations at pH 5.5 or 7.4. **(A)** $MuPrP^{90-231}$ and **(B)** $RaPrP^{90-231}$ 5 μM PrP^{90-231}. The experiments were performed in 50 mM Tris buffer containing 100 mM NaCl at pH 7.4 or 20 mM sodium acetate buffer containing 100 mM NaCl at pH 5.5. All experiments were performed at 25°C.

REFERENCES

Bian, J., Khaychuk, V., Angers, R. C., Fernández-Borges, N., Vidal, E., Meyerett-Reid, C., et al. (2017). Prion replication without host adaptation during interspecies transmissions. *Proc. Natl. Acad. Sci. U.S.A.* 114, 1141–1146. doi: 10.1073/pnas.1611891114

Castilla, J., and Requena, J. R. (2015). Prion-like diseases: Looking for their niche in the realm of infectious diseases. *Virus Res.* 207, 1–4. doi: 10.1016/j.virusres.2015.06.001

Castilla, J., Saá, P., Hetz, C., and Soto, C. (2005). In vitro generation of infectious scrapie prions. *Cell.* 121, 195–206. doi: 10.1016/j.cell.2005.02.011

Cavaliere, P., Pagano, B., Granata, V., Prigent, S., Rezaei, H., Giancola, C., et al. (2013). Cross-talk between prion protein and quadruplex-forming nucleic acids: a dynamic complex formation. *Nucleic Acids Res.* 41, 327–339. doi: 10.1093/nar/gks970

Chen, S., Mange, A., Dong, L., Lehmann, S., and Schachner, M. (2003). Prion protein as trans-interacting partner for neurons is involved in neurite outgrowth and neuronal survival. *Mol.Cell Neurosci.* 22, 227–233. doi: 10.1016/s1044-7431(02)00014-3

Chianini, F., Fernández-Borges, N., Eraña, H., Pang, Y., Vidal, E., Eaton, S. L., et al. (2013). Prion-resistant or prion-susceptible species, this is the question. *Virulence.* 4, 333–334. doi: 10.4161/viru.24456

Chianini, F., Fernández-Borges, N., Vidal, E., Gibbard, L., Pintado, B., De Castro, J., et al. (2012). Rabbits are not resistant to prion infection. *Proc. Natl. Acad. Sci. U.S.A.* 109, 5080–5085. doi: 10.1073/pnas.1120076109

Cordeiro, Y., Machado, F., Juliano, L., Juliano, M. A., Brentani, R. R., Foguel, D., et al. (2001). DNA converts cellular prion protein into the beta-sheet conformation and inhibits prion peptide aggregation. *J.Biol.Chem.* 276, 49400–49409. doi: 10.1074/jbc.M106707200

Cordeiro, Y., and Silva, J. L. (2005). The hypothesis of the catalytic action of nucleic acid on the conversion of prion protein. *Protein Pept.Lett.* 12, 251–255. doi: 10.2174/0929866053587138

Deleault, N. R., Harris, B. T., Rees, J. R., and Supattapone, S. (2007). Formation of native prions from minimal components in vitro. *Proc.Natl.Acad.Sci.U.S.A* 104, 9741–9746. doi: 10.1073/pnas.0702662104

Eraña, H., Fernández-Borges, N., Elezgarai, S. R., Harrathi, C., Charco, J. M., Chianini, F., et al. (2017). J. *Virol.* 91, e1543–e1517. doi: 10.1128/jvi.01543-17

Fernandez-Funez, P., Zhang, Y., Sanchez-Garcia, J., Jensen, K., Zou, W. Q., and Rincon-Limas, D. E. (2011). Pulling rabbits to reveal the secrets of the prion protein. *Commun Integr Biol* 4, 262–266. doi: 10.4161/cib.4.3.15054

Gibbs, C. J. Jr., and Gajdusek, D. C. (1973). Experimental subacute spongiform virus encephalopathies in primates and other laboratory animals. *Science.* 182, 67–68. doi: 10.1126/science.182.4107.67

Gjerde, D. T., Hoang, L., and Hornby, D. (2009). "Chromatographic separation equations and principles for rna separation," in *RNA Purification and Analysis: Sample Preparation, Extraction, Chromatography*, (Weinheim: Wiley-VCH), doi: 10.1002/9783527627196 *.

Godsave, S. F., Peters, P. J., and Wille, H. (2015). Subcellular distribution of the prion protein in sickness and in health. *Virus Res* 207, 136–145. doi: 10.1016/j.virusres.2015.02.004

Gomes, M. P. B., Millen, T. A., Ferreira, P. S., Cunha, E., Silva, N. L., Vieira, T. C. R. G., et al. (2008). Prion protein complexed to N2a cellular RNAs through its N-terminal domain forms aggregates and is toxic to murine neuroblastoma cells. *J. Biol. Chem.* 283, 19616–19625.

Hirschfield, G. M., and Hawkins, P. N. (2003). Amyloidosis: new strategies for treatment. *Int.J.Biochem.Cell Biol.* 35, 1608–1613. doi: 10.1016/s1357-2725(03)00169-9

Hornemann, S., Korth, C., Oesch, B., Riek, R., Wider, G., Wuthrich, K., et al. (1997). Recombinant full-length murine prion protein, mPrP(23-231): purification and spectroscopic characterization. *FEBS Lett.* 413, 277–281. doi: 10.1016/s0014-5793(97)00921-6

Horonchik, L., Tzaban, S., Ben Zaken, O., Yedidia, Y., Rouvinski, A., Papy-Garcia, D., et al. (2005). Heparan sulfate is a cellular receptor for purified infectious prions. *J.Biol.Chem.* 280, 17062–17067. doi: 10.1074/jbc.M500122200

Jameson, D. M. (2014). *Introduction to Fluorescence*. Boca Raton FL: CRC Press, doi: 10.1201/b16502

Kazlauskaite, J., Sanghera, N., Sylvester, I., Vénien-Bryan, C., and Pinheiro, T. J. (2003). Structural changes of the prion protein in lipid membranes leading to aggregation and fibrillization. *Biochemistry* 42, 3295–3304. doi: 10.1021/bi026872q

Khan, M. Q., Sweeting, B., Mulligan, V. K., Arslan, P. E., Cashman, N. R., Pai, E. F., et al. (2010). Prion disease susceptibility is affected by β-structure folding propensity and local side-chain interactions in PrP. *Proc. Natl. Acad. Sci. U. S. A.* 107, 19808–19813. doi: 10.1073/pnas.1005267107

Kim, S. Y., Zhang, F., Harris, D. A., and Linhardt, R. J. (2020). Structural Features of Heparin and Its Interactions With Cellular Prion Protein Measured by Surface Plasmon Resonance. *Front. Mol. Biosci.* 7:594497. doi: 10.3389/fmolb.2020.594497

Lawson, V. A., Priola, S. A., Wehrly, K., and Chesebro, B. (2001). N-terminal truncation of prion protein affects both formation and conformation of abnormal protease-resistant prion protein generated in vitro. *J.Biol.Chem.* 276, 35265–35271. doi: 10.1074/jbc.M103799200

Lima, L. M. T. R., Cordeiro, Y., Tinoco, W. L., Marques, A. F., Oliveira, C. L., Sampath, S., et al. (2006). Structural Insights into the Interaction between Prion Protein and Nucleic Acid. *Biochemistry* 45, 9180–9187. doi: 10.1021/BI060532D

Linden, R. (2017). The Biological Function of the Prion Protein: A Cell Surface Scaffold of Signaling Modules. *Front Mol. Neurosci.* 10:77. doi: 10.3389/fnmol.2017.00077

Linden, R., Martins, V. R., Prado, M. A., Cammarota, M., Izquierdo, I., and Brentani, R. R. (2008). Physiology of the prion protein. *Physiol. Rev.* 88, 673–728. doi: 10.1152/physrev.00007.2007

Loftus, B., and Rogers, M. (1997). Characterization of a prion protein (PrP) gene from rabbit; A species with apparent resistance to infection by prions. *Gene* 184, 215–219. doi: 10.1016/S0378-1119(96)00598-7

Lopes, M. H., Hajj, G. N. M., Muras, A. G., Mancini, G. L., Castro, R. M. P. S., Ribeiro, K. C. B., et al. (2005). Interaction of cellular prion and stress-inducible protein 1 promotes neuritogenesis and neuroprotection by distinct signaling pathways. *J. Neurosci.* 25, 11330–11339. doi: 10.1523/JNEUROSCI.2313-05.2005

M. Passos, Y., J. do Amaral, M., C. Ferreira, N., Macedo, B., Chaves, J. A. P., E. de Oliveira, V., et al. (2021). The interplay between a GC-rich oligonucleotide and copper ions on prion protein conformational and phase transitions. *Int. J. Biol. Macromol.* 173, 34–43. 10.1016/j.ijbiomac.2021.01.097

Macedo, B., Millen, T. A., Braga, C. A. C. A., Gomes, M. P. B., Ferreira, P. S., Kraineva, J., et al. (2012). Nonspecific Prion Protein–Nucleic Acid Interactions Lead to Different Aggregates and Cytotoxic Species. *Biochemistry* 51, 5402–5413. doi: 10.1021/bi300440e

Matos, C. O., Passos, Y. M., Amaral, M. J., Macedo, B., Tempone, M. H., Bezerra, O. C. L., et al. (2020). Liquid-liquid phase separation and fibrillation of the prion protein modulated by a high-affinity DNA aptamer. *FASEB J.* 34, 365–385. doi: 10.1096/fj.201901897R

Miller, M. B., Wang, D. W., Wang, F., Noble, G. P., Ma, J., Woods, V. L., et al. (2013). Cofactor molecules induce structural transformation during infectious prion formation. *Structure* 21, 2061–2068. doi: 10.1016/j.str.2013.08.025

Morillas, M., Swietnicki, W., Gambetti, P., and Surewicz, W. K. (1999). Membrane environment alters the conformational structure of the recombinant human prion protein. *J. Biol. Chem.* 274, 36859–36865. doi: 10.1074/jbc.274.52.36859

Myers, R., Cembran, A., and Fernandez-Funez, P. (2020). Insight From Animals Resistant to Prion Diseases: Deciphering the Genotype – Morphotype – Phenotype Code for the Prion Protein. *Front. Cell. Neurosci.* 14:254. doi: 10.3389/fncel.2020.00254

Nandi, P. K., Leclerc, E., Nicole, J. C., and Takahashi, M. (2002). DNA-induced partial unfolding of prion protein leads to its polymerisation to amyloid. *J.Mol.Biol.* 322, 153–161. doi: 10.1016/s0022-2836(02)00750-7

Nishina, K., Deleault, N. R., Lucassen, R. W., and Supattapone, S. (2004). In vitro prion protein conversion in detergent-solubilized membranes. *Biochemistry* 43, 2613–2621. doi: 10.1021/bi035889l

Pastore, A., and Zagari, A. (2007). A structural overview of the vertebrate prion proteins. *Prion.* 1, 185–197. doi: 10.4161/pri.1.3.5281

Polymenidou, M., Trusheim, H., Stallmach, L., Moos, R., Julius, C., Miele, G., et al. (2008). Canine MDCK cell lines are refractory to infection with human and mouse prions. *Vaccine* 26, 2601–2614. doi: 10.1016/j.vaccine.2008.03.035

Prusiner, S. B. (1982). Novel proteinaceous infectious particles cause scrapie. *Science.* 216, 136–144. doi: 10.1126/science.6801762

Prusiner, S. B. (1991). Molecular biology of prion diseases. *Science.* 252, 1515–1522. doi: 10.1126/science.1675487

Rauch, U., and Kappler, J. (2006). Chondroitin/Dermatan Sulfates in the Central Nervous System: Their Structures and Functions in Health and Disease. *Adv. Pharmacol.* 53, 337–356. doi: 10.1016/S1054-3589(05)53016-3

Saá, P., Castilla, J., and Soto, C. (2006). Ultra-efficient replication of infectious prions by automated protein misfolding cyclic amplification. *J. Biol. Chem.* 281, 35245–35252. doi: 10.1074/jbc.M603964200

Satoh, J., Obayashi, S., Misawa, T., Sumiyoshi, K., Oosumi, K., and Tabunoki, H. (2009). Protein microarray analysis identifies human cellular prion protein interactors. *Neuropathol Appl Neurobiol* 35, 16–35. doi: 10.1111/j.1365-2990.2008.00947.x

Schwartz, N. B., and Domowicz, M. S. (2018). Proteoglycans in brain development and pathogenesis. *FEBS Lett.* 592, 3791–3805.

Shyng, S. L., Huber, M. T., and Harris, D. A. (1993). A prion protein cycles between the cell surface and an endocytic compartment in cultured neuroblastoma cells. *J.Biol.Chem.* 268, 15922–15928. doi: 10.1016/s0021-9258(18)82340-7

Sigurdson, C. J., and Miller, M. W. (2003). Other animal prion diseases. *Br. Med. Bull.* 66, 199–212. doi: 10.1093/bmb/66.1.199

Silva, J. L., and Cordeiro, Y. (2016). The "Jekyll and Hyde" Actions of Nucleic Acids on the Prion-like Aggregation of Proteins. *J Biol Chem* 291, 15482–15490. doi: 10.1074/jbc.R116.733428

Silva, J. L. L. J. L., Gomes, M. P. B. M. P. B., Vieira, T. C. R. G. T. C. R. G., and Cordeiro, Y. (2010). PrP interactions with nucleic acids and glycosaminoglycans in function and disease. *Front. Biosci.* 15:132–150. doi: 10.2741/3611

Silva, J. L., Vieira, T. C., Gomes, M. P., Rangel, L. P., Scapin, S. M., and Cordeiro, Y. (2011). Experimental approaches to the interaction of the prion protein with nucleic acids and glycosaminoglycans: Modulators of the pathogenic conversion. *Methods.* 53, 306–317. doi: 10.1016/j.ymeth.2010.12.002

Singh, J., and Udgaonkar, J. B. (2016). Unraveling the Molecular Mechanism of pH-Induced Misfolding and Oligomerization of the Prion Protein. *J. Mol. Biol.* 428, 1345–1355. doi: 10.1016/j.jmb.2016.01.030

Srivastava, K. R., and Lapidus, L. J. (2017). Prion protein dynamics before aggregation. *Proc. Natl. Acad. Sci. U. S. A.* 114, 3572–3577. doi: 10.1073/pnas.1620400114

Supattapone, S. (2014). Elucidating the role of cofactors in mammalian prion propagation. *Prion.* 8, 100–105. doi: 10.4161/pri.27501

Sweeting, B., Khan, M. Q., Chakrabartty, A., and Pai, E. F. (2010). Structural factors underlying the species barrier and susceptibility to infection in prion disease. *Biochemistry and Cell Biology.* 88, 195–202. doi: 10.1139/O09-172

Tsiroulnikov, K., Shchutskaya, Y., Muronetz, V., Chobert, J. M., and Haertlé, T. (2009). Phospholipids influence the aggregation of recombinant ovine prions. From rapid extensive aggregation to amyloidogenic conversion. *Biochim Biophys Acta* 1794, 506–511. doi: 10.1016/j.bbapap.2008.12.002

Vidal, E., Fernández-Borges, N., Pintado, B., Eraña, H., Ordóñez, M., Márquez, M., et al. (2015). Transgenic Mouse Bioassay: Evidence That Rabbits Are Susceptible to a Variety of Prion Isolates. *PLoS Pathog.* 11:e1004977. doi: 10.1371/journal.ppat.1004977

Vieira, T. C., Cordeiro, Y., Caughey, B., and Silva, J. L. (2014). Heparin binding confers prion stability and impairs its aggregation. *FASEB J* 28, 2667–2676. doi: 10.1096/fj.13-246777

Vieira, T. C. R. G. C. R. G., and Silva, J. L. L. (2019). In Vitro Prion Amplification Methodology for Inhibitor Screening. *Methods Mol Biol* 1873, 305–316. doi: 10.1007/978-1-4939-8820-4_20

Vieira, T. C. R. G., Reynaldo, D. P., Gomes, M. P. B., Almeida, M. S., Cordeiro, Y., and Silva, J. L. (2011). Heparin Binding by Murine Recombinant Prion Protein Leads to Transient Aggregation and Formation of RNA-Resistant Species. *J. Am. Chem. Soc.* 133, 334–344. doi: 10.1021/ja106725p

Vieira, T., and Silva, J. (2016). "Glycosaminoglycans in Prion and Prion-Like Diseases," in *The Prion Phenomena in Neurodegenerative Diseases*, ed. G. G. Giuseppe Legname (Hauppauge NY: Nova Science Pub Inc), 67–87.

Vorberg, I., Groschup, M. H., Pfaff, E., and Priola, S. A. (2003). Multiple amino acid residues within the rabbit prion protein inhibit formation of its abnormal isoform. *J Virol* 77, 2003–2009. doi: 10.1128/jvi.77.3.2003-2009.2003

Wang, F., Yang, F., Hu, Y., Wang, X., Wang, X., Jin, C., et al. (2007). Lipid interaction converts prion protein to a PrPSc-like proteinase k-resistant conformation under physiological conditions. *Biochemistry.* 6, 7045–7053. doi: 10.1021/bi700299h

Wen, Y., Li, J., Xiong, M., Peng, Y., Yao, W., Hong, J., et al. (2010a). Solution structure and dynamics of the I214V mutant of the rabbit prion protein. *PLoS One* 5:e13273. doi: 10.1371/journal.pone.0013273

Wen, Y., Li, J., Yao, W., Xiong, M., Hong, J., Peng, Y., et al. (2010b). Unique structural characteristics of the rabbit prion protein. *J. Biol. Chem.* 285, 31682–31693. doi: 10.1074/jbc.M110.118844

Wulf, M. A., Senatore, A., and Aguzzi, A. (2017). The biological function of the cellular prion protein: an update. *BMC Biol* 15:34. doi: 10.1186/s12915-017-0375-5

Yan, X., Huang, J.-J., Zhou, Z., Chen, J., and Liang, Y. (2014). How Does Domain Replacement Affect Fibril Formation of the Rabbit/Human Prion Proteins. *PLoS One.* 9:e113238. doi: 10.1371/journal.pone.0113238.001

Yin, S., Fan, X., Yu, S., Li, C., and Sy, M. S. (2008). Binding of recombinant but not endogenous prion protein to DNA causes DNA internalization and expression in mammalian cells. *J.Biol.Chem.* 283, 25446–25454. doi: 10.1074/jbc.M800814200

Yokoyama, T., Takeuchi, A., Yamamoto, M., Kitamoto, T., Ironside, J. W., and Morita, M. (2011). Heparin enhances the cell-protein misfolding cyclic amplification efficiency of variant Creutzfeldt-Jakob disease. *Neurosci Lett* 498, 119–123. doi: 10.1016/j.neulet.2011.04.072

Yuan, Z., Zhao, D., and Yang, L. (2013). Decipher the mechanisms of rabbit's low susceptibility to prion infection. *Acta Biochim. Biophys. Sin. (Shanghai).* 45, 899–903. doi: 10.1093/abbs/gmt093

Zhang, J. (2010). Studies on the structural stability of rabbit prion probed by molecular dynamics simulations of its wild-type and mutants. *J. Theor. Biol.* 264, 119–122. doi: 10.1016/j.jtbi.2010.01.024

Zhang, J. (2011). Comparison studies of the structural stability of rabbit prion protein with human and mouse prion proteins. *J. Theor. Biol.* 269, 88–95. doi: 10.1016/j.jtbi.2010.10.020

Zhang, J., and Zhang, Y. (2014). Molecular dynamics studies on the NMR and X-ray structures of rabbit prion proteins. *J. Theor. Biol.* 342, 70–82. doi: 10.1016/j.jtbi.2013.10.005

Conflict of Interest: The authors declare that the research was conducted in the absence of any commercial or financial relationships that could be construed as a potential conflict of interest.

frontiers in Neuroscience

ORIGINAL RESEARCH
published: 22 June 2021
doi: 10.3389/fnins.2021.682172

Small, Seeding-Competent Huntingtin Fibrils Are Prominent Aggregate Species in Brains of zQ175 Huntington's Disease Knock-in Mice

*Franziska Schindler[1], Nicole Praedel[1], Nancy Neuendorf[1], Severine Kunz[1], Sigrid Schnoegl[1], Michael A. Mason[2], Bridget A. Taxy[2], Gillian P. Bates[2], Ali Khoshnan[3], Josef Priller[4,5,6], Jan Grimm[7], Marcel Maier[7], Annett Boeddrich[1] and Erich E. Wanker[1]**

[1] Neuroproteomics, Max Delbrück Center for Molecular Medicine in the Helmholtz Association, Berlin, Germany, [2] Huntington's Disease Centre, Department of Neurodegenerative Disease, UK Dementia Research Centre, UCL Queen Square Institute of Neurology, University College London, London, United Kingdom, [3] Division of Biology and Biological Engineering, California Institute of Technology, Pasadena, CA, United States, [4] Department of Psychiatry and Psychotherapy, Klinikum Rechts der Isar, Technical University of Munich, Munich, Germany, [5] Charité–Universitätsmedizin Berlin and DZNE, Berlin, Germany, [6] The University of Edinburgh, UK Dementia Research Institute, Edinburgh, United Kingdom, [7] Neurimmune AG, Schlieren, Switzerland

OPEN ACCESS

Edited by:
Cláudio M. Gomes,
University of Lisbon, Portugal

Reviewed by:
Rakez Kayed,
University of Texas Medical Branch at Galveston, United States
Federico Herrera,
University of Lisbon, Portugal

***Correspondence:**
Erich E. Wanker
erich.w@mdc-berlin.de

Specialty section:
This article was submitted to Neurodegeneration, a section of the journal Frontiers in Neuroscience

Received: 17 March 2021
Accepted: 31 May 2021
Published: 22 June 2021

Citation:
Schindler F, Praedel N, Neuendorf N, Kunz S, Schnoegl S, Mason MA, Taxy BA, Bates GP, Khoshnan A, Priller J, Grimm J, Maier M, Boeddrich A and Wanker EE (2021) Small, Seeding-Competent Huntingtin Fibrils Are Prominent Aggregate Species in Brains of zQ175 Huntington's Disease Knock-in Mice. Front. Neurosci. 15:682172. doi: 10.3389/fnins.2021.682172

The deposition of mutant huntingtin (mHTT) protein aggregates in neurons of patients is a pathological hallmark of Huntington's disease (HD). Previous investigations in cell-free and cell-based disease models showed mHTT exon-1 (mHTTex1) fragments with pathogenic polyglutamine (polyQ) tracts (>40 glutamines) to self-assemble into highly stable, β-sheet-rich protein aggregates with a fibrillar morphology. HD knock-in mouse models have not been extensively studied with regard to mHTT aggregation. They endogenously produce full-length mHTT with a pathogenic polyQ tract as well as mHTTex1 fragments. Here, we demonstrate that seeding-competent, fibrillar mHTT aggregates can be readily detected in brains of zQ175 knock-in HD mice. To do this, we applied a highly sensitive FRET-based protein amplification assay that is capable of detecting seeding-competent mHTT aggregate species down to the femtomolar range. Furthermore, we show that fibrillar structures with an average length of ∼200 nm can be enriched with aggregate-specific mouse and human antibodies from zQ175 mouse brain extracts through immunoprecipitations, confirming that such structures are formed *in vivo*. Together these studies indicate that small, fibrillar, seeding-competent mHTT structures are prominent aggregate species in brains of zQ175 mice.

Keywords: Huntington's disease, aggregates, seeding, mHTT, zQ175, brain, protein misfolding, FRASE assay

INTRODUCTION

Huntington's disease (HD) is a progressive neurodegenerative disorder that is characterized by motor, cognitive and psychiatric manifestations (Ross and Tabrizi, 2011; McColgan and Tabrizi, 2018). The disease is caused by a CAG repeat expansion encoding a polyglutamine (polyQ) tract within the N-terminus of huntingtin (HTT), a large α-helical protein (Guo et al., 2018), which plays a functional role in transcription regulation, autophagy and axonal transport processes (Saudou and Humbert, 2016).

Large neuronal intranuclear inclusion bodies (IBs) that contain mutant HTT (mHTT) protein aggregates, molecular chaperones and ubiquitin are the prominent hallmark of the pathology in HD patient brains (DiFiglia et al., 1997; Sieradzan et al., 1999), suggesting that misfolding and abnormal aggregation of mHTT may contribute to pathogenesis or even drive the disease process (Wanker et al., 2019). Besides nuclear IBs, however, also neuropil structures with mHTT aggregates and cytoplasmic IBs are commonly detected in neurons (Gutekunst et al., 1999), demonstrating that different types of mHTT aggregates are formed in HD patient brains that may have distinct roles in pathogenesis. This view is supported by studies in transgenic and knock-in (KI) HD mice, indicating that formation of neuropil mHTT aggregates is an early pathological event associated with axonal degeneration (Li et al., 2001; Tallaksen-Greene et al., 2005).

Our current understanding of HD is largely based on studies of mHTT-induced pathogenesis in transgenic and KI mouse models (Farshim and Bates, 2018). Among these, the KI mouse models carry expanded CAG repeats contained within the native murine *Htt* gene (Menalled et al., 2003; Heng et al., 2007). Thus, in comparison to transgenic models that were generated by inserting either a fragment or a full-length copy of the human *HTT* gene into the mouse genome (Mangiarini et al., 1996) they are closer to the situation in patients because they express the CAG mutation in the appropriate genetic context (Menalled et al., 2003; Farshim and Bates, 2018). The zQ175 KI line is a particularly useful model to study the molecular mechanisms of HD since it exhibits extensive behavioral, histopathological and molecular phenotypes reminiscent of human disease (Menalled, 2005; Heikkinen et al., 2012). Amongst the defects reported, zQ175 mice display behavioral deficits, especially in the dark phase of the diurnal cycle, from 4.5 months of age and overt rotarod impairments by 8 months of age (Menalled et al., 2012). Also, a progressive increase of nuclear and extranuclear inclusions with mHTT aggregates was observed in the striatum and cortex of zQ175 heterozygous mice (Carty et al., 2015), indicating that abnormal mHTT aggregation is associated with the appearance of disease symptoms in this model.

Currently, it remains unclear whether different types of mHTT aggregate species play a role in the observed disease process in zQ175 KI mice. Previous evidence has been obtained that N-terminal mHTT exon-1 (mHTTex1) fragments spontaneously self-assemble into stable β-sheet fibrillar structures *in vitro* and *in vivo* (Scherzinger et al., 1997, 1999; Waelter et al., 2001) and are also able to spread from cell to cell (Babcock and Ganetzky, 2015; Maxan et al., 2020). Whether such seeding- and spreading-competent structures are directly involved in pathogenesis is still a matter of debate (Hoffner and Djian, 2015). The formation of small seeding-competent mHTTex1 fibrils in adult neurons was recently shown to dramatically shorten the lifespan of HD transgenic flies (Ast et al., 2018), suggesting that similar structures may also contribute to pathogenesis in brains of zQ175 KI mice.

Here, we utilized a recently developed Förster resonance energy transfer (FRET)-based protein aggregate amplification assay (FRASE) (Ast et al., 2018) as well as various biochemical techniques to investigate whether seeding-competent, fibrillar mHTT aggregates are formed in brains of zQ175 mice. We found that such structures are detectable in brain extracts prepared from zQ175 KI mice but not in age-matched controls. Also, utilizing immunoprecipitation experiments, fibrillar, seeding-competent mHTT aggregates were enriched from zQ175 mouse brain extracts with various aggregate-specific mHTT antibodies, supporting our hypothesis that such structures are formed *in vivo*. Our findings will enable future studies to evaluate the effects of therapeutic molecules both on mHTT fibrillogenesis and disease symptoms in zQ175 KI mice.

RESULTS

Preformed Recombinant mHTTex1 Fibrils Stimulate Ex1Q48-CyPet/-YPet Co-aggregation in FRASE Assays

Previously, we have developed a FRET-based mHTT aggregate seeding assay (FRASE) that enables the quantification of mHTT seeding activity (HSA) in complex biosamples such as crude human brain extracts (Ast et al., 2018). For quantification of HSA, two purified glutathione S-transferase (GST)-tagged HTT exon-1 fusion proteins with 48 glutamines C-terminally fused to CyPet and YPet (GST-Ex1Q48-CyPet and -YPet) are utilized as reporter proteins (**Figure 1A**). They are soluble in aqueous solutions as long as they contain the N-terminal GST tag. When they are cleaved with PreScission protease (PP) the Ex1Q48-CyPet and -YPet fragments are released and they spontaneously form SDS-stable fibrillar co-aggregates after a lag phase of 8–10 h in a time-dependent manner. Their co-aggregation can be quantified by measuring FRET as the fluorescent tags CyPet and YPet are brought into close proximity when fibrillar mHTTex1 aggregates are formed (**Figure 1A**). Time-dependent co-aggregation can be accelerated by the addition of preformed fibrillar mHTT seeds, which function as templates for the conversion of the reporter proteins from a soluble into an aggregated state (Wagner et al., 2018). To benchmark the assay, control experiments with preformed fibrillar mHTTex1 seeds were performed. First, the recombinant fusion proteins GST-Ex1Q48-CyPet and -YPet were produced in *Escherichia coli* and purified to ∼90% homogeneity using glutathione agarose columns. Furthermore, GST-tagged HTTex1 fusion protein with 48 glutamines (GST-Ex1Q48) was produced and purified from *E. coli* protein extracts. This protein was later utilized for the production of recombinant seeds to stimulate the co-aggregation of the reporter proteins Ex1Q48-CyPet and -YPet in FRASE assays (**Figure 1A**). All purified recombinant fusion proteins were characterized by SDS-PAGE and Coomassie blue R staining. The fusion proteins GST-Ex1Q48-CyPet and -YPet migrated at ∼80 kDa in SDS-gels (**Supplementary Figure 1A**), while for the GST-Ex1Q48 fusion protein a molecular weight of ∼60 kDa was determined. The purified GST fusion proteins' molecular mass corresponds to the molecular weights expected from their amino acid sequence.

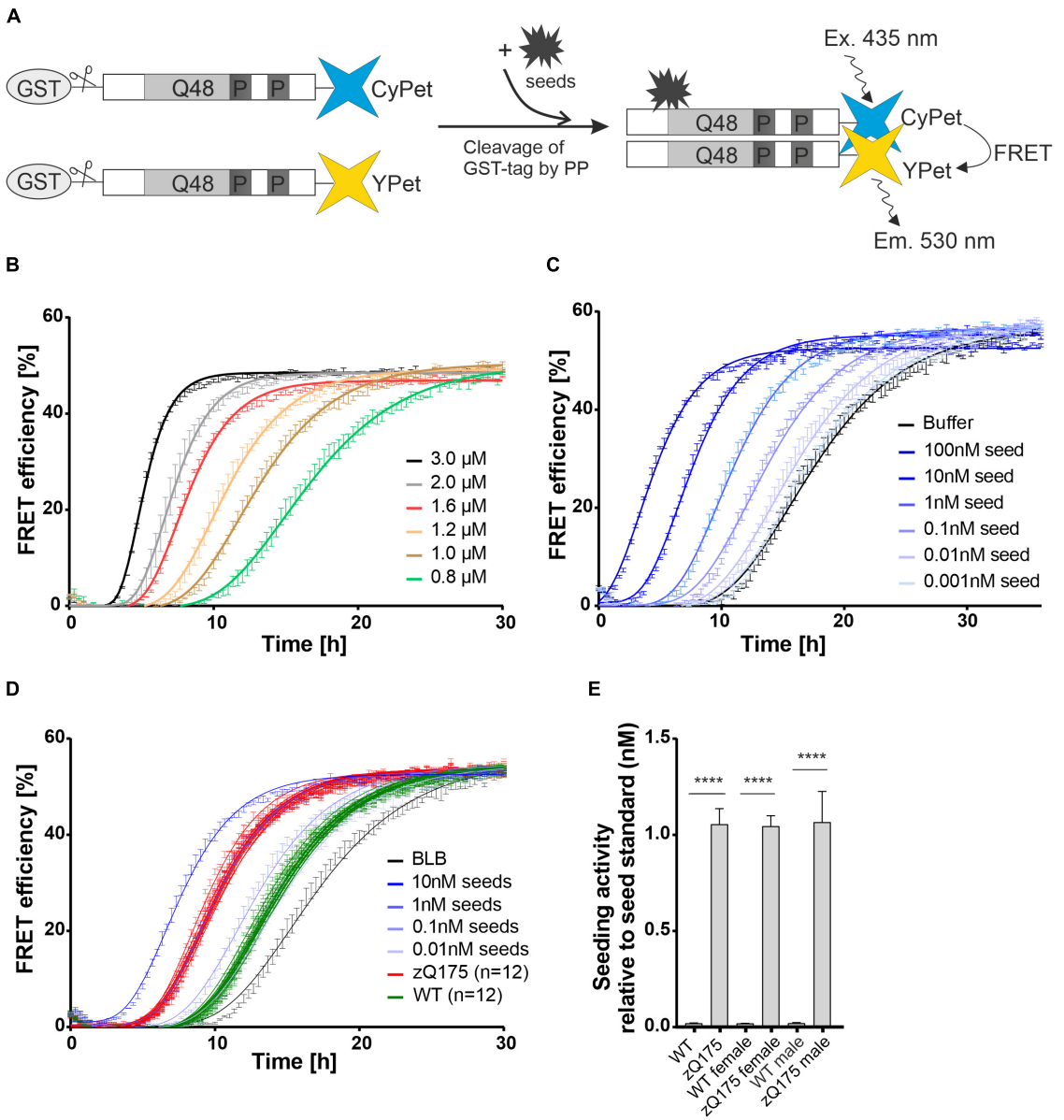

FIGURE 1 | Establishment of FRET-based mHTT aggregate seeding assay (FRASE) for testing biological samples. **(A)** Schematic representation of FRASE. PP, PreScission Protease. **(B)** Time- and concentration-dependent co-aggregation of Ex1Q48-CyPet and Ex1Q48-YPet sensor proteins (1:1 mixture, 0.8–3.0 µM) monitored by repeated FRET measurements. FRET efficiency is displayed as mean ± SEM of technical triplicates. **(C)** Effect of different concentrations of preformed Ex1Q48 seeds on Ex1Q48-CyPet and Ex1Q48-YPet (1:1 mixture, 1.2 µM) co-aggregation. Data are mean ± SEM of technical replicates. **(D)** FRASE analysis of crude brain extracts prepared from 6-month-old WT and zQ175 mice. Whole hemispheres were used for preparation. Different concentrations of preformed sonicated recombinant Ex1Q48 aggregates were used as seed standard. 4 µg total mouse protein per replicate was applied. BLB, brain lysis buffer. Data are mean ± SEM of three technical replicates. Number of biological replicates is indicated. **(E)** Quantification of seeding activity in mouse brain extracts investigated in panel **(D)**. Seeding activities were normalized to the seed standard. The first bars (WT and zQ175 mice) represent all 12 biological replicates analyzed in panel **(D)**. Six of these mice were female and six were male. The following bars represent six biological replicates of female and male mice, respectively. Data are mean ± SEM of biological replicates. Statistical analysis: Unpaired *t*-test between WT and zQ175 mice (****, *p* value < 0.0001).

To assess the aggregation propensity of the purified fusion proteins, we incubated different concentrations of GST-Ex1Q48-CyPet and -YPet (1:1 molar ratio) in 384-well plates with PP and quantified the time- and concentration-dependent appearance of FRET. We observed a steep increase in FRET efficiency after 4–10 h (**Figure 1B**), indicating that the released fragments Ex1Q48-CyPet and -YPet spontaneously form fibrillar mHTTex1 co-aggregates *in vitro*.

Next, preformed fibrillar Ex1Q48 aggregates were produced by cleavage and sonication of GST-Ex1Q48 fusion protein (**Supplementary Figure 1B**). We observed that the generated Ex1Q48 fibrils show a change in fluorescence upon addition

of the amyloid dye thioflavin T (**Supplementary Figure 1C**), confirming that they consist of β-sheets (Wagner et al., 2018). Preformed seeds were then added to Ex1Q48-CyPet and -YPet co-aggregation reactions to assess their activity. We found a concentration-dependent shortening of the lag phase when preformed fibrillar Ex1Q48 seeds were added to reactions (**Figure 1C**), indicating that these structures potently stimulate Ex1Q48-CyPet and -YPet co-polymerization in cell-free assays. Thus, preformed Ex1Q48 fibrils can be utilized as positive control when complex biosamples with unknown concentrations of mHTT fibrils are analyzed for their HSA in FRASE assays.

Detection of Seeding-Competent mHTT Aggregates in Brains of zQ175 Knock-in Mice Using FRASE Assays

Immunohistological investigations showed that IBs with mHTT aggregates are present in brains of 6-month-old zQ175 mice (Carty et al., 2015). We hypothesized that mHTT fibrils with seeding activity might also be detectable in brains of these mice. To address this question, we produced crude brain extracts from male and female heterozygous zQ175 and age-matched wild-type (WT) controls (six brains each) and quantified HSA using the established FRASE assay. All mouse brain samples were assessed on one 384-well plate together with different concentrations of preformed recombinant Ex1Q48 seeds as positive controls. Measurements were taken in three technical replicates. We observed similar HSA in all zQ175 brain samples, while HSA was not detected in brain extracts from age-matched control mice (**Figures 1D,E**). This indicates that fibrillar, seeding-competent mHTT aggregates are formed in brains of zQ175 mice but not in controls. Also, HSA was similar in brain extracts prepared from female and male zQ175 mice, indicating that sex does not significantly influence the formation of mHTT fibrils. Similar HSAs were determined when brain extracts prepared from 12-month-old zQ175 and wild-type control mice were analyzed with the FRASE assay (**Supplementary Figures 2A,B**).

Detection of Large, SDS-Stable mHTT Aggregates in R6/2 and zQ175 Mouse Brains by SDS-PAGE and Immunoblotting

Previous experiments demonstrated that seeding-competent mHTTex1 aggregates are SDS-stable, high molecular weight (HMW) structures readily detected in brains of transgenic R6/2 HD mice (Ast et al., 2018). In this HD model, a human mHTTex1 fragment with a pathogenic polyQ tract has a high propensity to form SDS-stable fibrillar protein aggregates (Scherzinger et al., 1999). Here, we first assessed whether a set of reported anti-HTT antibodies can detect mHTTex1 aggregates in crude mouse brain extracts of 12-week-old R6/2 mice by SDS-PAGE and immunoblotting. In R6/2 mouse brains, neuronal IBs are observed after 4 weeks with immunohistochemical methods (Landles et al., 2020). This suggests that HMW aggregates are also detectable by biochemical assays. We systematically tested 10 anti-HTT antibodies (**Figure 2A**, **Supplementary Table 1** and **Supplementary Figure 3**) for their ability to detect SDS-stable aggregates in crude HD and control mouse brain extracts. Most of them were previously shown to recognize N-terminal mHTT fragments (**Supplementary Table 1**; Ko et al., 2001, 2018), suggesting that they are immunoreactive for mHTTex1 fragments that are formed in R6/2 HD brains. We found that five of the tested antibodies (aAgg, MW8, MAB5492, PHP1, and PHP2) indeed detect SDS-stable, HMW mHTTex1 aggregates in HD mouse brains, which are retained in the stacking gel (**Figure 2A**). It is important to note that with none of tested anti-HTT antibodies soluble mHTTex1 protein with a pathogenic polyQ tract was identified, indicating that this protein at an age of 12 weeks is exclusively present in its aggregated form in R6/2 brains.

Next, we assessed whether HMW, SDS-stable mHTT aggregates can also be detected in brains of zQ175 KI mice that express full-length mHTT. Crude brain extracts prepared from 12-month-old KI and wild-type control animals were systematically investigated by SDS-PAGE and immunoblotting using the same set of antibodies. In addition, the polyclonal antibody S830 was assessed. We could detect HMW mHTT aggregates with the antibodies aAgg and S830 (**Figure 2B**). However, aggregates were not detected with the antibodies MW8, MAB5492, PHP1, and PHP2, which showed immunoreactivity in R6/2 mouse brains (**Figure 2A**). This may be due to lower abundance of SDS-stable, HMW mHTT aggregates in zQ175 compared to R6/2 brains or to structural and morphological differences between mHTT aggregates in zQ175 and R6/2 mouse brains. However, we observed that the anti-HTT antibodies MW1, PHP3, and PHP4 recognize FL mHTT protein migrating at ∼350 kDa in SDS-gels (**Figure 2B**). This indicates that these antibodies preferentially recognize FL soluble mHTT but not the HMW aggregates retained in the stacking gel. Interestingly, both wild-type and mutant FL HTT were detected with the antibody MAB2166, which recognizes an epitope located downstream of the polyQ tract (**Supplementary Figure 3**). Only with the polyclonal antibody S830 both HMW aggregates and soluble FL mHTT were detected on immunoblots (**Figure 2B**). However, with none of the applied antibodies soluble truncated N-terminal mHTT fragments could be detected on immunoblots, suggesting that such fragments are only present in an aggregated form in zQ175 mouse brains. Together these biochemical experiments show that HMW, SDS-stable mHTT aggregates can be detected in brains of R6/2 and zQ175 KI mice under denaturing conditions by immunoblotting using different anti-HTT antibodies.

Enrichment of mHTT Aggregates From zQ175 Mouse Brain Extracts by Immunoprecipitation

To investigate the morphology and seeding activity of mHTT aggregates formed in zQ175 mouse brains, we first established an antibody-based immunoprecipitation (IP) method using magnetic beads (Vila et al., 2010). We then systematically tested 8 different anti-HTT antibodies for their ability to IP mHTT aggregates under native conditions from crude brain extracts. Analysis of immunoprecipitates by SDS-PAGE and immunoblotting revealed that the anti-HTT antibodies MW8, PHP2 and S830 can enrich HMW, SDS-stable mHTT

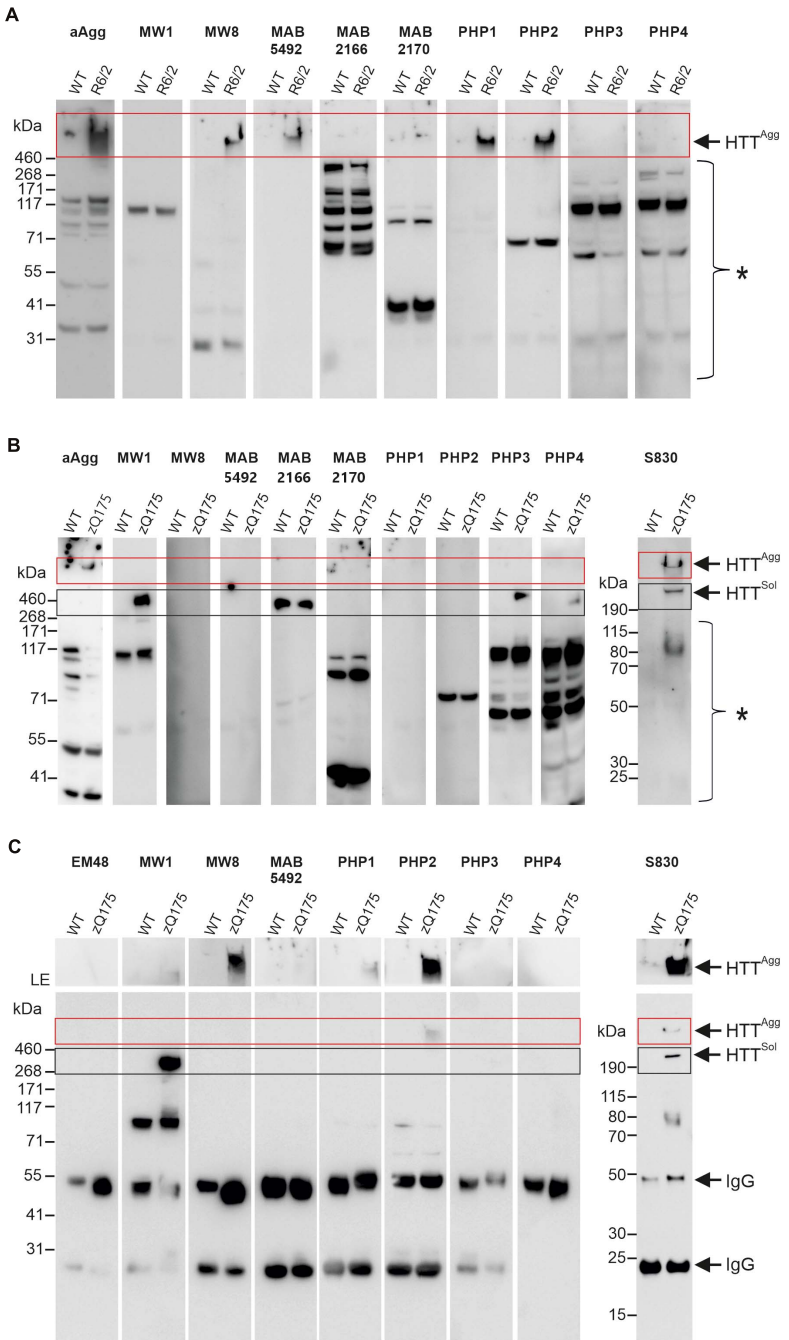

FIGURE 2 | Analysis of mHTT aggregates and soluble protein in brain homogenates from R6/2 and zQ175 mice. **(A)** 50 μg of total brain homogenates prepared from 12-week-old R6/2 and wild-type (WT) mice were analyzed on a denaturing NuPage gel and by immunoblotting using the antibodies indicated above the lanes. For preparation of brain homogenates, BLB was used. HTT^{Agg} and a red box indicate mHTT aggregates in the gel pockets. A bracket with an asterisk indicates immunoreactive bands which cannot be assigned to specific proteins. **(B)** 100 μg of total brain homogenate prepared from 12-month-old zQ175 and wild-type (WT) mice was analyzed on a denaturing NuPage gel and by immunoblotting using the indicated antibodies. For preparation of brain homogenates RIPA buffer was used. HTT^{Agg} and a red box indicate mHTT aggregates in the gel pockets. HTT^{sol} indicates soluble ∼350 kDa HTT protein. A black box indicates soluble HTT, migrating at the expected size of ∼350 kDa. A bracket with an asterisk indicates immunoreactive bands which cannot be assigned to specific proteins. **(C)** Immunoprecipitations using different antibodies, as indicated on top of the gels; total brain homogenates (in BLB) derived from 12-month-old zQ175 and wild-type (WT) mice were applied. Immunoblots were developed with the respective antibodies used for immunoprecipitation and exposed for 20 s, with the exception of the S830 immunoblot, which was exposed for 30 s. The upper parts of blots were exposed separately for 5 min, to better visualize mHTT aggregates. LE, long exposure. HTT^{Agg} and a red box indicate mHTT aggregates in the gel pockets. HTT^{sol} and a black box indicate soluble FL HTT protein migrating at ∼350 kDa. IgG indicates heavy (∼50 kDa) and light (∼25 kDa) antibody chains.

aggregates from zQ175 brain extracts (**Figure 2C**), while no or very low amounts of aggregates were immunoprecipitated with the antibodies MW1, MAB5492, PHP1, PHP3, and PHP4. Interestingly, we observed that the antibodies MW8 and PHP2 can IP mHTT aggregates from zQ175 mouse brain extracts, while they did not react with HMW, SDS-stable mHTT structures on immunoblots (**Figure 2B**). This suggests that these antibodies bind to mHTT aggregates under native conditions and can enrich such structures from crude mouse brain extracts. However, our investigations also indicate that the MW8 antibody, which recognizes a neoepitope that is only exposed at the C-terminus of HTTex1 fragments but not on FL HTT (Landles et al., 2010) can readily IP mHTT aggregates from mouse brain extracts (**Figure 2C**). This suggests that this antibody recognizes aggregates that are formed of mHTTex1 fragments. Such specific N-terminal mHTT fragments are known to be formed by alternative splicing in brains of HD KI mice and patient brains, which express FL mHTT (Sathasivam et al., 2013; Neueder et al., 2017). To assess whether MW8 can indeed immunoprecipitate mHTTex1 aggregates, we also performed immunoprecipitations with brain extracts prepared from R6/2 mice, which exclusively express a mHTTex1 fragment with a pathogenic polyQ tract but no FL mHTT protein (Mangiarini et al., 1996). We found that HMW, SDS-stable mHTTex1 aggregates can be immunoprecipitated from R6/2 mouse brain extracts but not from WT controls using the MW8 antibody (**Supplementary Figure 4**), confirming that this antibody recognizes *in vivo* aggregated mHTTex1 fragments under native conditions. It is important to note that neither from zQ175 nor from R6/2 brain extracts soluble mHTTex1 fragments could be enriched with MW8 IPs (**Figure 2C** and **Supplementary Figure 4**), suggesting that this N-terminal fragment is only present in its aggregated form in HD mouse brains.

Finally, we demonstrated that the polyclonal antibody S830 can enrich both insoluble aggregates and soluble mHTT from crude protein extracts, while the antibody MW1 exclusively precipitates soluble FL mHTT (**Figure 2C**).

Antibody-Enriched mHTT Aggregates From zQ175 Mouse Brain Extracts Are Seeding-Competent, Fibrillar Structures

To address the question of whether mHTT aggregates enriched from crude mouse brain extracts are seeding-competent, we added immunoprecipitates from zQ175 and WT control brains to FRASE assays. We found that the HMW, SDS-stable mHTT aggregates, which are immunoprecipitated with the antibodies S830, MW8 and PHP2 from zQ175 mouse brain extracts are highly seeding-competent structures (**Figure 3A**). In strong contrast, immunoprecipitated FL mHTT, which was enriched from zQ175 brain extracts with the MW1 antibody did not show seeding activity in FRASE assays, indicating that mHTT aggregates rather than the soluble FL protein stimulate the spontaneous aggregation of reporter proteins Ex1Q48-CyPet and -YPet in FRASE assays.

Next, we utilized immunoelectron microscopy (IEM) to investigate the morphology of antibody-enriched mHTT protein aggregates. We observed multiple mHTT fibrils in S830, PHP2 and MW8 immunoprecipitates but not in controls (**Figure 3B**), indicating that indeed fibrillar, structures are responsible for the observed seeding activity in FRASE assays (**Figure 3A**).

Finally, we quantified the lengths of the antibody-enriched mHTT fibrils, which were released from antibody beads by short-time treatment with an acidic buffer solution. We found that mHTT fibrils immunoprecipitated with the antibodies MW8, PHP2, and S830 on average have lengths of ∼192, ∼177, and ∼226 nm, respectively (**Figure 3C**), indicating that relatively small fibrillar mHTT aggregate species are enriched with different aggregate-specific HTT antibodies from 12-month-old zQ175 mouse brains. Together, these biochemical investigations strongly support our hypothesis that ordered, seeding-competent mHTT fibrils are present in brains of zQ175 KI mice.

Soluble Fractions Prepared From zQ175 Mouse Brains Contain Seeding-Competent mHTT Structures

Previous investigations indicate that mHTT fibrils in cells accumulate as insoluble protein aggregates in IBs (Waelter et al., 2001; Bauerlein et al., 2017). However, evidence was also presented that they are soluble, diffusible structures (Sahoo et al., 2016; Ast et al., 2018) that potentially can spread from cell to cell (Iadanza et al., 2018). To assess whether soluble, seeding-competent mHTT structures are present in mouse brain extracts and can be enriched with antibodies, we performed a centrifugation experiment to separate soluble from insoluble proteins. Crude protein homogenates prepared from 12-month-old zQ175 and control mouse brains were centrifuged for 20 min at 18,000 × *g* and the resulting supernatant and pellet fractions were analyzed by FRASE (**Figure 4A**). We found highHSA in the supernatant fraction, indicating that soluble, seeding-competent mHTT fibrils are present in HD mouse brains. In strong contrast, such activity was not detected in the supernatant and pellet fractions prepared from wild-type control brains (**Figure 4B**).

Next, we performed immunoprecipitation experiments with both pellet and supernatant fractions using the S830 anti-HTT antibody. The precipitated material was analyzed for HSA in FRASE assays. We obtained a similar result as with the initial supernatant and pellet fractions (**Figure 4B**), supporting our hypothesis that soluble, seeding-competent mHTT aggregates are detectable in HD mouse brains.

Finally, we assessed whether the seeding-competent mHTT structures present in supernatant fractions consist of truncated N-terminal fragments. To address this question mHTT aggregates were first precipitated from the soluble fraction using the MW8 antibody and subsequently treated with formic acid (FA), which was previously shown to promote the dissociation of amyloidogenic mHTT fibrils into monomers (Hazeki et al., 2000). Samples were finally analyzed by SDS-PAGE and immunoblotting using the antibodies S830 and MW1. We observed that upon FA treatment a smear of S830- and MW1-reactive mHTT fragments (∼80–190 kDa) was detectable (**Figure 4C**), indicating that the HMW mHTT assemblies present in the soluble fraction predominantly consist of

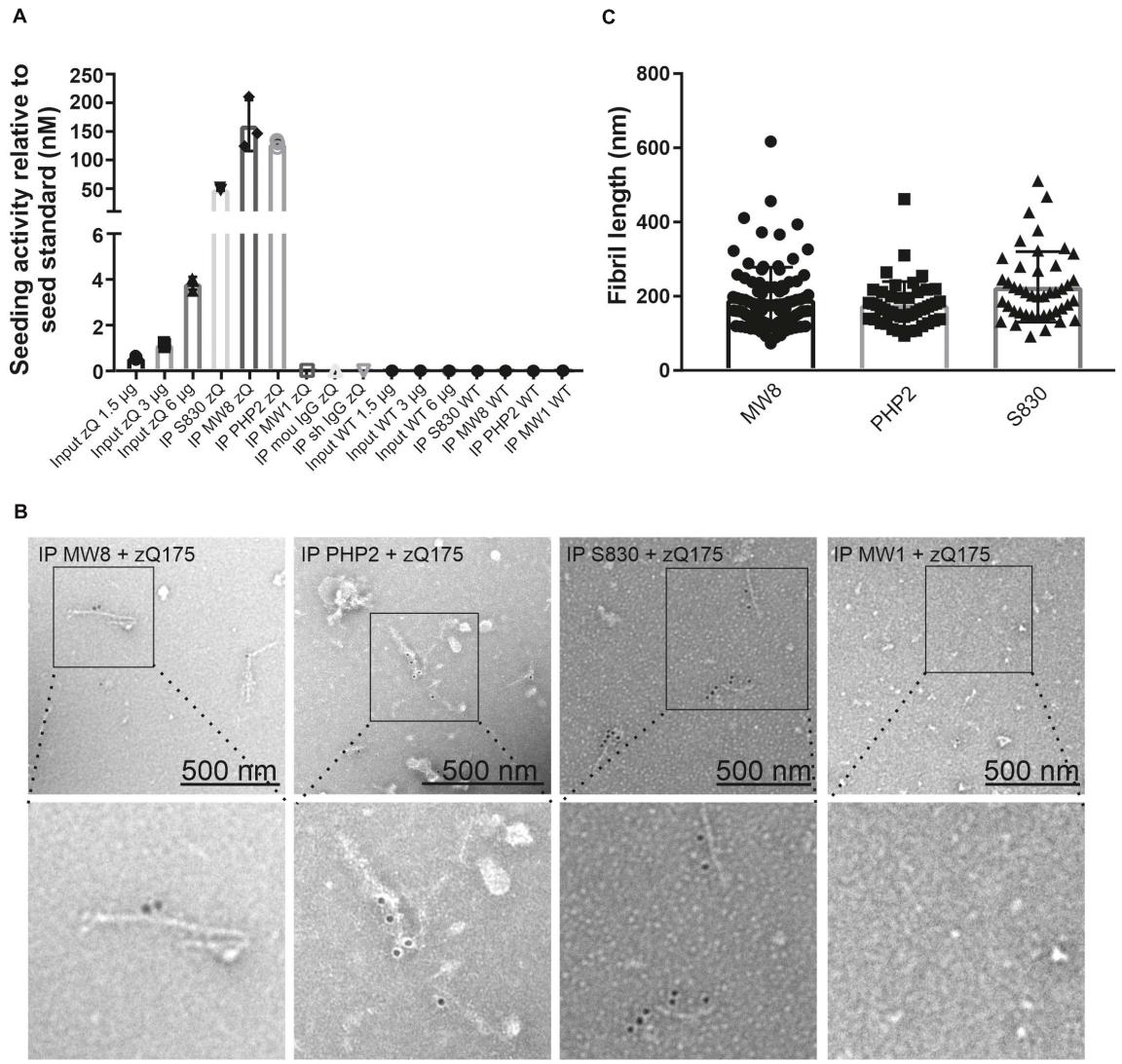

FIGURE 3 | Quantification of mHTT seeding activity and detection of mHTT fibrils in immunoprecipitates enriched from zQ175 mouse brain homogenates. **(A)** Immunoprecipitates and total brain homogenates (input) prepared from WT and zQ175 (zQ) mice were analyzed by FRASE assay. Seeding activities were normalized to the seed standard. Data are mean ± SD of three technical replicates. **(B)** TEM analysis with aAgg-immunogold labeling of eluates derived from S830, PHP2, and MW8 immunoprecipitations of zQ175 mouse brain homogenates. As a control, an eluate from a MW1 immunoprecipitation experiment with a zQ175 brain homogenate is shown. Pictures in the bottom row show magnifications of areas indicated in pictures in the top row. Fibril length was determined with the iTEM software **(C)**. For the MW8 IP, $n = 95$, for the PHP2 IP, $n = 48$ and for the S830 IP, $n = 44$ fibrils were measured. Mean fibril length is 192 nm ± 87 for the MW8 IP, 177 nm ± 63 for the PHP2 IP and 226 nm ± 95 for the S830 IP.

truncated N-terminal fragments. Together, these studies indicate that small seeding-competent mHTT aggregates consisting of N-terminal fragments are indeed present in soluble protein factions in brains of zQ175 KI mice.

The Human Antibodies Ab-A and Ab-B Immunoprecipitate Seeding-Competent, Fibrillar mHTT Aggregate Species From HD Mouse Brains

By screening human memory B cell repertoires of healthy elderly subjects and HD patients, we generated recombinant antibodies that preferentially bind to aggregated recombinant mHTTex1 fragments with a pathogenic polyQ tract (Sevigny et al., 2016; Maier et al., 2018). Two high-affinity human-derived anti-HTT antibodies (Ab-A and Ab-B) and a human isotype control antibody (Ab-Ctrl) were analyzed for their ability to immunoprecipitate mHTT aggregates under native conditions from crude brain extracts from 12-week-old R6/2 and 9-month-old zQ175 HD mice. Analysis of immunoprecipitates by SDS-PAGE and immunoblotting revealed that both anti-HTT antibodies Ab-A and Ab-B precipitated HMW SDS-stable mHTT aggregates from R6/2 (**Figure 5A**) and zQ175 mouse brain homogenates (**Figure 5B**), while no or only minimal amounts

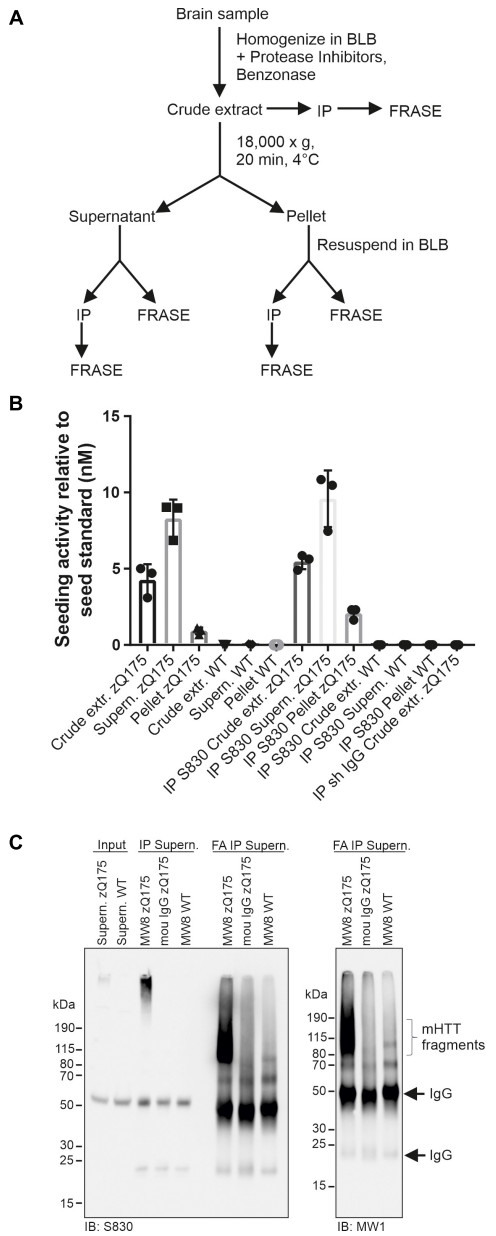

FIGURE 4 | Analysis of HTT seeding activity in soluble and insoluble zQ175 brain fractions. **(A)** Schematic representation of fractionation and analysis steps. **(B)** Analysis of mHTT seeding activity using different samples derived from fractionations of zQ175 and WT mouse brain homogenates following panel **(A)**. Immunoprecipitations (IP) were performed with the antibody S830 and a control IgG. Seeding activity was normalized to the seed standard. Data are mean ± SD of three technical replicates. **(C)** IP was performed with supernatant fraction (shown in panel **(A)**) derived from WT and zQ175 mouse brain homogenates using antibody MW8 and mouse (mou) IgG. Immunoprecipitates were treated with formic acid (FA). Antibodies used for immunoblotting (IB) are indicated below the blots. Input, 200 μg supernatant of zQ175 and WT brain homogenate.

of aggregates were detectable after immunoprecipitation with the human isotype control. Electron microscopy analysis of immunoprecipitates revealed the presence of fibrillar structures following precipitation with Ab-A and -B but not the isotype control antibody (**Supplementary Figure 5**).

To address the question whether human anti-HTT antibodies can bind and deplete seeding-competent mHTT aggregates from HD mouse brain homogenates, we quantified HSA in crude protein extracts after immunodepletion. We found that HSA was significantly decreased after treatment with the anti-HTT antibodies A and B but not the isotype control (**Figures 5C,D**). Thus, both human mHTT aggregate-specific antibodies are capable of removing fibrillar, seeding-competent mHTT aggregates from crude brain homogenates of R6/2 and zQ175 HD mice.

DISCUSSION

Several lines of experimental evidence indicate that the formation of mHTT aggregates is associated with the appearance of behavioral symptoms in HD mouse models (Li et al., 2001; Ast et al., 2018). Whether aggregate assembly plays a causative role in the pathogenic process or rather is an epiphenomenon that does not significantly contribute to disease development (Slow et al., 2005), however, is still a matter of debate.

Here, we systematically applied a FRASE assay, immunoprecipitations and high-resolution imaging methods to investigate the formation of fibrillar mHTT protein aggregates in brains of heterozygous zQ175 KI HD mice, which endogenously express FL mHTT with a pathogenic polyQ tract (Menalled et al., 2012). We measured high HSA in crude brain protein extracts prepared from 6-month-old zQ175 KI mice, indicating that seeding-competent mHTT fibrils are a prominent aggregate species in this HD model.

Previous investigations with HD transgenic mice and cell models have demonstrated that neuronal IBs are densely packed with fibrillar mHTT aggregates (Davies et al., 1997; Waelter et al., 2001; Bauerlein et al., 2017). This might suggest that mHTT fibrils in neurons are predominantly insoluble structures that either accumulate at specific subcellular locations by nucleation (Wagner et al., 2018) or are actively transported to IBs for deposition (Kopito, 2000). The local concentration of insoluble aggregated mHTT fibrils in IBs may be an important coping mechanism to protect neurons from aggregate toxicity (Arrasate et al., 2004). Our investigations of mouse brain extract with FRASE assays, however, suggest that a large fraction of the mHTT fibrils formed in HD mouse brains is soluble rather than insoluble (**Figure 4B**). The relatively small ∼200 nm long mHTT fibrils observed by IEM (**Figure 3B**) are likely to be diffusible structures that can move from one place to another in the cytoplasm and have the potential to perturb multiple biological functions such as axonal transport (Lee et al., 2004) or the release of neurotransmitters in synapses (Li et al., 2001). Our observation that mHTT fibrils in neurons are largely small soluble structures (**Figure 4B**) is supported by previous investigations showing that mHTTex1 fibrils accumulate rapidly as insoluble aggregates in large spherical IBs but at the same time are also present in a soluble form in the cytoplasm of mammalian cells (Sahl et al., 2016). It is important to note that IBs are very complex

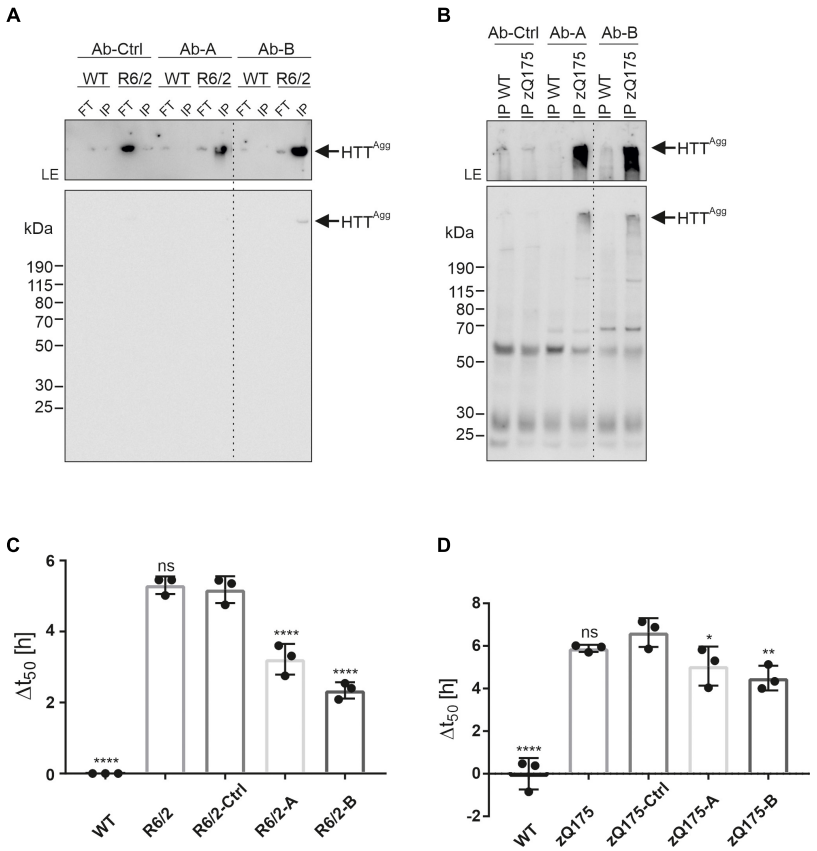

FIGURE 5 | Enrichment of mHTT aggregates from mouse brain extracts using human anti-HTT antibodies. **(A)** The human HTT antibodies Ab-A and Ab-B and an isotype control (Ab-Ctrl) were used for immunoprecipitation of mHTT aggregates from WT and R6/2 brain homogenates. Immunoprecipitates (IP) and flow-through samples (FT) were analyzed by immunoblotting on a denaturing gel using MW8 antibody. The western blot was exposed for 5 s. To better visualize the aggregates in the gel pockets, the upper part of the blot was exposed separately for 5 min. LE, longer exposure. HTT^{Agg} indicates mHTTex1 aggregates. **(B)** Antibodies Ab-A, -B, and -Ctrl were used for immunoprecipitation of mHTT aggregates from WT and zQ175 mouse brain homogenates. Immunoprecipitates (IP) were analyzed by immunoblotting on a denaturing gel using the PHP2 antibody. The western blot was exposed for 10 s. The upper part of the blot was exposed separately for 1 min. LE, longer exposure **(C)** Analysis of WT and R6/2 brain homogenates, and FT samples derived from immunoprecipitations using Ab-A (R6/2-A), Ab-B (R6/2-B), and Ab-Ctrl (R6/2-Ctrl) in the FRASE assay. Δt50 is displayed as mean ± SD of four technical replicates. Statistical analysis: One-way ANOVA followed by Dunnett's multiple-comparisons test reveals a significant difference in Δt50 values between WT and R6/2-Ctrl (****), R6/2-A and R6/2-Ctrl (****), and R6/2-B and R6/2-Ctrl (****) samples. ****, adjusted (adj.) p value = 0.0001. **(D)** Analysis of WT and zQ175 brain homogenates, and FT samples derived from immunoprecipitations using Ab-Ctrl (zQ175-Ctrl), Ab-A (zQ175-A), and Ab-B (zQ175-B) in the FRASE assay. Δt50 is displayed as mean ± SD of four technical replicates. Statistical analysis: One-way ANOVA followed by Dunnett's multiple-comparisons test reveals a significant difference in Δt50 values between WT and zQ175-Ctrl (****, adj. p value = 0.0001), zQ175-A and zQ175-Ctrl (*, adj. p value = 0.049) and zQ175-B and zQ175-Ctrl (**, adj. p value = 0.0091) samples.

protein condensates that contain many other cellular proteins besides insoluble mHTTex1 fibrils, as e.g., chaperones, ubiquitin or different components of the ubiquitin proteasome system (Waelter et al., 2001; Hosp et al., 2017). The composition of small, soluble mHTT fibrils in HD models and patient brains still needs to be investigated in depth with mass spectrometry-based methods.

The detection of seeding-competent mHTT fibrils in brains of zQ175 mice with immunoprecipitations and IEM (**Figure 3B**) is not unexpected. Previously, fibrillar mHTT aggregates were successfully enriched from brains of R6/2 and *Hdh*Q150 KI mice using a Seprion ligand (Sathasivam et al., 2010) that binds large, amyloidogenic protein assemblies, soluble oligomers and protofibrils. Similarly, small ordered mHTTex1 aggregates with a typical fibrillar morphology were isolated from HD mouse brain extracts using biochemical methods (Diaz-Hernandez et al., 2004; Ast et al., 2018). Finally, utilizing IEM methods, it was demonstrated that neuropil EM48-reactive inclusions in brains of HD KI mice contain fibrillar N-terminal mHTT assemblies (Li et al., 2001). Strikingly, such aggregates are formed early in the disease process in HD-relevant brain regions such as the striatum and are associated with axonal degeneration, suggesting that they play a critical role in pathogenesis. We propose here that the antibody-enriched mHTT fibrils from brain extracts of zQ175 mice might predominantly originate from the cytoplasm, which likely contains high amounts of mHTT aggregates (Maat-Schieman et al., 1999; Cicchetti et al., 2014). However, it may well be that small, seeding-competent mHTT fibrils formed in neuronal nuclei are also enriched with the mHTT aggregate-specific antibodies. Further studies are necessary to assess the

relative abundance of mHTT aggregate species in different subcellular compartments and their seeding activity.

Through immunoprecipitations followed by IEM experiments, we could show that antibodies such as MW8 and PHP2 are able to enrich seeding-competent, fibrillar mHTT aggregates from mouse brain extracts (**Figures 3A,B**). In strong contrast, FL mHTT migrating at ∼350 kDa was specifically enriched from brain extracts utilizing the MW1 antibody. These results are in agreement with previous studies indicating that aggregated and non-aggregated forms of mHTT expose distinct epitopes and therefore require different anti-HTT antibodies to be detected. While the pathogenic polyglutamine (polyQ) tract in FL mHTT is exposed on the protein surface and can be recognized by the polyQ-specific MW1 antibody, it is not exposed in β-sheet-rich fibrillar mHTT aggregates (Wagner et al., 2018). Thus, such structures cannot be immunoprecipitated with the MW1 antibody. Other domains such an α-helical proline-rich domain (PRD) are predominantly exposed in fibrillar mHTT aggregates, which can be recognized by aggregate-specific mHTT antibodies such as PHP2 (Ko et al., 2018).

Interestingly, fibrillar mHTT aggregates could be enriched from zQ175 brain extracts using the monoclonal antibody MW8 (**Figure 3B**). This conformation-sensitive antibody was previously shown to specifically recognize the C-terminus of HTTex1 fragments, which is not present in longer N-terminal HTT fragments or the FL protein (Landles et al., 2010). Thus, the MW8 antibody possibly enriches structures from mouse brain extracts that contain mHTTex1 fragments. Our results are therefore consistent with previous observations indicating that mHTTex1 fragments are produced in brains of zQ175 mice through abnormal splicing (Sathasivam et al., 2013). These peptides are highly aggregation-prone; they may function as seeds and drive the co-aggregation of longer N-terminal HTT fragments with pathogenic and non-pathogenic polyQ tracts, likely formed in HD brains by proteolytic cleavage of FL HTT (Ratovitski et al., 2009). Cell-free aggregation studies with recombinant proteins have shown that N-terminal HTT fragments with short and long polyQ tracts indeed can co-assemble into stable mixed fibrils (Busch et al., 2003), suggesting that polymorphic mHTT fibrils with distinct biological activities may also form *in vivo*. Furthermore, it is likely that at least a fraction of the mHTT fibrils formed in neurons undergoes post-translational modification, e.g., through the attachment of ubiquitin chains, which additionally enhances their polymorphic nature (Juenemann et al., 2015).

MW8-based ELISAs and homogenous time-resolved fluorescence (HTRF) assays were recently applied successfully to detect mHTT aggregates in zQ175 mouse brain extracts (Reindl et al., 2019). However, this approach does not provide information about the morphology and structure of the mHTT aggregates. Our investigations suggest that seeding-competent mHTT aggregate species indeed are detected with MW8 in ELISAs. However, it is important to note that current antibody-based mHTT aggregate detection assays (Reindl et al., 2019; Landles et al., 2021), in strong contrast to the FRASE method applied here, might also detect non-fibrillar mHTT assemblies in tissue samples. Such assemblies were previously described in different HD model systems (Sathasivam et al., 2010) and are thought to play a key role in pathogenesis (Hoffner and Djian, 2014). Similar to small mHTT fibrils, they are highly mobile structures. A soluble pool of MW1-immunoreactive mHTT oligomers formed of N-terminal fragments was previously identified in brains of HdhQ150 KI mice using the SEC-FRET technology (Marcellin et al., 2012). Such structures are less stable than β-sheet-rich mHTT fibrils. PolyQ tracts, readily recognized by the MW1 antibody, are exposed on their surface. Via their polyQ sequences, these dynamic mHTT structures may interact with other cellular proteins and perturb their cellular functions (Kwon et al., 2018). However, we suggest that both fibrillar and non-fibrillar mHTT structures are formed in neurons of zQ175 KI mice and contribute independently to the pathogenic process.

Together our studies show that small, seeding-competent mHTT fibrils are prominent aggregate species in brains of zQ175 HD mice. We suggest that they have the potential of driving the pathogenic process in zQ175 HD KI mice and patients, for these reasons: They are detected in brains of very young mice; they appear before the onset of symptoms; finally, their abundance increases progressively with disease development in typically affected brain regions such as the striatum.

MATERIALS AND METHODS

Antibodies

Most monoclonal antibodies used in this study were obtained by commercial suppliers (see **Supplementary Table 1**). Production and characterization of the antibodies aAgg (Scherzinger et al., 1999), PHP1-4 (Ko et al., 2018), and S830 (Neueder et al., 2017) were described previously. The concentrations of antibodies used for immunoprecipitations, immunoblots, and immuno-EM studies are described in the methods section below. Secondary colloidal gold-labeled anti-rabbit antibodies were used for transmission electron microscopy (TEM) studies, while peroxidase or HRP-labeled secondary antibodies were used for western blotting. For immunoprecipitations mouse IgG1 (Thermo Scientific) or sheep IgG (Millipore) were utilized as controls. Human anti-HTT antibodies A and B were derived from a de-identified blood lymphocyte library collected from healthy elderly subjects or HD patients utilizing previously reported procedures (Maier et al., 2018). High-affinity anti-HTT antibodies Ab-A and Ab-B were selected based on their preferential binding to aggregated recombinant human mHTTex1 fragments with a pathogenic polyQ49 tract compared to HTTex1 fragments with a normal polyQ21 tract using dot-blot and filter-retardation assays (Wagner et al., 2018).

Mouse Breeding and Maintenance

All procedures were performed in accordance with the Animals (Scientific Procedures) Act 1986, complied with ARRIVE guidelines and were approved by the University College London Ethical Review Process Committee. zQ175 knock-in mice were generated by replacing exon 1 of mouse *Htt* with exon 1 from human *HTT*, carrying a highly expanded CAG repeat (Menalled et al., 2012), from which the neo-selectable marker

had been removed (delta neo) (Franich et al., 2019). Mice were either bred in-house by backcrossing males to C57Bl/6J females (Charles River) or obtained from the CHDI Foundation colony at the Jackson Laboratory (Bar Harbor, Maine) on a C57Bl/6J background. R6/2 mice (Mangiarini et al., 1996) were bred by backcrossing R6/2 males to C57BL/6JOlaHsd × CBA/CaOlaHsd F1 females (B6CBAF1/OlaHsd, Envigo, Netherlands).

Within each colony, genetically modified and wild-type mice were group housed with up to five mice per cage, dependent on gender, but genotypes were mixed. Mice were housed in individually ventilated cages with Aspen Chips 4 Premium bedding (Datesand) and with environmental enrichment, which included chew sticks and a play tunnel (Datesand). They had unrestricted access to food (Teklad global 18% protein diet, Envigo) and water. The temperature was regulated at 21°C ± 1°C and animals were kept on a 12 h light-dark cycle. The animal facility was barrier-maintained and quarterly non-sacrificial FELASA screens found no evidence of pathogens.

R6/2 and zQ175 mice were genotyped and CAG repeat sizing was performed as previously described (Landles et al., 2021). The mean CAG repeat size ± SD was 190.23 ± 4.53 for 6-month-old zQ175, 194.45 ± 3.15 for 12-month-old zQ175, and 181.0 ± 4.0 for 12-week-old R6/2 mice.

Protein Expression

Escherichia coli BL21-RP carrying pGEX-6P1_Ex1Q48, pGEX-6P1_Ex1Q48-CyPet, and pGEX-6P1_Ex1Q48-YPet were grown in 20 ml of LB medium containing 150 μg/ml ampicillin and 42 μg/ml chloramphenicol at 37°C and 210 rpm shaking overnight. On the next day, the culture was inoculated in 1 l of LB media and grown to an OD_{600} of 0.6. Then, expression was induced with 1 mM IPTG for 4 h. Cultures of induced bacteria were centrifuged at 3,501 × *g* for 20 min, and the resulting pellets were stored at −80°C. Cells were thawed on ice and resuspended in 20 ml of cold buffer I (50 mM NaH_2PO_4, 5 mM Tris, 150 mM NaCl, 1 mM EDTA, pH 8.0) containing 1 mg/ml lysozyme and protease inhibitors. After incubation for 30 min on ice, cells were sonicated on ice with eight 10 s bursts (45 s break between bursts) using a Branson sonicator 450 (output control 4, duty cycle constant). Then, TritonX-100 to a final concentration of 1% was added and incubation continued for 5 min on ice. The resulting lysate was clarified by centrifugation for 40 min at 26,892 g. Cleared lysates were incubated on a rotating wheel for 1 h at 4°C with 4 ml of 1:1 slurry of glutathione-agarose beads (Sigma-Aldrich) that had been washed three times and resuspended in buffer I. The beads were poured into a small polypropylene column, washed with 10 ml buffer I containing 0.1% Triton-X and protease inhibitors, followed by a wash with 10 ml buffer I without additives. The bound fusion protein was eluted with 4 ml of 20 mM glutathione (reduced) in buffer I (pH 8.6) and then dialyzed overnight in a 10 kDa MWCO membrane and buffer containing 50 mM Tris, 150 mM NaCl, 1 mM EDTA and 5% glycerol (pH 7.4).

Western Blot Analysis

Protein extracts or magnetic protein G beads with immunoprecipitated HTT species were boiled with NuPAGE 4× sample buffer for 5 min and then loaded onto NuPAGE Novex 4–12% Bis-Tris gels (Thermo-Fisher Scientific, Waltham, MA, United States). Electrophoresis was performed according to a standard protocol followed by transfer of proteins onto a nitrocellulose membrane (0.45 μm; GE Healthcare Life Sciences, Munich, Germany) using a wet blotting system (Bio-Rad, Munich, Germany). The generated blots were incubated with primary antibodies (1:1000) and HRP-conjugated secondary antibodies (1:2000, Sigma-Aldrich, Taufkirchen, Germany). Immunoreactive proteins on membranes were visualized with WesternBright Quantum chemiluminescence substrate (Advansta, Menlo Park, CA, United States).

Coomassie Staining

Protein extracts were boiled with NuPAGE 4× sample buffer for 5 min and then loaded onto NuPAGE Novex 4–12% Bis-Tris gels (Thermo Fisher Scientific, Waltham, MA, United States). After electrophoresis, gels were stained with Coomassie blue R (50% methanol, 9.2% acetic acid, 0.175 brilliant blue) overnight followed by destaining with water.

FRASE Assay and Quantification of mHTT Seeding Activity

The FRASE assay was performed as described in Ast et al. (2018). To obtain the t_{50} values, the aggregation kinetics were curve fitted by Richard's five-parameter dose-response curve using GraphPad Prism. To quantify seeding activity of mHTT aggregate species in tissue samples or IP eluates, a seed standard was employed. Delta t_{50} values of the different seed standard concentrations were used to generate an exponential function in MS Excel. Using this function, the seeding activity of samples relative to the seed standard (in nM) was calculated.

Preparation of Seed Standard

Mutant huntingtin exon-1 aggregates (Ex1Q48) were prepared as described in Ast et al. (2018). Aggregates were sonicated on ice with six 10 s bursts (30 s break between bursts) using a BRANSON Sonifier 450 (output control 1, duty cycle 90%). Then, the sonicated aggregates (seeds) were diluted to concentrations of 100, 10, 1, 0.1, 0.01, and 0.001 nM, aliquoted and stored at −80°C until use.

Thioflavin T Binding Assay

Ex1Q48 aggregates were mixed with 20 μM Thioflavin T (ThT) in 1× PBS in a volume of 25 μl. Fluorescence measurements of samples were performed in a plate reader (Infinite M200, Tecan, Männedorf, Switzerland) at an excitation wavelength of 420 nm and an emission wavelength of 485 nm (LeVine, 1999).

Preparation of Tissue Homogenates

Frozen tissue (400–600 mg) was homogenized in 1 ml ice-cold brain lysis buffer (BLB: 10 mM Tris, 1 mM EDTA, 0.8 M NaCl, 10% Sucrose, pH 7.4, EDTA-free protease inhibitors) using a Precellys homogeniser (5,000 rpm, 2 × 20 s, break: 15 s). Then, the buffer volume was adjusted to 10-fold of volume, Benzonase (0.25 U/μl) was added and the homogenate incubated for 1 h at

4°C. Protein concentration was determined with the Pierce BCA assay (Thermo Fisher Scientific, Waltham, MA, United States) using BSA as a standard. Homogenates were aliquoted and stored at −80°C until further use. For FRASE assays, samples in BLB buffer were used.

For preparation of mouse brain homogenates in RIPA buffer, 400–600 mg brain was homogenized in 1 ml ice-cold 50 mM Tris pH 7.5 buffer using the Precellys homogenizer (5000 rpm, 2×20 s, break: 15 s). Then, buffer volume was adjusted to 10-fold of volume using 50 mM Tris pH 7.5, 150 mM NaCl, 1% Triton, 0.1% SDS, 0.5% Sodium deoxycholate, EDTA-free protease inhibitors and Benzonase (0.25 U/μl). Homogenates were incubated for 1 h at 4°C. Protein concentration was determined using the Pierce BCA assay (Thermo Fisher Scientific, Waltham, MA, United States). Homogenates were aliquoted and stored at −80°C until further use.

Immunoprecipitations and Formic Acid Treatment

Huntingtin protein species were enriched from mouse brain homogenates through immunoprecipitation with magnetic protein G beads (Thermo Fisher Scientific, Waltham, MA, United States) coated with the respective antibodies. For IP experiments shown in **Figure 2**, 2 μl antibody was bound to 0.75 mg beads by incubation for 30 min at room temperature on a rotating wheel. Antibody-bound beads were washed three times in PBS and then incubated with 1.25 mg RIPA homogenate at 4°C overnight on a rotating wheel. After washing the beads three times in a buffer containing 50 mM Tris pH 7.5, 150 mM NaCl, 0.01% SDS, 0.05% sodium deoxycholate, 0.1% Triton X-100 and protease inhibitors, HTT protein species were released from the beads by denaturation (5 min, 95°C) in NuPage sample buffer. All other immunoprecipitations were performed with tissue homogenates prepared in BLB. Antibodies (0.5–1 μg) were bound to 0.375 mg beads as described above. After washing the beads, brain homogenates in BLB buffer were added and incubated at 4°C overnight. Unbound material was taken off (=Flow Through) and beads were washed three times in BLB. HTT protein species were released from the beads either by denaturation in NuPage sample buffer or by incubation in 12.5 μl elution buffer (100 M Glycine-HCl, pH 2.8) for 30 min at 4°C. Eluates were neutralized by addition of 1.2 μl 1 M Tris pH 10.

For formic acid treatment, after the last washing step in BLB, beads with immunoprecipitates were resuspended in 100 μl 98% formic acid and incubated for 1 h at 37°C with 300 rpm shaking. Then, the bead formic acid solution was put to a magnet and the supernatant transferred to a new tube. After evaporation of the supernatant, elution buffer and 1 M Tris pH 10 were added and pipetted several times up and down, to solubilize proteins.

Transmission Electron Microscopy (TEM)

For TEM investigations, samples (5 μl IP eluate) were adsorbed onto formvar-carbon coated grids (Plano) by 10 min incubation at room temperature. After two times washing in 1× PBS containing 1% BSA and 0.12% glycine (wash buffer) for 5 min, samples on grids were incubated with aAgg antibody, diluted 1:50 in wash buffer for 15 min at room temperature.

Samples were washed again and incubated with immunogold-labeled goat anti-rabbit antibody (S830 IP: 18 nm Colloidal Gold AffiniPure Goat Anti-Rabbit IgG; PHP2 and MW8 IP: 12 nm Colloidal Gold AffiniPure Goat Anti-Rabbit IgG), diluted 1:30 in wash buffer, for 10 min. Grids were washed two times in 1× PBS and five times in deionized water, before they were stained with 5% uranyl acetate, and analyzed using the Zeiss EM 910 microscope. Pictures were taken and analyzed with the iTEM software (EMSIS GmbH, Münster, Germany).

DATA AVAILABILITY STATEMENT

The original contributions presented in the study are included in the article/**Supplementary Material**, further inquiries can be directed to the corresponding author/s.

ETHICS STATEMENT

The animal study was reviewed and approved by University College London Ethical Review Process Committee.

AUTHOR CONTRIBUTIONS

FS, NP, NN, and AB planned and performed the immunoprecipitations, FRASE assays, TEM and biochemical analysis. SK performed TEM analysis. AK generated PHP1-4 antibodies. GB discussed the experiments and results. MM, JG, and JP provided and contributed to the generation and characterization of human antibodies Ab-A, -B, and -Ctrl antibodies. MAM, BT, and GB provided mouse tissues. FS, SS, AB, and EW co-ordinated the study and edited the manuscript. EW designed the study and wrote the manuscript, with contributions from JP, GB, MM, SS, and AB. All authors contributed to the article and approved the submitted version.

FUNDING

The research was funded by the CHDI Foundation, United States (to EW and GB), the UK Dementia Research Institute (UK Medical Research Council, Alzheimer's Society and Alzheimer's Research UK, to GB and JP), and the DFG SFB/TRR167-2 B07, Germany (to JP).

ACKNOWLEDGMENTS

We thank L. Delius for technical assistance and C. Hänig for support with editing of the manuscript.

SUPPLEMENTARY MATERIAL

The Supplementary Material for this article can be found online at: https://www.frontiersin.org/articles/10.3389/fnins.2021.682172/full#supplementary-material

REFERENCES

Arrasate, M., Mitra, S., Schweitzer, E. S., Segal, M. R., and Finkbeiner, S. (2004). Inclusion body formation reduces levels of mutant huntingtin and the risk of neuronal death. *Nature* 431, 805–810. doi: 10.1038/nature02998

Ast, A., Buntru, A., Schindler, F., Hasenkopf, R., Schulz, A., Brusendorf, L., et al. (2018). mHTT Seeding Activity: A Marker of Disease Progression and Neurotoxicity in Models of Huntington's Disease. *Mol. Cell* 71, 675–688 e676. doi: 10.1016/j.molcel.2018.07.032

Babcock, D. T., and Ganetzky, B. (2015). Transcellular spreading of huntingtin aggregates in the Drosophila brain. *Proc. Natl. Acad. Sci. U. S. A.* 112, E5427–E5433. doi: 10.1073/pnas.1516217112

Bauerlein, F. J. B., Saha, I., Mishra, A., Kalemanov, M., Martinez-Sanchez, A., Klein, R., et al. (2017). In Situ Architecture and Cellular Interactions of PolyQ Inclusions. *Cell* 171, 179–187 e110. doi: 10.1016/j.cell.2017.08.009

Busch, A., Engemann, S., Lurz, R., Okazawa, H., Lehrach, H., and Wanker, E. E. (2003). Mutant huntingtin promotes the fibrillogenesis of wild-type huntingtin: a potential mechanism for loss of huntingtin function in Huntington's disease. *J. Biol. Chem.* 278, 41452–41461.

Carty, N., Berson, N., Tillack, K., Thiede, C., Scholz, D., Kottig, K., et al. (2015). Characterization of HTT inclusion size, location, and timing in the zQ175 mouse model of Huntington's disease: an in vivo high-content imaging study. *PLoS One* 10:e0123527. doi: 10.1371/journal.pone.0123527

Cicchetti, F., Lacroix, S., Cisbani, G., Vallieres, N., Saint-Pierre, M., St-Amour, I., et al. (2014). Mutant huntingtin is present in neuronal grafts in Huntington disease patients. *Ann. Neurol.* 76, 31–42. doi: 10.1002/ana.24174

Davies, S. W., Turmaine, M., Cozens, B. A., DiFiglia, M., Sharp, A. H., Ross, C. A., et al. (1997). Formation of neuronal intranuclear inclusions underlies the neurological dysfunction in mice transgenic for the HD mutation. *Cell* 90, 537–548.

Diaz-Hernandez, M., Moreno-Herrero, F., Gomez-Ramos, P., Moran, M. A., Ferrer, I., Baro, A. M., et al. (2004). Biochemical, ultrastructural, and reversibility studies on huntingtin filaments isolated from mouse and human brain. *J. Neurosci.* 24, 9361–9371.

DiFiglia, M., Sapp, E., Chase, K. O., Davies, S. W., Bates, G. P., Vonsattel, J. P., et al. (1997). Aggregation of huntingtin in neuronal intranuclear inclusions and dystrophic neurites in brain. *Science* 277, 1990–1993. doi: 10.1126/science.277.5334.1990

Farshim, P. P., and Bates, G. P. (2018). Mouse Models of Huntington's Disease. *Methods Mol. Biol.* 1780, 97–120. doi: 10.1007/978-1-4939-7825-0_6

Franich, N. R., Hickey, M. A., Zhu, C., Osborne, G. F., Ali, N., Chu, T., et al. (2019). Phenotype onset in Huntington's disease knock-in mice is correlated with the incomplete splicing of the mutant huntingtin gene. *J. Neurosci. Res.* 97, 1590–1605. doi: 10.1002/jnr.24493

Guo, Q., Bin, H., Cheng, J., Seefelder, M., Engler, T., Pfeifer, G., et al. (2018). The cryo-electron microscopy structure of huntingtin. *Nature* 555, 117–120. doi: 10.1038/nature25502

Gutekunst, C. A., Li, S. H., Yi, H., Mulroy, J. S., Kuemmerle, S., Jones, R., et al. (1999). Nuclear and neuropil aggregates in Huntington's disease: relationship to neuropathology. *J. Neurosci.* 19, 2522–2534.

Hazeki, N., Tukamoto, T., Goto, J., and Kanazawa, I. (2000). Formic acid dissolves aggregates of an N-terminal huntingtin fragment containing an expanded polyglutamine tract: applying to quantification of protein components of the aggregates. *Biochem. Biophys. Res. Commun.* 277, 386–393. doi: 10.1006/bbrc.2000.3682

Heikkinen, T., Lehtimaki, K., Vartiainen, N., Puolivali, J., Hendricks, S. J., Glaser, J. R., et al. (2012). Characterization of neurophysiological and behavioral changes, MRI brain volumetry and 1H MRS in zQ175 knock-in mouse model of Huntington's disease. *PLoS One* 7:e50717. doi: 10.1371/journal.pone.0050717

Heng, M. Y., Tallaksen-Greene, S. J., Detloff, P. J., and Albin, R. L. (2007). Longitudinal evaluation of the Hdh(CAG)150 knock-in murine model of Huntington's disease. *J. Neurosci.* 27, 8989–8998. doi: 10.1523/JNEUROSCI.1830-07.2007

Hoffner, G., and Djian, P. (2014). Monomeric, oligomeric and polymeric proteins in huntington disease and other diseases of polyglutamine expansion. *Brain Sci.* 4, 91–122. doi: 10.3390/brainsci4010091

Hoffner, G., and Djian, P. (2015). Polyglutamine Aggregation in Huntington Disease: Does Structure Determine Toxicity? *Mol. Neurobiol.* 52, 1297–1314. doi: 10.1007/s12035-014-8932-1

Hosp, F., Gutierrez-Angel, S., Schaefer, M. H., Cox, J., Meissner, F., Hipp, M. S., et al. (2017). Spatiotemporal Proteomic Profiling of Huntington's Disease Inclusions Reveals Widespread Loss of Protein Function. *Cell Rep.* 21, 2291–2303. doi: 10.1016/j.celrep.2017.10.097

Iadanza, M. G., Jackson, M. P., Hewitt, E. W., Ranson, N. A., and Radford, S. E. (2018). A new era for understanding amyloid structures and disease. *Nat. Rev. Mol. Cell Biol.* 19, 755–773. doi: 10.1038/s41580-018-0060-8

Juenemann, K., Wiemhoefer, A., and Reits, E. A. (2015). Detection of ubiquitinated huntingtin species in intracellular aggregates. *Front. Mol. Neurosci.* 8:1. doi: 10.3389/fnmol.2015.00001

Ko, J., Isas, J. M., Sabbaugh, A., Yoo, J. H., Pandey, N. K., Chongtham, A., et al. (2018). Identification of distinct conformations associated with monomers and fibril assemblies of mutant huntingtin. *Hum. Mol. Genet* 27, 2330–2343. doi: 10.1093/hmg/ddy141

Ko, J., Ou, S., and Patterson, P. H. (2001). New anti-huntingtin monoclonal antibodies: implications for huntingtin conformation and its binding proteins. *Brain Res. Bull.* 56, 319–329. doi: 10.1016/s0361-9230(01)00599-8

Kopito, R. R. (2000). Aggresomes, inclusion bodies and protein aggregation. *Trends Cell Biol.* 10, 524–530. doi: 10.1016/s0962-8924(00)01852-3

Kwon, M. J., Han, M. H., Bagley, J. A., Hyeon, D. Y., Ko, B. S., Lee, Y. M., et al. (2018). Coiled-coil structure-dependent interactions between polyQ proteins and Foxo lead to dendrite pathology and behavioral defects. *Proc. Natl. Acad. Sci. U. S. A.* 115, E10748–E10757. doi: 10.1073/pnas.1807206115

Landles, C., Milton, R. E., Ali, N., Flomen, R., Flower, M., Schindler, F., et al. (2020). Subcellular Localization And Formation Of Huntingtin Aggregates Correlates With Symptom Onset And Progression In A Huntington'S Disease Model. *Brain Commun.* 2:fcaa066. doi: 10.1093/braincomms/fcaa066

Landles, C., Milton, R. E., Jean, A., McLarnon, S., McAteer, S. J., Taxy, B. A., et al. (2021). Development of novel bioassays to detect soluble and aggregated Huntingtin proteins on three technology platforms. *Brain Commun.* 3:fcaa231. doi: 10.1093/braincomms/fcaa231

Landles, C., Sathasivam, K., Weiss, A., Woodman, B., Moffitt, H., Finkbeiner, S., et al. (2010). Proteolysis of mutant huntingtin produces an exon 1 fragment that accumulates as an aggregated protein in neuronal nuclei in Huntington disease. *J. Biol. Chem.* 285, 8808–8823. doi: 10.1074/jbc.M109.075028

Lee, W. C., Yoshihara, M., and Littleton, J. T. (2004). Cytoplasmic aggregates trap polyglutamine-containing proteins and block axonal transport in a Drosophila model of Huntington's disease. *Proc. Natl. Acad. Sci. U. S. A.* 101, 3224–3229. doi: 10.1073/pnas.0400243101

LeVine, H. III (1999). Quantification of beta-sheet amyloid fibril structures with thioflavin T. *Methods Enzymol.* 309, 274–284.

Li, H., Li, S. H., Yu, Z. X., Shelbourne, P., and Li, X. J. (2001). Huntingtin aggregate-associated axonal degeneration is an early pathological event in Huntington's disease mice. *J. Neurosci.* 21, 8473–8481.

Maat-Schieman, M. L., Dorsman, J. C., Smoor, M. A., Siesling, S., Van Duinen, S. G., Verschuuren, J. J., et al. (1999). Distribution of inclusions in neuronal nuclei and dystrophic neurites in Huntington disease brain. *J. Neuropathol. Exp. Neurol.* 58, 129–137. doi: 10.1097/00005072-199902000-00003

Maier, M., Welt, T., Wirth, F., Montrasio, F., Preisig, D., McAfoose, J., et al. (2018). A human-derived antibody targets misfolded SOD1 and ameliorates motor symptoms in mouse models of amyotrophic lateral sclerosis. *Sci. Transl. Med.* 126:aah3924. doi: 1010.1126/scitranslmed.aah3924

Mangiarini, L., Sathasivam, K., Seller, M., Cozens, B., Harper, A., Hetherington, C., et al. (1996). Exon 1 of the HD gene with an expanded CAG repeat is sufficient to cause a progressive neurological phenotype in transgenic mice. *Cell* 87, 493–506. doi: 10.1016/s0092-8674(00)81369-0

Marcellin, D., Abramowski, D., Young, D., Richter, J., Weiss, A., Marcel, A., et al. (2012). Fragments of HdhQ150 mutant huntingtin form a soluble oligomer pool that declines with aggregate deposition upon aging. *PLoS One* 7:e44457. doi: 10.1371/journal.pone.0044457

Maxan, A., Sciacca, G., Alpaugh, M., Tao, Z., Breger, L., Dehay, B., et al. (2020). Use of adeno-associated virus-mediated delivery of mutant huntingtin to study the spreading capacity of the protein in mice and non-human primates. *Neurobiol. Dis.* 141:104951. doi: 10.1016/j.nbd.2020.104951

McColgan, P., and Tabrizi, S. J. (2018). Huntington's disease: a clinical review. *Eur. J. Neurol.* 25, 24–34. doi: 10.1111/ene.13413

Menalled, L. B. (2005). Knock-in mouse models of Huntington's disease. *NeuroRx* 2, 465–470. doi: 10.1602/neurorx.2.3.465

Menalled, L. B., Kudwa, A. E., Miller, S., Fitzpatrick, J., Watson-Johnson, J., Keating, N., et al. (2012). Comprehensive behavioral and molecular characterization of a new knock-in mouse model of Huntington's disease: zQ175. *PLoS One* 7:e49838. doi: 10.1371/journal.pone.0049838

Menalled, L. B., Sison, J. D., Dragatsis, I., Zeitlin, S., and Chesselet, M. F. (2003). Time course of early motor and neuropathological anomalies in a knock-in mouse model of Huntington's disease with 140 CAG repeats. *J. Comp. Neurol.* 465, 11–26. doi: 10.1002/cne.10776

Neueder, A., Landles, C., Ghosh, R., Howland, D., Myers, R. H., Faull, R. L. M., et al. (2017). The pathogenic exon 1 HTT protein is produced by incomplete splicing in Huntington's disease patients. *Scientific Rep.* 7:1307. doi: 10.1038/s41598-017-01510-z

Ratovitski, T., Gucek, M., Jiang, H., Chighladze, E., Waldron, E., D'Ambola, J., et al. (2009). Mutant huntingtin N-terminal fragments of specific size mediate aggregation and toxicity in neuronal cells. *J. Biol. Chem.* 284, 10855–10867. doi: 10.1074/jbc.M804813200

Reindl, W., Baldo, B., Schulz, J., Janack, I., Lindner, I., Kleinschmidt, M., et al. (2019). Meso scale discovery-based assays for the detection of aggregated huntingtin. *PLoS One* 14:e0213521. doi: 10.1371/journal.pone.0213521

Ross, C. A., and Tabrizi, S. J. (2011). Huntington's disease: from molecular pathogenesis to clinical treatment. *Lancet Neurol.* 10, 83–98. doi: 10.1016/S1474-4422(10)70245-3

Sahl, S. J., Lau, L., Vonk, W. I., Weiss, L. E., Frydman, J., and Moerner, W. E. (2016). Delayed emergence of subdiffraction-sized mutant huntingtin fibrils following inclusion body formation. *Q. Rev. Biophys.* 49:e2. doi: 10.1017/S0033583515000219

Sahoo, B., Arduini, I., Drombosky, K. W., Kodali, R., Sanders, L. H., Greenamyre, J. T., et al. (2016). Folding Landscape of Mutant Huntingtin Exon1: Diffusible Multimers, Oligomers and Fibrils, and No Detectable Monomer. *PLoS One* 11:e0155747. doi: 10.1371/journal.pone.0155747

Sathasivam, K., Lane, A., Legleiter, J., Warley, A., Woodman, B., Finkbeiner, S., et al. (2010). Identical oligomeric and fibrillar structures captured from the brains of R6/2 and knock-in mouse models of Huntington's disease. *Hum. Mol. Genet* 19, 65–78. doi: 10.1093/hmg/ddp467

Sathasivam, K., Neueder, A., Gipson, T. A., Landles, C., Benjamin, A. C., Bondulich, M. K., et al. (2013). Aberrant splicing of HTT generates the pathogenic exon 1 protein in Huntington disease. *Proc. Natl. Acad. Sci. U. S. A.* 110, 2366–2370. doi: 10.1073/pnas.1221891110

Saudou, F., and Humbert, S. (2016). The Biology of Huntingtin. *Neuron* 89, 910–926. doi: 10.1016/j.neuron.2016.02.003

Scherzinger, E., Lurz, R., Turmaine, M., Mangiarini, L., Hollenbach, B., Hasenbank, R., et al. (1997). Huntingtin-encoded polyglutamine expansions form amyloid-like protein aggregates in vitro and in vivo. *Cell* 90, 549–558. doi: 10.1016/s0092-8674(00)80514-0

Scherzinger, E., Sittler, A., Schweiger, K., Heiser, V., Lurz, R., Hasenbank, R., et al. (1999). Self-assembly of polyglutamine-containing huntingtin fragments into amyloid-like fibrils: implications for Huntington's disease pathology. *Proc. Natl. Acad. Sci. U. S. A.* 96, 4604–4609.

Sevigny, J., Chiao, P., Bussiere, T., Weinreb, P. H., Williams, L., Maier, M., et al. (2016). The antibody aducanumab reduces Abeta plaques in Alzheimer's disease. *Nature* 537, 50–56. doi: 10.1038/nature19323

Sieradzan, K. A., Mechan, A. O., Jones, L., Wanker, E. E., Nukina, N., and Mann, D. M. (1999). Huntington's disease intranuclear inclusions contain truncated, ubiquitinated huntingtin protein. *Exp. Neurol.* 156, 92–99. doi: 10.1006/exnr.1998.7005

Slow, E. J., Graham, R. K., Osmand, A. P., Devon, R. S., Lu, G., Deng, Y., et al. (2005). Absence of behavioral abnormalities and neurodegeneration in vivo despite widespread neuronal huntingtin inclusions. *Proc. Natl. Acad. Sci. U. S. A.* 102, 11402–11407. doi: 10.1073/pnas.0503634102

Tallaksen-Greene, S. J., Crouse, A. B., Hunter, J. M., Detloff, P. J., and Albin, R. L. (2005). Neuronal intranuclear inclusions and neuropil aggregates in HdhCAG(150) knockin mice. *Neuroscience* 131, 843–852. doi: 10.1016/j.neuroscience.2004.10.037

Vila, A. M., de Arrilucea, P. R., Pelaez, E. C., and Gago-Martinez, A. (2010). Development of a new magnetic beads-based immunoprecipitation strategy for proteomics analysis. *J. Proteomics* 73, 1491–1501. doi: 10.1016/j.jprot.2010.02.015

Waelter, S., Boeddrich, A., Lurz, R., Scherzinger, E., Lueder, G., Lehrach, H., et al. (2001). Accumulation of mutant huntingtin fragments in aggresome-like inclusion bodies as a result of insufficient protein degradation. *Mol. Biol. Cell* 12, 1393–1407. doi: 10.1091/mbc.12.5.1393

Wagner, A. S., Politi, A. Z., Ast, A., Bravo-Rodriguez, K., Baum, K., Buntru, A., et al. (2018). Self-assembly of Mutant Huntingtin Exon-1 Fragments into Large Complex Fibrillar Structures Involves Nucleated Branching. *J. Mol. Biol.* 430, 1725–1744. doi: 10.1016/j.jmb.2018.03.017

Wanker, E. E., Ast, A., Schindler, F., Trepte, P., and Schnoegl, S. (2019). The pathobiology of perturbed mutant huntingtin protein-protein interactions in Huntington's disease. *J. Neurochem.* 151, 507–519. doi: 10.1111/jnc.14853

Conflict of Interest: MM and JG are co-inventors on patent number WO2016016278A2 entitled "Human-derived anti-huntingtin (htt) antibodies and uses thereof." MM and JG are employees and shareholders of Neurimmune AG, Switzerland.

The remaining authors declare that the research was conducted in the absence of any commercial or financial relationships that could be construed as a potential conflict of interest.

frontiers in Chemistry

REVIEW
published: 07 July 2021
doi: 10.3389/fchem.2021.666585

α-Synuclein: An All-Inclusive Trip Around its Structure, Influencing Factors and Applied Techniques

Nicolò Bisi[1†], Lucia Feni[2†], Kaliroi Peqini[2†], Helena Pérez-Peña[3†], Sandrine Ongeri[1], Stefano Pieraccini[3] and Sara Pellegrino[2]*

[1]BioCIS, CNRS, Université Paris Saclay, Châtenay-Malabry Cedex, France, [2]DISFARM-Dipartimento di Scienze Farmaceutiche, Sezione Chimica Generale e Organica "A. Marchesini", Università degli Studi di Milano, Milan, Italy, [3]Dipartimento di Chimica, Università degli Studi di Milano, Milan, Italy

Alpha-synuclein (αSyn) is a highly expressed and conserved protein, typically found in the presynaptic terminals of neurons. The misfolding and aggregation of αSyn into amyloid fibrils is a pathogenic hallmark of several neurodegenerative diseases called synucleinopathies, such as Parkinson's disease. Since αSyn is an Intrinsically Disordered Protein, the characterization of its structure remains very challenging. Moreover, the mechanisms by which the structural conversion of monomeric αSyn into oligomers and finally into fibrils takes place is still far to be completely understood. Over the years, various studies have provided insights into the possible pathways that αSyn could follow to misfold and acquire oligomeric and fibrillar forms. In addition, it has been observed that αSyn structure can be influenced by different parameters, such as mutations in its sequence, the biological environment (e.g., lipids, endogenous small molecules and proteins), the interaction with exogenous compounds (e.g., drugs, diet components, heavy metals). Herein, we review the structural features of αSyn (wild-type and disease-mutated) that have been elucidated up to present by both experimental and computational techniques in different environmental and biological conditions. We believe that this gathering of current knowledge will further facilitate studies on αSyn, helping the planning of future experiments on the interactions of this protein with targeting molecules especially taking into consideration the environmental conditions.

Keywords: intrinsically disordered protein, synucleinopathy, secondary and tertiary structure, protein interaction, *in silico* studies

OPEN ACCESS

Edited by:
Jinghui Luo,
Paul Scherrer Institut (PSI), Switzerland

Reviewed by:
Daniel E. Otzen,
Aarhus University, Denmark
Martina Huber,
Leiden University, Netherlands

***Correspondence:**
Sara Pellegrino
sara.pellegrino@unimi.it

[†]These authors equally contributed to this work

Specialty section:
This article was submitted to Chemical Biology, a section of the journal Frontiers in Chemistry

Received: *10 February 2021*
Accepted: *02 June 2021*
Published: *07 July 2021*

Citation:
Bisi N, Feni L, Peqini K, Pérez-Peña H, Ongeri S, Pieraccini S and Pellegrino S (2021) α-Synuclein: An All-Inclusive Trip Around its Structure, Influencing Factors and Applied Techniques. Front. Chem. 9:666585. doi: 10.3389/fchem.2021.666585

INTRODUCTION

Alpha-synuclein (αSyn) is a relatively small protein formed by 140 residues, which is highly expressed and conserved. It is typically found in the presynaptic terminals of neurons. Its primary sequence can be divided into three regions, as shown in **Figure 1** (Fusco et al., 2014; Mori et al., 2020; Uversky and Eliezer, 2009) that are characterized by different physico-chemical properties due to their distinct aminoacidic composition. First, the *N*-terminal segment, (residues 1–60), shows numerous amphipathic 11-mer repetitions, and contains the consensus sequence KTKEGV. This is the αSyn region where most of the familial mutations are located. Then, the non-amyloid-β-component (NAC) central region (residues 61–95) is highly amyloidogenic giving the protein the ability to generate β-sheets. Finally, the *C*-terminal segment (residues 96–140) is rich in anionic residues and prevents αSyn aggregation by electrostatic repulsion.

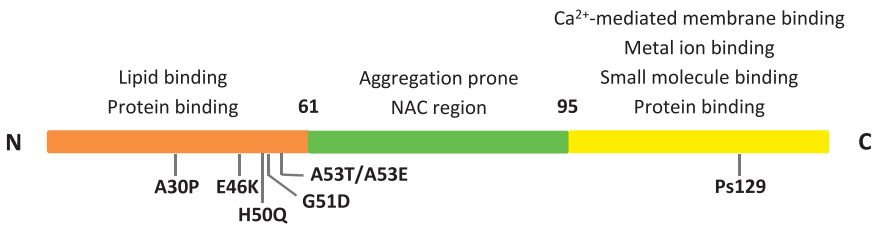

FIGURE 1 | The three αSyn regions are represented in different colors. Their properties, along with the main PD mutations and interacting sites are indicated.

In its native state, monomeric αSyn is unfolded, and thus is commonly considered as an intrinsically disordered protein (IDP). Yet, there is still a large controversy regarding αSyn secondary and tertiary structural tendencies and the data from literature are often conflicting. Changes in the environment conditions, mutations, interactions with endogenous and/or exogenous molecules can indeed induce αSyn to fold in different structures. αSyn misfolding and its subsequent aggregation into amyloid fibrils is a pathogenic hallmark of different synucleinopathies, such as Parkinson's disease (PD). As a consequence, the comprehension of αSyn structural and functional features is fundamental to progress in the study and finding of treatments for αSyn-related diseases.

Here, we provide a review on *in silico* and experimental data regarding the structural features of αSyn both in the WT form and in biologically relevant mutants. Moreover, we focus on different factors influencing αSyn structure, such as the biological environment, the interaction with lipids, with endogenous small molecules and proteins, as well as with exogenous compounds (e.g., drugs, diet components, heavy metals). We also discuss the different methods used to highlight αSyn structure in each case and the relation between the obtained results and the employed technique.

MONOMERIC WILD TYPE (WT) αSYN STRUCTURAL FEATURES

In 1996, Weinreb et al. observed that Wild-Type (WT) αSyn exists in solution as a dynamic ensemble of conformations lacking a single equilibrium structure and, therefore, classified it as an IDP (Weinreb et al., 1996). Many studies have advanced our knowledge in this field by applying experimental (for a recent review on NMR investigations see Kim et al., 2020) and computational (e.g., MD, Monte Carlo simulations) techniques (Jónsson et al., 2012), or a combination of both approaches (Brodie et al., 2019). However, due to αSyn structural heterogeneity that depends on many different biological and physico-chemical factors (Stephens et al., 2019), caution is needed when interpreting these results. To date, the general consensus is that monomeric WT αSyn is almost unstructured in solution (Fauvet et al., 2012). Anyway, variations of WT αSyn structural propensity can be detected. In order to rationalize the vast amount of literature data, we try to categorize them according to two different levels: global and local (**Table 1** and below).

Global-Level

Tertiary Structure Propensity

αSyn is able to interconvert between multiple states of the dynamic ensemble of conformations (Weinreb et al., 1996). Nonetheless, at the global-level, different research groups have reached different conclusions as to whether the conformational ensemble in solution is on average: (1) likely to be compact and acquire a globular-like structure driven mainly by long-range intra-molecular electrostatic interactions, as illustrated in **Figures 2** and **3** or (2) prone to exist as an extended random coil.

At physiological pH, WT αSyn has a very uneven distribution of physico-chemical properties along its sequence. The *N*-terminal region is amphipathic, the NAC region hydrophobic, and the *C*-terminal region highly negatively charged (Ilie and Caflisch, 2019). Flickering structural tendencies can be observed when viewing the hydrophobic effect as the major driving force for protein folding (Kauzmann, 1954). Based on this assumption, the contacts between the hydrophobic residues and the polar solvent are minimized. In turn, the regions formed by hydrophilic residues, such as the polar part of the *N*-terminal region and the *C*-terminal region, are expected to be more exposed to the cellular solvent and transiently interact with each other (Dułak et al., 2020). Experimental and computational techniques have suggested the presence of brief long-range intramolecular electrostatic interactions within αSyn structure (Dedmon et al., 2005b; Bertoncini et al., 2005; Allison et al., 2009; Fakhree et al., 2018; Brodie et al., 2019).

Dedmon et al. and Yu et al. lack of agreement on the exact residues that form the αSyn intra-electrostatic contacts, nonetheless, both agree on the existence of such interactions between the residues present in the *C*-terminal domain and those located in the central part of the protein. Moreover, Bertoncini et al. (2005) reported that perturbation of these long-range naturally occurring interactions could lead to the exposure of the NAC region (residues 61–95) toward the cellular environment, potentially promoting αSyn oligomerization. Furthermore, *in vivo* and *in vitro* experiments have shown that the truncation of the monomeric WT αSyn *C*-terminal

TABLE 1 | Reported experimental and computational data on monomeric wt αSyn.

Structural features		Technique		References
Global	**Local**	**Experimental**	**Computational**	
Compact, globular structure Electrostatic interactions (120–140 and 30–100 residues)	–	Technique: PRE[1] Spin label MTSL Cysteine mutations at Q24, S42, Q62, S87 and N103	Technique: MD[2]	Dedmon et al. (2005a)
Brief long-range intramolecular electrostatic interactions	–	Technique: NMR[3] 100uM WT αSyn in buffer (25mM Tris.Cl pH = 7.4/0.1M NaCl)	–	Bertoncini et al. (2005)
Extended tendency Brief long-range intramolecular electrostatic interactions	N-terminal: Helical elements	Technique: NMR[3]	Technique: restrained MD[2] Solvent: implicit	Allison et al., 2009
Compact structure at both neutral and low pH C- to N-terminal interchain interactions	–	Technique: PRE[1] Various pH, concentrations, solvents	–	Wu and Baum, (2010)
Compact structure (low pH)	–	Technique: Single-Molecule FRET[4] 50 pM solution of double-labeled WT αSyn	Technique: constrained excluded volume MC[5] Technique: All-atom MD[2] Solvent: explicit	Nath et al. (2012)
High-energy phase: Extended random coil Low-energy phase: Extended all-β	High-energy phase: N-terminal: Helical elements Low-energy phase: N-terminal + NAC + C-terminal (residues 30–100): β-strands C-terminal: β-structures + random coil	–	Technique: MC[5] Solvent: Implicit	Jónsson et al. (2012)
–	N-terminal + NAC + C-terminal (residues 1–100): Helical elements	–	Technique: REMD[6] Solvents: implicit Technique: MD[2] Solvents: explicit	Coskuner et al., (2013)
Compact structure Electrostatic interactions (118–130 and 38–53 residues) α+β	N-terminal: Helical elements + β-hairpin spanning residues 38–53 β-strands: β1 (38–44) and β2 (47–53) NAC: Helical elements C-terminal: Helical elements + β-structures	–	Technique: coarse-grained MD[2] Solvent: explicit	Yu et al. (2015)
Compact, globular structure Tail-like protrusions All-α	N-terminal: Helical elements NAC: Helical elements C-terminal: Helical elements	Technique: HS-AFM[7] 50nM WT αSyn in PBS	Technique: REX[8]/DMD[9] Solvent: Lazaridis-Karplus implicit	Zhang et al. (2018)
Compact, globular structure Brief long-range intramolecular electrostatic interactions α+β	N-terminal: Helical elements spanning residues 25–55 NAC: β-structures C-terminal: β-structures + random coil	Techniques: LD-CL[10], CD[11],HDX[12], LC-MS[13]/MS Analysis	Technique: REX[8]/DMD[9] Solvent: Lazaridis-Karplus implicit	Brodie et al., 2019
Compact, globular structure Tail-like protrusions All-α	N-terminal: Helical elements NAC: Helical elements C-terminal: Helical elements + random coil	–	Technique: MD[2] Solvents: explicit	Bhattacharya et al. (2019)
–	N-terminal: Helical elements spanning residues 10–30 and a weak helix centered around residue 50 NAC: tendency to form β-structures helix centered around residue 90	Technique: NMR[3]	–	Kim et al. (2020) (review)

[1]*Paramagnetic Relaxation Enhancement.*
[2]*Molecular Dynamics simulations.*
[3]*Nuclear magnetic resonance.*
[4]*Fluorescence resonance energy transfer.*
[5]*Monte Carlo simulations.*
[6]*Replica Exchange Molecular Dynamics simulations.*
[7]*High-Speed Atomic Force Microscopy.*
[8]*All-atom Replica Exchange.*
[9]*Discrete Molecular Dynamics.*
[10]*Long-distance crosslinking.*
[11]*Circular dichroism.*
[12]*Hydrogen-deuterium exchange.*
[13]*Liquid chromatography–mass spectrometry.*

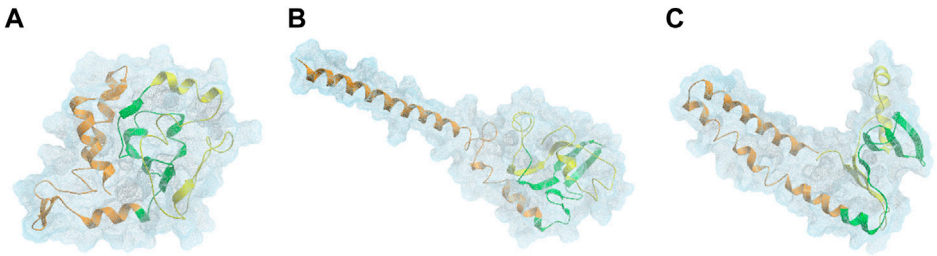

FIGURE 2 | DMD centroids of the most frequent monomeric WT αSyn lowest energy clusters. Clusters representing a **(A)** ~76%, **(B)** 15%, and **(C)** ~4% of the overall population. αSyn N-terminal region (residues 1–60) is colored in orange, the NAC-region (residues 61–95) is colored in green and the C-terminal region (residues 96–140) is colored in yellow (Zhang et al., 2018).

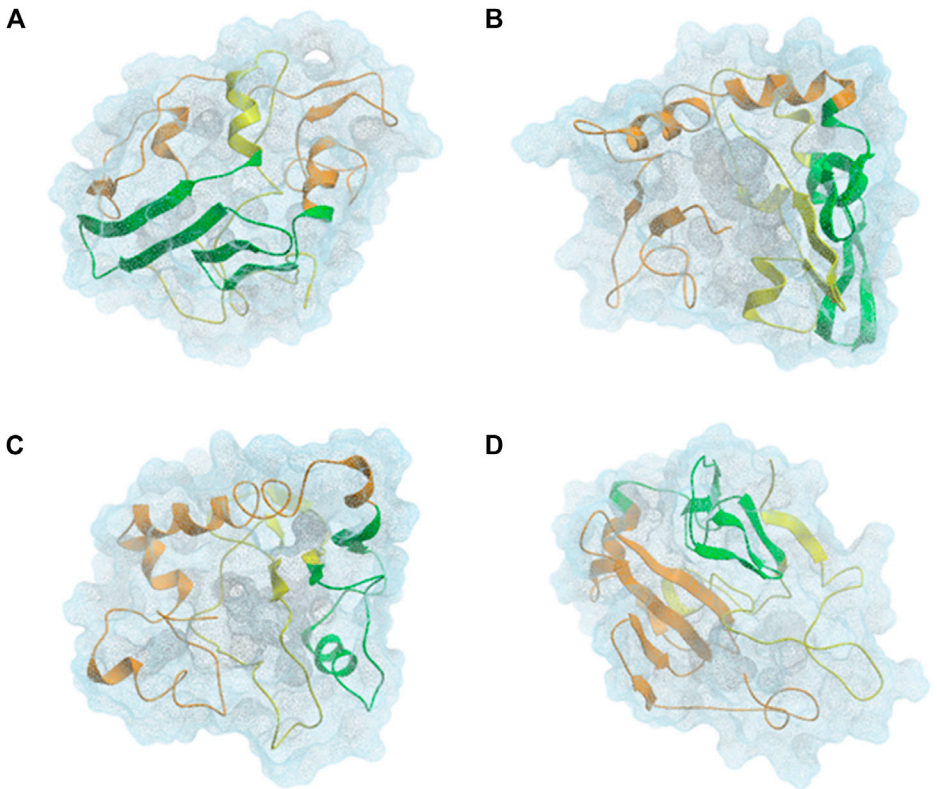

FIGURE 3 | CL-DMD WT monomeric αSyn models. Centroids from the most relevant conformational clusters containing **(A)** 37%, **(B)** 28%, **(C)** 20%, and **(D)** 8% of the overall population. αSyn *N*-terminal region (residues 1–60) is colored in orange, the NAC-region (residues 61–95) is colored in green and the *C*-terminal region (residues 96–140) is colored in yellow (Brodie et al., 2019).

region can induce the formation of amyloid aggregates (Iyer et al., 2017; Vasili et al., 2019). Hence, several studies hypothesized that these detected intra-molecular contacts reduce the accessibility of the central part of the protein, preventing it from establishing inter-molecular interactions and inhibiting monomeric WT αSyn oligomerization and aggregation. As a consequence, some authors have rationalized the possibility of αSyn *C*-terminal region demonstrating a protective role against the formation of amyloid fibrils (Dedmon et al., 2005b; Bertoncini et al., 2005; Yu et al., 2015).

The temperamental nature of these aggregation-resistant globular conformations can be affected by changes in the environment; for example, changes in pH alters the distribution of charges throughout αSyn, which can lead to the loss of these transient intra-molecular electrostatic interactions. The *C*-terminal domain, (residues 96–140), presents a high content of acidic residues at physiological pH which are thought to play a major role inhibiting αSyn aggregation (Dedmon et al., 2005b; Bertoncini et al., 2005; Bhattacharya et al., 2019). Studies suggest that, this self-inhibition against

fibrillation conformation can be lost when changing the pH from neutral to acidic (Plotegher et al., 2014).

Contrarily, Nath et al. observed that αSyn acquires a more compact conformation at low pH (Nath et al., 2012). However, this should be taken with caution as these are predictions and not conclusive observation. Moreover, some research groups point out that the interactions between the *C*-terminal region and the rest of the molecule is rather small and, therefore, the contacts established within the native structure provide limited protection against solvent exposure for the NAC region (Jónsson et al., 2012).

Further criticism suggests that monomeric WT αSyn acquires more extended or tail-like global conformations, which aligns with the fact that it is unstructured in solution. Zhang et al. reported the structural dynamics of αSyn in aqueous solution, demonstrating its ability to interchange its structure dynamically, mainly between the primary overall globular morphology and both one-tail and two-tail structures. These tails are parts of the protein that protrude from the main globular segment (**Figure 2**) (Zhang et al., 2018). The tendency of αSyn to adopt a tail-like structure has also been reported by other researchers, based on MD simulations, Small-Angle X-ray Scattering (SAXS) and Electron Microscopy (EM) experiments (Tsigelny et al., 2012; Lorenzen et al., 2014). These transient tail-like structures are often seen in IDPs because they are implicated in diverse biological functions (Uversky, 2013).

Lastly, other studies stated that, in aqueous solvent, monomeric WT αSyn has a weak preference for adopting globular conformations (Weinreb et al., 1996; Ilie and Caflisch, 2019). For instance, Allison et al. observed that, over time, monomeric WT αSyn has a propensity to expand (Allison et al., 2009). Also, others have reported relevant clusters of αSyn monomers detected in their experiments presenting extended conformations (Jónsson et al., 2012).

The controversial results about the globular or extended preferences obtained by various groups may be ascribed to the rapid interconversion between conformers affecting αSyn and the use of different methodologies to carry out their investigations.

Overall Secondary Structure Propensity

Knowing that monomeric WT αSyn is unstructured in solution, the classification of its transient secondary structural elements can be useful for further investigations. Attempts to determine a structure of native αSyn has been mainly classified it as an all-α protein, whose secondary structure is composed exclusively of α-helices allowing a small number of isolated β-sheets (**Figure 2**) (Bhattacharya et al., 2019; Cartelli et al., 2016; Meade et al., 2019; Zhang et al., 2018) or as an α+β protein when along the αSyn backbone α-helices and β-strands are intercalated (**Figures 3** and **4**) (Yu et al., 2015; Brodie et al., 2019).

Conversely, Jónsson et al. predicted that αSyn could adopt an all-β secondary structure in which αSyn was almost entirely composed by β-sheets with some peripherical small α-helices in several of the detected relevant conformers obtained.

They also reported that these results match with experimental data obtained at neutral pH and low temperatures, around 15°C (Jónsson et al., 2012). Zhang et al. (2018) found this

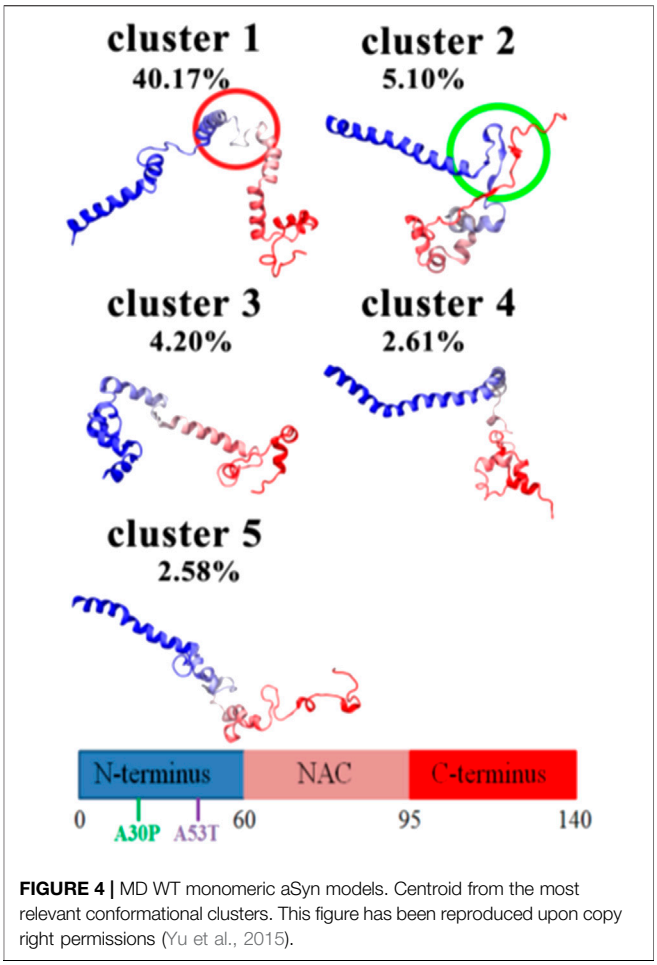

FIGURE 4 | MD WT monomeric aSyn models. Centroid from the most relevant conformational clusters. This figure has been reproduced upon copy right permissions (Yu et al., 2015).

conformational extended β-sheet pattern to be unfavorable in the WT αSyn monomeric state.

Some studies argue that folded helical conformers are not anticipated to be pathogenic (Meade et al., 2019) and impede amyloidogenic aggregation (Bhattacharya et al., 2019) whereas the presence of β-sheets drive this process. In fact, the design of novel small molecules or biological therapeutics to stabilize α-helical monomers is a strategy for blocking the neurotoxic pathway switching off β-sheet structure formation (Plotegher et al., 2014; Ciechanover and Kwon, 2015).

Local-Level

Since we face the problem of the lack of technical resources to irrefutably determine a series of conformations that full-length WT αSyn monomers can adopt in solution, attempts have been made to use available techniques to identify structural trends at the local-level, that is, if it even has a determinable structure. Despite its unstructured nature, αSyn can be analyzed in terms of its transient secondary structures. This allows us to hypothesize the conformational changes αSyn undergoes before the molecular aggregation process is carried out and identify possible target-sites that facilitate the design of drugs to avoid the formation of amyloid fibrils in earlier stages. As a matter of fact, due to the intrinsic dynamic equilibrium of this protein in solution, as

mentioned, different tools and techniques for proteins characterization capture different structural trends. However, there is an identifiable trend in which several research groups outline that the *N*-terminus of WT αSyn is prone to fold into a helical conformation, whereas the *C*-terminus contains many fragments found as random coils. There is less agreement as to whether the NAC region folds into β-sheets, which is the key secondary structure that directs protein aggregation, or whether it maintains a helical structure.

N-Terminal Region

Monomeric WT αSyn N-terminal region can adopt different transient secondary structural features in aqueous solution due to its intrinsically disordered nature. Several studies observed a tendency in the αSyn *N*-terminus to acquire a helical secondary structure (Vilar et al., 2008; Allison et al., 2009; Jónsson et al., 2012; Coskuner and Wise-Scira, 2013; Zhang et al., 2018; Bhattacharya et al., 2019; Brodie et al., 2019; Meade et al., 2019; Kim et al., 2020). This helical pattern has been proposed to be essential for vesicle and membrane binding (Coskuner and Wise-Scira, 2013; Vasili et al., 2019). Hence, this local conformation is prone to be energetically favorable, especially in the presence of factors known to drive this helical structural feature, such as acidic negatively charged membranes (Vasili et al., 2019).

Contrarily, Jónsson et al. predictedan αSyn conformational low-energy phase in solution, in which residues spanning from 30 to 100 contained a high average strand population (Jónsson et al., 2012). Additionally, Yu et al. identified in residues 38–53 a high probability of assuming a β-hairpin conformation, formed by antiparallel β-strands β1 (38–44) and β2 (47–53), connected by a turn in region 44–47 (**Figure 4**) (Yu et al., 2015). This protein region includes some of the residues belonging to two of the five αSyn segments suggested to be involved in the core of αSyn fibrils (37–43, 52–59) (Vilar et al., 2008). Other computational and bioinformatic studies have also reported a higher propensity for regions 38–40 and 50–53 to form β-strand structures (Vilar et al., 2008).

NAC Region

There is presently no clear agreement as to whether the NAC region (residues 61–95) adopts a helical or a β-sheet structure or, indeed, whether it acquires a structure at all. As this region is involved in triggering protein aggregation, its structure depends to a great extent on the environmental conditions. This is probably why it contains numerous distinct energetically favorable secondary structures.

A combination of experimental and computational approaches (Brodie et al., 2019) and NMR measurements (Eliezer, 2009) have seen a tendency of the αSyn NAC region to form β-structures (**Figure 3**) (Kim et al., 2020). This supports the significance of the presence of these transient structures in the native protein, alluding to their resemblance to hairpins that form inter-molecular interactions in amyloid fibrils constituting the core of this mature fibrillar form of αSyn (Tuttle et al., 2016; Guerrero-Ferreira et al., 2018). In contrast, in previous NMR studies, it was not possible to detect free αSyn conformations that would lead to the formation of partially folded aggregation intermediates (Wu and Baum, 2010).

Since the αSyn aggregation process is extremely slow, ensemble solution techniques such as NMR may not succeed in identifying the molecules that are prone to drive this process because they may appear in very small percentages (Plotegher et al., 2014). Nonetheless, Zhang et al. (2018) via HS-AFM documented that the extended β-sheet pattern in the WT αSyn monomeric state is unfavorable.

Other experiments show the sporadic formation of helical structures in the NAC region (**Figure 2**) (Coskuner and Wise-Scira, 2013; Zhang et al., 2018)

C-Terminal Region

The *C*-terminus of IDPs has been identified as the most important region since it has numerous functionalities (Uversky, 2013). It follows that this protein area adopts different structures depending on the function that it is required to perform. The results of the investigations that have tried to structurally characterize αSyn in an aqueous medium, either by experimental or computational methods, indicate that the *C*-terminal end tends to present a random coil structure for the most part under physiological conditions (Jónsson et al., 2012; Brodie et al., 2019).

Despite this tendency to present fewer secondary structure elements than the other protein regions, a propensity to form β-structures (Eliezer, 2009; Jónsson et al., 2012; Yu et al., 2015) and helical elements (Lorenzen et al., 2014; Yu et al., 2015; Zhang et al., 2018) has been observed in some studies.

EFFECT OF PD MUTATIONS ON αSYN STRUCTURAL FEATURES

αSyn is a protein involved in PD, not only as the main component of Lewy bodies, but because of its several mutations observed in PD patients. It is well known that mutations can change the phenotype, having several effects on the structure of a protein. Understanding how PD mutations affect αSyn structure and its functions is thus essential for gaining a profound understanding of the protein itself and for developing more effective pharmacological strategies.

A53T, A30P, and E46K Mutations

In 1997, Polymeropoulos et al. (1997) identified the A53T mutation in the αSyn gene in an Italian kindred and in three unrelated families of Greek origin with autosomal dominant inheritance for the PD phenotype. A year after, Krüger et al. (1998) reported the A30P mutation in the αSyn gene. A third mutation, namely E46K, was identified in 2004 (Zarranz et al., 2004). During the years, it has been highlighted that mutations could impact both the free state of αSyn and its aggregated form. In this context, studies were performed using different techniques such as NMR spectroscopy, CD, and FTIR.

Initial CD studies on WT αSyn and the first two identified mutations, A30P and A53T, showed that the three proteins lack a preferred conformation in solution (Conway et al., 1998; Narhi

et al., 1999; Serpell et al., 2000). However, in 2001, by conducting NMR studies, Bussell and Eliezer reported, that the mutation A30P strongly attenuates the helical propensity of the *N*-terminus. They observed indeed a positive C^{α} secondary shift, indicative of a significant preference for helical secondary structure in the WT 18–31 sequence, which was absent in mutant A30P. Conversely, A53T mutation leaves this region unperturbed, exerting a more modest and local influence on structural propensity (Bussell and Eliezer, 2001). In particular, the A53T mutant exhibited a slightly enhanced local preference for extended, β-sheet-like conformations around the site of the mutation. Other NMR studies on the WT, A30P and A53T, revealed a similar β-sheet-rich core region spanning residues 38–94 in the sequence of the two mutants, whereas the *C*-terminus remained flexible and unfolded in both cases (Heise et al., 2005).

McLean et al. investigated the αSyn long-range interactions by fluorescence resonance energy transfer (FRET). They reported, for both the WT and mutant A53T, a weak interaction between the *N*-terminal and *C*-terminal regions, whereas for mutant A30P they observed a statistical increase in the magnitude of FRET signal, indicating a closer vicinity between the *N*- and *C*- terminal regions (McLean et al., 2000).

In 2007, Fredenburg et al. reported a similar random coil secondary structure for both E46K and WT αSyn when free in solution, as highlighted by CD experiments (Fredenburg et al., 2007). In 2009, Rospigliosi et al. studied the effect of mutation E46K on the long-range interactions by paramagnetic relaxation NMR(PRE) and residual dipolar coupling (RDC) measurements. Surprisingly, no decrease in long-range contacts was detected in the mutant E46K with respect to the WT. Furthermore, an increased interaction between the *C*-terminal tail, the NAC and the *N*-terminal regions was observed. The same experiments on A30P and A53T did not indicate any changes in the long-range structure. In the same work, the authors observed a slight increase in local helix propensity in the area immediately adjacent to the mutation of mutant E46K, by calculating its C^{α} chemical shifts deviations in comparison to the deviations of the random coil ones (Rospigliosi et al., 2009).

Kumar et al. used Molecular Dynamics (MD) to analyze the mutations A30P, A53T and E46K in water under explicit solvent conditions. These mutants showed variations, more specifically their RMSD scores were 0.529, 0.534, and 0.486 respectively, in their secondary structure compared to WT micelle-bound αSyn (PDB ID 1XQ8) simulated in sodium dodecyl sulfate (SDS) (**Figure 5**). The secondary structure of A53T recorded in this study was similar to that determined by quenched hydrogen/deuterium exchange NMR spectroscopy which states that five β-strands appear in the amyloid state of αSyn (Vilar et al., 2008; Kumar et al., 2009).

Passing from the last decade to the current one, computational techniques started being more intensively employed to shed light on the structures of the WT and the mutants. In 2011, Balesh et al. (2011) performed classical MD and annealing MD (AMD) simulations and reported similar helical and β-sheet contents for the WT and A53T mutant-type αSyn proteins. At the same time, A53T presented a more compact structure. In 2013, Coskuner and Wise-Scira performed all-atom replica exchange molecular dynamics (REMD) simulations on the full-length monomeric WT and A53T mutant-type αSyn proteins in aqueous solution utilizing implicit and explicit water models. From these results, they observed that the helical content is minimally affected by the mutation A53T except for a few residues in the *N*-terminal and *C*-terminal regions. Additionally, in contrast, to previous computational works (Kumar et al., 2009) they reported an increase in the β-sheet formation close to the mutation site in the *N*-terminal region (Coskuner and Wise-Scira, 2013).

In the same year, a similar MD study was published on mutant A30P by Wise-Scira et al., reporting that the mutation has local as well as long-range effects on the protein structure. More specifically, the helical content of region 18–31 is less prominent in mutant A30P than in the WT protein. The β-sheet structure abundance decreases in the *N*-terminal region upon mutation A30P of the WT αSyn, whereas the NAC and *C*-terminal regions possess larger tendencies for β-sheet structure formation. Long-range intramolecular protein interactions are less abundant upon mutation A30P, especially between the NAC and *C*-terminal regions, leading to a less compact and less stable structure with respect to the WT (Wise-Scira et al., 2013).

Recently Discovered Mutations

In 2013, a fourth mutation, namely H50Q, was identified (Appel-Cresswell et al., 2013; Kiely et al., 2013). Far-UV CD studies demonstrated that also the H50Q variant is a primarily unfolded protein in aqueous buffers (Chi et al., 2014; Ghosh et al., 2013; Khalaf et al., 2014). Also, Chi et al. (2014), by using heteronuclear single quantum coherence (HSQC) NMR observed that the chemical shifts of most residues between the WT and H50Q were unperturbed, although the *C*-terminal region of H50Q is more flexible than that of the WT. On the contrary, Ghosh et al. noticed chemical shift perturbations between WT αSyn and H50Q, by conducting the same experiments. In fact, they observed quite significant chemical shift perturbations in the mutation area and in the C-terminal region (Ghosh et al., 2013).

In 2014, a fifth mutation, G51D, was discovered (Kiely et al., 2013; Lesage et al., 2013). Fares et al. performed CD experiments where the WT and G51D proteins exhibited the same random coil secondary structure. The ^{1}H, ^{15}N-HSQC studies confirmed the lack of a preferred conformation for both proteins, while the analysis of the secondary structure propensity *via* C^{α} secondary shifts deviations showed no significant loss or gain of secondary structure compared to the WT. Furthermore, it was observed that the mutation G51D also does not significantly perturb transient long range contacts between *N*-and *C*-termini (Fares et al., 2014).

In the same year, mutation A53E was identified in a Finnish family (Pasanen et al., 2014). Ghosh et al. performed NMR studies with the WT, A53T, and A53E αSyn. Their data showed approximately similar spectra of the WT, A53T, and A53E with relatively narrow dispersions in the proton dimension for all proteins, characteristic for unfolded structures. The chemical shift differences, however, suggest perturbation of chemical shifts for residues surrounding the A53E mutation

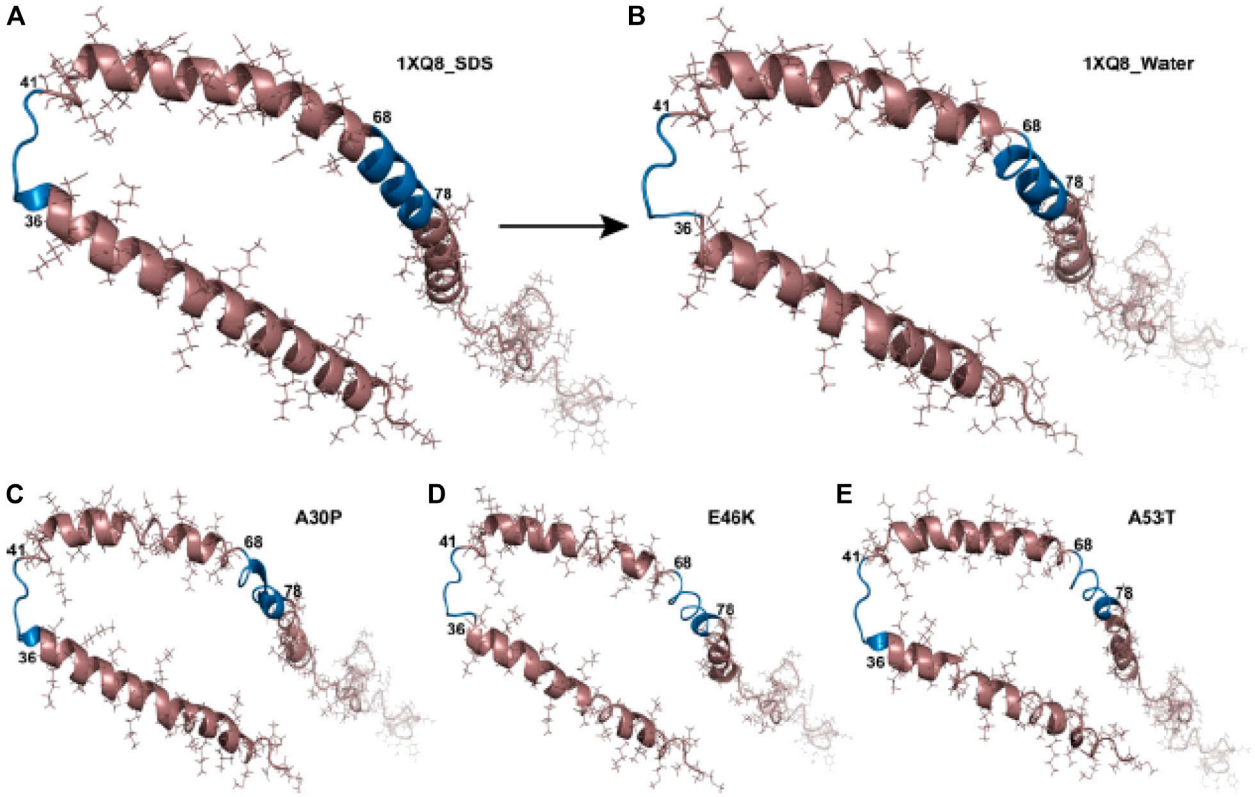

FIGURE 5 | Structural changes in αSyn and the hydrophobic regions. Structure of **(A)** wild type (1XQ8) in SDS solvent, **(B)** wild type (1XQ8) simulated in explicit water conditions, **(C)** A30P mutant in water solvent, **(D)** E46K mutant in water solvent, **(E)** A53T mutant in water solvent. The blue region depicts the 36–41 and 68–78 hydrophobic regions in αSyn showing aggregation propensity (Kumar et al., 2009).

site, as already observed for the other mutants. Significant chemical shift changes were also observed for the residues at the extreme *C*-terminus of αSyn. In contrast to chemical shift perturbation data, the secondary structural propensity did not show any major alteration due to mutation A53E or A53T (Ghosh et al., 2014).

Comparative Experiments on all Known Mutated Sequences

Recently, Tsigelny et al. generated by MD multiple structural conformations of the WT and all the different mutants, by developing a new combined modeling approach. In the beginning, they simulated WT αSyn and mutant conformers creating a 20-ns interval MD snapshot (**Figure 6**). From their analysis it can be deduced that the general α-helical content does not change more than 20% in all cases and that these α-helices transform into turns and loops within specific regions for each mutant over the 100 ns of the MD (Tsigelny et al., 2015).

In 2020, Okuwaki et al. examined all the NMR parameters, including the chemical shift and amide-proton exchange of the WT and the mutants. They observed in WT an α-helix structure in the 18–31 fragment, and a β-structure at the C-terminal region 120–140. The β-structure was destabilized by the mutations A30P and A53T. On the other hand, the α–helical structure might be stabilized by these mutations (Okuwaki et al., 2020).

Taken together, these data seem to point out that, among all the observed PD mutations, only A30P affects the overall αSyn structure. In addition, long-range interactions are less abundant. The contact between *N*- and *C*-terminal regions is thus perturbed and it might facilitate the aggregation.

EFFECT OF THE BIOLOGICAL ENVIRONMENT ON αSYN STRUCTURAL FEATURES

From the previous paragraphs, it can be deduced that the structure of the monomeric WT αSyn protein in solution tends to acquire diverse transient and dynamic conformations. αSyn will be likely to adopt specialized conformations upon different conditions (e.g., changes in pH, temperature, ionic strength, closeness to surfaces, etc. . .) in order to carry out certain biological or pathological functions. Hence, even though the study of WT αSyn conformation alone is useful, a more profitable course of action is to observe the conformational changes induced by different biological and physico-chemical factors triggering structure modifications. In

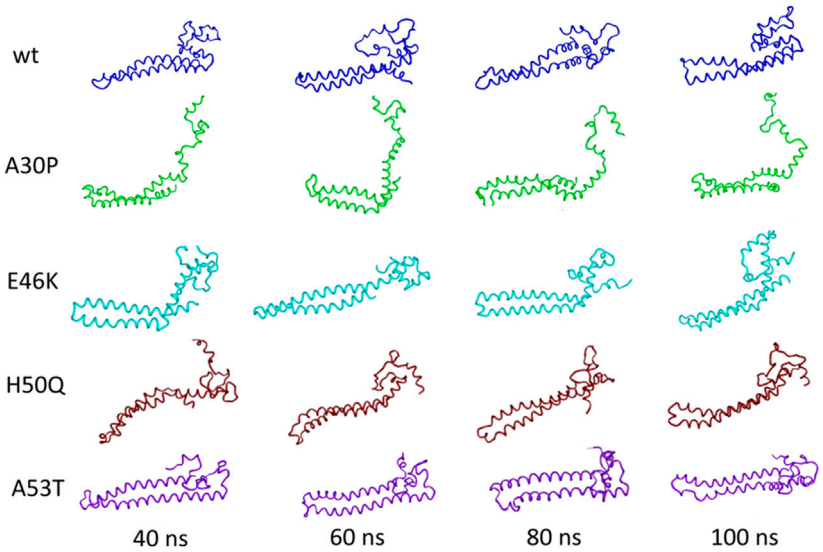

FIGURE 6 | Tertiary structure of the initial NMR conformations of the mutants containing a significant percentage of α-helices changes during MD. Figure modified from Tsigelny et al. (2015).

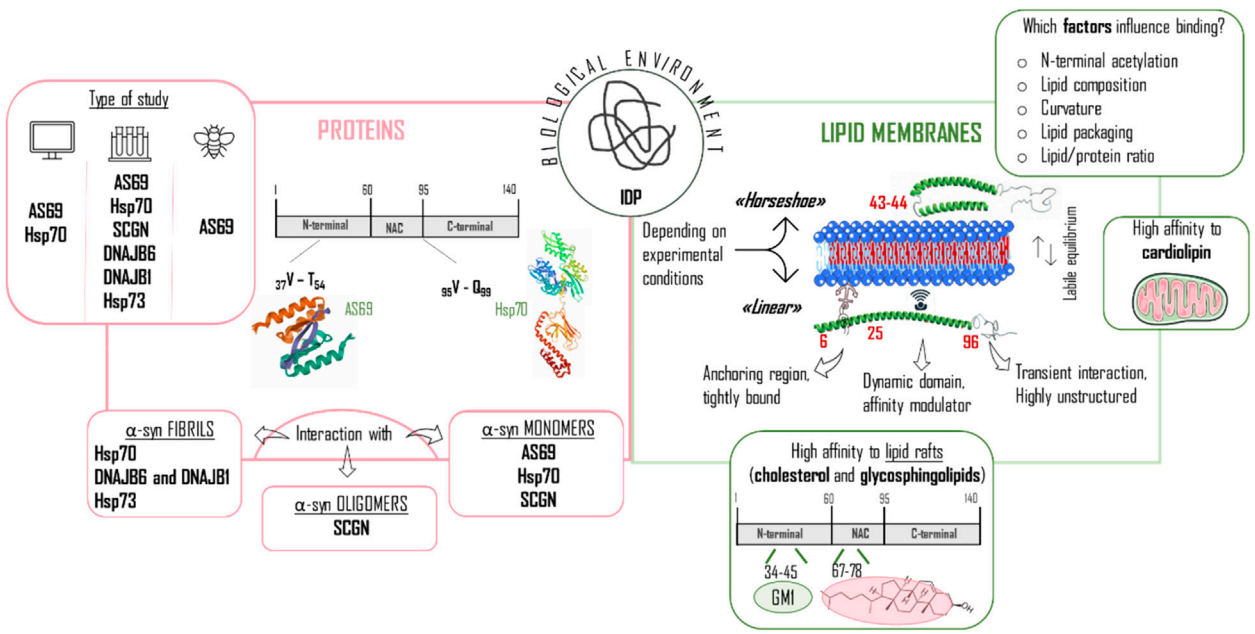

FIGURE 7 | Different biological factors/modulators influencing αSyn structure. The figure is composed of two sections referring to proteins **(left panel)** and lipid membranes **(right panel)**, which have an important role in the conformational change of αSyn from being an intrinsically disordered protein (IDP) to induce a more stable structure. Right panel: special emphasis is placed on the type of study performed, classified in computational, *in vitro* and *in vivo* experiments, and on the particular interaction of the proteins with the distinct αSyn configurations (fibrils, oligomers, monomers). Hsp70 and Hsp73 heat shock protein 70 and 73; SCGN: secretagogin. Left panel: The equilibrium between horseshoe and linear conformation is highlighted and the partition of αSyn in three regions is depicted to show the different behavior throughout the sequence when in contact with lipid membranes. The important interaction with mitochondrial membranes and lipid rafts is also mentioned here. GM1: monosialotetrahexosylganglioside.

this context, the interaction with endogenous molecules is an important factor to consider. It is commonly accepted that αSyn can bind lipids and phospholipids, as well as several proteins. Here below in **Figure 7**, the general features are presented, together with several highlights on the interaction with endogenous small molecules.

Lipids

In living organisms, lipids are mainly used as structural components in cell membranes, as energy stores or as signaling molecules. Various studies have investigated the possibility of αSyn monomer to bind lipids, in particular lipid membranes (plasma and mitochondrial membrane, axonal transport vesicles) (Sung and Eliezer, 2018). In the following paragraphs, we will present an overview of the most recent results, focusing our attention on the protein structure and the innovative strategies and techniques used to obtain these outcomes.

Phospholipids

Based on the specific binding properties to lipid layers and the location in synaptic nerve endings, the physiological function of αSyn has been related to circulation and transport of synaptic vesicles (Burré, 2015). Nevertheless, besides its physiological role in the synaptic transmission, the interaction with lipids can also lead to structural changes undergoing aggregation and contributing to amyloidogenesis. Membranes have been reported to both accelerate and inhibit αSyn fibril formation. In fact, the helical fold has been suggested to stabilize the protein and prevent aggregation by hindering the structural transition to β-sheet (Högen et al., 2012) but, at the same time, the helical state has also been proposed as being an intermediate in the aggregation process because it stabilizes intermolecular interactions through hydrophobic contacts (Eliezer et al., 2001). In the latter case, cell membrane surfaces would act as a fibrillation template favoring nucleation and participating in the fibrillation cascade while the NAC region would be essential for the self-polymerization of the protein (Pineda and Burré, 2017; Martial et al., 2019; O'Leary and Lee, 2019). A fact that argues in favor of the role of αSyn/lipid interaction in the etiopathogenesis of synucleinopathies is that all missense mutations responsible for familial PD (e.g., A30P and E46K) are localized in the 11-residue repeat domain; indeed, these mutations alter the lipid binding properties modifying membrane interaction (Bodner et al., 2010; Robotta et al., 2017). Therefore, it is particularly critical to understand how this interaction can regulate the equilibrium between the soluble intrinsically disordered monomer and the structured membrane-bound monomer/oligomer *in vivo*.

The first preliminary hypothesis about αSyn binding to membranes was developed by Davidson et al. (1998), who reported αSyn binding to acidic small unilamellar vesicles (SUVs), underlining the importance of membrane charge and curvature. In particular, an increase in α-helicity from 3 to 80% was measured. Browne and coworkers first tried in 2001, by means of modern multi-dimensional heteronuclear NMR spectroscopy, to characterize the conformational properties of αSyn as a free monomer and when bound to lipid-mimetic SDS detergent micelles and lipid vesicles. A prevalent disposition toward α-helical conformation in the *N*-terminal region was suggested in the free monomer in comparison to the *C*-terminus that, on the contrary, displays a highly unfolded and extended structure. Not surprisingly this tendency could be fulfilled after association to phospholipids, showing an extended α-helical structure stretching among residues 1–100 (Eliezer et al., 2001). Few years later, this idea of an extended conformation was revised by Chandra et al., who asserted that the *N*-terminal region, interacting with SDS, surprisingly configures itself in two helical regions that are interrupted by a short break around residues 43–44, as demonstrated by NMR studies and proteolysis experiments. This interruption has been explained with a more favorable binding of hydrophobic residues to the interior of the membrane or, alternatively, a more advantageous binding to highly curved vesicles (Chandra et al., 2003). By means of following studies based on EPR, Jao et al. could successfully provide important details about αSyn interaction with lipid bilayers, emphasizing the influence of the membrane features on the conformation of the membrane bound αSyn. The authors observed an extended, curved α-helical structure that is significantly different from the antiparallel helices formed in the presence of the detergent SDS (Jao et al., 2008). However, the experimental evidences provided by EPR are also consistent with different binding modes, involving an extensive membrane rearrangement, as suggested by Bodner et al. (Bodner et al., 2009). In this context of contradictory results, Robotta et al. (2011) presented αSyn as a coexistence of the two conformations: extended α-helix and horseshoe, i.e. two antiparallel α-helices, even if with a preference toward the extended form. The authors obtained these results by site-directed spin labeling in combination with pulsed electron paramagnetic resonance on large unilamellar vesicles (LUVs) and they concluded that the two conformations are closely related to the experimental conditions used and that the equilibrium is very labile, which means the molecule is highly flexible. In this way, they could explain why previous studies were in opposition (Robotta et al., 2011).

The interconversion between these two states has been represented as functionally relevant to the protein; in fact, physiologically, αSyn could effectively connect a synaptic vesicle to the plasma membrane by switching from an extended state to a broken-helix conformation (more tightly bound state). For this purpose, in order to characterize the extended helical structure by high-resolution solution-state NMR, a fluorinated alcohol (HFIP) has been employed, able to induce a highly helical state. Indeed, the central region corresponding to the non-helical linker displays a certain instability in the helical structure suggesting the possibility of this transition (Sung and Eliezer, 2018).

Solid state NMR (ssNMR) helped in providing new insights in the structural conformation of the membrane-bound αSyn. In fact, since the *N*-terminus is tightly bound to the lipid bilayer, these residues cannot be identified by solution NMR because they are invisible. The results of these experiments on acidic SUVs indicated that residues 6–25 are tightly bound to the membrane and no differences are detected when 1,2-dioleoyl-sn-glycero-3-[phospho-rac-(1-glycerol)] (DOPG) SUVs are used, even if the calculated affinity between αSyn and these vesicles is higher. We already know that the most dynamic part of the molecule is identified with the *C*-terminal region and INEPT (insensitive nuclei enhanced by polarization transfer) MAS (magic-angle spinning) measurements enabled to also characterize this domain as highly unstructured. In general, three domains could be identified: an anchoring *N*-terminal region (6–25), followed by an intermediate dynamic domain (26–96) and an

unstructured *C*-terminal domain that only transiently interact with the membrane surface. The central region is shown to be critical in modulating the affinity for the membrane surface and it is subsequently called membrane "sensor." Furthermore, MAS measurements indicated that the binding occurs at the surface of the membrane and not in the membrane bilayer (Fusco et al., 2014). Following ssNMR experiments helped also to understand the contribution of *N*-terminal acetylation on αSyn. This post-translational modification leads to a stronger membrane affinity and an increased propensity to adopt α helical structures in the *N*-terminal region. According to Runfola et al., *N*-terminal acetylation seems to regulate the binding affinity of αSyn for synaptic vesicles without altering the structural properties of the bound state (Runfola et al., 2020). Considering all these determinant aspects affecting the binding of αSyn to membranes, one can easily understand how the protein binding is sensitive to the experimental conditions used. In particular, a physiological environment should be used to mimic the naturally occurring features and obtain an ultimate description of the αSyn monomer when bound to membranes. In this framework, another factor to be taken into consideration is the influence of calcium ions on the membrane binding propensity of αSyn. This ion, localized at the presynaptic terminals, is able to bind to the *C*-terminus and favors its binding to lipid membranes, as verified by CEST-NMR experiments, leading to the so-called "double anchor mechanism" emphasizing its role in neurotransmitter release (Lautenschläger et al., 2018).

Summarizing, experimental evidences of association with lipid membranes support the strong dependence of the binding on the lipid composition and surface curvature. In general, αSyn binding to membrane is based on electrostatic interactions between the cationic groups of the basic *N*-terminal region (rich in Lys residues) and the anionic phospholipids, which in fact represent excellent models to mimic synaptic vesicles.

Similar considerations can be done for the αSyn fragment 71–82, included in the NAC region, as observed by Bédard et al., who described its role on the structural and assembly behavior of αSyn. As deduced from CD and IR measurements, in the presence of 1-palmitoyl-2-oleoyl-sn-glycero-3-phosphocholine (POPC) membranes, the fragment is mostly disordered as it is in solution, but when in contact with negatively charged membranes (1-palmitoyl-2-oleoylglycero-3-phosphoglycerol, POPG) the peptide adopts an intermolecular parallel β-sheet configuration (Bédard et al., 2014). In a more recent study, its behavior has been analyzed in the presence of partially anionic membranes to mimic in the best way neuronal membranes and an in-register configuration could be validated by means of IR and ssNMR DQF-DRAWS experiments. The amyloid aggregation driver is the electrostatic interaction as it happened also with the *N*-terminal sequence (Martial et al., 2020).

In addition to the curvature degree, the interaction of αSyn and membranes is also regulated by lipid packaging. In view of this, Stöckl et al. proved by confocal microscopy that αSyn preferentially interacts with liquid-disordered giant unilamellar vesicles (GUVs): the binding requires anionic lipids in a liquid disordered state, and this is in good correlation with the synaptic vesicles composition (Stöckl et al., 2008). This is also valid for fragment 71–82 (Martial et al., 2020). A comprehensive model for the interaction of αSyn with lipid bilayers has been proposed by Ouberai et al. based on many converging independent studies and new results generated by the combination of dual polarization interferometry, atomic force microscopy and CD spectroscopy. Connecting to membranes with strong curvature and stressed surfaces (cone-shaped lipids), αSyn monomers are apparently able to close the packing defects. In fact, after binding of αSyn to the phospholipid polar heads and insertion of the hydrophobic residues, lipids are induced to laterally expand provoking membrane remodeling and this process is promoted in the presence of packing defects or imperfections (Ouberai et al., 2013). αSyn ordering effect on the membrane has been also investigated by fluorescence anisotropy and it has been concluded that this is concentration dependent and it occurs in the liquid-crystalline state and not in the gel phase. This means that αSyn is able to stabilize the membrane of synaptic vesicles and thereby can be essential to prevent the premature vesicle fusion to the presynaptic membranes (Pirc and Ulrih, 2015). The higher binding affinity to fluid compared to gel phases has been also investigated by Galvagnion et al. by means of CD and DSC studies, suggesting that the higher exposure of hydrophobic area is essential for the binding. Notably, the authors also asserted that shorter and more soluble lipids greatly improve αSyn aggregation and, consequently, its pathological effect (Galvagnion et al., 2016).

Together with the lipid composition, the lipid to protein ratio is a discriminant factor for amyloidogenesis, being able to switch the equilibrium between physiological and pathological paths, as first described by Galvagnion et al. (2015) and later discussed in a detailed review by Kiechle et al. (2020). When this value is high, due to the low local concentration of αSyn, the aggregation can be suppressed. On the contrary, when this value is low or intermediate, αSyn-bound monomers could lead to nucleation and amyloid formation (Terakawa et al., 2018).

Although αSyn has a mainly cytosolic distribution, its ability to adhere to cell membranes, predisposes it to have other cellular localizations. A certain selectivity of αSyn toward mitochondrial membranes has been observed and this propensity has been related to the abundance of the phospholipid cardiolipin. Nevertheless, cardiolipin is mostly present in the inner membrane of the mitochondria. It has been demonstrated that αSyn enters mitochondria *via* import channels and not *via* direct interaction with the lipids of the outer membrane and afterward it is localized in the inner membrane (Zigoneanu et al., 2012). On the other hand, recent studies demonstrated that cardiolipin translocates to the outer mitochondrial membrane in response to cellular stress and binds αSyn species. In this position, cardiolipin can also pull αSyn monomer away from oligomeric/fibrillar aggregates and facilitate its refolding in α-helix. Cardiolipin exposure is therefore a key signal in PD pathogenesis (Ryan et al., 2018). In agreement to these results Ghio et al. also demonstrated that cardiolipin enhances αSyn lipid membrane binding and also favors the membrane pore-forming activity of αSyn oligomers (Ghio et al., 2019).

Lipid Rafts

In general, it seems that αSyn specifically binds to anionic phospholipids, when these are embedded in liquid-disordered domains (Stöckl et al., 2008). Nevertheless, various studies demonstrate that lipid rafts can also have a very important role in αSyn binding. Lipid rafts are specialized areas of the plasma where tightly packed cholesterol and sphingolipids accumulate, surrounded by more fluid phospholipids. In fact, these dynamic microdomains adopt a liquid-ordered state and float in the remaining liquid-disordered plasma membrane (Sezgin et al., 2017). Fortin et al. demonstrated by a double fluorescent labeling that αSyn specifically associates with lipid rafts and this interaction can be crucial for its synaptic localization and physiological function (Fortin et al., 2004). Furthermore, many other publications illustrated how lipid rafts are closely connected with neurodegenerative diseases (Sebastião et al., 2013; Canerina-Amaro et al., 2019; Mesa-Herrera et al., 2019; Grassi et al., 2020).

In this framework, the analysis of αSyn interaction with cholesterol and gangliosides is fundamental since both have been considered as critical elements that could synergically favor the insertion of αSyn in lipid rafts and influence its pathological and physiological function (Fantini et al., 2011).

Cholesterol

Together with phospholipids, cholesterol plays an important role in regulating permeability and fluidity of the membrane. As expected, it also interacts with αSyn modulating its binding to synaptic-like vesicles, cholesterol being a very important component of these structures (Pfrieger, 2003). In particular, two domains of αSyn were recognized by Fantini et al. to bind cholesterol. Especially, residues 67–78 display a high affinity binding with a tilt angle of 46°, as measured by MD. Notably, they asserted that the tilted peptide could probably insert in the membrane and intercalate with the apolar regions of cholesterol leading to a higher affinity. On the contrary, residues 37–43 probably just associated to the hydroxyl group of cholesterol (Fantini et al., 2011). Other authors showed how cholesterol reduced or completely blocked, depending on the concentration used, αSyn binding to non-anionic membranes but, at the same time, this effect was much lower in the presence of negatively charged membranes (Shvadchak et al., 2011). Recently, surface plasmon resonance (SPR) was employed to measure the binding of αSyn monomers to lipid vesicles and this resulted decreased with the addition of cholesterol molecules to the membrane composition. The effect was detected also in the presence of negatively charged vesicles (Jakubec et al., 2019). A very recent publication from Fusco and coworkers confirmed these results showing by CD experiments that αSyn binding is reduced in the presence of cholesterol. However, the weaker interaction was detected by CEST (chemical exchange saturation transfer) experiments only at the NAC region. The previously described property of αSyn of binding two different membranes at the same time, the "double anchor mechanism", has been also evaluated by DLS (dynamic light scattering) and the ability of αSyn to interact with two vesicles was promoted with the increasing concentration of cholesterol showing that the NAC region is effectively crucial in this step modulating this important biological property (Man et al., 2020). At the same time, Jakubec et al. questioned whether cholesterol could influence αSyn fibrillation and they observed that the aggregation was effectively promoted by analyzing ThT (thioflavin T) and TPE-TPP (bis(triphenylphosphonium) tetraphenylethene) fluorescence assays. This outcome could be explained taking into consideration that cholesterol could act as a nucleation site (Jakubec et al., 2019).

Glycosphingolipids

The interaction of αSyn with glycosphingolipids, in particular gangliosides as GM1, has been reported in many articles, revealing their key role in the physiological and pathological function of this protein (Chiricozzi et al., 2020). In 2006, Martinez et al. concluded from SEC (size-exclusion chromatography) HPLC, CD and TEM (transmission electron microscopy) that αSyn displays a very high binding affinity and specificity toward GM1, in comparison to the other gangliosides (Martinez et al., 2007). Differently from cholesterol, the high-affinity binding site of αSyn to glycosphingolipids includes residues 34–45 (Fantini et al., 2011). This affinity is even intensified when αSyn is *N*-acetylated and at the same time the fibrillation is reduced together with enhancement of the helical folding propensity (Bartels et al., 2014). Based on these outcomes, Schneider et al. reported that GM1 displays neuroprotective effects after *in vivo* administration with a decreased αSyn aggregation (Schneider et al., 2019).

Proteins

The investigation of the interplay between αSyn and proteins is of high relevance for understanding both the physiological and the pathological role of αSyn. To see how this interaction influences its monomeric structure, in the following paragraphs and in **Table 2** we will summarize various biomolecules and how they affect not only its conformation but also its aggregation tendency.

Tubulin

Tubulin is a highly conserved αβ dimeric protein that is the main component of microtubules. αβ-Tubulin dimers assembly and disassembly are finely tuned within the cell and a huge number of proteins interact with them, affecting the stability of microtubules and their function. Recently, it has been found that αSyn binds to microtubules and tubulin $\alpha_2\beta_2$ tetramer. This interaction induces helical αSyn folding, enabling it to promote microtubule nucleation and to enhance microtubule growth rate and catastrophe frequency. On the other hand, PD αSyn mutants do not undergo tubulin-induced folding, causing tubulin aggregation rather than polymerization (Cartelli et al., 2016). However, the precise sequence of α-Syn binding site to tubulin has not been fully elucidated yet, and molecular studies aimed to deciphering the interaction at an atomic level are still missing.

Heat Shock Protein 70 (Hsp70) and Heat Shock Protein 73 (Hsp73)

Hsp70 is a 70 kDa protein from the "chaperone" family, involved in cell defense against protein misfolding (**Figure 8**). Concerning

TABLE 2 | Reported proteins interactions with monomeric and aggregated states of αSyn.

Compound	α-Syn interaction region	α-Syn state conversion upon interaction	Common features (class)	References
Tubulin	Not specified	Folding into helical structure	Microtubule protein	Cartelli et al. (2016)
Hsp70	NAC and $_{95}$VKKDQ$_{99}$ (at the border between NAC and C-terminal)	Fibrils → soluble conformers	Chaperone	Ebrahimi-Fakhari et al. (2011)
		Monomers → stabilized monomers		Dedmon et al. (2005a) Luk et al. (2008) Klucken et al. (2006)
Hsp73	Not specified	Monomers → stabilized monomers	Chaperone	Chaari et al. (2016)
DNAJB6	Not specified	Non specified	Co-chaperone	Månsson et al. (2014) Aprile et al. (2017)
DNAJB1	Non specified	Fibrils → shorter fibrils → monomers	Co-chaperone	Gao et al. (2015)
SCGN	Non specified	Monomers and early-stage oligomers → soluble conformers	Ca^{2+}-binding protein	Chidananda et al. (2019)
AS69	Y_{39}, H_{50}	Monomers → stabilized monomers	Engineered protein	Mirecka et al. (2014) Agerschou et al. (2019)

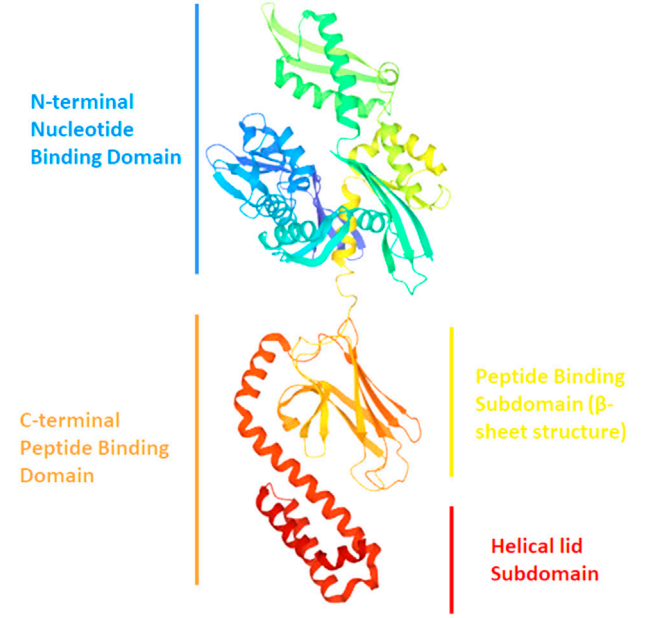

FIGURE 8 | Ribbon drawing illustrating the structure of Hsp70 with its different domains (PDB file 2KHO).

αSyn interaction, *in silico* and ThT assays suggest that Hsp70 binds to several conformers (monomers, protofibrils and fibrils) but it shows preference for the protofilaments involved in fibrils. In this regard, Fakhari et al. highlighted the binding of Hsp70 to the pre-fibrillar species of αSyn, which leads to their disassembly into soluble entities *in vitro* (Ebrahimi-Fakhari et al., 2011). Furthermore, experiments by Dedmon et al. show that Hsp70 interacts with αSyn fibrils instead of monomers. These results suggest that the protein adopts a folded structure which protects the central hydrophobic region and does not allow further inter-molecular binding. As shown by NMR data, this happens when the *C*-terminal domain makes contacts with the NAC region. If these interactions are perturbed (early stages of aggregation), the central region becomes exposed and this can lead to protein-protein interaction with the formation of pre-fibrillar aggregates. In this case, the chaperone binds to these aggregates and prevents the fibrils formation (Dedmon et al., 2005a). The hypothesis of Hsp70 interacting with the NAC region of αSyn is sustained also by Luk et al. As previously mentioned, this element represents the core of αSyn fibrils, and it contains the sequence required for αSyn to aggregate. Interestingly, ThT assay demonstrated that αSyn residues $_{95}$VKKDQ$_{99}$, at the border between NAC and the *C*-terminal domain, are crucial for interaction with Hsp70 (Luk et al., 2008).

Regarding monomers, Hsp70 is able to modify αSyn conformation by forcing it to a different open conformational state in which the *N*- and *C*-termini are distant from each other. αSyn-αSyn interactions are observed but are probably modified and NAC-NAC domain interactions among monomers are lost, increasing αSyn solubility (Klucken et al., 2006).

Another important chaperone is Hsp73 (Hsc70). Concerning its interaction with αSyn, Chaari et al. found out that the chaperone binds αSyn at the peptide binding sub domain (SBSD) corresponding to residues 386–509. These interactions involve unfolded monomers, and this is coherent with the role of Hsp73, which normally binds to unfolded proteins to mediate their refolding. At the same time, the helical subdomain (510–646) stabilizes the chaperone/αSyn complex, counteracting the formation of nuclei and/or the elongation of fibrils, as shown by *in vitro* experiments (Chaari et al., 2016).

DNAJB6 and DNAJB1

DNAJB6, the co-chaperone of Hsp70, is able to counteract αSyn and amyloid β aggregation *in vitro* by combining with its partner (Månsson et al., 2014). In particular, its effect is linked to the J domain, which catalyzes the transfer of the misfolded αSyn to the chaperone. Furthermore, *post-mortem* analysis on PD patients' brains reveals the presence of the protein in Lewy Bodies, suggesting that its misregulation may provide early PD onset. Finally, this may reveal an interaction of DNAJB6 with αSyn and its direct role in aggregation inhibition. However, this hypothesis needs to be proved *in vivo* (Aprile et al., 2017). Focusing on the

DNAJB family, *DNAJB1* efficiently works with Hsp70 and Hsp110 in fibrils disassembling. The system binds pre-formed fibrils both *in vitro* and *in vivo*, converting them into shorter fibrils later depolymerized into monomers (Gao et al., 2015). However, the interaction sites on αSyn still remain unknown.

Secretagogin (SCGN)

Studies suggest that neurodegeneration may be associated with Ca^{2+} dis-homeostasis, since a misregulation in this ion signaling system can be detected in neuropathologic patient brains. Considering this, scientists from Chidananda research team focused on SCGN, a Ca^{2+}-sensor protein expressed in the brain which plays a key role in insulin regulation (Chidananda et al., 2019).

To study its effect over αSyn, the authors developed a method able to lead to protein fibrillation with entities of the range of 5–10 nm. Notably, TEM analysis revealed that no fibril was formed when αSyn was incubated with SCGN. These results are explained by considering that SCGN can bind both to monomers and early-stage oligomers, according to ThT and MTT (3-(4,5-dimethylthiazol-2-yl)-2,5-diphenyltetrazolium bromide) assays. In this case, soluble αSyn is preserved, without any further aggregation (Chidananda et al., 2019).

All in all, SCGN is shown to bind to αSyn and prevent it from fibrillation and nucleation *in vitro*. This may impede its binding to membranes, its misfolding and its aggregation. Finally, NMR studies show that anti-fibrillar activity is attributed to the central region and *C*-terminal domain of SCGN (Chidananda et al., 2019).

AS69

AS69 was engineered from Mirecka et al., who developed a new phage library, obtained by random mutagenesis of the gene encoding ZAβ3. (Mirecka et al., 2014). This protein was proven to be an efficient $A\beta_{1-42}$ aggregation inhibitor. In particular, due to its structure it is classified as "β-wrappin." This protein shows two identical subunits, each formed by two α-helix and one β-strand spanning residues 13–58, linked by a disulphide bond involving the Cys28 residues of both of them. Moreover, NMR analyses showed that Phe31 residues of both AS69 subunits are involved in π-stacking interactions with Tyr39 and His50 of αSyn. Furthermore, molecular modeling studies suggest that AS69, by interacting with αSyn, folds into two β-strands and four α-helices forming a hydrophobic cavity where αSyn is buried (**Figure 9**) (Mirecka et al., 2014).

ThT analysis suggests that AS69 binds stoichiometrically to αSyn monomers, thus blocking the fibril elongation step by sequestrating free monomers. Also, the complex αSyn/protein can act as an inhibitor of the secondary nucleation process. Together, these results suggest that AS69 may display a broad activity against fibrillation, as demonstrated both *in vitro* and *in vivo* (*Drosophila* flies and mice) (Agerschou et al., 2019).

Endogenous Small Molecules

The role of endogenous small molecules (e.g., neurotransmitters) is important when it comes to understanding the function and structure of amyloids. Interestingly, some neurotransmitters are able to alter αSyn folding while interacting with it, which enables to better understand how the protein behaves and which binding sites are pivotal in that circumstance. The structures of the endogenous small molecules that will be reviewed in the next paragraphs are represented in **Figure 10** and the effect are summarized in **Table 3**.

Dopamine (DA)

Dopamine, one of our principal neurotransmitter, is a catecholamine implicated in several physiological process whose biosynthesis decreases in neuropathologies, like PD. Its role in αSyn aggregation modulation has been widely discussed and there is not a clear consensus whether it has a direct or indirect implication. In fact, some researchers hypothesize that DA can decrease αSyn fibrillation and oligomerization by binding to the protein *via* hydrophobic and hydrophilic interactions. These lead to non-stable complexes, which include its NAC or *C*-terminal region. Furthermore, studies showed that DA can mediate anti-fibrillar effect both *in vitro* and *in vivo*, while forming off-pathway oligomers (Oliveri, 2019).

The role of dopamine concerning αSyn modulation has been explored by Rekas et al. SAXS data suggest that the catecholamine mediates the formation of trimers made by αSyn overlapped structures. CD data suggest that their structure lacks β-sheets, which are crucial for amyloid aggregates (Rekas et al., 2010).

Recently, Post et al. reviewed the interaction between DA and αSyn, providing features over the protein structure and its binding sites. In particular, oxidized DA can interact with αSyn, producing a complex which enhances the formation of oligomers rather than fibrils (Post et al., 2018). Moreover, *in vitro* studies underline that its formation is due to a non-covalent binding between DA and the $_{125}$YEMPS$_{129}$ region of αSyn (Mazzulli et al., 2007). Furthermore, this complex seems to be stabilized by a salt-bridge between DA and E_{83} in the NAC region (Post et al., 2018).

Finally, the binding of DA to αSyn has an important effect on the conformation of the protein domains. In fact, fluorescence lifetime imaging microscopy data showed that the *N*- and *C*-termini of αSyn come closer, adopting a conformation which may inhibit fibril formation.

Arginine

Arginine is an amino acid able to affect αSyn behavior. This natural compound is well-known for its neuroprotective effect both *in vitro* and *in vivo* against glutamate excitotoxicity.

Regarding arginine/αSyn interaction, this molecule can inhibit protein late state aggregation, according to ThT, DLS and AFM (Atomic Force Microscopy) data. Isothermal calorimetry (ITC) and MS (Mass Spectrometry) analyses show that arginine binds to αSyn, forcing it to acquire a conformation thought to slow down the early-stage oligomerization. From a structural point of view, this conformer leads to a unified compaction of unfolded monomers. Since this intermediate is stabilized by clusters of arginine, the oligomerization and further fibrillation are avoided. Furthermore, MALDI-TOF mass spectrometry, ITC (Isothermal Titration Calorimetry) and MD analyses show that the aromatic residues of αSyn and the guanidine moiety of arginine interact *via*

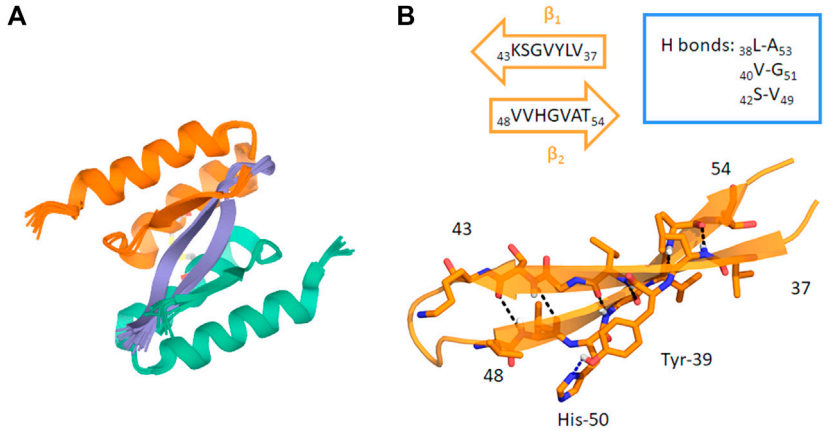

FIGURE 9 | (A) Ribbon drawing of the AS69 structure interacting with the αSyn β-hairpin (residues 36–55). In light orange and green, the two subunits of AS69 are shown. Each subunit spans residues 13–58 of AS69. **(B)** Ribbon drawing of the αSyn β-hairpin (orange, β1 and β2 strands). H-bonds are depicted by dashed lines. The main interacting residues are shown as sticks (Mirecka et al., 2014).

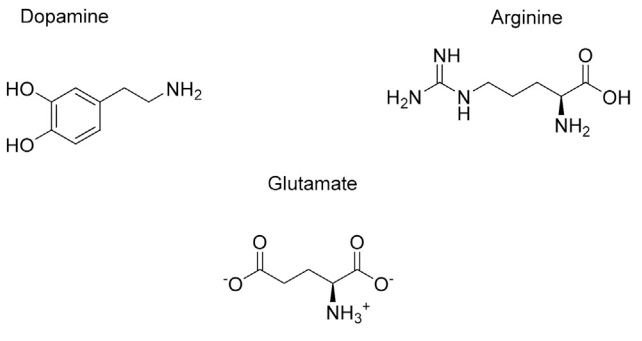

FIGURE 10 | Endogenous small molecules affecting αSyn conformation and aggregation.

cation-π forces. Finally, arginine protective effect against αSyn toxicity was also proven in HeLa and SH-SY5Y cells line (S. Ghosh et al., 2018).

Glutamate

Glutamate is an excitatory neurotransmitter whose concentration in blood is around 50 μM. In the brain, it is the precursor of glutamine in presynaptic terminals and glial cells (Ghosh et al., 2018). Importantly, glutamate is shown to influence αSyn conformation and promote its aggregation. However, as an osmolyte, it tends not to directly interact with the protein; thus, its activity on αSyn may derive from its exclusion from the protein surface. The impact of glutamate on the conformation of αSyn is shown in *in vitro* assays. Interestingly, the more the concentration of glutamate is increased, the more unfolded monomers convert into β-sheet rich oligomers. In particular, small oligomers (10–15 nm diameter) predominate when glutamate is present at a concentration of less than 100 mM. Furthermore, AFM analysis proved that in glutamate treated samples, after 3 h of incubation two kinds of oligomeric aggregates appeared. The most representing one had a diameter of 20–35 nm, while the second one of 60–85 nm. Finally, this early stage oligomerization could be a critical factor to enhance fibrillation (Ghosh et al., 2018).

EFFECT OF EXOGENOUS FACTORS ON αSYN STRUCTURAL FEATURES

In general, the interaction of IDPs with exogenous compounds plays a crucial role for conformational stabilization and induction of aggregation. These chemicals can be found in the daily diet (e.g., flavonoids) or can derive from pharmacological treatments or habits (e.g., nicotine from smoking). Recognizing which elements are essential, beneficial or toxic is a very important topic, displaying each substance a bivalent effect as summed up by the sentence "The dose makes the poison", asserted by Paracelsus. This is valid for every element, including metals, which have crucial physiological roles but at the same time can induce toxicity according to their therapeutic window. Thus, by analyzing the interaction between αSyn monomers and those molecules, a better insight of αSyn structural changes can be given. Finally, thanks to modern spectroscopy and molecular dynamics, the sites of interactions can be investigated. In the end, these data will help to better comprehend the structure of αSyn, whose details have not yet been fully elucidated. In this context, the main classes of chemicals that interact with αSyn are presented below (**Figure 11**).

Metals

Metals are everywhere. These so-called trace elements, have an indispensable physiological role in normal brain functions, being often used by enzymes and proteins, due to their redox potential (Garza-Lombó et al., 2018). On the other hand, many recent epidemiological studies detected a significant higher level of metals in the affected brain regions of Parkinson's disease

TABLE 3 | Reported endogenous and exogenous small molecules interactions with monomeric and aggregated states of αSyn.

Compound	α-Syn interaction region	α-Syn state conversion upon interaction	Common features (class)	References
Dopamine	$_{125}$YEMPS$_{129}$ (C-terminal) and E_{83} (NAC)	Oligomers → complex/trimers lacking β-sheets	Neurotransmitter	Oliveri, (2019) Rekas et al. (2010) Post et al. (2018)
Arginine	Aromatic residues	Monomers → unstructured conformer	Neurotransmitter	S. Ghosh et al. (2018)
Glutamate	Not specified	Monomers → β-sheet rich oligomers	Neurotransmitter	S. Ghosh et al. (2018)
EGCG	Residues 23–55 (N-terminal)	Monomers and fibrils → non-toxic entities	Polyphenol	Xu et al. (2020) Caruana et al. (2011) Pujols et al. (2018) Sternke-Hoffmann et al. (2020)
Baicalein	Lysine and tyrosine side chains (mainly N-terminal)	Monomers and fibrils → non-toxic oligomers	Polyphenol	Kurnik et al. (2018) Morshedi et al. (2015) Oliveri, (2019) Javed and Ojha, (2020)
NDGA	V_3, F_4, Met_5 and H_{50} (N-terminal)	Monomers → stabilized monomers Fibrils → low β-sheet complexes	Polyphenol	Caruana et al. (2011) Daniels et al. (2019) Perni et al. (2017)
Squalamine	Residues 113–139 (C-terminal)	Not specified	Triterpenoid	Perni et al. (2017)
Nicotine	Not specified	Monomers → soluble oligomers	Alkaloid	Kardani et al. (2017)
Caffeine	Not specified	Oligomers → mature aggregates	Alkaloid	Oliveri, (2019) Kardani and Roy, (2015)
Mannitol	Not specified	Oligomers → non-toxic entities	Sugar alcohol	Shaltiel-Karyo et al. (2013)
Scyllo-inositol	NAC	Monomers → stabilized monomers	Sugar alcohol	Ibrahim and McLaurin, (2016)
TANI and TAN IIA	Not specified	Monomers/oligomers/fibrils → non-toxic entities	Phenanthrenequinone	Ji et al. (2016) Ren et al. (2017)
Cuminaldehyde	Lysine side chains (N-terminal)	Monomers → α-helix-like complexes	Aldehyde	Morshedi et al. (2015)
PcTs	F_4 and Y_{39} (N-terminal), residues 93–95 (C-terminal)	Monomers → α-helix stabilized monomers	Phthalocyanines	Lamberto et al. (2009) Oliveri, (2019)
C41	N-terminal	Monomers/oligomers/fibrils → non-toxic entities	4-Hydroxynaphthalen-1-yl)sulphonamide derivatives	Kurnik et al. (2018)
NQTrp	Not specified	Monomers → non-toxic entities	Naphtoquinone-Tryptophan derivative	Paul et al. (2019)
M2N and M3N	Not specified	Fibrils → amorphic conformers	Mannitol derivatives	Paul et al. (2019)

(PD) patients. In particular, high concentrations of iron, zinc and aluminum have been found in the *substantia nigra*, while copper accumulation has been detected in cerebrospinal fluid of PD patients. Furthermore, long-term metal exposure has been frequently related to parkinsonism (Bjørklund et al., 2019, 2020). Despite these numerous examples, there is still a controversial debate among experts whether metals are directly related to the cause of the disease. In general, we can state that the exact role of metals in the mechanism to neurodegeneration is still ambiguous. Indeed, it has been observed that metals catalyze the formation of reactive oxygen species causing oxidative stress but also enhance the aggregation of several proteins, among which αSyn, by complexing to them. At the same time, current studies have also shown how Mn and Ca levels can be regulated by αSyn itself (Dučić et al., 2015). But how can metals affect αSyn assembly? A possible explanation regarding the increased tendency to fibrillation is the subsequent conformational change after metal binding, resulting in abnormal folding and oligomer stabilization, as demonstrated for various metal ions (Kostka et al., 2008; Rcom-H'cheo-Gauthier et al., 2014; Uversky et al., 2001).

Regarding metal-protein complexation, many recent studies have been focused on determining the structural complexity of this interaction reaching some important milestones. A low affinity binding site exists at the *C*-terminus of αSyn, where carboxylates of Asp and Glu residues are the major contributors for metal binding. In particular residues 119–124 are involved in electrostatic interactions and can bind all divalent metal cations, without specificity. Additionally, the affinity to this binding site can be drastically increased after phosphorylation of Tyr-125 and Ser-129 as demonstrated by ESI-MS and fluorescence spectroscopy in the case of Cu(II), Fe(II) and Pb(II) (Lu et al., 2011).

In the hierarchical order of divalent metal cations binding to αSyn, copper has been recognized to be the most affine and efficacious metal in promoting aggregation. Its binding has peculiar features in comparison to other ions and an exhaustive structural description of its coordination to αSyn

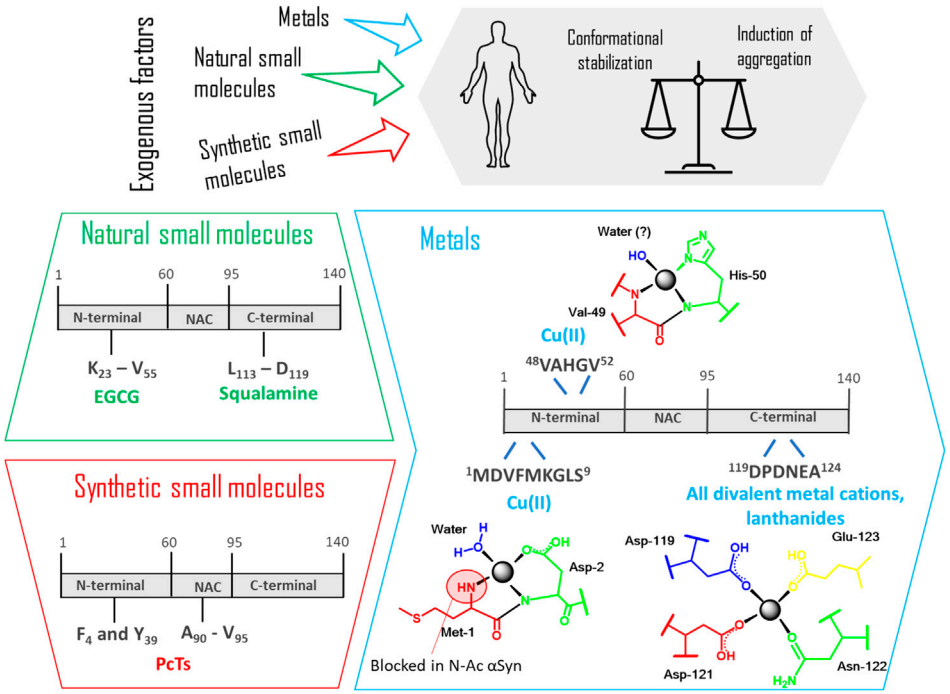

FIGURE 11 | Binding sites recognized in the interaction between αSyn monomer and different exogenous factors (natural and synthetic small molecules, metals). The coordination between the protein and these factors leads to a balance that is always shifting between conformational stabilization and induction of aggregation. In the box regarding "metals," the specific coordination modes of Cu(II), all divalent cations, lanthanides with the specific amino acid residues are detailed. EGCG: Epigallocatechin gallate; PcTs: phthalocyanine tetra sulfonate.

has been comprehensively summed up by Binolfi et al. (2012). The authors took into consideration the intrinsically disordered monomer of αSyn and recognized three different binding sites for Cu(II). Apart from the common *C*-terminal binding site, as previously described, two independent sites in the *N*-terminal portion have been defined as high-affinity binding site 1 (residues 1–5) and low-affinity binding site 2 (associated to His-50). Binding constants vary depending on the experimental conditions, so a comparison between results from different publications is not always appropriate. Anyhow, the authors could conclude that, differently from the binding to the *C*-terminal region typical of all the other cations, the *N*-terminal coordination might occur under physiological conditions and be significantly relevant to the beginning of PD.

After this review from 2012, many new experimental data have been published but still many questions remain open. In fact, current studies have partially undermined some of the previously described conclusions. In the following paragraphs, the influence of different metals on the αSyn structure will be analyzed and the most recent results in this field will be shown, taking into account contradictory point of views.

Copper

A very important issue pointed out by the research group of Lucas in 2019 is the fact that αSyn is mainly present *in vivo* as a *N*-terminally acetylated protein (Abeyawardhane et al., 2019). It is immediately clear how this post-translational modification could have an important consequence in the copper-protein interaction, perturbing the high affinity *N*-terminal binding site, since the Met1 site is now blocked. Through electron paramagnetic resonance (EPR) spectroscopy based on the Peisach-Blumberg correlation diagram and the DFT calculations previously reported by Ramis et al., two new correlation modes have been described (Ramis et al., 2017). A N3O1 binding involving His50, Val49 and a water molecule has been identified as the preferential *N*-terminal binding site and the principal binding site of the *N*-terminal-acetylated αSyn. On the contrary, a *C*-terminal binding site including residues Asp119, Asp121 and Glu123 have a great impact on fibrillation of the H50Q missense mutation, enhancing the protein aggregation propensity. In a recent comparison study carried out by Lorentzon et al., Cu(II) was found to accelerate non acetylated αSyn aggregation at biologically-relevant metal ion concentrations, while this reaction was not affected at all in the presence of the acetylated protein, of the A53T mutant and of the 1–97 truncated version. This is probably correlated with the intrinsic aggregation speed of the various αSyn variants: since the velocity with which the variants form the amyloid is higher than that of the wild type, the effect of metal binding is not detectable anymore (Lorentzon et al., 2020).

Cu(I) has also been investigated even if less information has been generated about it. αSyn, in fact, interacts with both oxidation states of copper ions that are involved in a copper catalyzed oxidation reaction, with the subsequent formation of

reactive oxygen species (ROS) that leads to oxidative stress and to a possible formation of amyloid fibrils (Bisaglia and Bubacco, 2020). Also, in the case of Cu(I), three binding sites have been recognized by NMR at the *N*- and *C*-termini, respectively residues 1–5 (high affinity), His-50 and residues 116–127 (Binolfi et al., 2011; Camponeschi et al., 2013; Miotto et al., 2014; Okita et al., 2017). In particular Met1 and Met5 are the main coordinating center for this ion with a 2S2N/O coordination mode (De Ricco et al., 2015).

Iron

Also iron undergoes an oxidation cycle between two oxidative states Fe(II) and Fe(III) with production of ROS through the Fenton-Haber Weiss reaction (McDowall and Brown, 2016). Even in this case, as for copper, Lucas and coworkers investigated the influence of iron on the aggregation propensity and the secondary structure of the *N*-acetyl-αSyn (Abeyawardhane et al., 2018). Experiments performed in aerobic conditions showed that Fe(II) yielded a distinctive, highly toxic αSyn-metal complex in comparison to Fe(III). Fe(II), in fact, can react with O_2 and oxidize to Fe(III) with the production of H_2O_2 and the subsequent development of a right-twisted antiparallel β-sheet conformation based on CD analyses and descriptive deconvolution of the secondary structure. These results display how the Fe(II) reactivity can have a very important impact in the protein conformation and its aggregated structural properties. Most importantly, the same does not occur with copper ions, proving a distinguished aggregation process.

Calcium

Calcium dysregulation has been connected with neurodegenerative disorders and high levels of this metal have been detected in Lewy bodies. For its central role in αSyn aggregation, Kim and his research group took Ca^{2+} as representative metal ion to understand metal influence on the formation of large interfibrillar aggregates (Han et al., 2018). The authors could demonstrate that Ca^{2+} mediates the rapid formation of αSyn fibrils *via* the structural transition of monomeric αSyn into an extended conformation, which is prone to aggregation. It is interesting to discover how the structure of the α-syn monomer develops after binding to Ca^{2+}. By using ion mobility-mass spectrometry (IM-MS) and synchrotron small-angle X-ray scattering (SAXS), Han et al. could demonstrate a structural transition of monomeric α-syn into an extended conformation with the exposure of the NAC region, which is more prone to aggregation.

Lanthanide (Trivalent) Metal Ions

Investigation on lanthanides is a very crucial topic since they are increasingly applied in various fields of industry and agriculture. As divalent metal ions, trivalent metal ions non-specifically bind to the *C*-terminus of αSyn but also transiently interact with carboxylates in the N-terminal and NAC regions as interpreted from 1H to 15N HSQC NMR spectroscopy. In addition, they accelerate fibrillation much faster than divalent cations (Bai et al., 2015).

All the *in vitro* experiments carried out so far do not necessarily translate *in vivo* metal binding. Lothian et al. pointed out that there is a lack of evidence that the metal binding observed *in vitro* also occurs *in vivo* (Lothian et al., 2019). This work does not exclude the possibility that a very small percent (1%) of the whole protein can effectively bind to metals, promoting their aggregation with the consequent formation of oligomers and fibrils but, in general, according to the authors, αSyn cannot be considered as a metalloprotein *in vivo*. However, also these last results have some limitations because they considered non-pathogenic tissues, while in PD many factors can be combined and lead to the ultimately conclusion, like e. g post translational modification, molecular binding, ionic strength, salt concentration.

Natural Small Molecules

Natural products are gaining importance in drug discovery since they are an environmental-friendly source for hit compounds. Moreover, with modern extraction and purification techniques, researchers are able to obtain these small molecules with moderate efforts. Also, they offer low-cost production and possible improvement of their activity. However, natural compounds have some limitations such as low reproducibility and yield, but also lack of safety and tolerability. Finally, their multi-target activity can be a problem when the aim is to be selective toward a single target.

Since these molecules present low selectivity, they can bind to both αSyn aggregates and monomers. However, when they bind to monomers, few of them have a characteristic binding site, hence more studies are needed to look further into this topic. Here, we present an overview over the main classes of natural small molecules able to influence monomeric αSyn aggregation. Their structures are depicted in **Figure 12**.

Polyphenols

Flavonoids

Epigallocatechin Gallate (EGCG)

EGCG is a natural compound known for its antioxidant properties and anti-aggregation activity against amyloid proteins. This latter effect against multiple targets (αSyn, $A\beta_{1-42}$, Tau, hIAPP) is due to its lack of selectivity. Concerning αSyn, NMR studies suggest that EGCG binds to the *N*-terminal domain, in particular to residues 23–55 (Xu et al., 2020). This binding is mainly governed by Van der Waals and π-stacking interactions due to the structure of EGCG, characterized by electron-rich aromatic rings bearing three consecutive OH substituents. Even if the mechanism behind the anti-aggregation effect is ambiguous, EGCG can bind fibrils and convert them into smaller, non-toxic aggregates. Moreover, EGCG is also able to bind to monomers and induce their aggregations into non-cytotoxic, off-pathway entities, thus avoiding the nucleation process (Caruana et al., 2011). EGCG efficacy has been tested both *in vitro* and *in vivo* (Pujols et al., 2018). Also, the compound is currently under clinical trials for Multiple System Atrophy (Xu et al., 2020). Recent studies have reported that the species responsible for EGCG anti-aggregating properties is its oxidized form

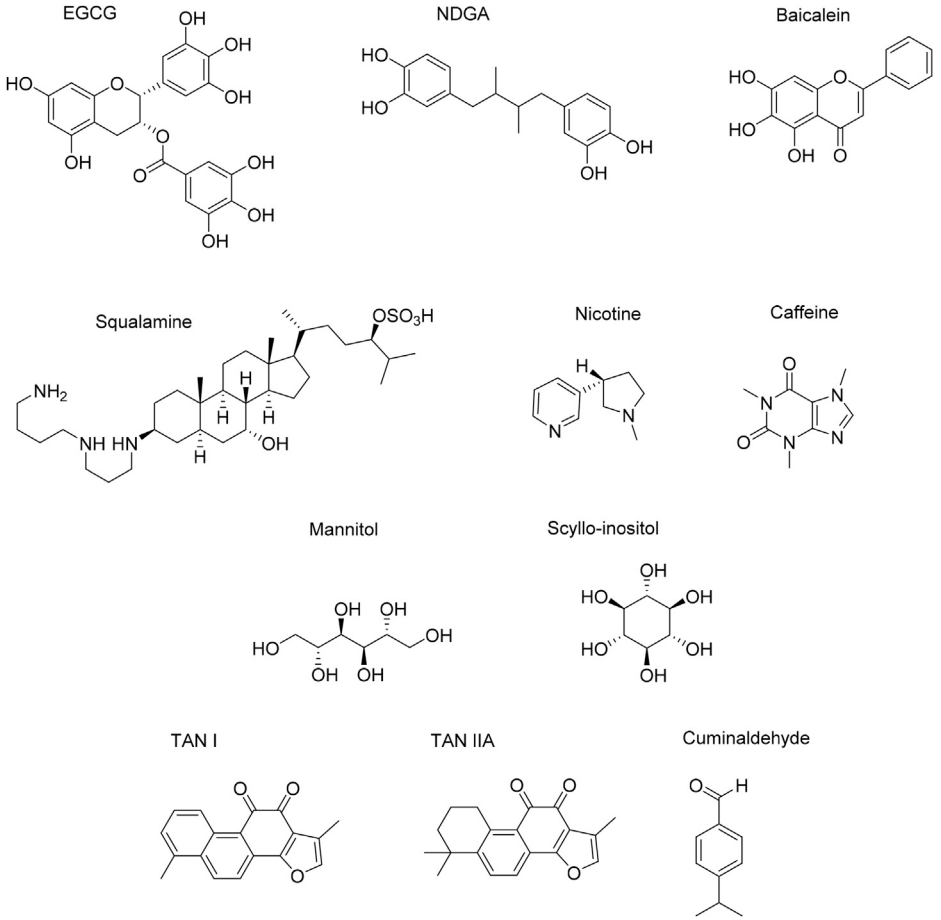

FIGURE 12 | Natural small molecules influencing αSyn conformation properties.

(oxEGCG). In fact, most of the EGCG efficacy studies were performed at pH 7, at which the compound is not stable and comes across oxidation. When EGCG is tested at pH six or less, the molecule is stable and its anti-aggregation properties are lost (Sternke-Hoffmann et al., 2020).

Baicalein

Baicalein is a flavonoid extracted from *Scutellaria* baicalensis. This molecule is known to disassemble αSyn fibrils into smaller, non-toxic oligomers by binding to them once they are mature (Kurnik et al., 2018). As EGCG, baicalein is also active toward αSyn monomers: the polyphenol can interact and convert them into off-pathway aggregates with very low cellular toxicity (Morshedi et al., 2015).

Recently, Javed et al. reviewed the interaction between baicalein and αSyn. Here, the oxidized form of baicalein (quinone) is crucial for αSyn aggregation inhibition. In fact, its effectiveness against αSyn aggregation has been tested both in cells (HeLa and SH-SY5Y) and *in vivo* models (Oliveri, 2019). When baicalein quinones interact with early-stage aggregates, it leads to quite soluble αSyn oligomers. In this case, the polyphenol covalently binds to the protein and creates a Schiff base with lysine side chains, expressed in the *N*-terminal domain of αSyn. Tyrosine residues are also involved in this binding (Javed and Ojha, 2020).

As mentioned before, Baicalein binds to a broad region of αSyn, thus it is not selective toward a specific binding site. Indeed, other studies showed that baicalein is an efficient aggregation inhibitor also for Aβ, Tau, IAPP and other amyloid proteins, which is a common characteristic for polyphenols (Oliveri, 2019).

Nordihydroguaiaretic Acid (NDGA)

Nordihydroguaiaretic acid is a natural compound deriving from *Larrea tridentata*. Concerning its interaction with αSyn, confocal single-molecule fluorescence spectroscopy studies showed that the compound binds to toxic inclusions and that it is able to inhibit the formation and/or to disaggregate mature oligomers (Caruana et al., 2011). Moreover, recent studies pointed out that oxidation and consecutive cyclization of NDGA is required for its activity. In fact, its oxidized form (oxNDGA) can interact with monomers and convert them into quinone-modified species, which are less prone to aggregate in comparison to the non-modified ones. However, these monomers can still carry out their physiological function: probably this modification does not alter

their normal activity. In fact, as CD data suggest, monomers preserve the ability to fold into α-helix conformations while interacting with SDS *in vitro*. Also, in the same work, oxNDGA was shown to inhibit *in vivo* oligomers and fibrils formation (*C. elegans*) (Daniels et al., 2019).

Furthermore, the compound is also able to interact with preformed fibrils. In fact, ThT assays displayed that cyclized NDGA can reduce the contents of β-sheets in a dose-dependent manner (Perni et al., 2017). However, it is important to inquire if these interactions have an effect over αSyn structure. In particular, ESI-MS analysis showed no covalent binding, which means that the protein primary structure is unmodified. Moreover, this interaction leads to a more compact conformation of the protein, which may mask the NAC region and discourage aggregation. Nevertheless, this hypothesis still needs additional analyses to be confirmed.

Regarding the sequences of αSyn involved in this interaction, NMR studies suggested that the most engaged domain is the *N*-terminus (Val3, Phe4, Met5 and His50 in particular). Especially, this domain is involved in the monomer's helix folding while interacting with membranes: as we saw before, the dynamic flexibility of the protein is not altered by the interaction with oxNDGA.

All in all, these results show that NDGA and in particular oxNDGA can modify the conformation of the protein aggregates. However, the structural properties of these entities as well as the involved domains of αSyn have yet to be elucidated.

Non polyphenols

Triterpenoids

Squalamine

Squalamine is a steroid-polyamine conjugate found in sharks and is known for its anticancer and antiviral activity. Its main characteristic is the polyamine chain attached to the cyclopentanoperhydrophenanthrene structure, which is positively charged in the cell's physiological environment. This moiety allows the compound to interact with membranes, in particular with the phospholipids negatively charged heads (Perni et al., 2017). Finally, the salt bridges formed between squalamine and the lipidic bilayer may avoid the pathological formation of αSyn oligomers, since there is a competition for the same sites of interactions between misfolded αSyn monomers and the triterpenoid. These hypotheses were confirmed by CD experiments. In fact, when αSyn is incubated with squalamine in the presence of phospholipidic membranes, a decrease of the α-helix character is noticed. Thus, one can speculate that the displacement of helical-folded αSyn from membranes leads to the refolding of the protein in a random-coil configuration. This last structure is the one in which monomers are usually found and it represents the most populated state of soluble cytosolic αSyn. However, further studies are required to confirm this idea.

Concerning αSyn-squalamine interactions, NMR analyses showed that the *C*-terminal domain is the most involved region of the protein (Perni et al., 2017). This is consistent with the fact that the positively charged chain of squalamine can create electrostatic interactions with the negatively charged domain of αSyn. In particular, the sequence engaged spans residues 113–139. However, this interaction is attenuated when squalamine and αSyn are incubated in the presence of membranes. Furthermore, this contact does not seem to directly alter the conformation of the protein. In fact, squalamine prefers to interact with phospholipids instead of αSyn in the cells. Nevertheless, more studies are required to confirm this speculation to be sure that αSyn refolding merely refers to its displacement by membranes.

Finally, the prevention of toxic oligomers formation provided by squalamine was proven *in vitro,* and the antiaggregant properties were later tested and confirmed *in vivo* using a *Caernohabditis elegans* PD model (Perni et al., 2017).

Alkaloids

Nicotine and Caffeine

Nicotine and caffeine can interact with αSyn and inhibit its aggregation pathway. However, since they can bind to αSyn simultaneously, their respective binding sites may be different. Also, the mechanism of the inhibition of aggregation is still unclear.

Concerning nicotine, *in vitro* studies demonstrated that this alkaloid can induce a conformational change in αSyn monomers, leading to nucleation slowdown and the formation of soluble, less toxic oligomers (Kardani et al., 2017).

At the same time, caffeine can decrease αSyn aggregates toxicity, while accelerating the apparent fibrillation rate (Oliveri, 2019). Interestingly, CD and TEM data suggest that caffeine does not alter the conformation of αSyn monomers (Kardani and Roy, 2015). Also, an increased transformation of oligomers into mature aggregates by administration of caffeine in yeast cell is remarked in literature. These data suggest a role of this alkaloid in the field of synucleinopathologies (Kardani and Roy, 2015).

Finally, nicotine is proven to be active against Aβ aggregates, while caffeine displays an activity also toward hIAPP and Tau toxic species both *in vitro* and *in vivo* (Ma et al., 2020).

Sugar Alcohols

Mannitol

Mannitol is a polyol approved by the Food and Drug Administration as an osmotic agent. Also, it is used as an osmotic diuretic in the therapy of hypertension and as a weak laxative in case of constipation. Furthermore, mannitol is known for its BBB disruption activity and its hyperosmotic solution is widely used in clinics. CD studies show that this compound is able to inhibit the aggregation of αSyn monomers into fibrils, likely through interaction with oligomers by leading them to an alternative pattern of aggregation acting as a "chemical chaperone". Finally, its neuroprotection activity was tested and proven *in vivo* in *Drosophila* flies and in mice (Shaltiel-Karyo et al., 2013).

Focusing on αSyn-mannitol interaction, CD experiments show that the polyalcohol does not affect the conformation of β-sheet rich fibrils, so no interaction is detected with the mature aggregates of the protein. However, the compound is able to change the secondary structure of αSyn oligomers. In fact, CD analysis spots a refolding in the early-stage aggregates outline.

However, more studies are required to understand the structural properties of the entities derived by oligomers refolding. Also, the protein domains involved in this interaction have yet to be discovered (Shaltiel-Karyo et al., 2013).

Scyllo-Inositol

Scyllo-inositol is one of the inositol stereoisomers, rare in nature, having attracted the attention of the scientific community in the field of $A\beta_{1-42}$ peptide inhibition. In fact, scyllo-inositol was shown to stabilize a non-toxic form of $A\beta_{1-42}$ peptide and to ameliorate cognitive deficit together with lowering amyloid plaques *in vivo* (AD mouse model) (Ibrahim and McLaurin, 2016). Interestingly, this molecule was proven to have an effect also toward αSyn. In fact, TEM experiments suggest that it can reduce both human and mouse αSyn aggregation. An explanation for its activity may lay in its planar structure, which is expected to interact with αSyn monomers through hydrophobic and hydrophilic interactions, possibly entrapping the NAC domain of the protein. Since this condition is crucial in fibrillation, its inaccessibility can discourage protein–protein interactions and, finally, aggregation. Considering αSyn conformation upon the interaction with scyllo-inositol, soluble monomers seem to be stabilized *in vitro*. This may allow these species to conserve their random coil structure and prevent them from the nucleation phase. However, further analyses are needed to determine the binding sites involved and the monomers behavior (Ibrahim and McLaurin, 2016).

Others

Tanshinone I (TAN I) and Tanshinone IIA (TAN IIA)

TAN I and TAN IIA are the main phenanthrenequinone compounds found in *Salvia miltiorrhiza,* a plant widely studied in Chinese traditional medicine. Concerning the interactions between these compounds and αSyn, ThT and TEM studies suggest that they both prolong the lag time of αSyn aggregation and disaggregate mature fibrils (Ji et al., 2016). This effect is related to their role in decreasing toxic oligomers formation, which contributes to their multi-target activity. Moreover, they seem to interact with αSyn monomers and oligomers through hydrophobic interactions, blocking them from aggregation in the same way they do with $A\beta_{1-42}$ peptide (Ren et al., 2017).

Regarding αSyn conformational aspects, CD data show that TANI and TANIIA keep the protein in a random coil structure, while in their absence monomers tend to misfold and aggregate in β-sheet structures (Ren et al., 2017). Although evidence suggests that the two compounds can avoid αSyn nucleation and fibrillation, the binding sites as well as a detailed description of the complex formed should still be investigated.

Cuminaldehyde

Cuminaldehyde is an aldehydic compound present in *Cuminum cyminum* essential oil. It is thought that the molecule interacts with αSyn monomers, thus preventing them from nucleation. Furthermore, cuminaldehyde showed a lower activity in fibrillar disaggregation than baicalein. These data suggest that Cuminaldehyde is more selective toward monomers rather than aggregated species (Morshedi et al., 2015).

Interestingly, far-UV CD gives an interesting insight over the structural behavior of αSyn while interacting with cuminaldehyde. When cuminaldehyde is incubated with αSyn, the strong negative peak at 200 nm disappears, in favor of one at 208 nm. This result highlights the conversion of random-coil monomers into entities whose structure is still unknow. However, no β-sheet peaks are detected and the shape of the graph refers to a characteristic α-helical conformation. All in all, one can speculate that the new complexes may adopt a helical structure, which is not prone to fold into β-sheet nor to convert into unfolded coils (Morshedi et al., 2015).

Interestingly, NMR studies suggest that the aldehydic function of cuminaldehyde may interact with lysine amino groups in the *N*-terminal domain of αSyn monomers (Morshedi et al., 2015). Thus, this interaction can be one of the main cause which leads to the conformational transition occurred in αSyn interacting with the compound. Finally, it may provide details about the binding site of the protein.

Synthetic Small Molecules

Synthetic small molecules have been widely investigated as putative inhibitors of αSyn aggregation. Here, some of the principal compounds currently being studied are described, highlighting the interaction with the protein (**Figure 13**). Other important molecules that play a role as inhibitors are omitted, since they mainly interact with αSyn aggregates rather than monomers. An example is the pyrazole Anle 138, widely described in Fields and Shvadchak works (Shvadchak et al., 2018; Fields et al., 2019).

Phthalocyanines

Phthalocyanines are tetrapyrrole macrocycles largely investigated in the field of αSyn aggregation. Their structure is correlated to the mechanism by which they bind to the protein: both the electron-dense pyrrolic core and the substituent carried by the peripherical rings play a pivotal role. In fact, NMR studies show that phthalocyanine tetra sulfonate (**PcTs**, a synthetic derivative of this group) interacts with αSyn at the *N*-terminal region residues Phe4 and Tyr39 mainly by π–π stacking interactions and salt bridges. This leads to a stabilization of the α-helical folding of monomers, thus delaying their misfolding and aggregation. However, data about the binding mode of PcTs to αSyn are controversial. In contrast with the previous studies, high resolution $^{1}H–^{15}N$ HSQC-NMR data of Lamberto et al. demonstrated that the compound binds to the *C*-terminal domain of αSyn monomers. Thus, these studies suggest the existence of another important binding site, involving residues 93–95 of the protein (Lamberto et al., 2009). Considering this contradiction, further studies are needed to understand which site plays a role in the interaction between αSyn and phthalocyanines.

Interestingly, PcTs can form a complex with Cu^{2+}, an important ion for αSyn accumulation in tissues. Also, this compound is able to inhibit fibrillation by forming off-pathway non-toxic oligomers *in vitro* (Oliveri, 2019). Finally, the compound is active not only against αSyn, but also amyloid β,

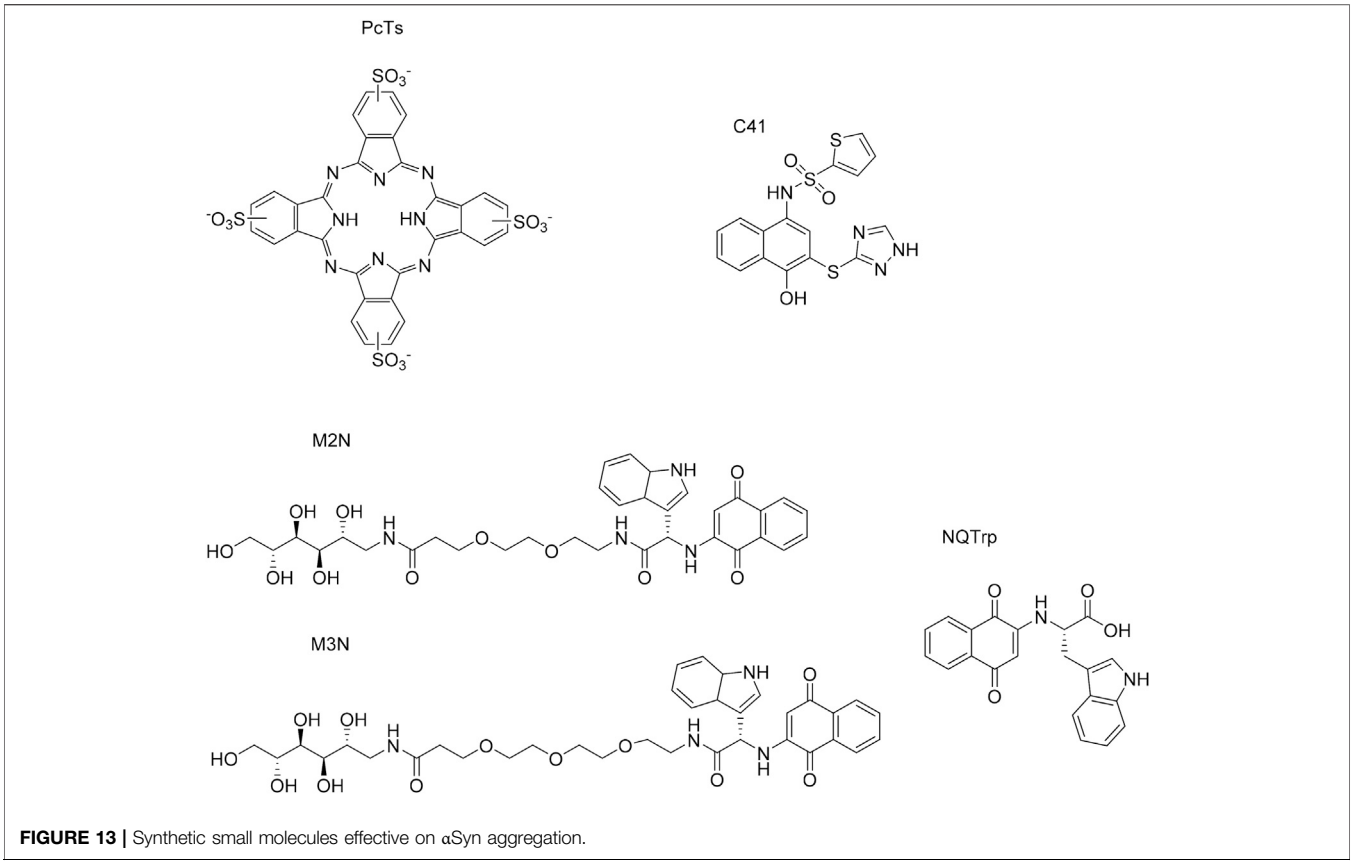

FIGURE 13 | Synthetic small molecules effective on αSyn aggregation.

Tau and PrP protein aggregates *in vitro* (Valiente-Gabioud et al., 2016).

4-Hydroxynaphthalen-1-yl)sulphonamide Derivatives

These compounds are novel inhibitors revealed by High-Throughput Screening (HTS). Among them, one of the most active compounds is **C41**. *In vitro* studies show that this molecule binds to αSyn monomers, on-pathway oligomers, and fibrillary precursors. In particular, the interaction with soluble monomers was confirmed by Size Exclusion Chromatography–Multi Angle Light Scattering (SEC–MALS). Furthermore, C41 also binds to off-pathway small aggregates and this can prevent both vesicle interaction and nucleation. $^{1}H–^{15}N$ HSQC analysis demonstrated that C41 mainly interacts with αSyn *N*-terminal domain through hydrophobic forces. As we saw before, this domain is involved in αSyn interaction with membrane, which is crucial for αSyn physiological role. MS data show that covalent adducts can be formed, but more studies are needed to identify them and understand the conformational changes of αSyn (Kurnik et al., 2018).

D3.3 Mannitol Derivatives

M2N and M3N

These compounds are αSyn aggregation inhibitors that consist of mannitol, covalently linked to NQTrp via two or three molecules of PEG. **NQTrp**, a generic amyloids inhibitor formed by NQ (Naphtoquinone) and Trp (Tryptophan), is effective against fibrils formation due to the possibility to share π-π interactions with αSyn monomers. However, even if the inhibition occurs at low concentration (0.1 μm), the compound is characterized by a poor BBB penetration (Paul et al., 2019).

To overcome this problem, researchers conjugated it with mannitol, known for its BBB disruption properties and anti-αSyn aggregation effect. Notably, the conjugates were non-toxic to SH-SY5Y cells and could reduce the cytotoxicity of αSyn aggregates. Moreover, results suggest that the longer PEG chain in M3N might confer better flexibility for a more efficient inhibition.

Concerning αSyn conformational aspects, CD studies were performed to elucidate the protein behavior during the interaction with the compounds. In this analysis, αSyn alone shows a negative peak at 218 nm and a positive one around 198 nm, which are typical of β-sheet rich structures. By adding incremental doses of the M2N and M3N, the peak at 218 decreases in a dose-dependent manner. This means that the secondary structure of the protein refolds during the interaction with the molecules, with a decrement of β-sheets. However, more studies are needed to identify the conformation of the new formed complexes (Paul et al., 2019).

Finally, TEM studies show that in the presence of M2N and M3N, the fibrillar outline of αSyn inclusions turns into an amorphic conformation (Paul et al., 2019). This is in accordance with the previous results and suggests that these

inhibitors can be interesting to investigate αSyn behavior while interacting with polyalcohol compounds.

CONCLUSION AND FUTURE PERSPECTIVE

After this trip around αSyn structure, the factors influencing it and the applied techniques, it is clear that the fundamental structural features of this rather small protein of 140 residues have not yet been elucidated. The main hurdle to thoroughly understand its behavior is its intrinsically disordered nature and high susceptibility to the environment. αSyn tends to acquire diverse transient and dynamic conformations depending on the presence of different biological and physico-chemical factors. In physiological conditions, αSyn is thought to be a compact monomer acquiring an aggregation-resistant globular structure. This conformation is stabilized by long-range electrostatic interactions between the residues present in the *C*-terminal domain and those located in the central part of the protein. On the other hand, when αSyn is driven to adopt a more extended structure, exposing the NAC region, protein aggregation is triggered. It is assumed that folded stable helical conformers impede amyloidogenic aggregation. However, to date, there is not a clear consensus on its *in vivo* structural propensity. αSyn will likely adopt specialized conformations depending on different conditions (e.g., changes in pH, temperature, ionic strength, closeness to surfaces) that might trigger different biological or pathological functions. For instance, a helical pattern at the *N*-terminal end has been observed upon vesicle and membrane interaction. Conversely, there are limited comprehensive structural data about αSyn interactions with various partners such as proteins and both endogenous (e.g., neurotransmitters, and lipids) and exogenous (e.g., metals and drugs) molecules. This information is limited due to the difficulty to create, isolate and analyze complexes of αSyn with these partners. This lack of comprehensive knowledge is also due to the absence of crystallographic data and of other experimental techniques able to reproduce the *in vivo* physiological and/or pathological conditions. In addition, experimental data in the literature are obtained from the study of αSyn in very different conditions, hampering a significant comparison of the obtained results. In our opinion, it would be appropriate for studies to converge upon standardized set up and protocols. As an example, *N*-terminal acetylation has been demonstrated to be a constitutive element of the protein, so this modification should be applied in every experiment to achieve reliable conclusions. Other aspects to be considered are the source of αSyn, its post-translational modifications and pathological mutations. Finally, a combination of experimental and computational approaches can be a good strategy for future research. By extracting information from different experimental techniques and constraining molecular dynamic simulations based on that information, more meaningful results could be obtained, allowing us to address some of the experimental issues observed so far. The more reliable information obtained, the more effective their translation into the development of bioactive compounds able to modulate pathological αSyn effects will be.

AUTHOR CONTRIBUTIONS

NB, LF, HP-P, and KP equallly contributed to this work. HP-P and KP: wt and mutated synuclein structural features; LF: Lipids and Metals; NB: Proteins and small molecules. SPi and SO: analysis, writing modifications, and revision through all the text. SPe: writing, analysis and interpretation throughout all the text, and editing of the manuscript.

FUNDING

This research has received funding from the European Union's Horizon 2020 research and innovation program H2020-MSCA-ITN-2019-EJD: Marie Skłodowska-Curie Innovative Training Networks (European Joint Doctorate)—Grant Agreement No: 860070—TubInTrain.

REFERENCES

Abeyawardhane, D. L., Fernández, R. D., Murgas, C. J., Heitger, D. R., Forney, A. K., Crozier, M. K., et al. (2018). Iron Redox Chemistry Promotes Antiparallel Oligomerization of α-Synuclein. *J. Am. Chem. Soc.* 140 (15), 5028–5032. doi:10.1021/jacs.8b02013

Abeyawardhane, D. L., Heitger, D. R., Fernández, R. D., Forney, A. K., and Lucas, H. R. (2019). C-terminal CuII Coordination to α-Synuclein Enhances Aggregation. *ACS Chem. Neurosci.* 10 (3), 1402–1410. doi:10.1021/acschemneuro.8b00448

Agerschou, E. D., Saridaki, T., Flagmeier, P., Galvagnion, C., Komnig, D., Nagpal, A., et al. (2019). An Engineered Monomer Binding-Protein Forα-Synuclein Efficiently Inhibits the Proliferation of Amyloid Fibrils. *Elife* 8, e46112. doi:10.7554/eLife.46112

Allison, J. R., Varnai, P., Dobson, C. M., and Vendruscolo, M. (2009). Determination of the Free Energy Landscape of α-Synuclein Using Spin Label Nuclear Magnetic Resonance Measurements. *J. Am. Chem. Soc.* 131 (51), 18314–18326. doi:10.1021/ja904716h

Appel-Cresswell, S., Vilarino-Guell, C., Encarnacion, M., Sherman, H., Yu, I., Shah, B., et al. (2013). Alpha-synuclein p.H50Q, a Novel Pathogenic Mutation for Parkinson's Disease. *Mov Disord.* 28 (6), 811–813. doi:10.1002/mds.25421

Aprile, F. A., Arosio, P., Fusco, G., Chen, S. W., Kumita, J. R., Dhulesia, A., et al. (2017). Inhibition of α-Synuclein Fibril Elongation by Hsp70 Is Governed by a Kinetic Binding Competition between α-Synuclein Species. *Biochemistry* 56 (9), 1177–1180. doi:10.1021/acs.biochem.6b01178

Bai, J., Zhang, Z., Liu, M., and Li, C. (2015). α-synuclein-lanthanide Metal Ions Interaction: Binding Sites, Conformation and Fibrillation. *BMC Biophys.* 9 (1), 1–10. doi:10.1186/s13628-016-0026-1

Balesh, D., Ramjan, Z., and Floriano, W. B. (2011). Unfolded Annealing Molecular Dynamics Conformers for Wild-type and Disease-Associated Variants of Alpha-Synuclein Show No Propensity for Beta-Sheetformation. *Jbpc* 02 (2), 124–134. doi:10.4236/jbpc.2011.22015

Bartels, T., Kim, N. C., Luth, E. S., and Selkoe, D. J. (2014). N-Alpha-Acetylation of α-Synuclein Increases its Helical Folding Propensity, GM1 Binding Specificity and Resistance to Aggregation. *PLoS ONE* 9 (7), e103727. doi:10.1371/journal.pone.0103727

Bédard, L., Lefèvre, T., Morin-Michaud, É., and Auger, M. (2014). Besides Fibrillization: Putative Role of the Peptide Fragment 71-82 on the Structural and Assembly Behavior of α-Synuclein. *Biochemistry* 53 (41), 6463–6472. doi:10.1021/bi5008707

Bertoncini, C. W., Jung, Y.-S., Fernandez, C. O., Hoyer, W., Griesinger, C., Jovin, T. M., et al. (2005). From the Cover: Release of Long-Range Tertiary Interactions Potentiates Aggregation of Natively Unstructured -synuclein. *Proc. Natl. Acad. Sci.* 102 (5), 1430–1435. doi:10.1073/pnas.0407146102

Bhattacharya, S., Xu, L., and Thompson, D. (2019). Molecular Simulations Reveal Terminal Group Mediated Stabilization of Helical Conformers in Both Amyloid-β42 and α-Synuclein. *ACS Chem. Neurosci.* 10 (6), 2830–2842. doi:10.1021/acschemneuro.9b00053

Binolfi, A., Valiente-Gabioud, A. A., Duran, R., Zweckstetter, M., Griesinger, C., and Fernandez, C. O. (2011). Exploring the Structural Details of Cu(I) Binding to α-Synuclein by NMR Spectroscopy. *J. Am. Chem. Soc.* 133 (2), 194–196. doi:10.1021/ja107842f

Binolfi, A., Quintanar, L., Bertoncini, C. W., Griesinger, C., and Fernández, C. O. (2012). Bioinorganic Chemistry of Copper Coordination to Alpha-Synuclein: Relevance to Parkinson's Disease. *Coord. Chem. Rev.* 256 (19–20), 2188–2201. doi:10.1016/j.ccr.2012.05.004

Bisaglia, M., and Bubacco, L. (2020). Copper Ions and Parkinson's Disease: Why Is Homeostasis So Relevant? *Biomolecules* 10 (2), 195. doi:10.3390/biom10020195

Bjørklund, G., Hofer, T., Nurchi, V. M., and Aaseth, J. (2019). Iron and Other Metals in the Pathogenesis of Parkinson's Disease: Toxic Effects and Possible Detoxification. *J. Inorg. Biochem.* 199, 110717. doi:10.1016/j.jinorgbio.2019.110717

Bjørklund, G., Dadar, M., Chirumbolo, S., and Aaseth, J. (2020). The Role of Xenobiotics and Trace Metals in Parkinson's Disease. *Mol. Neurobiol.* 57 (3), 1405–1417. doi:10.1007/s12035-019-01832-1

Bodner, C. R., Dobson, C. M., and Bax, A. (2009). Multiple Tight Phospholipid-Binding Modes of α-Synuclein Revealed by Solution NMR Spectroscopy. *J. Mol. Biol.* 390 (4), 775–790. doi:10.1016/j.jmb.2009.05.066

Bodner, C. R., Maltsev, A. S., Dobson, C. M., and Bax, A. (2010). Differential Phospholipid Binding of α-Synuclein Variants Implicated in Parkinson's Disease Revealed by Solution NMR Spectroscopy. *Biochemistry* 49 (5), 862–871. doi:10.1021/bi901723p

Brodie, N. I., Popov, K. I., Petrotchenko, E. V., Dokholyan, N. V., and Borchers, C. H. (2019). Conformational Ensemble of Native α-synuclein in Solution as Determined by Short-Distance Crosslinking Constraint-Guided Discrete Molecular Dynamics Simulations. *Plos Comput. Biol.* 15 (3), e1006859–21. doi:10.1371/journal.pcbi.1006859

Burré, J. (2015). The Synaptic Function of α-Synuclein. *Jpd* 5 (4), 699–713. doi:10.3233/JPD-150642

Bussell, R., and Eliezer, D. (2001). Residual Structure and Dynamics in Parkinson's Disease-Associated Mutants of α-Synuclein. *J. Biol. Chem.* 276 (49), 45996–46003. doi:10.1074/jbc.M106777200

Camponeschi, F., Valensin, D., Tessari, I., Bubacco, L., Dell'Acqua, S., Casella, L., et al. (2013). Copper(I)-α-Synuclein Interaction: Structural Description of Two Independent and Competing Metal Binding Sites. *Inorg. Chem.* 52 (3), 1358–1367. doi:10.1021/ic302050m

Canerina-Amaro, A., Pereda, D., Diaz, M., Rodriguez-Barreto, D., Casañas-Sánchez, V., Heffer, M., et al. (2019). Differential Aggregation and Phosphorylation of Alpha Synuclein in Membrane Compartments Associated with Parkinson Disease. *Front. Neurosci.* 13 (382), 1–21. doi:10.3389/fnins.2019.00382

Cartelli, D., Aliverti, A., Barbiroli, A., Santambrogio, C., Ragg, E. M., Casagrande, F. V. M., et al. (2016). α-Synuclein Is a Novel Microtubule Dynamase. *Sci. Rep.* 6 (33289), 1–13. doi:10.1038/srep33289

Caruana, M., Högen, T., Levin, J., Hillmer, A., Giese, A., and Vassallo, N. (2011). Inhibition and Disaggregation of α-synuclein Oligomers by Natural Polyphenolic Compounds. *FEBS Lett.* 585 (8), 1113–1120. doi:10.1016/j.febslet.2011.03.046

Chaari, A., Eliezer, D., and Ladjimi, M. (2016). The C-Terminal α-helices of Mammalian Hsc70 Play a Critical Role in the Stabilization of α-synuclein Binding and Inhibition of Aggregation. *Int. J. Biol. Macromolecules* 83, 433–441. doi:10.1016/j.ijbiomac.2015.10.089

Chandra, S., Chen, X., Rizo, J., Jahn, R., and Südhof, T. C. (2003). A Broken α-Helix in Folded α-Synuclein. *J. Biol. Chem.* 278 (17), 15313–15318. doi:10.1074/jbc.M213128200

Chi, Y.-C., Armstrong, G. S., Jones, D. N. M., Eisenmesser, E. Z., and Liu, C.-W. (2014). Residue Histidine 50 Plays a Key Role in Protecting α-Synuclein from Aggregation at Physiological pH. *J. Biol. Chem.* 289 (22), 15474–15481. doi:10.1074/jbc.M113.544049

Chidananda, A. H., Sharma, A. K., Khandelwal, R., and Sharma, Y. (2019). Secretagogin Binding Prevents α-Synuclein Fibrillation. *Biochemistry* 58 (46), 4585–4589. doi:10.1021/acs.biochem.9b00656

Chiricozzi, E., Lunghi, G., Di Biase, E., Fazzari, M., Sonnino, S., and Mauri, L. (2020). GM1 Ganglioside Is a Key Factor in Maintaining the Mammalian Neuronal Functions Avoiding Neurodegeneration. *Ijms* 21 (3), 868–929. doi:10.3390/ijms21030868

Ciechanover, A., and Kwon, Y. T. (2015). Degradation of Misfolded Proteins in Neurodegenerative Diseases: Therapeutic Targets and Strategies. *Exp. Mol. Med.* 47, e147. doi:10.1038/emm.2014.117

Conway, K. A., Harper, J. D., and Lansbury, P. T. (1998). Accelerated *In Vitro* Fibril Formation by a Mutant α-synuclein Linked to Early-Onset Parkinson Disease. *Nat. Med.* 4 (11), 1318–1320. doi:10.1038/3311

Coskuner, O., and Wise-Scira, O. (2013). Structures and Free Energy Landscapes of the A53T Mutant-type α-Synuclein Protein and Impact of A53T Mutation on the Structures of the Wild-type α-Synuclein Protein with Dynamics. *ACS Chem. Neurosci.* 4 (7), 1101–1113. doi:10.1021/cn400041j

Daniels, M. J., Nourse, J. B., Kim, H., Sainati, V., Schiavina, M., Murrali, M. G., et al. (2019). Cyclized NDGA Modifies Dynamic α-synuclein Monomers Preventing Aggregation and Toxicity. *Sci. Rep.* 9 (1), 1–17. doi:10.1038/s41598-019-39480-z

Davidson, W. S., Jonas, A., Clayton, D. F., and George, J. M. (1998). Stabilization of α-Synuclein Secondary Structure upon Binding to Synthetic Membranes. *J. Biol. Chem.* 273 (16), 9443–9449. doi:10.1074/jbc.273.16.9443

De Ricco, R., Valensin, D., Dell'Acqua, S., Casella, L., Hureau, C., and Faller, P. (2015). Copper(I/II), α/β-Synuclein and Amyloid-β: Menage à Trois? *ChemBioChem* 16 (16), 2319–2328. doi:10.1002/cbic.201500425

Dedmon, M. M., Christodoulou, J., Wilson, M. R., and Dobson, C. M. (2005a). Heat Shock Protein 70 Inhibits α-Synuclein Fibril Formation via Preferential Binding to Prefibrillar Species. *J. Biol. Chem.* 280 (15), 14733–14740. doi:10.1074/jbc.M413024200

Dedmon, M. M., Lindorff-Larsen, K., Christodoulou, J., Vendruscolo, M., and Dobson, C. M. (2005b). Mapping Long-Range Interactions in α-Synuclein Using Spin-Label NMR and Ensemble Molecular Dynamics Simulations. *J. Am. Chem. Soc.* 127 (2), 476–477. doi:10.1021/ja044834j

Dučić, T., Carboni, E., Lai, B., Chen, S., Michalke, B., Lázaro, D. F., et al. (2015). Alpha-Synuclein Regulates Neuronal Levels of Manganese and Calcium. *ACS Chem. Neurosci.* 6 (10), 1769–1779. doi:10.1021/acschemneuro.5b00093

Dułak, D., Gadzała, M., Banach, M., Konieczny, L., and Roterman, I. (2020). Alternative Structures of α-Synuclein. *Molecules* 25 (3). doi:10.3390/molecules25030600

Ebrahimi-Fakhari, D., Wahlster, L., and McLean, P. J. (2011). Molecular Chaperones in Parkinson's Disease—Present and Future. *J. Parkinson's Dis.* 1 (4), 299–320. doi:10.3233/JPD-2011-11044

Eliezer, D., Kutluay, E., Bussell, R., and Browne, G. (2001). Conformational Properties of α-synuclein in its Free and Lipid-Associated States 1 1Edited by P. E. Wright. *J. Mol. Biol.* 307 (4), 1061–1073. doi:10.1006/jmbi.2001.4538

Eliezer, D. (2009). Biophysical Characterization of Intrinsically Disordered Proteins. *Curr. Opin. Struct. Biol.* 19 (1), 23–30. doi:10.1016/j.sbi.2008.12.004

Fakhree, M. A. A., Nolten, I. S., Blum, C., and Claessens, M. M. A. E. (2018). Different Conformational Subensembles of the Intrinsically Disordered Protein α-Synuclein in Cells. *J. Phys. Chem. Lett.* 9 (6), 1249–1253. doi:10.1021/acs.jpclett.8b00092

Fantini, J., Carlus, D., and Yahi, N. (2011). The Fusogenic Tilted Peptide (67-78) of α-synuclein Is a Cholesterol Binding Domain. *Biochim. Biophys. Acta (Bba) - Biomembranes* 1808 (10), 2343–2351. doi:10.1016/j.bbamem.2011.06.017

Fares, M.-B., Ait-Bouziad, N., Dikiy, I., Mbefo, M. K., Jovii, A., Kiely, A., et al. (2014). The Novel Parkinson's Disease Linked Mutation G51D Attenuates *In Vitro* Aggregation and Membrane Binding of -synuclein, and Enhances its Secretion and Nuclear Localization in Cells. *Hum. Mol. Genet.* 23 (17), 4491–4509. doi:10.1093/hmg/ddu165

Fauvet, B., Mbefo, M. K., Fares, M.-B., Desobry, C., Michael, S., Ardah, M. T., et al. (2012). α-Synuclein in Central Nervous System and from Erythrocytes, Mammalian Cells, and *Escherichia coli* Exists Predominantly as Disordered Monomer*. *J. Biol. Chem.* 287 (19), 15345–15364. doi:10.1074/jbc.M111.318949

Fields, C. R., Bengoa-Vergniory, N., and Wade-Martins, R. (2019). Targeting Alpha-Synuclein as a Therapy for Parkinson's Disease. *Front. Mol. Neurosci.* 12, 1–14. doi:10.3389/fnmol.2019.00299

Fortin, D. L., Troyer, M. D., Nakamura, K., Kubo, S. I., Anthony, M. D., and Edwards, R. H. (2004). Lipid Rafts Mediate the Synaptic Localization of -Synuclein. *J. Neurosci.* 24 (30), 6715–6723. doi:10.1523/JNEUROSCI.1594-04.2004

Fredenburg, R. A., Rospigliosi, C., Meray, R. K., Kessler, J. C., Lashuel, H. A., Eliezer, D., et al. (2007). The Impact of the E46K Mutation on the Properties of α-Synuclein in its Monomeric and Oligomeric States. *Biochemistry* 46 (24), 7107–7118. doi:10.1021/bi7000246

Fusco, G., De Simone, A., Gopinath, T., Vostrikov, V., Vendruscolo, M., Dobson, C. M., et al. (2014). Direct Observation of the Three Regions in α-synuclein that Determine its Membrane-Bound Behaviour. *Nat. Commun.* 5 (3827), 1–8. doi:10.1038/ncomms4827

Galvagnion, C., Buell, A. K., Meisl, G., Michaels, T. C. T., Vendruscolo, M., Knowles, T. P. J., et al. (2015). Lipid Vesicles Trigger α-synuclein Aggregation by Stimulating Primary Nucleation. *Nat. Chem. Biol.* 11 (3), 229–234. doi:10.1038/nchembio.1750

Galvagnion, C., Brown, J. W. P., Ouberai, M. M., Flagmeier, P., Vendruscolo, M., Buell, A. K., et al. (2016). Chemical Properties of Lipids Strongly Affect the Kinetics of the Membrane-Induced Aggregation of α-synuclein. *Proc. Natl. Acad. Sci. USA* 113 (26), 7065–7070. doi:10.1073/pnas.1601899113

Gao, X., Carroni, M., Nussbaum-Krammer, C., Mogk, A., Nillegoda, N. B., Szlachcic, A., et al. (2015). Human Hsp70 Disaggregase Reverses Parkinson's-Linked α-Synuclein Amyloid Fibrils. *Mol. Cel* 59 (5), 781–793. doi:10.1016/j.molcel.2015.07.012

Garza-Lombó, C., Posadas, Y., Quintanar, L., Gonsebatt, M. E., and Franco, R. (2018). Neurotoxicity Linked to Dysfunctional Metal Ion Homeostasis and Xenobiotic Metal Exposure: Redox Signaling and Oxidative Stress. *Antioxid. Redox Signal.* 28 (18), 1669–1703. doi:10.1089/ars.2017.7272

Ghio, S., Camilleri, A., Caruana, M., Ruf, V. C., Schmidt, F., Leonov, A., et al. (2019). Cardiolipin Promotes Pore-Forming Activity of Alpha-Synuclein Oligomers in Mitochondrial Membranes. *ACS Chem. Neurosci.* 10 (8), 3815–3829. doi:10.1021/acschemneuro.9b00320

Ghosh, D., Mondal, M., Mohite, G. M., Singh, P. K., Ranjan, P., Anoop, A., et al. (2013). The Parkinson's Disease-Associated H50Q Mutation Accelerates α-Synuclein Aggregation *In Vitro*. *Biochemistry* 52 (40), 6925–6927. doi:10.1021/bi400999d

Ghosh, D., Sahay, S., Ranjan, P., Salot, S., Mohite, G. M., Singh, P. K., et al. (2014). The Newly Discovered Parkinson's Disease Associated Finnish Mutation (A53E) Attenuates α-Synuclein Aggregation and Membrane Binding. *Biochemistry* 53 (41), 6419–6421. doi:10.1021/bi5010365

Ghosh, S., Kundu, A., and Chattopadhyay, K. (2018). Small Molecules Attenuate the Interplay between Conformational Fluctuations, Early Oligomerization and Amyloidosis of Alpha Synuclein. *Sci. Rep.* 8 (1), 1–16. doi:10.1038/s41598-018-23718-3

Grassi, S., Giussani, P., Mauri, L., Prioni, S., Sonnino, S., and Prinetti, A. (2020). Lipid Rafts and Neurodegeneration: Structural and Functional Roles in Physiologic Aging and Neurodegenerative Diseases. *J. Lipid Res.* 61 (5), 636–654. doi:10.1194/jlr.TR119000427

Guerrero-Ferreira, R., Taylor, N. M., Mona, D., Ringler, P., Lauer, M. E., Riek, R., et al. (2018). Cryo-EM Structure of Alpha-Synuclein Fibrils. *ELife* 7, e36402. doi:10.7554/eLife.36402

Han, J. Y., Choi, T. S., and Kim, H. I. (2018). Molecular Role of Ca2+ and Hard Divalent Metal Cations on Accelerated Fibrillation and Interfibrillar Aggregation of α-Synuclein. *Sci. Rep.* 8 (1), 1–11. doi:10.1038/s41598-018-20320-5

Heise, H., Hoyer, W., Becker, S., Andronesi, O. C., Riedel, D., and Baldus, M. (2005). Molecular-level Secondary Structure, Polymorphism, and Dynamics of Full-Length -synuclein Fibrils Studied by Solid-State NMR. *Proc. Natl. Acad. Sci.* 102 (44), 15871–15876. doi:10.1073/pnas.0506109102

Högen, T., Levin, J., Schmidt, F., Caruana, M., Vassallo, N., Kretzschmar, H., et al. (2012). Two Different Binding Modes of α-Synuclein to Lipid Vesicles Depending on its Aggregation State. *Biophysical J.* 102 (7), 1646–1655. doi:10.1016/j.bpj.2012.01.059

Ibrahim, T., and McLaurin, J. (2016). α-Synuclein Aggregation, Seeding and Inhibition by Scyllo-Inositol. *Biochem. Biophysical Res. Commun.* 469 (3), 529–534. doi:10.1016/j.bbrc.2015.12.043

Ilie, I. M., and Caflisch, A. (2019). Simulation Studies of Amyloidogenic Polypeptides and Their Aggregates. *Chem. Rev.* 119 (12), 6956–6993. doi:10.1021/acs.chemrev.8b00731

Iyer, A., Roeters, S. J., Kogan, V., Woutersen, S., Claessens, M. M. A. E., and Subramaniam, V. (2017). C-terminal Truncated α-Synuclein Fibrils Contain Strongly Twisted β-Sheets. *J. Am. Chem. Soc.* 139 (43), 15392–15400. doi:10.1021/jacs.7b07403

Jakubec, M., Bariås, E., Furse, S., Govasli, M. L., George, V., Turcu, D., et al. (2019). Cholesterol Is a strong Promotor of an α-Synuclein Membrane Binding Mode that Accelerates Oligomerization. *BioRxiv* 12, 725762. doi:10.1101/725762

Jao, C. C., Hegde, B. G., Chen, J., Haworth, I. S., and Langen, R. (2008). Structure of Membrane-Bound -synuclein from Site-Directed Spin Labeling and Computational Refinement. *Proc. Natl. Acad. Sci.* 105 (50), 19666–19671. doi:10.1073/pnas.0807826105

Javed, H., and Ojha, S. (2020). Therapeutic Potential of Baicalein in Parkinson's Disease: Focus on Inhibition of α-Synuclein Oligomerization and Aggregation. *Synucleins - Biochem. Role Dis.* 14, 1–16. doi:10.5772/intechopen.83589

Ji, K., Zhao, Y., Yu, T., Wang, Z., Gong, H., Yang, X., et al. (2016). Inhibition Effects of Tanshinone on the Aggregation of α-synuclein. *Food Funct.* 7 (1), 409–416. doi:10.1039/c5fo00664c

Jónsson, S. A., Mohanty, S., and Irbäck, A. (2012). Distinct Phases of Free α-synuclein-A Monte Carlo Study. *Proteins* 80 (9), 2169–2177. doi:10.1002/prot.24107

Kardani, J., and Roy, I. (2015). Understanding Caffeine's Role in Attenuating the Toxicity of α-Synuclein Aggregates: Implications for Risk of Parkinson's Disease. *ACS Chem. Neurosci.* 6 (9), 1613–1625. doi:10.1021/acschemneuro.5b00158

Kardani, J., Sethi, R., and Roy, I. (2017). Nicotine Slows Down Oligomerisation of α-synuclein and Ameliorates Cytotoxicity in a Yeast Model of Parkinson's Disease. *Biochim. Biophys. Acta (Bba) - Mol. Basis Dis.* 1863 (6), 1454–1463. doi:10.1016/j.bbadis.2017.02.002

Kauzmann, W. (1954). "Denaturation of Proteins and Enzymes," in *The Mechanism of Enzyme Action*, Berlin: Springer, 71.

Khalaf, O., Fauvet, B., Oueslati, A., Dikiy, I., Mahul-Mellier, A.-L., Ruggeri, F. S., et al. (2014). The H50Q Mutation Enhances α-Synuclein Aggregation, Secretion, and Toxicity. *J. Biol. Chem.* 289 (32), 21856–21876. doi:10.1074/jbc.M114.553297

Kiechle, M., Grozdanov, V., and Danzer, K. M. (2020). The Role of Lipids in the Initiation of α-Synuclein Misfolding. *Front. Cel Dev. Biol.* 8, 957. doi:10.3389/fcell.2020.562241

Kiely, A. P., Asi, Y. T., Kara, E., Limousin, P., Ling, H., Lewis, P., et al. (2013). α-Synucleinopathy Associated with G51D SNCA Mutation: a Link between Parkinson's Disease and Multiple System Atrophy? *Acta Neuropathol.* 125 (5), 753–769. doi:10.1007/s00401-013-1096-7

Kim, D.-H., Lee, J., Mok, K., Lee, J., and Han, K.-H. (2020). Salient Features of Monomeric Alpha-Synuclein Revealed by NMR Spectroscopy. *Biomolecules* 10 (3), 428–515. doi:10.3390/biom10030428

Klucken, J., Outeiro, T. F., Nguyen, P., McLean, P. J., and Hyman, B. T. (2006). Detection of Novel Intracellular O-synuclein Oligomeric Species by Fluorescence Lifetime Imaging. *FASEB j.* 20 (12), 2050–2057. doi:10.1096/fj.05-5422com

Kostka, M., Högen, T., Danzer, K. M., Levin, J., Habeck, M., Wirth, A., et al. (2008). Single Particle Characterization of Iron-Induced Pore-Forming α-Synuclein Oligomers. *J. Biol. Chem.* 283 (16), 10992–11003. doi:10.1074/jbc.M709634200

Krüger, R., Kuhn, W., Müller, T., Woitalla, D., Graeber, M., Kosel, S., et al. (1998). Ala30Pro Mutation in the Gene Encoding A-Synuclein in Parkinson's Disease. *Nat. Genet.* 18 (3), 231–236. doi:10.1038/ng0298-106

Kumar, S., Sarkar, A., and Sundar, D. (2009). Controlling Aggregation Propensity in A53T Mutant of Alpha-Synuclein Causing Parkinson's Disease. *Biochem. Biophys. Res. Commun.* 387 (2), 305–309. doi:10.1016/j.bbrc.2009.07.008

Kurnik, M., Sahin, C., Andersen, C. B., Lorenzen, N., Giehm, L., Mohammad-Beigi, H., et al. (2018). Potent α-Synuclein Aggregation Inhibitors, Identified by High-Throughput Screening, Mainly Target the Monomeric State. *Cel Chem. Biol.* 25 (11), 1389–1402. doi:10.1016/j.chembiol.2018.08.005

Lamberto, G. R., Binolfi, A., Orcellet, M. L., Bertoncini, C. W., Zweckstetter, M., Griesinger, C., et al. (2009). Structural and Mechanistic Basis behind the Inhibitory Interaction of PcTS on α-synuclein Amyloid Fibril Formation. *Pnas* 106 (50), 21057–21062. doi:10.1073/pnas.0902603106

Lautenschläger, J., Stephens, A. D., Fusco, G., Ströhl, F., Curry, N., Zacharopoulou, M., et al. (2018). C-terminal Calcium Binding of α-synuclein Modulates Synaptic Vesicle Interaction. *Nat. Commun.* 9 (1), 712. doi:10.1038/s41467-018-03111-4

Lesage, S., Anheim, M., Letournel, F., Bousset, L., Honoré, A., Rozas, N., et al. (2013). G51D α-synuclein Mutation Causes a Novel Parkinsonian-Pyramidal Syndrome. *Ann. Neurol.* 73 (4), 459–471. doi:10.1002/ana.23894

Lorentzon, E., Kumar, R., Horvath, I., and Wittung-Stafshede, P. (2020). Differential Effects of Cu2+ and Fe3+ Ions on *In Vitro* Amyloid Formation of Biologically-Relevant α-synuclein Variants. *Biometals* 33, 97–106. doi:10.1007/s10534-020-00234-4

Lorenzen, N., Lemminger, L., Pedersen, J. N., Nielsen, S. B., and Otzen, D. E. (2014). The N-Terminus of α-synuclein Is Essential for Both Monomeric and Oligomeric Interactions with Membranes. *FEBS Lett.* 588 (3), 497–502. doi:10.1016/j.febslet.2013.12.015

Lothian, A., Lago, L., Mukherjee, S., Connor, A. R., Fowler, C., McLean, C. A., et al. (2019). Characterization of the Metal Status of Natively Purified Alpha-Synuclein from Human Blood, Brain Tissue, or Recombinant Sources Using Size Exclusion ICP-MS Reveals No Significant Binding of Cu, Fe or Zn. *Metallomics* 11 (1), 128–140. doi:10.1039/c8mt00223a

Lu, Y., Prudent, M., Fauvet, B., Lashuel, H. A., and Girault, H. H. (2011). Phosphorylation of α-Synuclein at Y125 and S129 Alters its Metal Binding Properties: Implications for Understanding the Role of α-Synuclein in the Pathogenesis of Parkinson's Disease and Related Disorders. *ACS Chem. Neurosci.* 2 (11), 667–675. doi:10.1021/cn200074d

Luk, K. C., Mills, I. P., Trojanowski, J. Q., and Lee, V. M.-Y. (2008). Interactions between Hsp70 and the Hydrophobic Core of α-Synuclein Inhibit Fibril Assembly. *Biochemistry* 47 (47), 12614–12625. doi:10.1021/bi801475r

Ma, L., Yang, C., Zheng, J., Chen, Y., Xiao, Y., and Huang, K. (2020). Non-polyphenolic Natural Inhibitors of Amyloid Aggregation. *Eur. J. Med. Chem.* 192, 112197. doi:10.1016/j.ejmech.2020.112197

Månsson, C., Arosio, P., Hussein, R., Kampinga, H. H., Hashem, R. M., Boelens, W. C., et al. (2014). Interaction of the Molecular Chaperone DNAJB6 with Growing Amyloid-Beta 42 (Aβ42) Aggregates Leads to Sub-stoichiometric Inhibition of Amyloid Formation. *J. Biol. Chem.* 289 (45), 31066–31076. doi:10.1074/jbc.M114.595124

Man, W. K., De Simone, A., Barritt, J. D., Vendruscolo, M., Dobson, C. M., and Fusco, G. (2020). A Role of Cholesterol in Modulating the Binding of α-Synuclein to Synaptic-like Vesicles. *Front. Neurosci.* 14, 1–11. doi:10.3389/fnins.2020.00018

Martial, B., Lefèvre, T., Buffeteau, T., and Auger, M. (2019). Vibrational Circular Dichroism Reveals Supramolecular Chirality Inversion of α-Synuclein Peptide Assemblies upon Interactions with Anionic Membranes. *ACS Nano* 13 (3), 3232–3242. doi:10.1021/acsnano.8b08932

Martial, B., Raîche-Marcoux, G., Lefèvre, T., Audet, P., Voyer, N., and Auger, M. (2020). Structure of a Parkinson's Disease-Involved α-Synuclein Peptide Is Modulated by Membrane Composition and Physical State. *J. Phys. Chem. B.* 124 (17), 3469–3481. doi:10.1021/acs.jpcb.0c00945

Martinez, Z., Zhu, M., Han, S., and Fink, A. L. (2007). GM1 Specifically Interacts with α-Synuclein and Inhibits Fibrillation. *Biochemistry* 46 (7), 1868–1877. doi:10.1021/bi061749a

Mazzulli, J. R., Armakola, M., Dumoulin, M., Parastatidis, I., and Ischiropoulos, H. (2007). Cellular Oligomerization of α-Synuclein Is Determined by the Interaction of Oxidized Catechols with a C-Terminal Sequence. *J. Biol. Chem.* 282 (43), 31621–31630. doi:10.1074/jbc.M704737200

McDowall, J. S., and Brown, D. R. (2016). Alpha-synuclein: Relating Metals to Structure, Function and Inhibition. *Metallomics* 8 (4), 385–397. doi:10.1039/c6mt00026f

McLean, P. J., Kawamata, H., Ribich, S., and Hyman, B. T. (2000). Membrane Association and Protein Conformation of α-Synuclein in Intact Neurons. *J. Biol. Chem.* 275 (12), 8812–8816. doi:10.1074/jbc.275.12.8812

Meade, R. M., Fairlie, D. P., and Mason, J. M. (2019). Alpha-synuclein Structure and Parkinson's Disease - Lessons and Emerging Principles. *Mol. Neurodegener.* 14 (1), 29. doi:10.1186/s13024-019-0329-1

Mesa-Herrera, F., Taoro-González, L., Valdés-Baizabal, C., Diaz, M., and Marín, R. (2019). Lipid and Lipid Raft Alteration in Aging and Neurodegenerative Diseases: A Window for the Development of New Biomarkers. *Ijms* 20 (15), 3810. doi:10.3390/ijms20153810

Miotto, M. C., Binolfi, A., Zweckstetter, M., Griesinger, C., and Fernández, C. O. (2014). Bioinorganic Chemistry of Synucleinopathies: Deciphering the Binding Features of Met Motifs and His-50 in AS-Cu(I) Interactions. *J. Inorg. Biochem.* 141, 208–211. doi:10.1016/j.jinorgbio.2014.08.012

Mirecka, E. A., Shaykhalishahi, H., Gauhar, A., Akgül, Ş., Lecher, J., Willbold, D., et al. (2014). Sequestration of a β-Hairpin for Control of α-Synuclein Aggregation. *Angew. Chem. Int. Ed.* 53 (16), 4227–4230. doi:10.1002/anie.201309001

Mori, A., Imai, Y., and Hattori, N. (2020). Lipids: Key Players that Modulate α-Synuclein Toxicity and Neurodegeneration in Parkinson's Disease. *Ijms* 21 (9), 3301. doi:10.3390/ijms21093301

Morshedi, D., Aliakbari, F., Tayaranian-Marvian, A., Fassihi, A., Pan-Montojo, F., and Pérez-Sánchez, H. (2015). Cuminaldehyde as the Major Component ofCuminum Cyminum, a Natural Aldehyde with Inhibitory Effect on Alpha-Synuclein Fibrillation and Cytotoxicity. *J. Food Sci.* 80 (10), H2336–H2345. doi:10.1111/1750-3841.13016

Narhi, L., Wood, S. J., Steavenson, S., Jiang, Y., Wu, G. M., Anafi, D., et al. (1999). Both Familial Parkinson's Disease Mutations Accelerate α-Synuclein Aggregation. *J. Biol. Chem.* 274 (14), 9843–9846. doi:10.1074/jbc.274.14.9843

Nath, A., Sammalkorpi, M., Dewitt, D. C., Trexler, A. J., Elbaum-Garfinkle, S., O'Hern, C. S., et al. (2012). The Conformational Ensembles of α-Synuclein and Tau: Combining Single-Molecule FRET and Simulations. *Biophysical J.* 103 (9), 1940–1949. doi:10.1016/j.bpj.2012.09.032

O'Leary, E. I., and Lee, J. C. (2019). Interplay between α-synuclein Amyloid Formation and Membrane Structure. *Biochim. Biophys. Acta - Proteins Proteomics* 1867 (5), 483–491. doi:10.1016/j.bbapap.2018.09.012

Okita, Y., Rcom-H'cheo-Gauthier, A. N., Goulding, M., Chung, R. S., Faller, P., and Pountney, D. L. (2017). Metallothionein, Copper and Alpha-Synuclein in Alpha-Synucleinopathies. *Front. Neurosci.* 11, 114. doi:10.3389/fnins.2017.00114

Okuwaki, R., Shinmura, I., Morita, S., Matsugami, A., Hayashi, F., Goto, Y., et al. (2020). Distinct Residual and Disordered Structures of Alpha-Synuclein Analyzed by Amide-Proton Exchange and NMR Signal Intensity. *Biochim. Biophys. Acta (Bba) - Proteins Proteomics* 1868 (9), 140464. doi:10.1016/j.bbapap.2020.140464

Oliveri, V. (2019). Toward the Discovery and Development of Effective Modulators of α-synuclein Amyloid Aggregation. *Eur. J. Med. Chem.* 167, 10–36. doi:10.1016/j.ejmech.2019.01.045

Ouberai, M. M., Wang, J., Swann, M. J., Galvagnion, C., Guilliams, T., Dobson, C. M., et al. (2013). α-Synuclein Senses Lipid Packing Defects and Induces Lateral Expansion of Lipids Leading to Membrane Remodeling. *J. Biol. Chem.* 288 (29), 20883–20895. doi:10.1074/jbc.M113.478297

Pasanen, P., Myllykangas, L., Siitonen, M., Raunio, A., Kaakkola, S., Lyytinen, J., et al. (2014). A Novel α-synuclein Mutation A53E Associated with Atypical Multiple System Atrophy and Parkinson's Disease-type Pathology. *Neurobiol. Aging* 35 (9), 2180.e1–2180.e5. doi:10.1016/j.neurobiolaging.2014.03.024

Paul, A., Zhang, B.-D., Mohapatra, S., Li, G., Li, Y.-M., Gazit, E., et al. (2019). Novel Mannitol-Based Small Molecules for Inhibiting Aggregation of α-Synuclein Amyloids in Parkinson's Disease. *Front. Mol. Biosci.* 6, 1–10. doi:10.3389/fmolb.2019.00016

Perni, M., Galvagnion, C., Maltsev, A., Meisl, G., Müller, M. B. D., Challa, P. K., et al. (2017). A Natural Product Inhibits the Initiation of α-synuclein Aggregation and Suppresses its Toxicity. *Proc. Natl. Acad. Sci. USA* 114 (6), E1009–E1017. doi:10.1073/pnas.1610586114

Pfrieger, F. W. (2003). Role of Cholesterol in Synapse Formation and Function. *Biochim. Biophys. Acta (Bba) - Biomembr.* 1610 (2), 271–280. doi:10.1016/S0005-2736(03)00024-5

Pineda, A., and Burré, J. (2017). Modulating Membrane Binding of α-synuclein as a Therapeutic Strategy. *Proc. Natl. Acad. Sci. USA* 114 (6), 1223–1225. doi:10.1073/pnas.1620159114

Pirc, K., and Ulrih, N. P. (2015). α-Synuclein Interactions with Phospholipid Model Membranes: Key Roles for Electrostatic Interactions and Lipid-Bilayer Structure. *Biochim. Biophys. Acta (Bba) - Biomembr.* 1848 (10), 2002–2012. doi:10.1016/j.bbamem.2015.06.021

Plotegher, N., Greggio, E., Bisaglia, M., and Bubacco, L. (2014). Biophysical Groundwork as a Hinge to Unravel the Biology of α-synuclein Aggregation and Toxicity. *Quart. Rev. Biophys.* 47 (1), 1–48. doi:10.1017/S0033583513000097

Polymeropoulos, M. H., Lavedan, C., Leroy, E., Ide, S. E., Dehejia, A., Dutra, A., et al. (1997). Mutation in the -Synuclein Gene Identified in Families with Parkinson's Disease. *Science* 276 (5321), 2045–2047. doi:10.1126/science.276.5321.2045

Post, M. R., Lieberman, O. J., and Mosharov, E. V. (2018). Can Interactions between α-Synuclein, Dopamine and Calcium Explain Selective Neurodegeneration in Parkinson's Disease? *Front. Neurosci.* 12, 161. doi:10.3389/fnins.2018.00161

Pujols, J., Peña-Díaz, S., Lázaro, D. F., Peccati, F., Pinheiro, F., González, D., et al. (2018). Small Molecule Inhibits α-synuclein Aggregation, Disrupts Amyloid Fibrils, and Prevents Degeneration of Dopaminergic Neurons. *Proc. Natl. Acad. Sci. USA* 115 (41), 10481–10486. doi:10.1073/pnas.1804198115

Ramis, R., Ortega-Castro, J., Vilanova, B., Adrover, M., and Frau, J. (2017). Copper(II) Binding Sites in N-Terminally Acetylated α-Synuclein: A Theoretical Rationalization. *J. Phys. Chem. A.* 121 (30), 5711–5719. doi:10.1021/acs.jpca.7b03165

Rcom-H'cheo-Gauthier, A., Goodwin, J., and Pountney, D. L. (2014). Interactions between Calcium and Alpha-Synuclein in Neurodegeneration. *Biomolecules* 4 (3), 795–811. doi:10.3390/biom4030795

Rekas, A., Knott, R. B., Sokolova, A., Barnham, K. J., Perez, K. A., Masters, C. L., et al. (2010). The Structure of Dopamine Induced α-synuclein Oligomers. *Eur. Biophys. J.* 39 (10), 1407–1419. doi:10.1007/s00249-010-0595-x

Ren, B., Liu, Y., Zhang, Y., Zhang, M., Sun, Y., Liang, G., et al. (2017). Tanshinones Inhibit hIAPP Aggregation, Disaggregate Preformed hIAPP Fibrils, and Protect Cultured Cells. *J. Mater. Chem. B.* 6 (1), 56–67. doi:10.1039/c7tb02538f

Robotta, M., Braun, P., Van Rooijen, B., Subramaniam, V., Huber, M., and Drescher, M. (2011). Direct Evidence of Coexisting Horseshoe and Extended helix Conformations of Membrane-Bound Alpha-Synuclein. *ChemPhysChem* 12 (2), 267–269. doi:10.1002/cphc.201000815

Robotta, M., Cattani, J., Martins, J. C., Subramaniam, V., and Drescher, M. (2017). Alpha-Synuclein Disease Mutations Are Structurally Defective and Locally Affect Membrane Binding. *J. Am. Chem. Soc.* 139 (12), 4254–4257. doi:10.1021/jacs.6b05335

Rospigliosi, C. C., McClendon, S., Schmid, A. W., Ramlall, T. F., Barré, P., Lashuel, H. A., et al. (2009). E46K Parkinson's-Linked Mutation Enhances C-Terminal-To-N-Terminal Contacts in α-Synuclein. *J. Mol. Biol.* 388 (5), 1022–1032. doi:10.1016/j.jmb.2009.03.065

Runfola, M., De Simone, A., Vendruscolo, M., Dobson, C. M., and Fusco, G. (2020). The N-Terminal Acetylation of α-Synuclein Changes the Affinity for Lipid Membranes but Not the Structural Properties of the Bound State. *Sci. Rep.* 10 (1), 1–10. doi:10.1038/s41598-019-57023-4

Ryan, T., Bamm, V. V., Stykel, M. G., Coackley, C. L., Humphries, K. M., Jamieson-Williams, R., et al. (2018). Cardiolipin Exposure on the Outer Mitochondrial Membrane Modulates α-synuclein. *Nat. Commun.* 9 (1), 1–17. doi:10.1038/s41467-018-03241-9

Schneider, J. S., Aras, R., Williams, C. K., Koprich, J. B., Brotchie, J. M., and Singh, V. (2019). GM1 Ganglioside Modifies α-Synuclein Toxicity and Is Neuroprotective in a Rat α-Synuclein Model of Parkinson's Disease. *Sci. Rep.* 9 (1), 1–12. doi:10.1038/s41598-019-42847-x

Sebastião, A. M., Colino-Oliveira, M., Assaife-Lopes, N., Dias, R. B., and Ribeiro, J. A. (2013). Lipid Rafts, Synaptic Transmission and Plasticity: Impact in Age-Related Neurodegenerative Diseases. *Neuropharmacology* 64, 97–107. doi:10.1016/j.neuropharm.2012.06.053

Serpell, L. C., Berriman, J., Jakes, R., Goedert, M., and Crowther, R. A. (2000). Fiber Diffraction of Synthetic Alpha -synuclein Filaments Shows Amyloid-like Cross-Beta Conformation. *Proc. Natl. Acad. Sci.* 97 (9), 4897–4902. doi:10.1073/pnas.97.9.4897

Sezgin, E., Levental, I., Mayor, S., and Eggeling, C. (2017). The Mystery of Membrane Organization: Composition, Regulation and Roles of Lipid Rafts. *Nat. Rev. Mol. Cel Biol.* 18 (6), 361–374. doi:10.1038/nrm.2017.16

Shaltiel-Karyo, R., Frenkel-Pinter, M., Rockenstein, E., Patrick, C., Levy-Sakin, M., Schiller, A., et al. (2013). A Blood-Brain Barrier (BBB) Disrupter Is Also a Potent α-Synuclein (α-Syn) Aggregation Inhibitor. *J. Biol. Chem.* 288 (24), 17579–17588. doi:10.1074/jbc.M112.434787

Shvadchak, V. V., Falomir-Lockhart, L. J., Yushchenko, D. A., and Jovin, T. M. (2011). Specificity and Kinetics of α-Synuclein Binding to Model Membranes Determined with Fluorescent Excited State Intramolecular Proton Transfer (ESIPT) Probe. *J. Biol. Chem.* 286 (15), 13023–13032. doi:10.1074/jbc.M110.204776

Shvadchak, V. V., Afitska, K., and Yushchenko, D. A. (2018). Inhibition of α-Synuclein Amyloid Fibril Elongation by Blocking Fibril Ends. *Angew. Chem. Int. Ed.* 57 (20), 5690–5694. doi:10.1002/anie.201801071

Stephens, A. D., Zacharopoulou, M., and Kaminski Schierle, G. S. (2019). The Cellular Environment Affects Monomeric α-Synuclein Structure. *Trends Biochem. Sci.* 44 (5), 453–466. doi:10.1016/j.tibs.2018.11.005

Sternke-Hoffmann, R., Peduzzo, A., Bolakhrif, N., Haas, R., and Buell, A. K. (2020). The Aggregation Conditions Define whether EGCG Is an Inhibitor or Enhancer of α-Synuclein Amyloid Fibril Formation. *Ijms* 21 (6), 1995. doi:10.3390/ijms21061995

Stöckl, M., Fischer, P., Wanker, E., and Herrmann, A. (2008). α-Synuclein Selectively Binds to Anionic Phospholipids Embedded in Liquid-Disordered Domains. *J. Mol. Biol.* 375 (5), 1394–1404. doi:10.1016/j.jmb.2007.11.051

Sung, Y.-H., and Eliezer, D. (2018). Structure and Dynamics of the Extended-helix State of Alpha-Synuclein: Intrinsic Lability of the Linker Region. *Protein Sci.* 27 (7), 1314–1324. doi:10.1002/pro.3426

Terakawa, M. S., Lee, Y.-H., Kinoshita, M., Lin, Y., Sugiki, T., Fukui, N., et al. (2018). Membrane-induced Initial Structure of α-synuclein Control its Amyloidogenesis on Model Membranes. *Biochim. Biophys. Acta (Bba) - Biomembr.* 1860 (3), 757–766. doi:10.1016/j.bbamem.2017.12.011

Tsigelny, I. F., Sharikov, Y., Wrasidlo, W., Gonzalez, T., Desplats, P. A., Crews, L., et al. (2012). Role of α-synuclein Penetration into the Membrane in the Mechanisms of Oligomer Pore Formation. *FEBS J.* 279 (6), 1000–1013. doi:10.1111/j.1742-4658.2012.08489.x

Tsigelny, I. F., Sharikov, Y., Kouznetsova, V. L., Greenberg, J. P., Wrasidlo, W., Overk, C., et al. (2015). Molecular Determinants of α-Synuclein Mutants' Oligomerization and Membrane Interactions. *ACS Chem. Neurosci.* 6 (3), 403–416. doi:10.1021/cn500332w

Tuttle, M. D., Comellas, G., Nieuwkoop, A. J., Covell, D. J., Berthold, D. A., Kloepper, K. D., et al. (2016). Solid-state NMR Structure of a Pathogenic Fibril of Full-Length Human α-synuclein. *Nat. Struct. Mol. Biol.* 23 (5), 409–415. doi:10.1038/nsmb.3194

Uversky, V., and Eliezer, D. (2009). Biophysics of Parkinsons Disease: Structure and Aggregation of α- Synuclein. *Cpps* 10 (5), 483–499. doi:10.2174/138920309789351921

Uversky, V. N., Li, J., and Fink, A. L. (2001). Evidence for a Partially Folded Intermediate in α-Synuclein Fibril Formation. *J. Biol. Chem.* 276 (14), 10737–10744. doi:10.1074/jbc.M010907200

Uversky, V. N. (2013). The Most Important Thing Is the Tail: Multitudinous Functionalities of Intrinsically Disordered Protein Termini. *FEBS Lett.* 587 (13), 1891–1901. doi:10.1016/j.febslet.2013.04.042

Valiente-Gabioud, A. A., Miotto, M. C., Chesta, M. E., Lombardo, V., Binolfi, A., and Fernández, C. O. (2016). Phthalocyanines as Molecular Scaffolds to Block Disease-Associated Protein Aggregation. *Acc. Chem. Res.* 49 (5), 801–808. doi:10.1021/acs.accounts.5b00507

Vasili, E., Dominguez-Meijide, A., and Outeiro, T. F. (2019). Spreading of α-Synuclein and Tau: A Systematic Comparison of the Mechanisms Involved. *Front. Mol. Neurosci.* 12, 1–23. doi:10.3389/fnmol.2019.00107

Vilar, M., Chou, H.-T., Lührs, T., Maji, S. K., Riek-Loher, D., Verel, R., et al. (2008). The Fold of -synuclein Fibrils. *Proc. Natl. Acad. Sci.* 105 (25), 8637–8642. doi:10.1073/pnas.0712179105

Weinreb, P. H., Zhen, W., Poon, A. W., Conway, K. A., and Lansbury, P. T. (1996). NACP, A Protein Implicated in Alzheimer's Disease and Learning, Is Natively Unfolded. *Biochemistry* 35 (43), 13709–13715. doi:10.1021/bi961799n

Wise-Scira, O., Aloglu, A. K., Dunn, A., Sakallioglu, I. T., and Coskuner, O. (2013). Structures and Free Energy Landscapes of the Wild-type and A30P Mutant-type α-Synuclein Proteins with Dynamics. *ACS Chem. Neurosci.* 4 (3), 486–497. doi:10.1021/cn300198q

Wu, K.-P., and Baum, J. (2010). Detection of Transient Interchain Interactions in the Intrinsically Disordered Protein α-Synuclein by NMR Paramagnetic Relaxation Enhancement. *J. Am. Chem. Soc.* 132 (16), 5546–5547. doi:10.1021/ja9105495

Xu, M.-M., Ryan, P., Rudrawar, S., Quinn, R. J., Zhang, H.-Y., and Mellick, G. D. (2020). Advances in the Development of Imaging Probes and Aggregation Inhibitors for Alpha-Synuclein. *Acta Pharmacol. Sin* 41 (4), 483–498. doi:10.1038/s41401-019-0304-y

Yu, H., Han, W., Ma, W., and Schulten, K. (2015). Transient β-hairpin Formation in α-synuclein Monomer Revealed by Coarse-Grained Molecular Dynamics Simulation. *J. Chem. Phys.* 143 (24), 243142. doi:10.1063/1.4936910

Zarranz, J. J., Alegre, J., Gómez-Esteban, J. C., Lezcano, E., Ros, R., Ampuero, I., et al. (2004). The New Mutation, E46K, of α-synuclein Causes Parkinson and Lewy Body Dementia. *Ann. Neurol.* 55 (2), 164–173. doi:10.1002/ana.10795

Zhang, Y., Hashemi, M., Lv, Z., Williams, B., Popov, K. I., Dokholyan, N. V., et al. (2018). High-speed Atomic Force Microscopy Reveals Structural Dynamics of α-synuclein Monomers and Dimers. *J. Chem. Phys.* 148 (12), 123322. doi:10.1063/1.5008874

Zigoneanu, I. G., Yang, Y. J., Krois, A. S., Haque, M. E., and Pielak, G. J. (2012). Interaction of α-synuclein with Vesicles that Mimic Mitochondrial Membranes. *Biochim. Biophys. Acta (Bba) - Biomembr.* 1818 (3), 512–519. doi:10.1016/j.bbamem.2011.11.024

Conflict of Interest: The authors declare that the research was conducted in the absence of any commercial or financial relationships that could be construed as a potential conflict of interest.

frontiers in Neuroscience

ORIGINAL RESEARCH
published: 13 July 2021
doi: 10.3389/fnins.2021.696440

A β-Wrapin Targeting the N-Terminus of α-Synuclein Monomers Reduces Fibril-Induced Aggregation in Neurons

*Éva M. Szegő[1†], Fabian Boß[2†], Daniel Komnig[2†], Charlott Gärtner[1], Lennart Höfs[1], Hamed Shaykhalishahi[3,4], Michael M. Wördehoff[3], Theodora Saridaki[2], Jörg B. Schulz[2,5], Wolfgang Hoyer[3,4] and Björn H. Falkenburger[1,2,5,6]**

[1] Department of Neurology, Technische Universität Dresden, Dresden, Germany, [2] Department of Neurology, RWTH Aachen University, Aachen, Germany, [3] Institut für Physikalische Biologie, Heinrich-Heine-Universität Düsseldorf, Düsseldorf, Germany, [4] Institute of Biological Information Processing (IBI-7), Forschungszentrum Jülich GmbH, Jülich, Germany, [5] JARA-Institute Molecular Neuroscience and Neuroimaging, Forschungszentrum Jülich GmbH and RWTH Aachen University, Aachen, Germany, [6] Deutsches Zentrum für Neurodegenerative Erkrankungen, Dresden, Germany

OPEN ACCESS

Edited by:
Cláudio M. Gomes, University of Lisbon, Portugal

Reviewed by:
Andreas Martin Grabrucker, University of Limerick, Ireland
Nelson Ferreira, Aarhus University, Denmark

***Correspondence:**
Björn H. Falkenburger
bfalken@ukdd.de

† These authors have contributed equally to this work

Specialty section:
This article was submitted to Neurodegeneration, a section of the journal Frontiers in Neuroscience

Received: *16 April 2021*
Accepted: *28 May 2021*
Published: *13 July 2021*

Citation:
Szegő ÉM, Boß F, Komnig D, Gärtner C, Höfs L, Shaykhalishahi H, Wördehoff MM, Saridaki T, Schulz JB, Hoyer W and Falkenburger BH (2021) A β-Wrapin Targeting the N-Terminus of α-Synuclein Monomers Reduces Fibril-Induced Aggregation in Neurons. Front. Neurosci. 15:696440. doi: 10.3389/fnins.2021.696440

Reducing α-synuclein pathology constitutes a plausible strategy against Parkinson's disease. As we recently demonstrated, the β-wrapin protein AS69 binds an N-terminal region in monomeric α-synuclein, interferes with fibril nucleation, and reduces α-synuclein aggregation *in vitro* and in a fruit fly model of α-synuclein toxicity. The aim of this study was to investigate whether AS69 also reduces α-synuclein pathology in mammalian neurons. To induce α-synuclein pathology, primary mouse neurons were exposed to pre-formed fibrils (PFF) of human α-synuclein. PFF were also injected into the striatum of A30P-α-synuclein transgenic mice. The extent of α-synuclein pathology was determined by phospho-α-synuclein staining and by Triton X-100 solubility. The degeneration of neuronal somata, dendrites, and axon terminals was determined by immunohistochemistry. AS69 and PFF were taken up by primary neurons. AS69 did not alter PFF uptake, but AS69 did reduce PFF-induced α-synuclein pathology. PFF injection into mouse striatum led to α-synuclein pathology and dystrophic neurites. Co-injection of AS69 abrogated PFF-induced pathology. AS69 also reduced the PFF-induced degeneration of dopaminergic axon terminals in the striatum and the degeneration of dopaminergic dendrites in the substantia nigra pars reticulata. AS69 reduced the activation of astroglia but not microglia in response to PFF injection. Collectively, AS69 reduced PFF-induced α-synuclein pathology and the associated neurodegeneration in primary neurons and in mouse brain. Our data therefore suggest that small proteins binding the N-terminus of α-synuclein monomers are promising strategies to modify disease progression in Parkinson's disease.

Keywords: α-synuclein, pre-formed fibrils, protein aggregation, molecular chaperones, nanobodies

Abbreviations: aSyn, alpha-synuclein; BSA, bovine serum albumin; DN, dystrophic neurite; GFAP, glial fibrillary acidic protein; Iba1, ionized calcium-binding adapter molecule 1; LB, Lewy body; LN, Lewy neurite; PBS, phosphate buffered saline solution; PD, Parkinson's disease; PFF, pre-formed fibrils; SA, somatic accumulation; TH, tyrosine hydroxylase; WT, wild-type DIV, day in vitro; GFAP,glial fibrillary acidic protein; Iba1, ionized calciumbinding adapter molecule 1; SNr, substantia nigra pars reticulata.

BACKGROUND

In Parkinson's disease (PD) and other synucleinopathies, aggregation and accumulation of α-synuclein (aSyn) is considered a central event. In PD and dementia with Lewy bodies (LBs), the major hallmarks of aSyn pathology are large inclusions in the neuronal soma (LB) and dystrophic, aSyn-containing neurites [Lewy neurites (LN)]. Reducing the extent of aSyn pathology thus represents an attractive neuroprotective strategy against synucleinopathies (Obeso et al., 2017).

Molecular chaperones can prevent protein aggregation (Muchowski and Wacker, 2005). Naturally occurring chaperones interact with aSyn *via* weak and transient interaction (Jia et al., 2019). The engineered β-wrapin AS69, in contrast, binds monomeric aSyn with high effectivity and high specificity (Mirecka et al., 2014). AS69 wraps around a sequence region of monomeric aSyn comprising residues 37–54 and stabilizes a β-hairpin conformation (Mirecka et al., 2014). AS69 therefore represents a new paradigm in amyloid inhibition. The aSyn N-terminal region is critical for aSyn aggregation (Mirecka et al., 2014; Shaykhalishahi et al., 2015; Doherty et al., 2020; Khammari et al., 2020). On a biophysical level, AS69 binding interferes with primary and secondary nucleation processes and inhibits the proliferation of aSyn fibrils (Agerschou et al., 2019). In HEK293T cells, AS69 reduces oligomerization and aggregation of aSyn; in a fruit fly model of A53T aSyn toxicity, AS69 reduces aggregation of aSyn in neurons and rescues the locomotor deficit resulting from neuronal aSyn expression (Agerschou et al., 2019).

So far, AS69 has not been studied in mammalian neurons. We therefore tested the effect of AS69 on aSyn pathology induced by pre-formed fibrils (PFF) in primary cortical neurons using a standard protocol (Volpicelli-Daley et al., 2014). In addition, we tested AS69 in the more complex biological environment of a mammalian brain using PFF injection in transgenic mice expressing human A30P-aSyn.

METHODS

The sources of chemicals are listed in **Table 1**. The source and concentration of antibodies are listed in **Table 2**. **Supplementary Table 1** lists the composition of buffers, equipment, and software.

Recombinant Proteins and Atomic Force Microscopy

Human wild-type (WT) aSyn and AS69 were produced in bacteria and purified as previously described (Gauhar et al., 2014). PFF were generated using a standard protocol (Volpicelli-Daley et al., 2014) as previously described (Agerschou et al., 2019). Fibril formation was confirmed by Thioflavin T fluorescence and atomic force microscopy (AFM) (Agerschou et al., 2019).

Fibrils were analyzed by AFM. One microliter of sonicated PFF solution (5 mg/ml α-synuclein) was diluted with phosphate buffered saline solution (PBS) to 50 μl and adsorbed for 30 min onto a freshly cleaved mica surface followed by washing with milliQ water and drying with a gentle stream of N2 gas. Imaging was performed under air-dried conditions in intermittent contact mode in a JPK Nano Wizard II atomic force microscope using a silicon cantilever with a silicon tip (OMCL-AC160TS, Olympus) with a typical tip radius of 9 ± 2 nm, a force constant of 42 N/m, and a line rate of 0.5 Hz. The images were processed using JPK Data Processing software. Fibril lengths were determined using ImageJ software (Schindelin et al., 2012; Schneider et al., 2012) and the Ridge Detection plugin v1.4.0 (Steger, 1998). **Supplementary Figure 1A** shows a representative AFM image of our sonicated PFF, and **Supplementary Figure 1B** shows the size distribution of the PFF fragments.

Animals and Surgery

C57BL6/J-Thy1-A30P-α-synuclein mice (Kahle et al., 2000) were bred as homozygous, housed, and handled in a pathogen-free animal facility at 20–24°C with a 12-h light/dark cycle and food and water *ad libitum*, in accordance with guidelines of the Federation for European Laboratory Animal Science Associations (FELASA). Breeding and surgery were approved by the local authorities (Landesamt für Natur, Umwelt und Verbraucherschutz Nordrhein-Westfalen, license numbers 84.02.04.2015.A027 and 84-02.04.2014.A321).

Mice (47–57 weeks old; males:females = 2:3 in PBS only, 2:4 in PFF only, 2:4 in PFF + ASS) were randomly assigned to one of the three experimental groups. The injected solution was prepared from frozen aliquots and sonicated on the day of the experiment. The final solutions contained (1) PBS only, (2) 1.4 mg/ml aSyn equivalent PFF, and (3) 1.4 mg/ml aSyn equivalent PFF + 98 nm. AS69. (98 μM AS69 is roughly equimolar to 1.4 mg/ml aSyn.).

Stereotaxic injection into the right striatum (AP: 1; ML: 1.5 relative to Bregma; DV: 1.55 from dura) and tissue preparations were performed as described earlier (Krenz et al., 2009), under ketamine (100 mg/kg)/xylazine (10 mg/kg) anesthesia (Guillen, 2012); 2.5 μl solution was injected with a flow rate of 0.2 μl/min. Surgeries and animal perfusions were performed between 8:00

TABLE 1 | Source of chemicals.

Reagent	Source	ID
Thioflavin T	Sigma-Aldrich	Cat# T3516
Poly-L-ornithine hydrobromide (0.1 mg/ml)	Sigma-Aldrich	Cat# 3655
LDH Cytotoxity Detection Kit	Roche	Cat# 11644793001
Bovine Serum Albumin (BSA)	Sigma-Aldrich	Cat# A2153
6× Loading Dye	Thermo Fisher	Cat# R0611
SuperSignal™ West Femto Maximum Sensitivity Substrate	Thermo Fisher	Cat# 34096
Avidin-Biotin Complex from VECTASTAIN® Elite ABC-HRP Kit (1:200)	Vector Laboratories	Cat# PK6100
SIGMAFAST™ DAB with Metal Enhancer	Sigma-Aldrich	Cat# D0426
Entellan	Merck Millipore	Cat# 1079600500
Fluoromount-G	Southern Biotech	Cat# 0100-01
Hoechst 33342	Thermo Fisher	Cat# H3570
Novex™ 4-20% Tris-Glycin Plus Gel	Thermo Fisher	Cat# NP0343

TABLE 2 | Source and concentration of antibodies.

Antibody	Source	ID	Dilution
Mouse anti-α-Synuclein	BD Transduction Laboratories	Cat# 610787	1:2000
Goat anti-affibody	Abcam	Cat# ab50345	1:500
Rabbit anti-tubulin	Abcam	Cat# ab6046	1:2000
Rabbit anti-phospho-α-synuclein	Abcam	Cat# ab51253	1:500
Mouse anti-phospho-α-synuclein	Wako	Cat# 015-25191	1:1000
Rat monoclonal anti-human-α-synuclein (15G7)	Enzo Life Sciences	Cat# ALX-804-258-L001	1:500
Rabbit anti-microtubule-associated protein 2	Merck Millipore	Cat# AB5622	1:1000
Rabbit anti-TH	Merck Millipore	Cat# AB152	1:1000
Chicken anti-GFAP	Abcam	Cat# ab4674	1:2000
Rabbit anti-Iba1	Wako	Cat# 019-19741	1:1000
Rabbit monoclonal rodent specific anti-α-synuclein (D37A6)	Cell Signaling	Cat# mAb4179	1:1000
Mouse monoclonal anti-aggregated-α-synuclein (5G4)	Merck Millipore	Cat# MABN389	1:1000
HRP-conjugated donkey anti-goat IgG	Jackson ImmunoResearch	Cat# 705-035-147	1:5000
HRP-conjugated donkey anti-mouse IgG	Jackson ImmunoResearch	Cat# 715-035-150	1:5000
HRP-conjugated donkey anti-rabbit IgG	Jackson ImmunoResearch	Cat# 711-035-152	1:5000
Biotinylated goat anti-rabbit IgG	Vector Laboratories	Cat# BA-1000	1:200
Alexa 405-conjugated donkey anti-rabbit	Jackson ImmunoResearch	Cat# 711-475-152	1:1000
Alexa 488-conjugated donkey anti-rat	Invitrogen	Cat# A21208	1:1000
Alexa 555-conjugated donkey anti-goat	Invitrogen	Cat# A21432	1:1000
Alexa 555-conjugated donkey anti-rabbit	Invitrogen	Cat# A31572	1:1000
Alexa 647-conjugated donkey anti-mouse	Invitrogen	Cat# A31571	1:1000
Alexa 488-conjugated goat anti-rabbit	Invitrogen	Cat# A-11008	1:1000
Alexa 488-conjugated goat anti-chicken	Invitrogen	Cat# A-11039	1:1000

and 16:00. After surgery, animals were kept in the original cage (3–5 mice per cage) and monitored every day for 10 days. Weight, wound healing, fell condition, and general behavior were scored according to the local Animal Welfare Authorities and the FELASA recommendations (Guillen, 2012). Mice were sacrificed 90 days later by an overdose of ketamine. Brains were fixed at 4°C (4% paraformaldehyde, 24 h) and cryoprotected (30% sucrose). Free-floating, 30-μm serial coronal sections were cut in a cryostat and were stored at −20°C until use. Nineteen mice started the experiment. Two animals died during the course of the experiment; the brains of these animals were not used for analysis. No power analysis was conducted to determine group size.

Primary Neuronal Cultures

Primary neuronal cultures were prepared from 1- to 3-day-old C57BL6/J mouse pups (mixed sex, 4–6 pups/preparation). Dissociated neurons were plated onto poly-L-ornithine-coated glass coverslip (100,000 cells per well in 24-well dishes), and maintained in Neurobasal A medium [2% B27, 0.5 mM glutamax, antibiotics as previously (Szegő et al., 2019)]. One-third of the medium was changed on every third day, and from the second change on, no antibiotics were added. For image analysis, bovine serum albumin (BSA) (1 μg/ml, protein control), 50 nM AS69, PFF corresponding to 50 nM aSyn monomer, or the same concentration of PFF + 50 nM AS69 was added to neurons on day *in vitro* (DIV) 12. For detergent solubility fractionation, 150 nM AS69 and 150 nM aSyn were used. Neurons were analyzed on DIV 13 (24 h after adding PFF), DIV 15 (72 h after PFF), or DIV 22 (10 days after PFF). Experiments were repeated with three to four independent preparations (n = 3–4).

Detergent-Solubility Fractionation

For detection of Triton X-100-insoluble proteins, neuronal cultures were lysed in buffer containing 1% Triton X-100 as previously described (Szegő et al., 2019). After centrifugation (14,000 × g, 30 min, 4°C), the supernatant was used as the Triton X-100 soluble fraction. The pellet (Triton X-100-insoluble fraction) was washed in ice-cold PBS, centrifuged, and re-dissolved with sonication (10 s) in 50 μl of buffer containing 2% SDS. Ten micrograms of the Triton X-100 soluble fraction or 10 μl from the Triton X-100-insoluble fraction was loaded onto a 4%–20% Tris/glycine SDS gel for Western blot analysis. aSyn, AS69, and tubulin were detected using an LAS-3000 Luminescent Image Analyzer with CCD camera. In the detergent-insoluble fraction, aSyn was not detected in the control conditions, "BSA only" and "AS69 only" (**Figure 2D**). The ratio of aSyn/tubulin is therefore presented as percent of the PFF-treated values (**Figure 2E**). In the detergent-soluble fraction (**Supplementary Figure 2A**), the ratio of aSyn/tubulin is reported as percent of the control condition BSA (**Supplementary Figures 2B,C**).

Immunostaining–Brain Sections

To visualize the α-synuclein pathology, every sixth section of the striatum was used. After blocking endogenous peroxidase activity (0.3% H_2O_2), sections were first blocked (3% normal goat serum, 60 min), then incubated with a primary anti-phospho-aSyn antibody (overnight, 4°C, in blocking solution), followed by biotinylated secondary antibody and Avidin-Biotin Complex (30 min, 21°C each). Antibody labeling was visualized by 3,3′ diaminobenzidine (4 mg/ml). After mounting and dehydration in xylene, sections were coverslipped with Entellan.

To determine density of striatal dopaminergic axon terminals, three sections [0.26–0.98 mm to Bregma (Paxinos and Franklin, 2001)] per animal were stained for tyrosine hydroxylase (TH) as previously described (Komnig et al., 2016). In brief, after blocking, sections were incubated with TH antibody (overnight, 4°C) followed by secondary antibody (Alexa 488 conjugated goat anti-rabbit, 60 min). Sections were mounted with Fluoromount-G.

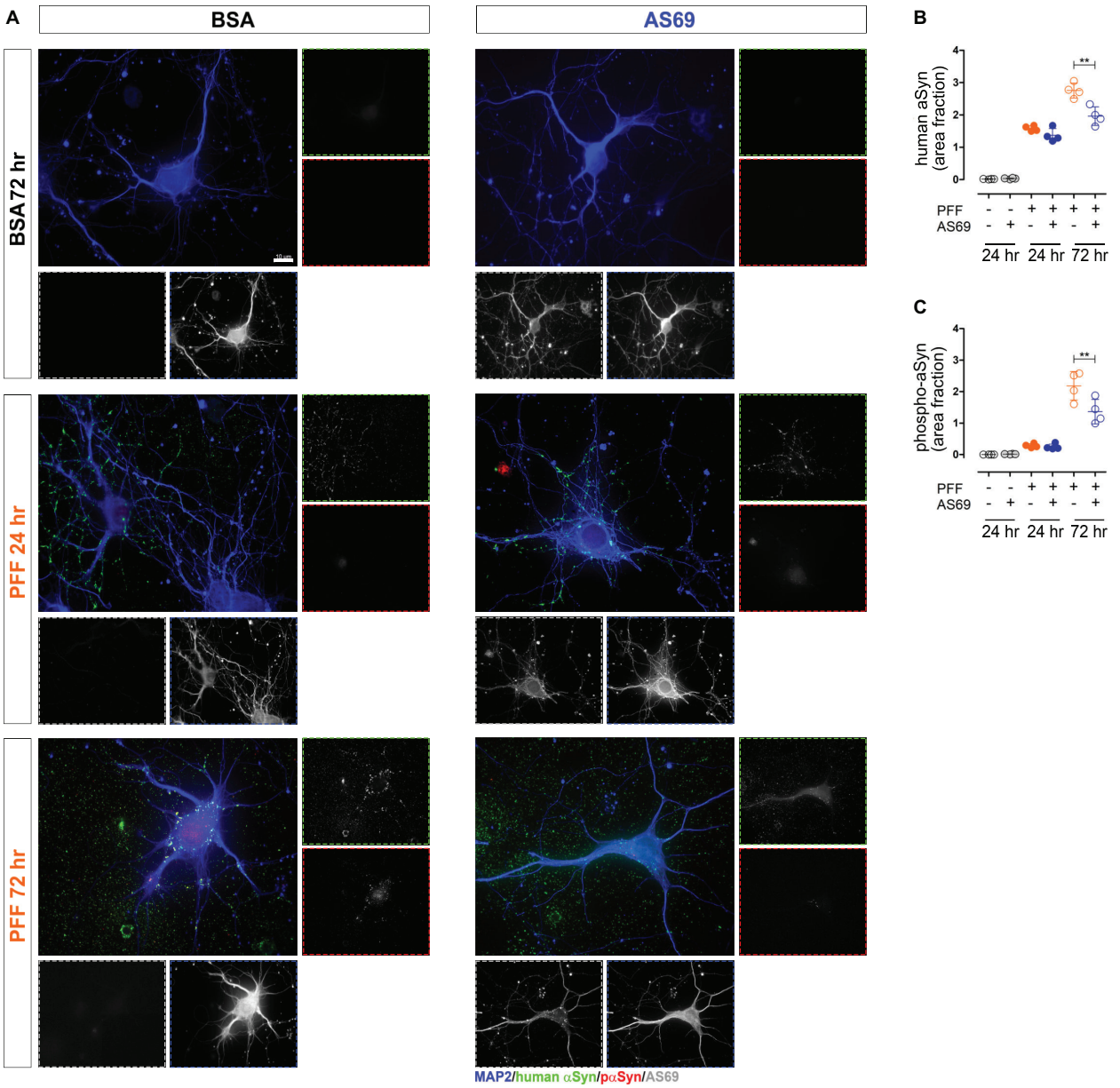

FIGURE 1 | AS69 does not affect PFF uptake, but reduces early pathology. **(A)** Representative images of primary neurons acquired 24 or 72 h after treatment with either PFF or BSA, and in addition either AS69 or BSA. Neurons were stained for AS69 (inset with white border, not included in merged image), phospho-aSyn (red border inset and red channel in merged image), human aSyn (green border inset and green channel), and neuronal markers [microtubule-associated protein 2 (MAP2) + βIII-tubulin, blue border inset and blue channel]. Scale bar: 10 μm. **(B)** Quantification of the area positive for human aSyn within the area delineated by the neuronal markers in neurons as depicted in panel **(A)** (n = 4 independent preparations, ≥10 neurons per experimental group, p = 0.007 for PFF + BSA vs. PFF + AS69 at 72 h, two-way ANOVA followed by Bonferroni *post hoc* test). **(C)** Quantification of phospho-aSyn within the same neurons as in panel **(B)** (p = 0.009 for PFF + BSA vs. PFF + AS69 at 72 h, two-way ANOVA followed by Bonferroni *post hoc* test). All markers represent the mean of all technical replicates of one individual preparation; lines represent mean ± SD of independent preparations. $^{**}p < 0.01$.

To determine the density of dopaminergic apical dendrites in the substantia nigra pars reticulata (SNr), every third section spanning the substantia nigra was stained for TH with DAB as described for the striatal sections.

To determine neuroinflammation, every sixth striatal sections was incubated with the astroglia marker glial fibrillary acidic protein (GFAP) and the microglia marker ionized calcium-binding adapter molecule 1 (Iba1) (overnight, 4°C). After incubation with fluorescently labeled secondary antibodies (Alexa 488-conjugated goat anti-chicken and Alexa 555-conjugated donkey anti-rabbit, 120 min), sections were counterstained with Hoechst and mounted with Fluoromount-G.

Immunostaining–Primary Neurons

To determine aSyn uptake and pathology in primary neurons, cells were fixed 24 or 72 h after treatment and permeabilized (0.2% Triton X-100), unspecific sites were blocked (2% BSA), and cells were incubated in the presence of the following primary antibodies (4°C, overnight): phospho-aSyn, human-aSyn, affibody, and MAP2.

To address Triton X-100-insoluble aSyn pathology 10 days after seeding, neurons were fixed for 10 min (4% paraformaldehyde, 4% sucrose, and 1% Triton X-100), and washed with 0.1% Triton X-100. Neurons were stained with anti-MAP2, an antibody against aggregated aSyn, and an antibody recognizing mouse and rat aSyn, but not human aSyn (Villar-Piqué et al., 2016). After incubation with fluorescently labeled secondary antibodies, coverslips were mounted with Fluoromount G. To measure toxicity of compounds, neurons were fixed 10 days after treatment and stained for MAP2.

Image Analyses–Brain Sections

Image analyses were carried out blinded for the experimental group by assigning random numbers to slides. aSyn pathology in the striatum was quantified in every third section spanning the entire striatum using stereological techniques and the optical fractionator method. In this method, phospho-aSyn positive somatic inclusions and dystrophic neurites (DNs) were counted manually (63× oil objective, Axio Imager 2 microscope, Carl Zeiss Vision) in counting frames presented by the software (StereoInvestigator, MicroBrightfield Bioscience, grid size: 200 μm × 200 μm, counting frame: 100 μm × 100 μm).

To quantify the density of striatal dopaminergic axon terminals ("fibers"), z-stack images were acquired (five planes, 1 μm apart, 60× oil objective, IX81S1F microscope, Olympus). TH-positive fibers were delineated from the maximal intensity projection (ImageJ, 1.47v) and expressed as percent area. Three sections per animal and five images per section were analyzed in a hierarchically nested design. A generalized linear mixed model (glm) was applied as noted in the *Statistical analysis and data visualization* section as previously described (Szegő et al., 2013).

For quantification of the density of TH-positive apical dendrites in the SNr, bright-field images were acquired (DAB staining) using a 20× objective (NA 0.8) with an Axio Imager 2 microscope (Zeiss). Area fraction of dendrites in the entire SNr was determined from a minimum of three sections per animal, and the ratio of ipsilateral and contralateral densities was analyzed.

For quantification of gliosis, fluorescent images were acquired (20× objective, Axio Imager 2 microscope, Zeiss). The area fraction of GFAP or Iba1 staining was determined from two sections per animal and from 10 images per section (ImageJ). Results were analyzed as described for TH-positive fibers. Fluorescent intensity of the GFAP signal was measured within the astroglia as follows using ImageJ. First, the image was duplicated, and one image was despeckled. The background was subtracted from the duplicate and then it was binarized and noise removal (despeckling) was applied. A mask was created from the binarized image. The mask was restored in the first image, and signal integrated density was measured within the mask. For quantification of microglia morphology, skeleton analysis was used (Young and Morrison, 2018). Briefly, individual glia cells were cropped from the binarized images (see above), and after noise removal (despeckling), using the close function (connecting two pixels that are separated by up to two pixels) and removing outliers (pixel radius of 2, threshold of 50), cells were skeletonized. Total branch length per cell was calculated by summing up the length of branches over a cutoff value of 2.

Image Analyses–Primary Neurons

To measure aSyn uptake and pathology in neurons, a minimum of 10 neurons were imaged randomly for each experiment and experimental group using a 100× oil objective on a Zeiss Axio Imager 2 microscope and constant exposure times for each staining across all experimental groups. To outline neurons, a mask was created based on the MAP2 channel. In this mask, the area fraction of staining for (a) phospho-aSyn, (b) human aSyn, (c) mouse aSyn, or (d) aggregated aSyn was determined, using ImageJ. Images are pseudo colored for better visualization. For phospho-aSyn and human aSyn, values are reported as "raw" area fraction (**Figures 1B,C**). For the staining after incubation with 1% Triton X-100 (**Figures 2B,C**), area fractions are normalized to values of only PFF-treated neurons.

Neuronal integrity was quantified by measuring the area of MAP2-positive signal from the primary cultures. For that, images were acquired with a 20× objective, background was subtracted, and images were despeckled and binarized by thresholding. Outliers (pixel radius of 2, threshold of 50) were removed from the binary image. The area fraction was determined from the binary image.

LDH Assay

To determine the toxic effects of aSyn PFF on primary neuronal cultures, the concentration of extracellular LDH was measured in the medium 24 h after the last medium change using the Cytotoxicity Detection Kit according to the manufacturer's protocol. Briefly, for each independent preparation, three to four technical replicates were measured and the results were averaged. Absorbances were measured at 492 nm; reference wavelength was 620 nm. Background (medium) absorbance was subtracted from all values, and values were normalized to control cells (non-treated) and to maximal lysed cells (treated with 2% Triton X-100), according to the protocol.

Statistical Analysis and Data Visualization

"*n*" was set to the number of individual preparations for cell culture experiments or to the number of animals for the animal experiments. Sample sizes are based on previous experience and not on a calculation performed prior to the experiment. Data are presented as markers for each experiment/animal and summarized as mean ± standard deviation of these markers. Data normality was tested by the Shapiro–Wilk test (R). No test

for outliers was performed and no data points were removed. To compare experimental groups, we used *t*-test, one-way or two-way ANOVA in GraphPad Prism 5 (Version 5.01), or a linear mixed effect model that allows both fixed and random effects (animal and image in the hierarchically nested design) as previously described (Szegő et al., 2013) in R (version 2.8.0).

$p < 0.05$ was considered statistically significant. *p*-values are depicted on the graphs as $^{*}p < 0.05$, $^{**}p < 0.01$, and $^{***}p < 0.001$, and exact *p*-values and r^2 values are noted in the figure legends.

RESULTS

AS69 Decreases Intracellular aSyn Pathology in Primary Neurons

AS69 is a small (15 kDa) protein that interferes with aSyn aggregation in a substoichiometric way (Mirecka et al., 2014; Agerschou et al., 2019). Its mechanism includes the inhibition of secondary nucleation, which is a critical part of the prion-like behavior of aSyn (Törnquist et al., 2018). Here, we modeled secondary nucleation in primary neurons by applying PFF prepared from human WT aSyn. In neurons exposed to PFF, human aSyn staining was detected intracellularly 24 h after adding PFF (**Figures 1A,B**), confirming that primary neurons take up PFF–as demonstrated previously by others (Volpicelli-Daley et al., 2014). The extent of early PFF-induced aSyn pathology was determined by staining for phospho-aSyn 24 and 72 h after seeding (**Figures 1A,C**). Phosphorylation of aSyn is widely used to quantify seeded aSyn pathology (Mahul-Mellier et al., 2020; Weston et al., 2021).

We demonstrated previously that AS69 does not dissociate aSyn fibrils (Gauhar et al., 2014; Mirecka et al., 2014; Agerschou et al., 2019) and therefore added AS69 together with the PFF; BSA was used as negative control. In neurons incubated with AS69 but not PFF, we observed intracellular AS69 staining (**Figure 1A**, BSA + AS69 group), confirming that neurons can take up AS69 independently of PFF. AS69 did not alter the amount of intracellular human aSyn at 24 h (**Figure 1B**), indicating that AS69 does not affect aSyn uptake–in agreement with our previous finding that AS69 does not directly affect aSyn fibrils.

When neurons were exposed to PFF with AS69, the extent of phospho-aSyn pathology after 72 h was reduced by 37% compared to PFF alone (**Figure 1C**), consistent with our previous finding that AS69 reduces secondary nucleation *in vitro* (Agerschou et al., 2019). The area positive for human aSyn at 72 h was also reduced by 29% by AS69 (**Figure 1B**).

In order to investigate the effect of AS69 on PFF-induced aSyn pathology over a longer time period, we measured the fraction of detergent-insoluble aSyn 10 days after PFF seeding, as described earlier by others (Volpicelli-Daley et al., 2014). Detergent-insoluble aSyn is considered a pathological form (Klucken et al., 2006). Thus, PFF-treated neurons were incubated with 1% Triton X-100 after fixation to remove soluble aSyn. Neurons were then stained for endogenous mouse aSyn and aggregated aSyn (**Figure 2A**). We observed aSyn-positive puncta (arrowheads), bigger, roundish aggregates (open arrowheads), and longer aggregates (arrows). Quantification of Triton X-100-insoluble mouse aSyn (green in **Figure 2A**) and aggregated aSyn (red in **Figure 2A**) showed that AS69 treatment reduced the amount of aSyn aggregates after PFF seeding by 65% and 67% (**Figures 2B,C**).

In addition, we performed detergent solubility fractionation of neuronal protein lysates obtained 10 days after adding PFF. Primary neurons exposed to PFF showed a strong accumulation of aSyn in the detergent-insoluble fraction (**Figure 2D**). AS69 reduced the amount of aSyn in the detergent-insoluble fraction by 63% (**Figure 2E**). The amount of aSyn in the soluble fraction was not altered (**Supplementary Figure 2**).

AS69 Decreases aSyn-Induced Degeneration in Primary Neurons

In order to determine the functional relevance of the AS69 effects in primary neurons, we quantified the area covered by the MAP2-positive neuropil (**Figures 3A,B**) and measured cell death using the LDH assay (**Figure 3C**). aSyn monomers slightly decreased neuronal integrity, but to a much lesser extent than observed for PFF. PFF decreased the extent of neuronal processes substantially (**Figures 3A,B**) and induced cell death (**Figure 3C**). AS69 significantly reduced the extent of PFF-induced neuronal damage whereas BSA did not (**Figures 3B,C**).

AS69 Reduces PFF-Induced α-Synuclein Pathology *in vivo*

Since AS69 reduced aSyn pathology in primary neurons, we next asked whether AS69 can also reduce PFF-induced aSyn pathology in mice. PFF were injected into the striatum of 47- to 57-week-old mice with neuronal expression of human A30P-aSyn. We used aSyn transgenic mice because the higher concentration of aSyn neurons in these mice facilitates aSyn aggregation, and because the human isoform expressed from the transgene may circumvent the species barrier between PFF prepared from human aSyn and the endogenous mouse aSyn observed in some studies (Luk et al., 2016). A30P-aSyn transgenic mice have been used for PFF-based seeding less frequently than transgenic mice with other aSyn variants. We used this line because we have worked with it extensively in the past (Rathke-Hartlieb et al., 2001; Krenz et al., 2009; Szegő et al., 2012). Mouse brains were analyzed 90 days after the injection (**Figure 4A**). To reveal PFF-induced striatal aSyn pathology, we visualized phospho-aSyn positive structures (**Figure 4B**) and discriminated two phenotypes: (i) somatic accumulations of phospho-aSyn ("SA," solid arrows in **Figure 4B**, 100× images) and (ii) dystrophic, phospho-aSyn positive neurites ["DN," open arrows in **Figure 4B** 100× images]. These changes are reminiscent of the somatic LB and LN in human brain.

Even in vehicle-injected mice, we saw a relevant number of SA (**Figures 4B,C**) and DN (**Figures 4B,D**), as demonstrated previously for A30P-aSyn mice (Schell et al., 2009; Fagerqvist et al., 2013). The injection of PFF induced the formation of additional SA and DN; the number of SA and DN was significantly higher in the injected hemisphere than in the non-injected hemisphere (**Supplementary Figures 3A,B**). To account

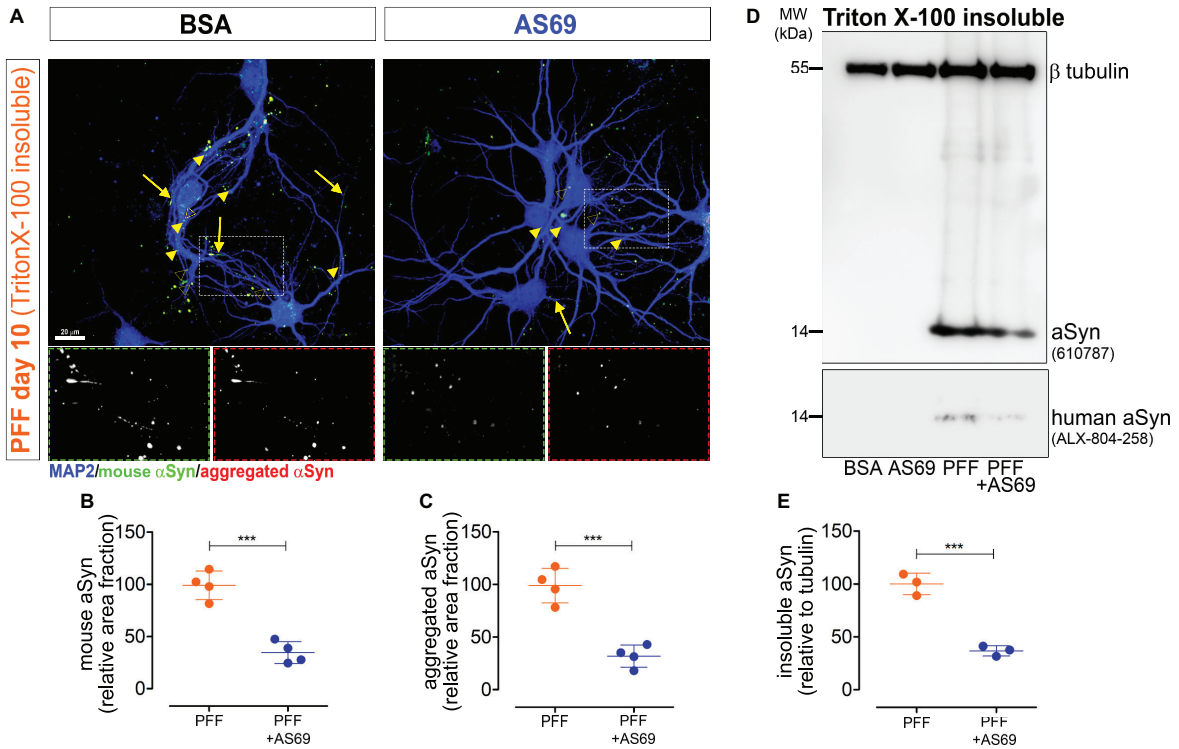

FIGURE 2 | AS69 inhibits PFF-induced aggregation of endogenous aSyn monomers in primary neurons. **(A)** Representative images of primary neurons acquired 10 days after seeding with PFF + BSA or PFF + AS69. Neurons were incubated with 1% Triton X-100 before staining to remove Triton X-100 soluble aSyn and stain only Triton X-100-insoluble aSyn. Channels: mouse aSyn (green), aggregated aSyn (red), and neuronal markers (blue). Arrowheads: dot-like aSyn inclusions; open arrowheads: bigger, round inclusions; arrow: fibrillary inclusions. Scale bar: 20 μm. **(B)** Quantification of endogenous mouse aSyn in primary neurons treated as in panel **(A)**, normalized to the "PFF only" condition (n = 4 independent preparations, ≥10 neurons per experimental group, p = 0.0003, t-test). **(C)** Quantification of aggregated aSyn staining in the same neurons as in panel **(A)**, normalized to the "PFF only" condition (p = 0.0004, t-test). **(D)** Immunoblot of the Triton X-100-insoluble fraction of primary neuron lysates obtained 10 days after PFF treatment. Blots were incubated with an antibody detecting both mouse and human aSyn (BD 610787) and with an antibody against βIII-tubulin as loading control. The immunoblot of the Triton X-100 soluble fraction of the same lysate and its quantification are in **Supplementary Figure 2**. **(E)** Quantification of the 14 kDa band of n = 3 independent blots as in panel **(D)**, showing intensity of the aSyn band relative to the βIII-tubulin band with the "PFF-only" condition set to 100% (p = 0.0006, t-test). All markers represent the mean of all technical replicates of one individual preparation; lines represent mean ± SD of independent preparations. ***$p < 0.001$.

for variability between animals and compare between treatment groups, baseline was subsequently defined as the non-injected hemisphere of the same animal and numbers normalized to this baseline. We observed a significant difference between PFF-injected animals and PBS-injected controls for the number of DN in the striatum (**Figure 4D**). The difference was not statistically significant for SA (**Figure 4C**).

Co-injection of AS69 decreased PFF-induced formation of DN by 49% (**Figure 4D**, values for individual hemispheres are in **Supplementary Figure 3**). These findings are consistent with our results in cultured neurons (**Figures 1–3**).

AS69 Reduces Degeneration of Dopaminergic Axon Terminals and Dendrites

A30P-aSyn transgenic mice do not show spontaneous degeneration of dopaminergic neurons in the substantia nigra or degeneration of their axon terminals in the striatum (Rathke-Hartlieb et al., 2001). Similarly, injection of PBS did not reduce the density of striatal dopaminergic axon terminals (**Figures 5A,B**), or the density of dopaminergic apical dendrites that extend from the SNc into the SNr (**Figures 5C,D**). Injection of PFF, in contrast, reduced the density of striatal dopaminergic axon terminals by 22% (**Figures 5A,B**) and the density of dopaminergic dendrites in the SNr by 28% (**Figures 5C,D**). This is consistent with previous findings in mice transgenic for A53T aSyn (Luk et al., 2012b).

Co-injection of AS69 abrogated the PFF-induced degeneration of dopaminergic axon terminals: The relative density was not significantly different from PBS-injected mice, and it was significantly higher than in PFF-injected animals (54% rescue; **Figures 5A,B**). Similarly, co-injection of AS69 abrogated the PFF-induced loss of dopaminergic dendrites in the SNr (51% rescue; **Figures 5C,D**). Across treatment groups, the density of dopaminergic dendrites in the SNr correlated strongly with the density of dopaminergic axon terminals in the striatum (**Figure 5E**; r^2 = 0.6843; p = 0.00067), indicating that aSyn pathology affects the entire neuron.

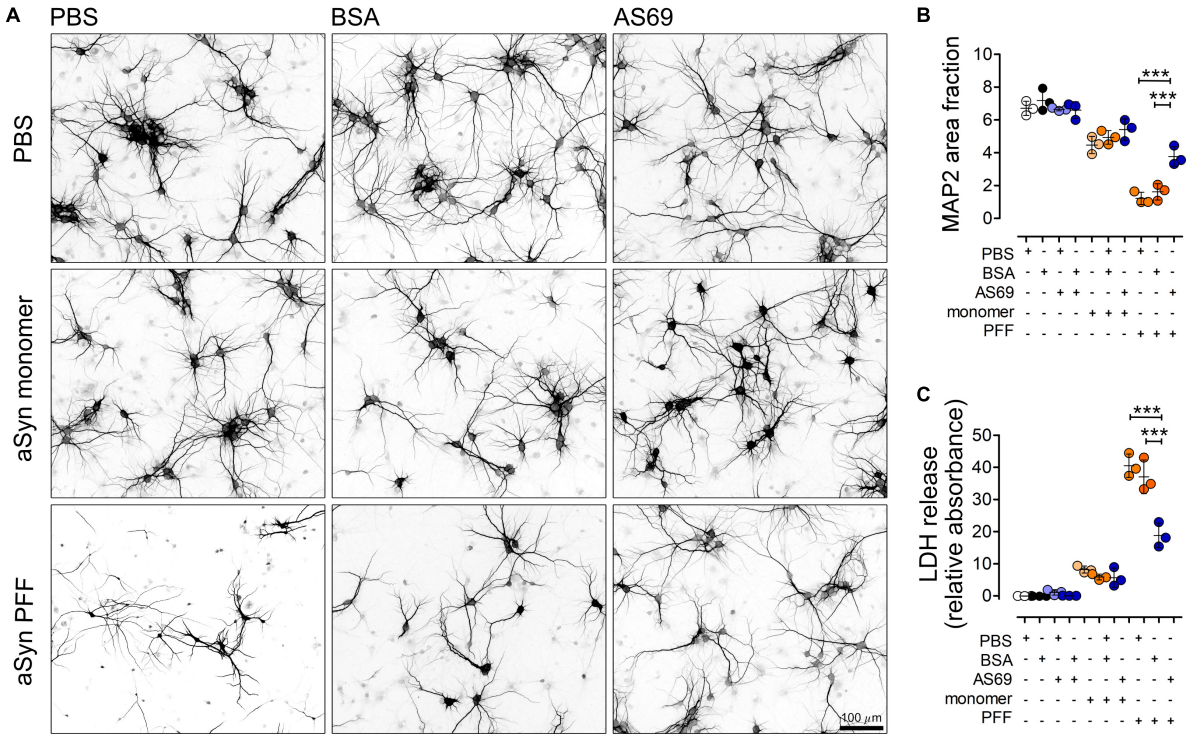

FIGURE 3 | AS69 decreases aSyn-induced degeneration in primary neurons. **(A)** Representative images of primary neurons stained for MAP2 10 days after treatments as indicated. Scale bar: 100 µm. **(B)** Quantification of the area positive for MAP2 in neurons as depicted in panel **(A)** (n = 3 independent preparations, ≥10 image fields per experiment/group). Two-way ANOVA showed positive interaction (p = 0.004) (p-values of Bonferroni *post hoc* tests depicted). **(C)** Quantification of LDH release in primary neuronal cultures with groups as in panel **(A)**. Two-way ANOVA showed positive interaction (p = 0.004) (p-values of Bonferroni *post hoc* tests depicted). All markers represent the mean of all technical replicates of one individual preparation; lines represent mean ± SD of n = 3 independent preparations. ***$p < 0.001$.

Although it is widely accepted that aSyn pathology is a major hallmark of PD and a driver of neurodegeneration, it is still a matter of debate which type of aSyn inclusions correlates best with neurotoxicity and functional impairment (Schulz-Schaeffer, 2012). We therefore correlated on an animal basis the extent of SA and DN pathology with the density of dopaminergic fibers. We observed a strong and significant correlation between DN pathology and the reduction in dopaminergic fibers in the striatum (r^2 = 0.8063; p = 0.00005; **Figure 5F**), and also with the reduction of dopaminergic dendrites in the SNr (**Figure 5G**, r^2 = 0.6535, p = 0.00007). The extent of SA pathology, in contrast, did not correlate significantly with dopaminergic fiber loss in the striatum (r^2 = 0.0335; p = 0.5067; **Supplementary Figure 4A**) or with the loss of dopaminergic dendrites in the SNr (**Supplementary Figure 4B**, r^2 = 0.04519, p = 0.4127). This difference suggests that, in our model, neuritic aSyn pathology is more closely linked to the degeneration of dopaminergic axon terminals than the presence of SA.

AS69 Reduces Activation of Astroglia by PFF

Finally, we measured the glial response to PFF injection in the striatum by measuring the area positive for the astroglia marker GFAP (**Figure 6A**). PFF injection increased the area positive for GFAP (160% of PBS control; **Figures 6A,B**), suggesting activation of astroglia. PFF injection also increased the intensity of GFAP staining (**Figure 6C**) and the morphology of GFAP-positive cells (branch length per cell, **Figures 6D,E**). Injection of PBS alone did not produce a significant glial activation (**Figures 6A–E**), confirming that that the observed effects can be attributed to the PFF. AS69 reduced activation of astroglia by 43% (**Figures 6A–D**). The extent of astroglia activation correlated inversely with the density of dopaminergic fibers (r^2 = 0.3298; p = 0.0159; **Figure 6F**) and positively with the relative density of DN (r^2 = 0.4238; p = 0.046; **Figure 6G**). This correlation can best be explained by astroglia activation downstream of neuronal damage. The correlation of astroglia activation with the density of SA was not statistically significant (**Supplementary Figure 4C**).

In addition, we determined the response of microglia by measuring the area positive for Iba1 (**Figure 6A**). PFF injection induced activation of microglia (110% of PBS control, **Supplementary Figure 4E**), consistent with the finding by others that microglia plays an active role in the PFF-induced degeneration (Duffy et al., 2018; Earls et al., 2019). Microglia activation was not affected by AS69 (**Figure 6A** and **Supplementary Figure 4E**).

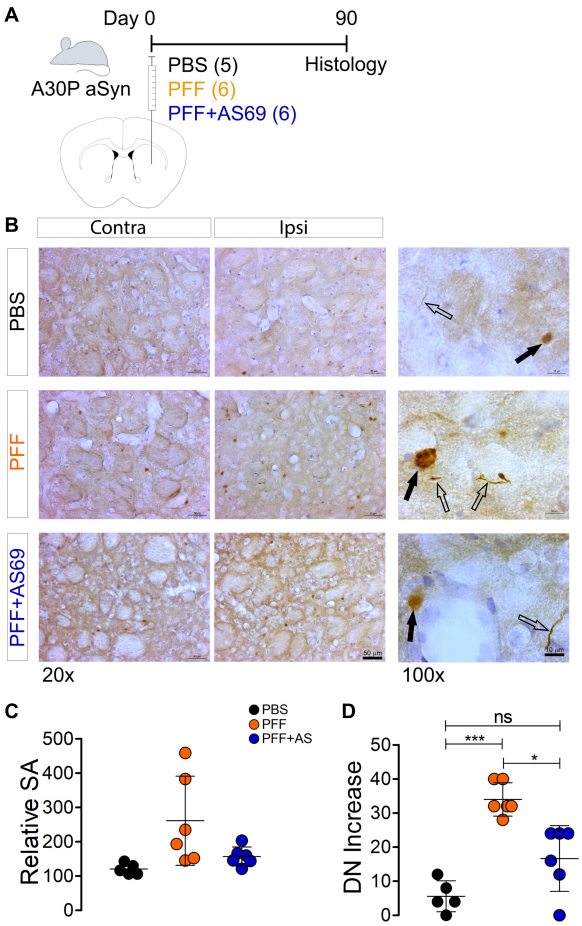

FIGURE 4 | AS69 inhibits PFF-induced aSyn-pathology in mouse brain. **(A)** Injection scheme: Transgenic mice expressing human A30P-aSyn received injections into the striatum of either PBS as control, PFF prepared from human WT aSyn, or PFF + AS69. aSyn pathology was analyzed 90 days later. Nineteen mice started the experiment. Two animals died during the course of the experiment; brains of these animals were not used for analysis. **(B)** Representative, low-magnification (20×) and high-magnification (100×) images of striatal sections stained for phospho-aSyn. Dystrophic neurites (DN, open arrows) and somatic accumulations (SA, black arrows) are indicated. Scale bars: 50 μm (20×) and 10 μm (100×). **(C)** Quantification of the number of SA in the injected striatum normalized by the non-injected hemisphere to control for variance between animals (100 × ipsilateral/contralateral). Differences between groups were not statistically significant (one-way ANOVA followed by Bonferroni *post hoc* test). **(D)** Number of DN per section in the injected striatum normalized by the non-injected hemisphere (ipsilateral–contralateral; $p = 0.0007$ for PBS vs. PFF; $p = 0.004$ for PFF vs. PFF + AS69, one-way ANOVA followed by Bonferroni *post hoc* test). Absolute values for panels **(C,D)** are depicted in **Supplementary Figures 3A,B**. Markers represent values for individual animals; lines represent mean ± SD of these values, $n = 5$ (PBS) or 6 (PFF, PFF + AS69) animals. ns: not significant; $^{*}p < 0.05$; $^{***}p < 0.001$.

DISCUSSION

Here, we investigated the effect of AS69, which binds the aSyn monomer with high affinity, in PFF-based models of secondary nucleation. In primary neurons, AS69 did not alter PFF uptake, but reduced aggregation of endogenous mouse aSyn after seeding with PFF. In mouse brain, AS69 ameliorated PFF-induced striatal aSyn pathology. AS69 also abrogated the degeneration of striatal dopaminergic axon terminals and the reduction of dopaminergic dendrites in the SNr, demonstrating the functional relevance of the aggregate reduction (summarized in **Figure 7**).

In primary neurons exposed to PFF, staining for human aSyn was already observed after 24 h whereas the extent of phospho-aSyn staining increased mainly between 24 and 72 h, consistent with previous findings that seeding of aSyn pathology by extracellular PFF takes time (Flavin et al., 2017; Rodriguez et al., 2018). During this time, PFF exit from endosomes, interact with endogenous aSyn, and seed the pathology visualized by the phospho-aSyn staining (Karpowicz et al., 2017; Wu et al., 2019). AS69 reduced the extent of phospho-aSyn pathology after 72 h (**Figure 1C**) and the extent of Triton X-100-insoluble aSyn after 10 days (**Figure 2**), indicating that AS69 reduces aSyn pathology. Staining for mouse aSyn showed Triton X-100-insoluble aggregates after PFF treatment (**Figure 2B**), confirming that the PFF made from human aSyn seeded aggregation of endogenous aSyn (Karpowicz et al., 2017; Wu et al., 2019). We used an antibody against "aggregated" aSyn, and conformation-specific antibodies have their limitations (Kumar et al., 2020). Yet, the strong co-localization with mouse aSyn staining after 1% Triton X-100 treatment (**Figure 2A**) suggests that the staining for aggregated aSyn in this paradigm represents for the most part Triton X-100-insoluble aSyn. Interestingly, AS69 also reduced the area positive for human aSyn after 72 h (**Figure 1B**). Therefore, the reduced extent of aSyn pathology observed with AS69 could alleviate the known inhibition of autophagy by aSyn pathology (Mazzulli et al., 2016; Hoffmann et al., 2019) and facilitate clearance of (human) aSyn. Improved clearance of human aSyn could also result from improved cellular health as suggested by the denser neuropil and the reduced LDH release in the presence of AS69 (**Figure 3**).

Despite the abundance of aSyn pathology (**Figures 4B–D**), nigral dopaminergic neurons and their striatal axon terminals are preserved in the A30P-aSyn transgenic mice used in this study (**Figures 5A–D**; Rathke-Hartlieb et al., 2001). In aSyn transgenic mice and in PFF-based models, pathology originates in the presynaptic compartment and propagates retrogradely to the cell body (Schaser et al., 2020). The presence of SA in the A30P-aSyn transgenic mice (**Figure 4C**) therefore suggests that retrograde transport to assemble aSyn aggregates in perinuclear accumulations is preserved in A30P-aSyn mice. PFF injection triggered a robust increase in aSyn pathology (**Figures 4C,D**), consistent with previous work using PFF in other aSyn transgenic mice (Luk et al., 2012a; Zhang et al., 2019). The PFF-induced increase was particularly strong for DN (**Figure 4D**). The predominant formation of DN in our paradigm can be explained: (1) by a very rapid formation of aSyn aggregates when PFF "seeds" are added to the high concentration of aSyn in neurons resulting from the combined expression of endogenous

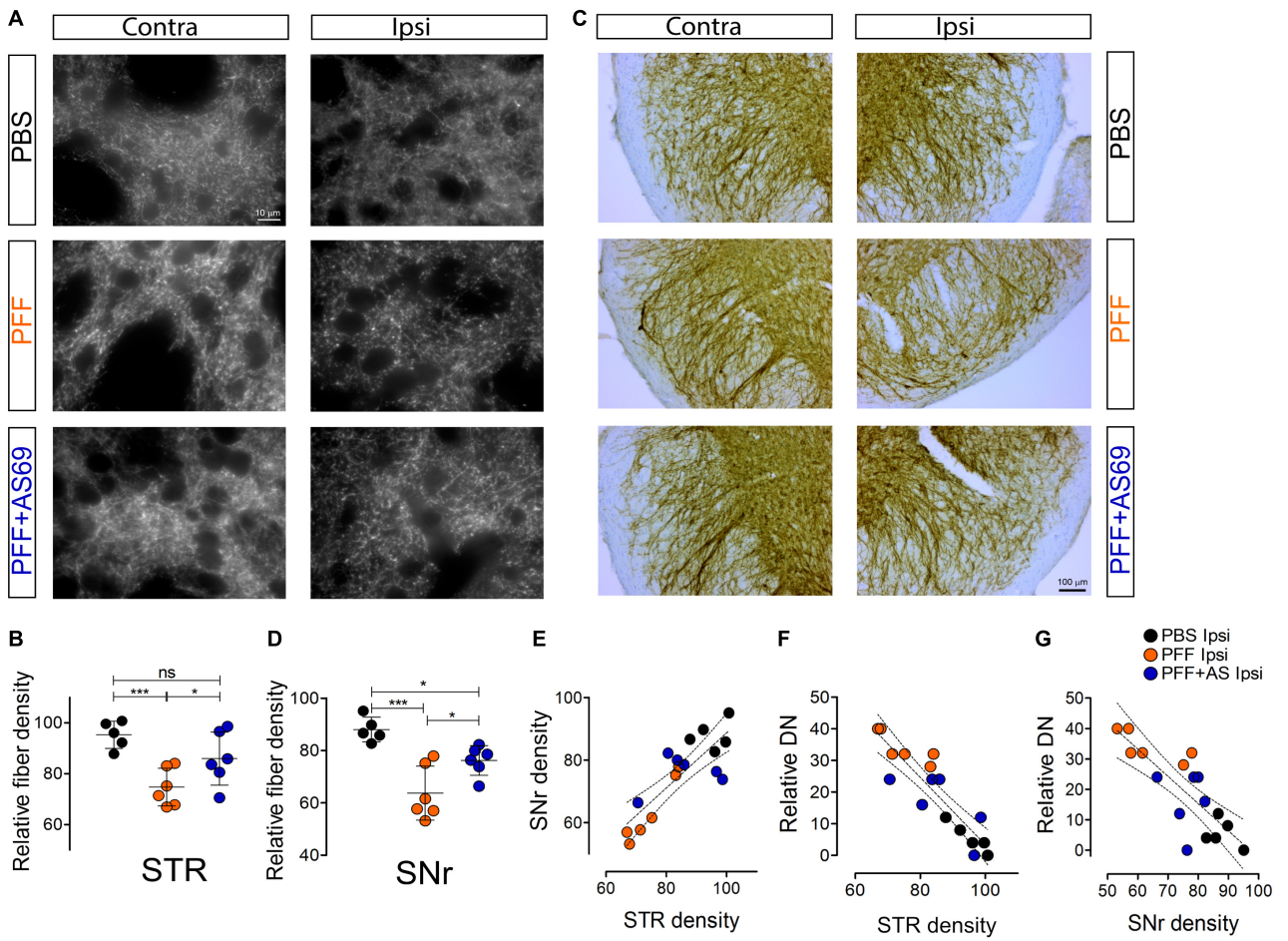

FIGURE 5 | AS69 decreases PFF-induced degeneration of dopaminergic fibers. **(A)** Representative images of striatal sections ipsilateral and contralateral to the PFF injection stained for dopaminergic (TH positive) fibers 90 days after PFF injection. Scale bar: 10 µm. **(B)** Relative density of striatal dopaminergic fibers in the striatum (STR), 100 × ipsilateral/contralateral hemisphere, $p = 0.0009$ for PBS vs. PFF; $p = 0.041$ for PFF vs. PFF + AS69, linear mixed model. Absolute values are in **Supplementary Figure 3C**. **(C)** Representative images of TH-positive dendrites in the substantia nigra pars reticulata (SNr) 90 days after PFF injection. Scale bar: 100 µm. **(D)** Relative density of dopaminergic dendrites in the SNr, 100 × ipsilateral/contralateral hemisphere, $p = 0.0008$ for PBS vs. PFF; $p = 0.012$ for PFF vs. PFF + AS69, linear mixed model. **(E)** Linear regression of dopaminergic axon terminals in STR (from panel **B**) vs. dopaminergic dendrites in SNr (from panel **D**); $p = 0.00067$; $r^2 = 0.6843$. **(F)** Linear regression of dopaminergic fibers in STR (from panel **B**) vs. DN (from **Figure 2D**); $p = 0.00005$; $r^2 = 0.8063$. **(G)** Linear regression of dopaminergic dendrites in SNr (from panel **D**) vs. DN (from **Figure 2D**); $p = 0.00072$; $r^2 = 0.6535$. In panels **(B,D–G)**, markers represent individual animals. In B and D, lines represent mean ± SD of these values. In panels **(E–G)**, dotted lines represent linear regression and 95% confidence interval. $n = 5$ (PBS) or 6 (PFF, PFF + AS69) animals. ns, not significant; $^*p < 0.05$; $^{***}p < 0.001$.

aSyn and the transgene; and (2) by the known inhibition of retrograde axonal transport by aSyn (Chung et al., 2009; Koch et al., 2015; Prots et al., 2018). In previous studies with PFF, SA-like aSyn pathology was mainly observed 4–6 months after PFF injection (Luk et al., 2012a,b; Osterberg et al., 2015; Zhang et al., 2019), thus later than our 3-month time point (**Figure 4A**). Consistent with the concept of retrograde progression noted above, we therefore assume that the abundance of SA would be more pronounced at a later time point. In addition, a slightly different phenotype in our model could be explained by the fact that 12-month-old mice were used in our experiments whereas most previous studies used younger animals. In our paradigm, the tight correlation between DN and (i) degeneration of dopaminergic axon terminals in the striatum (**Figure 5F**), (ii) degeneration of dopaminergic dendrites in the SNr (**Figure 5G**), and (iii) astrogliosis (**Figure 6G**) suggests that the DN pathology is responsible for these observed effects. The functional importance of aSyn pathology in neuronal processes is consistent with the finding of presynaptic aSyn microaggregates in the absence of somatic inclusions (Spinelli et al., 2014), earlier aSyn-induced oxidative stress in the synaptic terminals than in the soma (Szegő et al., 2019; Schaser et al., 2020), and the observation that presynaptic aSyn is a primary target for phosphorylation (Weston et al., 2021). As noted above, however, neuritic aSyn pathology often precedes somatic pathology, and cortical neurons with aSyn inclusions degenerate over time (Osterberg et al., 2015).

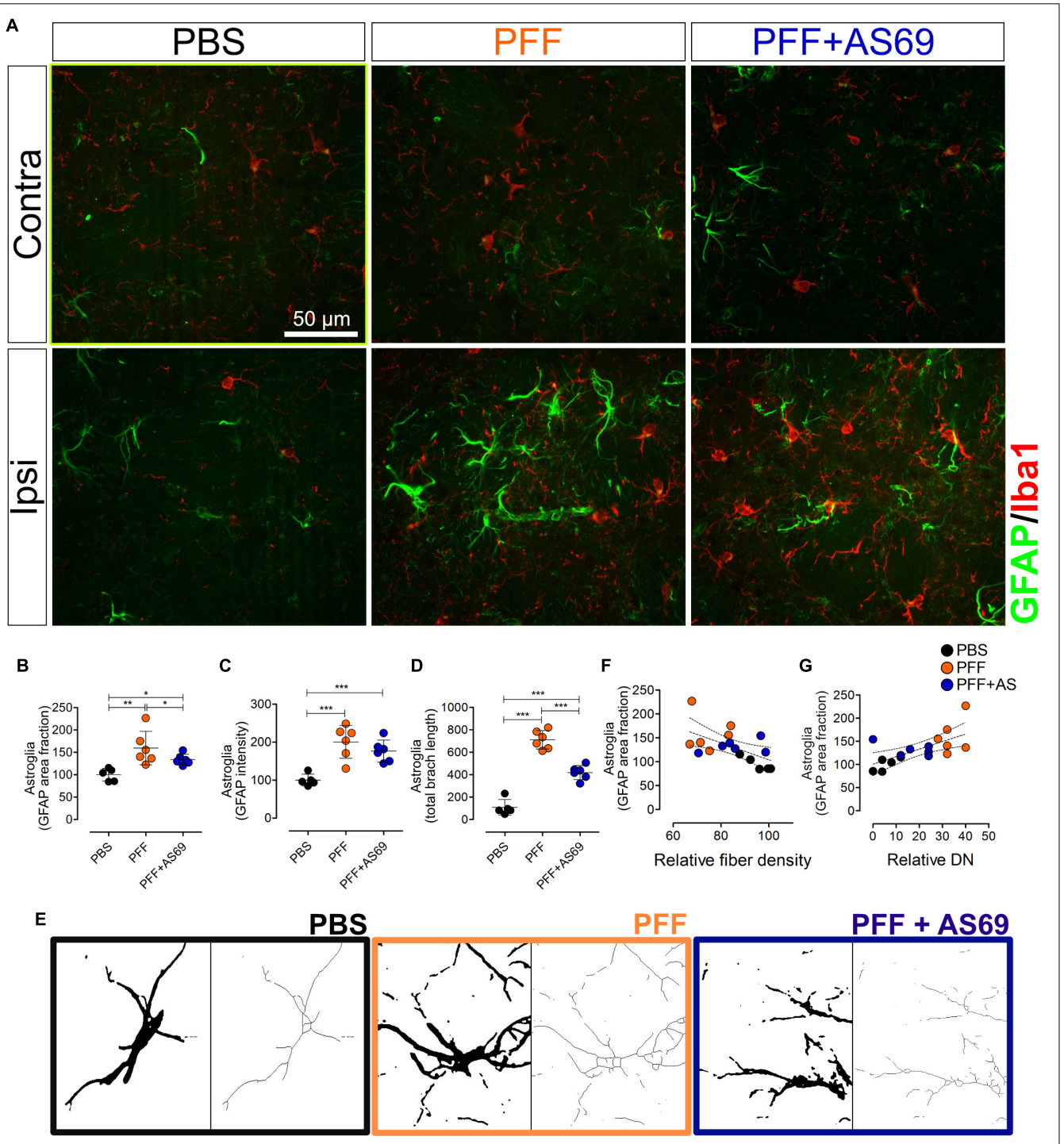

FIGURE 6 | AS69 decreases PFF-induced astrogliosis. **(A)** Representative images of striatal sections ipsilateral and contralateral to the PFF injection stained for astroglia (GFAP, green) and microglia (Iba1, red) 90 days after PFF injection. Scale bar: 50 µm. **(B–D)** Astroglia reaction expressed as GFAP-positive area fraction **(B)**, GFAP staining intensity **(C)**, and skeleton branch length **(D)** in the injected hemisphere relative to the contralateral hemisphere with the PBS-injected group set to 100%. *p*-values from one-way ANOVA followed by Bonferroni *post hoc* test. Absolute values for individual hemispheres are in **Supplementary Figures 3D–F**. **(E)** Representative images of individual astroglia after binarization (left panels) and after skeletonization (right panels) as used for panel **(D)**. **(F)** Linear regression of astroglia activation (from panel **B**) vs. density of dopaminergic fibers in the striatum (from **Figure 5B**), $p = 0.0159$; $r^2 = 0.3298$. **(G)** Linear regression of astroglia activation (from panel **B**) vs. DN in the striatum (from **Figure 3D**), $p = 0.0046$; $r^2 = 0.4238$. In panels **(B–G)**, markers represent individual animals. In panels **(B–D)**, lines represent mean ± SD. In panels **(F,G)**, dotted lines represent linear regression and 95% confidence interval. $n = 5$ (PBS) or 6 (PFF, PFF + AS69) animals. $^*p < 0.05$; $^{**}p < 0.01$; $^{***}p < 0.001$.

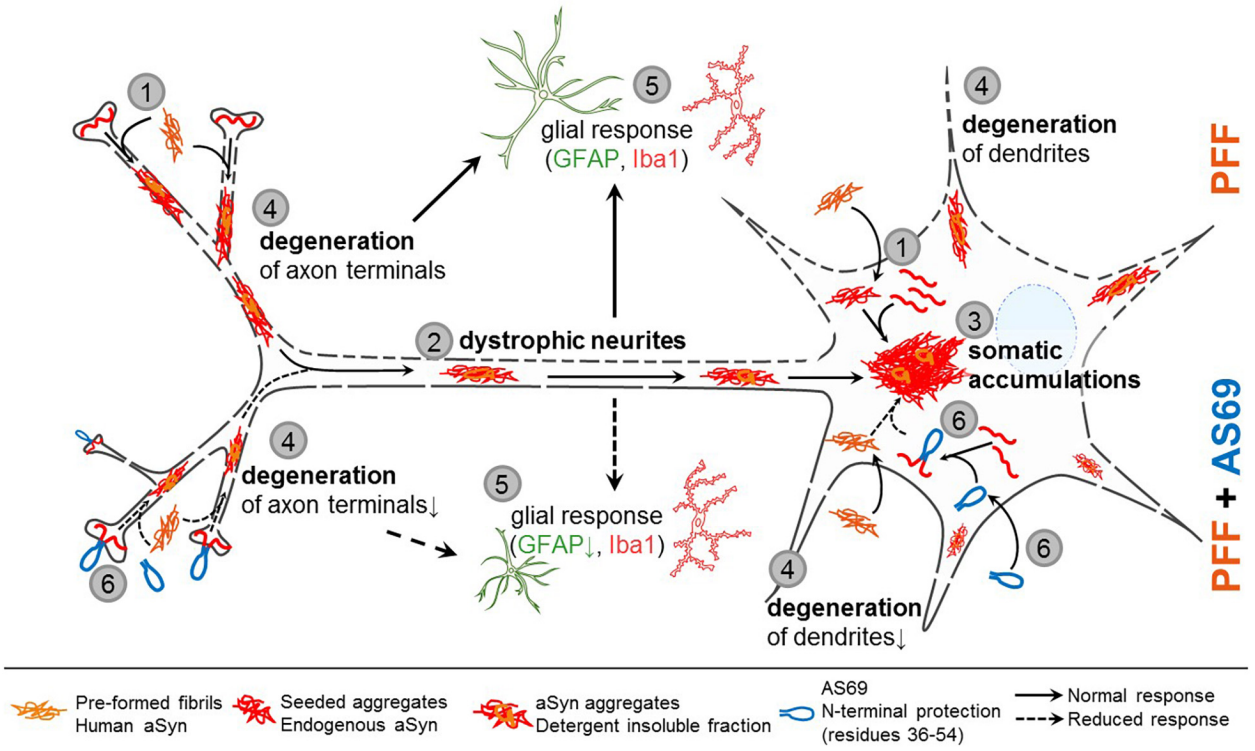

FIGURE 7 | Proposed model of aSyn pathology and AS69 protection. **(1)** aSyn pre-formed fibrils (PFF) are taken up by neurons and accelerate aggregation of aSyn monomers into detergent-insoluble aggregates (see **Figures 1D–G**). **(2)** Phospho-aSyn positive aggregates accumulate in dystrophic neurites reminiscent of Lewy-neurites and to a lesser extent in somatic inclusions reminiscent of Lewy bodies (see **Figure 2**). **(3)** Neuritic aSyn aggregates are retrogradely transported to the neuronal soma, where they are collected into somatic accumulations. **(4)** aSyn pathology causes degeneration of dopaminergic axon terminals in the striatum and degeneration of dopaminergic dendrites in the SNr (see **Figure 3**). **(5)** Dystrophic neurites and their degeneration leads to a glial response (see **Figure 4**). **(6)** AS69 is taken up by neurons, binds to N-terminal residues of the aSyn monomer, and through this mechanism reduces nucleation of aSyn aggregates (see **Figures 1C,E,G**), dystrophic neurites (see **Figure 2D**), degeneration of axon terminals and dendrites (see **Figures 3B,D**) and the astroglial response (see **Figure 4C**).

AS69 reduced PFF-induced DN formation (**Figure 3D**), and we propose that this underlies the protection of striatal axon terminals in the striatum (**Figure 5B**), dopaminergic dendrites in the SNr (**Figure 5D**), and the reduced astrogliosis (**Figures 6B–D**), consistent with our findings in primary neurons. The pathway of aSyn pathology and the proposed mechanism of AS69 action are summarized in **Figure 7**. We acknowledge that the reduction of PFF-induced aSyn pathology by AS69 was incomplete. The incomplete rescue might result from degradation of AS69 over time while the aSyn pathology increases (Patterson et al., 2019). In addition, due to the high concentration of human A30P-aSyn resulting from the transgene, aSyn fibrils–after PFF seeding–might grow mainly by fibril elongation, bypassing the need for fibril amplification by secondary nucleation. It will be important to test in future studies whether the effect of AS69 increases with repeated administration. From a translational standpoint, slowing down disease progression by 50% would already constitute a clinically meaningful effect in PD patients.

Limitations of this study include the use of transgenic mouse lines expressing human A30P-aSyn and the injection of PFF into the striatum. Both the distribution of aSyn pathology throughout the nervous system and the precise composition of the aSyn aggregates differ from PD patients. Also, we did not investigate the effects of AS69 on the propagation of aSyn pathology from the enteric nervous system to the central nervous system (Borghammer and Van Den Berge, 2019; Van Den Berge et al., 2019; Ferreira et al., 2021) that likely occurs in PD patients.

The N-terminal aSyn residues 35–43 constitute one of the hotspots controlling aSyn aggregation (Doherty et al., 2020; Khammari et al., 2020). They are targeted not only by AS69 but also by some of the aSyn antibodies tested for application in PD patients. Our findings about AS69 therefore indicate that molecules binding residues 35–43 of the aSyn monomer are promising candidates against PD.

DISCLOSURES

ÉS, FB, DK, CG, LH, HS, MW, and TS have no disclosure. JS has received payment from Biogen and grants from Deutsche Forschungsgemeinschaft, the Christina Foundation, and Pfizer. WH has received research support from the European Research Council. BF has received payment for talks from UCB and a grant from Deutsche Forschungsgemeinschaft.

DATA AVAILABILITY STATEMENT

The original contributions presented in the study are included in the article/**Supplementary Material**, further inquiries can be directed to the corresponding author/s.

ETHICS STATEMENT

The animal study was reviewed and approved by Landesamt für Natur, Umwelt und Verbraucherschutz Nordrhein-Westfalen, license numbers 84.02.04.2015.A027 and 84-02.04.2014.A321.

AUTHOR CONTRIBUTIONS

ÉS, JS, WH, and BF conceived the research. ÉS, FB, DK, CG, LH, HS, MW, and TS performed the research. ÉS, WH, and BF wrote the manuscript. All authors contributed and approved the manuscript.

FUNDING

This work was supported by the German Research Foundation (DFG, FA 658/3-1, to BF) and by the Interdisciplinary Center for Clinical Research (IZKF) Aachen (to TS). Support by a European Research Council (ERC) Consolidator Grant (grant agreement no. 726368, to WH) is acknowledged. Funders had no role in data analysis and did not have access to the data set.

ACKNOWLEDGMENTS

We thank Sabine Hamm and Andrea Kempe for excellent technical assistance, Akanksha Nagpal and Natalie Gasterich for their contributions to this project, and Filip Hasecke for help with AFM data analysis.

SUPPLEMENTARY MATERIAL

The Supplementary Material for this article can be found online at: https://www.frontiersin.org/articles/10.3389/fnins.2021.696440/full#supplementary-material

Supplementary Figure 1 | Characterization of sonicated PFFs by atomic force microscopy (AFM). **(A)** AFM amplitude image of sonicated PFFs. **(B)** Violin plot of PFF lengths determined AFM. The white dot at 41 μm represents the median. The thick gray bar represents the interquartile range, the thin gray line represents the rest of the distribution, except for points that are determined to be outliers using a method that is a function of the interquartile range.

Supplementary Figure 2 | (A) Representative immunoblot showing the Triton X-100 soluble fraction of primary neuron lysates obtained 10 days after PFF treatment. Blots were first incubated with an antibody detecting only rodent aSyn (D37A6, upper image), then with an antibody detecting both rodent and human aSyn (BD610787, middle image), finally βIII-tubulin was detected as loading control (lower image). **(B)** Quantification of the rodent aSyn signal at the 14 kDa band of $n = 3$ independent blots as in panel **(A)**, showing intensity of the aSyn band relative to the βIII-tubulin band with the signal in the BSA-treated condition set to 100%. **(C)** Quantification of the total aSyn signal at the 14 kDa band of $n = 3$ independent blots as in panel **(A)**, showing intensity of the aSyn band relative to the βIII-tubulin band with the signal in the BSA-treated condition set to 100%.

Supplementary Figure 3 | (A,B) DN and SA in the striatum in absolute numbers for each hemisphere, related to **Figures 4C,D**. **(C)** Density of dopaminergic axon terminals in the striatum in absolute numbers for each hemisphere, related to **Figure 5B**. **(D–F)** GFAP area fraction **(D)**, GFAP staining intensity **(E)** and total branch length after skeletonization of GFAP positive cells **(F)** in the striatum in absolute numbers for each hemisphere, related to **Figures 6B–D**. **(G)** Iba1 area fraction in the striatum in absolute numbers for each hemisphere, related to **Supplementary Figure 4E**. $^{*}p < 0.5$; $^{**}p < 0.01$; $^{***}p < 0.001$.

Supplementary Figure 4 | (A) Linear regression of dopaminergic axon terminals in the striatum (from **Figure 5B**) vs. SA (from **Figure 4C**), $p = 0.5067$; $r^2 = 0.0335$. **(B)** Linear regression of SA (from **Figure 4C**) vs. dendrites in SNr (from **Figure 5D**), $p = 0.4127$; $r^2 = 0.04519$. **(C)** Linear regression of astroglia activation (from **Figure 6B**) vs. SA (from **Figure 4C**). $p = 0.0609$; $r^2 = 0.2288$. **(D)** Linear regression of microglia activation (from panel **E**) vs. SA (from **Figure 3C**). $p = 0.7713$; $r^2 = 0.0062$. **(E)** Microglia reaction expressed as Iba1 positive area fraction in the injected hemisphere relative to the contralateral hemisphere with the PBS-injected group set to 100%. $p = 0.00078$ for PBS vs. PFF; $p = 0.029$ for PBS vs. PFF + AS69, one-way ANOVA followed by Bonferroni *post hoc* test. Absolute values for individual hemispheres are in **Supplementary Figure 3G**. $^{*}p < 0.05$; $^{**}p < 0.01$.

REFERENCES

Agerschou, E. D., Flagmeier, P., Saridaki, T., Galvagnion, C., Komnig, D., Heid, L., et al. (2019). An engineered monomer binding-protein for α-synuclein efficiently inhibits the proliferation of amyloid fibrils. *eLife* 8:e46112.

Borghammer, P., and Van Den Berge, N. (2019). Brain-First versus Gut-First Parkinson's Disease: a hypothesis. *J. Parkinsons. Dis.* 9, S281–S295.

Chung, C. Y., Koprich, J. B., Siddiqi, H., and Isacson, O. (2009). Dynamic changes in presynaptic and axonal transport proteins combined with striatal neuroinflammation precede dopaminergic neuronal loss in a rat model of AAV α-synucleinopathy. *J. Neurosci.* 29, 3365–3373. doi: 10.1523/jneurosci.5427-08.2009

Doherty, C. P. A., Ulamec, S. M., Maya-Martinez, R., Good, S. C., Makepeace, J., Khan, G. N., et al. (2020). A short motif in the N-terminal region of α-synuclein is critical for both aggregation and function. *Nat. Struct. Mol. Biol.* 27, 249–259. doi: 10.1038/s41594-020-0384-x

Duffy, M. F., Collier, T. J., Patterson, J. R., Kemp, C. J., Luk, K. C., Tansey, M. G., et al. (2018). Lewy body-like alpha-synuclein inclusions trigger reactive microgliosis prior to nigral degeneration. *J. Neuroinflammation* 15:129.

Earls, R. H., Menees, K. B., Chung, J., Barber, J., Gutekunst, C. A., Hazim, M. G., et al. (2019). Intrastriatal injection of preformed alpha-synuclein fibrils alters central and peripheral immune cell profiles in non-transgenic mice. *J. Neuroinflammation* 16:250.

Fagerqvist, T., Lindström, V., Nordström, E., Lord, A., Tucker, S. M. E., Su, X., et al. (2013). Monoclonal antibodies selective for α-synuclein oligomers/protofibrils recognize brain pathology in Lewy body disorders and α-synuclein transgenic mice with the disease-causing A30P mutation. *J. Neurochem.* 126, 131–144. doi: 10.1111/jnc.12175

Ferreira, N., Gonçalves, N. P., Jan, A., Jensen, N. M., van der Laan, A., Mohseni, S., et al. (2021). Trans-synaptic spreading of alpha-synuclein pathology through sensory afferents leads to sensory nerve degeneration and neuropathic pain. *Acta Neuropathol. Commun.* 9:31.

Flavin, W. P., Bousset, L., Green, Z. C., Chu, Y., Skarpathiotis, S., Chaney, M. J., et al. (2017). Endocytic vesicle rupture is a conserved mechanism of cellular invasion by amyloid proteins. *Acta Neuropathol.* 134, 629–653. doi: 10.1007/s00401-017-1722-x

Gauhar, A., Shaykhalishahi, H., Gremer, L., Mirecka, E. A., and Hoyer, W. (2014). Impact of subunit linkages in an engineered homodimeric binding protein

to α-synuclein. *Protein Eng. Des. Sel.* 27, 473–479. doi: 10.1093/protein/gzu047

Guillen, J. (2012). FELASA guidelines and recommendations. *J. Am. Assoc. Lab. Anim. Sci.* 51, 311–321.

Hoffmann, A. C., Minakaki, G., Menges, S., Salvi, R., Savitskiy, S., Kazman, A., et al. (2019). Extracellular aggregated alpha synuclein primarily triggers lysosomal dysfunction in neural cells prevented by trehalose. *Sci. Rep.* 9, 1–18.

Jia, C., Ma, X., Liu, Z., Gu, J., Zhang, X., Li, D., et al. (2019). Different heat shock proteins bind α-Synuclein with distinct mechanisms and synergistically prevent its amyloid aggregation. *Front. Neurosci.* 13:1124. doi: 10.3389/fnins.2019.01124

Kahle, P. J., Neumann, M., Ozmen, L., Muller, V., Jacobsen, H., Schindzielorz, A., et al. (2000). Subcellular localization of wild-type and Parkinson's disease-associated mutant alpha -synuclein in human and transgenic mouse brain. *J. Neurosci.* 20, 6365–6373. doi: 10.1523/jneurosci.20-17-06365.2000

Karpowicz, R. J., Haney, C. M., Mihaila, T. S., Sandler, R. M., Petersson, E. J., and Lee, V. M. Y. (2017). Selective imaging of internalized proteopathic -synuclein seeds in primary neurons reveals mechanistic insight into transmission of synucleinopathies. *J. Biol. Chem.* 292, 13482–13497. doi: 10.1074/jbc.m117.780296

Khammari, A., Arab, S. S., and Ejtehadi, M. R. (2020). The hot sites of α-synuclein in amyloid fibril formation. *Sci. Rep.* 10:12175.

Klucken, J., Ingelsson, M., Shin, Y., Irizarry, M. C., Hedley-Whyte, E. T., Frosch, M. P., et al. (2006). Clinical and biochemical correlates of insoluble α-synuclein in dementia with Lewy bodies. *Acta Neuropathol.* 111, 101–108. doi: 10.1007/s00401-005-0027-7

Koch, J. C., Bitow, F., Haack, J., D'Hedouville, Z., Zhang, J.-N. N., Tönges, L., et al. (2015). Alpha-Synuclein affects neurite morphology, autophagy, vesicle transport and axonal degeneration in CNS neurons. *Cell Death Dis.* 6:e1811. doi: 10.1038/cddis.2015.169

Komnig, D., Schulz, J. B., Reich, A., and Falkenburger, B. H. (2016). Mice lacking Faim2 show increased cell death in the MPTP mouse model of Parkinson disease. *J. Neurochem.* 139, 848–857. doi: 10.1111/jnc.13847

Krenz, A., Falkenburger, B. H., Gerhardt, E., Drinkut, A., and Schulz, J. B. (2009). Aggregate formation and toxicity by wild-type and R621C synphilin-1 in the nigrostriatal system of mice using adenoviral vectors. *J. Neurochem.* 108, 139–146. doi: 10.1111/j.1471-4159.2008.05755.x

Kumar, S. T., Jagannath, S., Francois, C., Vanderstichele, H., Stoops, E., and Lashuel, H. A. (2020). How specific are the conformation-specific α-synuclein antibodies? Characterization and validation of 16 α-synuclein conformation-specific antibodies using well-characterized preparations of α-synuclein monomers, fibrils and oligomers with distinct structures and morphology. *Neurobiol. Dis.* 146:105086. doi: 10.1016/j.nbd.2020.105086

Luk, K. C., Kehm, V., Carroll, J., Zhang, B., Brien, P. O., Trojanowski, J. Q., et al. (2012a). Pathological a-synuclein transmission initiates Parkinson-like neurodegeneration in nontransgenic mice. *Science* 338, 949–954. doi: 10.1126/science.1227157

Luk, K. C., Kehm, V., Zhang, B., O'Brien, P., Trojanowski, J., and Lee, V. (2012b). Intracerebral inoculation of pathological α-synuclein initiates a rapidly progressive neurodegenerative α-synucleinopathy in mice. *J. Exp. Med.* 209, 975–986. doi: 10.1084/jem.20112457

Luk, K. C., Covell, D. J., Kehm, V. M., Zhang, B., Song, I. Y., Byrne, M. D., et al. (2016). Molecular and biological compatibility with host alpha-synuclein influences fibril pathogenicity. *Cell Rep.* 16, 3373–3387. doi: 10.1016/j.celrep.2016.08.053

Mahul-Mellier, A. L., Burtscher, J., Maharjan, N., Weerens, L., Croisier, M., Kuttler, F., et al. (2020). The process of Lewy body formation, rather than simply α-synuclein fibrillization, is one of the major drivers of neurodegeneration. *Proc. Natl. Acad. Sci. U.S.A.* 117, 4971–4982. doi: 10.1073/pnas.1913904117

Mazzulli, J. R., Zunke, F., Tsunemi, T., Toker, N. J., Jeon, S., Burbulla, L. F., et al. (2016). Activation of β-glucocerebrosidase reduces pathological α-synuclein and restores lysosomal function in Parkinson's patient midbrain neurons. *J. Neurosci.* 36, 7693–7706. doi: 10.1523/jneurosci.0628-16.2016

Mirecka, E. A., Shaykhalishahi, H., Gauhar, A., Akgül, Ş, Lecher, J., Willbold, D., et al. (2014). Sequestration of a β-hairpin for control of α-synuclein aggregation. *Angew. Chem. Int. Ed.* 53, 4227–4230. doi: 10.1002/anie.201309001

Muchowski, P. J., and Wacker, J. L. (2005). Modulation of neurodegeneration by molecular chaperones. *Nat. Rev. Neurosci.* 6, 11–22. doi: 10.1038/nrn1587

Obeso, J. A., Stamelou, M., Goetz, C. G., Poewe, W., Lang, A. E., Weintraub, D., et al. (2017). Past, present, and future of Parkinson's disease: a special essay on the 200th anniversary of the shaking palsy. *Mov. Disord.* 32, 1264–1310.

Osterberg, V. R., Spinelli, K. J., Weston, L. J., Luk, K. C., Woltjer, R. L., and Unni, V. K. (2015). Progressive aggregation of alpha-synuclein and selective degeneration of lewy inclusion-bearing neurons in a mouse model of Parkinsonism. *Cell Rep.* 10, 1252–1260. doi: 10.1016/j.celrep.2015.01.060

Patterson, J. R., Duffy, M. F., Kemp, C. J., Howe, J. W., Collier, T. J., Stoll, A. C., et al. (2019). Time course and magnitude of alpha-synuclein inclusion formation and nigrostriatal degeneration in the rat model of synucleinopathy triggered by intrastriatal α-synuclein preformed fibrils. *Neurobiol. Dis.* 130:104525. doi: 10.1016/j.nbd.2019.104525

Paxinos, G., and Franklin, K. B. J. (2001). *Paxinos and Franklin's the Mouse Brain in Stereotaxic Coordinates*. Amsterdam: Elsevier.

Prots, I., Grosch, J., Brazdis, R. M., Simmnacher, K., Veber, V., Havlicek, S., et al. (2018). α-Synuclein oligomers induce early axonal dysfunction in human iPSC-based models of synucleinopathies. *Proc. Natl. Acad. Sci. U.S.A.* 115, 7813–7818. doi: 10.1073/pnas.1713129115

Rathke-Hartlieb, S., Kahle, P. J., Neumann, M., Ozmen, L., Haid, S., Okochi, M., et al. (2001). Sensitivity to MPTP is not increased in Parkinson' s disease-associated mutant α-synuclein transgenic mice. *J. Neurochem.* 77, 1181–1184. doi: 10.1046/j.1471-4159.2001.00366.x

Rodriguez, L., Marano, M. M., and Tandon, A. (2018). Import and export of misfolded α-Synuclein. *Front. Neurosci.* 12:344. doi: 10.3389/fnins.2018.00344

Schaser, A. J., Stackhouse, T. L., Weston, L. J., Kerstein, P. C., Osterberg, V. R., López, C. S., et al. (2020). Trans-synaptic and retrograde axonal spread of Lewy pathology following pre-formed fibril injection in an in vivo A53T alpha-synuclein mouse model of synucleinopathy. *Acta Neuropathol. Commun.* 8:150.

Schell, H., Hasegawa, T., Neumann, M., and Kahle, P. J. (2009). Nuclear and neuritic distribution of serine-129 phosphorylated α-synuclein in transgenic mice. *Neuroscience* 160, 796–804. doi: 10.1016/j.neuroscience.2009.03.002

Schindelin, J., Arganda-Carreras, I., Frise, E., Kaynig, V., Longair, M., Pietzsch, T., et al. (2012). Fiji: an open-source platform for biological-image analysis. *Nat. Methods* 9, 676–682. doi: 10.1038/nmeth.2019

Schneider, C. A., Rasband, W. S., and Eliceiri, K. W. (2012). NIH Image to ImageJ: 25 years of image analysis. *Nat. Methods* 9, 671–675. doi: 10.1038/nmeth.2089

Schulz-Schaeffer, W. J. (2012). Neurodegeneration in Parkinson disease: moving lewy bodies out of focus. *Neurology* 79, 2298–2299. doi: 10.1212/wnl.0b013e318278b6a7

Shaykhalishahi, H., Gauhar, A., Wördehoff, M. M., Grüning, C. S. R., Klein, A. N., Bannach, O., et al. (2015). Contact between the β1 and β2 Segments of α-Synuclein that inhibits amyloid formation. *Angew. Chem. Int. Ed.* 54, 8837–8840. doi: 10.1002/anie.201503018

Spinelli, K. J., Taylor, J. K., Osterberg, V. R., Churchill, M. J., Pollock, E., Moore, C., et al. (2014). Presynaptic alpha-synuclein aggregation in a mouse model of Parkinson's disease. *J. Neurosci.* 34, 2037–2050. doi: 10.1523/jneurosci.2581-13.2014

Steger, C. (1998). An unbiased detector of curvilinear structures. *IEEE Trans. Anal. Mach. Intell.* 20, 113–125. doi: 10.1109/34.659930

Szegő, ÉM., Dominguez-Meijide, A., Gerhardt, E., König, A., Koss, D. J., Li, W., et al. (2019). Cytosolic trapping of a mitochondrial heat shock protein is an early pathological event in synucleinopathies. *Cell Rep.* 28, 65.e6–77.e6.

Szegő, ÉM., Gerhardt, E., Kermer, P., and Schulz, J. B. (2012). A30P α-synuclein impairs dopaminergic fiber regeneration and interacts with L-DOPA replacement in MPTP-treated mice. *Neurobiol. Dis.* 45, 591–600. doi: 10.1016/j.nbd.2011.09.017

Szegő, ÉM., Outeiro, T. F., Kermer, P., and Schulz, J. B. (2013). Impairment of the septal cholinergic neurons in MPTP-treated A30P α-synuclein mice. *Neurobiol. Aging* 34, 589–601. doi: 10.1016/j.neurobiolaging.2012.04.012

Törnquist, M., Michaels, T. C. T., Sanagavarapu, K., Yang, X., Meisl, G., Cohen, S. I. A., et al. (2018). Secondary nucleation in amyloid formation. *Chem. Commun.* 54, 8667–8684.

Van Den Berge, N., Ferreira, N., Gram, H., Mikkelsen, T. W., Alstrup, A. K. O., Casadei, N., et al. (2019). Evidence for bidirectional and trans-synaptic

parasympathetic and sympathetic propagation of alpha-synuclein in rats. *Acta Neuropathol.* 138, 535–550. doi: 10.1007/s00401-019-02040-w

Villar-Piqué, A., Da Fonseca, T. L., Sant'Anna, R., Szegö, ÉM., Fonseca-Ornelas, L., Pinho, R., et al. (2016). Environmental and genetic factors support the dissociation between α-synuclein aggregation and toxicity. *Proc. Natl. Acad. Sci. U.S.A* 113, E6506–E6515.

Volpicelli-Daley, L. A., Luk, K. C., and Lee, V. M.-Y. (2014). Addition of exogenous α-synuclein preformed fibrils to primary neuronal cultures to seed recruitment of endogenous α-synuclein to Lewy body and Lewy neurite-like aggregates. *Nat. Protoc.* 9, 2135–2146. doi: 10.1038/nprot.2014.143

Weston, L. J., Stackhouse, T. L., Spinelli, K. J., Boutros, S. W., Rose, E. P., Osterberg, V. R., et al. (2021). Genetic deletion of Polo-like kinase 2 reduces alpha-synuclein serine-129 phosphorylation in presynaptic terminals but not Lewy bodies. *J. Biol. Chem.* 296:100273. doi: 10.1016/j.jbc.2021.100273

Wu, Q., Takano, H., Riddle, D. M., Trojanowski, J. Q., Coulter, D. A., and Lee, V. M. Y. (2019). α-Synuclein (αsyn) preformed fibrils induce endogenous αsyn aggregation, compromise synaptic activity and enhance synapse loss in cultured excitatory hippocampal neurons. *J. Neurosci.* 39, 5080–5094. doi: 10.1523/jneurosci.0060-19.2019

Young, K., and Morrison, H. (2018). Quantifying microglia morphology from photomicrographs of immunohistochemistry prepared tissue using imagej. *J. Vis. Exp.* 2018:57648.

Zhang, B., Kehm, V., Gathagan, R., Leight, S. N., Trojanowski, J. Q., Lee, V. M. Y., et al. (2019). Stereotaxic targeting of alpha-synuclein pathology in mouse brain using preformed fibrils. *Methods Mol. Biol.* 1948, 45–57. doi: 10.1007/978-1-4939-9124-2_5

Conflict of Interest: The authors declare that the research was conducted in the absence of any commercial or financial relationships that could be construed as a potential conflict of interest.

frontiers in Neuroscience

REVIEW
published: 14 September 2021
doi: 10.3389/fnins.2021.718188

Green Tea Polyphenol Epigallocatechin-Gallate in Amyloid Aggregation and Neurodegenerative Diseases

*Luiza Fernandes†, Thyago R. Cardim-Pires†, Debora Foguel and Fernando L. Palhano**

Instituto de Bioquímica Médica Leopoldo de Meis, Programa de Biologia Estrutural, Universidade Federal do Rio de Janeiro, Rio de Janeiro, Brazil

The accumulation of protein aggregates in human tissues is a hallmark of more than 40 diseases called amyloidoses. In seven of these disorders, the aggregation is associated with neurodegenerative processes in the central nervous system such as Alzheimer's disease (AD), Parkinson's disease (PD), and Huntington's disease (HD). The aggregation occurs when certain soluble proteins lose their physiological function and become toxic amyloid species. The amyloid assembly consists of protein filament interactions, which can form fibrillar structures rich in β-sheets. Despite the frequent incidence of these diseases among the elderly, the available treatments are limited and at best palliative, and new therapeutic approaches are needed. Among the many natural compounds that have been evaluated for their ability to prevent or delay the amyloidogenic process is epigallocatechin-3-gallate (EGCG), an abundant and potent polyphenolic molecule present in green tea that has extensive biological activity. There is evidence for EGCG's ability to inhibit the aggregation of α-synuclein, amyloid-β, and huntingtin proteins, respectively associated with PD, AD, and HD. It prevents fibrillogenesis (*in vitro* and *in vivo*), reduces amyloid cytotoxicity, and remodels fibrils to form non-toxic amorphous species that lack seed propagation. Although it is an antioxidant, EGCG in an oxidized state can promote fibrils' remodeling through formation of Schiff bases and crosslinking the fibrils. Moreover, microparticles to drug delivery were synthesized from oxidized EGCG and loaded with a second anti-amyloidogenic molecule, obtaining a synergistic therapeutic effect. Here, we describe several pre-clinical and clinical studies involving EGCG and neurodegenerative diseases and their related mechanisms.

Keywords: amyloidosis, epigallocatechin-gallate, anti-amyloidogenic, Alzheimer's disease, Parkinson's disease, Huntington's disease

OPEN ACCESS

Edited by:
Jinghui Luo, Paul Scherrer Institute (PSI), Switzerland

Reviewed by:
Jan Bieschke, University College London, United Kingdom
Martin Lothar Duennwald, Western University, Canada

***Correspondence:**
Fernando L. Palhano
palhano@bioqmed.ufrj.br

† These authors have contributed equally to this work

Specialty section:
This article was submitted to Neurodegeneration, a section of the journal Frontiers in Neuroscience

Received: *31 May 2021*
Accepted: *27 July 2021*
Published: *14 September 2021*

Citation:
Fernandes L, Cardim-Pires TR, Foguel D and Palhano FL (2021) Green Tea Polyphenol Epigallocatechin-Gallate in Amyloid Aggregation and Neurodegenerative Diseases. Front. Neurosci. 15:718188. doi: 10.3389/fnins.2021.718188

PROTEIN AGGREGATION AND AMYLOID DISEASES (AmD)

Amyloid fibrils are proteinaceous, insoluble structures that can be formed and accumulated inside or outside cells in response to mutations, stress conditions (pH, temperature, ionic strength, etc.), increase in protein concentration, and cellular protein quality-control failure, among others (Husby and Sletten, 1986; Brange et al., 1992; Chi et al., 2003; Alford et al., 2008). The vast majority of amyloid fibrils is composed of cross-beta structure and is found in different organs and tissues, causing a heterogeneous group of intractable diseases collectively called amyloid diseases (AmD) or amyloidoses (Husby and Sletten, 1986). The common structural features of all amyloid fibrils

have allowed the use of specific probes such as Congo red (reviewed by Yakupova et al., 2019) and thioflavin-T (Biancalana and Koide, 2010) to evaluate their formation in the test tube or in the diagnosis of AmD. Universal antibodies against fibrils have also been developed (Kayed et al., 2007). This homogeneity in fibril structure has been exploited in the search for anti-amyloidogenic compounds with some success, at least in the test tube (Trivella et al., 2012; Sant'anna et al., 2013). Epigallocatechin-gallate (EGCG) is one of these successful examples, as described in this review.

Amyloid diseases can be either systemic or localized. In the former, amyloid deposits are mainly found dispersed among peripheral tissues/organs, while in the latter the aggregates are restricted to a specific tissue/organ; if they occur in the central nervous system (CNS) a neurodegenerative disorder can develop (Muchowski, 2002; Wechalekar et al., 2016), as in the case of Huntington's disease (HD), Parkinson's disease (PD), and Alzheimer's disease (AD) (DiFiglia et al., 1997; Rocha et al., 2018; Busche and Hyman, 2020). Although they all share the amyloid fibrils as a hallmark, the proteins that compose the fibrils and the regions of the brain where the deposits are found, at least at the onset of each disease, are different, which gives rise to different clinical manifestations and demands the use of different palliative treatments, since up to now, there are no drugs against these diseases (Rubinsztein, 2006; Bloom, 2014). Tafamidis is an exception since it has been used with great success in several countries in recent years to treat patients with familial amyloid polyneuropathy, a transthyretin (TTR)-related amyloidosis (Coelho et al., 2012), and more recently, familial cardiomyopathy (Maurer et al., 2018). TTR is a tetrameric protein with two thyroxin binding pockets in the dimer-dimer interface. This structural feature allowed the development of compounds (such as Tafamidis and tolcapone) that fit with high affinity into these pockets, locking TTR in its tetrameric, non-amyloidogenic state. Tafamidis is now commercially available. This fortunate circumstance has not occurred with other amyloidogenic proteins, some of which even belong to the family of intrinsically disordered proteins, which makes it very difficult to find compounds that trap these proteins in a non-aggregating conformation. Thus, strategies or compounds that target very early aggregate species, blocking the progress of aggregation, are lacking.

Nowadays, there is a consensus that most of the toxicity/damage observed in AmD is due mainly to the oligomeric, soluble species that are formed in the process of fibril formation (Verma et al., 2015). In addition, amyloid fibrils can serve as a reservoir of toxic, soluble oligomers contributing to disease progression (Azevedo et al., 2012). Despite their different protein origins, oligomers share morphologies and biological activities (Kayed and Lasagna-Reeves, 2013). Their toxicity is associated with their binding to different cellular receptors, their pore-forming capacity, and their ability to modulate different cell pathways, among other properties (Chong et al., 2006; Choi et al., 2013; Miller et al., 2014). In the case of neurodegenerative AmD, dysregulation of synapses (pre- or post-synaptic neurons) (Scheff et al., 2007; Koffie et al., 2009; da Silva et al., 2020; Marcantoni et al., 2020), induction of reactive oxygen species (ROS) and oxidative stress (Figueiredo et al., 2013; Deas et al., 2016), calcium imbalance and mitochondrial dysfunction (Luth et al., 2014; Ludtmann et al., 2018), apoptosis induction (Chong et al., 2006), cell membrane adhesion and toxicity (Choi et al., 2013; Burré et al., 2014) and other cellular effects have been observed.

Amyloid diseases are multifactorial diseases since in addition to the damage caused by protein deposition *per se* and oligomer-related injuries, inflammation also plays an important role in disease progression and prognosis (Azevedo et al., 2019; La Vitola et al., 2021). Promising compounds must cross the blood–brain barrier (BBB) when neurodegenerative disorders are considered. All this complexity has to be considered in the search for new therapeutic approaches, which are urgent in an aging population.

NATURAL PRODUCTS AS THERAPEUTIC MOLECULES: FLAVONOIDS OF GREEN TEA

The use of natural therapeutic approaches was described more than 3,000 years ago, mostly by Chinese and Indian medicine (Nestler, 2002; Saini, 2016). The secondary metabolites from plants represent an endless frontier to be explored in the search for compounds with pharmaceutical and medical purpose. We know only a tiny fraction of our biodiversity worldwide, which makes our responsibility to preserve the environment very important.

Secondary metabolism provides several groups of molecules with different chemical properties and biochemical activities such as alkaloids, tannins, quinones, saponins, methylxanthines, and flavonoids (Kumar and Pandey, 2013). Flavonoids consist of molecules of a phenolic nature that share the flavone group as the primary skeleton. Its complexity allows different substitutions in the structure, leading to formation of a diversity of compounds such as rutin, quercetin, hesperidin, and epigallocatechin-3-gallate (Manach et al., 2004; Wen et al., 2017). The diversity of these molecules is vital to the plants, since they act as antioxidant and vegetal hormones to protect them from ultraviolet rays, bugs and opportunistic microorganisms (Wen et al., 2017).

Flavonoids display multiple biological properties such as antioxidation, through direct interaction with ROS; anticancer, by modulating several cellular pathways involved in tumor growth and apoptosis, anti-inflammation, and other effects (de Almeida et al., 2020; de Amorim et al., 2020; Lakshmi et al., 2020; Xuan et al., 2020).

Tea, the second most consumed beverage in the world, is rich in flavonoids. The predominant flavonoids of tea are catechins: (–)-epicatechin, (–)-epicatechin gallate, (–)-epigallocatechin, and (–)-epigallocatechin gallate. Tea also contains other phenolic acids (e.g., gallic acid), minerals (e.g., potassium and calcium), and amino acids (e.g., theanine) that contribute to its nutraceutical properties (Balentine et al., 1997).

Different types of tea (e.g., black and green) are prepared from the leaves of *Camellia sinensis*, whose production and consumption are widespread in China (Yan et al., 2020). The dry weight of a fresh leaf contains 2.5 to 4% caffeine and 30% flavonoids (Balentine et al., 1997).

The flavonoid EGCG is a polyphenolic compound having seven hydroxyl radicals distributed among three aromatic rings (**Figure 1**). This feature confers water solubility, allowing this molecule to be extracted merely by boiling in water (Wang et al., 2008).

Epigallocatechin-gallate oxidation can form a quinone state that can self-polymerize and crosslink with amines and sulfhydryl groups of proteins (Palhano et al., 2013). The quinone state is also related to amyloid fibril remodeling and conserves its anti-amyloidogenic activity (Palhano et al., 2013; An et al., 2017).

HISTORY OF THE INHIBITORY EFFECTS OF EPIGALLOCATECHIN-GALLATE IN PROTEIN AGGREGATION AND ITS USE IN NEURODEGENERATIVE AMYLOID DISEASES

Epigallocatechin-Gallate in Prion Diseases

The prion diseases are characterized by the conversion of the cellular isoform of the prion protein (PrP^{C}) to scrapie (PrP^{Sc}), a pathogenic conformation (reviewed by Prusiner et al., 1998; Colby and Prusiner, 2011). In this process, some of the α-helices present in PrP^{C} are refolded into β-sheets, which changes the protein physicochemical characteristics and leads to the formation of proteinaceous infectious particles, PrP^{Sc} (Pan et al., 1993; Prusiner et al., 1998). High-throughput screenings were performed to find effective therapeutic agents that could cross the BBB as well as inhibit the formation of PrP^{Sc}; reduce the PrP^{C} precursor of infectious PrP^{Sc}; and disaggregate pre-existing PrP^{Sc} (reviewed by Giles et al., 2017). In the screening of 2,000 drugs and natural products, some polyphenols such as tannin, 2′2‴-bisepigallocatechin digallate, and katacine were identified as anti-PrP^{Sc} agents (Kocisko et al., 2003). These compounds prevented PrP^{Sc} formation and accumulation in infected cells and inhibited the induced conversion of radiolabeled hamster PrP^{C} to PrP^{Sc}, resistant to protease degradation (Kocisko et al., 2003). Other polyphenols, including epicatechin and epigallocatechin, were ineffective against PrP^{Sc} formation, indicating that structural variations can lead to opposite results (Kocisko et al., 2003). After cellular screening *in vitro* (Kocisko et al., 2003), some inhibitors such as polyphenolic extracts of tea, grape seed and pine bark, tannic acid, amodiaquine, thioridazine, thiothixene, trifluoperazine, and tetrandrine were tested in scrapie-infected mice, and the positive results observed previously did not occur *in vivo* (Kocisko et al., 2004). Multiple variables can be involved in this lack of an effect *in vivo*, such as dosage, vehicle, timing for beginning or ending treatment, the compound's inability to cross the BBB and its metabolization (Kocisko et al., 2004).

A subsequent study specifically evaluated the effect of green tea extract on PrP^{Sc} formation (Rambold et al., 2008). It was demonstrated that EGCG and gallocatechin-gallate (GCG), abundant polyphenols in green tea, induced rapid transition of mature PrP^{C} into detergent-insoluble conformations, favoring the cellular protein internalization and its lysosomal degradation (Rambold et al., 2008). Consequently, PrP^{Sc} formation was reduced because the PrP^{C} precursor was depleted by the EGCG or GCG treatment (Rambold et al., 2008). Furthermore, the greater efficacy of EGCG compared to epicatechin-gallate (ECG) was attributed to the presence of three hydroxyl groups in the trihydroxyphenyl side chain and their meta-position in EGCG (Rambold et al., 2008). The gallate group at the side chain was described as essential for the observed anti-PrP^{Sc} effect (Rambold et al., 2008). Next, the effect of EGCG was also evaluated in the yeast prion protein Sup35 (Roberts et al., 2009). In these experiments, EGCG inhibited fibrillogenesis of Sup35's prion domain *in vitro* at 25 or 37°C as measured by Congo red, ThT fluorescence, and sedimentation assays (Roberts et al., 2009), while epicatechin and gallic acid had no inhibitory effects (Roberts et al., 2009). Pre-formed fibers of Sup35 prion were incubated with EGCG and the drug promoted fibril remodeling after 24 h (Roberts et al., 2009). The treatment reduced the fibrillar content and promoted an enrichment of soluble oligomeric species (Roberts et al., 2009). These oligomers were not recognized by specific conformational antibodies for amyloid species and presented lower seeding capacity (Roberts et al., 2009). The yeast phenotype termed [PSI^{+}] indicates a strain containing Sup35 in prion state aggregates and resistant to the action of proteases (Paushkin et al., 1997). The effect of EGCG on this phenotype was investigated, and the treatment reduced weak [PSI^{+}] colonies (susceptible prion strain) more effectively than strong [PSI^{+}] (resistant prion strain) (Roberts et al., 2009). Finally, EGCG and 4,5-bis- (4-methoxyanilino)

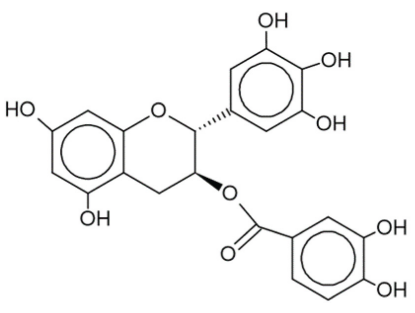

Molecular Formula: $C_{22}H_{18}O_{10}$
Formula Weight: 442.37232
Density: 1.80 ± 0.1 g/cm^3
Polarizability: 42.37 ± 0.5 10^{-24}cm^3

FIGURE 1 | Molecular structure of epigallocatechin-gallate.

phthalimide (DAPH-12) were co-applied to increase activity against prionogenesis, since DAPH-12 was able to cure strong colonies [PSI^+] (Roberts et al., 2009). Therefore, the synergy with EGCG increased the elimination of several Sup35 prion strains and enhanced the polyphenol therapeutic potential (Roberts et al., 2009; Duennwald and Shorter, 2010).

The studies presented above have demonstrated the efficacy of EGCG in inhibiting prionogenesis (Kocisko et al., 2003; Rambold et al., 2008; Roberts et al., 2009), although the mechanism has not yet been clarified. Investigations using nuclear magnetic resonance (NMR) spectroscopy revealed that EGCG bound non-specifically with PrP^C (Kamatari et al., 2013). This bond promoted the structural stabilization of PrP^C, interfering in the intermolecular interaction between PrP^C and PrP^{Sc} during the pathogenic conversion process (Kamatari et al., 2013). The neuroprotective action was also evaluated: neurotoxicity was induced by the PrP fragment (106–126) in human neuroblastoma cells and the consequences of EGCG pre-treatment were analyzed (Lee et al., 2015). When EGCG was present, it inhibited mitochondrial dysfunctions, preventing Bax translocation and cytochrome c release, and induced autophagy activated by sirt1 (silent mating type information regulation 2-homolog), increasing cell survival (Lee et al., 2015). Thus, these results suggest that EGCG may be useful for therapy in prion diseases.

Effects of Epigallocatechin-Gallate in Huntingtin Aggregation

Huntington's disease treatment is restricted to reducing symptoms (Kumar and Kumar, 2009; Dickey and La Spada, 2018; Varga et al., 2020) and the focus of research has been on disease-modifying treatments. For the first time, after the screening of 5,000 natural molecules, EGCG demonstrated potential modulatory effects against the early steps in huntingtin (htt) aggregation (Ehrnhoefer et al., 2006). A fluorescence microscopy assay revealed a reduction of protein aggregates by approximately 40% in a yeast model overexpressing htt (expanded with 72 glutamines and fused to green fluorescent protein), and the cell- extract evaluation confirmed the lower quantity of insoluble species (Ehrnhoefer et al., 2006). In yeast, EGCG decreased the toxicity promoted by htt and in HD transgenic flies the compound diminished the photoreceptor degeneration and motor impairments (Ehrnhoefer et al., 2006). Accordingly, the EGCG becomes attractive as an anti-amyloidogenic therapeutic strategy (Ehrnhoefer et al., 2006). Subsequently, EGCG was tested against fibrillar oligomers, which are globular structures, soluble in detergent and detected by an antibody that recognizes the fibrillar conformation of amyloid pathogenic proteins (Kumar and Kumar, 2009). The EGCG reduced these oligomers in pheochromocytoma cells (PC12) expressing htt and also reduced the formation of inclusion bodies (Kumar and Kumar, 2009). Given the complexity of amyloidoses and the influence of changes in the aggregation environment, the effectiveness of EGCG was also assessed in the presence of lipid membranes and the study demonstrated that EGCG efficacy was not impaired (Beasley et al., 2019). In addition to EGCG, the effect on HD of an infusion of green tea like that consumed by humans was analyzed using a *Drosophila* model. The green tea improved the neurodegeneration presented in HD flies but did not influence their viability or prolong the lifespan of wild-type *Drosophila* (Varga et al., 2020). The authors' discussion highlights the modest positive effect of the tea infusion consumption on symptoms of HD and states that the results obtained can be limited by the genetic condition of *Drosophila*, the fly husbandry and the composition and concentration of green tea used for the test (Varga et al., 2020).

Effects of EGCG on Amyloidogenesis of α-Synuclein Protein and Parkinson's Disease Prevention

Effects on α-Synuclein Aggregation

The aggregation of α-synuclein (α-syn) is a process that occurs in PD (Cascella et al., 2021). Analysis of the therapeutic potential of EGCG have shown that it inhibits α-syn amyloidogenesis (Ehrnhoefer et al., 2008; Jha et al., 2017; Dominguez-Meijide et al., 2020) and protects rat PC12 and neuroblastoma cells against aggregate-induced cytotoxicity (Ehrnhoefer et al., 2008; Jha et al., 2017). Even with the presence of metal ions to accelerate the fibrillation process, EGCG has been shown to be an effective anti-amyloid agent (Zhao et al., 2017; Teng et al., 2019). The amyloid aggregation pathway was redirected to the formation of stable spherical oligomers when EGCG was added (Ehrnhoefer et al., 2008). These oligomers were identified as non-toxic amorphous species unable to promote seeding and disassembly under denaturing conditions (resistance to sodium dodecyl sulfate) (Ehrnhoefer et al., 2008). The presence of protein dimers, tetramers and hexamers was observed after treatment with EGCG, indicating crosslinking between α-syn and the compound (Ehrnhoefer et al., 2008). Moreover, it has been shown that EGCG binds specifically to intrinsically disordered proteins (α-syn and Aβ), preventing the conversion of random-coil structures into β-sheets (Ehrnhoefer et al., 2008). The EGCG interacted with flexible regions in natively structured proteins and natively disordered proteins (α-syn and Aβ) and the binding occurred uniformly throughout the protein sequence (Fusco et al., 2018). In addition, the protein oligomerization promoted by EGCG, which redirects the pathway of amyloid formation to amorphous species, probably occurs by the establishment of multiple hydrogen bonds and aromatic interaction with backbone atoms that inducing aggregation by protein-protein interaction (Fusco et al., 2018). It has been suggested that the aggregation process can be reduced by EGCG through the oxidation of α-syn methionines (Ponzini et al., 2019). A later study discriminated between the conformational states of α-syn in neutral pH solution in the absence and presence of EGCG, proposing that EGCG binds preferentially to compact α-syn species and does not depend on covalent modifications to establish the protein-ligand interaction (Konijnenberg et al., 2016).

Šneideris et al. (2015, 2019) argued that the EGCG may be not an inhibitor of amyloidogenesis and demonstrated the possibility of false-positive results related to the method of analysis applied and the influence of environmental conditions. When the ThT fluorescence assay, based on aggregation half-time, was used,

Šneideris et al. (2015) observed that EGCG did not inhibit the formation of α-syn and Aβ fibrils. The same was observed when the pH was reduced from 7.0 to 6.0: the EGCG lost its anti-amyloid effectiveness (Šneideris et al., 2019). However, despite this controversy, several studies have reported the effectiveness of EGCG (Ehrnhoefer et al., 2008; Caruana et al., 2011; Jha et al., 2017; Zhao et al., 2017; Teng et al., 2019; Dominguez-Meijide et al., 2020).

The potential of EGCG was also evaluated in the inhibition of pre-formed amyloid fibrils (Bae et al., 2010; Bieschke et al., 2010; Yoshida et al., 2013; Haney et al., 2017; Jha et al., 2017). Similar to that described with α-syn monomers, new findings indicated that EGCG bound directly to β-sheets of fibrils, altering the amyloid conformation without disassembling them into toxic oligomeric intermediates (Bieschke et al., 2010). The remodeling of fibrils by the action of EGCG reduced the deposition of amyloid and transformed them into amorphous non-cytotoxic aggregates (Bieschke et al., 2010). Additionally, the effectiveness of EGCG was assessed in simulations of physiological conditions in a crowded macromolecular environment (Gautam et al., 2017). EGCG, in synergy with β-cyclodextrin, which also acts alone against aggregation (reviewed by Oliveri and Vecchio, 2016; Gautam et al., 2017), increased the inhibition of amyloidogenesis and the disaggregation of pre-formed fibrils (Gautam et al., 2017).

Based on the three-dimensional structure of the α-syn fibril, an analysis of the molecular dynamics of the atoms was performed to understand the remodeling process that occurs during the binding between EGCG and the mature fibril (Liu et al., 2018). The main types of EGCG interaction were hydrophobic and hydrogen bonding, affecting three different fibril sites and with participation to binding of some residues such as LYS58, GLU61, THR64, LYS96, and ASP98 (Liu et al., 2018). The remodeling promoted by EGCG occurred by generated disturbances in β-sheets and hydrogen bonds in turn of the structure of the peptide, disordering the fibril (Liu et al., 2018). It has been reported that EGCG reduced the ordered structure of the fibril (Liu et al., 2017; Yao et al., 2020) and enhanced the rupture of the β-sheets occurred mainly in the regions of residues 45–55 and 86–96, affecting the overall structure of the fibril (Yao et al., 2020). Furthermore, the EGCG interacted preferentially with the charged residues E46, E61, K80, and E83 and the polar residue S87 and with the hydrophobic residues H50, V66, V82, V95, and F94, besides destroying the saline bridge E46-K80, stabilizer of the amyloid structure (Yao et al., 2020). However, although these studies demonstrate the ability of EGCG to remodel fibrils, Sternke-Hoffmann et al. (2020) proposed that EGCG cannot inhibit its α-syn seeding capacity. Sternke-Hoffmann et al. (2020) argued that EGCG can interact with the fibril surface and block binding to ThT. Additionally, the conditions used during the tests, such as the types of plaques or pH of the solutions, alter the results of the remodeling of fibrils. It has been shown that, although EGCG promotes fibril remodeling, ThT may not be the best probe to assess the occurrence of this process (Kelley et al., 2021). Immediately after incubating the fibril with EGCG, a reduction in ThT fluorescence was observed, but this did not represent remodeling and when the washing protocol was applied, the free EGCG was removed and ThT levels were restored to a level similar to that observed prior to treatment (Kelley et al., 2021). Thus, the authors suggested the use of pentameric thiophene as an alternative to the use of ThT in addition to the application of complementary techniques and centrifugation/washing protocols to avoid unspecific results (Kelley et al., 2021).

Effects on Cellular Mechanism and Neuroprotection

The EGCG also proved to be an efficient amyloid antagonist when pre-formed oligomers were subjected to treatment (Caruana et al., 2011). These amyloid aggregation intermediates, soluble oligomers, can induce pore formation and permeabilization of the lipid bilayer, leading to cell death. Indeed, they are known as the most pathogenic amyloid species (Danzer et al., 2007). The treatment with EGCG was able to inhibit cytotoxicity induced by pre-fibrillar species in mouse neuroblastoma cells (Gautam et al., 2017). The inhibition promoted by EGCG may be related to its binding with the flexible C-terminal region of α-syn oligomers, reducing damage to the membrane (Lorenzen et al., 2014). The evidence points to a decrease in the oligomer-membrane interaction after treatment of vesicles with EGCG, which may be consequently associated to the protection of rat brain cells against oligomer toxicity (Lorenzen et al., 2014). Another proposition suggests that EGCG accelerates the formation of amyloid fibrils, reducing the active toxic oligomers (Yang et al., 2017). Thus, the cellular protection displayed after treatment with EGCG would be to facilitate the conversion of active oligomers into amyloid fibrils, decreasing rupture of the cell membrane and the cytotoxicity of the aggregates (Yang et al., 2017).

A different mechanism has been suggested for the action of EGCG in the yeast model of α-synucleinopathy (Griffioen et al., 2006). Due to its antioxidant and metal-chelating properties, EGCG inhibited aggregation and cytotoxicity. The polyphenol also preserved dopaminergic neurons and motor functions, decreasing the accumulation of amyloid in the brain of non-human primates with induced parkinsonism (Chen et al., 2015). The reduction in amyloid promoted by EGCG was observed in tissues of patients with PD (Xu et al., 2016), suggesting therapeutic potential. In addition, the neuroblastoma cells expressing wild-type or mutant α-syn were challenged by 6-hydroxydopamine (6-OHDA) and the genomic response was measured after EGCG treatment (Ma et al., 2010). The expression of α-syn sensitizes the cell to the insult and the effect of EGCG can be evaluated under the combination of genetic risk factors and environmental stress (simulated by 6-OHDA) that leads to oxidative damages similar to occurred in PD disease (Ma et al., 2010). The EGCG inhibited 70% of changes in the transcriptome induced by 6-OHDA, including the block of genes associated with erythroid-related nuclear factor 2 (Nrf2)-mediated antioxidant response (Ma et al., 2010). The knowledge about the modulation promoted by EGCG, an antioxidant, in stress response pathways may be used to understand the molecular bases of therapeutic strategies (Ma et al., 2010). Despite the 6-OHDA toxicity can be related to generation of ROS and both promote the caspase activation, it is important to identify the transcriptional network involved in neurotoxicity and EGCG action to search for new treatments (Ma et al., 2010).

Effects of EGCG in Alzheimer's Disease

Amyloid plaques and neurofibrillary tangles are hallmarks of AD. These structures are composed of amyloid-β peptide (Aβ) and tau protein, respectively (reviewed by Vaz and Silvestre, 2020). The Aβ formation and consequent aggregation depend on the sequential cleavage of amyloid precursor protein (APP) (Vaz and Silvestre, 2020). When APP is cleaved by α- and γ-secretase, the soluble product is non-amyloidogenic, but when cleavage occurs by β- and γ-secretase, amyloid-β is generated (Vaz and Silvestre, 2020). The Aβ is toxic and can aggregate, depositing in the brain tissue (Vaz and Silvestre, 2020). The new therapies focus on anti-amyloid compounds, increasing attention to the tau protein and aiming to act against the progression of the disease, not just alleviating symptoms (Vaz and Silvestre, 2020).

Indirect Effects of EGCG

The main green-tea polyphenol, EGCG, was first investigated for action against neuronal toxicity promoted by amyloid-β peptide with the focus on the antioxidant property of EGCG (Choi et al., 2001). The EGCG reduced the death of hippocampal neurons, and its protective effect was attributed to the scavenging of ROS (Choi et al., 2001). Furthermore, it has been reported that EGCG can restore nerve growth factor balance, reducing apoptosis and neurodegeneration through activation of the tropomyosin kinase A receptor (TrkA) (Liu et al., 2014). The EGCG neuroprotection also involved the nicotinic acetylcholine receptor α7 (nAChR α7) signaling cascade (Zhang X. et al., 2014). In rat neurons, EGCG protected against Aβ neurotoxicity by activating nAChR α7, which consequently activated phosphoinositide-3-kinase (PI3K), leading to Akt (protein kinase B) phosphorylation and attenuating the reduction of the anti-apoptotic Bcl-2 effector (Zhang X. et al., 2014). In a mouse model of AD, EGCG restored mitochondrial respiratory rates, adenosine triphosphate (ATP), and ROS levels and the membrane potential (Dragicevic et al., 2011). This investigation indicated that the EGCG action occurred in part by its antioxidant property and in part by stabilization of the electron transport chain (Dragicevic et al., 2011). The mitochondrial dysfunction can also be associated with prolonged exposure to oligomeric species of Aβ (He et al., 2011). These toxic species stimulate the ROS production that depends on the NADPH oxidase pathway and attenuate Ca^{2+} influx mediated by *N*-methyl-D-aspartate (NMDA)-receptor activity (He et al., 2011). The treatment with EGCG was able to protect against neurotoxic effects induced by Aβ oligomers, inhibiting ROS generation and mitigating mitochondrial damage (He et al., 2011). Moreover, the EGCG treatment can also prevented neuronal apoptosis induced by endoplasmic reticulum (ER) stress after Aβ exposure (Du et al., 2018). This array of mechanisms related to EGCG activity indicate a remarkably broad spectrum of molecular actions performed.

Activity of EGCG in APP Processing and Aβ Generation

It was found that EGCG can also suppress the increase in β-secretase expression (Shimmyo et al., 2008) and inhibit β-secretase activity directly (Jeon et al., 2003). Furthermore, in murine neuroblastoma cells transfected with the human APP mutant, EGCG inhibited the generation of $A\beta_{1-40}$ and $A\beta_{1-42}$ by increasing the action of α-secretase, which promotes the non-amyloidogenic processing of APP (Rezai-Zadeh et al., 2005).

Although the mechanism of action of EGCG has not yet been elucidated, metalloproteases and protein kinase C (PKC) may be involved. It was observed that EGCG depends on PKC and metalloproteinases for APP processing into soluble non-amyloidogenic products (Levites et al., 2003; Obregon et al., 2006). The increase in APP non-amyloidogenic processing promoted with EGCG treatment was attributed to activation of disintegrin and metalloproteinase domain-containing protein 10 (ADAM10) through estrogen receptor/phosphoinositide (Fernandez et al., 2010). Moreover, EGCG inhibited the activation of extracellular signal-regulated kinase (ERK) and the nuclear transcription factor-kB (NF-kB) induced by Aβ (Lee et al., 2009). Concomitantly, in AD mice, EGCG attenuated the reduction in α-secretase expression and the increase in β-secretase and Aβ that AD causes in the brain, suggesting that memory dysfunction was prevented by changes in APP processing (Lee et al., 2009). Thus, these changes in APP cleavage by secretases were correlated with the inactivation of ERK and NF-kB promoted by EGCG and the observations suggest that ERK and NF-kB may be modulating secretase activity (Lee et al., 2009). The EGCG also can decrease the Aβ levels by enhancing APP non-amyloidogenic processing when affecting c-Abl (Abelson tyrosine kinase) distribution in cells. The polyphenol can reduce nuclear translocation of c-Abl (Lin et al., 2009), involved in the regulation of cellular apoptosis (Yuan et al., 1997), and the interaction between c-Abl and FE65 (Lin et al., 2009), an adaptor protein involved in cellular movement and APP proteolytic processing (Wiley et al., 2007; Minopoli et al., 2012). In addition, it was demonstrated that EGCG can mitigate the expression of β-secretase and Aβ generation via nuclear peroxisome receptor activated by gamma receptor proliferator (PPARγ) (Zhang et al., 2017). Thus, reducing inflammatory agents, oxidative stress and apoptotic proteins (Zhang et al., 2017). The reduction in nuclear translocation of c-Abl inhibited glycogen synthase kinase-3β activity, an enzyme responsible for phosphorylating tau protein (Lin et al., 2009). Thus, the decrease in tyrosine phosphorylation of tau, which was indirectly generated by EGCG, can protect the cells (Lin et al., 2009).

EGCG Reduction in Aβ Levels and Amyloid Plaques

Analysis of the transgenic AD mouse model showed a reduction in brain amyloid plaques after treatment with EGCG and validated the results found in cells (Rezai-Zadeh et al., 2005). The reduction in amyloid plaques, Aβ levels and cognitive deficits was observed with intraperitoneal injection of EGCG (Rezai-Zadeh et al., 2005), as well as with oral administration in drinking water (Rezai-Zadeh et al., 2008). Furthermore, it was observed that the reduction in Aβ levels in mice treated with EGCG was accompanied by the inhibition in signaling to tumor necrosis factor alpha/c-Jun N-terminal kinase (TNF-α/JNK) and a decrease in insulin receptor substrate-1 (IRS-1), suggesting a correlation with the restoration of memory impairment by EGCG and the attenuation of insulin resistance (Jia et al., 2013).

Overall, it has been demonstrated that EGCG can reduce Aβ levels, inhibiting the deposition of plaques and recovering learning and memory functions that have been depleted by

neurotoxic effects of aggregates (Chang et al., 2015; Schimidt et al., 2017; Mori et al., 2019; Bao et al., 2020). EGCG was effective in decreasing amyloid fibrillation (Wang et al., 2017; Rho et al., 2019), redirecting to non-toxic, amorphous species of oligomers (Ehrnhoefer et al., 2008; Sinha et al., 2012) and remodeling pre-formed fibrils (Ehrnhoefer et al., 2008; Palhano et al., 2013; Ahmed et al., 2017; Wang et al., 2017; Lee et al., 2020). However, the protective effects of EGCG in neurons are not restricted to the reduction of Aβ levels. It also protects against mitochondrial damage (Dragicevic et al., 2011), induced metal toxicity (Reznichenko et al., 2006; Hyung et al., 2013; Chan et al., 2016; Ayyalasomayajula et al., 2019), stress by ROS generation (Shimmyo et al., 2008; Kim et al., 2009; Ayyalasomayajula et al., 2019) and neuroinflammation events (Lee et al., 2009; Cheng-Chung Wei et al., 2016) related to AD. A study developed in transgenic *Caenorhabditis elegans* demonstrated that EGCG inhibited oligomerization and Aβ deposition, and in the worms exposed only to oxidative stress, the EGCG reduced the levels of small heat shock protein, under the control of DAF-2/insulin-like signaling pathway (Abbas and Wink, 2010). Thus, suggesting that EGCG can protect against age-related diseases, like AD, and ROS-mediated damages (Abbas and Wink, 2010).

EGCG Binding to β-Amyloid

To better understand the mechanism of EGCG binding to amyloid protein, thermodynamic analyses were performed (Wang et al., 2010). Hydrophobic interactions and hydrogen bonds appeared to be the main actors in the process of Aβ-EGCG interaction (Wang et al., 2010). There were gradual changes from hydrogen bonding to hydrophobic interactions during the increase in the EGCG/Aβ ratio and the experimental conditions as such increase in temperature, salt concentration or changes in pH facilitated the formation of the EGCG-protein bond (Wang et al., 2010). Hydrogen interactions have been shown to occur primarily in the protein backbone and hydrophobic interactions in the side-chains (Liu et al., 2011). In addition, it was found that van der Waals interactions and the participation of 12 amino-acid residues (F4, R5, F19, F20, E22, K28, G29, L34, M35, V36, G37, and I41) occurred during EGCG contacts with the Aβ peptide, preventing the conformation conversion of α-helices into β-sheets that is characteristic of $A\beta_{1-42}$ (Liu et al., 2011). During analysis of $A\beta_{1-42}$ fragments, it was observed that hydrogen bonds occur in $A\beta_{1-16}$ more frequently, while hydrophobic interactions occur mainly in $A\beta_{17-42}$. However, thermodynamic evaluations performed in different solutions containing the peptide fragments and EGCG did not suggest specific binding sites for EGCG (Wang et al., 2012). NMR characterizations of oligomers formed in the presence of EGCG showed that the compound interacts with the aromatic hydrophobic nucleus of Aβ (residues 17–20) (Lopez del Amo et al., 2012). There was an immobilization of 1–20 Aβ-peptide residues after EGCG interaction, inhibiting the characteristic β-sheet formation of amyloid aggregation (Lopez del Amo et al., 2012). Subsequent investigations demonstrated that 3 molecules of EGCG were attached to Aβ and the planar ring of EGCG prevented the β-sheets formation (Bleiholder et al., 2013). However, solid-state NMR assay indicated that the oligomers generated with EGCG treatment were not amorphous as previously described (Ehrnhoefer et al., 2008), but instead were well structured (Lopez del Amo et al., 2012). In the same study, it was reported that EGCG may have prevented the metal ions' coordination with residues Y10, H13, and H14, justifying the loss of neurotoxicity by oligomers generated in the presence of EGCG (Lopez del Amo et al., 2012). This interaction with Y10 of Aβ peptide and the His influence was confirmed subsequently (Zhang B. et al., 2013). Furthermore, the metal-Aβ interaction was associated with neuronal toxicity and pathogenesis of AD, and evaluation of the effects of EGCG demonstrated that in the presence of metal that was free or complexed with the peptide, the induced neurotoxicity was reduced (Hyung et al., 2013). EGCG can bind to metal-Aβ species and also promote metal chelation, both related to this positive action of the compound (Hyung et al., 2013).

The first investigation of the binding between EGCG and the Aβ dimers (smallest aggregates) showed higher number of contacts of three aromatic rings of EGCG with Aβ and its preferential interaction with residues G29, A30, G37, G38, V39, and A42 of the backbone and strong with residues F4, F19, F20, T10, I31, I32, M35, V36, V39, and I41 of the side-chains (Zhang T. et al., 2013). Furthermore, analysis of the molecular mechanism of EGCG interactions during the remodeling of mature amyloid fibrils identified as the main factor the interactions between the compound and hydrophobic fiber sites (Palhano et al., 2013). This remodeling process depended on EGCG auto-oxidation, which generates a mixture of EGCG-quinone monomers and polymers (Palhano et al., 2013). The EGCG's oxidized molecules formed Schiff bases with amyloid fibrils by reaction with free amines in the protein (Palhano et al., 2013). The crosslink thus generated was responsible for preventing fibril dissociation in toxic oligomeric species (Palhano et al., 2013). Despite the observation that oxidized EGCG was able to bind to fibrils, the role of EGCG auto-oxidation in driving the amyloid fibril remodeling remains unclear (Palhano et al., 2013). Through NMR spectroscopy analysis, it was observed that the flavon-3-ol unit of catechins was essential for the interaction with the Aβ oligomers and the EGCG interaction affinity can be enhanced by the presence of the gallate motif (Sironi et al., 2014). Later, it was observed that EGCG can interfere in the interaction of residues in the central region of Aβ (F19 and L34) that are important in the structure of amyloid fibrils (Tavanti et al., 2020). Molecular dynamics simulations indicated that EGCG alters the Aβ protofibril conformation by breaking the hydrogen bond between H6 and E11 residues, interacting with H14/Y10, and interacting with residue A42, disrupting the salt bridge with the side chain of K28 (Zhan et al., 2020). This same lysine also interacted with the gallic acid of EGCG, confirming that group's critical role in protofibril disruption (Zhan et al., 2020). Thus, it was observed that the central interference promoted by EGCG in fibril formation is the disruption of inter-chain hydrogen bonds and salt bridges crucial to amyloid structure (Acharya et al., 2020). Even though the mechanism of action of EGCG has not been elucidated, the knowledge of some forms of interaction between the compound and amyloid

proteins can generate valuable information for therapeutic strategies against aggregation. The EGCG seems to interact preferably with intrinsically disordered proteins as such Aβ and α-syn (Ehrnhoefer et al., 2008) and with flexible regions of ordered proteins (Fusco et al., 2018). The aromatic rings, hydroxyls groups and gallate motif of EGCG appear to be essential for the interactions with proteins and the anti-amyloid effectiveness (Rambold et al., 2008; Sironi et al., 2014; Fusco et al., 2018). Moreover, the hydrophobic interactions and hydrogen bonds represent the main form of protein-compound interaction, resulting in inhibition of the conversion in β amyloid toxic structures (Wang et al., 2010), and the break of saline bridges promoted by EGCG can be crucial to interrupt the fibril structuration (Acharya et al., 2020; Yao et al., 2020; Zhan et al., 2020).

DRUG DELIVERY SYSTEMS CONTAININ EPIGALLOCATECHIN-GALLATE

Despite the several benefits promoted by EGCG treatment of AmD, their low intestinal absorbance and instability constitute an important limitation to consider in developing new therapeutic strategies (reviewed by Granja et al., 2017). Different types of nanocarriers have been evaluated for their ability to enhance EGCG efficacy, mainly related to this catechin's antioxidant and anti-inflammatory properties (Granja et al., 2017). Nanolipid particles (lipid complexes: EGCG; formation of non-traditional micelles) have been synthesized to improve oral bioavailability of EGCG and BBB penetration and prevent APP cleavage of Aβ peptide by inducing α-secretase activity (Smith et al., 2010). The increased bioavailability of these particles may be important to reduce the required concentration of EGCG in promoting benefits and its future success in clinical trials (Smith et al., 2010). New types of nanoparticles containing EGCG have been evaluated for their ability to inhibit amyloid aggregation (Zhang J. et al., 2014; Debnath et al., 2016; Liu et al., 2017; Li et al., 2018; Singh et al., 2018; Fernandes et al., 2020). Selenium nanoparticles bound to EGCG and coated by the TET-1 peptide, which increases their delivery to neuronal cells, were effective at inhibiting amyloid cytotoxicity, blocking the Aβ aggregation and disaggregating mature fibrils (Zhang J. et al., 2014). These anti-amyloidogenic effects have also been shown during the evaluation of EGCG nanoparticles produced from polysuccinimide and functionalized with octadecylamine, dopamine and ethylenediamine and loaded with EGCG (Debnath et al., 2016). Enhancement of the chemical stability of EGCG by nanoparticle formation, their improvement in ease of cellular internalization, and stronger binding with amyloids were considered to contribute to their better performance (Debnath et al., 2016). In addition, when the EGCG was linked to negatively charged polymeric nanoparticles (NP10) it showed synergistic action against aggregation of Aβ and seeding capacity using a low concentration of the polyphenol (Liu et al., 2017). The NP10 inhibits the aggregation through hydrophobic binding and electrostatic repulsion and the hydrophobicity of EGCG stabilizes the Aβ in a stable oligomeric state, preventing the amyloid structuration (Liu et al., 2017). Both NP10 and EGCG, individually could act as anti-aggregating compounds, however in dual system were more efficient (Liu et al., 2017). In rats in which AD was induced by the administration of aluminum chloride, nanoparticles loaded with EGCG (synthesized by the solvent evaporation method in double emulsion) showed greater protective efficiency than free EGCG (Singh et al., 2018). These EGCG nanoparticles inhibited the accumulation of amyloid plaques and neurofibrillary tangles and reduced the immunoreactivity of the Aβ peptide and the ROS production in the brain tissues of AD rat model (Singh et al., 2018). Thus, the EGCG nanoparticles led to an increase in locomotor activity and recognition memory in these rats (Singh et al., 2018). In addition, EGCG together with ascorbic acid (AA) were encapsulated by a dual formulation of chemical polymers and also demonstrated a reduction in amyloid plaques and Aβ content in mice with familial AD (Cano et al., 2019). The increase in synapses and decrease in neuroinflammation generated after the treatment with encapsulated EGCG/AA were accompanied by improved learning and memory (Cano et al., 2019). The AA was responsible for creating an antioxidative environment for EGCG and promoted an increase in the positive effects of nanoparticles (Cano et al., 2019). In the mouse model with PD, similar results were observed when nanolipid particles carrying EGCG improved motor performance, decreased α-syn aggregation in neurons and protected dopaminergic cells (Li et al., 2018). These nanoparticles were more permeable and accumulated in brain tissue because of the link with the B6 peptide, which has a high affinity for the transferrin endothelial receptor, and also because of the loading with supermagnetic iron oxide nanocubes (Li et al., 2018). Furthermore, liposomes assembled with 1-palmitoyl-2-oleoyl-sn-glycero-3-phosphate and leptin used for EGCG delivery were more permeable than unmodified liposomes, reducing MPTP toxin-induced neurotoxicity and the cellular expression of α-syn and proteins involved in apoptotic processes (Kuo et al., 2021). Finally, a different concept was introduced by the synthesis of functional spheres of EGCG, synthesized by a simple method of catechin auto-oxidation under controlled heating and in the presence of a specific metal concentration (Chen et al., 2013). These functional microparticles, with oxidized EGCG as carrier, have been shown to inhibit α-syn aggregation, reduce the cytotoxicity of oligomers and, modestly, remodel mature fibrils (Fernandes et al., 2020). Moreover, when the EGCG microparticle was loaded with an additional amyloidogenesis inhibitor, ortho-iminoquinone (Largeron and Fleury, 2012; Fernandes et al., 2017), its activity increased, demonstrating a synergistic action between the microcarrier and the loaded molecule (Fernandes et al., 2020).

CLINICAL TRIALS INVOLVING GREEN TEA AND EGCG

Since green tea components are well absorbed and bioavailable in humans (Nakagawa et al., 1997; van het Hof et al., 1998; Chow et al., 2003), several clinical trials have been conducted to dissect

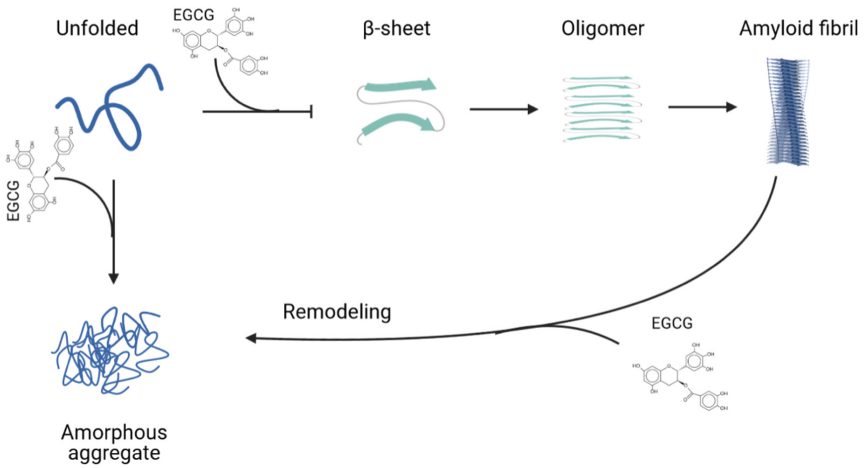

FIGURE 2 | Epigallocatechin-gallate (EGCG) interferes in different steps of amyloid formation. EGCG can bind to unfolded monomers and inhibit the formation of amyloid fibrils or amorphous aggregates. It also is able to remodel amyloid fibrils to form amorphous aggregates. Created with BioRender.com.

the role of complete green tea or its purified constituents in different conditions and diseases.

In human clinical trials, green tea extracts and EGCG were shown to be safe for use in children and adults, including during prolonged periods (Kumar et al., 2016; de la Torre et al., 2020; Vilela et al., 2020), which reinforces the treatment potential of those components.

Most clinical trials involving green tea and EGCG are related to several cancer types, cardiovascular diseases, and metabolic disorders such as diabetes, dyslipidemia and obesity. Despite evidence from *in vitro* and *in vivo* studies involving amyloidoses and EGCG, only a few clinical trials are registered, and even fewer have produced accessible results. In phase 1 clinical trials, green tea reduced cardiac TTR amyloidosis-related symptoms and amyloid plaques (Kristen et al., 2012; Aus dem Siepen et al., 2015) and improved health quality in patients.

Neurological clinical trials are almost entirely restricted to cognitive performance studies. In a study conducted in 2012, EGCG (300 mg) improved neurological effects during alpha, beta, and theta brainwave stimulation, promoting, among other effects, increased calmness and reduced stress self-evaluated by healthy individuals over periods of 120 min (Scholey et al., 2012). These studies are corroborated by a more recent phase 1 trial conducted by de la Torre et al. (2020). EGCG improved cognition and functional competence when combined with cognitive training during a 3-month follow-up (de la Torre et al., 2020).

Epigallocatechin-gallate also abrogated cognitive deficits related to Down syndrome, an amyloid-related disease (reviewed by Abrahamson et al., 2019), since its administration during 3 or 12 months induced episodic memory and working memory improvement and visual recognition memory and adaptive behavior, respectively (de la Torre et al., 2014, 2016). The consumption of green tea was related to a reduced risk of dementia n elderly Japanese (Tomata et al., 2016), suggesting that its use may be related to a better prognosis in AD.

In patients with multiple system atrophy, a disease related to α-synuclein aggregation, EGCG administered daily for 48 weeks showed no effect against disease progression (Levin et al., 2019).

As reviewed here, green tea EGCG is a potent molecule with several therapeutic properties against different neurological diseases. However, there is a lack of clinical trials involving this promising molecule against these types of disease and amyloidoses especially.

FINAL CONSIDERATIONS

Considering the evidence presented above, the use of EGCG in amyloidogenic neurodegenerative diseases is a very promising therapeutic tool, since it has been used in pre-clinical and clinical studies to treat several amyloidoses. **Figure 2** summarizes the interference and anti-amyloid effects of EGCG in different steps of protein aggregation and amyloid formation.

AUTHOR CONTRIBUTIONS

LF and TRCP both wrote the manuscript. DF and FLP edited, approved, and finalized the manuscript.

FUNDING

This work was supported by Conselho Nacional de Desenvolvimento Científico e Tecnológico (CNPq), Fundação de Amparo a Pesquisa do Estado do Rio de Janeiro (FAPERJ), and Coordenação de Aperfeiçoamento de Pessoal de Nível Superior (CAPES).

ACKNOWLEDGMENTS

We thank Martha Sorenson for the critical reading of the manuscript.

REFERENCES

Abbas, S., and Wink, M. (2010). Epigallocatechin gallate inhibits beta amyloid oligomerization in Caenorhabditis elegans and affects the daf-2/insulin-like signaling pathway. *Phytomedicine* 17, 902–909. doi: 10.1016/j.phymed.2010.03.008

Abrahamson, E. E., Head, E., Lott, I. T., Handen, B. L., Mufson, E. J., Christian, B. T., et al. (2019). Neuropathological correlates of amyloid PET imaging in Down syndrome. *Dev. Neurobiol.* 79, 750–766. doi: 10.1002/dneu.22713

Acharya, A., Stockmann, J., Beyer, L., Rudack, T., Nabers, A., Gumbart, J. C., et al. (2020). The effect of (-)-epigallocatechin-3-gallate on the amyloid-β secondary structure. *Biophys. J.* 119, 349–359. doi: 10.1016/j.bpj.2020.05.033

Ahmed, R., VanSchouwen, B., Jafari, N., Ni, X., Ortega, J., and Melacini, G. (2017). Molecular Mechanism for the (-)-epigallocatechin gallate-induced toxic to nontoxic remodeling of Aβ oligomers. *J. Am. Chem. Soc.* 139, 13720–13734. doi: 10.1021/jacs.7b05012

Alford, J. R., Kendrick, B. S., Carpenter, J. F., and Randolph, T. W. (2008). High concentration formulations of recombinant human interleukin-1 receptor antagonist: II. aggregation kinetics. *J. Pharmaceut. Sci.* 97, 3005–3021. doi: 10.1002/jps.21205

An, T. T., Feng, S., and Zeng, C. M. (2017). Oxidized epigallocatechin gallate inhibited lysozyme fibrillation more strongly than the native form. *Redox Biol.* 11, 315–321. doi: 10.1016/j.redox.2016.12.016

Aus dem Siepen, F., Bauer, R., Aurich, M., Buss, S. J., Steen, H., Altland, K., et al. (2015). Green tea extract as a treatment for patients with wild-type transthyretin amyloidosis: an observational study. *Drug Design Dev. Ther.* 9, 6319–6325. doi: 10.2147/DDDT.S96893

Ayyalasomayajula, N., Ajumeera, R., Chellu, C. S., and Challa, S. (2019). Mitigative effects of epigallocatechin gallate in terms of diminishing apoptosis and oxidative stress generated by the combination of lead and amyloid peptides in human neuronal cells. .*J. Biochem. Mol. Toxicol.* 33:22393. doi: 10.1002/jbt.22393

Azevedo, E. P., Guimaraes-Costa, A. B., Bandeira-Melo, C., Chimelli, L., Waddington-Cruz, M., Saraiva, E. M., et al. (2019). Inflammatory profiling of patients with familial amyloid polyneuropathy. *BMC Neurol.* 19:1369–1364. doi: 10.1186/s12883-019-1369-4

Azevedo, E. P., Guimarães-Costa, A. B., Torezani, G. S., Braga, C. A., Palhano, F. L., Kelly, J. W., et al. (2012). Amyloid fibrils trigger the release of neutrophil extracellular traps (NETs), causing fibril fragmentation by NET-associated elastase. *J. Biol. Chem.* 287, 37206–37218. doi: 10.1074/jbc.M112.369942

Bae, S. Y., Kim, S., Hwang, H., Kim, H. K., Yoon, H. C., Kim, J. H., et al. (2010). Amyloid formation and disaggregation of α-synuclein and its tandem repeat (α-TR). *Biochem. Biophys. Res. Commun.* 400, 531–536. doi: 10.1016/j.bbrc.2010.08.088

Balentine, D. A., Wiseman, S. A., and Bouwens, L. C. (1997). The chemistry of tea flavonoids. *Crit. Rev. Food Sci. Nutrit.* 37, 693–704. doi: 10.1080/10408399709527797

Bao, J., Liu, W., Zhou, H. Y., Gui, Y. R., Yang, Y. H., Wu, M. J., et al. (2020). Epigallocatechin-3-gallate alleviates cognitive deficits in APP/PS1 mice. *Curr. Med. Sci.* 40, 18–27. doi: 10.1007/s11596-020-2142-z

Beasley, M., Stonebraker, A. R., Hasan, I., Kapp, K. L., Liang, B. J., Agarwal, G., et al. (2019). Lipid membranes influence the ability of small molecules to inhibit huntingtin fibrillization. *Biochemistry* 58, 4361–4373. doi: 10.1021/acs.biochem.9b00739

Biancalana, M., and Koide, S. (2010). Molecular mechanism of thioflavin-T binding to amyloid fibrils. *Biochim. Biophys. Acta* 1804, 1405–1412. doi: 10.1016/j.bbapap.2010.04.001

Bieschke, J., Russ, J., Friedrich, R. P., Ehrnhoefer, D. E., Wobst, H., Neugebauer, K., et al. (2010). EGCG remodels mature alpha-synuclein and amyloid-beta fibrils and reduces cellular toxicity. *Proc. Natl. Acad. Sci. U S A.* 107, 7710–7715. doi: 10.1073/pnas.0910723107

Bleiholder, C., Do, T. D., Wu, C., Economou, N. J., Bernstein, S. S., Buratto, S. K., et al. (2013). Ion mobility spectrometry reveals the mechanism of amyloid formation of Aβ(25-35) and its modulation by inhibitors at the molecular level: epigallocatechin gallate and scyllo-inositol. *J. Am. Chem. Soc.* 135, 16926–16937. doi: 10.1021/ja406197f

Bloom, G. S. (2014). Amyloid-β and tau: the trigger and bullet in Alzheimer disease pathogenesis. *JAMA Neurol.* 71, 505–508. doi: 10.1001/jamaneurol.2013.5847

Brange, J., Havelund, S., and Hougaard, P. (1992). Chemical stability of insulin. 2. Formation of higher molecular weight transformation products during storage of pharmaceutical preparations. *Pharmaceut. Res.* 9, 727–734. doi: 10.1023/a:1015887001987

Burré, J., Sharma, M., and Südhof, T. C. (2014). α-Synuclein assembles into higher-order multimers upon membrane binding to promote SNARE complex formation. *Proc. Natl. Acad. Sci. U S A.* 111, e4274–e4283. doi: 10.1073/pnas.1416598111

Busche, M. A., and Hyman, B. T. (2020). Synergy between amyloid-β and tau in Alzheimer's disease. *Nat. Neurosci.* 23, 1183–1193. doi: 10.1038/s41593-020-0687-6

Cano, A., Ettcheto, M., Chang, J. H., Barroso, E., Espina, M., Kühne, B. A., et al. (2019). Dual-drug loaded nanoparticles of epigallocatechin-3-gallate (EGCG)/ascorbic acid enhance therapeutic efficacy of EGCG in a APPswe/PS1dE9 Alzheimer's disease mice model. *J. Control. Rel.* 301, 62–75. doi: 10.1016/j.jconrel.2019.03.010

Caruana, M., Högen, T., Levin, J., Hillmer, A., Giese, A., and Vassallo, N. (2011). Inhibition and disaggregation of α-synuclein oligomers by natural polyphenolic compounds. *FEBS Lett.* 585, 1113–1120. doi: 10.1016/j.febslet.2011.03.046

Cascella, R., Chen, S. W., Bigi, A., Camino, J. D., Xu, C. K., Dobson, C. M., et al. (2021). The release of toxic oligomers from α-synuclein fibrils induces dysfunction in neuronal cells. *Nat. Commun.* 12, 21937–21933. doi: 10.1038/s41467-021-21937-3

Chan, S., Kantham, S., Rao, V. M., Palanivelu, M. K., Pham, H. L., Shaw, P. N., et al. (2016). Metal chelation, radical scavenging and inhibition of Aβ42 fibrillation by food constituents in relation to Alzheimer's disease. *Food Chem.* 199, 185–194. doi: 10.1016/j.foodchem.2015.11.118

Chang, X., Rong, C., Chen, Y., Yang, C., Hu, Q., Mo, Y., et al. (2015). (-)-Epigallocatechin-3-gallate attenuates cognitive deterioration in Alzheimer's disease model mice by upregulating neprilysin expression. *Exp. Cell Res.* 334:004. doi: 10.1016/j.yexcr.2015.04.004

Chen, M., Wang, T., Yue, F., Li, X., Wang, P., Li, Y., et al. (2015). Tea polyphenols alleviate motor impairments, dopaminergic neuronal injury, and cerebral α-synuclein aggregation in MPTP-intoxicated parkinsonian monkeys. *Neuroscience* 286, 383–392. doi: 10.1016/j.neuroscience.2014.12.003

Chen, Z., Wang, C., Chen, J., and Li, X. (2013). Biocompatible, functional spheres based on oxidative coupling assembly of green tea polyphenols. *J. Am. Chem. Soc.* 135:ja311374b. doi: 10.1021/ja311374b

Cheng-Chung Wei, J., Huang, H. C., Chen, W. J., Huang, C. N., Peng, C. H., and Lin, C. L. (2016). Epigallocatechin gallate attenuates amyloid β-induced inflammation and neurotoxicity in EOC 13.31 microglia. *Eur. J. Pharmacol.* 770, 16–24. doi: 10.1016/j.ejphar.2015.11.048

Chi, E. Y., Krishnan, S., Randolph, T. W., and Carpenter, J. F. (2003). Physical stability of proteins in aqueous solution: mechanism and driving forces in nonnative protein aggregation. *Pharmaceut. Res.* 20:a:1025771421906. doi: 10.1023/a:1025771421906

Choi, B. K., Choi, M. G., Kim, J. Y., Yang, Y., Lai, Y., Kweon, D. H., et al. (2013). Large α-synuclein oligomers inhibit neuronal SNARE-mediated vesicle docking. *Proc. Natl. Acad. Sci. U S A.* 110:1218424110. doi: 10.1073/pnas.1218424110

Choi, Y. T., Jung, C. H., Lee, S. R., Bae, J. H., Baek, W. K., Suh, M. H., et al. (2001). The green tea polyphenol (-)-epigallocatechin gallate attenuates beta-amyloid-induced neurotoxicity in cultured hippocampal neurons. *Life Sci.* 70, 603–614. doi: 10.1016/s0024-3205(01)01438-2

Chong, Y. H., Shin, Y. J., Lee, E. O., Kayed, R., Glabe, C. G., and Tenner, A. J. (2006). ERK1/2 activation mediates Abeta oligomer-induced neurotoxicity via caspase-3 activation and tau cleavage in rat organotypic hippocampal slice cultures. *J. Biol. Chem.* 281, 20315–20325. doi: 10.1074/jbc.M601016200

Chow, H. H., Cai, Y., Hakim, I. A., Crowell, J. A., Shahi, F., Brooks, C. A., et al. (2003). Pharmacokinetics and safety of green tea polyphenols after multiple-dose administration of epigallocatechin gallate and polyphenon E in healthy individuals. *Clin. Cancer Res.* 9, 3312–3319.

Coelho, T., Maia, L. F., Martins, da Silva, A., Waddington Cruz, M., Planté-Bordeneuve, V., et al. (2012). Tafamidis for transthyretin familial amyloid polyneuropathy: a randomized, controlled trial. *Neurology* 79, 785–792. doi: 10.1212/WNL.0b013e3182661eb1

Colby, D. W., and Prusiner, S. B. (2011). Prions. *Cold Spring Harb. Perspect. Biol.* 3:a006833. doi: 10.1101/cshperspect.a006833

da Silva, J. S., Nonose, Y., Rohden, F., Lukasewicz Ferreira, P. C., Fontella, F. U., Rocha, A., et al. (2020). Guanosine neuroprotection of presynaptic mitochondrial calcium homeostasis in a mouse study with amyloid-β oligomers. *Mol. Neurobiol.* 57, 4790–4809. doi: 10.1007/s12035-020-02064-4

Danzer, K. M., Haasen, D., Karow, A. R., Moussaud, S., Habeck, M., Giese, A., et al. (2007). Different species of alpha-synuclein oligomers induce calcium influx and seeding. *J. Neurosci.* 27, 9220–9232. doi: 10.1523/JNEUROSCI.2617-07.2007

de Almeida, M., Pieropan, F., de Mattos Oliveira, L., Dos Santos, Junior, M. C., David, J. M., et al. (2020). The flavonoid agathisflavone modulates the microglial neuroinflammatory response and enhances remyelination. *Pharmacol. Res.* 159:104997. doi: 10.1016/j.phrs.2020.104997

de Amorim, V., Júnior, M., da Silva, A. B., David, J. M., David, J., de Fátima Dias, et al. (2020). Agathisflavone modulates astrocytic responses and increases the population of neurons in an in vitro model of traumatic brain injury. *Naunyn-Schmiedeberg's Archiv. Pharmacol.* 393, 1921–1930. doi: 10.1007/s00210-020-01905-2

de la Torre, R., de Sola, S., Farré, M., Xicota, L., Cuenca-Royo, A., Rodriguez, J., et al. (2020). A phase 1, randomized double-blind, placebo controlled trial to evaluate safety and efficacy of epigallocatechin-3-gallate and cognitive training in adults with Fragile X syndrome. *Clin. Nutrit.* 39, 378–387. doi: 10.1016/j.clnu.2019.02.028

de la Torre, R., de Sola, S., Hernandez, G., Farré, M., Pujol, J., Rodriguez, J., et al. (2016). Safety and efficacy of cognitive training plus epigallocatechin-3-gallate in young adults with Down's syndrome (TESDAD): a double-blind, randomised, placebo-controlled, phase 2 trial. *Lancet Neurol.* 15, 801–810. doi: 10.1016/S1474-4422(16)30034-5

de la Torre, R., de Sola, S., Pons, M., Duchon, A., de Lagran, M. M., Farré, M., et al. (2014). Epigallocatechin-3-gallate, a DYRK1A inhibitor, rescues cognitive deficits in Down Syndrome mouse models and in humans. *Mol. Nutrit. Food Res.* 58, 278–288. doi: 10.1002/mnfr.201300325

Deas, E., Cremades, N., Angelova, P. R., Ludtmann, M. H., Yao, Z., Chen, S., et al. (2016). Alpha-synuclein oligomers interact with metal ions to induce oxidative stress and neuronal death in Parkinson's Disease. *Antioxidants Redox Signal.* 24, 376–391. doi: 10.1089/ars.2015.6343

Debnath, K., Shekhar, S., Kumar, V., Jana, N. R., and Jana, N. R. (2016). Efficient Inhibition of Protein Aggregation, Disintegration of Aggregates, and Lowering of Cytotoxicity by Green Tea Polyphenol-Based Self-Assembled Polymer Nanoparticles. *ACS Appl. Mater. Interf.* 8, 20309–20318. doi: 10.1021/acsami.6b06853

Dickey, A. S., and La Spada, A. R. (2018). Therapy development in Huntington disease: from current strategies to emerging opportunities. *Am. J. Med. Genet. Part A* 176, 842–861. doi: 10.1002/ajmg.a.38494

DiFiglia, M., Sapp, E., Chase, K. O., Davies, S. W., Bates, G. P., Vonsattel, J. P., et al. (1997). Aggregation of huntingtin in neuronal intranuclear inclusions and dystrophic neurites in brain. *Science* 277, 1990–1993. doi: 10.1126/science.277.5334.1990

Dominguez-Meijide, A., Vasili, E., König, A., Cima-Omori, M. S., Ibáñez, de Opakua, A., et al. (2020). Effects of pharmacological modulators of α-synuclein and tau aggregation and internalization. *Sci. Rep.* 10:12827. doi: 10.1038/s41598-020-69744-y

Dragicevic, N., Smith, A., Lin, X., Yuan, F., Copes, N., Delic, V., et al. (2011). Green tea epigallocatechin-3-gallate (EGCG) and other flavonoids reduce Alzheimer's amyloid-induced mitochondrial dysfunction. *J. Alzheimer's Dis.* 26, 507–521. doi: 10.3233/JAD-2011-101629

Du, K., Liu, M., Zhong, X., Yao, W., Xiao, Q., Wen, Q., et al. (2018). Epigallocatechin gallate reduces amyloid β-induced neurotoxicity via inhibiting endoplasmic reticulum stress-mediated apoptosis. *Mol. Nutrit. Food Res.* 62:201700890. doi: 10.1002/mnfr.201700890

Duennwald, M. L., and Shorter, J. (2010). Countering amyloid polymorphism and drug resistance with minimal drug cocktails. *Prion* 4, 244–251. doi: 10.4161/pri.4.4.13597

Ehrnhoefer, D. E., Bieschke, J., Boeddrich, A., Herbst, M., Masino, L., Lurz, R., et al. (2008). EGCG redirects amyloidogenic polypeptides into unstructured, off-pathway oligomers. *Nat. Struct. Mol. Biol.* 15, 558–566. doi: 10.1038/nsmb.1437

Ehrnhoefer, D. E., Duennwald, M., Markovic, P., Wacker, J. L., Engemann, S., Roark, M., et al. (2006). Green tea (-)-epigallocatechin-gallate modulates early events in huntingtin misfolding and reduces toxicity in Huntington's disease models. *Hum. Mol. Genet.* 15, 2743–2751. doi: 10.1093/hmg/ddl210

Fernandes, L., Messias, B., Pereira-Neves, A., Azevedo, E. P., Araújo, J., Foguel, D., et al. (2020). Green Tea Polyphenol Microparticles Based on the Oxidative Coupling of EGCG Inhibit Amyloid Aggregation/Cytotoxicity and Serve as a Platform for Drug Delivery. *ACS Biomater. Sci. Engine.* 6, 4414–4423. doi: 10.1021/acsbiomaterials.0c00188

Fernandes, L., Moraes, N., Sagrillo, F. S., Magalhães, A. V., de Moraes, M. C., Romão, L., et al. (2017). An ortho-iminoquinone compound reacts with lysine inhibiting aggregation while remodeling mature amyloid fibrils. *ACS Chem. Neurosci.* 8, 1704–1712. doi: 10.1021/acschemneuro.7b00017

Fernandez, J. W., Rezai-Zadeh, K., Obregon, D., and Tan, J. (2010). EGCG functions through estrogen receptor-mediated activation of ADAM10 in the promotion of non-amyloidogenic processing of APP. *FEBS Lett.* 584, 4259–4267. doi: 10.1016/j.febslet.2010.09.022

Figueiredo, C. P., Clarke, J. R., Ledo, J. H., Ribeiro, F. C., Costa, C. V., Melo, H. M., et al. (2013). Memantine rescues transient cognitive impairment caused by high-molecular-weight aβ oligomers but not the persistent impairment induced by low-molecular-weight oligomers. *J. Neurosci.* 33, 9626–9634. doi: 10.1523/JNEUROSCI.0482-13.2013

Fusco, G., Sanz-Hernandez, M., Ruggeri, F. S., Vendruscolo, M., Dobson, C. M., and De Simone, A. (2018). Molecular determinants of the interaction of EGCG with ordered and disordered proteins. *Biopolymers* 109:23117. doi: 10.1002/bip.23117

Gautam, S., Karmakar, S., Batra, R., Sharma, P., Pradhan, P., Singh, J., et al. (2017). Polyphenols in combination with β-cyclodextrin can inhibit and disaggregate α-synuclein amyloids under cell mimicking conditions: A promising therapeutic alternative. *Biochim. Biophys. Acta Prot. Proteom.* 1865, 589–603. doi: 10.1016/j.bbapap.2017.02.014

Giles, K., Olson, S. H., and Prusiner, S. B. (2017). Developing Therapeutics for PrP Prion Diseases. *Cold Spring Harb. Perspect. Med.* 7:a023747. doi: 10.1101/cshperspect.a023747

Granja, A., Frias, I., Neves, A. R., Pinheiro, M., and Reis, S. (2017). Therapeutic potential of epigallocatechin gallate nanodelivery systems. *BioMed Res. Int.* 2017:5813793. doi: 10.1155/2017/5813793

Griffioen, G., Duhamel, H., Van Damme, N., Pellens, K., Zabrocki, P., Pannecouque, C., et al. (2006). A yeast-based model of alpha-synucleinopathy identifies compounds with therapeutic potential. *Biochim. Biophys. Acta* 1762, 312–318. doi: 10.1016/j.bbadis.2005.11.009

Haney, C. M., Cleveland, C. L., Wissner, R. F., Owei, L., Robustelli, J., Daniels, M. J., et al. (2017). Site-specific fluorescence polarization for studying the disaggregation of α-synuclein fibrils by small molecules. *Biochemistry* 56, 683–691. doi: 10.1021/acs.biochem.6b01060

He, Y., Cui, J., Lee, J. C., Ding, S., Chalimoniuk, M., Simonyi, A., et al. (2011). Prolonged exposure of cortical neurons to oligomeric amyloid-β impairs NMDA receptor function via NADPH oxidase-mediated ROS production: protective effect of green tea (-)-epigallocatechin-3-gallate. *ASN Neuro* 3:AN20100025. doi: 10.1042/AN20100025

Husby, G., and Sletten, K. (1986). Chemical and clinical classification of amyloidosis. *Scand. J. Immunol.* 23, 253–265. doi: 10.1111/j.1365-3083.1986.tb01966.x

Hyung, S. J., DeToma, A. S., Brender, J. R., Lee, S., Vivekanandan, S., Kochi, A., et al. (2013). Insights into antiamyloidogenic properties of the green tea extract (-)-epigallocatechin-3-gallate toward metal-associated amyloid-β species. *Proc. Natl. Acad. Sci. U S A.* 110, 3743–3748. doi: 10.1073/pnas.1220326110

Jeon, S. Y., Bae, K., Seong, Y. H., and Song, K. S. (2003). Green tea catechins as a BACE1 (beta-secretase) inhibitor. *Bioorganic Med. Chem. Lett.* 13, 3905–3908. doi: 10.1016/j.bmcl.2003.09.018

Jha, N. N., Kumar, R., Panigrahi, R., Navalkar, A., Ghosh, D., Sahay, S., et al. (2017). Comparison of α-synuclein fibril inhibition by four different amyloid inhibitors. *ACS Chem. Neurosci.* 8, 2722–2733. doi: 10.1021/acschemneuro.7b00261

Jia, N., Han, K., Kong, J. J., Zhang, X. M., Sha, S., Ren, G. R., et al. (2013). (-)-Epigallocatechin-3-gallate alleviates spatial memory impairment in APP/PS1 mice by restoring IRS-1 signaling defects in the hippocampus. *Mol. Cell. Biochem.* 380, 211–218. doi: 10.1007/s11010-013-1675-x

Kamatari, Y. O., Hayano, Y., Yamaguchi, K., Hosokawa-Muto, J., and Kuwata, K. (2013). Characterizing antiprion compounds based on their binding properties

to prion proteins: implications as medical chaperones. *Prot. Sci.* 22, 22–34. doi: 10.1002/pro.2180

Kayed, R., and Lasagna-Reeves, C. A. (2013). Molecular mechanisms of amyloid oligomers toxicity. *J. Alzheimer's Dis.* 33:129001. doi: 10.3233/JAD-2012-129001

Kayed, R., Head, E., Sarsoza, F., Saing, T., Cotman, C. W., Necula, M., et al. (2007). Fibril specific, conformation dependent antibodies recognize a generic epitope common to amyloid fibrils and fibrillar oligomers that is absent in prefibrillar oligomers. *Mol. Neurodegenerat.* 2:18. doi: 10.1186/1750-1326-2-18

Kelley, M., Sant'Anna, R., Fernandes, L., and Palhano, F. L. (2021). Pentameric Thiophene as a Probe to Monitor EGCG's Remodeling Activity of Mature Amyloid Fibrils: Overcoming Signal Artifacts of Thioflavin T. *ACS Omega* 6, 8700–8705. doi: 10.1021/acsomega.1c00680

Kim, C. Y., Lee, C., Park, G. H., and Jang, J. H. (2009). Neuroprotective effect of epigallocatechin-3-gallate against beta-amyloid-induced oxidative and nitrosative cell death via augmentation of antioxidant defense capacity. *Archiv. Pharmacal. Res.* 32, 869–881. doi: 10.1007/s12272-009-1609-z

Kocisko, D. A., Baron, G. S., Rubenstein, R., Chen, J., Kuizon, S., and Caughey, B. (2003). New inhibitors of scrapie-associated prion protein formation in a library of 2000 drugs and natural products. *J. Virol.* 77, 10288–10294. doi: 10.1128/jvi.77.19.10288-10294.2003

Kocisko, D. A., Morrey, J. D., Race, R. E., Chen, J., and Caughey, B. (2004). Evaluation of new cell culture inhibitors of protease-resistant prion protein against scrapie infection in mice. *J. General Virol.* 85, 2479–2483. doi: 10.1099/vir.0.80082-0

Koffie, R. M., Meyer-Luehmann, M., Hashimoto, T., Adams, K. W., Mielke, M. L., Garcia-Alloza, M., et al. (2009). Oligomeric amyloid beta associates with postsynaptic densities and correlates with excitatory synapse loss near senile plaques. *Proc. Natl. Acad. Sci. U S A.* 106, 4012–4017. doi: 10.1073/pnas.0811698106

Konijnenberg, A., Ranica, S., Narkiewicz, J., Legname, G., Grandori, R., Sobott, F., et al. (2016). Opposite structural effects of epigallocatechin-3-gallate and dopamine binding to α-synuclein. *Analyt. Chem.* 88, 8468–8475. doi: 10.1021/acs.analchem.6b00731

Kristen, A. V., Lehrke, S., Buss, S., Mereles, D., Steen, H., Ehlermann, P., et al. (2012). Green tea halts progression of cardiac transthyretin amyloidosis: an observational report. *Clin. Res. Cardiol.* 101, 805–813. doi: 10.1007/s00392-012-0463-z

Kumar, N. B., Pow-Sang, J., Spiess, P. E., Park, J., Salup, R., Wiliams, C. R., et al. (2016). Randomized, placebo-controlled trial evaluating the safety of one-year administration of green tea catechins. *Oncotarget* 7, 70794–70802. doi: 10.18632/oncotarget.12222

Kumar, P., and Kumar, A. (2009). Effect of lycopene and epigallocatechin-3-gallate against 3-nitropropionic acid induced cognitive dysfunction and glutathione depletion in rat: A novel nitric oxide mechanism. *Food Chem. Toxicol.* 47, 2522–2530. doi: 10.1016/j.fct.2009.07.011

Kumar, S., and Pandey, A. K. (2013). Chemistry and biological activities of flavonoids: an overview. *Sci. World J.* 29:162750. doi: 10.1155/2013/162750

Kuo, Y. C., Wang, I. H., and Rajesh, R. (2021). Use of leptin-conjugated phosphatidic acid liposomes with resveratrol and epigallocatechin gallate to protect dopaminergic neurons against apoptosis for Parkinson's disease therapy. *Acta Biomaterial.* 119, 360–374. doi: 10.1016/j.actbio.2020.11.015

La Vitola, P., Balducci, C., Baroni, M., Artioli, L., Santamaria, G., Castiglioni, M., et al. (2021). Peripheral inflammation exacerbates α-synuclein toxicity and neuropathology in Parkinson's models. *Neuropathol. Appl. Neurobiol.* 47, 43–60. doi: 10.1111/nan.12644

Lakshmi, S. P., Reddy, A. T., Kodidhela, L. D., and Varadacharyulu, N. C. (2020). The tea catechin epigallocatechin gallate inhibits NF-κB-mediated transcriptional activation by covalent modification. *Arch. Biochem. Biophys.* 695:108620. doi: 10.1016/j.abb.2020.108620

Largeron, M., and Fleury, M. B. (2012). A biologically inspired Cu(I)/topaquinone-like co-catalytic system for the highly atom-economical aerobic oxidation of primary amines to imines. *Angewandte Chemie* 51, 5409–5412. doi: 10.1002/anie.201200587

Lee, J. H., Moon, J. H., Kim, S. W., Jeong, J. K., Nazim, U. M., Lee, Y. J., et al. (2015). EGCG-mediated autophagy flux has a neuroprotection effect via a class III histone deacetylase in primary neuron cells. *Oncotarget* 6, 9701–9717. doi: 10.18632/oncotarget.3832

Lee, J. W., Lee, Y. K., Ban, J. O., Ha, T. Y., Yun, Y. P., Han, S. B., et al. (2009). Green tea (-)-epigallocatechin-3-gallate inhibits beta-amyloid-induced cognitive dysfunction through modification of secretase activity via inhibition of ERK and NF-kappaB pathways in mice. *J. Nutrit.* 139, 1987–1993. doi: 10.3945/jn.109.109785

Lee, S. B., Choi, E. H., Jeong, K. H., Kim, K. S., Shim, S. M., and Kim, G. H. (2020). Effect of catechins and high-temperature-processed green tea extract on scavenging reactive oxygen species and preventing $A\beta_{1-42}$ fibrils' formation in brain microvascular endothelium. *Nutrit. Neurosci.* 23, 363–373. doi: 10.1080/1028415X.2018.1507618

Levin, J., Maaß, S., Schuberth, M., Giese, A., Oertel, W. H., Poewe, W., et al. (2019). Safety and efficacy of epigallocatechin gallate in multiple system atrophy (PROMESA): a randomised, double-blind, placebo-controlled trial. *Lancet Neurol.* 18, 724–735. doi: 10.1016/S1474-4422(19)30141-3

Levites, Y., Amit, T., Mandel, S., and Youdim, M. B. (2003). Neuroprotection and neurorescue against Abeta toxicity and PKC-dependent release of nonamyloidogenic soluble precursor protein by green tea polyphenol (-)-epigallocatechin-3-gallate. *Federat. Am. Soc. Exp. Biol.* 17, 952–954. doi: 10.1096/fj.02-0881fje

Li, Y., Chen, Z., Lu, Z., Yang, Q., Liu, L., Jiang, Z., et al. (2018). "Cell-addictive" dual-target traceable nanodrug for Parkinson's disease treatment via flotillins pathway. *Theranostics* 8, 5469–5481. doi: 10.7150/thno.28295

Lin, C. L., Chen, T. F., Chiu, M. J., Way, T. D., and Lin, J. K. (2009). Epigallocatechin gallate (EGCG) suppresses beta-amyloid-induced neurotoxicity through inhibiting c-Abl/FE65 nuclear translocation and GSK3 beta activation. *Neurobiol. Aging* 30, 81–92. doi: 10.1016/j.neurobiolaging.2007.05.012

Liu, F. F., Dong, X. Y., He, L., Middelberg, A. P., and Sun, Y. (2011). Molecular insight into conformational transition of amyloid β-peptide 42 inhibited by (-)-epigallocatechin-3-gallate probed by molecular simulations. *J. Phys. Chem. B* 115, 11879–11887. doi: 10.1021/jp202640b

Liu, H., Yu, L., Dong, X., and Sun, Y. (2017). Synergistic effects of negatively charged hydrophobic nanoparticles and (-)-epigallocatechin-3-gallate on inhibiting amyloid β-protein aggregation. *J. Colloid Interf. Sci.* 491, 305–312. doi: 10.1016/j.jcis.2016.12.038

Liu, M., Chen, F., Sha, L., Wang, S., Tao, L., Yao, L., et al. (2014). (-)-Epigallocatechin-3-gallate ameliorates learning and memory deficits by adjusting the balance of TrkA/p75NTR signaling in APP/PS1 transgenic mice. *Mol. Neurobiol.* 49, 1350–1363. doi: 10.1007/s12035-013-8608-2

Liu, X., Zhou, S., Shi, D., Bai, Q., Liu, H., and Yao, X. (2018). Influence of EGCG on α-synuclein (αS) aggregation and identification of their possible binding mode: A computational study using molecular dynamics simulation. *Chem. Biol. Drug Design* 91, 162–171. doi: 10.1111/cbdd.13067

Lopez del Amo, J. M., Fink, U., Dasari, M., Grelle, G., Wanker, E. E., et al. (2012). Structural properties of EGCG-induced, nontoxic Alzheimer's disease Aβ oligomers. *J. Mol. Biol.* 421, 517–524. doi: 10.1016/j.jmb.2012.01.013

Lorenzen, N., Nielsen, S. B., Yoshimura, Y., Vad, B. S., Andersen, C. B., Betzer, C., et al. (2014). How epigallocatechin gallate can inhibit α-synuclein oligomer toxicity in vitro. *J. Biol. Chem.* 289, 21299–21310. doi: 10.1074/jbc.M114.554667

Ludtmann, M., Angelova, P. R., Horrocks, M. H., Choi, M. L., Rodrigues, M., Baev, A. Y., et al. (2018). α-synuclein oligomers interact with ATP synthase and open the permeability transition pore in Parkinson's disease. *Nat. Commun.* 9:2293. doi: 10.1038/s41467-018-04422-2

Luth, E. S., Stavrovskaya, I. G., Bartels, T., Kristal, B. S., and Selkoe, D. J. (2014). Soluble, prefibrillar α-synuclein oligomers promote complex I-dependent, Ca2+-induced mitochondrial dysfunction. *J. Biol. Chem.* 289, 21490–21507. doi: 10.1074/jbc.M113.545749

Ma, L., Cao, T. T., Kandpal, G., Warren, L., Fred Hess, J., Seabrook, G. R., et al. (2010). Genome-wide microarray analysis of the differential neuroprotective effects of antioxidants in neuroblastoma cells overexpressing the familial Parkinson's disease alpha-synuclein A53T mutation. *Neurochem. Res.* 35, 130–142. doi: 10.1007/s11064-009-0038-1

Manach, C., Scalbert, A., Morand, C., Rémésy, C., and Jiménez, L. (2004). Polyphenols: food sources and bioavailability. *Am. J. Clin. Nutrit.* 79, 727–747. doi: 10.1093/ajcn/79.5.727

Marcantoni, A., Cerullo, M. S., Buxeda, P., Tomagra, G., Giustetto, M., Chiantia, G., et al. (2020). Amyloid Beta42 oligomers up-regulate the excitatory synapses

by potentiating presynaptic release while impairing postsynaptic NMDA receptors. *J. Physiol.* 598, 2183–2197. doi: 10.1113/JP279345

Maurer, M. S., Schwartz, J. H., Gundapaneni, B., Elliott, P. M., Merlini, G., Waddington-Cruz, M., et al. (2018). Tafamidis treatment for patients with transthyretin amyloid cardiomyopathy. *N. Engl. J. Med.* 379, 1007–1016. doi: 10.1056/NEJMoa1805689

Miller, E. C., Teravskis, P. J., Dummer, B. W., Zhao, X., Huganir, R. L., and Liao, D. (2014). Tau phosphorylation and tau mislocalization mediate soluble Aβ oligomer-induced AMPA glutamate receptor signaling deficits. *Eur. J. Neurosci.* 39, 1214–1224. doi: 10.1111/ejn.12507

Minopoli, G., Gargiulo, A., Parisi, S., and Russo, T. (2012). Fe65 matters: new light on an old molecule. *IUBMB Life* 64, 936–942. doi: 10.1002/iub.1094

Mori, T., Koyama, N., Tan, J., Segawa, T., Maeda, M., and Town, T. (2019). Combined treatment with the phenolics (-)-epigallocatechin-3-gallate and ferulic acid improves cognition and reduces Alzheimer-like pathology in mice. *J. Biol. Chem.* 294, 2714–2731. doi: 10.1074/jbc.RA118.004280

Muchowski, P. J. (2002). Protein misfolding, amyloid formation, and neurodegeneration: a critical role for molecular chaperones? *Neuron* 35, 9–12. doi: 10.1016/s0896-6273(02)00761-4

Nakagawa, K., Okuda, S., and Miyazawa, T. (1997). Dose-dependent incorporation of tea catechins, (-)-epigallocatechin-3-gallate and (-)-epigallocatechin, into human plasma. *Biosci. Biotechnol. Biochem.* 61, 1981–1985. doi: 10.1271/bbb.61.1981

Nestler, G. (2002). Traditional Chinese medicine. *Med. Clin. North Am.* 86, 63–73. doi: 10.1016/s0025-7125(03)00072-5

Obregon, D. F., Rezai-Zadeh, K., Bai, Y., Sun, N., Hou, H., Ehrhart, J., et al. (2006). ADAM10 activation is required for green tea (-)-epigallocatechin-3-gallate-induced alpha-secretase cleavage of amyloid precursor protein. *J. Biol. Chem.* 281, 16419–16427. doi: 10.1074/jbc.M600617200

Oliveri, V., and Vecchio, G. (2016). Cyclodextrins as protective agents of protein aggregation: an overview. *Chemis. Asian J.* 11, 1648–1657. doi: 10.1002/asia.201600259

Palhano, F. L., Lee, J., Grimster, N. P., and Kelly, J. W. (2013). Toward the molecular mechanism(s) by which EGCG treatment remodels mature amyloid fibrils. *J. Am. Chem. Soc.* 135, 7503–7510. doi: 10.1021/ja3115696

Pan, K. M., Baldwin, M., Nguyen, J., Gasset, M., Serban, A., Groth, D., et al. (1993). Conversion of alpha-helices into beta-sheets features in the formation of the scrapie prion proteins. *Proc. Natl. Acad. Sci. U S A.* 90, 10962–10966. doi: 10.1073/pnas.90.23.10962

Paushkin, S. V., Kushnirov, V. V., Smirnov, V. N., and Ter-Avanesyan, M. D. (1997). In vitro propagation of the prion-like state of yeast Sup35 protein. *Science* 277, 381–383. doi: 10.1126/science.277.5324.381

Ponzini, E., De Palma, A., Cerboni, L., Natalello, A., Rossi, R., Moons, R., et al. (2019). Methionine oxidation in α-synuclein inhibits its propensity for ordered secondary structure. *J. Biol. Chem.* 294, 5657–5665. doi: 10.1074/jbc.RA118.001907

Prusiner, S. B., Scott, M. R., DeArmond, S. J., and Cohen, F. E. (1998). Prion protein biology. *Cell* 93, 337–348. doi: 10.1016/s0092-8674(00)81163-0

Rambold, A. S., Miesbauer, M., Olschewski, D., Seidel, R., Riemer, C., Smale, L., et al. (2008). Green tea extracts interfere with the stress-protective activity of PrP and the formation of PrP. *J. Neurochem.* 107, 218–229. doi: 10.1111/j.1471-4159.2008.05611.x

Rezai-Zadeh, K., Arendash, G. W., Hou, H., Fernandez, F., Jensen, M., Runfeldt, M., et al. (2008). Green tea epigallocatechin-3-gallate (EGCG) reduces beta-amyloid mediated cognitive impairment and modulates tau pathology in Alzheimer transgenic mice. *Brain Res.* 1214, 177–187. doi: 10.1016/j.brainres.2008.02.107

Rezai-Zadeh, K., Shytle, D., Sun, N., Mori, T., Hou, H., Jeanniton, D., et al. (2005). Green tea epigallocatechin-3-gallate (EGCG) modulates amyloid precursor protein cleavage and reduces cerebral amyloidosis in Alzheimer transgenic mice. *J. Neurosci.* 25, 8807–8814. doi: 10.1523/JNEUROSCI.1521-05.2005

Reznichenko, L., Amit, T., Zheng, H., Avramovich-Tirosh, Y., Youdim, M. B., Weinreb, O., et al. (2006). Reduction of iron-regulated amyloid precursor protein and beta-amyloid peptide by (-)-epigallocatechin-3-gallate in cell cultures: implications for iron chelation in Alzheimer's disease. *J. Neurochem.* 97, 527–536. doi: 10.1111/j.1471-4159.2006.03770.x

Rho, T., Choi, M. S., Jung, M., Kil, H. W., Hong, Y. D., and Yoon, K. D. (2019). Identification of fermented tea (Camellia sinensis) polyphenols and their inhibitory activities against amyloid-beta aggregation. *Phytochemistry* 160, 11–18. doi: 10.1016/j.phytochem.2018.12.013

Roberts, B. E., Duennwald, M. L., Wang, H., Chung, C., Lopreiato, N. P., Sweeny, E. A., et al. (2009). A synergistic small-molecule combination directly eradicates diverse prion strain structures. *Nat. Chem. Biol.* 5, 936–946. doi: 10.1038/nchembio.246

Rocha, E. M., De Miranda, B., and Sanders, L. H. (2018). Alpha-synuclein: Pathology, mitochondrial dysfunction and neuroinflammation in Parkinson's disease. *Neurobiol. Dis.* 109(Pt B), 249–257. doi: 10.1016/j.nbd.2017.04.004

Rubinsztein, D. C. (2006). The roles of intracellular protein-degradation pathways in neurodegeneration. *Nature* 443, 780–786. doi: 10.1038/nature05291

Saini, A. (2016). Physicians of ancient India. *J. Fam. Med. Primary Care* 5, 254–258. doi: 10.4103/2249-4863.192322

Sant'anna, R. O., Braga, C. A., Polikarpov, I., Ventura, S., Lima, L. M., and Foguel, D. (2013). Inhibition of human transthyretin aggregation by non-steroidal anti-inflammatory compounds: a structural and thermodynamic analysis. *Int. J. Mol. Sci.* 14, 5284–5311. doi: 10.3390/ijms14035284

Scheff, S. W., Price, D. A., Schmitt, F. A., DeKosky, S. T., and Mufson, E. J. (2007). Synaptic alterations in CA1 in mild Alzheimer disease and mild cognitive impairment. *Neurology* 68, 1501–1508. doi: 10.1212/01.wnl.0000260698.46517.8f

Schimidt, H. L., Garcia, A., Martins, A., Mello-Carpes, P. B., and Carpes, F. P. (2017). Green tea supplementation produces better neuroprotective effects than red and black tea in Alzheimer-like rat model. *Food Res. Int.* 100(Pt 1), 442–448. doi: 10.1016/j.foodres.2017.07.026

Scholey, A., Downey, L. A., Ciorciari, J., Pipingas, A., Nolidin, K., Finn, M., et al. (2012). Acute neurocognitive effects of epigallocatechin gallate (EGCG). *Appetite* 58, 767–770. doi: 10.1016/j.appet.2011.11.016

Shimmyo, Y., Kihara, T., Akaike, A., Niidome, T., and Sugimoto, H. (2008). Epigallocatechin-3-gallate and curcumin suppress amyloid beta-induced beta-site APP cleaving enzyme-1 upregulation. *Neuroreport* 19, 1329–1333. doi: 10.1097/WNR.0b013e32830b8ae1

Singh, N. A., Bhardwaj, V., Ravi, C., Ramesh, N., Mandal, A., and Khan, Z. A. (2018). EGCG Nanoparticles attenuate aluminum chloride induced neurobehavioral deficits, beta amyloid and tau pathology in a rat model of Alzheimer's Disease. *Front. Aging Neurosci.* 10:244. doi: 10.3389/fnagi.2018.00244

Sinha, S., Du, Z., Maiti, P., Klärner, F. G., Schrader, T., Wang, C., et al. (2012). Comparison of three amyloid assembly inhibitors: the sugar scyllo-inositol, the polyphenol epigallocatechin gallate, and the molecular tweezer CLR01. *ACS Chem. Neurosci.* 3, 451–458. doi: 10.1021/cn200133x

Sironi, E., Colombo, L., Lompo, A., Messa, M., Bonanomi, M., Regonesi, M. E., et al. (2014). Natural compounds against neurodegenerative diseases: molecular characterization of the interaction of catechins from green tea with Aβ1-42, PrP106-126, and ataxin-3 oligomers. *Chemistry* 20, 13793–13800. doi: 10.1002/chem.201403188

Smith, A., Giunta, B., Bickford, P. C., Fountain, M., Tan, J., and Shytle, R. D. (2010). Nanolipidic particles improve the bioavailability and alpha-secretase inducing ability of epigallocatechin-3-gallate (EGCG) for the treatment of Alzheimer's disease. *Int. J. Pharmaceut.* 389, 207–212. doi: 10.1016/j.ijpharm.2010.01.012

Šneideris, T., Baranauskienė, L., Cannon, J. G., Rutkienė, R., Meškys, R., and Smirnovas, V. (2015). Looking for a generic inhibitor of amyloid-like fibril formation among flavone derivatives. *PeerJ* 3:e1271. doi: 10.7717/peerj.1271

Šneideris, T., Sakalauskas, A., Sternke-Hoffmann, R., Peduzzo, A., Ziaunys, M., Buell, A. K., et al. (2019). The environment is a key factor in determining the anti-amyloid efficacy of EGCG. *Biomolecules* 9:855. doi: 10.3390/biom9120855

Sternke-Hoffmann, R., Peduzzo, A., Bolakhrif, N., Haas, R., and Buell, A. K. (2020). The aggregation conditions define whether EGCG is an inhibitor or enhancer of α-synuclein amyloid fibril formation. *Int. J. Mol. Sci.* 21:1995. doi: 10.3390/ijms21061995

Tavanti, F., Pedone, A., and Menziani, M. C. (2020). Insights into the effect of curcumin and (-)-epigallocatechin-3-gallate on the aggregation of Aβ(1-40) monomers by means of molecular dynamics. *Int. J. Mol. Sci.* 21:5462. doi: 10.3390/ijms21155462

Teng, Y., Zhao, J., Ding, L., Ding, Y., and Zhou, P. (2019). Complex of EGCG with Cu(II) suppresses amyloid aggregation and Cu(II)-induced cytotoxicity of α-synuclein. *Molecules* 24:2940. doi: 10.3390/molecules24162940

Tomata, Y., Sugiyama, K., Kaiho, Y., Honkura, K., Watanabe, T., Zhang, S., et al. (2016). Green tea consumption and the risk of incident dementia in elderly japanese: the Ohsaki Cohort 2006 Study. *Am. J. Geriatr. Psychiatry* 24, 881–889. doi: 10.1016/j.jagp.2016.07.009

Trivella, D. B., dos Reis, C. V., Lima, L. M., Foguel, D., and Polikarpov, I. (2012). Flavonoid interactions with human transthyretin: combined structural and thermodynamic analysis. *J. Struct. Biol.* 180, 143–153. doi: 10.1016/j.jsb.2012.07.008

van het Hof, K. H., Kivits, G. A., Weststrate, J. A., and Tijburg, L. B. (1998). Bioavailability of catechins from tea: the effect of milk. *Eur. J. Clin. Nutrit.* 52, 356–359. doi: 10.1038/sj.ejcn.1600568

Varga, J., Dér, N. P., Zsindely, N., and Bodai, L. (2020). Green tea infusion alleviates neurodegeneration induced by mutant Huntingtin in *Drosophila*. *Nutrit. Neurosci.* 23, 183–189. doi: 10.1080/1028415X.2018.1484021

Vaz, M., and Silvestre, S. (2020). Alzheimer's disease: recent treatment strategies. *Eur. J. Pharmacol.* 887, 173554. doi: 10.1016/j.ejphar.2020.173554

Verma, M., Vats, A., and Taneja, V. (2015). Toxic species in amyloid disorders: oligomers or mature fibrils. *Ann. Ind. Acad. Neurol.* 18, 138–145. doi: 10.4103/0972-2327.144284

Vilela, M. M., Salvador, S. L., Teixeira, I., Del Arco, M., and De Rossi, A. (2020). Efficacy of green tea and its extract, epigallocatechin-3-gallate, in the reduction of cariogenic microbiota in children: a randomized clinical trial. *Arch. Oral Biol.* 114:104727. doi: 10.1016/j.archoralbio.2020.104727

Wang, R., Zhou, W., and Jiang, X. (2008). Reaction kinetics of degradation and epimerization of epigallocatechin gallate (EGCG) in aqueous system over a wide temperature range. *J. Agricult. Food Chem.* 56, 2694–2701. doi: 10.1021/jf0730338

Wang, S. H., Dong, X. Y., and Sun, Y. (2012). Thermodynamic analysis of the molecular interactions between amyloid β-protein fragments and (-)-epigallocatechin-3-gallate. *J. Physic. Chem. B* 116, 5803–5809. doi: 10.1021/jp209406t

Wang, S. H., Liu, F. F., Dong, X. Y., and Sun, Y. (2010). Thermodynamic analysis of the molecular interactions between amyloid beta-peptide 42 and (-)-epigallocatechin-3-gallate. *J. Phys. Chem. B* 114, 11576–11583. doi: 10.1021/jp1001435

Wang, Y., Latshaw, D. C., and Hall, C. K. (2017). Aggregation of Aβ(17-36) in the presence of naturally occurring phenolic inhibitors using coarse-grained simulations. *J. Mol. Biol.* 429, 3893–3908. doi: 10.1016/j.jmb.2017.10.006

Wechalekar, A. D., Gillmore, J. D., and Hawkins, P. N. (2016). Systemic amyloidosis. *Lancet* 387, 2641–2654. doi: 10.1016/S0140-6736(15)01274-X

Wen, L., Jiang, Y., Yang, J., Zhao, Y., Tian, M., and Yang, B. (2017). Structure, bioactivity, and synthesis of methylated flavonoids. *Ann. N Y. Acad. Sci.* 1398, 120–129. doi: 10.1111/nyas.13350

Wiley, J. C., Smith, E. A., Hudson, M. P., Ladiges, W. C., and Bothwell, M. (2007). Fe65 stimulates proteolytic liberation of the beta-amyloid precursor protein intracellular domain. *J. Biol. Chem.* 282, 33313–33325. doi: 10.1074/jbc.M706024200

Xu, Y., Zhang, Y., Quan, Z., Wong, W., Guo, J., Zhang, R., et al. (2016). epigallocatechin gallate (egcg) inhibits alpha-synuclein aggregation: a potential agent for Parkinson's Disease. *Neurochem. Res.* 41, 2788–2796. doi: 10.1007/s11064-016-1995-9

Xuan, L., Zhang, J., Ji, J., Hu, J., and Li, F. (2020). oroxylin a exerts its antitumor effects in human gallbladder cancer via inhibition of the PTEN/PI3K/AKT signaling pathway. *Biol. Pharmaceut. Bull.* 43, 1511–1518. doi: 10.1248/bpb.b20-00262

Yakupova, E. I., Bobyleva, L. G., Vikhlyantsev, I. M., and Bobylev, A. G. (2019). Congo Red and amyloids: history and relationship. *Biosci. Rep.* 39:BSR20181415. doi: 10.1042/BSR20181415

Yan, Z., Zhong, Y., Duan, Y., Chen, Q., and Li, F. (2020). Antioxidant mechanism of tea polyphenols and its impact on health benefits. *Anim. Nutrit.* 6, 115–123. doi: 10.1016/j.aninu.2020.01.001

Yang, J. E., Rhoo, K. Y., Lee, S., Lee, J. T., Park, J. H., Bhak, G., et al. (2017). EGCG-mediated protection of the membrane disruption and cytotoxicity caused by the 'active oligomer' of α-synuclein. *Sci. Rep.* 7:17945. doi: 10.1038/s41598-017-18349-z

Yao, Y., Tang, Y., and Wei, G. (2020). epigallocatechin gallate destabilizes α-synuclein fibril by disrupting the E46-K80 salt-bridge and inter-protofibril interface. *ACS Chem. Neurosci.* 11, 4351–4361. doi: 10.1021/acschemneuro.0c00598

Yoshida, W., Kobayashi, N., Sasaki, Y., Ikebukuro, K., and Sode, K. (2013). Partial peptide of α-synuclein modified with small-molecule inhibitors specifically inhibits amyloid fibrillation of α-synuclein. *Int. J. Mol. Sci.* 14, 2590–2600. doi: 10.3390/ijms14022590

Yuan, Z. M., Huang, Y., Ishiko, T., Kharbanda, S., Weichselbaum, R., and Kufe, D. (1997). Regulation of DNA damage-induced apoptosis by the c-Abl tyrosine kinase. *Proc. Natl. Acad. Sci. U S A.* 94, 1437–1440. doi: 10.1073/pnas.94.4.1437

Zhan, C., Chen, Y., Tang, Y., and Wei, G. (2020). Green tea extracts EGCG and EGC display distinct mechanisms in disrupting $A\beta_{42}$ protofibril. *ACS Chem. Neurosci.* 11, 1841–1851. doi: 10.1021/acschemneuro.0c00277

Zhang, B., Cheng, X. R., da Silva, I. S., Hung, V. W., Veloso, A. J., Angnes, L., et al. (2013). Electroanalysis of the interaction between (-)-epigallocatechin-3-gallate (EGCG) and amyloid-β in the presence of copper. *Metallomics Integr. Biomet. Sci.* 5, 259–264. doi: 10.1039/c3mt20106f

Zhang, J., Zhou, X., Yu, Q., Yang, L., Sun, D., Zhou, Y., et al. (2014). Epigallocatechin-3-gallate (EGCG)-stabilized selenium nanoparticles coated with Tet-1 peptide to reduce amyloid-β aggregation and cytotoxicity. *ACS Appl. Mater. Interf.* 6, 8475–8487. doi: 10.1021/am501341u

Zhang, T., Zhang, J., Derreumaux, P., and Mu, Y. (2013). Molecular mechanism of the inhibition of EGCG on the Alzheimer Aβ(1-42) dimer. *J. Phys. Chemist. B* 117, 3993–4002. doi: 10.1021/jp312573y

Zhang, X., Wu, M., Lu, F., Luo, N., He, Z. P., and Yang, H. (2014). Involvement of α7 nAChR signaling cascade in epigallocatechin gallate suppression of β-amyloid-induced apoptotic cortical neuronal insults. *Mol. Neurobiol.* 49, 66–77. doi: 10.1007/s12035-013-8491-x

Zhang, Z. X., Li, Y. B., and Zhao, R. P. (2017). Epigallocatechin gallate attenuates β-amyloid generation and oxidative stress involvement of PPARγ in N2a/APP695 cells. *Neurochemic. Res.* 42, 468–480. doi: 10.1007/s11064-016-2093-8

Zhao, J., Xu, L., Liang, Q., Sun, Q., Chen, C., Zhang, Y., et al. (2017). Metal chelator EGCG attenuates Fe(III)-induced conformational transition of α-synuclein and protects AS-PC12 cells against Fe(III)-induced death. *J. Neurochem.* 143, 136–146. doi: 10.1111/jnc.14142

Conflict of Interest: The authors declare that the research was conducted in the absence of any commercial or financial relationships that could be construed as a potential conflict of interest.

Publisher's Note: All claims expressed in this article are solely those of the authors and do not necessarily represent those of their affiliated organizations, or those of the publisher, the editors and the reviewers. Any product that may be evaluated in this article, or claim that may be made by its manufacturer, is not guaranteed or endorsed by the publisher.

frontiers in Molecular Neuroscience

ORIGINAL RESEARCH
published: 11 February 2022
doi: 10.3389/fnmol.2022.804702

Amyloid Beta Is Internalized *via* Macropinocytosis, an HSPG- and Lipid Raft-Dependent and Rac1-Mediated Process

Keyoumu Nazere[1], *Tetsuya Takahashi*[1,2]*, *Naoyuki Hara*[1], *Kazuki Muguruma*[1], *Masahiro Nakamori*[1], *Yu Yamazaki*[1], *Hiroyuki Morino*[1,3] *and Hirofumi Maruyama*[1]

[1]*Department of Clinical Neuroscience and Therapeutics, Hiroshima University Graduate School of Biomedical and Health Sciences, Hiroshima, Japan,* [2]*Department of Rehabilitation, Faculty of Rehabilitation, Hiroshima International University, Hiroshima, Japan,* [3]*Department of Medical Genetics, Tokushima University Graduate School of Biomedical Sciences, Tokushima, Japan*

Intracellular amyloid β peptide (Aβ) accumulation has drawn attention in relation to the pathophysiology of Alzheimer's disease in addition to its extracellular deposition as senile plaque. Cellular uptake of extracellular Aβ is one of the possible mechanisms by which intracellular Aβ deposits form. Given the relevance of Aβ inside cells, it is important to understand the mechanism by which it is taken up by them. In this study, we elucidated that Neuro2A and SH-SY5Y cells internalize specifically oligomerized Aβ in a time- and dose-dependent manner. The depletion of plasma membrane cholesterol with methyl-β-cyclodextrin or treatment with trypsin diminished the internalization of oAβ, suggesting that the oAβ uptake might be both a lipid raft-dependent and heparan sulfate proteoglycan-mediated process. Treatment with a macropinocytosis inhibitor (ethylisopropyl amiloride and wortmannin) also drastically reduced the uptake of oligomer-Aβ (oAβ). oAβ-treated cells exhibited an increase in Rac1 activity, indicating that macropinocytosis induced by oAβ is regulated by these small GTPases. These findings suggest that macropinocytosis is a major endocytic route through which oAβ42 enters cells.

Keywords: Alzheimer's disease, amyloid – beta, HSPG, lipid raft, macropinocytosis, Rac1

OPEN ACCESS

Edited by:
Jinghui Luo,
Paul Scherrer Institut (PSI), Switzerland

Reviewed by:
Luis Gerardo Aguayo,
University of Concepcion, Chile
Homira Behbahani,
Karolinska Institutet (KI), Sweden

***Correspondence:**
Tetsuya Takahashi
tetakaha@mac.com

Specialty section:
This article was submitted to Brain Disease Mechanisms, a section of the journal Frontiers in Molecular Neuroscience

Received: *02 December 2021*
Accepted: *17 January 2022*
Published: *11 February 2022*

Citation:
Nazere K, Takahashi T, Hara N, Muguruma K, Nakamori M, Yamazaki Y, Morino H and Maruyama H (2022) Amyloid Beta Is Internalized via Macropinocytosis, an HSPG- and Lipid Raft-Dependent and Rac1-Mediated Process. Front. Mol. Neurosci. 15:804702. doi: 10.3389/fnmol.2022.804702

INTRODUCTION

Alzheimer's disease (AD) is the most common form of dementia, which is histopathologically characterized by the presence of senile plaques and neurofibrillary tangles (NFTs; Belyaev et al., 2010; Viola and Klein, 2015; Frost and Li, 2017). Senile plaques are extracellular deposits of aggregated amyloid β peptide (Aβ), while NFTs are intracellular aggregates composed mainly of hyperphosphorylated tau protein (Serrano-Pozo et al., 2011). Aβ is a 40- or 42-amino-acid peptide produced through the cleavage of amyloid precursor protein by β- and γ-secretase (Belyaev et al., 2010; Serrano-Pozo et al., 2011;

Abbreviations: AD, Alzheimer's disease; Aβ, amyloid beta; ANOVA, analysis of variance; CTB, cholera toxin B subunit; DAPI, 4',6-diamidino-2-phenylindole; DMEM, Dulbecco's Modified Eagle Medium; EIPA, 5-(N-ethyl-N-isopropyl)-amiloride; HFIP, 1,1,1,3,3,3-hexafluoro-2-propanol; HSPG, heparan sulfate proteoglycan; MβCD, methyl-β-cyclodextrin; NFT, neurofibrillary tangle; oAβ, oligomeric amyloid beta.

Frost and Li, 2017). In addition to both ends of monomer state and fibril, distinct intermediate species of Aβ42 in the form of low-molecular-weight oligomers, such as dimers, trimers, and larger spherical oligomers, so-called Aβ-derived diffusible ligands, have been reported (Serrano-Pozo et al., 2011). The overproduction of Aβ42 or impairment of its proper clearance is pivotal in the appearance of senile plaques, which is thought to be an event leading to the formation of NFTs (Singh et al., 2016). Apart from senile plaques as extracellular Aβ42 deposits, increasing evidence has demonstrated the pathological relevance of intracellular Aβ42 (Takahashi et al., 2004; Chafekar et al., 2008; Ansari et al., 2009; Bharadwaj et al., 2009; Thal et al., 2015); however, the precise mechanism that links NFT formation and intracellular as well as extracellular Aβ42 remains unclear. Regarding the mechanism behind the appearance of intracellular Aβ42, several studies have reported that the generation of Aβ42 might take place inside intracellular vesicles such as endosomes (Zhang and Song, 2013; Schützmann et al., 2021). Another plausible manner by which intracellular Aβ42 will appear is that cells actively take up the secreted Aβ42 and traffic it to multivesicular bodies (Friedrich et al., 2010). Although Aβ42 might appear inside cells not in an exclusive manner, information on the mechanism by which Aβ42 can be internalized should be valuable in the search for future therapeutics for AD.

Living cells can endocytose a diverse array of extracellular materials such as solute molecules, nutrients, and antigens, and the vast majority of viruses hijack these mechanisms at the initial step of infection (Doherty and McMahon, 2009). Among a variety of types of endocytosis, clathrin-dependent endocytosis is the most extensively studied, using transferrin as a representative marker (Mayor and Pagano, 2007). Recently, findings on macropinocytosis among the rest of endocytosis (non-clathrin endocytosis) have emerged. Macropinosome formation is driven by the rearrangement of actin filaments underlying the plasma membrane, which is regulated by PI3K, Rac1, and Arf6 (Swanson and Watts, 1995). Human immunodeficiency virus (HIV) virion and the technique of gene delivery of lipoplexes utilize macropinocytosis (Letoha et al., 2013). Interestingly, the oligomer of human amylin, a 37-amino-acid peptide produced by pancreatic beta cells, plays a role in the pathogenesis of type 2 diabetes mellitus, as Aβ does in AD. In the case of amylin, oligomeric amylin has been shown to be taken up into islet cells *via* macropinocytosis, which raises the possibility that the mechanism of oligomer-Aβ (oAβ)42 internalization is the same as that for amylin (Clark and Nilsson, 2004; Trikha and Jeremic, 2011, 2013).

To test this hypothesis, we examined the dynamics of Aβ42 internalization using culture cells, including non-neuronal cells, and found that cells take up Aβ42 in a time- and concentration-dependent manner. We next found that the uptake process requires both intact heparan sulfate proteoglycan (HSPG)s and lipid rafts. We also discovered that the macropinocytosis process regulated by Rac1 is involved in the uptake of oligomeric Aβ42 (oAβ42).

METHODS AND REAGENTS

Reagents

FITC-labeled Aβ42 was purchased from GL Biochem Ltd. (Shanghai, China); TMR-labeled Aβ42, FITC-dextran (MW: 70,000), a marker for the macropinocytosis pathway, FITC-Cholera Toxin B subunit (CTB), a marker of Lipid raft, heparin sodium salt an inhibitor of HSPGs, and methyl-β-cyclodextrin (MβCD) that can disrupt lipid raft, were obtained from Sigma-Aldrich (St. Louis, MO, USA); ethylisopropyl amiloride (EIPA) a blockef of macropinocytosis, SecinH3, an indirect inhibitor of Arf6, Grassofermata (NAV 2729) a direct inhibitor of Arf6, and EHT1864, a Rac1 inhibitor of were purchased from Cayman chemical (Ann Arbor, MI, USA); dynasore (ab120192), a dynamin inhibitor was from Abcam (Cambridge, MA, USA), Alexa Fluor 488 transferrin and phalloidin were obtained from Invitrogen (Carlsbad, CA, USA); wortmannin, a phosphoinositide 3-kinase inhibitor, Dulbecco's Modified Eagle Medium (DMEM) cell culture medium, phenol red-free Ham's F12 Medium, 0.25% trypsin-EDTA, and 1,1,1,3,3,3-hexafluoro-2-propanol (HFIP) were from Fujifilm Wako Pure Chemical Corporation (Osaka, Japan); fetal bovine serum was from COSMO BIO (Tokyo, Japan); and Hoechst 33342 and 4',6-diamidino-2-phenylindole (DAPI), were from Dojindo (Kumamoto, Japan). G-LISA (ELISA-based GTPase activation assay) kits obtained from Cytoskeleton (Denver, CO, USA) were used to measure the activities of Rac1 and Arf6.

Preparation of Amyloid Beta Monomers and Oligomers

We first allowed lyophilized Aβ42 to equilibrate at room temperature for 30 min, followed by the addition of 200 μl of HFIP to obtain a 1 mM solution and vortexing the solution for a few seconds. After evaporation of HFIP overnight in a fume hood, Aβ42 peptide in microtubes was transferred to a vacuum concentrator and dried down for 1 h without heating to remove any remaining traces of HFIP and moisture. The dried peptide films in microtubes were stored with a desiccant at -20°C. The stored peptide films were allowed to come to room temperature at the time of usage. Subsequently, the peptide film was reconstituted in dimethylsulfoxide (DMSO) and the solution was sonicated for 10 min in a bath sonicator to make 5 mM Aβ42 solution. Ice-cold H_2O was added to obtain a monomeric Aβ42 (mAβ42) solution with a final concentration of 100 μM, vortexed for 15 s, and used immediately. As for the preparation of oAβ42 (100 μM), dried peptide film of Aβ42 was dissolved in DMSO, mixed well with the phenol red-free Ham's F12 medium, and incubated for 6 h at 4°C.

The 5 μM of TMR-Aβ42 samples prepared as monomer or oligomer were subjected to non-reducing SDS-PAGE using 16.5% Tris-Tricine gel. After electrophoresis, the fluorescence in the gel was observed on a UV illuminator to check the monomeric or oligomeric status.

Cell Cultures and Treatments

Neuro2A, SH-SY5Y, HeLa, and HEK293T cells were cultured in DMEM supplemented with 10% (v/v) fetal bovine serum and

1% penicillin/streptomycin at 37°C in a humidified incubator with 5% CO_2. Cells were passaged bi-weekly. Passages 2–10 were used for all of the experiments. Cells were plated at a density of 50,000 cells/well and cultured for 24 h before the treatment with oAβ42 unless otherwise indicated. In the experiments using inhibitors, cells were pretreated with EIPA (80 μM), wortmannin (300 nM), or dynasore (80 mM) for 1 h, or 10 mM or 20 mM MβCD, and 50 ng/ml heparin sodium salt for 30 min, followed by the addition of oAβ42 at the indicated concentrations for 90 min.

To test whether Arf6, a small GTPase, is involved in the cellular uptake of oAβ42, Neuro2A cells were cultured with oAβ42 in the presence of the direct or indirect inhibitor of Arf6 (NAV 2729 at 5 μM or SecinH3 at 150 μM for 1 h), followed by washing with chilled PBS, fixing, and then staining of nuclei with DAPI. Neuro2A cells and SH-SY5Y cells were first incubated with 5 μM EHT1864, a Rac1 inhibitor, at 37°C for 60 min, and then treated with oAβ42 for 90 min.

To explore the effect of the mode of culture passage on the entry of oAβ42, two types of culture dishes were prepared. In one type, cells were passaged using a scraper to dissociate them and maintain the cell surface HSPGs. In the other dishes, cells were dissociated by 8 min of treatment with 0.25% trypsin-EDTA to cleave HSPGs. Each dissociated floating cell was treated with oAβ42 for 90 min, centrifuged at 500× *g* for 3 min, and then washed twice with DMEM to discard the free oAβ42. The cells were further incubated for 24 h before microscopic examination.

To visualize actin filaments with Alexa-488 phalloidin, cells were treated with oAβ42 for 90 min, followed by washing with chilled PBS, fixing with 4% paraformaldehyde (PFA) for 15 min, and then processing with permeabilization and blocking, using a mixed solution of 0.5% saponin and 5% normal goat serum, 137 mM sodium glutamate, 2 mM $MgCl_2$, and 1 mg/ml BSA, pH 6.8, for 4 h at 4°C. After two final washes in ice-cold PBS, coverslips were mounted on slides using DAPI.

Confocal Microscopy

The cells were incubated with TMR- or FITC-labeled oAβ42 and the FITC-labeled endocytosis marker dextran at 37°C for 90 min. After washing, the cells were fixed with 4% PFA and permeabilized. Images were obtained using a confocal laser scanning microscope (FV1000-D IX81; Olympus, Tokyo, Japan). Three 50 mW solid-state lasers (405, 488, and 568 nm) coupled to an acoustic-optical tunable filter were used. The degree of internalization of oAβ42 and its accumulation in Neuro2A and SH-SY5Y cells were determined using ImageJ. The integrated amount of oAβ42 accumulated in the cell corrected by the background represented the total ligand uptake. Briefly, the cell contour in each plane was determined by increasing the brightness of the image. In some cases, brightfield images were also taken to help identify cell contours. Upon various pharmacological treatments, all intact cells in each image area were evaluated for quantitative oAβ42 uptake, based on the FITC signal intensity of the green channel and the TMR signal of the red channel. Briefly, regions of interest corresponding to oAβ42 and dextran deposits that stained positively for DAPI were created by thresholding (auto-thresholding). Among several methods for auto-thresholding in ImageJ, we used default and B&W switches to minimize background noise and convert the original grayscale image to a binary image.

Measurements of Small GTPase Activities

Several GTPases have been shown to be activated in the course of macropinocytosis. To explore the possibility of this occurring in the process of oAβ42 internalization, we assessed the changes in the activity of small GTPases (Rac1 and Arf6) under oAβ42 treatment. Neruo2A cells were incubated with oAβ42 in 35 mm culture dishes for 7, 15, and 30 min (for the Arf6 activation assay, we additionally prepared 3 and 5 min culture dishes) as distinctive groups, and the cell lysates were collected. Rac1 and Arf6 activities in the lysates were measured using the respective G-LISA absorbance-based activation assay kits (Cytoskeleton Inc., Denver, CO, USA). Briefly, Neuro2A cells were lysed in a buffer provided by the manufacturer, and clarified lysates were incubated in Rac1/Arf6-GTP-binding protein-coated wells. Following washes to remove nonspecific binding, bound Rac1/Arf6-GTP was detected using anti-Rac1 or Arf6 primary and HRP-linked secondary antibodies. The read-out was obtained at a wavelength of 490 nm.

Statistics

Data are presented as mean ± standard error of the mean (SEM) of three replicate experiments. Statistical analysis was performed by one-way analysis of variance (ANOVA) using JMP Pro15 (SAS Institute, Cary, NC, USA), followed by multiple comparisons with Dunnett's test to test for differences in mean fluorescent intensity between samples and differences in the activities of GTPases (Rac1 and Arf6) among groups.

RESULTS

Time and Dose Dependence of Cellular Uptake of Amyloid Beta

Intracellular Aβ42 has attracted substantial attention over the past few years (Chafekar et al., 2008; Dorostkar et al., 2015). One of the possible reasons why Aβ42 is observed in cells is that extracellularly generated Aβ42 enters them. To test this possibility, we examined the dynamics of internalization of oAβ42 peptides of different concentrations using Neuro2A cells. The culture medium with 5 μM FITC-labeled oAβ42 was replaced with fresh DMEM without peptide at the time points of 30, 60, and 90 min. The representative photographs in **Figure 1** illustrate an increase in intracellularly accumulated punctate oAβ42. In the time-dependent uptake experiment (**Figures 1A–C**), the level of internalized oAβ42 was 4.2-fold higher at 60 min [95% confidence interval (CI) 3.99–4.36; $p < 0.0001$] and 7.5-fold higher at 90 min (95% CI 7.19–7.87; $p < 0.0001$) than that at 30 min (31.39 ± 8.3).

Next, we treated the cells with different concentrations of FITC-labeled oAβ42 (1, 2, and 5 μM) for 90 min at 37°C. In this dose-dependent uptake experiment (**Figures 1B–D**), compared with 1 μM (50.47 ± 3.6), the signal intensity of oAβ42 at 2 μM increased by 2.8- fold (95% CI 2.65–2.82; $p < 0.0001$) and that at 5 μM by 4.8-fold (95% CI 4.60–4.88;

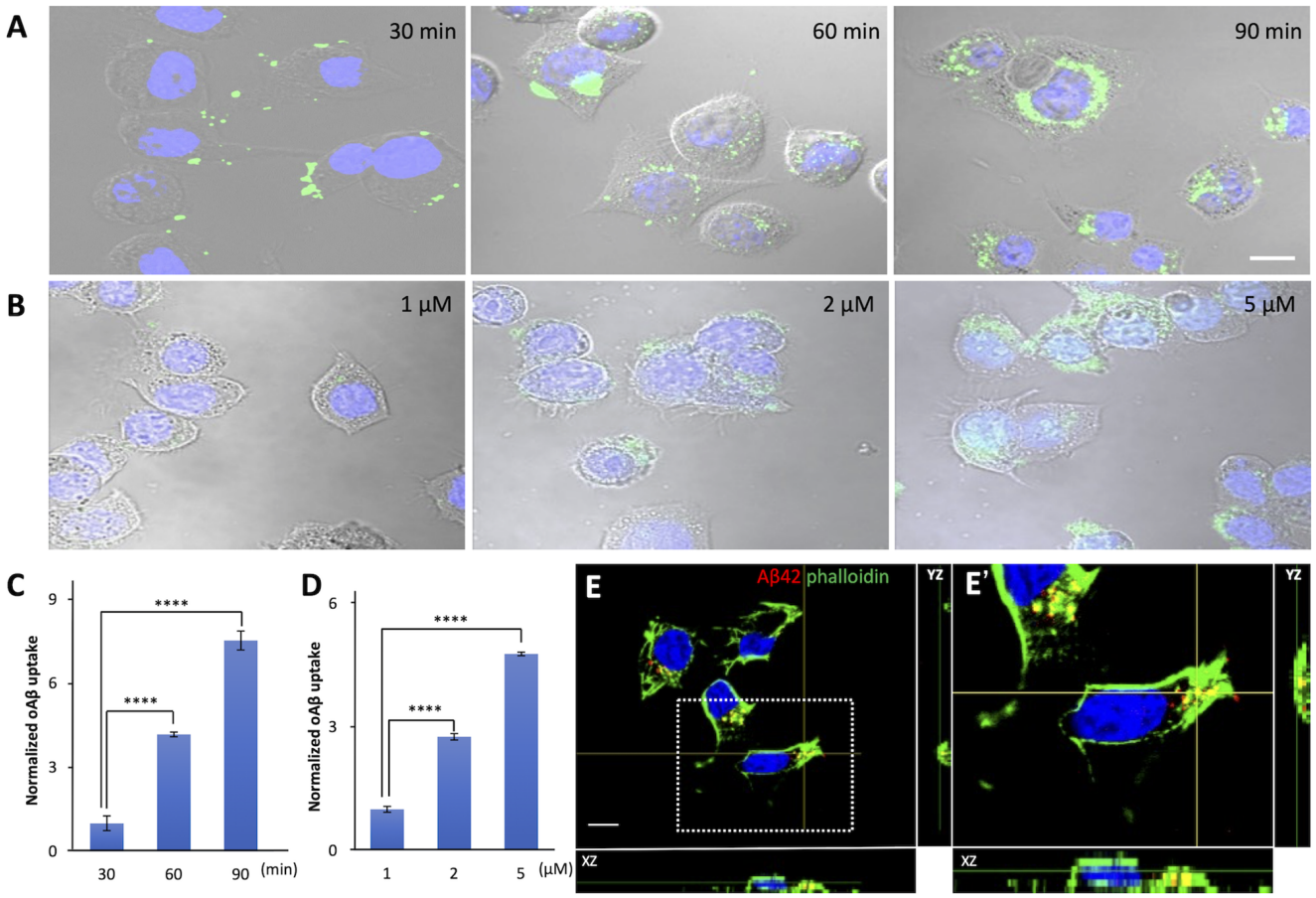

FIGURE 1 | The time and dose dependence of cellular uptake of amyloid beta in neuroblastoma cells. **(A)** Neuro2A cells were allowed to internalize 5 μM FITC-labeled oAβ42 for 30, 60, and 90 min, followed by washing and fixation. Nuclei were stained with DAPI (blue). **(B)** Neuro2A cells were treated with 1, 2, and 5 μM oAβ42 for 90 min and nuclei were stained with DAPI. All experiments were repeated three times. Quantification of the fluorescence intensity shows **(C)** a time-dependent increase in intracellular oAβ42 and **(D)** a dose-dependent increase in intracellular oAβ42. All experiments were repeated three times. Data are presented as mean ± SEM, and data are presented as mean fluorescence normalized to 30 min or 1 μM. Error bars indicate standard error ($n = 3$). Significance was established using ANOVA followed by the Dunnett–Square test. Scale bar = 10 μm. **(E)** The two orthogonal views (XZ and YZ) on confocal microscopy showed that oAβ42 labeled with TMR was surrounded by actin (arrows) labeled with phalloidin (green). The nuclei were visualized with DAPI (blue). An enlarged view of the boxed region is shown in **(E')**. Scale bar = 10 μm. ****$p < 0.0001$.

$p < 0.0001$). Taking these findings together, oAβ42 is taken up into cells in a time- and dose-dependent manner. We next tested the ability of 5 μM mAβ42 to enter Neuro2a cells after 90 min of incubation; however, mAβ42 exhibited a capacity for internalization only comparable to a lower concentration (1 μM) of oAβ42 (**Supplementary Figures 1A,B**). Next, both mAβ42 and oAβ42 were placed in a Tris-Tricine gel to check whether they were in a monomeric or oligomeric form. Here, peptides were dissolved in gel loading buffer and electrophoresed in a 16.5% Tris-Tricine gel at 100 V for 120 min, followed by observation under 312 nm UV light (**Supplementary Figure 1C**).

To confirm that oAβ was taken up into cells, we analyzed confocal micrographs three-dimensionally. The two orthogonal views from different planes (XZ and YZ) of the images showed that oAβ42 labeled with TMR localized not on the surface of cell membranes but inside the cells. Notably, the oAβ42 inside the cells was surrounded by actin, as visualized by phalloidin (**Figures 1E,E'**).

Amyloid Beta Oligomer Uptake Is Dependent on Intact Lipid Rafts

Lipid rafts are highly organized membrane domains enriched with cholesterol/sphingolipid and play roles in various types of endocytosis in the initial binding steps (Nichols, 2003; Rushworth and Hooper, 2010; Bieberich, 2018). We examined whether lipid rafts are also involved in the cellular uptake of oAβ42 using MβCD, which depletes cholesterol from the membrane, thereby disrupting lipid rafts. As shown in **Figures 2A,B**, MβCD decreased the uptake of oAβ42 (46.6% with 10 mM and 82.5% with 20 mM, respectively; $p < 0.0001$) in a manner dependent on the concentration of MβCD. This indicates that the lipid rafts are critical in the process of oAβ42 internalization.

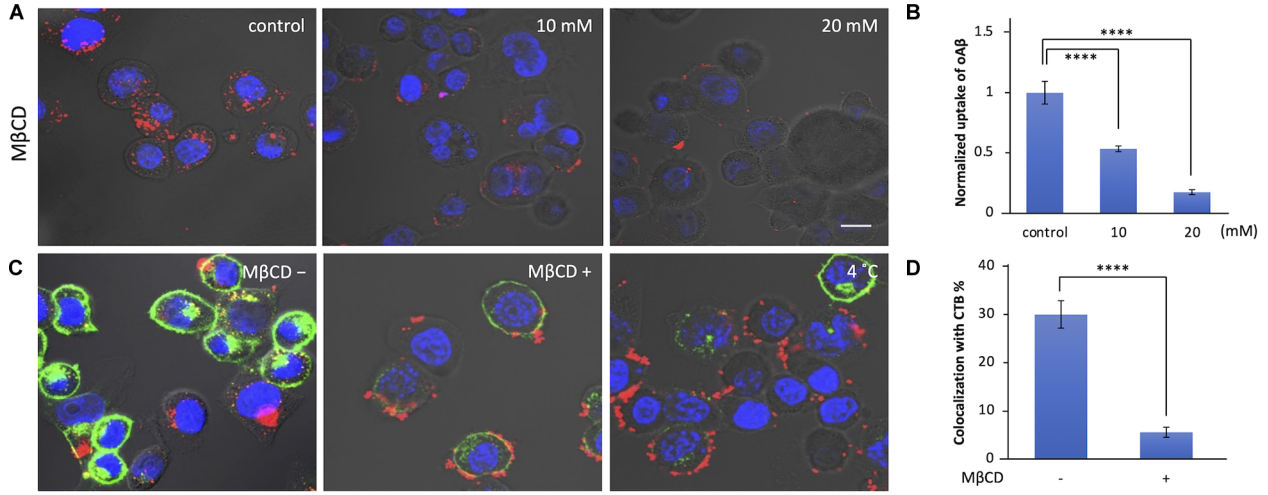

FIGURE 2 | Effect of lipid raft disruption with cyclodextrin on oAβ42 uptake. **(A)** Neuro2A cells were pretreated with MβCD (10 or 20 mM) for 30 min at 37°C; then, the cell culture medium was exchanged with that with 5 μM oAβ42 and incubated for 90 min at 37°C. Nuclei were visualized with Hoechst 33342 (blue). **(B)** Quantification of the fluorescence intensity shows the uptake of oAβ42, and data are presented as mean fluorescence normalized to control. Significance was established using ANOVA followed by the Dunnett–Square test. Data are presented as mean ± SEM. All experiments were repeated three times. **(C)** Neuro2A cells were incubated with or without 10 mM MβCD for 30 min at 37°C, followed by incubation with 20 μg/ml CTB for 10 min at 4°C. Subsequently, cells were further incubated at 37°C for 90 min in combination with oAβ42 (5 μM). Alternatively, Neuro2A cells were pretreated with 5 μM oAβ42 and 20 μg/ml CTB at 4°C for 10 min, and then at 37°C for 90 min. **(D)** Quantification of the colocalization of oAβ42 and CTB (colocalization/total) in the absence or presence of MβCD (10 mM). All experiments were repeated three times. Data are presented as mean ± SEM. Significance was established by Student's t-test. Scale bars = 10 μm. ****$p < 0.0001$.

To visualize lipid rafts, Neuro2A cells were incubated in the presence of CTB, a nontoxic portion of cholera toxin with high affinity to the GM1 ganglioside (Gupta and DeFranco, 2003). As shown in **Figures 2C,D**, we observed that 30.0% of CTB colocalized with oAβ42; in addition, in the presence of MβCD, the colocalization rate was significantly reduced to 5.6%. Alternatively, Neuro2A cells were simultaneously treated with oAβ42 and CTB at 4°C for 10 min to facilitate the staining of lipid rafts, and then at 37°C for 90 min (**Figure 2C**, right). In this case, prolonged attachment of oAβ42 to the surface of cells would facilitate the further accumulation of oAβ42 into aggregates, which appeared as deposits. Lowering the temperature might block molecules that are involved in the internalization of oAβ42.

HSPGs Mediate Amyloid Beta Oligomer Uptake

Heparan sulfate proteoglycans (HSPGs) on the cell surface can function as co-receptors of the diverse array of receptors and actively internalize various substrates into the cells. We examined whether oAβ42 internalization is an HSPG-mediated process using trypsin and heparin, given that trypsin can cleave HSPGs and heparin can block HSPGs. In the experiment using trypsin, we dissociated cells with 0.25% trypsin-EDTA at culture passage and treated them with oAβ42. Subsequently, the cells were collected and washed twice with medium to discard unincorporated oAβ42, followed by further incubationof the cells attached to the bottom of the dishes. For comparison, another group of cells was dissociated using a scraper to keep HSPGs intact during culture passage. As shown in **Figure 3G**, quantitative analysis of the results showed a clear reduction in the amount of oAβ42 inside the cells passaged using trypsin in both Neuro2A cells (scraper: 224.0 ± 20.3 vs. trypsin: 33.4 ± 4.1, $p < 0.0001$; **Figures 3A,B**) and SH-SY5Y cells (scraper: 214.8 ± 17.8 vs. trypsin: 37.4 ± 4.5, $p < 0.0001$; **Figures 3C,D**). Next, we used heparin as a blocker for HSPGs to examine whether it can interfere with the oAβ42 uptake activity of Neuro2A cells (**Figures 3E,F**). We found that 30 min of pretreatment with heparin significantly decreased intracellular oAβ42 by 6.9-fold compared with that of untreated cells (treated: 34.9 ± 8.8 vs. untreated: 241.6 ± 13.1, $p < 0.0001$; **Figure 3H**).

Amyloid Beta Oligomer Is Internalized Into Cells by Macropinocytosis

Evidence has demonstrated that, in neuronal cells, macropinocytosis is mediated by HSPGs (Holmes et al., 2013). It has also been reported that both HSPGs and lipid rafts are involved in the internalization of proteins released by eosinophils (Fan et al., 2007) and the HIV Tat protein transduction domain (Imamura et al., 2011). Since our results showed that oAβ42 is internalized in a lipid raft-dependent and HSPG-mediated manner, we examined whether oAβ42 was taken up by cells *via* macropinocytosis. Neuro2A cells were pretreated for 1 h with EIPA, a Na^+/H^+ exchanger inhibitor, or wortmannin, a phosphoinositide 3-kinase inhibitor, both of which can block macropinocytosis. Subsequently, cells were cultured in a medium containing oAβ42 with dextran or transferrin. The pretreatment with EIPA or wortmannin attenuated the signals from oAβ42 and dextran (**Figure 4A**). In contrast, these pretreatments did not noticeably change the amount of intracellular transferrin. To test the possible role of clathrin-dependent endocytosis in the internalization of oAβ42, cells were treated with dynasore, a cell-permeable inhibitor of dynamin. As

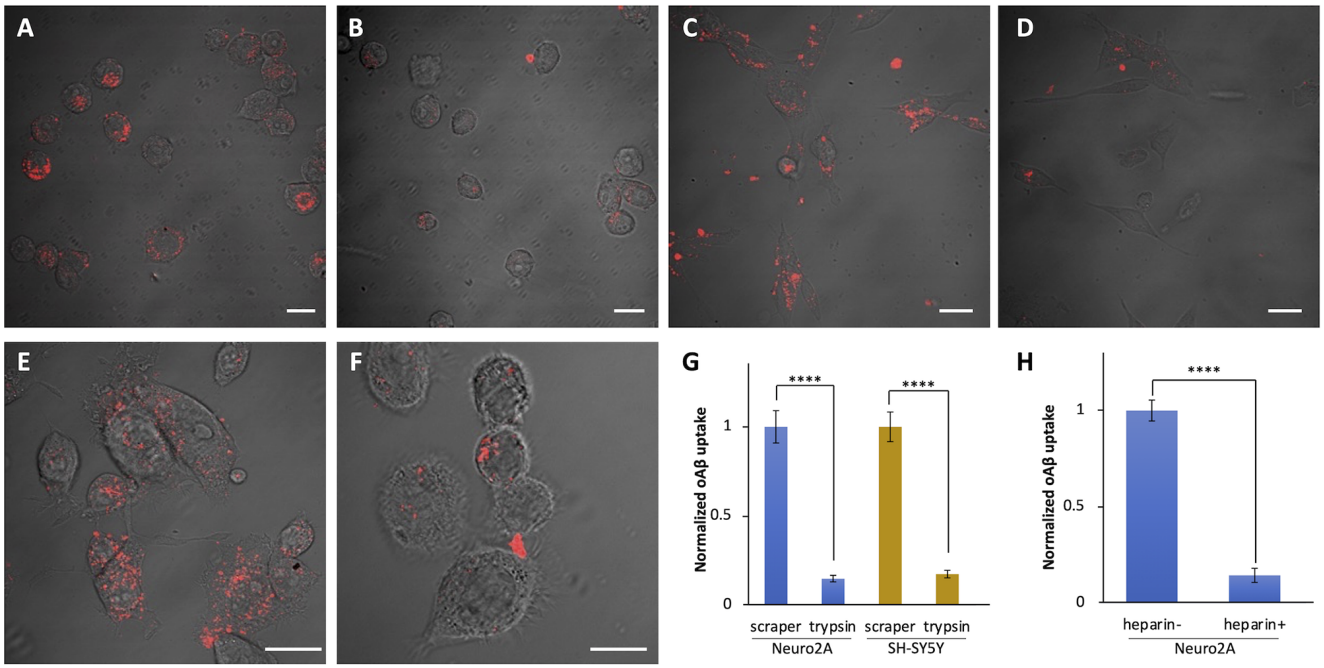

FIGURE 3 | Impaired uptake of oAβ42 by the treatment with heparin and trypsin. **(A,B)** Neuro2A cells were dissociated using a scraper **(A)** or by 8 min of treatment with 0.25% trypsin-EDTA **(B)**. After treatment with oAβ42 in 1.5 ml microcentrifuge tubes for 90 min, cells were washed and incubated for 24 h at 37°C in a medium free of oAβ42. The next day, cells were fixed and observed under a confocal microscope. SH-SY5Y cells were treated in the same manner using a scraper **(C)** or trypsin **(D)**. Neuro2A cells were cultured in the absence **(E)** or presence **(F)** of heparin (50 ng/ml) for 30 min; then, oAβ42 (5 μM) was added for 90 min and observed under a confocal microscope. Scale bars = 10 μm. **(G,H)** Fluorescent intensity of three independent experiments shows a marked reduction in the uptake of oAβ42 in the presence of trypsin and heparin. Data are presented as mean fluorescence normalized to scraper or heparin. Data are presented as mean ± SEM. Significance was established by Student's t-test. ****$p < 0.0001$.

a result, dynasore decreased the uptake of transferrin, but not that of oAβ42 and dextran (120 cells observed for each ligand). The same experiment using SH-SY5Y cells showed similar results (**Supplementary Figure 2A**). The rate of coexistence of oAβ42 and dextran (colocalization/total) after 90 min of treatment was 42.9% (**Figures 4B,C**) in the absence of EIPA, but it decreased significantly to 2.9% in the presence of EIPA ($p < 0.0001$). These results suggest that oAβ42 was internalized in Neuro2A cells *via* macropinocytosis. Next, we confirmed the internalization of oAβ42 by other cells to generalize our findings beyond the neuronal cells. We treated SH-SY5Y, HeLa, HEK293T, as well as Neuro2A cells with fluorescently labeled oAβ42. In all cells tested, oAβ42 was observed as punctate spots throughout the cell bodies (**Supplementary Figures 2B,C**).

Small GTPase Rac1 Is Involved in Amyloid Beta Oligomer Internalization

Macropinocytosis is regulated by small GTPases such as ADP ribosylation factor protein 6 (Arf6) and Rac1 (Désiré et al., 2005; Tang et al., 2015). To examine whether these GTPases are involved in the internalization of oAβ42, we used specific inhibitors. First, we treated Neuro2A cells with Arf6 inhibitors, NAV 2729, or an indirect inhibitor, SecinH3, and then incubated them with oAβ42. SecinH3 is a cytohesin-specific small-molecule inhibitor that blocks the activation of Arf6 through the inhibition of ARNO. In the presence of these inhibitors, the amount of intracellular oAβ42 did not significantly decrease (NAV 2729, $p = 0.849$; SecinH3, $p = 0.744$; **Figures 5A,B**), suggesting that Arf6 does not take part in oAβ42 uptake. In contrast, EHT1864, an inhibitor of Rac1, decreased intracellular oAβ42 in Neuro2A and SH-SY5Y cells by 61.4% and 85.1% respectively (Neuro2A, $p < 0.0001$; SH-SY5Y, $p < 0.0001$; **Figures 5D,E**). Taken together, these studies indicate that the internalization of oAβ42 is dependent solely on Rac1 activity. Next, we studied the change in activities of Arf6 and Rac1 during the entry of oAβ42. Lysates from Neuro2A cells incubated with 5 μM oAβ42 for 7, 15, and 30 min were subjected to Rac1 G-LISA assay. We used a lysate concentration of 0.5 mg/ml for the Rac1 G-LISA to keep the assay in the linear range. The signal was read by measuring absorbance at 490 nm using a microplate spectrophotometer. Wells with lysis buffer alone were designated as blanks for the assay. The results indicated that Rac1 activity at the time of 7 min showed a maximum increase of 3.0-fold (95% CI 2.89–3.12, $p < 0.0001$) compared with the control (1.13 ± 0.12), and then gradually decreased with increasing incubation (15 min, 1.79 ± 0.12, $p < 0.001$; 30 min, 1.29 ± 0.09, $p = 0.008$; **Figure 5F**). However, Arf6 activity upon treatment with oAβ42 at the times of 7 (0.14 ± 0.006, $p = 0.412$), 15 (0.13 ± 0.004, $p = 0.294$), and 30 min (0.12 ± 0.004, $p = 0.131$) did not change compared with that of the control (0.13 ± 0.006; **Figure 5C**). The activation and inhibition assays suggested that Arf6 is not involved in the endocytosis of oAβ42.

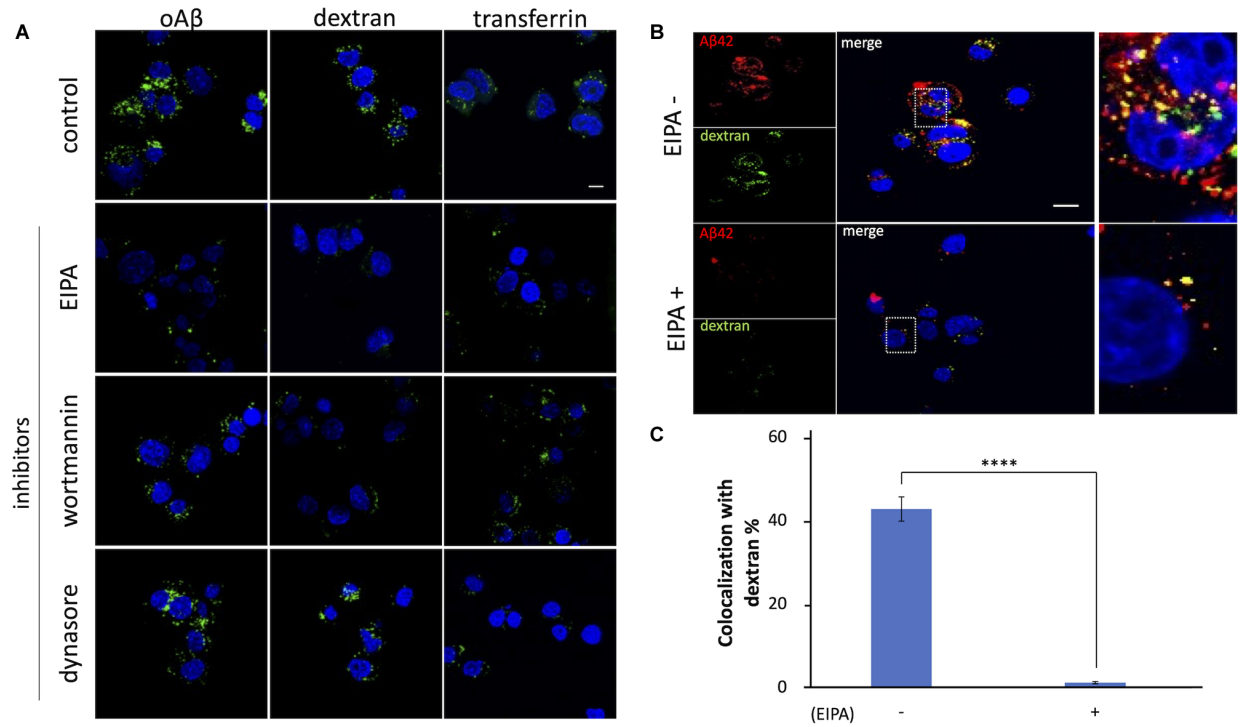

FIGURE 4 | Effects of inhibitors on the internalization of oAβ42 in Neuro2A cells. **(A)** Neuro2A cells were mock-treated or pretreated with 80 μM EIPA, 300 nM wortmannin, or 80 mM dynasore for 1 h, followed by incubation with 5 μM oAβ42, 2.5 mg/ml dextran, or 50 μg/ml transferrin for an additional 90 min at 37°C, respectively. Nuclei were visualized with DAPI (blue). Scale bar = 10 μm. **(B)** Neuro2A cells were treated with 5 μM TMR-oAβ42 (red) and 2.5 mg/ml FITC-dextran (green) for 90 min in the absence or presence of EIPA. Yellow indicates colocalization. Nuclei were visualized with DAPI (blue). Enlarged views of the boxed region are shown in **(B)** (far right line). Scale bar = 10 μm. **(C)** Quantification of the rate of coexistence of oAβ42 and dextran (colocalization/total) shows a marked reduction in the presence of EIPA. Experiments were repeated three times. Data are presented as mean ± SEM. Significance was established by Student's t-test. ****$p < 0.0001$.

DISCUSSION

To better understand the pathological association of extracellular Aβ42 deposition and neurodegeneration, we investigated the mode of Aβ42 entry into culture cells using synthetic Aβ42, based on the assumption that intracellular Aβ42 plays a role in neurodegeneration. Our study showed that oAβ42 is distinctively internalized *via* Rac1-mediated macropinocytosis, which requires HSPGs and lipid rafts. Although the pathological significance of this is not yet fully understood, there is a growing body of evidence that Aβ42 exists not only extracellularly but also intracellularly (Hu et al., 2009; Bayer and Wirths, 2010; Lai and McLaurin, 2010; Omtri et al., 2012; Ji et al., 2016; Wesén et al., 2017; Welikovitch et al., 2018). With regard to intracellular Aβ42, there is a possibility that Aβ42 is formed inside the cell and is secreted, resulting in senile plaque formation. Another source of senile plaque might be the dead cells bearing intracellular oAβ. In accordance with this notion, Tang et al. (2015) demonstrated that amyloid precursor protein is directly delivered *via* macropinocytosis to the lysosome where Aβ42 is generated from amyloid precursor protein (Tam et al., 2016). Another possibility is that the endocytic process internalizes extracellularly formed Aβ42. The presence of Aβ42 in the multivesicular bodies (Takahashi et al., 2002) supports both above-mentioned notions since multivesicular bodies are a central node that connects both the endosome–lysosome pathway and the exosome secretion pathway. A recent study demonstrated that amyloid precursor protein functions as adhesion molecules bridging presynaptic and postsynaptic membranes. Enhanced synaptic activity leads to increased APP processing and Aβ generation (Stahl et al., 2014). Our results demonstrate that the uptake of extracellular oAβ42 is one probable explanation for the presence of intracellular oAβ42.

Endocytosis encompassing a variety of routes is critical for living cells to take up extracellular materials (El-Sayed and Harashima, 2013). Clathrin-dependent endocytosis is the type of endocytosis that has been most extensively studied to date. Transferrin is well known to be incorporated *via* clathrin-dependent endocytosis driven by the motor protein dynamin (Mayor and Pagano, 2007). Dynasore, a dynamin inhibitor, was found to inhibit the endocytosis of transferrin but not oAβ42, indicating that clathrin-dependent endocytosis plays only a minor role. In our study, internalized oAβ42 was surrounded by actin filaments visualized by phalloidin. The pretreatment of Rac1 inhibitors significantly reduced the internalization of both oAβ42 and dextran, whereas the G-LISA assay showed that Rac1 was activated by oAβ42. Regarding Rac1 activity, Borin et al. (2018) reported no change in the activity at the time points of 1,

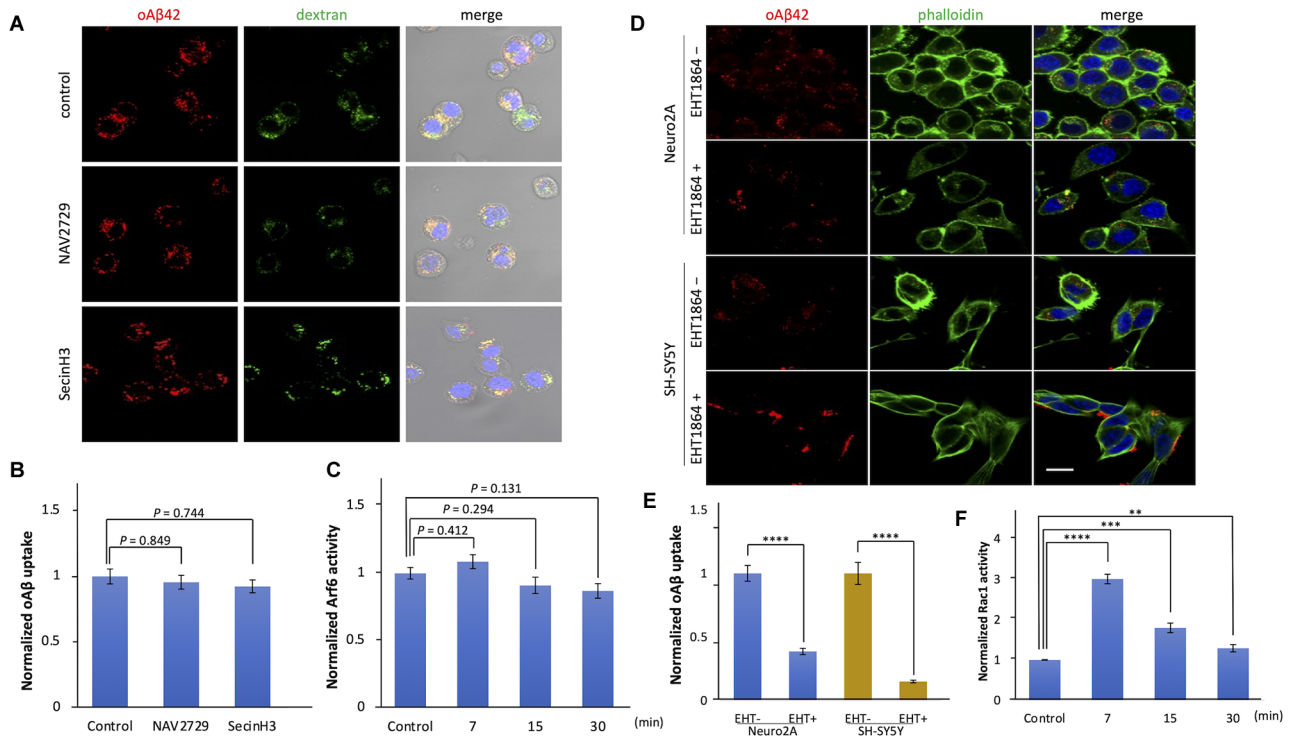

FIGURE 5 | The effects of Arf6 and Rac1 inhibitors on the uptake of oligomeric amyloid beta. **(A)** Cells were treated with NAV 2729 and SecinH3 for 1 h, followed by incubation with 5 μM TMR-oAβ42 (red) and 2.5 mg/ml FITC-dextran (green) for 90 min at 37°C. Nuclei were visualized with DAPI (blue). Scale bar = 10 μm. **(B)** Quantification of the uptake of oAβ42 by confocal microscopy in the presence of the Arf6 inhibitors, and data are presented as mean fluorescence normalized to control (n = 3). Significance was established by ANOVA followed by the Dunnett–Square test. **(C)** The change in Arf6 activity in Neuro2A cells by the treatment of oAβ42 was measured using G-LISA. Normalized data are presented as mean ± SEM. Significance was established by ANOVA followed by the Dunnett–Square test. **(D)** Actin and nuclei were visualized with Alexa Fluor 488 phalloidin conjugates (green) and DAPI, respectively. Scale bar = 10 μm. **(E)** Quantification of the uptake of oAβ42 by confocal microscopy in the presence of EHT1864. Data are presented as mean fluorescence normalized to without EHT (n = 3). Significance was established by Student's t-test. **(F)** The change in Rac-1 activity in Neuro2A cells upon oAβ42 treatment was measured using G-LISA. Normalized data are presented as mean ± SEM. Significance was established by ANOVA followed by the Dunnett–Square test. $^{**}p < 0.01$; $^{***}p < 0.001$; $^{****}p < 0.0001$.

3, 6, and 24 h after oAβ42 treatment. However, their results are not incompatible with our findings since we observed that the level of Rac1 activity returned to the basal level as early as 30 min. Rather, our results are in line with the fact that Rac1 is involved in the early stage of macropinocytosis (Kunita et al., 2007).

Eosinophil cationic protein (ECP), a superfamily member related to human RNase and asthma pathology, was reported to be another molecule incorporated *via* macropinocytosis. It was also shown that HSPGs and lipid rafts are indispensable for the internalization of ECP (Fan et al., 2007). Specifically, cell surface-bound HSPGs (syndecan, glypican) act as coreceptors for various growth factor receptors and several viruses (Sarrazin et al., 2011; Cagno et al., 2019). Interestingly, syndecan is found in senile plaques and neurofibrillary tangles of AD-affected brains (Verbeek et al., 1999). These findings prompted us to examine the dependence of oAβ42 on HSPGs and lipid rafts. The pretreatment of trypsin or coincubation with heparin to interfere with HSPGs reduced the amount of intracellular oAβ42. Likewise, cellular uptake of oAβ42 was decreased in the presence of MβCD that destroys lipid rafts. The dependence on lipid rafts was previously reported in the case of clathrin-mediated mAβ42 internalization (Hu et al., 2009). The mode of oAβ42 internalization is similar to that of ECP; however, Arf6 was not involved in the process in our study.

Imamura et al. (2011) reported that only multivalent but not monovalent HIV Tat protein could enter cells through the crosslinking of HSPGs and subsequent macropinocytosis. They showed that crosslinked HSPGs can recruit active Rac1 to lipid rafts, followed by the induction of macropinocytosis (Fan et al., 2007). The finding that monomeric Tat protein incapable of HSPG crosslinking is not internalized is compatible with our finding that mAβ42 scarcely entered cells. The similar dependence of oligomeric Aβ42 on HSPGs suggests that oAβ42 can also crosslink HSPGs and be endocytosed alongside syndecan. Letoha et al. (2019) found that syndecan-3, a neuron-specific syndecan isoform, facilitates not only cellular uptake but also fibrillization of Aβ42. In line with their findings, we observed that, at a low temperature, Aβ42 attached to the cell periphery as aggregates. The prolonged attachment to the cell surface covered with syndecan might facilitate the fibrillization of Aβ42. The fibrillated Aβ42 can no longer enter cells.

A previous study reported that astrocytes internalize both monomeric and oligomeric Aβ42, and another study showed that the monomer but not the oligomer is preferentially internalized

(Omtri et al., 2012; Li et al., 2014). In our research, mAβ42 was the major species in the prepared samples, as evidenced by PAGE. Nonetheless, when samples without oAβ42 were applied, only a trace amount of Aβ42 was found in the cells, in contrast to the sample containing oAβ42, indicating that oAβ42 preferentially enters cells. The difference may stem from the various types of cells and diverse experimental conditions, since the preference will be defined by the repertories of cell surface receptors, and dozens of receptors have been reported as candidates for Aβ42 (Jarosz-Griffiths et al., 2016). Recently, Marshall et al. (2020) applied oAβ42 to primary neurons from the hippocampus of P0–P1 rats and found that oAβ42 was associated with the cell surface at the timepoint of 1 h. It was internalized *via* clathrin-dependent endocytosis at a later stage of cell culture.

Amylin is a 37-amino-acid peptide produced by pancreatic beta cells, which causes islet cell damage in its fibrillar form. An experiment using EIPA or wortmannin demonstrated that both oligomeric and monomeric amylin peptides are endocytosed by cells *via* the macropinocytosis pathway (Clark and Nilsson, 2004; Trikha and Jeremic, 2011, 2013). Notably, in the early stage, monomeric amylin is internalized by clathrin endocytosis, although oligomers enter cells regardless of the timepoint. Furthermore, in the case of amylin, it has been reported that it is detoxified when taken up by cells since the amyloid form of amylin bound to the cell surface exerts cytotoxicity.

The detailed fate of endocytosed oAβ is not yet clarified. However, massive accumulation of Aβ outside and inside the cells might implicate that the degradation system, including lysosome, cannot work properly in the AD brain. If it is the case, an impaired lysosomal function might link with neuronal cell death. Given that the internalization of oAβ is the upstream event of such lysosomal impairment, any method that can impede macropinocytosis of oAβ is of clinical relevance.

Our study has several limitations. First, our results obtained from *in vitro* assay using culture cells cannot faithfully reflect the pathological process that has taken place in a diseased brain. However, if its supposed time dependence and wide dose dependence are taken into consideration, it is conceivable that a fraction of senile plaque components enter the cells in the long-term, as shown in this study. Second, we could not specifically isolate oAβ despite the effort to purify it; instead, we used a mixture of monomeric and oligomeric Aβ as oAβ. Nonetheless, the lower relative abundance of oAβ42 in samples used as oAβ42 supports our conclusion, as mentioned above.

In conclusion, we herein report the preferential entry of oAβ42 over mAβ42 into several types of cells, including neuronal cells, in a time- and dose-dependent fashion. The mode of internalization, although not exclusive, is macropinocytosis, which depends on HSPGs and lipid rafts. The requirement for Rac1 activation suggests that the entry of oAβ42 is an active process. Further delineation of the process of oAβ42 internalization and the biological implications of intracellular Aβ42 might provide information on the development of novel types of AD therapies.

DATA AVAILABILITY STATEMENT

The original contributions presented in the study are included in the article/**Supplementary Materials**, further inquiries can be directed to the corresponding author.

AUTHOR CONTRIBUTIONS

KN and TT designed the study. MN, YY, and HMo provided advice to KN. KN, KM, and NH performed the experiments. KN and TT analyzed the data. KN wrote the first draft of the manuscript. HMa supervised the study. All authors contributed to the article and approved the submitted version.

FUNDING

This work was supported by Grant-in-Aid for Scientific Research (C) (Grant Number JP19K07974) from the Ministry of Education, Culture, Sports, Science and Technology.

ACKNOWLEDGMENTS

We thank Ms. Yasuko Furuno and Ms. Miwako Sasanishi for their excellent technical assistance. Special appreciation goes to Dr. Chengyu Li for her helpful technical advice. We would also like to thank Edanz (https://jp.edanz.com/) for English language editing, and the Analysis Center of Life Science, Hiroshima University, Hiroshima, Japan, for the use of its facilities.

SUPPLEMENTARY MATERIALS

The Supplementary Material for this article can be found online at: https://www.frontiersin.org/articles/10.3389/fnmol.2022.804702/full#supplementary-material.

SUPPLEMENTARY FIGURE 1 | The monomeric or oligomeric status of Aβ42 was investigated using confocal microscopy and Tricine gel. **(A)** Neuro2A cells were treated with mAβ42 and oAβ42 at concentrations of 1, 2, and 5 μM for 90 min at 37°C, and then observed by confocal microscopy. Scale bar = 10 nm. **(B)** Graph of the levels of internalization of oAβ42 or mAβ42. Data are presented as mean ± SEM. a.u. = arbitrary units. Significance was established by Student's t-test. $^{****}p < 0.0001$. **(C)** Next, both mAβ42 and oAβ42 were subjected to 16.5% Tris-Tricine gel to check the monomeric or oligomeric status. The gel was observed on a UV (312 nm) illuminator.

SUPPLEMENTARY FIGURE 2 | Effects of inhibitors on the internalization of oAβ42 in SH-SY5Y cells. **(A)** SH-SY5Y cells were mock-treated or pretreated with 80 μM EIPA, 300 nM wortmannin, or 80 mM dynasore for 1 h, followed by 5 μM oAβ42, 2.5 mg/ml dextran, and 50 μg/ml transferrin for an additional 90 min at 37°C. Confocal microscopy in the presence of the macropinocytosis inhibitors compared with the controls. **(B)** Internalization of oAβ42 and dextran was investigated in four different cell lines: Neuro2A, SH-SY5Y, HEK293T, and HeLa cells. These cells were treated with 5 μM TMR-oAβ42 (red) and 2.5 mg/ml FITC-dextran (green) for 90 min. Nuclei were visualized with DAPI (blue). Yellow indicates colocalization. **(C)** Graph of the levels of internalization of oAβ42 by different cells. Data are presented as mean ± SEM. a.u. = arbitrary units. Scale bars = 10 μm.

REFERENCES

Ansari, M. A., Abdul, H. M., Joshi, G., Opii, W. O., and Butterfield, D. A. (2009). Protective effect of quercetin in primary neurons against Aβ (1–42): relevance to Alzheimer's disease. *J. Nutr. Biochem.* 20, 269–275. doi: 10.1016/j.jnutbio.2008.03.002

Bayer, T. A., and Wirths, O. (2010). Intracellular accumulation of amyloid-Beta-a predictor for synaptic dysfunction and neuron loss in Alzheimer's disease. *Front. Aging Neurosci.* 2:8. doi: 10.3389/fnagi.2010.00008

Belyaev, N. D., Kellett, K. A., Beckett, C., Makova, N. Z., Revett, T. J., Nalivaeva, N. N., et al. (2010). The transcriptionally active amyloid precursor protein (APP) intracellular domain is preferentially produced from the 695 isoform of APP in a β-secretase-dependent pathway. *J. Biol. Chem.* 285, 41443–41454. doi: 10.1074/jbc.M110.141390

Bharadwaj, P. R., Dubey, A. K., Masters, C. L., Martins, R. N., and Macreadie, I. G. (2009). Aβ aggregation and possible implications in Alzheimer's disease pathogenesis. *J. Cell. Mol. Med.* 13, 412–421. doi: 10.1111/j.1582-4934.2009.00609.x

Bieberich, E. (2018). Sphingolipids and lipid rafts: novel concepts and methods of analysis. *Chem. Phys. Lipids* 216, 114–131. doi: 10.1016/j.chemphyslip.2018.08.003

Borin, M., Saraceno, C., Catania, M., Lorenzetto, E., Pontelli, V., Paterlini, A., et al. (2018). Rac1 activation links tau hyperphosphorylation and Aβ dysmetabolism in Alzheimer's disease. *Acta Neuropathol. Commun.* 6:61. doi: 10.1186/s40478-018-0567-4

Cagno, V., Tseligka, E. D., Jones, S. T., and Tapparel, C. (2019). Heparan sulfate proteoglycans and viral attachment: true receptors or adaptation bias? *Viruses* 11:596. doi: 10.3390/v11070596

Chafekar, S. M., Baas, F., and Scheper, W. (2008). Oligomer-specific Aβ toxicity in cell models is mediated by selective uptake. *Biochim. Biophys. Acta* 1782, 523–531. doi: 10.1016/j.bbadis.2008.06.003

Clark, A., and Nilsson, M. R. (2004). Islet amyloid: a complication of islet dysfunction or an aetiological factor in type 2 diabetes? *Diabetologia* 47, 157–169. doi: 10.1007/s00125-003-1304-4

Désiré, L., Bourdin, J., Loiseau, N., Peillon, H., Picard, V., De Oliveira, C., et al. (2005). RAC1 inhibition targets amyloid precursor protein processing by γ-secretase and decreases Aβ production *in vitro* and *in vivo*. *J. Biol. Chem.* 280, 37516–37525. doi: 10.1074/jbc.M507913200

Doherty, G. J., and McMahon, H. T. (2009). Mechanisms of endocytosis. *Ann. Rev. Biochem.* 78, 857–902. doi: 10.1146/annurev.biochem.78.081307.110540

Dorostkar, M. M., Zou, C., Blazquez-Llorca, L., and Herms, J. (2015). Analyzing dendritic spine pathology in Alzheimer's disease: problems and opportunities. *Acta Neuropathol.* 130, 1–19. doi: 10.1007/s00401-015-1449-5

El-Sayed, A., and Harashima, H. (2013). Endocytosis of gene delivery vectors: from clathrin-dependent to lipid raft-mediated endocytosis. *Mol. Ther.* 21, 1118–1130. doi: 10.1038/mt.2013.54

Fan, T. C., Chang, H. T., Chen, I. W., Wang, H. Y., and Chang, M. D. T. (2007). A heparan sulfate-facilitated and raft-dependent macropinocytosis of eosinophil cationic protein. *Traffic* 8, 1778–1795. doi: 10.1111/j.1600-0854.2007.00650.x

Friedrich, R. P., Tepper, K., Rönicke, R., Soom, M., Westermann, M., Reymann, K., et al. (2010). Mechanism of amyloid plaque formation suggests an intracellular basis of Aβ pathogenicity. *Proc. Natl. Acad. Sci. U S A* 107, 1942–1947. doi: 10.1073/pnas.0904532106

Frost, G. R., and Li, Y. M. (2017). The role of astrocytes in amyloid production and Alzheimer's disease. *Open Biol.* 7:170228. doi: 10.1098/rsob.170228

Gupta, N., and DeFranco, A. L. (2003). Visualizing lipid raft dynamics and early signaling events during antigen receptor-mediated B-lymphocyte activation. *Mol. Biol. Cell* 14, 432–444. doi: 10.1091/mbc.02-05-0078

Holmes, B. B., DeVos, S. L., Kfoury, N., Li, M., Jacks, R., Yanamandra, K., et al. (2013). Heparan sulfate proteoglycans mediate internalization and propagation of specific proteopathic seeds. *Proc. Natl. Acad. Sci. U S A* 110, E3138–E3147. doi: 10.1073/pnas.1301440110

Hu, X., Crick, S. L., Bu, G., Frieden, C., Pappu, R. V., and Lee, J. M. (2009). Amyloid seeds formed by cellular uptake, concentration and aggregation of the amyloid-beta peptide. *Proc. Natl. Acad. Sci. U S A* 106, 20324–20329. doi: 10.1073/pnas.0911281106

Imamura, J., Suzuki, Y., Gonda, K., Roy, C. N., Gatanaga, H., Ohuchi, N., et al. (2011). Single particle tracking confirms that multivalent Tat protein transduction domain-induced heparan sulfate proteoglycan cross-linkage activates Rac1 for internalization. *J. Biol. Chem.* 286, 10581–10592. doi: 10.1074/jbc.M110.187450

Jarosz-Griffiths, H. H., Noble, E., Rushworth, J. V., and Hooper, N. M. (2016). Amyloid-β receptors: the good, the bad and the prion protein. *J. Biol. Chem.* 291, 3174–3183. doi: 10.1074/jbc.R115.702704

Ji, L., Zhao, X., Lu, W., Zhang, Q., and Hua, Z. (2016). Intracellular Aβ and its pathological role in Alzheimer's disease: lessons from cellular to animal models. *Curr. Alzheimer Res.* 13, 621–630. doi: 10.2174/1567205013666160322142226

Kunita, R., Otomo, A., Mizumura, H., Suzuki-Utsunomiya, K., Hadano, S., and Ikeda, J. E. (2007). The Rab5 activator ALS2/alsin acts as a novel Rac1 effector through Rac1-activated endocytosis. *J. Biol. Chem.* 282, 16599–16611. doi: 10.1074/jbc.M610682200

Lai, A. Y., and McLaurin, J. (2010). Mechanisms of amyloid-beta peptide uptake by neurons: the role of lipid rafts and lipid raft-associated proteins. *Int. J. Alzheimers Dis.* 2011:548380. doi: 10.4061/2011/548380

Letoha, T., Hudák, A., Kusz, E., Pettkó-Szandtner, A., Domonkos, I., Jósvay, K., et al. (2019). Contribution of syndecans to cellular internalization and fibrillation of amyloid-β(1–42). *Sci. Rep.* 9:1393. doi: 10.1038/s41598-018-37476-9

Letoha, T., Kolozsi, C., Ékes, C., Keller-Pintér, A., Kusz, E., Szakonyi, G., et al. (2013). Contribution of syndecans to lipoplex-mediated gene delivery. *Eur. J. Pharm. Sci.* 49, 550–555. doi: 10.1016/j.ejps.2013.05.022

Li, Y., Cheng, D., Cheng, R., Zhu, X., Wan, T., Liu, J., et al. (2014). Mechanisms of U87 astrocytoma cell uptake and trafficking of monomeric versus protofibril Alzheimer's disease amyloid-β proteins. *PLoS One* 9:e99939. doi: 10.1371/journal.pone.0099939

Marshall, K. E., Vadukul, D. M., Staras, K., and Serpell, L. C. (2020). Misfolded amyloid-β-42 impairs the endosomal-lysosomal pathway. *Cell. Mol. Life Sci.* 77, 5031–5043. doi: 10.1007/s00018-020-03464-4

Mayor, S., and Pagano, R. E. (2007). Pathways of clathrin-independent endocytosis. *Nat. Rev. Mol. Cell Biol.* 8, 603–612. doi: 10.1038/nrm2216

Nichols, B. (2003). Caveosomes and endocytosis of lipid rafts. *J. Cell Sci.* 116, 4707–4714. doi: 10.1242/jcs.00840

Omtri, R. S., Davidson, M. W., Arumugam, B., Poduslo, J. F., and Kandimalla, K. K. (2012). Differences in the cellular uptake and intracellular itineraries of amyloid beta proteins 40 and 42: ramifications for the Alzheimer's drug discovery. *Mol. Pharm.* 9, 1887–1897. doi: 10.1021/mp200530q

Rushworth, J. V., and Hooper, N. M. (2010). Lipid rafts: linking Alzheimer's amyloid-β production, aggregation and toxicity at neuronal membranes. *Int. J. Alzheimers Dis.* 2011:603052. doi: 10.4061/2011/603052

Sarrazin, S., Lamanna, W. C., and Esko, J. D. (2011). Heparan sulfate proteoglycans. *Cold Spring Harb. Perspect. Biol.* 3:a004952. doi: 10.1101/cshperspect.a004952

Schützmann, M. P., Hasecke, F., Bachmann, S., Zielinski, M., Hänsch, S., Schröder, G. F., et al. (2021). Endo-lysosomal Aβ concentration and pH trigger formation of Aβ oligomers that potently induce Tau missorting. *Nat. Commun.* 12:4634. doi: 10.1038/s41467-021-24900-4

Serrano-Pozo, A., Frosch, M. P., Masliah, E., and Hyman, B. T. (2011). Neuropathological alterations in Alzheimer disease. *Cold Spring Harb. Perspect. Med.* 1:a006189. doi: 10.1101/cshperspect.a006189

Singh, S. K., Srivastav, S., Yadav, A. K., Srikrishna, S., and Perry, G. (2016). Overview of Alzheimer's disease and some therapeutic approaches targeting Aβ by using several synthetic and herbal compounds. *Oxid. Med. Cell. Longev.* 2016:7361613. doi: 10.1155/2016/7361613

Stahl, R., Schilling, S., Soba, P., Rupp, C., Hartmann, T., Wagner, K., et al. (2014). Shedding of APP limits its synaptogenic activity and cell adhesion properties. *Front. Cell. Neurosci.* 8:410. doi: 10.3389/fncel.2014.00410

Swanson, J. A., and Watts, C. (1995). Macropinocytosis. *Trends Cell Biol.* 5, 424–428. doi: 10.1016/s0962-8924(00)89101-1

Takahashi, R. H., Almeida, C. G., Kearney, P. F., Yu, F., Lin, M. T., Milner, T. A., et al. (2004). Oligomerization of Alzheimer's β-amyloid within processes and synapses of cultured neurons and brain. *J, Neurosci.* 24, 3592–3599. doi: 10.1523/JNEUROSCI.5167-03.2004

Takahashi, R. H., Milner, T. A., Li, F., Nam, E. E., Edgar, M. A., Yamaguchi, H., et al. (2002). Intraneuronal Alzheimer Aβ42 accumulates in multivesicular bodies and is associated with synaptic pathology. *Am. J. Pathol.* 161, 1869–1879. doi: 10.1016/s0002-9440(10)64463-x

Tam, J. H., Cobb, M. R., Seah, C., and Pasternak, S. H. (2016). Tyrosine binding protein sites regulate the intracellular trafficking and processing of amyloid precursor protein through a novel lysosome-directed pathway. *PLoS One* 11:e0161445. doi: 10.1371/journal.pone.0161445

Tang, W., Tam, J. H., Seah, C., Chiu, J., Tyrer, A., Cregan, S. P., et al. (2015). Arf6 controls beta-amyloid production by regulating macropinocytosis of the amyloid precursor protein to lysosomes. *Mol. Brain* 8:41. doi: 10.1186/s13041-015-0129-7

Thal, D. R., Walter, J., Saido, T. C., and Fändrich, M. (2015). Neuropathology and biochemistry of Aβ and its aggregates in Alzheimer's disease. *Acta Neuropathol.* 129, 167–182. doi: 10.1007/s00401-014-1375-y

Trikha, S., and Jeremic, A. M. (2011). Clustering and internalization of toxic amylin oligomers in pancreatic cells require plasma membrane cholesterol. *J. Biol. Chem.* 286, 36086–36097. doi: 10.1074/jbc.M111.240762

Trikha, S., and Jeremic, A. M. (2013). Distinct internalization pathways of human amylin monomers and its cytotoxic oligomers in pancreatic cells. *PloS One* 8:e73080. doi: 10.1371/journal.pone.0073080

Verbeek, M. M., Otte-Höller, I., van den Born, J., van den Heuvel, L. P., David, G., Wesseling, P., et al. (1999). Agrin is a major heparan sulfate proteoglycan accumulating in Alzheimer's disease brain. *Am. J. Pathol.* 155, 2115–2125. doi: 10.1016/S0002-9440(10)65529-0

Viola, K. L., and Klein, W. L. (2015). Amyloid β oligomers in Alzheimer's disease pathogenesis, treatment and diagnosis. *Acta Neuropathol.* 129, 183–206. doi: 10.1007/s00401-015-1386-3

Welikovitch, L. A., Do Carmo, S., Maglóczky, Z., Szocsics, P., L'oke, J., Freund, T., et al. (2018). Evidence of intraneuronal Aβ accumulation preceding tau pathology in the entorhinal cortex. *Acta Neuropathol.* 136, 901–917. doi: 10.1007/s00401-018-1922-z

Wesén, E., Jeffries, G. D., Dzebo, M. M., and Esbjörner, E. K. (2017). Endocytic uptake of monomeric amyloid-β peptides is clathrin-and dynamin-independent and results in selective accumulation of Aβ(1–42) compared to Aβ(1–40). *Sci. Rep.* 7:2021. doi: 10.1038/s41598-017-02227-9

Zhang, X., and Song, W. (2013). The role of APP and BACE1 trafficking in APP processing and amyloid-β generation. *Alzheimers Res. Ther.* 5:46. doi: 10.1186/alzrt211

Conflict of Interest: The authors declare that the research was conducted in the absence of any commercial or financial relationships that could be construed as a potential conflict of interest.

Publisher's Note: All claims expressed in this article are solely those of the authors and do not necessarily represent those of their affiliated organizations, or those of the publisher, the editors and the reviewers. Any product that may be evaluated in this article, or claim that may be made by its manufacturer, is not guaranteed or endorsed by the publisher.

frontiers | Frontiers in Neuroscience

TYPE Review
PUBLISHED 16 November 2022
DOI 10.3389/fnins.2022.1003997

OPEN ACCESS

EDITED BY
Wolfgang Hoyer,
Heinrich Heine University Düsseldorf, Germany

REVIEWED BY
Thibault Viennet,
Dana-Farber Cancer Institute, United States
Bjoern Falkenburger,
Technical University Dresden, Germany

*CORRESPONDENCE
Aditya Iyer
linktoaditya@gmail.com
Vinod Subramaniam
v.subramaniam@utwente.nl

†PRESENT ADDRESS
Aditya Iyer,
Amyl Therapeutics,
Liège, Belgium

SPECIALTY SECTION
This article was submitted to Neurodegeneration, a section of the journal Frontiers in Neuroscience

RECEIVED 26 July 2022
ACCEPTED 26 October 2022
PUBLISHED 16 November 2022

CITATION
Iyer A, Sidhu A and Subramaniam V (2022) How important is the N-terminal acetylation of alpha-synuclein for its function and aggregation into amyloids? *Front. Neurosci.* 16:1003997. doi: 10.3389/fnins.2022.1003997

How important is the N-terminal acetylation of alpha-synuclein for its function and aggregation into amyloids?

Aditya Iyer[1*†], Arshdeep Sidhu[2] and Vinod Subramaniam[3*]

[1]Department of Biochemistry, Groningen Biomolecular Sciences and Biotechnology Institute, University of Groningen, Groningen, Netherlands, [2]Nitte University Centre for Science Education and Research, Nitte University (DU), Mangalore, India, [3]University of Twente, Enschede, Netherlands

N-α-acetylation is a frequently occurring post-translational modification in eukaryotic proteins. It has manifold physiological consequences on the regulation and function of several proteins, with emerging studies suggesting that it is a global regulator of stress responses. For decades, *in vitro* biochemical investigations into the precise role of the intrinsically disordered protein alpha-synuclein (αS) in the etiology of Parkinson's disease (PD) were performed using non-acetylated αS. The N-terminus of α-synuclein is now unequivocally known to be acetylated *in vivo*, however, there are many aspects of this post-translational modifications that are not understood well. Is *N*-α-acetylation of αS a constitutive modification akin to most cellular proteins, or is it spatio-temporally regulated? Is *N*-α-acetylation of αS relevant to the as yet elusive function of αS? How does the *N*-α-acetylation of αS influence the aggregation of αS into amyloids? Here, we provide an overview of the current knowledge and discuss prevailing hypotheses on the impact of *N*-α-acetylation of αS on its conformational, oligomeric, and fibrillar states. The extent to which *N*-α-acetylation of αS is vital for its function, membrane binding, and aggregation into amyloids is also explored here. We further discuss the overall significance of *N*-α-acetylation of αS for its functional and pathogenic implications in Lewy body formation and synucleinopathies.

KEYWORDS

protein aggregation, fibril structure, acetylation, post-translational modifications, alpha-synuclein

Introduction

N-terminal acetylation is a post-translational modification carried out by N-terminal acetyltransferases in nascent protein chains during translation (Aksnes et al., 2019). A protein can exist in full, partial and non-acetylated form. N-terminal acetylation involves the addition of an acetyl group to the free alpha-amino group (N-α-group) of

the first amino acid in the nascent protein chain by an N-terminal acetyltransferase (Nat) complex (Varland et al., 2015). To date, N-terminal acetylation is considered irreversible because an N-terminal de-acetyltransferase (Ndat) either does not exist in eukaryotic cells or remains to be discovered. We draw a clear distinction between N-terminal acetylation and *N*-α-acetylation in the context of this review. *N*-α-acetylation refers explicitly to the acetylation of the first amino acid (in most cases, methionine). In contrast, N-terminal acetylation may include the acetylation of amino acid residues in the N-terminal region in proteins comprising several amino acids. Protein acetylation also occurs on the ε-amino group of the lysine side chains (*N*-ε-acetylation) catalyzed by a different class of enzymes called lysine acetyltransferases (Choudhary et al., 2014) and on hydroxyl groups of tyrosine/serine/threonine referred to as *O*-acetylation (Yang and Grégoire, 2007). In contrast to Ndats, eukaryotic lysine deacetylases are well-known, and their functions are reviewed elsewhere (Yang and Grégoire, 2007; Choudhary et al., 2014; Xia et al., 2020). In humans, seven Nats have been identified to date — NatA, NatB, NatC, NatD, NatE, NatF, and NatH (Aksnes et al., 2019) — which are responsible for N-terminal acetylation of more than 80% of eukaryotic proteins (Arnesen et al., 2009; Johnson et al., 2010; Aksnes et al., 2016), the rest of the 20% proteome is not known to be acetylated (Ree et al., 2018). Six Nats (NatA to NatF) have broad substrate specificity, except for NatH, which is a dedicated acetylase for actin (Drazic et al., 2018). Each Nat exhibits a strong preference for specific N-terminal residues and (at least) one or two subsequent amino acids required to facilitate N-terminal acetylation (**Figure 1**).

There is ample evidence in the literature that *N*-α-acetylation of proteins, in general, is an essential mediator of protein function, stability, and localization. N-terminal acetylation impacts protein localization and targeting (Behnia et al., 2004; Setty et al., 2004; Forte et al., 2011; Dikiy and Eliezer, 2014; Park et al., 2015), multi-protein complex formation (Scott et al., 2011; Arnaudo et al., 2013; Monda et al., 2013; Yang et al., 2013; Gao et al., 2016), protein secondary structure (Maltsev et al., 2012; Miotto et al., 2015), protein degradation (Hwang et al., 2010; Shemorry et al., 2013) and aggregation into amyloid fibrils (Kang et al., 2013; Iyer et al., 2016; Watson and Lee, 2019). Of the seven identified Nats, NatB holds particular importance in the context of diseases. NatB acetylates essential proteins at the N-terminus such as tropomyosin, actin, and alpha-synuclein (αS); is required for stability of the actin cytoskeleton; is vital for cell-cycle progression (Starheim et al., 2008), cell proliferation (Ametzazurra et al., 2008); and is implicated in diseases such as hepatocellular carcinoma and Parkinson's disease (PD) (Polevoda and Sherman, 2003; Ametzazurra et al., 2008; Halliday et al., 2011; Neri et al., 2017).

αS is an intrinsically disordered protein found in high concentrations at the synaptic junctions of neuronal cells. Its precise role in the etiology of PD remains unknown. Several decades of research have not brought us much closer to pinning down its physiological function in eukaryotic cells. αS comprises three domains: the positively charged N-terminal region (aa 1-60) which is involved in membrane binding (Bartels et al., 2010; Lorenzen et al., 2014; Zarbiv et al., 2014; Viennet et al., 2018; Makasewicz et al., 2021), the amyloidogenic NAC domain (aa 61-95) crucial for amyloid formation (Waxman et al., 2009), and the highly charged C-terminal region (aa 96-140), that interacts with polyamines, metal ions, and cellular proteins (Antony et al., 2003; Eliezer, 2013). The observed binding of αS to phospholipid membranes is considered relevant for its function. It is also one of the proposed facilitators of the αS aggregation cascade in addition to point mutations, oxidative stress, truncations, possibly leading to neuronal cell death in PD. Like other eukaryotic proteins, αS is subjected to several post-translational modifications, including phosphorylation, ubiquitination, and acetylation; reviewed elsewhere in detail (Breydo et al., 2012; Barrett and Greenamyre, 2015; Iyer and Claessens, 2019; Zhang et al., 2019). αS is acetylated at the terminal methionine residue (*N*-α-acetylation) by NatB and several lysine residues *in vivo* (*N*-ε-acetylation) by other enzymes, but the physiological impact of acetylation of αS is unclear. We aim to give a critical perspective on the impact of *N*-α-acetylation of αS on its physiological role and pathological aggregation into amyloid fibrils.

N-terminal acetylation of αS

A brief history of *N*-α-acetylation

Much before the ongoing debate over its native state, αS was widely accepted as a monomeric, intrinsically disordered protein associated with intracellular membranes and found substantially in a fibrillar state in numerous synucleinopathies. Early investigations into αS focused on the mechanism of aggregation/toxicity and possibly overlooked the role of post-translational modifications occurring in αS. The loss of a positive charge from the N-terminal methionine of αS acetylation affects its secondary structure substantially (**Figure 2**). *N*-α-acetylation is considered crucial for aggregation of αS into amyloid fibrils (Kang et al., 2012; Yang et al., 2021) and interaction with other binding partners in its native cellular environment (Zabrocki et al., 2008; Runfola et al., 2020). The *N*-α-acetylated form is believed to represent the functional form of the protein, and the debate over its native state being monomeric or tetrameric continues as discussed in the following sections.

The earliest report drawing attention to the presence of *N*-α-acetylation of αS obtained from brain cells and Lewy bodies considered it a passive post-translational modification (**Figure 3**; Anderson et al., 2006). Before this report, αS was mainly purified and studied from mammalian and non-mammalian sources to ascertain its genetic basis in neurogenerative diseases like PD, multiple system atrophy (MSA), Lewy body dementia,

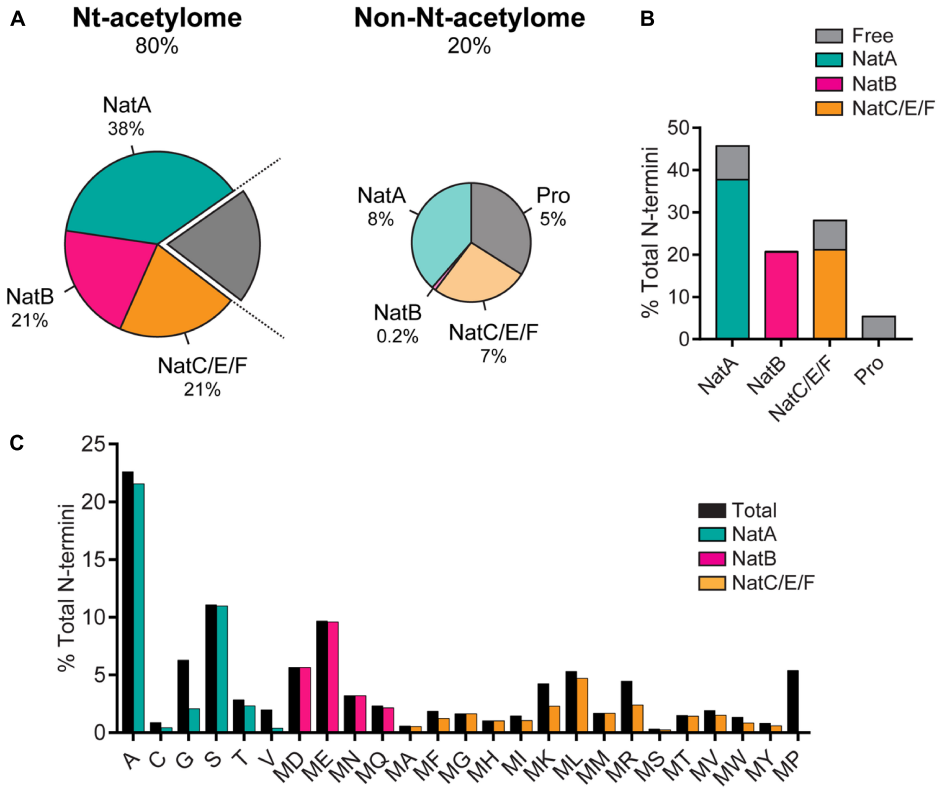

FIGURE 1
(A) The prevalence of N-terminal acetylation in human cells is depicted by separating the proteome into the N-terminal(Nt)-acetylome (80%) and the non-Nt-acetylome (20%). The human Nt-acetylome (the complete set of N-terminal acetylated proteins) was predicted by incorporating experimentally determined Nt-acetylation events (including NatC and NatF related data) to all SwissProt entries (version 57.8) based on the occurrence of the first two amino acids. The chance that a protein will be Nt-acetylated mainly depends on the identity of the first two amino acids. To visualize this concept, the Nt-acetylome can be grouped according to **(B)** NAT substrate class or **(C)** N-terminal amino acid frequency. NatD is not depicted due to its limited coverage. Image reproduced from Ree et al. (2018) licensed under CC BY 4.0. The figure legend is a modified excerpt of the original.

Lewy body variant of Alzheimer's disease (LBAD), and AD. The relevance of N-α-acetylation of αS gained prominence following a report by the Selkoe group (Bartels et al., 2011), who contradicted the established view of the native state of αS as an intrinsically disordered monomer. Using numerous cell lines and an array of analytical techniques, including EM imaging, circular dichroism spectroscopy, clear-native PAGE (CN-PAGE), and sedimentation-equilibrium analytical ultracentrifugation (SE-AUC), the study reported that native/endogenous αS is an aggregation-resistant helical tetramer in dynamic equilibrium with the monomeric αS species. The study drew parallels to transthyretin amyloidosis, wherein the destabilization of a metastable tetramer in human plasma causes aberrant aggregation of monomers (Quintas et al., 1999).

A widespread debate ensued challenging the tetramer hypothesis in several subsequent studies (Fauvet et al., 2012a,b; Burré et al., 2013), promptly responded to by the primary advocates of the tetramer hypothesis (Bartels and Selkoe, 2013; Dettmer et al., 2013, 2015a,b; Luth et al., 2015) and other groups (Ullman et al., 2011; Gurry et al., 2013; Fernández and Lucas, 2018a). The authors' conclusion that tetrameric αS may dissociate to its monomeric form during cell lysis and widely differing protein purification protocols across research groups gained little reconciliation. The primary authors further showed that the tetrameric species was sensitive to cell-lysis protocols using *in vivo* cross-linking studies that showed the apparent 60-kDa tetramer does not arise from aggregation and that minor 80- and 100-kDa species accompanying varying concentrations of free monomers occurs endogenously in primary neurons as well as neuroblastoma cells that overexpress αS (Dettmer et al., 2013).

Several new questions emerged as a consequence that have been answered in part with ensuing research, while others remain contentious. Could bacterial systems employed to express and purify αS before the Selkoe report (Bartels et al., 2011) not possess the necessary physiological environment for tetramer assembly? Could *N*-α-acetylation of αS *per se* be of enough biophysical consequence to trigger the formation of aggregation-resistant tetramers? These questions

10.3389/fnins.2022.1003997

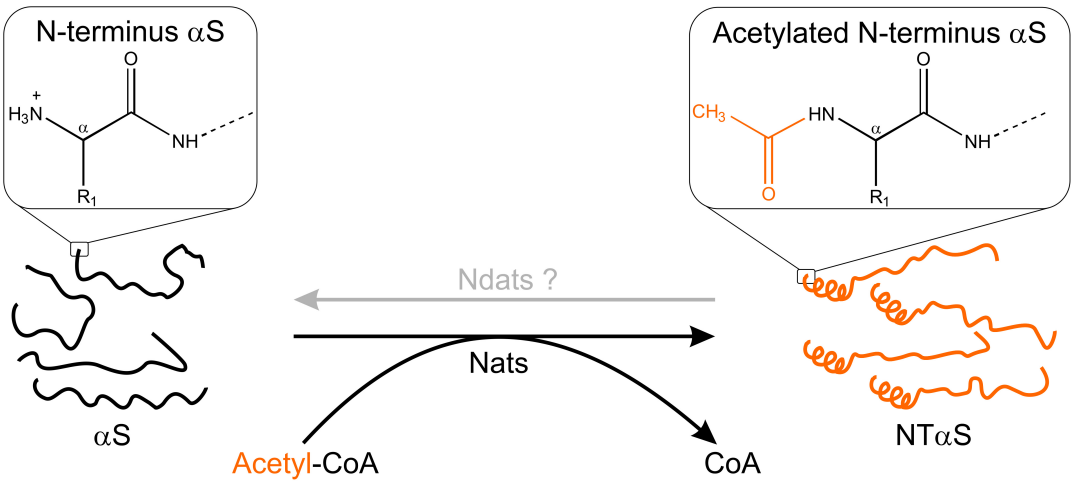

FIGURE 2
Schematic outline of N-terminal acetylation. N-terminal acetyltransferases (Nats) catalyze the transfer of an acetyl group (CH_3CO) from acetyl-CoA (Ac-CoA) to the free α-amino group of the protein N-terminus. The transferred acetyl group eliminates a positive charge at the protein N-terminus. In the case of αS, *N*-α-acetylation has been shown to induce helix formation in the first 16 residues (Maltsev et al., 2012). The existence of N-terminal de-acetyltransferases (Ndats) is unknown.

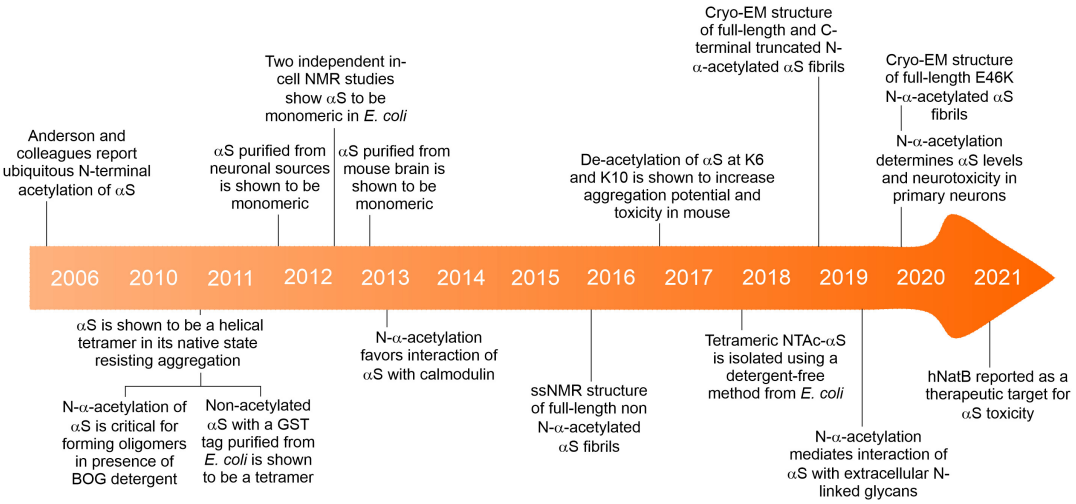

FIGURE 3
A brief timeline of key events about the *N*-α-acetylation of αS.

were answered, in part, by a report showing that non-acetylated αS purified from *Escherichia coli* (*E. coli*) closely resembled the aforementioned tetrameric species (Wang et al., 2011). However, this construct harbored a 10-residue N-terminal fusion-protein fragment (GPLGSPEFPG) post cleavage of the Glutathione S-transferase (GST) tag that could mimic the biophysical consequences of *N*-α-acetylation of αS. To test if *N*-α-acetylation of αS in bacterial cells could lead to the formation of a tetrameric species, a bacterial co-expression system was used to generate *N*-α-acetylated αS (NTAc-αS). The authors determined that N-terminal acetylation and non-denaturing purification protocols, including the non-ionic detergent octyl β-D-glucopyranoside (BOG), were necessary to observe helical oligomeric αS (Trexler and Rhoades, 2012). In this co-expression system, the NatB acetylase derived from yeast is cloned into a bacterial plasmid, allowing N-terminal acetylation of NatB peptide substrates (MD, ME, MN, MQ; see **Figure 1**) alongside the overexpression of a target protein (Johnson et al., 2010). The CD spectrum of NTAc-αS showed a helical and presumably tetrameric form when purified in the presence of BOG, while non-acetylated or BOG-free αS was disordered and monomeric. These results implicitly contradicted the hypothesis

of a folded αS tetramer in non-acetylation-competent *E. coli* cells used in the previous report (Wang et al., 2011). Could the detergents used during purification protocols lead to the proposed tetrameric state? Using the NatB bacterial co-expression system, Fernández and Lucas, 2018a,b demonstrated a detergent-free method to isolate recombinant tetrameric NTAc-αS. Subsequently, αS was shown to be monomeric by in-cell NMR studies in intact *E. coli* cells (Binolfi et al., 2012; Waudby et al., 2013) and numerous non-neuronal cells (Theillet et al., 2016). The monomer-tetramer debate is far from over but highlights the importance of how subtle environmental changes can cause significant molecular changes in αS. The physiological conditions governing the dynamic equilibrium between monomeric and tetrameric αS remain mysterious. Intuitively, an off-pathway, fibril-resistant αS tetramer can sequester aggregation-competent αS monomers. However, the irreproducibility across labs in isolating the tetrameric species, unknown factors affecting the monomer-tetramer equilibrium and tetramer stability have resulted in reluctant acceptance of its existence.

We speculate that *N*-α-acetylation alone or in combination with other post-translational modifications could be a regulatory step in maintaining an equilibrium between the monomeric and tetrameric states of αS. Tetrameric αS species have been purified from both endogenously expressing and overexpressing mammalian cell lines (Dettmer et al., 2013), ruling out pleiotropic effects of high concentrations. However, in gastrointestinal neuronal cells from rats, the population of tetrameric αS is absent, and these cells constitute primarily monomeric αS (Corbillé et al., 2016). Crowding within mammalian cells alone cannot explain the tetrameric state since in-cell NMR studies in bacterial cytoplasm (Binolfi et al., 2012; Waudby et al., 2013) and the periplasm (McNulty et al., 2006) that are significantly more crowded than mammalian cells (Swaminathan et al., 1997) affirm its monomeric state. Assuming there is an equilibrium between the tetrameric and monomeric species *in vivo*, how are the purified tetrameric αS species stably maintained, preventing their dissociation *in vitro*? A dynamic equilibrium between the tetrameric and monomeric state must be carefully regulated *in vivo*. Long-range interactions between acetyl groups and other amino acids within protein assemblies are well known (Langeberg and Scott, 2015), and transcriptional control via acetylation is one such example (Latham and Dent, 2007). It remains unclear whether *N*-α-acetylation, the purification methodology, the use of detergents, or the choice of a prokaryotic/eukaryotic expression system is crucial for tetramer formation. If *in vivo* cross-linking of tetrameric αS can be achieved, in-cell NMR studies may prove particularly useful in providing concrete evidence of such a species. In addition, how/if the distribution of the monomer-tetramer species depends on cell type and other biochemical factors needs investigation. For instance, glucocerebrosidase 1 deficiency in SH-SY5Y cells has been shown to disfavor the tetrameric αS populations over the monomeric αS population (Kim et al., 2018), while the tetrameric αS population is favored in primary neurons and erythroid cells (Dettmer et al., 2013). Addressing the *N*-α-acetylated state of αS is a promising avenue to probe the existence of a tetrameric species, to understand the possible mechanisms of amyloid formation, and to gain insights into the physiological function of αS.

Impact of *N*-α-acetylation of αS on biophysical properties and membrane binding

NTAc-αS is suggested to be a physiologically relevant brain species (Bartels et al., 2011; Fauvet et al., 2012b; Burré et al., 2013; Theillet et al., 2016), and several emerging studies have benchmarked its biophysical properties with non-acetylated αS. A summary of all biophysical properties of NTAc-αS is listed in **Table 1**. Early solution-NMR studies with NTAc-αS revealed that *N*-α-acetylation of αS triggered a helical conformation in the first 16 residues (Maltsev et al., 2012; Dikiy and Eliezer, 2014) *in vitro* and subsequently in live neuronal and non-neuronal cells using in-cell NMR (Theillet et al., 2016). The interactions of non-acetylated αS with membranes have been studied in detail, but interactions with NTAc-αS remain relatively less explored. To the best of our knowledge, membrane binding studies have been carried out only for monomeric NTAc-αS and not for the tetrameric NTAc-αS species. It is well known that the N-terminal region (aa 1–60) of αS is involved in membrane binding. However, emerging studies show that the first 15 residues in αS largely recapitulate the binding properties of full-length αS such as partition constants, molecular mobility, and membrane insertion (Pfefferkorn et al., 2012), and removal of the first 14 residues severely compromises membrane binding (Cholak et al., 2020). How *N*-α-acetylation affects the membrane binding ability of αS is unclear due to conflicting results and differing solvent conditions and membrane compositions used. For example, NTAc-αS showed enhanced membrane binding in two studies (Bartels et al., 2014; Viennet et al., 2018) and no enhancement in other studies (Fauvet et al., 2012a; Maltsev et al., 2012; Iyer et al., 2016).

Considering that *N*-α-acetylation leads to loss of a positive charge from the terminal methionine residue, *N*-α-acetylation may affect the interaction between αS and membranes or other binding partners in the cellular milieu. Intuitively, the loss of a positive charge upon *N*-α-acetylation is likely to result in a decreased affinity toward anionic lipid membranes. However, *N*-α-acetylation of αS does not affect its binding to anionic phospholipid membranes with increasing surface charge densities but shows enhanced binding to zwitterionic phospholipid membranes in a curvature-dependent manner (Dikiy and Eliezer, 2014; Iyer et al., 2016; O'Leary et al., 2018). The observation may be reasoned as follows: *N*-α-acetylation

TABLE 1 Effect of N-terminal acetylation on biophysical properties of αS.

Probed parameter		Technique used	Effect of *N*-α -acetylation compared to non-acetylated αS	References
Predominant native state		In-cell NMR	Monomeric	Fauvet et al., 2012a; Theillet et al., 2016
		Mass spectrometry, native-PAGE, CD spectroscopy, sedimentation equilibrium-analytical ultracentrifugation (SE-AUC)	Monomeric	Fauvet et al., 2012a,b; Maltsev et al., 2012; Burré et al., 2013; Iyer et al., 2016
			Tetrameric	Bartels et al., 2011; Wang et al., 2011; Luth et al., 2015; Fernández and Lucas, 2018a,b
Membrane binding of αS monomer		CD spectroscopy, isothermal calorimetry (ITC), nuclear magnetic resonance (NMR)	Enhanced binding to GM1 gangliosides	Bartels et al., 2014
			Comparable binding to GM3, POPS lipids	Maltsev et al., 2012; Bartels et al., 2014; Dikiy and Eliezer, 2014
			Moderately enhanced binding to zwitterionic lipids	Dikiy and Eliezer, 2014; Iyer et al., 2016; O'Leary et al., 2018
Aggregation properties	Amyloid formation rate	ThT fluorescence	Decreased	Kang et al., 2012; Bartels et al., 2014; Gallea et al., 2016; Ruzafa et al., 2017
			No significant effect	Fauvet et al., 2012a; Maltsev et al., 2012; Iyer et al., 2016
			Increased in presence of air-water interface	Viennet et al., 2018
	Heterogeneity in aggregation kinetics	ThT fluorescence	Decreased	Kang et al., 2012; Iyer et al., 2016
Dimer/ Oligomer formation	Oligomer formation	Solid-state nanopores and MD simulations	Decreased	Bu et al., 2017
		SE-AUC	Critically dependent on the presence of BOG detergent	Trexler and Rhoades, 2012
Fibril structure	Fibril height(nm)	Atomic force microscopy (AFM)	No significant effect	Iyer et al., 2016
	Secondary structure	CD spectroscopy	Increased β-sheet content	Iyer et al., 2016; Rossetti et al., 2016
		Raman spectroscopy	Decreased β-sheet content	Watson and Lee, 2019
	Proteinase-K digestion	ThT fluorescence and SDS-PAGE	Increased proteolysis	Iyer et al., 2016; Watson and Lee, 2019
	Periodicity	Scanning transmission electron microscopy (STEM), AFM	Increased no. of monomers per nm of fibril	Iyer et al., 2016

of αS increases the propensity of the first 16 residues in the N-terminus to organize into helices (Figure 2). The binding of αS to lipid membranes results in a loss of conformational entropy compensated for by favorable electrostatic interactions and hydrogen bonding. Since NTAc-αS binds with a pre-existing helical conformation, the loss in conformational entropy upon binding to anionic membranes is probably lower for NTAc-αS than for the non-acetylated αS. The lower entropy cost associated with helix formation is balanced by losing the positive charge upon *N*-α-acetylation. The binding of non-acetylated and NTAc-αS to anionic lipid membranes is therefore comparable. In the absence of strong, attractive forces between neutral lipid membranes and αS, the effect of *N*-α-acetylation is likely dominated by the increased propensity of αS to fold into an amphipathic helix. Since the final helical content of both NTAc-αS and non-acetylated αS is comparable, the net free energy gain upon binding of NTAc-αS is higher with neutral lipid membranes resulting in enhanced affinity for NTAc-αS.

Although monomeric non-acetylated αS faithfully mimics NTAc-αS in specific biophysical properties like hydrodynamic radii and conformational change upon binding anionic lipid membranes, it does not reflect the importance of NTAc-αS. *N*-α-acetylation may have yet unknown physiological roles that may not be realized in experiments with purified proteins *in vitro*. For example, a recent study showed that abolishing *N*-α-acetylation of αS led to lower levels of αS and substantially reduced neurotoxicity in substantia nigra of rats (Vinueza-Gavilanes et al., 2020). *N*-α-acetylation of αS may also be possibly prevented *in vivo* by mutating the aspartic acid residue (D) in the second position to a proline residue (P) as recently shown for αS (Vinueza-Gavilanes et al., 2020) and numerous other proteins (Goetze et al., 2009).

Compared to its non-acetylated counterpart, NTAc-αS binds faster to model lipid membranes but forms amyloid aggregates and fibrils slower (Ruzafa et al., 2017; Cholak et al., 2020). However, in the presence of air-water interfaces, the apparent lag-time for NTAc-αS aggregation into amyloid fibrils is nearly twofold lesser than that observed with non-acetylated-αS (Viennet et al., 2018). Further, the presence of the neuronal ganglioside GM1 in model lipid membranes impaired the ability of NTAc-αS to form ThT-positive aggregates (Bartels et al., 2014). Given that the final helical content of both NTAc-αS and non-acetylated αS are comparable, the kinetic barrier for a membrane-bound helical conformation to a β-sheet conformation would also be comparable. If so, why would NTAc-αS aggregate slower on lipid membranes? Perhaps *N*-α-acetylation stabilizes interactions within the helical conformation and orients residues along with the interface such that αS dips further in the membrane, leading to a robust anchoring. While the above-mentioned model lipid membranes provide valuable biochemical insights, the next step must be to validate these observations in mammalian cells. Despite differences in the kinetics of membrane binding, the membrane-bound conformation and the morphology of micelle-induced aggregates of NTAc-αS are invariant with non-acetylated αS. Mimicking the biophysical consequences of N-α-acetylation of αS with or without PD familial mutations, for example, charge swap on terminal methionine, conformational restriction/stabilization of the N-terminal region, are needed to understand the monomer-tetramer equilibrium, aggregation on or in presence of lipid membranes will provide valuable mechanistic and functional insights into the role *N*-α-acetylation of αS.

How does acetylation of αS impact aggregation in amyloid structures?

The effect of *N*-α-acetylation on the structure of αS monomer and amyloid conformation has been investigated using multiple techniques in recent years. At the monomer level, *N*-α-acetylation does not affect the hydrodynamic radius, electrophoretic properties, and oligomerization potential of αS, suggesting minimal changes in the overall structure and biochemistry as compared to non-acetylated αS (Fauvet et al., 2012a; Kang et al., 2012; Gallea et al., 2016; Ni et al., 2019). However, NMR studies using ^{1}H-^{15}N HSQC show a significant difference in the chemical environment of the first nine residues and increased helical propensity of the first 12 residues (Fauvet et al., 2012a; Kang et al., 2012; Maltsev et al., 2012). The increased helicity of the N-terminus on acetylation mirrors the structural transitions observed in αS in the presence of model membranes, albeit only in a small region of the protein (Davidson et al., 1998; Eliezer et al., 2001; Georgieva et al., 2008). The acetyl carbonyl (C=O) group can participate in a hydrogen bond with the amino H (N-H) group from subsequent amino acids, which can stabilize a helix by sealing its fraying end (Fairman et al., 1989; Chakrabartty et al., 1993; Doig et al., 1994). NTAc-αS with helical N-terminus may facilitate its transition from a random coil to an α-helix *in vivo*, on interaction with a membrane surface, due to lower entropic cost and favorable dipole interactions associated with adding residues to an α-helix rather than initiating the helix (Zimm and Bragg, 1959; Creighton, 1993). In addition to the N-terminus, weak long-range interactions around residues 28–31, 43–46, 50, and 50–66 were also reported in acetylated αS (Kang et al., 2012). All these sites, toward the end of the N-terminal region (aa 1–60) and the beginning of the NAC region (aa 61–95) of αS, are associated with αS function and familial forms of PD (Polymeropoulos et al., 1997; Krüger et al., 1998; Zarranz et al., 2004; Lesage et al., 2013; Proukakis et al., 2013; Pasanen et al., 2014).

Histidine-50 is one of the copper (I) binding sites of αS that is mutated in the familial form of PD (H50Q mutation) (Sung et al., 2006; Proukakis et al., 2013). Non-acetylated αS binds copper via a coordination complex involving the N-terminal amine group of methionine-1, backbone and side chain of aspartate-2, and the imidazole ring of histidine-50 (Dudzik et al., 2011). A clear difference in methionine-1 and aspartate-2 environment on acetylation in NMR studies (Fauvet et al., 2012a; Kang et al., 2012) is predictive of different αS-copper interaction in acetylated and non-acetylated form. H50Q mutation in non-acetylated αS increases the aggregation of monomeric αS into amyloid structures, with minor changes in the secondary structure and negligible effect on the overall copper binding capacity (Uversky et al., 2001; Ghosh et al., 2013). Copper binding in *N*-α-acetylated H50Q protein (the *in vivo* form of H50Q mutation) is impaired, likely due to a double hit at the copper coordination complex; lack of the N-terminal amine, and the absence of the imidazole side chain at position 50 (Mason et al., 2016). Loss of copper-binding in acetylated H50Q is likely to interfere with the proposed ferrireductase activity of αS, leading to defects in metal homeostasis *in vivo* (Davies et al., 2011; Mezzaroba et al., 2019).

N-α-acetylated αS, like non-acetylated αS, aggregates into oligomers and fibrils under various experimental conditions (Kang et al., 2012; Maltsev et al., 2012; Gallea et al., 2016; Lima et al., 2019; Watson and Lee, 2019). There are varying reports for the effect of acetylation on both oligomers and fibrils. The extent of oligomerization of acetylated αS has been reported to be the same (Fauvet et al., 2012a; Kang et al., 2012) as well as reduced (Bu et al., 2017). Further, acetylated oligomers and fibrils show morphological and spectral features similar to unmodified αS, except for increased β-sheet and helical content in acetylated αS oligomers (Gallea et al., 2016; Iyer et al., 2016). The acetylated forms of familial PD mutants, E46K, H50Q, and A53T, show increased aggregation in 3,4-dihydroxyphenylacetaldehyde (DOPAL), dopamine, and SDS micelles, in comparison to wild-type acetylated αS (Ruzafa et al., 2017; Lima et al., 2019). Changes in fibrillization kinetics of wild-type αS upon acetylation are also ambiguous. Some studies report no significant difference (Fauvet et al., 2012a; Maltsev et al., 2012; Iyer et al., 2016), while others report slower kinetics, especially in the elongation rate (Kang et al., 2012; Ruzafa et al., 2017; Watson and Lee, 2019). This reduced elongation rate could be due to a helical secondary structure at the N-terminus that likely hinders the conversion of a monomer into the typical fibrillar β-sheet conformation (Kang et al., 2012). Acetylated αS is reported to yield distinct polymorphs (Watson and Lee, 2019) with likely increased structural homogeneity within a population (Iyer et al., 2016). The increased structural homogeneity in a fibril population may arise from a monomeric pool that is "structurally homogenous" (**Figure 2**). *N*-α-acetylation of αS results in a homogenous ensemble wherein 16 amino acids are in a helical conformation, leading to the nucleation of a homogenous population of fibrils. In a distinct polymorph, the reduced elongation rate can also be due to lower Thioflavin-T sensitivity toward acetylated αS, as Thioflavin-T fluorescence assay is sensitive to changes in topological features (Sidhu et al., 2018; Watson and Lee, 2019).

Structurally, fibrils formed by acetylated and non-acetylated αS show a mix of similar and distinct features. An overlay of four full-length αS structures, two with acetylation and two without acetylation, reveal an analogous backbone arrangement (**Figure 4A**; Tuttle et al., 2016; Li B. et al., 2018; Li Y. et al., 2018; Ni et al., 2019). Both types of fibril structures are formed of two protofilaments that intertwine in a twisted fibril morphology along a 21 screw axis – placing two monomers ∼180° to each other with an interaction surface in the center (Li B. et al., 2018; Li Y. et al., 2018; Ni et al., 2019). The N-α-acetylated protofilaments show a left-handed helical twist of –0.72° and a rise of ∼4.8 Å (Li Y. et al., 2018; Ni et al., 2019), while the non-acetylated protofilaments show a right-handed helical twist of 179.1° and a rise of 2.4 Å (Li B. et al., 2018). The dimer interaction surface in acetylated fibrils is formed by a hydrophobic steric zipper between residues histidine-50 to glutamate-57. Additionally, electrostatic interactions between histidine-50 and lysine-45 from one monomer and glutamate-57 from another monomer, and salt bridges between lysine-58: glutamate-61 (K58-E61) and glutamate-46: lysine-80 (E46-K80) stabilize the fibril core (Li Y. et al., 2018; Ni et al., 2019). In non-acetylated fibrils, the steric zipper is formed by residues further in the NAC region. Residues 55–62 are disordered (ssNMR studies) or do not form the steric zipper (cryoEM studies). The dimer interaction surface is formed by valine-71 to valine-82 in ssNMR studies and by glycine-68 to alanine-78 in cryoEM structures. Moreover, lysine-58 is flipped outward, resulting in the absence of the K58-E61 salt bridge (**Figure 4A**; Tuttle et al., 2016; Li Y. et al., 2018).

The stabilizing effect of the salt-bridges on protein structure is well known, particularly in the case of αS. The compromised salt bridge between E46 and K80 side chains in an E46K variant of αS leads to a structurally homogenous yet entirely different fibril structure (consisting of one fibril species) and is more pathogenic compared to the wild-type αS (Boyer et al., 2020). A summary of all the available fibril structures of αS in PDB is listed in **Table 2**, with corresponding indicators for the K58-E61 salt bridge in each structure. An exciting facet of the αS fibril structure emerges concerning the K58-E61 salt bridge. Full-length *N*-α-acetylated αS fibrils have the K58-E61 salt bridge intact in sharp contrast to non-*N*-α-acetylated αS fibrils. The presence of the K58-E61 salt bridge is not influenced by *N*-α-acetylation alone but also by C-terminal truncation, phosphorylation of Tyr39, E46K mutation, and fibril polymorphism. The stark differences in the orientation of K58 cannot be an artifact of differing aggregation conditions since, in a single study employing identical aggregation conditions, the K58-E61 salt bridge was preserved in full-length *N*-α-acetylated αS fibrils and 1–103 *N*-α-acetylated αS fibrils but broken in 1–122 *N*-α-acetylated αS fibrils (Ni et al., 2019). Further, comparing structures of C-terminal truncated 1–121/2 αS fibrils suggests little or no role of *N*-α-acetylation on the orientation of K58 (**Figure 4B**). Why is the orientation of K58 sensitive to *N*-α-acetylation in full-length αS fibrils but not in C-terminal truncated αS fibrils? Further experiments elucidating the driving force for the K58-E61 salt bridge could be exciting and may give us a better understanding of salt-bridges in the stability of αS fibrils. It is unclear if the orientation of K58 and the salt bridge between K58-E61 is physiologically relevant to its cellular function or pathological aggregation of αS. The outward orientation of K58 may render non-acetylated, and C-terminally truncated fibrils exposed to ubiquitination or SUMOylation (signal for proteasome-induced degradation) or acetylation by lysine acetylases.

N-terminal de-acetyltransferases (Ndats) are not known in eukaryotic cells as yet, suggesting constitutional *N*-α-acetylation of αS by N-terminal acetyltransferases (Nats). Could it be possible that Nats decline in function or decrease in expression levels in an age-dependent manner? Such a scenario would result in a decrease in *N*-α-acetylated αS over time and possibly

10.3389/fnins.2022.1003997

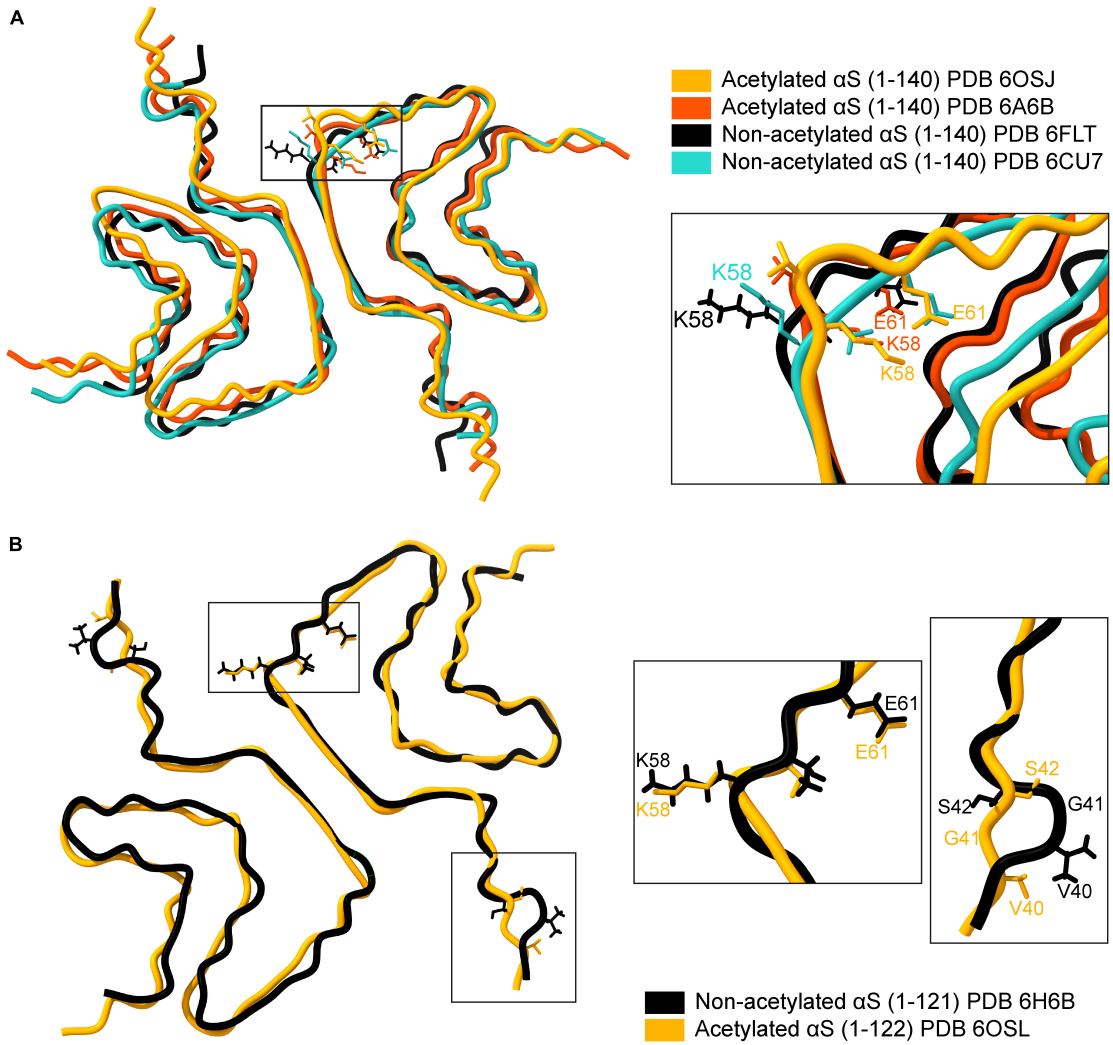

FIGURE 4
Comparison of available cryo-EM structures of the full-length acetylated (yellow, PDB ID: 6OSJ and orange, PDB ID:6A6B) and non-acetylated αS fibrils (black, PDB ID: 6FLT and blue, PDB ID:6CU7). **(A)** The backbone overlay of acetylated and non-acetylated αS fibrils is shown. The residue K58 in both acetylated αS fibrils is flipped inward, forming a salt bridge between K58-E61 (see inset). In contrast, the salt bridge is broken in acetylated αS fibrils due to the outward flip of K58. **(B)** The backbone overlay generated using ChimeraX of truncated (1-121/2) acetylated (yellow, PDB ID: 6OSL) and non-acetylated αS fibrils (black, PDB ID: 6H6B) depicting flipped K58 residues irrespective of acetylation state and minor loop fluctuations around the G41 residue.

affect its function and interaction with its binding partners. It has been shown by several groups that *N*-α-acetylated αS fibrils are less cytotoxic compared to non-*N*-α-acetylated αS fibrils. Studies investigating the absolute amounts of *N*-α-acetylated αS and non-*N*-α-acetylated αS in healthy and diseased patients would be a significant step forward. The proposed hypothesis on Nats draws parallels from a study investigating the effect of the NAD-dependent deacetylase sirtuin 2 (SIRT2) on the aggregation potential and cytotoxicity of αS. The authors showed that lysine residues acetylated at the ε-amino positions in the N-terminal region of αS (K6 and K10) from mice brains could be deacetylated by SIRT2. The deacetylation event exacerbated its aggregation potential and toxicity *in vitro* and in the substantia nigra of rats (de Oliveira et al., 2017). Furthermore, mutating K6 and K10 residues to create αS variants that are acetylation-resistant or mimic constitutive acetylation showed that acetylation at these residues prevents αS aggregation in the substantia nigra of rats. The remarkable changes in aggregation potential and toxicity of αS *in vivo* resulting from acetylation of N-terminal lysine residues are intriguing. The authors proposed a model in which the age-dependent increase of SIRT2 in the brain, with the concomitant decrease of acetylated αS, leads to increased αS aggregation and the worsening of the expected defects in the autophagy-lysosome pathway (ALP) associated with aging.

TABLE 2 Comparison of available αS fibril structures and an overview of K58-E61 salt bridge.

N-terminal-αS	Salt bridge K58-E61	Orientation		PDB ID	Method	References
		K58	E61			
Full-length						
NH2-αS, 1–140	Broken	Out	In	2N0A	ssNMR	Tuttle et al., 2016
N-α-acetyl-αS, 1–140	Present	In	In	6A6B	cryoEM	Li Y. et al., 2018
N-α-acetyl-αS, 1–140	Present	In	In	6OSJ	cryoEM	Ni et al., 2019
NH2-αS, 1–140	Broken	Out	In	6FLT	cryoEM	Guerrero-Ferreira et al., 2018
Polymorph						
NH2-αS rod	Broken	Out	In	6CU7	cryoEM	Li B. et al., 2018
NH2-αS twister	Broken	Out	In	6CU8	cryoEM	Li B. et al., 2018
NH2-αS fibril polymorph 2A	Broken	Out	Out	6SSX	cryoEM	Guerrero-Ferreira et al., 2019
NH2-αS fibril polymorph 2B	Broken	Out	Out	6SST	cryoEM	Guerrero-Ferreira et al., 2019
**N*-α-acetyl-αS filament: MSA Type I	Broken	Out	In	6XYO	cryoEM	Schweighauser et al., 2020
**N*-α-acetyl-αS filament: MSA Type II-1	Broken	Out	In	6XYP	cryoEM	Schweighauser et al., 2020
**N*-α-acetyl-αS filament: MSA II-2	Broken	Out	In	6XYQ	cryoEM	Schweighauser et al., 2020
Truncations/Modifications						
NH2-αS,1-121	Broken	Out	In	6H6B	cryoEM	Guerrero-Ferreira et al., 2018
N-α-acetyl-αS, 1–103	Present	In	In	6OSM	cryoEM	Ni et al., 2019
N-α-acetyl-αS, 1–122	Broken	Out	In	6OSL	cryoEM	Ni et al., 2019
NH2-αS phosphoTyr39 (twist dimer)	Broken	Out	Out	6L1T	cryoEM	Zhao et al., 2020b
NH2-αS phosphoTyr39 (twist trimer)	Broken	Out	Out	6L1U	cryoEM	Zhao et al., 2020b
PD mutants						
NH2-αS E46K, 1–140	Broken	Out	Out	6UFR	cryoEM	Boyer et al., 2020
N-α-acetyl-αS E46K, 1–140	Broken	Out	Out	6L4S	cryoEM	Zhao et al., 2020a
N-α-acetyl-αS A53T, 1–140	Present	In	In	6LRQ	cryoEM	Sun et al., 2020
NH2-αS H50Q Wide Fibril	Present	In	In	6PES	cryoEM	Boyer et al., 2019
NH2-αS H50Q Narrow Fibril	Present	In	In	6PEO	cryoEM	Boyer et al., 2019

The wild-type interactions of αS protofibrils are perturbed in familial PD mutations. The observation is not surprising as most of the mutations associated with the familial form of PD (H50Q, G51D, A53T, A53E) are located at the dimerization interface. The H50Q mutation disrupts the H50-K45-E57 interaction, while the E46K mutation breaks the E46-K80 salt bridge (Li B. et al., 2018). In A53T mutations, the dimerization core is formed by only two residues, Tyr-59 and Lys-60, instead of seven residues (H50-E57) in wild-type αS (Sun et al., 2020). Thus, these mutations can be expected to weaken the fibril core, resulting in morphological differences and greater fragmentation that consequently may increase seeding potential (Zhao et al., 2020a).

In structural studies, acetylated and non-acetylated αS fibrils could seed aggregation reactions and were cytotoxic (Tuttle et al., 2016; Li B. et al., 2018; Li Y. et al., 2018). In wild-type αS, acetylated αS seeds faithfully template fibril morphology across multiple seeding reactions, while non-acetylated αS seeds show poorer templating (Watson and Lee, 2019). Since the seed molecule's conformation is critical in templating reactions, an unstable fibril core in non-acetylated αS, due to the absence of the K58-E61 salt bridge, may lead to poor templating (Sidhu et al., 2016). NMR studies show that in seeded aggregations of acetylated αS monomers with fibril seeds and off-pathway oligomers, the first 11 residues interact with the seeds in both the cases—successful templating with fibril seeds and unsuccessful templating with off-pathway oligomers. The observation suggests that the N-terminal interaction of acetylated αS is the first point of contact between a seed and a free monomer, irrespective of templating outcome (Yang et al., 2021). The differences between oligomers and fibrils from acetylated and non-acetylated αS monomers are likely due to the acetyl group. Still, some of the differences, at least, could also be due to differences in fibril preparation protocols used in each study. Differences in protein concentration; solution conditions like buffer, salt, metal ions, small molecules; agitation; incubation time have a significant effect on the kinetics and morphology of αS fibrils (Hoyer et al., 2002; Heise et al., 2005; Powers and Powers, 2006; Vilar et al., 2008; Knowles et al., 2009; Morel et al., 2010; Bousset et al., 2013; Buell et al., 2013, 2014; Sidhu et al., 2014; Buell, 2019; Panuganti and Roy, 2020). Since all the studies compared here have differences in

the parameters mentioned above, a direct comparison to arrive at an empirical conclusion is challenging.

Effect of N-terminal acetylation on the physiological function of αS

More than 300 post-translational modifications (PTMs) are known to occur in proteins (Clark et al., 2005), but a handful of these are known for αS, and their implications have been discussed in detail (Beyer, 2006; Zhang et al., 2019). These modifications include acetylation, phosphorylation, nitration, glycosylation, SUMOylation, ubiquitination, di-tyrosine crosslinking, and methionine oxidation. While the impact of PTMs in αS has been studied extensively in isolation, very few studies have considered the impact of *N*-α-acetylation in concert with the modifications mentioned above. Experiments in yeast show that deletion of NatB selectively increased localization of αS to cytoplasm and not plasma membrane as in wild-type yeast (Zabrocki et al., 2008). Evidence for the role of N-terminal acetylation of αS in its function are scarce and are still emerging. Since *in vivo* αS is universally present in the acetylated form (Bartels et al., 2011; Fauvet et al., 2012b; Burré et al., 2013; Theillet et al., 2016), all the studies with endogenous αS represent functions of acetylated αS. However, most of the studies with recombinant αS report behavior of non-acetylated αS. Only systematic comparative studies of αS behavior from endogenous and recombinant αS can delineate the effects of N-terminal acetylation. Limited studies that focus on the acetylated αS show that acetylated forms are involved in Lewy body associated pathology, metal homeostasis and synaptic function. Mass-spectrometry based studies from postmortem tissue of dementia with Lewy bodies (DLB) and PD patients, show full-length and truncated acetylated αS forms (Ac-αS_{1-139}, Ac-αS_{1-119} Ac-αS_{1-103}) and no non-acetylated forms, suggesting that in both disease and healthy conditions acetylation is present (Öhrfelt et al., 2011). This is consistent with another study that identified multiple truncated acetylated forms (Ac- αS_{1-6}, Ac- αS_{13-21}, Ac- αS_{35-43}, Ac- αS_{46-58}, Ac- αS_{61-80}, Ac- αS_{81-96}, Ac- $\alpha S_{103-119}$) of αS in Lewy body enriched fractions of PD patient samples (Bhattacharjee et al., 2019). In addition to brain tissues, only NTAc-αS can be detected in blood from Alzheimer's patients and not the non-acetylated form, which is an indicator of neuronal death (Pero-Gascon et al., 2020). These studies highlight the importance to study physiologically relevant biochemistry of αS in acetylated forms to find better inhibitors for αS aggregation and to identify biomarkers.

αS is a copper binding protein with two sites for interaction with copper: Met 1-Met 5 and Ala 49-His 50 (Dudzik et al., 2011). Copper binding at Met 1–Met 5 is different for acetylated and non-acetylated αS forms. Copper binding in non-acetylated form at position Met 1–Met 5 results in a redox active state that can reduce metals while acetylated αS, though binds Cu^{2+}, does not exhibit redox behavior (Garza-Lombó et al., 2018). The copper binding behavior of αS at the N-terminus is observed both in solution and membrane bound conformations (Dudzik et al., 2013). Since both N-terminal acetylation and copper binding increase the propensity of αS to adopt α-helical conformation, it is likely that they synergistically contribute to αS interaction with synaptic vesicles.

Could N-terminal acetylation of αS be a priming event?

Post-translational modifications can be reversible or irreversible, and the regulatory dynamics of these modifications may give vital insights into protein function. Unlike reversible PTMs, like phosphorylation, glycosylation, ubiquitination, SUMOylation, methionine oxidation, nitration that may be rapidly added or removed from a protein under varied metabolic or pathologic cues, N-α-acetylation has been thought to be irreversible and occurring co-translationally. However, there is emerging evidence that acetylation of N-termini of proteins does necessarily occur co-translationally (Dormeyer et al., 2007). When ^{15}N isotope-enriched non-acetylated αS was delivered into A2780, HeLa, RCSN-3, B65, and SK-N-SH cells using electroporation and was found to be *N*-α-acetylated entirely within 5 h (Theillet et al., 2016). These evidences suggest that cells prefer *N*-α-acetylated αS. It may be energetically more favorable for ubiquitous acetylation of αS to occur co-translationally.

There is no evidence of the existence of N-terminal de-acetyltransferases (Ndats), suggesting the irreversible nature of *N*-α-acetylation. This observation opens new avenues to investigate the existence of N-terminal de-acetyltransferases (Ndats) and other regulatory mechanisms that could (dys)regulate *N*-α-acetylation of αS. NMR studies have shown that *N*-α-acetylation induces stable α-helix formation in the first 16 amino acid residues in αS (Maltsev et al., 2012). *N*-α-acetylation of αS occurs co-translationally in eukaryotes and therefore precedes all other PTMs. Not surprisingly, the various permutations of PTMs mentioned above in αS preparations have consistently reported *N*-α-acetylation of αS at the least. We speculate that *N*-α-acetylation may "prime" αS for subsequent PTMs vital to its function and explain the cellular need to acetylate the N-terminus co-translationally. Our speculation is based on several observations: (a) *N*-α-acetylation led to plasma membrane localization of acetylated αS in yeast while non-acetylated αS remained in the cytoplasm. Further, the study showed decreased levels of Ser129 phosphorylation in non-acetylated αS compared to acetylated αS (Zabrocki et al., 2008). (b) Crosstalk between acetylation and other PTMs in a given protein is well known in eukaryotes (Yang and Seto, 2008) and impacts cell fate, and has implications for aging (Ree et al., 2018). For example, acetylation of histone H3 at K9/27 positions crosstalk with phosphorylation at S10/28 positions,

respectively, to affect downstream gene expression (Latham and Dent, 2007). (c) The formation of a stabilized helix upon *N*-α-acetylation may provide lysine acetylases a helical scaffold (compared to disordered chain in non-acetylated αS) to effectively acetylate lysine residues in the 6th and 10th position in αS. Such scaffolds are well known in the context of signaling proteins and multi-protein complexes in eukaryotes (Langeberg and Scott, 2015). (d) The lack of Ndats potentially highlights the importance of *N*-α-acetylation of αS, with as yet unknown modes of regulation. Typically, modifications closely involved in regulatory processes are reversible processes (Martin, 2007). Examples of such reversible processes include protein (de)phosphorylation, (de)acetylation, (de)adenylylation, and (de)ADP-ribosylation. Additionally, Acetyl-CoA is a key metabolite in cellular metabolism and its consumption for the *N*-α-acetylation of αS indicates a necessary protein modification. (e) *N*-α-acetylation has been shown to inhibit protein targeting to the endoplasmic reticulum (Forte et al., 2011).

The priming role of *N*-α-acetylation of αS suggested here may have evaded sight as it likely does not require genomic regulation or quantitative changes in αS levels. Thus, *in vivo* studies investigating the impact of *N*-α-acetylation of αS on subsequent PTMs, especially phosphorylation, may help us understand if *N*-α-acetylation has a priming function. Understanding the crosstalk between *N*-α-acetylation and S129 phosphorylation is vital since several reports show accelerated inclusion formation and cellular toxicity in different models triggered by S129 phosphorylation (Smith et al., 2005; Sugeno et al., 2008). Additionally, more than 90% of αS deposited in Lewy bodies (LBs) in PD patients is phosphorylated at S129 while healthy individuals exhibit roughly 4% S129 phosphorylation (Arawaka et al., 2017).

Directions for future research

The physiologically native state of αS is unquestionably *N*-α-acetylated. The observation has been determined exhaustively in numerous mammalian cells and organisms. It remains irrefutably an irreversible modification in αS so far. The impact of *N*-α-acetylation of αS in the context of pathological consequences (aggregation into toxic oligomers, fibrils, and higher-ordered aggregates) is increasingly being investigated. With the advent of cryo-EM, we are beginning to see structural details of αS fibrils at unprecedented spatial resolutions. Emerging studies are benchmarking the fibril structure of NTAc-αS housing PD familial mutations with endogenous αS fibrils isolated from diseased patients. However, despite these achievements, the impact of *N*-α-acetylation on the function of αS is still murky.

It is vital to understand how acetylation imbalance in αS manifests *in vivo* and which physiological consequences of the imbalance lead to neurotoxicity (de Oliveira et al., 2017). In this respect, a detailed proteomics study documenting the ratio of acetylated and non-acetylated αS over the progress of Lewy body formation would be remarkable. Emerging studies have shown enough evidence of *N*-α-acetylation affecting several downstream processes in living cells. A recent study demonstrated that *N*-α-acetylation of αS determines αS levels and subsequent toxicity in primary neurons (Vinueza-Gavilanes et al., 2020). Using point mutants that altered or blocked *N*-α-acetylation, the authors demonstrated that blocking *N*-α-acetylation led to a decrease in αS levels in live primary neurons and concomitantly reduced neurotoxicity. The prospect of blocking *N*-α-acetylation of αS by NatB is exciting, yet, maybe challenging for drug discovery strategies given that NatB acetylates ∼20% of cellular proteins. CRISPR-based strategies in the future may be able to edit the first two N-terminal amino acids and demonstrate if *in vivo* blocking *N*-α-acetylation of αS may help to decrease αS levels. Although NTAc-αS is recognized as the physiologically relevant species in healthy brain cells – in both the soluble and insoluble fractions of brain tissues of PD patients (Anderson et al., 2006) – the use of non-acetylated αS is rampant in emerging literature. The use of NTAc-αS must be encouraged, and NTAc-αS should be a gold standard for all studies investigating this multi-faceted protein (Lashuel et al., 2013) concerning conformational changes, oligomerization and aggregation propensities, lipid interactions, and other cellular binding partners.

In the future, we must focus our efforts toward elucidating (a) the effect of co-occurring *N*-α-acetylation and other PTMs in αS on its membrane (un)binding, oligomer/fibril structure, and corresponding aggregation kinetics, (b) the effect of co-occurring *N*-α-acetylation and familial PD mutations on αS function and aggregation into fibrillar structures, (c) the relation between the level of *N*-α-acetylation of αS and the progression rate of neurodegeneration in synucleinopathies, (d) the relation between metal-ion (dys)homeostasis and cellular models of synucleinopathies wherein levels of *N*-α-acetylation can be modulated, and (e) the complex relation between aggregation rates, diffusion coefficients, macromolecular crowding and *N*-α-acetylated αS *in vivo*. We may also want to investigate the interplay of regulatory factors (sirtuins) or genetic circuits triggered in PD patients and *N*-α-acetylation levels. While the physiological function of αS remains evasive, *N*-α-acetylation of αS presents an exciting path for future research.

Author contributions

AI, AS, and VS wrote the manuscript. All authors contributed to the article and approved the submitted version.

Funding

This work presented here was part of a FOM-program entitled "A Single Molecule View on Protein Aggregation" (No. 127). We acknowledge generous funding from the work funded by the erstwhile Foundation for Fundamental Research on Matter (FOM), now subsumed by the Dutch Research Council (NWO). We also acknowledge support from NanoNextNL, a micro- and nanotechnology consortium of the Government of The Netherlands and 130 partners.

Acknowledgments

We thank Mireille Claessens (University of Twente, Enschede, Netherlands) for many helpful and stimulating discussions.

Conflict of interest

The authors declare that the research was conducted in the absence of any commercial or financial relationships that could be construed as a potential conflict of interest.

Publisher's note

References

Aksnes, H., Drazic, A., Marie, M., and Arnesen, T. (2016). First things first: Vital protein marks by N-terminal acetyltransferases. *Trends Biochem. Sci.* 41, 746–760. doi: 10.1016/j.tibs.2016.07.005

Aksnes, H., Ree, R., and Arnesen, T. (2019). Co-translational, post-translational, and non-catalytic roles of N-terminal acetyltransferases. *Mol. Cell* 73, 1097–1114. doi: 10.1016/j.molcel.2019.02.007

Ametzazurra, A., Larrea, E., Civeira, M. P., Prieto, J., and Aldabe, R. (2008). Implication of human N-α-acetyltransferase 5 in cellular proliferation and carcinogenesis. *Oncogene* 27, 7296–7306. doi: 10.1038/onc.2008.332

Anderson, J. P., Walker, D. E., Goldstein, J. M., De Laat, R., Banducci, K., Caccavello, R. J., et al. (2006). Phosphorylation of Ser-129 is the dominant pathological modification of α-synuclein in familial and sporadic Lewy body disease. *J. Biol. Chem.* 281, 29739–29752. doi: 10.1074/jbc.M600933200

Antony, T., Hoyer, W., Cherny, D., Heim, G., Jovin, T. M., and Subramaniam, V. (2003). Cellular polyamines promote the aggregation of α-synuclein. *J. Biol. Chem.* 278, 3235–3240. doi: 10.1074/jbc.M208249200

Arawaka, S., Sato, H., Sasaki, A., Koyama, S., and Kato, T. (2017). Mechanisms underlying extensive Ser129-phosphorylation in α-synuclein aggregates. *Acta Neuropathol. Commun.* 5:48. doi: 10.1186/s40478-017-0452-6

Arnaudo, N., Fernández, I. S., McLaughlin, S. H., Peak-Chew, S. Y., Rhodes, D., and Martino, F. (2013). The N-terminal acetylation of Sir3 stabilizes its binding to the nucleosome core particle. *Nat. Struct. Mol. Biol.* 20, 1119–1121. doi: 10.1038/nsmb.2641

Arnesen, T., Van Damme, P., Polevoda, B., Helsens, K., Evjenth, R., Colaert, N., et al. (2009). Proteomics analyses reveal the evolutionary conservation and divergence of N-terminal acetyltransferases from yeast and humans. *Proc. Natl. Acad. Sci. U.S.A.* 106, 8157–8162. doi: 10.1073/pnas.0901931106

Barrett, P. J., and Greenamyre, T. J. (2015). Post-translational modification of α-synuclein in Parkinson's disease. *Brain Res.* 1628, 247–253. doi: 10.1016/j.brainres.2015.06.002

Bartels, T., Ahlstrom, L. S., Leftin, A., Kamp, F., Haass, C., Brown, M. F., et al. (2010). The N-terminus of the intrinsically disordered protein α-synuclein triggers membrane binding and helix folding. *Biophys. J.* 99, 2116–2124. doi: 10.1016/j.bpj.2010.06.035

Bartels, T., Choi, J. G., and Selkoe, D. J. (2011). α-Synuclein occurs physiologically as a helically folded tetramer that resists aggregation. *Nature* 477, 107–111. doi: 10.1038/nature10324

Bartels, T., Kim, N. C., Luth, E. S., and Selkoe, D. J. (2014). N-alpha-acetylation of α-synuclein increases its helical folding propensity, GM1 binding specificity and resistance to aggregation. *PLoS One* 9:e103727. doi: 10.1371/journal.pone.0103727

Bartels, T., and Selkoe, D. J. (2013). Bartels & Selkoe reply. *Nature* 498, E6–E7. doi: 10.1038/nature12126

Behnia, R., Panic, B., Whyte, J. R. C., and Munro, S. (2004). Targeting of the Arf-like GTPase Arl3p to the Golgi requires N-terminal acetylation and the membrane protein Sys1p. *Nat. Cell Biol.* 6, 405–413. doi: 10.1038/ncb1120

Beyer, K. (2006). α-Synuclein structure, posttranslational modification and alternative splicing as aggregation enhancers. *Acta Neuropathol.* 112, 237–251. doi: 10.1007/s00401-006-0104-6

Bhattacharjee, P., Öhrfelt, A., Lashley, T., Blennow, K., Brinkmalm, A., and Zetterberg, H. (2019). Mass spectrometric analysis of Lewy body-enriched α-synuclein in Parkinson's disease. *J. Proteome Res.* 18, 2109–2120. doi: 10.1021/acs.jproteome.8b00982

Binolfi, A., Theillet, F. X., and Selenko, P. (2012). Bacterial in-cell NMR of human α-synuclein: A disordered monomer by nature? *Biochem. Soc. Trans.* 40, 950–954. doi: 10.1042/BST20120096

Bousset, L., Pieri, L., Ruiz-Arlandis, G., Gath, J., Jensen, P. H., Habenstein, B., et al. (2013). Structural and functional characterization of two alpha-synuclein strains. *Nat. Commun.* 4:2575. doi: 10.1038/ncomms3575

Boyer, D. R., Li, B., Sun, C., Fan, W., Sawaya, M. R., Jiang, L., et al. (2019). Structures of fibrils formed by α-synuclein hereditary disease mutant H50Q reveal new polymorphs. *Nat. Struct. Mol. Biol.* 26, 1044–1052.

Boyer, D. R., Li, B., Sun, C., Fan, W., Zhou, K., Hughes, M. P., et al. (2020). The α-synuclein hereditary mutation E46K unlocks a more stable, pathogenic fibril structure. *Proc. Natl. Acad. Sci. U.S.A.* 117, 3592–3602. doi: 10.1073/pnas.1917914117

Breydo, L., Wu, J. W., and Uversky, V. N. (2012). α-Synuclein misfolding and Parkinson's disease. *Biochim. Biophys. Acta* 1822, 261–285.

Bu, B., Tong, X., Li, D., Hu, Y., He, W., Zhao, C., et al. (2017). N-terminal acetylation preserves α-synuclein from Oligomerization by blocking intermolecular hydrogen bonds. *ACS Chem. Neurosci.* 8, 2145–2151. doi: 10.1021/acschemneuro.7b00250

Buell, A. K. (2019). The growth of amyloid fibrils: Rates and mechanisms. *Biochem. J.* 476, 2677–2703. doi: 10.1042/BCJ20160868

Buell, A. K., Galvagnion, C., Gaspar, R., Sparr, E., Vendruscolo, M., Knowles, T. P. J., et al. (2014). Solution conditions determine the relative importance of nucleation and growth processes in α-synuclein aggregation. *Proc. Natl. Acad. Sci. U.S.A.* 111, 7671–7676. doi: 10.1073/pnas.1315346111

Buell, A. K., Hung, P., Salvatella, X., Welland, M. E., Dobson, C. M., and Knowles, T. P. J. (2013). Electrostatic effects in filamentous protein aggregation. *Biophys. J.* 104, 1116–1126. doi: 10.1016/j.bpj.2013.01.031

Burré, J., Vivona, S., Diao, J., Sharma, M., Brunger, A. T., and Südhof, T. C. (2013). Properties of native brain α-synuclein. *Nature* 498, E4–E6. doi: 10.1038/nature12125

Chakrabartty, A., Doig, A. J., and Baldwin, R. L. (1993). Helix capping propensities in peptides parallel those in proteins. *Proc. Natl. Acad. Sci. U.S.A.* 90, 11332–11336. doi: 10.1073/pnas.90.23.11332

Cholak, E., Bugge, K., Khondker, A., Gauger, K., Pedraz-Cuesta, E., Pedersen, M. E., et al. (2020). Avidity within the N-terminal anchor drives α-synuclein membrane interaction and insertion. *FASEB J.* 34, 7462–7482. doi: 10.1096/fj.202000107R

Choudhary, C., Weinert, B. T., Nishida, Y., Verdin, E., and Mann, M. (2014). The growing landscape of lysine acetylation links metabolism and cell signalling. *Nat. Rev. Mol. Cell Biol.* 15, 536–550. doi: 10.1038/nrm3841

Clark, R. S. B., Bayir, H., and Jenkins, L. W. (2005). Posttranslational protein modifications. *Crit. Care Med.* 33, S407–S409. doi: 10.1097/01.CCM.0000191712.96336.51

Corbillé, A. G., Neunlist, M., and Derkinderen, P. (2016). Cross-linking for the analysis of α-synuclein in the enteric nervous system. *J. Neurochem.* 139, 839–847. doi: 10.1111/jnc.13845

Creighton, T. E. (1993). *Proteins: Structures and molecular properties*, 2nd Edn. New York, NY: W.H.Freeman.

Davidson, W. S., Jonas, A., Clayton, D. F., and George, J. M. (1998). Stabilization of α-Synuclein secondary structure upon binding to synthetic membranes. *J. Biol. Chem.* 273, 9443–9449. doi: 10.1074/jbc.273.16.9443

Davies, P., Moualla, D., and Brown, D. R. (2011). Alpha-synuclein is a cellular ferrireductase. *PLoS One* 6:e15814. doi: 10.1371/journal.pone.0015814

de Oliveira, R. M., Vicente Miranda, H., Francelle, L., Pinho, R., Szegö, É. M., Martinho, R., et al. (2017). The mechanism of sirtuin 2–mediated exacerbation of alpha-synuclein toxicity in models of Parkinson disease. *PLoS Biol.* 15:e2000374. doi: 10.1371/journal.pbio.2000374

Dettmer, U., Newman, A. J., Luth, E. S., Bartels, T., and Selkoe, D. (2013). In vivo cross-linking reveals principally oligomeric forms of α-synuclein and β-synuclein in neurons and non-neural cells. *J. Biol. Chem.* 288, 6371–6385. doi: 10.1074/jbc.M112.403311

Dettmer, U., Newman, A. J., Von Saucken, V. E., Bartels, T., and Selkoe, D. (2015b). KTKEGV repeat motifs are key mediators of normal α-synuclein tetramerization: Their mutation causes excess monomers and neurotoxicity. *Proc. Natl. Acad. Sci. U.S.A.* 112, 9596–9601. doi: 10.1073/pnas.1505953112

Dettmer, U., Newman, A. J., Soldner, F., Luth, E. S., Kim, N. C., Von Saucken, V. E., et al. (2015a). Parkinson-causing α-synuclein missense mutations shift native tetramers to monomers as a mechanism for disease initiation. *Nat. Commun.* 6:7314. doi: 10.1038/ncomms8314

Dikiy, I., and Eliezer, D. (2014). N-terminal Acetylation stabilizes N-terminal Helicity in Lipid- and Micelle-bound α-Synuclein and increases its affinity for Physiological Membranes. *J. Biol. Chem.* 289, 3652–3665. doi: 10.1074/jbc.M113.512459

Doig, A. J., Chakrabartty, A., Klingler, T. M., and Baldwin, R. L. (1994). Determination of Free Energies of N-Capping in α-Helices by Modification of the Lifson-Roig Helix-Coil Theory To Include N- and C-Capping. *Biochemistry* 33, 3396–3403. doi: 10.1021/bi00177a033

Dormeyer, W., Mohammed, S., Van Breukelen, B., Krijgsveld, J., and Heck, A. J. R. (2007). Targeted analysis of protein termini. *J. Proteome Res.* 6, 4634–4645. doi: 10.1021/pr070375k

Drazic, A., Aksnes, H., Marie, M., Boczkowska, M., Varland, S., Timmerman, E., et al. (2018). NAA80 is actin's N-terminal acetyltransferase and regulates cytoskeleton assembly and cell motility. *Proc. Natl. Acad. Sci. U.S.A.* 115, 4399–4404. doi: 10.1073/pnas.1718336115

Dudzik, C. G., Walter, E. D., Abrams, B. S., Jurica, M. S., and Millhauser, G. L. (2013). Coordination of copper to the membrane-bound form of α-synuclein. *Biochemistry* 52, 53–60. doi: 10.1021/bi301475q

Dudzik, C. G., Walter, E. D., and Millhauser, G. L. (2011). Coordination features and affinity of the Cu2+ site in the α-synuclein protein of Parkinson's disease. *Biochemistry* 50, 1771–1777. doi: 10.1021/bi101912q

Eliezer, D. (2013). The mysterious C-terminal tail of alpha-synuclein: Nanobody's guess. *J. Mol. Biol.* 425, 2393–2396. doi: 10.1016/j.jmb.2013.03.031

Eliezer, D., Kutluay, E., Bussell, R., and Browne, G. (2001). Conformational properties of α-synuclein in its free and lipid-associated states. *J. Mol. Biol.* 307, 1061–1073. doi: 10.1006/jmbi.2001.4538

Fairman, R., Shoemaker, K. R., York, E. J., Stewart, J. M., and Baldwin, R. L. (1989). Further studies of the helix dipole model: Effects of a free α−NH3+ or α−COO- group on helix stability. *Proteins* 5, 1–7. doi: 10.1002/prot.340050102

Fauvet, B., Fares, M. B., Samuel, F., Dikiy, I., Tandon, A., Eliezer, D., et al. (2012a). Characterization of semisynthetic and naturally N α- acetylated α-synuclein in vitro and in intact cells: Implications for aggregation and cellular properties of α-synuclein. *J. Biol. Chem.* 287, 28243–28262. doi: 10.1074/jbc.M112.383711

Fauvet, B., Mbefo, M. K., Fares, M. B., Desobry, C., Michael, S., Ardah, M. T., et al. (2012b). α-Synuclein in central nervous system and from erythrocytes, mammalian cells, and *Escherichia coli* exists predominantly as disordered monomer. *J. Biol. Chem.* 287, 15345–15364. doi: 10.1074/jbc.M111.318949

Fernández, R. D., and Lucas, H. R. (2018a). Isolation of recombinant tetrameric N-acetylated α-synuclein. *Protein Expr. Purif.* 152, 146–154. doi: 10.1016/j.pep.2018.07.008

Fernández, R. D., and Lucas, H. R. (2018b). Mass spectrometry data confirming tetrameric α-synuclein N-terminal acetylation. *Data Brief* 20, 1686–1691. doi: 10.1016/j.dib.2018.09.026

Forte, G. M. A., Pool, M. R., and Stirling, C. J. (2011). N-terminal acetylation inhibits protein targeting to the endoplasmic reticulum. *PLoS Biol.* 9:e1001073. doi: 10.1371/journal.pbio.1001073

Gallea, J. I., Sarroukh, R., Yunes-Quartino, P., Ruysschaert, J. M., Raussens, V., and Celej, M. S. (2016). Structural remodeling during amyloidogenesis of physiological Nα-acetylated α-synuclein. *Biochim. Biophys. Acta* 1864, 501–510. doi: 10.1016/j.bbapap.2016.01.011

Gao, J., Barroso, C., Zhang, P., Kim, H. M., Li, S., Labrador, L., et al. (2016). N-terminal acetylation promotes synaptonemal complex assembly in *C. elegans*. *Genes Dev.* 30, 2404–2416. doi: 10.1101/gad.277350.116

Garza-Lombó, C., Posadas, Y., Quintanar, L., Gonsebatt, M. E., and Franco, R. (2018). Neurotoxicity linked to dysfunctional metal ion homeostasis and xenobiotic metal exposure: Redox signaling and oxidative stress. *Antioxid. Redox Signal.* 28, 1669–1703. doi: 10.1089/ars.2017.7272

Georgieva, E. R., Ramlall, T. F., Borbat, P. P., Freed, J. H., and Eliezer, D. (2008). Membrane-bound α-synuclein forms an extended helix: Long-distance pulsed ESR measurements using vesicles, bicelles, and rodlike micelles. *J. Am. Chem. Soc.* 130, 12856–12857. doi: 10.1021/ja804517m

Ghosh, D., Mondal, M., Mohite, G. M., Singh, P. K., Ranjan, P., Anoop, A., et al. (2013). The parkinson's disease-associated H50Q mutation accelerates α-synuclein aggregation in vitro. *Biochemistry* 52, 6925–6927. doi: 10.1021/bi400999d

Goetze, S., Qeli, E., Mosimann, C., Staes, A., Gerrits, B., Roschitzki, B., et al. (2009). Identification and functional characterization of N-terminally acetylated proteins in *Drosophila melanogaster*. *PLoS Biol.* 7:e1000236. doi: 10.1371/journal.pbio.1000236

Guerrero-Ferreira, R., Taylor, N. M. I., Arteni, A. A., Kumari, P., Mona, D., Ringler, P., et al. (2019). Two new polymorphic structures of human full-length alpha-synuclein fibrils solved by cryo-electron microscopy. *eLife* 8:e48907. doi: 10.7554/eLife.48907

Guerrero-Ferreira, R., Taylor, N. M. I., Mona, D., Ringler, P., Lauer, M. E., Riek, R., et al. (2018). Cryo-EM structure of alpha-synuclein fibrils. *eLife* 7:e36402. doi: 10.7554/eLife.36402

Gurry, T., Ullman, O., Fisher, C. K., Perovic, I., Pochapsky, T., and Stultz, C. M. (2013). The dynamic structure of α-synuclein multimers. *J. Am. Chem. Soc.* 135, 3865–3872. doi: 10.1021/ja310518p

Halliday, G. M., Holton, J. L., Revesz, T., and Dickson, D. W. (2011). Neuropathology underlying clinical variability in patients with synucleinopathies. *Acta Neuropathol.* 122, 187–204. doi: 10.1007/s00401-011-0852-9

Heise, H., Hoyer, W., Becker, S., Andronesi, O. C., Riedel, D., and Baldus, M. (2005). Molecular-level secondary structure, polymorphism, and dynamics of full-length α-synuclein fibrils studied by solid-state NMR. *Proc. Natl. Acad. Sci. U.S.A.* 102, 15871–15876. doi: 10.1073/pnas.0506109102

Hoyer, W., Antony, T., Cherny, D., Heim, G., Jovin, T. M., and Subramaniam, V. (2002). Dependence of α-synuclein aggregate morphology on solution conditions. *J. Mol. Biol.* 322, 383–393. doi: 10.1016/S0022-2836(02)00775-1

Hwang, C. S., Shemorry, A., and Varshavsky, A. (2010). N-terminal acetylation of cellular proteins creates specific degradation signals. *Science* 327, 973–977. doi: 10.1126/science.1183147

Iyer, A., and Claessens, M. M. A. E. (2019). Disruptive membrane interactions of alpha-synuclein aggregates. *Biochim. Biophys. Acta Proteins Proteom.* 1867, 468–482. doi: 10.1016/j.bbapap.2018.10.006

Iyer, A., Roeters, S. J., Schilderink, N., Hommersom, B., Heeren, R. M. A., Woutersen, S., et al. (2016). The impact of N-terminal acetylation of α-synuclein on phospholipid membrane binding and fibril structure. *J. Biol. Chem.* 291, 21110–21122. doi: 10.1074/jbc.M116.726612

Johnson, M., Coulton, A. T., Geeves, M. A., and Mulvihill, D. P. (2010). Targeted amino-terminal acetylation of recombinant proteins in E. coli. *PLoS One* 5:e15801. doi: 10.1371/journal.pone.0015801

Kang, L., Janowska, M. K., Moriarty, G. M., and Baum, J. (2013). Mechanistic Insight into the Relationship between N-Terminal Acetylation of α-Synuclein

and Fibril Formation Rates by NMR and Fluorescence. *PLoS One* 8:e75018. doi: 10.1371/journal.pone.0075018

Kang, L., Moriarty, G. M., Woods, L. A., Ashcroft, A. E., Radford, S. E., and Baum, J. (2012). N-terminal acetylation of α-synuclein induces increased transient helical propensity and decreased aggregation rates in the intrinsically disordered monomer. *Protein Sci.* 21, 911–917. doi: 10.1002/pro.2088

Kim, S., Yun, S. P., Lee, S., Umanah, G. E., Bandaru, V. V. R., Yin, X., et al. (2018). GBA1 deficiency negatively affects physiological α-synuclein tetramers and related multimers. *Proc. Natl. Acad. Sci. U.S.A.* 115, 798–803. doi: 10.1073/pnas.1700465115

Knowles, T. P. J., Waudby, C. A., Devlin, G. L., Cohen, S. I. A., Aguzzi, A., Vendruscolo, M., et al. (2009). An analytical solution to the kinetics of breakable filament assembly. *Science* 326, 1533–1537. doi: 10.1126/science.1178250

Krüger, R., Kuhn, W., Müller, T., Woitalla, D., Graeber, M., Kösel, S., et al. (1998). Ala30Pro mutation in the gene encoding α-synuclein in Parkinson's disease. *Nat. Genet.* 18, 106–108. doi: 10.1038/ng0298-106

Langeberg, L. K., and Scott, J. D. (2015). Signalling scaffolds and local organization of cellular behaviour. *Nat. Rev. Mol. Cell Biol.* 16, 232–244. doi: 10.1038/nrm3966

Lashuel, H. A., Overk, C. R., Oueslati, A., and Masliah, E. (2013). The many faces of α-synuclein: From structure and toxicity to therapeutic target. *Nat. Rev. Neurosci* 14, 38–48. doi: 10.1038/nrn3406

Latham, J. A., and Dent, S. Y. R. (2007). Cross-regulation of histone modifications. *Nat. Struct. Mol. Biol.* 14, 1017–1024. doi: 10.1038/nsmb1307

Lesage, S., Anheim, M., Letournel, F., Bousset, L., Honoré, A., Rozas, N., et al. (2013). G51D α-synuclein mutation causes a novel Parkinsonian-pyramidal syndrome. *Ann. Neurol* 73, 459–471. doi: 10.1002/ana.23894

Li, B., Ge, P., Murray, K. A., Sheth, P., Zhang, M., Nair, G., et al. (2018). Cryo-EM of full-length α-synuclein reveals fibril polymorphs with a common structural kernel. *Nat. Commun.* 9:3609. doi: 10.1038/s41467-018-05971-2

Li, Y., Zhao, C., Luo, F., Liu, Z., Gui, X., Luo, Z., et al. (2018). Amyloid fibril structure of α-synuclein determined by cryo-electron microscopy. *Cell Res.* 28, 897–903. doi: 10.1038/s41422-018-0075-x

Lima, V. D. A., Do Nascimento, L. A., Eliezer, D., and Follmer, C. (2019). Role of Parkinson's disease-linked mutations and N-Terminal acetylation on the Oligomerization of α-Synuclein Induced by 3,4-Dihydroxyphenylacetaldehyde. *ACS Chem. Neurosci.* 10, 690–703. doi: 10.1021/acschemneuro.8b00498

Lorenzen, N., Lemminger, L., Pedersen, J. N., Nielsen, S. B., and Otzen, D. E. (2014). The N-terminus of α-synuclein is essential for both monomeric and oligomeric interactions with membranes. *FEBS Lett.* 588, 497–502. doi: 10.1016/j.febslet.2013.12.015

Luth, E. S., Bartels, T., Dettmer, U., Kim, N. C., and Selkoe, D. J. (2015). Purification of α-synuclein from human brain reveals an instability of endogenous multimers as the protein approaches purity. *Biochemistry* 54, 279–292. doi: 10.1021/bi501188a

Makasewicz, K., Wennmalm, S., Stenqvist, B., Fornasier, M., Andersson, A., Jönsson, P., et al. (2021). Cooperativity of α-Synuclein binding to lipid membranes. *ACS Chem. Neurosci.* 12, 2099–2109. doi: 10.1021/acschemneuro.1c00006

Maltsev, A. S., Ying, J., and Bax, A. (2012). Impact of N-terminal acetylation of α-synuclein on its random coil and lipid binding properties. *Biochemistry* 51, 5004–5013. doi: 10.1021/bi300642h

Martin, B. L. (2007). Regulation by covalent modification. *eLS* 1–7. doi: 10.1002/9780470015902.a0000866.pub2

Mason, R. J., Paskins, A. R., Dalton, C. F., and Smith, D. P. (2016). Copper binding and subsequent aggregation of α-Synuclein Are Modulated by N-terminal acetylation and ablated by the H50Q Missense Mutation. *Biochemistry* 55, 4737–4741. doi: 10.1021/acs.biochem.6b00708

McNulty, B. C., Young, G. B., and Pielak, G. J. (2006). Macromolecular crowding in the *Escherichia coli* periplasm maintains α-synuclein disorder. *J. Mol. Biol.* 355, 893–897. doi: 10.1016/j.jmb.2005.11.033

Mezzaroba, L., Alfieri, D. F., Colado Simão, A. N., and Vissoci Reiche, E. M. (2019). The role of zinc, copper, manganese and iron in neurodegenerative diseases. *Neurotoxicology* 74, 230–241. doi: 10.1016/j.neuro.2019.07.007

Miotto, M. C., Valiente-Gabioud, A. A., Rossetti, G., Zweckstetter, M., Carloni, P., Selenko, P., et al. (2015). Copper binding to the N-terminally acetylated, naturally occurring form of Alpha-Synuclein induces local helical folding. *J. Am. Chem. Soc.* 137, 6444–6447. doi: 10.1021/jacs.5b01911

Monda, J. K., Scott, D. C., Miller, D. J., Lydeard, J., King, D., Harper, J. W., et al. (2013). Structural conservation of distinctive N-terminal acetylation-dependent interactions across a family of mammalian NEDD8 ligation enzymes. *Structure* 21, 42–53. doi: 10.1016/j.str.2012.10.013

Morel, B., Varela, L., Azuaga, A. I., and Conejero-Lara, F. (2010). Environmental conditions affect the kinetics of nucleation of amyloid fibrils and determine their morphology. *Biophys. J.* 99, 3801–3810. doi: 10.1016/j.bpj.2010.10.039

Neri, L., Lasa, M., Elosegui-Artola, A., D'Avola, D., Carte, B., Gazquez, C., et al. (2017). NatB-mediated protein N-α-terminal acetylation is a potential therapeutic target in hepatocellular carcinoma. *Oncotarget* 8, 40967–40981. doi: 10.18632/oncotarget.17332

Ni, X., McGlinchey, R. P., Jiang, J., and Lee, J. C. (2019). Structural Insights into α-Synuclein Fibril Polymorphism: Effects of Parkinson's Disease-Related C-Terminal Truncations. *J. Mol. Biol.* 431, 3913–3919. doi: 10.1016/j.jmb.2019.07.001

Öhrfelt, A., Zetterberg, H., Andersson, K., Persson, R., Secic, D., Brinkmalm, G., et al. (2011). Identification of novel α-synuclein isoforms in human brain tissue by using an online NanoLC-ESI-FTICR-MS method. *Neurochem. Res.* 36, 2029–2042. doi: 10.1007/s11064-011-0527-x

O'Leary, E. I., Jiang, Z., Strub, M. P., and Lee, J. C. (2018). Effects of phosphatidylcholine membrane fluidity on the conformation and aggregation of N-terminally acetylated α-Synuclein. *J. Biol. Chem.* 293, 11195–11205. doi: 10.1074/jbc.RA118.002780

Panuganti, V., and Roy, I. (2020). Oligomers, fibrils and aggregates formed by alpha-synuclein: role of solution conditions. *J. Biomol. Struct. Dyn.* 40, 4389–4398. doi: 10.1080/07391102.2020.1856721

Park, S. E., Kim, J. M., Seok, O. H., Cho, H., Wadas, B., Kim, S. Y., et al. (2015). Control of mammalian g protein signaling by N-terminal acetylation and the N-end rule pathway. *Science* 347, 1249–1252. doi: 10.1126/science.aaa3844

Pasanen, P., Myllykangas, L., Siitonen, M., Raunio, A., Kaakkola, S., Lyytinen, J., et al. (2014). A novel α-synuclein mutation A53E associated with atypical multiple system atrophy and Parkinson's disease-type pathology. *Neurobiol. Aging* 35:2180.e1-5. doi: 10.1016/j.neurobiolaging.2014.03.024

Pero-Gascon, R., Benavente, F., Minic, Z., Berezovski, M. V., and Sanz-Nebot, V. (2020). On-line aptamer affinity solid-phase extraction capillary electrophoresis-mass spectrometry for the analysis of blood α-Synuclein. *Anal. Chem.* 92, 1525–1533. doi: 10.1021/acs.analchem.9b04802

Pfefferkorn, C. M., Heinrich, F., Sodt, A. J., Maltsev, A. S., Pastor, R. W., and Lee, J. C. (2012). Depth of α-synuclein in a bilayer determined by fluorescence, neutron reflectometry, and computation. *Biophys. J.* 102, 613–621. doi: 10.1016/j.bpj.2011.12.051

Polevoda, B., and Sherman, F. (2003). N-terminal acetyltransferases and sequence requirements for N-terminal acetylation of eukaryotic proteins. *J. Mol. Biol.* 325, 595–622. doi: 10.1016/S0022-2836(02)01269-X

Polymeropoulos, M. H., Lavedan, C., Leroy, E., Ide, S. E. E., Dehejia, A., Dutra, A., et al. (1997). Mutation in the α-synuclein gene identified in families with Parkinson's disease. *Science* 276, 2045–2047. doi: 10.1126/science.276.5321.2045

Powers, E. T., and Powers, D. L. (2006). The kinetics of nucleated polymerizations at high concentrations: Amyloid fibril formation near and above the "supercritical concentration.". *Biophys. J.* 91, 122–132. doi: 10.1529/biophysj.105.073767

Proukakis, C., Dudzik, C. G., Brier, T., MacKay, D. S., Cooper, J. M., Millhauser, G. L., et al. (2013). A novel α-synuclein missense mutation in Parkinson disease. *Neurology* 80, 1062–1064. doi: 10.1212/WNL.0b013e31828727ba

Quintas, A., Saraiva, M. J. M., and Britot, R. M. M. (1999). The tetrameric protein transthyretin dissociates to a non-native monomer in solution. A novel model for amyloidogenesis. . *J. Biol. Chem.* 274, 32943–32949. doi: 10.1074/jbc.274.46.32943

Ree, R., Varland, S., and Arnesen, T. (2018). Spotlight on protein N-terminal acetylation. *Exp. Mol. Med.* 50, 1–13. doi: 10.1038/s12276-018-0116-z

Rossetti, G., Musiani, F., Abad, E., Dibenedetto, D., Mouhib, H., Fernandez, C. O., et al. (2016). Conformational ensemble of human α-synuclein physiological form predicted by molecular simulations. *Phys. Chem. Chem. Phys.* 18, 5702–5706. doi: 10.1039/c5cp04549e

Runfola, M., De Simone, A., Vendruscolo, M., Dobson, C. M., and Fusco, G. (2020). The N-terminal Acetylation of α-Synuclein changes the affinity for lipid membranes but not the structural properties of the bound state. *Sci. Rep* 10:204. doi: 10.1038/s41598-019-57023-4

Ruzafa, D., Hernandez-Gomez, Y. S., Bisello, G., Broersen, K., Morel, B., and Conejero-Lara, F. (2017). The influence of N-terminal acetylation on micelle-induced conformational changes and aggregation of α-Synuclein. *PLoS One* 12:e0178576. doi: 10.1371/journal.pone.0178576

Schweighauser, M., Shi, Y., Tarutani, A., Kametani, F., Murzin, A. G., Ghetti, B., et al. (2020). Structures of α-synuclein filaments from multiple system atrophy. *Nature* 585, 464–469. doi: 10.1038/s41586-020-2317-6

Scott, D. C., Monda, J. K., Bennett, E. J., Harper, J. W., and Schulman, B. A. (2011). N-terminal acetylation acts as an avidity enhancer within an interconnected multiprotein complex. *Science* 334, 674–678. doi: 10.1126/science.1209307

Setty, S. R. G., Strochlic, T. I., Tong, A. H. Y., Boone, C., and Burd, C. G. (2004). Golgi targeting of Arf-like GTPase Arl3p requires its Nα-acetylation and the integral membrane protein Sys1p. *Nat. Cell Biol.* 6, 414–419. doi: 10.1038/ncb1121

Shemorry, A., Hwang, C. S., and Varshavsky, A. (2013). Control of protein quality and stoichiometries by N-Terminal acetylation and the N-End rule pathway. *Mol. Cell* 50, 540–551. doi: 10.1016/j.molcel.2013.03.018

Sidhu, A., Segers-Nolten, I., and Subramaniam, V. (2014). Solution conditions define morphological homogeneity of α-synuclein fibrils. *Biochim. Biophys. Acta* 1844, 2127–2134. doi: 10.1016/j.bbapap.2014.09.007

Sidhu, A., Segers-Nolten, I., and Subramaniam, V. (2016). Conformational compatibility is essential for heterologous aggregation of α-Synuclein. *ACS Chem. Neurosci.* 7, 719–727. doi: 10.1021/acschemneuro.5b00322

Sidhu, A., Vaneyck, J., Blum, C., Segers-Nolten, I., and Subramaniam, V. (2018). Polymorph-specific distribution of binding sites determines thioflavin-T fluorescence intensity in α-synuclein fibrils. *Amyloid* 25, 189–196. doi: 10.1080/13506129.2018.1517736

Smith, W. W., Margolis, R. L., Li, X., Troncoso, J. C., Lee, M. K., Dawson, V. L., et al. (2005). α-synuclein phosphorylation enhances eosinophilic cytoplasmic inclusion formation in SH-SY5Y cells. *J. Neurosci.* 25, 5544–5552. doi: 10.1523/JNEUROSCI.0482-05.2005

Starheim, K. K., Arnesen, T., Gromyko, D., Ryningen, A., Varhaug, J. E., and Lillehaug, J. R. (2008). Identification of the human Nα-acetyltransferase complex B (hNatB): A complex important for cell-cycle progression. *Biochem. J.* 415, 325–331. doi: 10.1042/BJ20080658

Sugeno, N., Takeda, A., Hasegawa, T., Kobayashi, M., Kikuchi, A., Mori, F., et al. (2008). Serine 129 phosphorylation of α-synuclein induces unfolded protein response-mediated cell death. *J. Biol. Chem.* 283, 23179–23188. doi: 10.1074/jbc.M802223200

Sun, Y., Hou, S., Zhao, K., Long, H., Liu, Z., Gao, J., et al. (2020). Cryo-EM structure of full-length α-synuclein amyloid fibril with Parkinson's disease familial A53T mutation. *Cell Res.* 30, 360–362. doi: 10.1038/s41422-020-0299-4

Sung, Y. H., Rospigliosi, C., and Eliezer, D. (2006). NMR mapping of copper binding sites in alpha-synuclein. *Biochim. Biophys. Acta* 1764, 5–12. doi: 10.1016/j.bbapap.2005.11.003

Swaminathan, R., Hoang, C. P., and Verkman, A. S. (1997). Photobleaching recovery and anisotropy decay of green fluorescent protein GFP-S65T in solution and cells: Cytoplasmic viscosity probed by green fluorescent protein translational and rotational diffusion. *Biophys. J.* 72, 1900–1907. doi: 10.1016/S0006-3495(97)78835-0

Theillet, F. X., Binolfi, A., Bekei, B., Martorana, A., Rose, H. M., Stuiver, M., et al. (2016). Structural disorder of monomeric α-synuclein persists in mammalian cells. *Nature* 530, 45–50. doi: 10.1038/nature16531

Trexler, A. J., and Rhoades, E. (2012). N-terminal acetylation is critical for forming α-helical oligomer of α-synuclein. *Protein Sci.* 21, 601–605. doi: 10.1002/pro.2056

Tuttle, M. D., Comellas, G., Nieuwkoop, A. J., Covell, D. J., Berthold, D. A., Kloepper, K. D., et al. (2016). Solid-state NMR structure of a pathogenic fibril of full-length human α-synuclein. *Nat. Struct. Mol. Biol.* 23, 409–415. doi: 10.1038/nsmb.3194

Ullman, O., Fisher, C. K., and Stultz, C. M. (2011). Explaining the structural plasticity of α-synuclein. *J. Am. Chem. Soc.* 133, 19536–19546. doi: 10.1021/ja208657z

Uversky, V. N., Li, J., and Fink, A. L. (2001). Metal-triggered structural transformations, aggregation, and fibrillation of human α-synuclein: A possible molecular link between parkinson's disease and heavy metal exposure. *J. Biol. Chem.* 276, 44284–44296. doi: 10.1074/jbc.M105343200

Varland, S., Osberg, C., and Arnesen, T. (2015). N-terminal modifications of cellular proteins: The enzymes involved, their substrate specificities and biological effects. *Proteomics* 15, 2385–2401. doi: 10.1002/pmic.201400619

Viennet, T., Wördehoff, M. M., Uluca, B., Poojari, C., Shaykhalishahi, H., Willbold, D., et al. (2018). Structural insights from lipid-bilayer nanodiscs link α-Synuclein membrane-binding modes to amyloid fibril formation. *Commun. Biol.* 1:44. doi: 10.1038/s42003-018-0049-z

Vilar, M., Chou, H. T., Lührs, T., Maji, S. K., Riek-Loher, D., Verel, R., et al. (2008). The fold of α-synuclein fibrils. *Proc. Natl. Acad. Sci. U.S.A.* 105, 8637–8642. doi: 10.1073/pnas.0712179105

Vinueza-Gavilanes, R., Íñigo-Marco, I., Larrea, L., Lasa, M., Carte, B., Santamaría, E., et al. (2020). N-terminal acetylation mutants affect alpha-synuclein stability, protein levels and neuronal toxicity. *Neurobiol. Dis.* 137:104781. doi: 10.1016/j.nbd.2020.104781

Wang, W., Perovic, I., Chittuluru, J., Kaganovich, A., Nguyen, L. T. T., Liao, J., et al. (2011). A soluble α-synuclein construct forms a dynamic tetramer. *Proc. Natl. Acad. Sci. U.S.A.* 108, 17797–17802. doi: 10.1073/pnas.1113260108

Watson, M. D., and Lee, J. C. (2019). N-Terminal Acetylation Affects α-Synuclein Fibril Polymorphism. *Biochemistry* 58, 3630–3633. doi: 10.1021/acs.biochem.9b00629

Waudby, C. A., Camilloni, C., Fitzpatrick, A. W. P., Cabrita, L. D., Dobson, C. M., Vendruscolo, M., et al. (2013). In-Cell NMR characterization of the secondary structure populations of a disordered conformation of α-Synuclein within E. coli Cells. *PLoS One* 8:e72286. doi: 10.1371/journal.pone.0072286

Waxman, E. A., Mazzulli, J. R., and Giasson, B. I. (2009). Characterization of hydrophobic residue requirements for α-synuclein fibrillization. *Biochemistry* 48, 9427–9436. doi: 10.1021/bi900539p

Xia, C., Tao, Y., Li, M., Che, T., and Qu, J. (2020). Protein acetylation and deacetylation: An important regulatory modification in gene transcription (Review). *Exp. Ther. Med.* 20, 2923–2940. doi: 10.3892/etm.2020.9073

Yang, D., Fang, Q., Wang, M., Ren, R., Wang, H., He, M., et al. (2013). Nα-acetylated Sir3 stabilizes the conformation of a nucleosome-binding loop in the BAH domain. *Nat. Struct. Mol. Biol.* 20, 1116–1118. doi: 10.1038/nsmb.2637

Yang, X., Wang, B., Hoop, C. L., Williams, J. K., and Baum, J. (2021). NMR unveils an N-terminal interaction interface on acetylated-α-synuclein monomers for recruitment to fibrils. *Proc. Natl. Acad. Sci. U.S.A.* 118:e2017452118. doi: 10.1073/pnas.2017452118

Yang, X. J., and Grégoire, S. (2007). Metabolism, cytoskeleton and cellular signalling in the grip of protein Nε- and O-acetylation. *EMBO Rep.* 8, 556–562. doi: 10.1038/sj.embor.7400977

Yang, X. J., and Seto, E. (2008). Lysine Acetylation: Codified Crosstalk with Other Posttranslational Modifications. *Mol. Cell* 31, 449–461. doi: 10.1016/j.molcel.2008.07.002

Zabrocki, P., Bastiaens, I., Delay, C., Bammens, T., Ghillebert, R., Pellens, K., et al. (2008). Phosphorylation, lipid raft interaction and traffic of α-synuclein in a yeast model for Parkinson. *Biochim. Biophys. Acta* 1783, 1767–1780. doi: 10.1016/j.bbamcr.2008.06.010

Zarbiv, Y., Simhi-Haham, D., Israeli, E., Elhadi, S. A., Grigoletto, J., and Sharon, R. (2014). Lysine residues at the first and second KTKEGV repeats mediate α-Synuclein binding to membrane phospholipids. *Neurobiol. Dis.* 70, 90–98. doi: 10.1016/j.nbd.2014.05.031

Zarranz, J. J., Alegre, J., Gómez-Esteban, J. C., Lezcano, E., Ros, R., Ampuero, I., et al. (2004). The New Mutation, E46K, of α-Synuclein Causes Parkinson and Lewy Body Dementia. *Ann. Neurol.* 55, 164–173. doi: 10.1002/ana.10795

Zhang, J., Li, X., and Li, J. D. (2019). The Roles of Post-translational Modifications on α-Synuclein in the Pathogenesis of Parkinson's Diseases. *Front. Neurosci.* 13:381. doi: 10.3389/fnins.2019.00381

Zhao, K., Li, Y., Liu, Z., Long, H., Zhao, C., Luo, F., et al. (2020a). Parkinson's disease associated mutation E46K of α-synuclein triggers the formation of a distinct fibril structure. *Nat. Commun.* 11:2643. doi: 10.1038/s41467-020-16386-3

Zhao, K., Lim, Y. J., Liu, Z., Long, H., Sun, Y., Hu, J. J., et al. (2020b). Parkinson's disease-related phosphorylation at Tyr39 rearranges α-synuclein amyloid fibril structure revealed by cryo-EM. *Proc. Natl. Acad. Sci. U.S.A.* 117, 20305–20315. doi: 10.1073/PNAS.1922741117

Zimm, B. H., and Bragg, J. K. (1959). Theory of the phase transition between helix and random coil in polypeptide chains. *J. Chem. Phys.* 31, 526–535. doi: 10.1063/1.1730390

frontiers | Frontiers in Neuroscience

TYPE Original Research
PUBLISHED 06 February 2023
DOI 10.3389/fnins.2023.1110311

OPEN ACCESS

EDITED BY
Jinghui Luo,
Paul Scherrer Institut (PSI), Switzerland

REVIEWED BY
Jorge Alí-Torres,
National University of Colombia, Colombia
Jamie Platts,
Cardiff University, United Kingdom

*CORRESPONDENCE
Mariona Sodupe
✉ mariona.sodupe@uab.cat
Jean-Didier Maréchal
✉ jeandidier.marechal@uab.cat

SPECIALTY SECTION
This article was submitted to Neurodegeneration, a section of the journal Frontiers in Neuroscience

RECEIVED 28 November 2022
ACCEPTED 10 January 2023
PUBLISHED 06 February 2023

CITATION
Roldán-Martín L, Sodupe M and Maréchal J-D (2023) Computational assessment of the impact of Cu(II) and Al(III) on β -amyloid$_{42}$ fibrils: Binding sites, structural stability, and possible physiological implications. *Front. Neurosci.* 17:1110311. doi: 10.3389/fnins.2023.1110311

Computational assessment of the impact of Cu(II) and Al(III) on β -amyloid$_{42}$ fibrils: Binding sites, structural stability, and possible physiological implications

Lorena Roldán-Martín, Mariona Sodupe* and Jean-Didier Maréchal*

Departament de Química, Universitat Autònoma de Barcelona, Cerdanyola del Vallès, Spain

One of Alzheimer's disease major hallmarks is the aggregation of β-amyloid peptide, a process in which metal ions play an important role. In the present work, an integrative computational study has been performed to identify the metal-binding regions and determine the conformational impact of Cu(II) and Al(III) ion binding to the β-amyloid (Aβ$_{42}$) fibrillary structure. Through classical and Gaussian accelerated molecular dynamics, it has been observed that the metal-free fiber shows a hinge fan-like motion of the S-shaped structure, maintaining the general conformation. Upon metal coordination, distinctive patterns are observed depending on the metal. Cu(II) binds to the flexible N-terminal region and induces structural changes that could ultimately disrupt the fibrillary structure. In contrast, Al(III) binding takes place with the residues Glu22 and Asp23, and its binding reinforces the core stability of the system. These results give clues on the molecular impact of the interaction of metal ions with the aggregates and sustain their non-innocent roles in the evolution of the illness.

KEYWORDS

molecular modeling and simulation, molecular dynamic (MD), amyloid Aβ-42, protein-ligand docking, metal

Introduction

Nowadays, neurodegenerative diseases are hot topics in a broad spectrum of the scientific community. The most predominant one is Alzheimer's disease (AD) with six out of 10 dementia cases (WHO, 2019). AD first affects the memory areas but as it spreads, other areas of the brain get damaged including those controlling language, reasoning, and cognitive skills. Many efforts have been placed into discovering the onset of the disease and how to reverse it, but no effective treatments have been proposed so far (Breijyeh et al., 2020).

Amyloid plaques and neurofibrillary tangles are the main hallmarks of AD and are caused by the accumulation of β-amyloid (Aβ) and tau protein, respectively (Kepp, 2012; Deture and Dickson, 2019). How these proteins start their aggregation process is still widely unknown. Aβ arises from the cleavage of the amyloid precursor protein (APP) and several hypotheses exist regarding its aggregation mechanism. The most accepted is the amyloid cascade (Hardy and Higgins, 1992), which suggests that the aggregation of Aβ, arising from an imbalance between Aβ production and clearance, is the main causative agent of Alzheimer's disease

pathology. Nonetheless, such aggregation is also observed in healthy patients (Bennett et al., 2006). Another possibility is the metal ion hypothesis (Maynard et al., 2005), derived from the high concentration of metal ions [Zn(II), Fe(III), Al(III), and Cu(II)] in Aβ plaques, which postulates that a loss of metal homeostasis could enhance the aggregation process. Regardless of the onset process, once the aggregation has started, the monomeric forms expand forming oligomers, the most neurotoxic forms, that bind together to form protofibrils and ultimately the entire fibrils. Along all these stages, though, the aggregation unit can be broken producing smaller subunits with seed properties capable of inducing disease in new areas. Accordingly, it is extremely important to properly understand the different phases of the aggregation process to produce effective drugs either to prevent the raise of the disease or slow down its advance (Kepp, 2012).

In the last decades, numerous studies have focused on decoding the folding and aggregation process of Aβ systems (Groh et al., 2017; Almeida and Brito, 2020; Ke et al., 2020; Krishnamurthy et al., 2022; Rahman et al., 2022). Despite these efforts, the elucidation at the molecular level of the aggregation mechanism has not been reached yet. For monomers, the major challenge arises from their intrinsic flexibility, becoming even more complex when they are merged with metal ion binding. To date, several experimental (Drew and Barnham, 2011; Faller et al., 2013; Stefaniak et al., 2021) and theoretical (Huy et al., 2016; Liao et al., 2018; Mutter et al., 2018; Pham et al., 2018; Khatua et al., 2019; Strodel and Coskuner-Weber, 2019; Turner et al., 2019; Boopathi et al., 2020; Roldán-Martín et al., 2021) studies have been performed with respect to different metals (Cu, Zn, and Al) binding to monomeric Aβ. In our previous study, it was demonstrated that monomeric Aβ can adopt a U-shaped structure with two antiparallel α-helix regions, whose secondary and tertiary structure can be modified upon Cu(II) and Al(III) coordination, increasing β-sheet content in the latter case (Roldán-Martín et al., 2021).

However, when it comes to larger aggregated forms such as fibrillary Aβ complexes, the experiments lack the techniques to precisely identify the binding site of metal ions (Miller, 2022). Therefore, there are scarce experimental details on plausible metal-binding sites in fibrils (Parthasarathy et al., 2011), and computational approaches have been shown as suitable techniques to determine the impact of metal binding on Aβ fibril dynamics. Contrary to monomers, aggregate forms are less flexible and several forms of fibrillary structures have been recently reported by X-ray and ss-NMR techniques (Xiao et al., 2015; Wälti et al., 2016; Kollmer et al., 2019; Liberta et al., 2019), providing a solid ground for computational studies to unravel the effect of metal ion binding to amyloid fibrils.

To shed light on those questions, we decided to apply a multi-scale protocol focusing on Cu(II) and Al(III) bound forms of $A\beta_{42}$ fibril, which are known to be more aggregation-prone. The work stands on (1) BioMetAll (Sánchez-Aparicio et al., 2021), a recently released structural predictor of metal-binding sites in proteins, (2) protein-ligand dockings compatible with metallic ligands (Sciortino et al., 2018), and (3) classical and accelerated molecular dynamics. The impact of the metal on Aβ fibril formation and stabilization is assessed with the purpose of providing structural knowledge that could help in understanding the role of metal in the aggregation processes associated with Alzheimer's disease.

Materials and methods

The computational protocol followed in this study is summarized in **Figure 1**.

Initial models

Several fibrillary structures of the β-amyloid fibril are available in the Protein Data Bank. The most complete PDB structure, with code 2NAO (Wälti et al., 2016), corresponds to the sequence 1–42 of the amyloid for each strand, though it retrieves poor punctuation in all the PDB parameters (clashes score 22, Ramachandran 12.4% and Sidechain 26.7%). On the other hand, the PDB structure with code 2MXU (Xiao et al., 2015) presents far better punctuation (clashes score 0, Ramachandran 3.8% and sidechain 6.22%) at the expense of residues 1 to 11 being missing, an observation consistent with the high flexibility of the N_{Ter} region of the peptide. Therefore, for this study, we selected the latest and elongated each strand with the 11 missing residues using homology modeling through the UCSF Chimera Software Modeler tool (Pettersen et al., 2004) to obtain the N-terminal missing region. Chimera minimization was performed to reduce the clashes, with the Amber ff14SB force field (Maier et al., 2015) and 100 steps of steepest descent.

Once the complete fibrillary structure was obtained, several preliminary molecular dynamics calculations were performed. We considered the systems with different numbers of strands, namely 4, 6, 8, and 10 aiming at identifying the minimal number of strands necessary for the fiber to remain stable in the fibrillar form during the trajectory. This is also particularly important to avoid possible drawbacks inherent to force field propensity to stabilize certain secondary structures against others (Case et al., 2005). With the Amber force field, we observed that at least 6 strands are necessary to obtain a fibril, though at least 10 strands should be considered for a stable core. In this study, only the fibrillary structure of 10 strands is discussed.

Metal-binding areas: BioMetAll and GOLD

Putative metal-binding areas were detected by applying the BioMetAll software (Sánchez-Aparicio et al., 2021) to the $A\beta_{11-42}$ crystallographic structure available in the PDB 2MXU, which was configured to include the backbone atoms and a minimum of three residues as possible coordinating groups. BioMetAll only considers the backbone and the residues that are within a suitable distance to coordinate the metal, but their orientation may not be optimized for coordination. Therefore, protein-ligand dockings calculations were performed with the program GOLD (Jones et al., 1997) using the GoldScore scoring (Jones et al., 1995) function, whose parameter file was modified to include atom types for metal ions and their possible coordinating amino acids (Sciortino et al., 2018). Genetic algorithm (GA) parameters were set to 50 GA runs and a minimum of 100,000 operations each. The remaining parameters, including pressure, number of islands, crossovers, or mutations, were set to default. Finally, docking solutions were analyzed through GaudiView (Rodríguez-Guerra Pedregal et al., 2017) an in-house developed GUI tool built as an extension of UCSF Chimera.

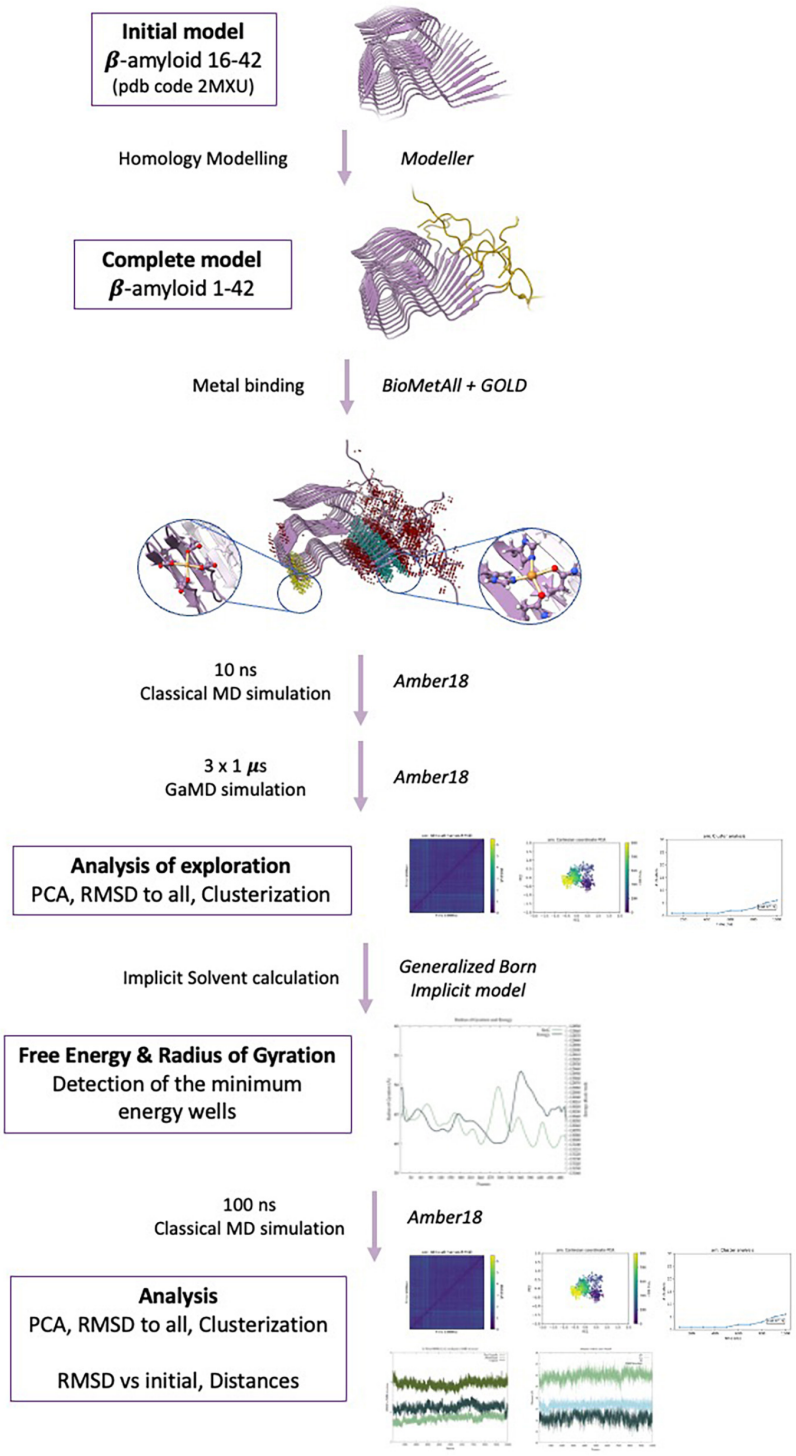

FIGURE 1
Methodological protocol used in the present study.

Classical molecular dynamics simulations for metalloaggregates

Metal parameters were obtained using the MCPB.py package (Li and Merz, 2016) from quantum mechanical calculations with DFT (B3LYP) (Lee et al., 1988; Becke, 1998) and adding Grimme's D3 correction for dispersion (Grimme et al., 2010). For aluminum complexes, the 6-31 + G (d,p) basis set was used for all atoms (Rassolov et al., 2001). For Cu(II) complexes, we used the 6-31 + G (d,p) basis set for C, H, N, and O atoms; and the SDD pseudo-potential and the corresponding basis-set supplemented with f-polarization function for Cu (Ehlers et al., 1993). Solvent-polarizable dielectric continuum model (SMD) was considered to account for the solvent effects in water (Marenich et al., 2009). Force constants and equilibrium parameters for metal-coordinating atoms were obtained through the Seminarios's method (Seminario, 1996)

while point charges were derived using the RESP (restrained electrostatic potential) model (Bayly et al., 1993).

Molecular dynamics simulations were then performed with AMBER18 (Case et al., 2018) using the AMBER ff14SB (Maier et al., 2015) force field in the NPT ensemble, with a 1 fs integration time step. The initial models were embedded within a cubic box of pre-equilibrated TIP3P (Jorgensen et al., 1998) water molecules and Na^+ ions were included to balance the total charge depending on the system: 30 for the metal-free system, 20 for the copper-bound system, and 15 for the aluminum-bound system. Constant temperature and pressure were set by coupling the system to a Monte Carlo barostat (Duane et al., 1987) at 1.01325 bar and a Langevin thermostat at 300 K (Loncharich et al., 1992). The SHAKE algorithm (Ryckaert et al., 1977) was used to constrain the bonds involving hydrogen atoms. Classical MD simulations were performed for 10 ns for all the systems, just to equilibrate the system before running Gaussian accelerated molecular dynamics (GaMDs). Moreover, MD simulations have also been performed on the lowest energy wells obtained in the GaMD simulations.

GaMDs simulations

Enhanced conformational sampling was performed with the Gaussian accelerated molecular dynamics (GaMDs) (Miao et al., 2015). For these simulations, the AMBER ff14SB force field in the NVT ensemble was used, constraining the bonds involving H atoms with SHAKE, with an integration time step of 2 fs. A boost on both dihedral and total potential energy (igamd = 3) was applied. In total, three GaMD replicas of 1 μs were produced for each system.

Analysis

The energy of the systems was calculated along the trajectory with the Generalized Born Implicit model (Onufriev et al., 2000, 2004), for 1,000 frames extracted from each 1 μs GaMD trajectory, stripping water molecules, and performing a short minimization (maxcyc = 500 steps) previously to the energy extraction. The radius of gyration (RoG) was computed over the same 1,000 frames, so a graphic with the different minima was obtained. For each system, the well with the minimum energy was selected for an MD, to test its stability, and for the analysis.

Principal component analysis (PCA) (Wold et al., 1987), RMSD all-to-all, and clustering were performed over both the GaMD and MD simulations to test whether the exploration was exhaustive enough. For the MD simulations performed on the lowest energy wells from the GaMDs, the RMSD with respect to the initial structure was also computed. The last analysis performed consisted of studying the PCA movements of the fibers along the trajectories with the VMD tool NMWiz and counterchecked by normal mode analysis performed with WEBnma software (Humphrey et al., 1996; Bakan et al., 2011) to study the global low-energy internal motions of the systems.

Results and discussion

This work aims at investigating the effect of the binding of Cu(II) and Al(III) to the $A\beta_{1-42}$ fibers through molecular modeling. We first present the study of the metal-free fiber to generate a point of comparison and then pursue metal-bound systems.

Dynamical behavior of metal-free fibril

The initial structure of the metal-free fibril has been obtained from the solid-state NMR (ss-NMR) structure of $A\beta_{11-42}$ (pdb code 2MXU). Since the N_{Ter} end of the system is missing (residues 1 to 10), the structure was completed by homology modeling using modeller (Martí-Renom et al., 2000; **Figure 2A**). Then, long GaMD simulations were performed using a biased potential and the results were analyzed using several statistical tools.

The total 3 μs GaMD simulation spread over three replicas of 1 μs. The three replicas exhibit similar behaviors in terms of global breathing motions and exhaustive exploration of the conformational space. Accordingly, PCA and energetic profiles of the replica with the lowest energetic conformation identified are presented in the main text (**Figures 2B, C**) while the other ones are reported in ESI (**Supplementary Figure 1**). Principal component analysis shows a displacement of the system at the end of the first 100 ns, then, it explores a limited region of the space until approximately 600 ns, and finally, it explores back the previous region, so that the simulation is converged (**Figure 2B**). The potential energy profile clearly indicates that during the trajectory, a series of low-energy wells are explored with a radius of gyration slowly raising–meaning a geometric expansion of the system (**Figure 2C**). This is in line with the results reported by Miller et al. (2012), who suggest that fibers do not show a unique lower energy state but different conformers with barriers between them, which are expected to be more or less favorable upon metal binding.

The trajectories present a series of interesting features. The first one is that only the six central strands maintain the fibrillary structure while the two at each extreme tend to unfold. This is related to the fact that these extremes are more exposed to the solvent and naturally start to adopt a more molten globule geometry with some helical contents, a situation reminiscent of the simulations of monomeric peptides. The second is that the terminal regions of each strand represented by the amino acids from 1 to 10 are overall disorganized. This is consistent with the absence of atomic density in the pdb structure and suggests that the overall geometry of the amyloid is barely affected by the N_{Ter} region adopting quite random conformations. Based on this, the N_{Ter} region and the four strands at the extremes are discarded for the rest of the analyses, which focuses on the core formed by the six central strands and from residues 11 to 42.

The major motion observed is a fan-like movement of the $A\beta_{11-20}$ β-sheet, which appears to be the natural breathing movement of the system (**Figure 2D**) as counterchecked by normal mode analysis performed using WEBnma software (Tiwari et al., 2014). This fan-like motion consists of a hinge that can be defined as the angle between the principal axes of the sets of atoms of residues 11 to 15 and 39 to 41 (**Figure 2E**). The angle obtained between these two principal axes for a representative structure of the most populated cluster reaches 48.5° against the 7.8° of the ss-NMR structure. For the lowest energy structure, the same analysis shows a hinge of 46.7° (**Figure 2F**), which still represents the main distortion with respect to the ss-NMR structure. These simulations and analyses show that the metal-free fiber mostly retains the experimental geometry although it

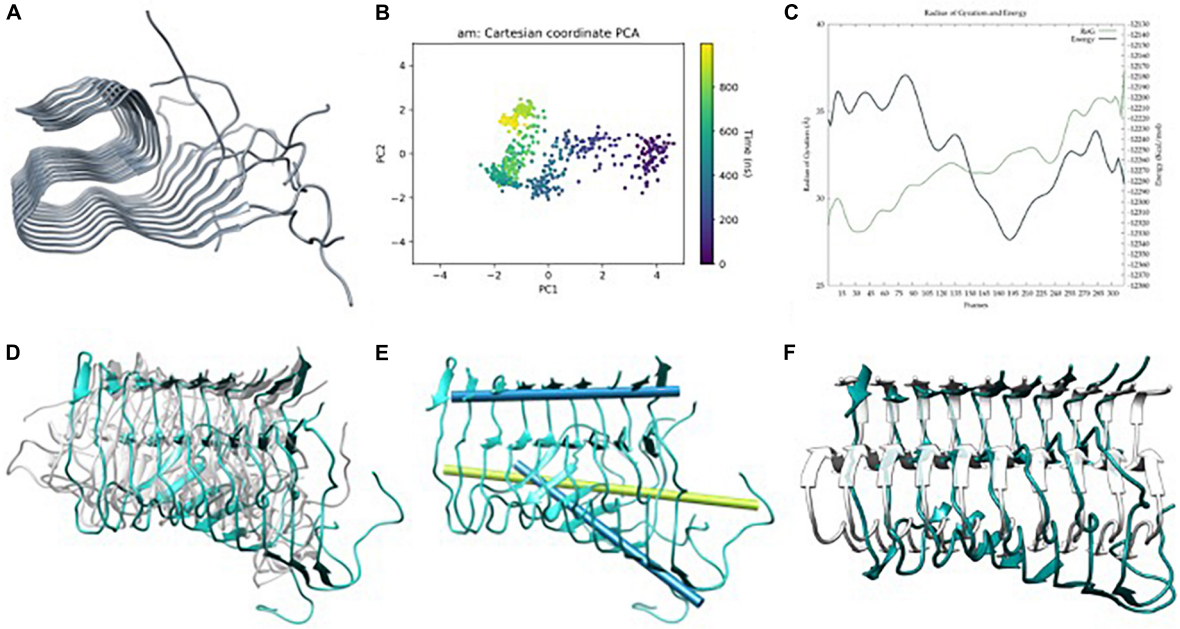

FIGURE 2
(A) $A\beta_{42}$ model built from $A\beta_{11-42}$ (2MXU) (Xiao et al., 2015) after adding the 1–11 residues, **(B)** principle component analysis (PCA) of Gaussian accelerated molecular dynamics (GaMD) simulation, **(C)** energy profile and radius of gyration (RoG) along the GaMD simulation, **(D)** overlap of representative structures of most populated clusters obtained from GaMD simulations, **(E)** in blue, metal-free fibril axis representation of 39–41 (top) and 11–15 β-sheets (bottom), in green; 11–15 β-sheets axis of NMR-structure, and **(F)** overlap between the solid-state NMR (ss-NMR) structure and the lowest energy structure of the GaMD simulation.

can display the dynamic motions not observed in the experimental structures.

Predicting metal-binding sites in amyloid aggregated structures

The binding of metal ions to amyloids has been the source of an extensive number of studies (Faller, 2009; Mutter et al., 2018; Pham et al., 2018; Roldán-Martín et al., 2021; Miller, 2022). Today, a relatively clear picture of metal binding has emerged in the monomeric systems, either theoretically for Al(III) (Mujika et al., 2017) or experimentally for Cu(II) (Drew and Barnham, 2011), which has narrowed the location and type of amino acids that bind the metal ions with only few candidates, all part of the N_{Ter} region of the peptide. For aggregates, though, there is still a substantial level of uncertainty.

The previous part of our study sustains an intrinsically disordered protein (IDP) behavior of the N_{Ter} region of the aggregate. This flexibility indicates that the binding of the metal ions to this region would be similar to what occurs in monomeric species. It also shows that the core of the aggregate is quite rigid, and one would naturally wonder if this rigidity induces some pre-organizations for metal binding.

To identify putative metal-binding sites in the aggregates, we performed BioMetAll calculations, a software recently released by our group for the prediction of metal-binding sites in biomolecules. Based on the backbone pre-organization hypothesis, BioMetAll has shown excellent success rates in identifying metal-binding locations for a wide sample of proteins and ions (Sánchez-Aparicio et al., 2021). To search for site-specific binding areas for copper and aluminum, the search was first performed looking for a minimum of three coordinating amino acids and any amino acid known to participate in the coordination sphere of transition metals. With this screening, BioMetAll finds the geometries compatible with the simultaneous coordination of two His residues in the N_{Ter} region of the Aβ fibril as identified in the monomers (Alí-Torres et al., 2011, 2014) from the experiments and QM calculations. However, this only occurs in a few strands due to the intrinsic flexibility of that region. Since other metal-binding sites are more frequently found in the core region of the fibril, indicating that in this system, the situation is different from what happens in monomers, we discarded N_{Ter} monomer-like binding sites and focused on the core region, favoring Asp and Glu for Al(III) (Mujika et al., 2017) and His and Gln for Cu(II). For the latter, it is important to notice that Gln residues have been included in the search since, although rare, the coordination of Gln to Cu(II) is observed in a series of X-ray structures from the protein data bank, it has also been proposed as a possible coordinate residue (Parthasarathy et al., 2011), and Gln15 shows the proper location for metal coordination in the selected structures.

In total, two areas were found for metal binding in the core of the fibril: one consistent with copper and the other with aluminum. The former, named Cu_F, stands at the linker between the N_{Ter} loop and the β-strand regions (from residue 12–15) and is composed of histidine His13 of two adjacent strands and two glutamine Gln15 of the same strands (**Figure 3A**). The latter, named Al_F, is located at the beginning of the coil with residues Glu22 and Asp23 of adjacent strands (**Figure 3B**). This latter site agrees with the work reported by Yang et al. (2022) which shows that this area is likely to be bound to a metal ion. With these two sites identified, we pursued generating realistic three-dimensional models of the metal-aggregate systems by carrying out protein-ligand dockings. Those were performed with

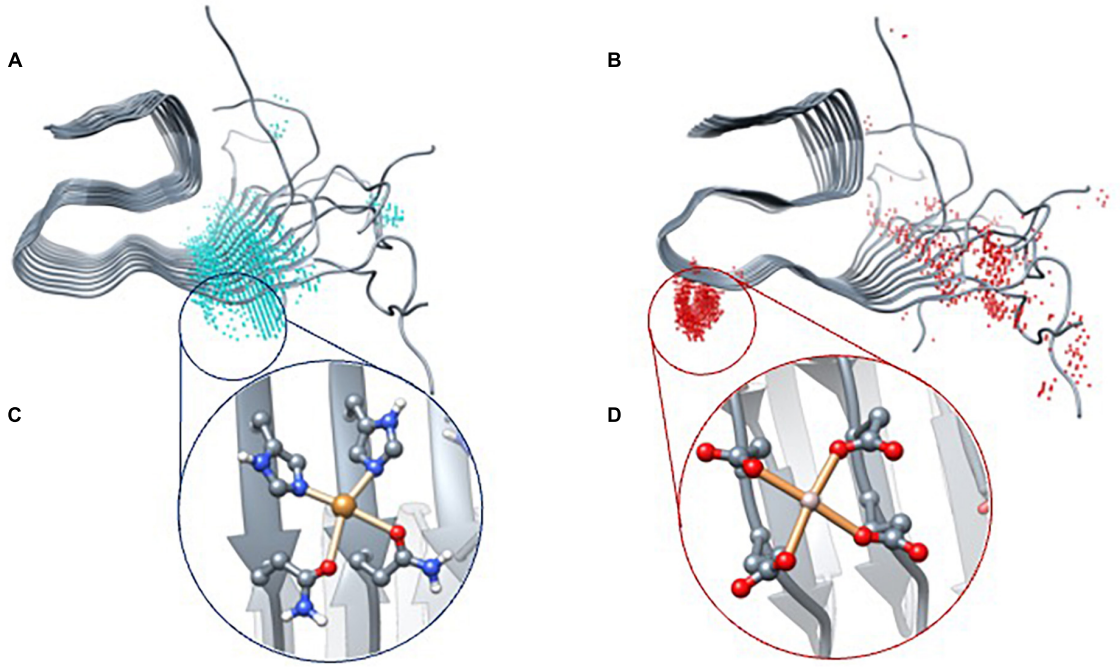

FIGURE 3
BioMetAll results of Cu(II) **(A)** and Al(III) **(B)** coordination. Once the areas were identified, docking results with Gold software were obtained for Cu(II) **(C)** and Al(III) **(D)**.

GOLD, assuming a square planar environment for Cu(II) and an octahedral one for Al(III) (Figures 3C, D).

The results indicate that Cu(II) can achieve a square planar coordination with two His and two Gln from adjacent strands. However, for Al(III), docking results only find an incomplete octahedral coordination in which two Glu and two Asp of adjacent strands are involved, thereby leaving vacant sites that would probably be occupied by the solvent molecules. Each model was then submitted to triplicated Gaussian accelerated molecular dynamic simulations to evaluate its stability and dynamics properties as well as to compare with the metal-free system.

GaMD of metal bound fibers

Data of the triplicated simulations on Cu_F are given in Figure 4 and Supplementary Figure 2 of ESI. In all cases, the trajectories tend to converge around 400 ns (Figure 4B and Supplementary Figures 4D–F) and show the presence of a series of minima (Figure 4C). Such minima agree with the fact that amyloids are highly polymorphic, metal binding shifting the population toward a certain conformation (Miller et al., 2010). Overall, the 3 μs GaMD simulations depict the same fan-like motion observed in the metal-free fiber (Figure 4D). Strikingly though, the geometry variability of the N_{Ter} loop (residues 1–11) is significantly more pronounced in Cu_F; i.e., each metal-bounded pairs of strands have their motions uncoupled from adjacent pairs. Consequently, the β-sheet H-bonds between these adjacent pairs are significantly weakened, which favors the change in their secondary structure increasing the α-helix content in the N_{Ter} ends, particularly on the first strands. Such α-helix regions are reminiscent of the monomeric forms, a behavior more pronounced than in the metal-free system (Roldán-Martín et al., 2021). However, the hinge movement previously observed in the metal-free fiber appears to be reduced, the angle between the two principal axes (considering the six central strands as done previously for the metal-free fiber) in a representative structure of the most populated cluster being 6.1° (Figure 4E). Note that in this case, the motion is not globally spread all other the fibril since there is a disruption of the fibrillar form that arises from a higher displacement of the first strands with respect to the remaining ones, probably due to the repulsion between Cu(II) ions (Figure 4F). Such observations may indicate that Cu(II) binding tends to disrupt the fibrillar form to lower-aggregation structures or amorphous aggregates without fibrillary structure.

For Al(III), the preferred binding site in the fiber involves the residues Glu22 and Asp23 of adjacent strands (Figure 5A). In this last case, the GaMD explores a series of minima until finding a well it cannot escape during the last 400 ns (Figure 5B and Supplementary Figure 3). Despite the energy profile highlighting a remarkable minimum (Figure 5C), the whole trajectory displays a very stable fold with minor motions (Figure 5D). In particular, the amplitude of the fan-like movement is far more limited in Al_F than in the other two systems. For example, one of the most representative structures presents an inter-axial angle of only 2.7°, similar–even lower–than that in the ss-NMR structure (7.8°) (Figures 5E, F). Therefore, GaMD simulations show that the aluminum-bound aggregate displays a more compact structure than both free-metal and copper-bound ones and remains closer to the static view provided by experimental ss-NMR geometry (Figure 5F).

Further analysis

To further analyze how the metal ions impact the conformation landscape and stability of the aggregates, classical MDs of 100 ns were carried out starting from the structure of the lowest energy well

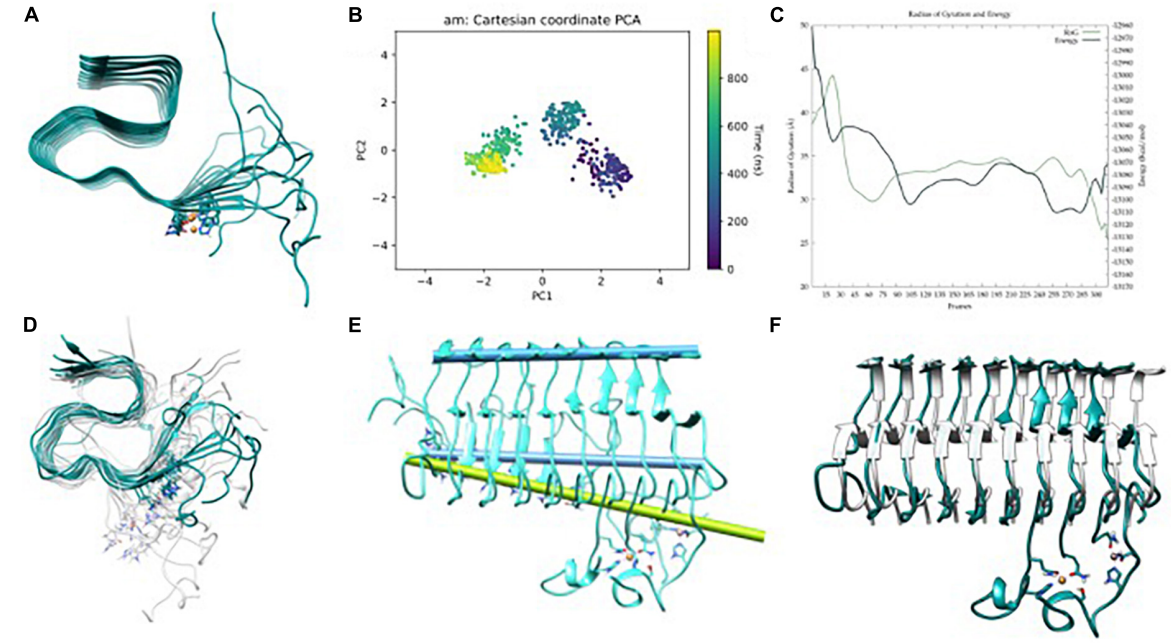

FIGURE 4
(A) $A\beta_{42}$-Cu(II) model, **(B)** principle component analysis (PCA) of Gaussian accelerated molecular dynamics (GaMD) simulation, **(C)** energy profile and radius of gyration (RoG) along the GaMD simulation, **(D)** overlap of representative structures of most populated clusters obtained from GaMD simulations, **(E)** in blue, axis representation of 39–41 residues (top) and 13–16 β-sheets (bottom); in green; 13–16 β-sheets axis of NMR-structure, and **(F)** overlap between the solid-state NMR (ss-NMR) structure and the lowest energy structure of the GaMD simulation.

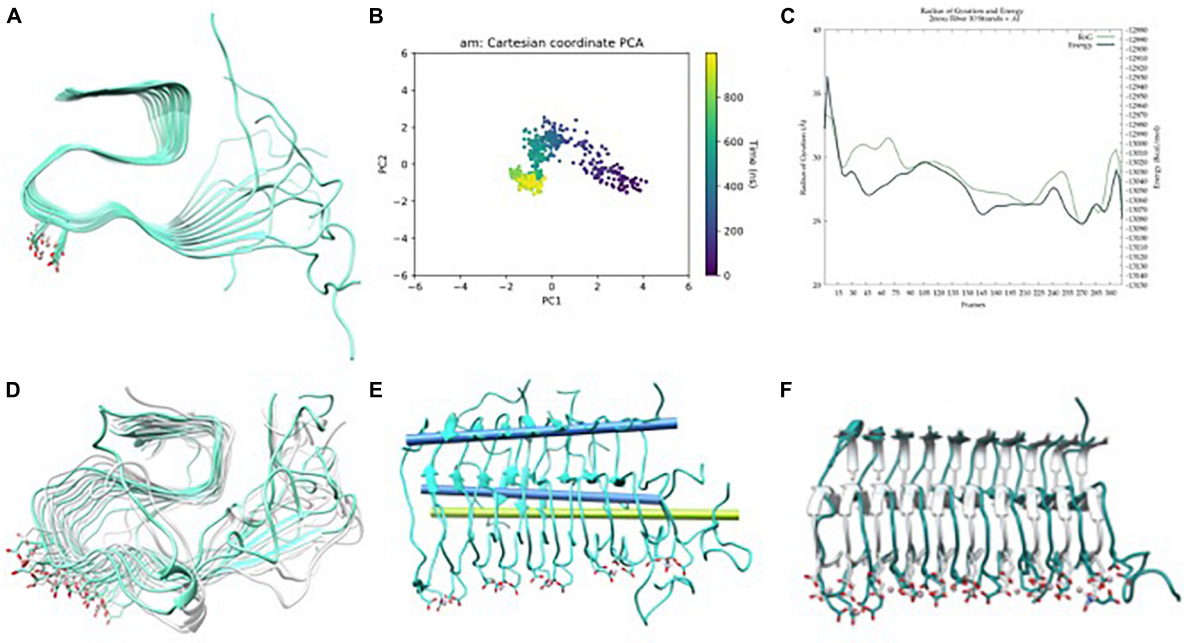

FIGURE 5
(A) $A\beta_{42}$-Al(III) model, **(B)** principle component analysis (PCA) of Gaussian accelerated molecular dynamics (GaMD) simulation, **(C)** energy profile and radius of gyration (RoG) along the GaMD simulation, **(D)** overlap of representative structures of most populated clusters obtained from GaMD simulations, **(E)** in blue, axis representation of 39–41 residues (top) and 13–15 residues β-sheets (bottom); in green; 13–16 β-sheets axis of NMR-structure, and **(F)** overlap between the solid-state NMR (ss-NMR) structure and the lowest energy structure of the GaMD simulation.

obtained from the GaMD simulations. To test the exhaustiveness of the exploration and their stability, RMSD and PCA were performed on the trajectories (Supplementary Figure 4). Emphasis is given to how metal binding alters the fiber's low collective modes and breathing motions. For that, five distances were evaluated using the carbon α of each residue and considering only the six central strands of the fibril. To ease the labeling and the reading, we use the X-ResNum identification format where X is the number of the strand

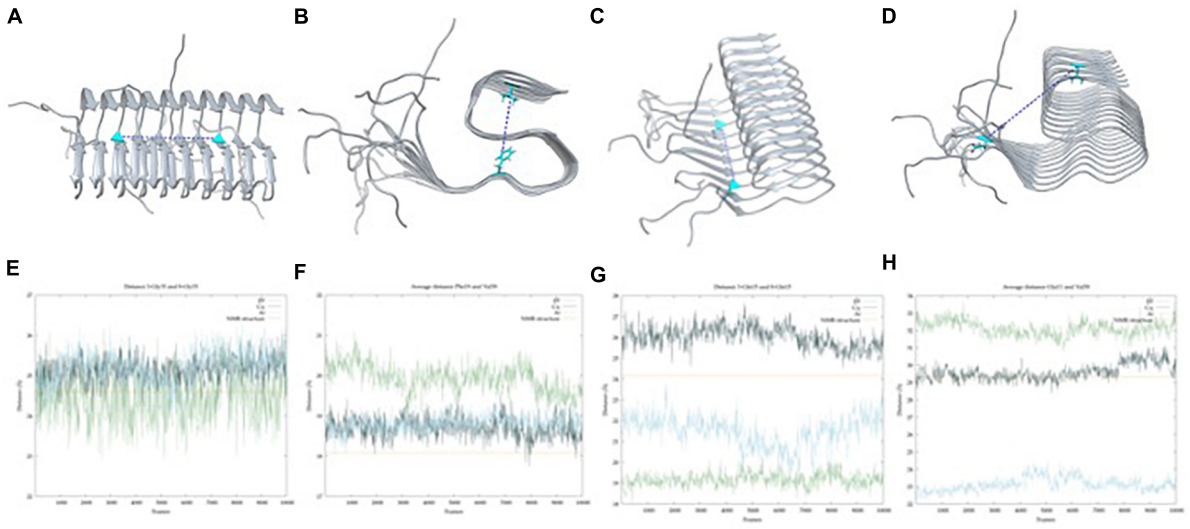

FIGURE 6
Atoms chosen for the horizontal distance **(A)**, vertical distance **(B)**, 11–15 β-strand intersheet distance **(C)** and opening of the 1–18 region **(D)** represented in the solid-state NMR (ss-NMR) model. Results of the horizontal **(E)**, with an average distance of 24.6 (± 5.6)Å, 25.2 (±1.6)Å and 25.5 (±10.9)Å for metal-free, Cu(II) and Al(III) systems; vertical **(F)**, with an average distance of 19.9 (±0.3)Å, 18.7 (±0.2)Å and 18.8 (±0.2)Å for metal-free, Cu(II) and Al(III) systems; intersheet **(G)**; with an average distance of 19.3 (±5.2)Å, 26.06 (±1.1)Å and 21.5 (±0.7)Å for metal-free, Cu(II) and Al(III) systems; and opening **(H)**, with an average distance of 32.1 (±0.4)Å, 29.6 (±0.5)Å and 23.1 (±0.4)Å for metal-free, Cu(II) and Al(III) systems; along the MD simulation, with ss-NMR distance represented in yellow line.

the residue belongs to, Res is the type of the residue, and Num is its number in the sequence.

1. The distance between 3-Gly33 and 8-Gly33 measures how the fiber opens horizontally in the core region and indicates if the β-sheet interaction is weakened (longer distance) or strengthened (shorter distance) (Figure 6A).
2. The average distance from Phe19 to Val39 of each core strand indicates how the fiber opens vertically and measures the compactness of the S-shaped supramolecular structure (Figure 6B).
3. The distance between 3-Gln15 and 8-Gln15 measures how the fiber opens horizontally in the N_{Ter} region and is indicative of the β-sheet interaction at this region (Figure 6C).
4. The average distance from Glu11 to Val39 of each core strand describes the separation movement of the N_{Ter} tail from the core region of the fiber (Figure 6D).
5. The average distance between His14 of each core strand describes if the fiber movement is collective (equal distance between strands) or individual (Figure 7).

With these descriptors, it is possible to see that the three complexes behave similarly both in the horizontal and in the vertical axes (measures 1 and 2). For measure 1 (Figure 6E), the metal-free fiber shows a distance of 24.64 (±5.6) Å, while Al(III) and Cu(II) exhibit values around 25 Å, which are very similar to the 24.6 Å of the ss-NMR structure. Distances of measure 2 (Figure 6F) are also similar, with the values of 19.9 (±0.3) Å for the metal-free fiber, 18.7 (±0.3) Å and 18.8 (±0.2) Å for the Cu and Al bound complexes and 18.3 Å for the ss-NMR structure, respectively. The other distances, though, demonstrate the substantial differences between the metal-free fiber and the metal-bound complexes.

Measure 3 relates to the disruption of the fibrillary structure in the N_{Ter} region. It is observed that Cu(II) coordination produces an increase in this distance, from 24.3 Å in the ss-NMR to 26 (±1.1) Å. In contrast, both the metal-free fibril and Al(III)-bound structure show shorter distances, of 19.93 (±0.3) Å and 21.5 (±0.7) Å, respectively, in comparison with the ss-NMR structure (Figure 6G). Measure 4, on its side, is remarkably increased in the metal-free fibril [32.1 (± 0.4) Å] with respect to the ss-NMR (29.3 Å), due to the hinge fan-like movement. Cu(II) system is maintained in a similar value to the ss-NMR structure, with a distance of 29.6 (±0.5) Å. Note, however, that this distance is an average of six values and the displacement of the terminal strands is faded by the shorter distance retrieved by the other ones. Indeed, the two most external strands included in the average exhibit values of 35 and 42 Å, respectively, whereas the four inner ones show values that range between 20 and 25 Å. Finally, the Al(III) system is even more compact than the ss-NMR structure, with an average distance of 23.1 (±0.4) Å, supporting the fact that aluminum binding increases the stability of the fibrillary conformation (Figure 6H).

The distances between each pair of strands (measure 5) were also measured (Figure 7). Calculations confirm the trends previously observed. The metal-free fibril has approximately the same distance between each pair of strands. Such system has a higher flexibility on the vertical axis, as measures 2 and 4 also support, while the horizontal axis is more compact and shows a collective movement of all the strands, which corresponds to the hinge fan-like movement. However, upon metal coordination, the distance between the strands differs.

First, Cu(II) ion, which binds to the N_{Ter} region, increases the distance between each pair of strands, even between those bound to the same metal ion. The most remarkable is the increase in the 4-His14–5-His14 distance, which indicates a disruption in the collective movement of the strands (Figure 7). This only happens in the Cu-bound system. For Al(III), the distance between the

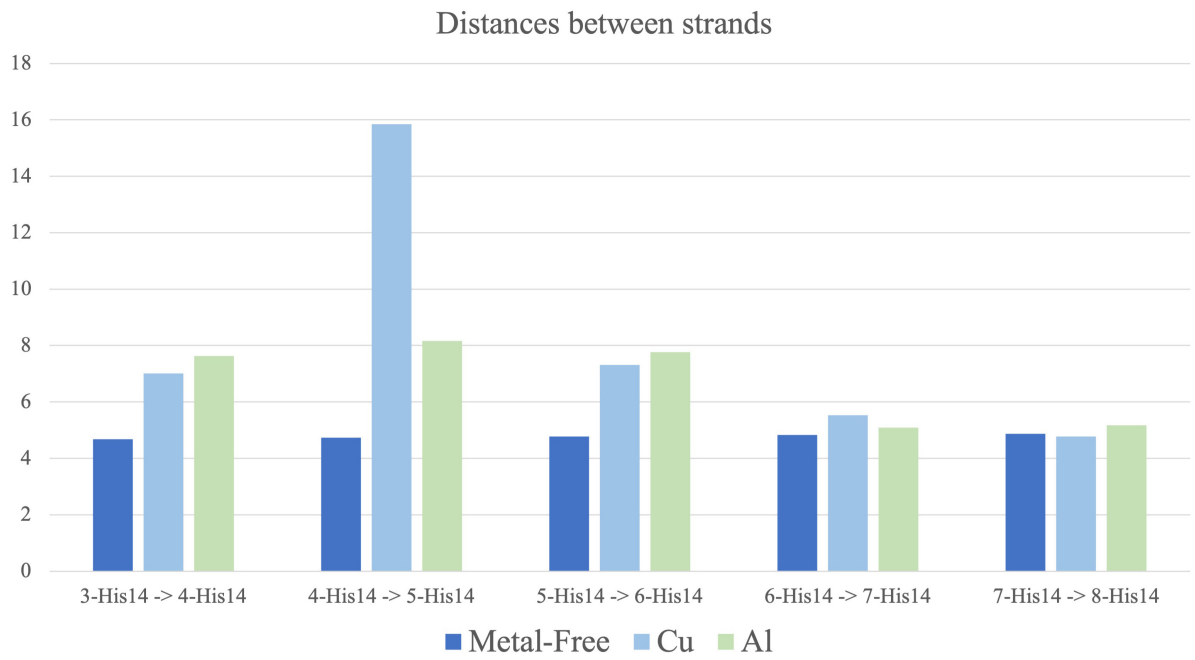

FIGURE 7
Average distance between His14 from each core strand to the adjacent one along 100 ns molecular dynamic (MD) simulation for metal-free fibril (dark blue), Cu(II) (light blue) and Al(III) (green). Standard deviation range from 0.1 to 0.7. Strands 3–4, 5–6, and 7–8 are bound by metal coordination in Cu(II) and Al(III) systems.

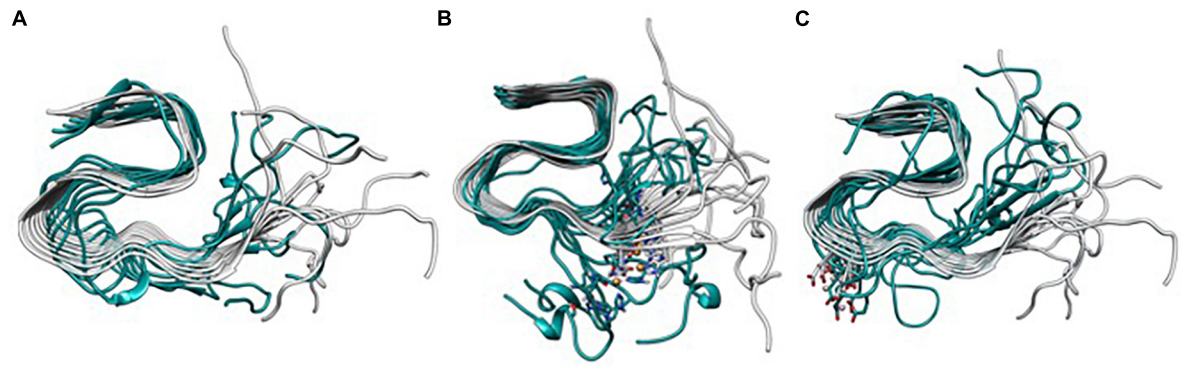

FIGURE 8
Overlapping of the lowest energy structure obtained from the Gaussian accelerated molecular dynamics (GaMD) simulation of Metal-Free Fibril **(A)**, Cu(II) **(B)**, and Al(III) **(C)** against the $A\beta_{42}$ model.

pairs of strands is also increased, especially in strands 3 to 6, but the collective movement is preserved. This points to the fact that, although Al(III) binding increases the compactness and stability of the core region, as measures 1 to 4 support, the (N_{Ter}) region is still highly flexible.

The mentioned changes in metal coordination are also clearly observed if the systems are overlapped against the ss-NMR structure (Figure 8), which demonstrates that the metal-free fiber has a collective hinge fan-like movement, increasing the flexibility of the system but without its disruption. In contrast, Cu(II) leads to the partial dismantling of the fibrillary conformation in the (N_{Ter}) region by breaking the collective movement of the fiber. Finally, Al(III)-bound system is more compact in the core region, though the (N_{Ter}) region is still highly flexible.

Conclusion

One of the Alzheimer's disease main hallmarks is the formation of amyloid plaques, constituted by the aggregates of β-amyloid peptides. In this process, metal ions have been shown to play an important role. In the present study, an integrative computational study has been performed to unravel the role of Cu(II) and Al(III) ion binding in the β-amyloid fibrillary structure (pdb code 2MXU). To do so, the binding site and the coordination sphere of the metallic ions were identified with a combined protocol of BioMetAll and Gold Software. Once binding sites were properly detected and the tridimensional models properly set up, the complexes were submitted to an exhaustive conformational exploration through MD and Gaussian accelerated MD, with three replicas of 1 μs each,

achieving a total of 3 μs for the metal-free fiber, Cu(II)-bound, and Al(III)-bound systems. The resulting simulations were analyzed and compared between them and in front of the initial ss-NMR structure.

Metal-free simulations allowed us to characterize the collective low-energy vibrational modes that constitute the natural breathing motions of the S-shaped structure. The main one could be described as a hinge fan-like movement due to the opening–closing tendency of the (N_{Ter}) region of the fiber. Such movement could be linked to the dynamic process of aggregating and dismantling β-amyloid fibers. Metal-bound complexes show a differential behavior that, interestingly, depends on the metal ion. On the one side, Cu(II) binding is at the (N_{Ter}) region with two His13 and Gln15 from adjacent strands, at a site very close to where it happens in the monomeric species. The binding of copper ion introduces the charges in the (N_{Ter}) region and the analyses of the simulations show that the system tends to disrupt the fibrillary structure of the most extreme strands that adopt α-helix configurations, resembling the monomeric structure of the β-amyloid peptide. This fact supports the hypothesis that copper is more prone to lead to amorphous aggregates (Huy et al., 2016), as shown experimentally (Innocenti et al., 2010). In contrast, Al(III) binding takes place in the first coil region of the S-shape, on the residues Glu22 and Asp23 from adjacent strands, which compensates for the Al(III) charge. In this case, aluminum ion binding reinforces the stability of the system in the core region, even reducing the hinge movement observed in the metal-free fiber complex and obtaining structures with the lowest difference with respect to the ss-NMR structure. Such fact reinforces the idea that Al(III) stabilizes neurotoxic species (Miller et al., 2012). In contrast, the larger stability of the fibril has been related to a higher aggregation rate (Thu and Li, 2022). However, mature fibril deposits are less relevant than oligomers with respect to AD etiology and severity (Miller et al., 2012).

Overall, the computational study carried out in this work shows that the binding of metal ions to β-amyloid fiber indeed affects its dynamical behavior, though in a different manner depending on the metal ion involved: while Cu(II) leads to less organized tertiary structures than the unbound system, Al(III) retrieves the opposite behavior, with a high stable S-shaped structure. This is in line with the study of Bolognin et al. (2011), which demonstrates that while Cu(II) prevents the formation of fibrillary aggregates, Al(III) induces the aggregation of fibrillary oligomers. The next steps are being performed to merge the influence of metal-ion coordination with the relevant familiar mutated forms of the β-amyloid fiber.

Data availability statement

The original contributions presented in this study are included in this article/**Supplementary material**, further inquiries can be directed to the corresponding authors.

Author contributions

LR-M carried out the experiment. LR-M, J-DM, and MS wrote the manuscript. J-DM and MS supervised the project and conceived the original idea. All authors contributed to the article and approved the submitted version.

Funding

This work was supported by the projects PID2020-116861GB-I00 and PID2020-112715GB-I00 from the Spanish Ministerio de Ciencia y Educación. LR-M would like to thank Generalitat de Catalunya (grant 2020FI_B2_01000).

Conflict of interest

The authors declare that the research was conducted in the absence of any commercial or financial relationships that could be construed as a potential conflict of interest.

Publisher's note

Supplementary material

The Supplementary Material for this article can be found online at: https://www.frontiersin.org/articles/10.3389/fnins.2023.1110311/full#supplementary-material

References

Alí-Torres, J., Maréchal, J. D., Rodríguez-Santiago, L., and Sodupe, M. (2011). Three dimensional models of Cu 2+-Aβ(1-16) complexes from computational approaches. *J. Am. Chem. Soc.* 133, 15008–15014. doi: 10.1021/ja203407v

Alí-Torres, J., Mirats, A., Maréchal, J. D., Rodríguez-Santiago, L., and Sodupe, M. (2014). 3D structures and redox potentials of Cu2+-Aβ(1-16) complexes at different pH: A computational study. *J. Phys. Chem. B* 118, 4840–4850. doi: 10.1021/jp5019718

Almeida, Z. L., and Brito, R. M. M. (2020). Structure and aggregation mechanisms in amyloids. *Molecules* 25:1195. doi: 10.3390/molecules25051195

Bakan, A., Meireles, L. M., and Bahar, I. (2011). ProDy: Protein dynamics inferred from theory and experiments. *Bioinformatics* 27, 1575–1577. doi: 10.1093/bioinformatics/btr168

Bayly, C. I., Cieplak, P., Cornell, W. D., and Kollman, P. A. (1993). A well-behaved electrostatic potential based method using charge restraints for deriving atomic charges: The RESP model. *J. Phys. Chem.* 97, 10269–10280. doi: 10.1021/j100142a004

Becke, A. D. (1998). Density-functional thermochemistry. III. The role of exact exchange. *J. Chem. Phys.* 98:5648. doi: 10.1063/1.464913

Bennett, D. A., Schneider, J. A., Arvanitakis, Z., Kelly, J. F., Aggarwal, N. T., Shah, R. C., et al. (2006). Neuropathology of older persons without cognitive impairment from two community-based studies. *Neurology* 66, 1837–1844. doi: 10.1212/01.wnl.0000219668.47116.e6

Bolognin, S., Messori, L., Drago, D., Gabbiani, C., Cendron, L., and Zatta, P. (2011). Aluminum, copper, iron and zinc differentially alter amyloid-Aβ(1-42) aggregation and toxicity. *Int. J. Biochem. Cell Biol.* 43, 877–885. doi: 10.1016/j.biocel.2011.02.009

Boopathi, S., Dinh Quoc, Huy, P., Gonzalez, W., Theodorakis, P. E., and Li, M. S. (2020). Zinc binding promotes greater hydrophobicity in Alzheimer's Aβ42 peptide than copper binding: Molecular dynamics and solvation thermodynamics studies. *Proteins* 88, 1285–1302. doi: 10.1002/prot.25901

Breijyeh, Z., Karaman, R., Muñoz-Torrero, D., and Dembinski, R. (2020). Comprehensive review on Alzheimer's disease: Causes and treatment. *Molecules* 25:5789. doi: 10.3390/molecules25245789

Case, D. A. I, Ben-Shalom, Y., Brozell, S. R., Cerutti, D. S., Cheatham, T. E., Cruzeiro, V. W. D., et al. (2018). *Amber 2018*. San Francisco, CA: University of California.

Case, D. A., Cheatham, T. E., Darden, T., Gohlke, H., Luo, R., Merz, K. M., et al. (2005). The amber biomolecular simulation programs. *J. Comput. Chem.* 26, 1668–1688. doi: 10.1002/jcc.20290

Deture, M. A., and Dickson, D. W. (2019). The neuropathological diagnosis of Alzheimer's disease. *Mol. Neurodegener.* 14:32. doi: 10.1186/s13024-019-0333-5

Drew, S. C., and Barnham, K. J. (2011). The heterogeneous nature of Cu2+ interactions with Alzheimer's amyloid-β peptide. *Acc. Chem. Res.* 44, 1146–1155. doi: 10.1021/ar200014u

Duane, S., Kennedy, A. D., Pendleton, B. J., and Roweth, D. (1987). Hybrid monte carlo. *Phys. Lett. B* 195, 216–222. doi: 10.1016/0370-2693(87)91197-X

Ehlers, A. W., Böhme, M., Dapprich, S., Gobbi, A., Höllwarth, A., Jonas, V., et al. (1993). A set of f-polarization functions for pseudo-potential basis sets of the transition metals Sc-Cu, Y-Ag and La-Au. *Chem. Phys. Lett.* 208, 111–114. doi: 10.1016/0009-2614(93)80086-5

Faller, P. (2009). Copper and zinc binding to amyloid-beta: Coordination, dynamics, aggregation, reactivity and metal-ion transfer. *Chembiochem* 10, 2837–2845. doi: 10.1002/cbic.200900321

Faller, P., Hureau, C., and Berthoumieu, O. (2013). Role of metal ions in the self-assembly of the Alzheimer's amyloid-β peptide. *Inorg. Chem.* 52, 12193–12206. doi: 10.1021/ic4003059

Grimme, S., Antony, J., Ehrlich, S., and Krieg, H. (2010). A consistent and accurate ab initio parametrization of density functional dispersion correction (DFT-D) for the 94 elements H-Pu. *J. Chem. Phys.* 132:154104. doi: 10.1063/1.3382344

Groh, N., Bühler, A., Huang, C., Li, K. W., van Nierop, P., Smit, A. B., et al. (2017). Age-dependent protein aggregation initiates amyloid-β aggregation. *Front. Aging Neurosci.* 9:138. doi: 10.3389/fnagi.2017.00138

Hardy, J. A., and Higgins, G. A. (1992). Alzheimer's disease: The amyloid cascade hypothesis. *Science* 256, 184–185. doi: 10.1126/science.1566067

Humphrey, W., Dalke, A., and Schulten, K. (1996). VMD: Visual molecular dynamics. *J. Mol. Graph.* 14, 33–38. doi: 10.1016/0263-7855(96)00018-5

Huy, P. D. Q., Vuong, Q., van, la Penna, G., Faller, P., and Li, M. S. (2016). Impact of Cu(II) binding on structures and dynamics of Aβ42 monomer and dimer: Molecular dynamics study. *ACS Chem. Neurosci.* 7, 1348–1363. doi: 10.1021/acschemneuro.6b00109

Innocenti, M., Salvietti, E., Guidotti, M., Casini, A., Bellandi, S., Foresti, M. L., et al. (2010). Trace copper(II) or zinc(II) ions drastically modify the aggregation behavior of amyloid-beta1-42: An AFM study. *J. Alzheimers Dis.* 19, 1323–1329. doi: 10.3233/JAD-2010-1338

Jones, G., Willett, P., and Glen, R. C. (1995). Molecular recognition of receptor sites using a genetic algorithm with a description of desolvation. *J. Mol. Biol.* 245, 43–53. doi: 10.1016/S0022-2836(95)80037-9

Jones, G., Willett, P., Glen, R. C., Leach, A. R., and Taylor, R. (1997). Development and validation of a genetic algorithm for flexible docking. *J. Mol. Biol.* 267, 727–748. doi: 10.1006/jmbi.1996.0897

Jorgensen, W. L., Chandrasekhar, J., Madura, J. D., Impey, R. W., and Klein, M. L. (1998). Comparison of simple potential functions for simulating liquid water. *J. Chem. Phys.* 79:926. doi: 10.1063/1.445869

Ke, P. C., Zhou, R., Serpell, L. C., Riek, R., Knowles, T. P. J., Lashuel, H. A., et al. (2020). Half a century of amyloids: Past, present and future. *Chem. Soc. Rev.* 49, 5473–5509. doi: 10.1039/C9CS00199A

Kepp, K. P. (2012). Bioinorganic chemistry of Alzheimer's disease. *Chem. Rev.* 112, 5193–5239. doi: 10.1021/cr300009x

Khatua, P., Mondal, S., and Bandyopadhyay, S. (2019). Effects of metal ions on Aβ42 peptide conformations from molecular simulation studies. *J. Chem. Inf. Model.* 59, 2879–2893. doi: 10.1021/acs.jcim.9b00098

Kollmer, M., Close, W., Funk, L., Rasmussen, J., Bsoul, A., Schierhorn, A., et al. (2019). Cryo-EM structure and polymorphism of Aβ amyloid fibrils purified from Alzheimer's brain tissue. *Nat. Commun.* 10, 1–8. doi: 10.1038/s41467-019-12683-8

Krishnamurthy, S., Sudhakar, S., and Mani, E. (2022). Kinetics of aggregation of amyloid β under different shearing conditions: Experimental and modelling analyses. *Colloids Surf. B Biointerfaces* 209:112156. doi: 10.1016/j.colsurfb.2021.112156

Lee, C., Yang, W., and Parr, R. G. (1988). Development of the colle-salvetti correlation-energy formula into a functional of the electron density. *Phys. Rev. B Condens. Matter* 37:785. doi: 10.1103/PhysRevB.37.785

Li, P., and Merz, K. M. (2016). MCPB.py: A python based metal center parameter builder. *J. Chem. Inf. Model.* 56, 599–604. doi: 10.1021/acs.jcim.5b00674

Liao, Q., Owen, M. C., Bali, S., Barz, B., and Strodel, B. (2018). Aβ under stress: The effects of acidosis, Cu 2+ -binding, and oxidation on amyloid β-peptide dimers. *Chem. Comm.* 54, 7766–7769. doi: 10.1039/C8CC02263A

Liberta, F., Loerch, S., Rennegarbe, M., Schierhorn, A., Westermark, P., Westermark, G. T., et al. (2019). Cryo-EM fibril structures from systemic AA amyloidosis reveal the species complementarity of pathological amyloids. *Nat. Commun.* 2019, 1–10. doi: 10.1038/s41467-019-09033-z

Loncharich, R. J., Brooks, B. R., and Pastor, R. W. (1992). Langevin dynamics of peptides: The frictional dependence of isomerization rates of N-acetylalanyl-N'-methylamide. *Biopolymers* 32, 523–535. doi: 10.1002/bip.360320508

Maier, J. A., Martinez, C., Kasavajhala, K., Wickstrom, L., Hauser, K. E., and Simmerling, C. (2015). ff14SB: Improving the accuracy of protein side chain and backbone parameters from ff99SB. *J. Chem. Theory Comput.* 11, 3696–3713. doi: 10.1021/acs.jctc.5b00255

Marenich, A. V., Cramer, C. J., and Truhlar, D. G. (2009). Universal solvation model based on solute electron density and on a continuum model of the solvent defined by the bulk dielectric constant and atomic surface tensions. *J. Phys. Chem. B* 113, 6378–6396. doi: 10.1021/jp810292n

Martí-Renom, M. A., Stuart, A. C., Fiser, A., Sánchez, R., Melo, F., and Šali, A. (2000). Comparative protein structure modeling of genes and genomes. *Annu. Rev. Biophys. Biomol. Struct.* 29, 291–325. doi: 10.1146/annurev.biophys.29.1.291

Maynard, C. J., Bush, A. I., Masters, C. L., Cappai, R., and Li, Q. X. (2005). Metals and amyloid-β in Alzheimer's disease. *Int. J. Exp. Pathol.* 86:147. doi: 10.1111/j.0959-9673.2005.00434.x

Miao, Y., Feher, V. A., and McCammon, J. A. (2015). Gaussian accelerated molecular dynamics: Unconstrained enhanced sampling and free energy calculation. *J. Chem. Theory Comput.* 11, 3584–3595. doi: 10.1021/acs.jctc.5b00436

Miller, Y. (2022). Molecular insights into the effect of metals on amyloid aggregation. *Methods Mol. Biol.* 2340, 121–137. doi: 10.1007/978-1-0716-1546-1_7

Miller, Y., Ma, B., and Nussinov, R. (2010). Zinc ions promote alzheimer aβ aggregation via population shift of polymorphic states. *Proc. Natl. Acad. Sci. U.S.A.* 107, 9490–9495. doi: 10.1073/pnas.0913114107

Miller, Y., Ma, B., and Nussinov, R. (2012). Metal binding sites in amyloid oligomers: Complexes and mechanisms. *Coord. Chem. Rev.* 256, 2245–2252. doi: 10.1016/j.ccr.2011.12.022

Mujika, J. I., Rodríguez-Guerra Pedregal, J., Lopez, X., Ugalde, J. M., Rodríguez-Santiago, L., Sodupe, M., et al. (2017). Elucidating the 3D structures of Al(III)-Aβ complexes: A template free strategy based on the pre-organization hypothesis. *Chem. Sci.* 8, 5041–5049. doi: 10.1039/C7SC01296A

Mutter, S. T., Turner, M., Deeth, R. J., and Platts, J. A. (2018). Metal binding to amyloid-β1-42: A ligand field molecular dynamics study. *ACS Chem. Neurosci.* 9, 2795–2806. doi: 10.1021/acschemneuro.8b00210

Onufriev, A., Bashford, D., and Case, D. A. (2000). Modification of the generalized born model suitable for macromolecules. *J. Phys. Chem. B* 104, 3712–3720. doi: 10.1021/jp994072s

Onufriev, A., Bashford, D., and Case, D. A. (2004). Exploring protein native states and large-scale conformational changes with a modified generalized born model. *Proteins* 55, 383–394. doi: 10.1002/prot.20033

Parthasarathy, S., Long, F., Miller, Y., Xiao, Y., McElheny, D., Thurber, K., et al. (2011). Molecular-level examination of Cu2+ binding structure for amyloid fibrils of 40-residue alzheimer's β by solid-state NMR spectroscopy. *J. Am. Chem. Soc.* 133, 3390–3400. doi: 10.1021/ja1072178

Pettersen, E. F., Goddard, T. D., Huang, C. C., Couch, G. S., Greenblatt, D. M., Meng, E. C., et al. (2004). UCSF chimera–a visualization system for exploratory research and analysis. *J. Comput. Chem.* 25, 1605–1612. doi: 10.1002/jcc.20084

Pham, D. Q. H., Li, M. S., and la Penna, G. (2018). Copper binding induces polymorphism in amyloid-β peptide: Results of computational models. *J. Phys. Chem. B* 122, 7243–7252. doi: 10.1021/acs.jpcb.8b03983

Rahman, A., Saikia, B., Gogoi, C. R., and Baruah, A. (2022). Advances in the understanding of protein misfolding and aggregation through molecular dynamics simulation. *Prog. Biophys. Mol. Biol.* 175, 31–48. doi: 10.1016/j.pbiomolbio.2022.08.007

Rassolov, V. A., Ratner, M. A., Pople, J. A., Redfern, P. C., and Curtiss, L. A. (2001). 6-31G* basis set for third-row atoms. *J. Comput. Chem.* 22, 976–984. doi: 10.1002/jcc.1058

Rodríguez-Guerra Pedregal, J., Sciortino, G., Guasp, J., Municoy, M., and Maréchal, J.-D. (2017). GaudiMM: A modular multi-objective platform for molecular modeling. *J. Comput. Chem.* 38, 2118–2126. doi: 10.1002/jcc.24847

Roldán-Martín, L., Peccati, F., Sciortino, G., Sodupe, M., and Maréchal, J. D. (2021). Impact of Cu(II) and Al(III) on the conformational landscape of amyloidβ1-42. *Phys. Chem. Chem. Phys.* 23, 13023–13032. doi: 10.1039/D1CP01561C

Ryckaert, J.-P., Ciccotti, G., and Berendsen, H. J. C. (1977). Numerical integration of the cartesian equations of motion of a system with constraints: Molecular dynamics of n-Alkanes. *J. Comput. Phys.* 23, 321–341. doi: 10.1016/0021-9991(77)90098-5

Sánchez-Aparicio, J. E., Tiessler-Sala, L., Velasco-Carneros, L., Roldán-Martín, L., Sciortino, G., and Maréchal, J. D. (2021). BioMetAll: Identifying metal-binding sites in proteins from backbone preorganization. *J. Chem. Inf. Model.* 61, 311–323. doi: 10.1021/acs.jcim.0c00827

Sciortino, G., Rodríguez-Guerra Pedregal, J., Lledós, A., Garribba, E., and Maréchal, J.-D. (2018). Prediction of the interaction of metallic moieties with proteins: An update for protein-ligand docking techniques. *J. Comput. Chem.* 39, 42–51. doi: 10.1002/jcc.25080

Seminario, J. (1996). Calculation of intramolecular force fields from second-derivative tensors. *Int. J. Quantum Chem.* 60, 1271–1277. doi: 10.1002/(SICI)1097-461X(1996)60:7<1271::AID-QUA8>3.0.CO;2-W

Stefaniak, E., Atrian-Blasco, E., Goch, W., Sabater, L., Hureau, C., and Bal, W. (2021). The aggregation pattern of Aβ1–40 is altered by the presence of N-truncated Aβ4–40 and/or CuII in a similar way through ionic interactions. *Chem. Eur. J.* 27, 2798–2809. doi: 10.1002/chem.202004484

Strodel, B., and Coskuner-Weber, O. (2019). Transition metal ion interactions with disordered amyloid-β peptides in the pathogenesis of Alzheimer's disease: Insights from computational chemistry studies. *J. Chem. Inf. Model.* 59, 1782–1805. doi: 10.1021/acs.jcim.8b00983

Thu, T. T. M., and Li, M. S. (2022). Protein aggregation rate depends on mechanical stability of fibrillar structure. *J. Chem. Phys.* 157:055101. doi: 10.1063/5.0088689

Tiwari, S. P., Fuglebakk, E., Hollup, S. M., Skjærven, L., Cragnolini, T., Grindhaug, S. H., et al. (2014). WEBnmat v2.0: Web server and services for comparing protein flexibility. *BMC Bioinformatics* 15:427. doi: 10.1186/s12859-014-0427-6

Turner, M., Mutter, S. T., Kennedy-Britten, O. D., and Platts, J. A. (2019). Molecular dynamics simulation of aluminium binding to amyloid-β and its effect on peptide structure. *PLoS One* 14:e0217992. doi: 10.1371/journal.pone.0217992

Wälti, M. A., Ravotti, F., Arai, H., Glabe, C. G., Wall, J. S., Böckmann, A., et al. (2016). Atomic-resolution structure of a disease-relevant Aβ(1-42) amyloid fibril. *Proc. Natl. Acad. Sci. U.S.A.* 113, E4976–E4984. doi: 10.1073/pnas.1600749113

WHO (2019). *Dementia*. Geneva: World Health Organization.

Wold, S., Esbensen, K., and Geladi, P. (1987). Principal component analysis. *Chemom. Intell. Lab. Syst.* 2, 37–52. doi: 10.1016/0169-7439(87)80084-9

Xiao, Y., Ma, B., McElheny, D., Parthasarathy, S., Long, F., Hoshi, M., et al. (2015). Aβ(1–42) fibril structure illuminates self-recognition and replication of amyloid in Alzheimer's disease. *Nat. Struct. Mol. Biol.* 6, 499–505. doi: 10.1038/nsmb.2991

Yang, Y., Arseni, D., Zhang, W., Huang, M., Lövestam, S., Schweighauser, M., et al. (2022). Cryo-EM structures of amyloid-β 42 filaments from human brains. *Science* 375, 167–172. doi: 10.1126/science.abm7285

frontiers | Frontiers in Neuroscience

TYPE Original Research
PUBLISHED 21 March 2023
DOI 10.3389/fnins.2023.1162741

OPEN ACCESS

EDITED BY
Jerson L. Silva,
Federal University of Rio de Janeiro, Brazil

REVIEWED BY
Karishma Bhasne,
University of Massachusetts Amherst, United States
Sukanya Saha,
National Institute of Environmental Health Sciences (NIH), United States
Mayra De Amorim Marques,
Federal University of Rio de Janeiro, Brazil

*CORRESPONDENCE
Cláudio M. Gomes
✉ cmgomes@fc.ul.pt

SPECIALTY SECTION
This article was submitted to Neurodegeneration, a section of the journal Frontiers in Neuroscience

RECEIVED 09 February 2023
ACCEPTED 06 March 2023
PUBLISHED 21 March 2023

CITATION
Figueira AJ, Saavedra J, Cardoso I and Gomes CM (2023) S100B chaperone multimers suppress the formation of oligomers during Aβ42 aggregation. *Front. Neurosci.* 17:1162741. doi: 10.3389/fnins.2023.1162741

S100B chaperone multimers suppress the formation of oligomers during Aβ42 aggregation

António J. Figueira[1,2], Joana Saavedra[3,4,5], Isabel Cardoso[3,4,5] and Cláudio M. Gomes[1,2]*

[1]BioISI–Instituto de Biosistemas e Ciências Integrativas, Faculdade de Ciências, Universidade de Lisboa, Lisbon, Portugal, [2]Departamento de Química e Bioquímica, Faculdade de Ciências, Universidade de Lisboa, Lisbon, Portugal, [3]i3S–Instituto de Investigação e Inovação em Saúde, Universidade do Porto, Porto, Portugal, [4]IBMC–Instituto de Biologia Molecular e Celular, Universidade do Porto, Porto, Portugal, [5]ICBAS–Instituto de Ciências Biomédicas Abel Salazar, Universidade do Porto, Porto, Portugal

Extracellular aggregation of the amyloid-β 1–42 (Aβ42) peptide is a major hallmark of Alzheimer's disease (AD), with recent data suggesting that Aβ intermediate oligomers (AβO) are more cytotoxic than mature amyloid fibrils. Understanding how chaperones harness such amyloid oligomers is critical toward establishing the mechanisms underlying regulation of proteostasis in the diseased brain. This includes S100B, an extracellular signaling Ca^{2+}-binding protein which is increased in AD as a response to neuronal damage and whose holdase-type chaperone activity was recently unveiled. Driven by this evidence, we here investigate how different S100B chaperone multimers influence the formation of oligomers during Aβ42 fibrillation. Resorting to kinetic analysis coupled with simulation of AβO influx distributions, we establish that supra-stoichiometric ratios of dimeric S100B-Ca^{2+} drastically decrease Aβ42 oligomerization rate by 95% and AβO levels by 70% due to preferential inhibition of surface-catalyzed secondary nucleation, with a concomitant redirection of aggregation toward elongation. We also determined that sub-molar ratios of tetrameric apo-S100B decrease Aβ42 oligomerization influx down to 10%, while precluding both secondary nucleation and, more discreetly, fibril elongation. Coincidently, the mechanistic predictions comply with the independent screening of AβO using a combination of the thioflavin-T and X-34 fluorophores. Altogether, our findings illustrate that different S100B multimers act as complementary suppressors of Aβ42 oligomerization and aggregation, further underpinning their potential neuroprotective role in AD.

KEYWORDS

molecular chaperones, protein aggregation, amyloid-β oligomers, aggregation kinetics and mechanism, amyloid beta (1–42)

Introduction

Aggregation of the disordered amyloid-β peptide (Aβ) into extracellular plaques constitutes a major hallmark in Alzheimer's disease (AD) neurodegeneration (Hardy and Higgins, 1992; Knowles et al., 2014; Selkoe and Hardy, 2016). Indeed, the conversion of monomeric Aβ into mature amyloid fibrils involves a complex self-assembly process that

leads to the formation of transient and off-pathway soluble/fibrillar species (Kayed et al., 2007), globally designated as Aβ oligomers (AβO) (Michaels et al., 2018). Increasing evidence suggests that AβO, rather than mature amyloid fibrils, are the key AD etiological drivers responsible for disease progression (Holtzman et al., 2011; Benilova et al., 2012). Various populations of AβO were reported to trigger multiple deleterious events that ultimately contribute to neuronal loss and cognitive decline (Cline et al., 2018). Examples include tau hyperphosphorylation and missorting (Ma et al., 2009; Schützmann et al., 2021), oxidative stress (De Felice et al., 2007; Wang et al., 2014), metallostasis dysregulation (Lazzari et al., 2015; Cristóvão et al., 2016), cell membrane damage (Williams et al., 2011), axonal transport impairment (Decker et al., 2010), synaptic receptor redistribution (Lacor et al., 2007), and astroglia activation (Heneka et al., 2015; Forloni and Balducci, 2018). In particular, reactive astrocytes surround Aβ proteinaceous aggregates (Kato et al., 1998) and prompt local neuroinflammation by secreting several alarmins into the synaptic milieu (Li et al., 2011).

This is the case of the small homodimeric (2 × 10.7 kDa) Ca^{2+}-binding S100B protein (Mrak and Griffinbc, 2001; Donato et al., 2009), which is upregulated in AD (Marshak et al., 1992) and is known to contribute to the late neuroinflammatory response (Cuello, 2017; Hagmeyer et al., 2019). Apart from its pro-inflammatory role, we have recently unveiled that the Ca^{2+}-bound form of dimeric S100B inhibits the *in vitro* aggregation and toxicity of the Aβ forty two amino-acid variant (Aβ42) (Cristóvão et al., 2018, 2020) and the microtubule-associated protein tau (Moreira et al., 2021), thus acting as a neuroprotective holdase-type chaperone. Not only, and although mainly present in the brain as a homodimer, S100B is also found as higher order functional oligomers such as octamers, hexamers and tetramers (Ostendorp et al., 2007), the latter described as suppressors of Aβ42 aggregation (Figueira et al., 2022). Indeed, we recently established that S100B tetramerization spawns an extended hydrophobic surface which is formed by the lateral juxtaposition of homodimer C-terminal helices and whose solvent accessibility is independent of Ca^{2+} binding. This novel regulatory cleft leads to a significant increase of Aβ42 anti-aggregation activity, also observable in the apo-form of tetrameric S100B (Figueira et al., 2022). Structural nuclear magnetic resonance (NMR), immunogold labeling electron microscopy and computational studies show that dimeric and tetrameric S100B target monomeric and fibrillar Aβ42 conformers (Cristóvão et al., 2018; Rodrigues et al., 2021), which indicates a modulation of Aβ42 primary nucleation, fibril elongation and, particularly, fibril catalyzed secondary nucleation of monomers into small aggregates (Arosio et al., 2016; Cristóvão et al., 2018). Given that secondary nucleation constitutes a major source of on-pathway Aβ42 oligomers (Arosio et al., 2015; Tornquist et al., 2018), aggregation suppressors able to impair this microscopic reaction step result in a significant depletion of AβO formed along the aggregation process, thus being attractive candidates for disease-modifying approaches. This is the case of the Brichos chaperone domain (Cohen et al., 2015; Chen et al., 2020), numerous bexarotene derivatives (Chia et al., 2018), and the anti-Aβ Aducanumab antibody (Linse et al., 2020). Driven by this evidence, we here investigate if dimeric and tetrameric S100B, the two most abundant non-covalent S100B multimers present in the human brain (Ostendorp et al., 2007), could exert an analogous effect over AβO generation.

While several biophysical approaches are available for the kinetic monitoring of mature amyloid fibrils (Biancalana and Koide, 2010), the detection of intermediate species is particularly challenging due to the conformational heterogeneity and residual amounts of AβO. Although experimental methods based on ELISA immunodetection (Aprile Francesco et al., 2020), mass spectrometry and tritium scintillation (Michaels et al., 2020) were previously employed to timely screen pre-fibrillar AβO populations, a simpler approach builds in the kinetic simulation of the nucleation rates throughout Aβ aggregation (Chia et al., 2018). This represents a robust and relatively simple method to estimate fibrillar AβO distributions exclusively based in the rate constants drawn from thioflavin-T (ThT) aggregation kinetics assays (Gade Malmos et al., 2017). Interestingly, some amyloid binding fluorophores are reported to detect ThT negative conformers early in the aggregation reaction. Indeed, fluorescent dyes such as the p-FTAA luminescent conjugated oligothiophene (Klingstedt et al., 2011), the Congo red derivative X-34 (Barton et al., 2019) and the molecular rotors DCVJ (Nagarajan and Lapidus, 2017) and ThX (Needham et al., 2020), were described to have enhanced selectivity for oligomers in particular aggregation systems. In this study, we take advantage of these properties and combine different amyloid fluorescent dyes to monitor Aβ42 aggregation kinetics and infer on the extent of formed oligomers through differential analysis. Interestingly, we find this to correlate adequately with AβO distributions determined independently through mechanistic analysis.

Results and discussion

S100B multimers modulate multiple pathways governing Aβ42 aggregation

To establish the impact of S100B on the generation of Aβ42 oligomers, we started by characterizing the mechanistic properties contributing for S100B anti-aggregation activity in the Ca^{2+}-bound dimeric and apo-tetrameric states. For this, we employed Aβ42 thioflavin-T (ThT) monitored aggregation assays coupled with global fitting analysis, which provides information about the microscopic mechanisms accounting for the macroscopic kinetic traces (**Figures 1A–F**).

Complying with our prior observations, we observe that the calcium bound form of dimeric S100B (S100B-Ca^{2+}) suppresses Aβ42 aggregation at supra-stoichiometric conditions (**Figures 1A, C**). Global fitting of the kinetic traces implies that Aβ42 aggregation secondary pathways, a combination of the secondary nucleation and elongation rates constants (k_2k_+), are properly suppressed by an excess of S100B-Ca^{2+} dimer (**Figure 1E**). This inhibitory behavior is indeed consistent with the multiple Aβ42 conformers previously shown to interact with S100B-Ca^{2+}, and which include monomers, oligomers and fibril surfaces (Cristóvão et al., 2018). Primary pathway rates (k_nk_+) are contrastingly enhanced in the presence of the chaperone (**Figure 1E**), settling with the mild acceleration of Aβ42 fibrillation observed at lower S100B:Aβ42 ratios (**Figure 1C**). In fact, an increase over primary nucleation rates was reported to occur in other amyloid suppressors (Linse et al., 2020; Poska et al., 2020),

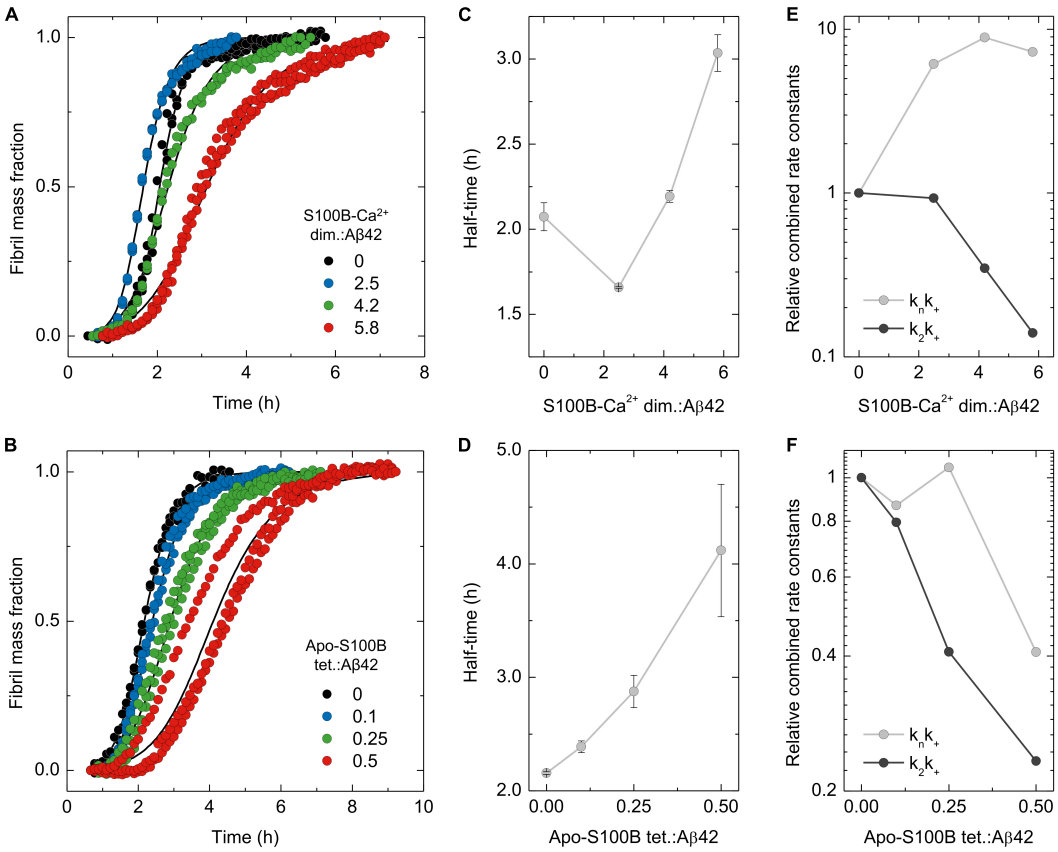

FIGURE 1
Analysis of dimeric and tetrameric S100B effect over Aβ42 aggregation mechanisms. Normalized traces of ThT-monitored aggregation of monomeric Aβ42 [6 μM in panel **(A)** or 2 μM in panel **(B)**] in the presence of increasing molar ratios of **(A)** S100B-Ca^{2+} dimer:Aβ42 (0–5.8) or **(B)** apo-S100B tetramer:Aβ42 (0–0.5) with the **(C,D)** respective values of aggregation half-times ($t_{1/2}$). Solid lines depict global fits of each curve obtained by varying the rate constants of primary (k_nk_+) and secondary (k_2k_+) Aβ42 aggregation pathways, with the relative values of each combined rate constant plotted as a function of S100B **(E)** dimer and **(F)** tetramer ratios. In all cases, error bars represent standard deviation of three experiments.

particularly for proteins exposing aggregation-prone surfaces as Ca^{2+}-bound S100B (Cristóvão et al., 2021). Such effect yields, however, a negligible perturbation over the amounts and formation rates of intermediate Aβ42 oligomers, as previously characterized (Arosio et al., 2015). To gain further insights in the specific mechanisms influenced by S100B-Ca^{2+}, we performed global fitting of the kinetic data but, this time, allowing only a specific rate constant (k_n, k_2 or k_+) to be the free fitting-parameter transversely to all conditions (**Supplementary Figures 1A–C**). This semiempirical analysis reveal that the experimental data is best described by a specific reduction of the surface catalyzed nucleation rate constant k_2 (**Supplementary Figure 1B**). Consequently, results support that dimeric S100B-Ca^{2+} effect over Aβ42 secondary paths is largely caused by an impairment of surface catalyzed nucleation events.

Using an analogous procedure, we set out to investigate the mechanistic aspects driving the activity of tetrameric apo-S100B under sub-stoichiometric conditions. We tested tetrameric S100B in a Ca^{2+} free state, as this allow us to selectively investigate the catalytic activity of the novel extended cleft present in tetrameric S100B (Figueira et al., 2022). As reported, tetrameric apo-S100B displays an enhanced anti-aggregation activity with respect to dimer, being able to delay Aβ42 fibrillation even at sub-molar ratios (**Figures 1B, D**). Global fitting analysis reveal a simultaneous suppression of both Aβ42 combined aggregation rate constants, with a higher impact on k_2k_+values (**Figure 1F**). As this scenario is compatible with an inhibition of any Aβ42 aggregation micro-steps, we again performed global fitting allowing variations of each individual rate constant (**Supplementary Figures 1D–F**). We observed that only selective perturbations in secondary nucleation (k_2) and elongation rate (k_+) constants lead to appropriate explanation of the experimental kinetic traces (**Supplementary Figures 1E, F**). Therefore, we are guided to conjecture that the decrease over primary and secondary pathway rate constants results from a concomitant and more balanced inhibition of secondary nucleation and fibril elongation.

Dimeric and tetrameric S100B preferentially suppress Aβ42 secondary nucleation and minimize oligomer generation

To quantitatively dissect the partial contributions of secondary nucleation and fibril elongation for the observed k_2k_+ depletions,

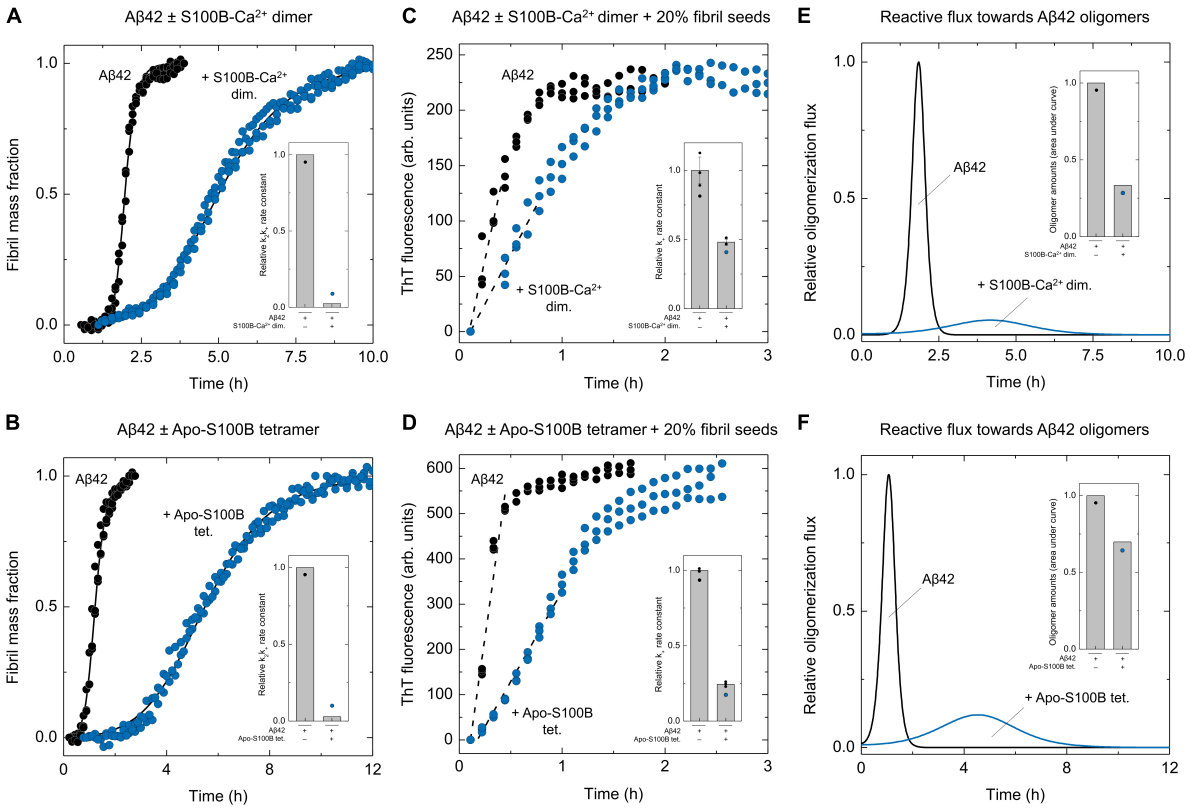

FIGURE 2
Effect of S100B dimer and tetramer over Aβ42 oligomerization flux distributions. Normalized kinetic traces and global fits (solid lines) of unseeded ThT-monitored aggregation of Aβ42 [6 μM in panel **(A)** or 4 μM in panel **(B)**] in the absence and presence of **(A)** dimeric S100B-Ca^{2+} (S100B:Aβ42 = 5.8) or **(B)** tetrameric apo-S100B (S100B:Aβ42 = 0.5) with indication of the relative secondary pathways combined rate constants (k_2k_+, insets). Kinetic traces of high-seeded (20% Aβ42 fibrils). ThT-monitored aggregation of Aβ42 [6 μM in panel **(C)** or 4 μM in panel **(D)**] in the absence and presence of **(C)** dimeric S100B-Ca^{2+} (S100B:Aβ42 = 5.8) or **(D)** tetrameric apo-S100B (S100B:Aβ42 = 0.5), depicting the plot regions used for linear fits (dashed lines) and the calculated relative elongation rate constants (k_+, insets). Error bars represent standard deviation of three experiments. Relative Aβ42 oligomerization flux/nucleation rate distributions (solid lines) in the absence/presence of **(E)** dimeric S100B-Ca^{2+} (S100B:Aβ42 = 5.8) or **(F)** tetrameric apo-S100B (S100B:Aβ42 = 0.5) and total amounts of oligomers calculated by integration of each distribution in respect to time (insets).

we then performed experiments at high seeding conditions (20% of Aβ42 fibrils), and employing the highest S100B:Aβ42 ratios assayed (Figures 2A–F). Indeed, under these conditions Aβ42 aggregation is completely dominated by elongations events, and the initial slope of the resulting kinetic profile can be used to estimate the correspondent elongation rate constants k_+ (Meisl et al., 2014). Results show that unlike the unseeded condition, in which dimeric S100B-Ca^{2+} strongly reduces to <5% the combined rate constant k_2k_+ (Figure 2A), under a high seeding kinetic regime the k_+ reduction is limited to 50% (Figure 2C). We thus conclude that the S100B-Ca^{2+} dimer effect on the apparent k_2k_+ value is mainly caused by an inhibition of Aβ42 nucleation on fibril surfaces. With respect to tetrameric apo-S100B, high-seeding assays denote a more vigorous inhibition over the mechanism of fibril elongation, associated with a 75% k_+ reduction (Figures 2B, D). Nonetheless, and despite this stronger effect, we find that the k_2k_+ depletion is still mostly prompted by an impairment of Aβ42 secondary nucleation.

Given the pivotal role of secondary nucleation in AβO catalytic cycle (Tornquist et al., 2018), we posited that the activity of S100B multimers could result in a depletion of nucleation units/oligomers formed throughout Aβ42 fibrillation. To test this hypothesis, the determined relative k_+ values were used to derive primary nucleation (k_n) and secondary nucleation (k_2) individual rate constants, which in turn were employed to simulate Aβ42 oligomerization flux distributions (Figures 2E, F). Simulations reveal that an excess of S100B-Ca^{2+} dimer results in a substantial suppression of Aβ42 oligomers formation during the fibrillation process. We observe a drastic 95% reduction in the maximum reactive flux toward Aβ42 oligomers and peak integration reveals that the number of AβO is decreased by 70% in the presence of S100B (Figure 2E). A similar effect is noticed for the apo-S100B tetramer under sub-stoichiometric conditions, with the maximum rate of Aβ42 oligomer formation being diminished down to 10% (Figure 2F). Nonetheless, and contrastingly to the activity of dimeric S100B, we find that the tetramer has a more modest 30% reduction effect in AβO total amounts. This is, however, in line with the improved inhibitory effect of the S100B tetramer over fibril elongation, as this mechanism constitutes the major reactive path by which nucleated aggregates can be converted into more matured fibrils (Staats et al., 2020).

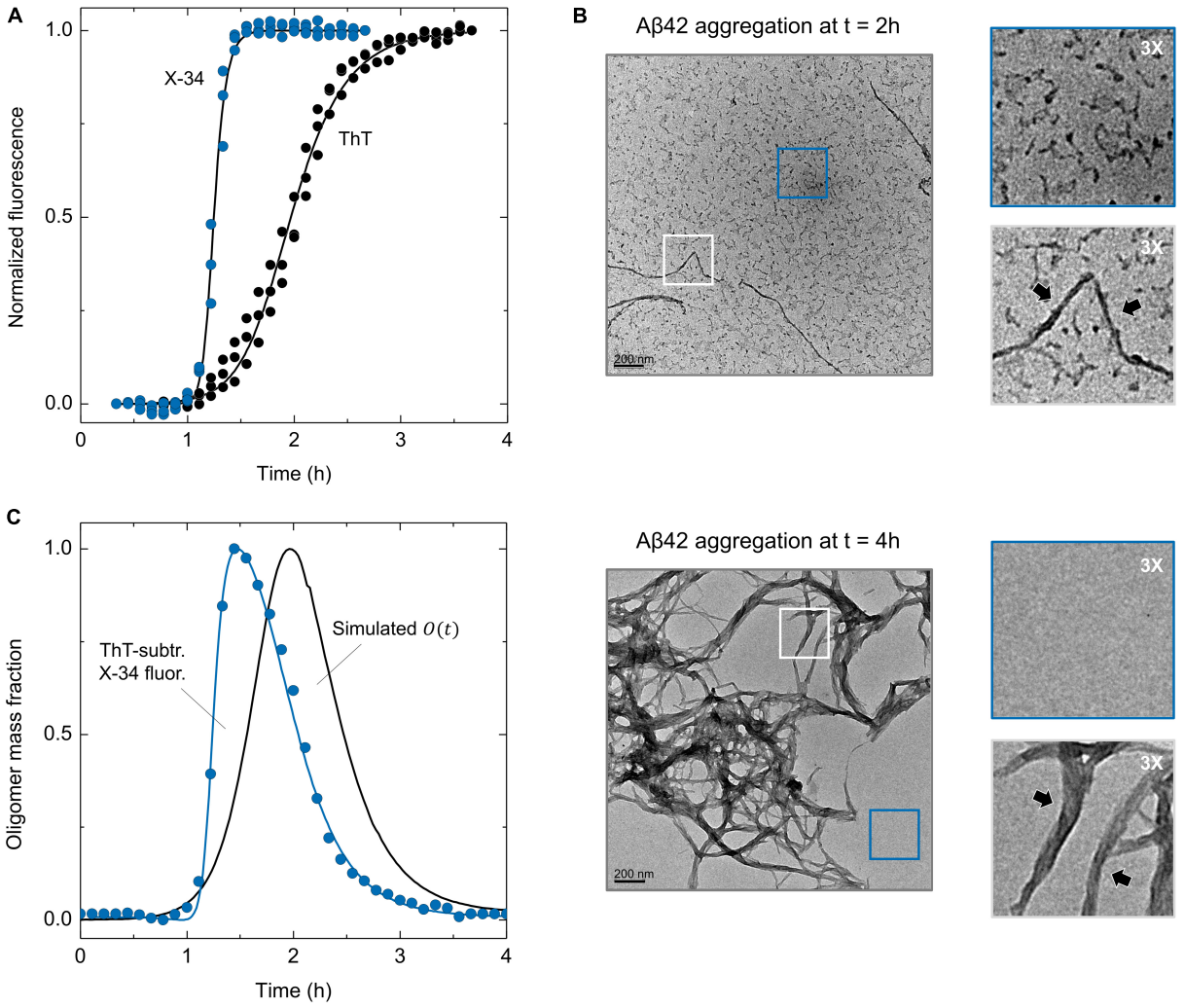

FIGURE 3
ThT and X-34 differential fluorescence analysis of Aβ42 aggregation and TEM imaging of X-34 positive oligomers. **(A)** Comparison of Aβ42 (6 μM) aggregation kinetics monitored by the ThT and X-34 fluorophores. **(B)** Representative transmission electron microscopy images of Aβ42 aggregation at the time-points of (top) 2 and (bottom) 4 h. Gray and blue insets represent three-times ampliation of Aβ42 amyloid-like fibrils and small oligomers/background, respectively. Black arrows pinpoint Aβ42 amyloid fibrils. **(C)** Temporal evolution of ThT subtracted X-34 positive species (average values, n = 3) overlayed with Aβ42 oligomer mass fraction progression [$O(t)$] calculated from aggregation rate constants (black solid line), portraying a significant intersection between experimental and simulated kinetics. See **Supplementary Figures 3A–C** for details on the mathematical formalism employed.

Taken together, kinetic assays show that both dimeric and tetrameric S100B strongly minimize the formation of oligomers during Aβ42 fibrillation. Such inhibitory profile arises from a preferential targeting of secondary nucleation, which causes a subsequent redirection of Aβ42 aggregation toward elongation events.

Estimation of Aβ42 oligomer distributions from differential fluorescence analysis

To gain further experimental insight about the effect of S100B over AβO populations, we resorted to a combination of the amyloid-binding fluorophores ThT and the Congo red derivative X-34. X-34 was reported to detect early amyloidogenic species in addition to mature amyloid fibrils (Rodriguez Camargo et al., 2021), including globular oligomers and small curly filaments (Barton et al., 2019). In agreement, when X-34 is employed to monitor the aggregation of Aβ42, a kinetic profile with a shorter lag phase and earlier plateau is observed, in respect to that obtained on a ThT-monitored aggregation (**Figure 3A**). To rule out that the possibility that either X-34 or DMSO (the dye solvent) might be causing acceleration of Aβ42 aggregation, we performed appropriate controls using increasing dye (1, 2 and 5 μM) and solvent concentration (1% in volume), which yielded superimposable kinetic traces (**Supplementary Figures 2A, B**). We also performed scaling exponent analysis of Aβ42 aggregation monitored with X-34 and obtained a scaling exponent (γ) of–1.26 ± 0.20, which indicates that, similarly to what is obtained with ThT (Cohen et al., 2013; Meisl et al., 2016), X-34 monitored Aβ42 aggregation kinetics follows a mechanism dominated by secondary nucleation

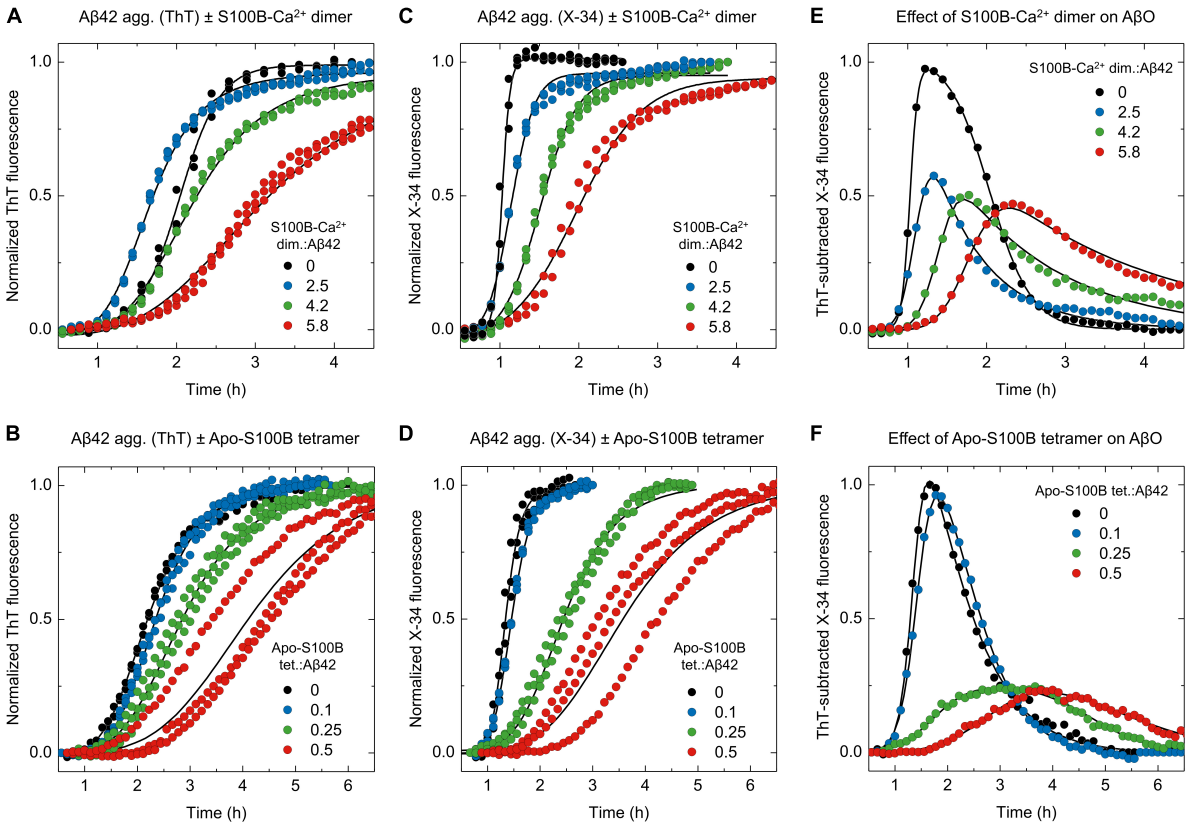

FIGURE 4
ThT and X-34 differential fluorescence analysis support the S100B dimer and tetramer suppressor effect over Aβ42 oligomeric species. Normalized kinetic traces of **(A,B)** ThT or **(C,D)** X-34 monitored aggregation of monomeric Aβ42 [6 μM in panels **(A,C)** or 2 μM in panels **(B,D)**] in the presence of increasing molar ratios **(A,C)** of S100B-Ca^{2+} dimer:Aβ42 (0–5.8) or **(B,D)** apo-S100B tetramer:Aβ42 (0–0.5). ThT subtracted X-34 kinetic traces (average values, n = 3) of all **(E)** S100B-Ca^{2+} dimer and **(F)** apo-S100B tetramer concentrations assayed. Non-normalized kinetic traces are depicted in Supplementary Figure 4.

(Supplementary Figures 2C, D). Therefore, the early increase in X-34 fluorescence observed during Aβ42 aggregation suggests that this fluorophore is effectively detecting Aβ42 oligomers. To obtain additional evidence we employed transmission electron microscopy (TEM) for morphological analysis of Aβ42 species at different time points of aggregation. At t = 2 h, which corresponds to the ThT half-time and to the X-34 plateau phase, we observed mostly small (<50 nm) Aβ42 aggregates in addition to sparse fibrillar materials (Figure 3B top). On the other hand, at t = 4 h, which corresponds to the ThT-plateau phase, we observed essentially mature Aβ42 fibrils with a high-level of self-association but no small oligomers (Figure 3B bottom). Therefore, TEM imaging confirms that X-34 detects early Aβ42 aggregates that are on pathway to the formation of mature amyloid fibrils. This result prompt us to establish a procedure through which the combined monitoring of Aβ42 aggregation kinetics using both X-34 and ThT, might result in a straightforward experimental estimate for formed AβO. This approach is based on the premise that the algebraic subtraction between X-34 and ThT normalized kinetic traces will yield a fair estimate of AβO, allowing a straightforward experimental estimate for the evolution of AβO during Aβ42 aggregation. To evaluate such possibility, we compared the mechanistically derived mass progression of Aβ42 oligomers [$O(t)$] obtained from the ThT-aggregation rate constants (Supplementary Figure 3) with the computed kinetic profile obtained from the algebraic subtraction between X-34 and ThT normalized kinetic traces (Figure 3C). Strikingly, the comparison of this experimentally derived trace with the simulated progression of Aβ42 oligomers revealed a significant overlap between the two distributions, whose maxima differ by only by ∼ 0.5 h. Given the complex and dynamic nature of AβO (Michaels et al., 2020), this fluorescence kinetics difference method provides a fairly reasonable estimate of these species obtained from straightforward kinetic experiments.

Effect of dimeric and tetrameric S100B on X-34 positive Aβ42 oligomers

Once we established the screening of AβO using X-34, the effects of S100B-Ca^{2+} dimer and apo-S100B tetramer were examined (Figures 4A–F; Supplementary Figure 4). Firstly, we monitored Aβ42 aggregation employing the two fluorophores side-by-side at increasing supra-stoichiometric ratios of S100B-Ca^{2+} dimer (Figures 4A, C). The evolution of X-34 positive non-thioflavin Aβ42 oligomers was again computed by subtracting each X-34 kinetic to the corresponding ThT trace, for a given S100B concentration. Corroborating the mechanistic predictions,

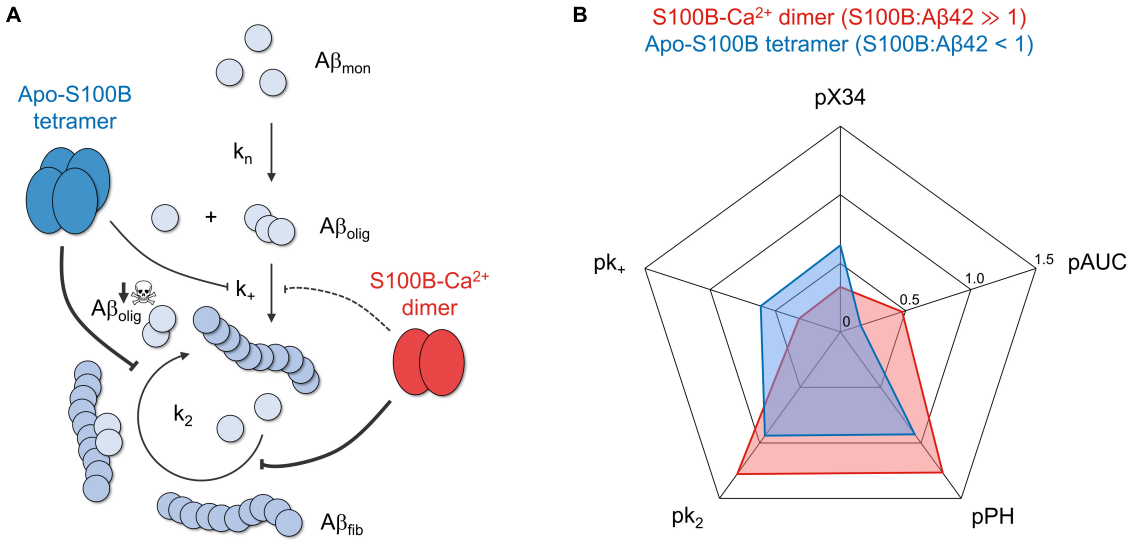

FIGURE 5
The chaperone activity of dimeric and tetrameric S100B suppresses the generation of intermediate oligomers during Aβ42 aggregation. **(A)** S100B dimer and tetramer suppression of Aβ42 oligomerization based on the discreetly distinct inhibition of multiple aggregation micro-steps and the preferential targeting of fibril catalyzed secondary nucleation. **(B)** Radar plot illustrating the complementary effect of dimeric (red) and tetrameric (blue) S100B, under the conditions tested, on the diverse parameters illustrating Aβ42 aggregation and oligomer formation: secondary nucleation and fibril elongation rate constants (k_2 and k_+, respectively), maximum oligomer influx and total number of oligomers (measured, respectively, by peak height, PH, and area under the curve, AUC, of Aβ42 oligomerization distributions) and relative amounts of X-34 positive oligomers. To facilitate data comparison, each parameter was transformed by applying the operator p ($-\log_{10}$), such that a higher inhibition will result in a more eccentric point in the plot.

experimental outcomes reveal that in addition to delay the time required for AβO emergence, an excess of dimeric S100B-Ca^{2+} suppresses the maximum formed amounts of X-34 positive Aβ42 oligomers down to 45%, in a concentration dependent manner (**Figure 4E**). This quantity was reduced to 65% even at the lowest ratio assayed, suggesting that the S100B-Ca^{2+} dimer has an anti-oligomerization effect even at such molar proportions. Correspondingly, the establishment of more mature and structured Aβ42 species that are simultaneously positive for X-34 and ThT also provides evidence for an S100B-induced redirection of Aβ42 aggregation toward elongation events. A similar phenomenon was actually verified in other nucleation suppressor chaperones, whose activity elicited the formation of longer and more ordered Aβ amyloid fibrils, as inferred by bio-imaging techniques (Cohen et al., 2015; Limbocker et al., 2019).

Lastly, we exploited the X-34 detection of Aβ42 oligomers to evaluate the effect of apo-S100B tetramer, at similar sub-stoichiometric conditions (**Figures 4B, D**). ThT-subtracted X-34 kinetic traces indicate that tetrameric S100B drastically inhibit the generation of X-34 positive AβO down to 25%, an effect that is produced even at a apo-S100B tetramer. Aβ42 molar ratio of 0.25 (**Figure 4F**). Indeed, we notice a close overlap between X-34 and ThT kinetics in the presence of tetrameric apo-S100B at molar proportions $\geq$ 0.25, again suggesting a predominance of more structured thioflavin-T positive species throughout Aβ42 fibrillation. We thus conclude that as postulated by a mechanistic-based analysis, Aβ42 binding by tetrameric S100B affords a potent oligomer suppressor effect which occurs at sub-stoichiometric concentrations and in a Ca^{2+} independent fashion.

Conclusion

Whereas a number of molecular and chemical chaperones were described to halt *in vitro* and *in vivo* Aβ42 fibrillation, only a limited set is able to target the specific microscopic mechanisms responsible for the generation of neurotoxic oligomers (Arosio et al., 2016; Mannini and Chiti, 2017). Noteworthy, previous work has shown that anti-oligomerization chaperones provide neuroprotection in Aβ-challenged murine brain models (Cohen et al., 2015; Chen et al., 2020), thus making such proteostasis regulators attractive inspirations for prospective AD therapies. Here we resorted to a combination of mechanistic and kinetic approaches to investigate the hypothesis that the S100B synaptic chaperone could also be able to minimize the formation of Aβ42 oligomers on-pathway to fibril formation.

Our results revealed that dimeric and tetrameric S100B, the latter operating under sub-stoichiometric conditions and in the Ca^{2+} free state, are able to drastically decrease the reactive influx toward oligomers and AβO total amounts—as inferred by reductions in the peak height (PH) and area under curve (AUC) of oligomerization rate distributions, in addition to X-34 positive Aβ42 oligomers (**Figure 5**). We demonstrate that such inhibitory behavior is a consequence of a preferential suppression of fibril catalyzed nucleation (k_2) of Aβ42 monomers into small aggregates (**Figure 5A**), in agreement with previous findings of an interaction between S100B and Aβ fibrils (Cristóvão et al., 2018; Figueira et al., 2022). With respect to fibril elongation, our results showed that although moderately, tetrameric apo-S100B is more competent than the dimer in suppressing the growth of aggregates (**Figure 5B**), a mechanism which constitute the main reactive sink for nucleated

oligomers (Staats et al., 2020). We speculate that this might be relevant *in vivo*, where both S100B multimers co-exist (Ostendorp et al., 2007) and act concertedly to target multiple Aβ42 aggregation microscopic steps responsible for AβO formation and growth.

Altogether, our study sheds new insights on the catalytic landscape of the S100B chaperone, suggesting its critical role in the regulation of protein aggregation and neurotoxic oligomer formation in AD.

Materials and methods

Materials and proteins

All reagents were of the highest grade commercially available. A chelex resin (Bio-Rad, CA, USA) was used to remove contaminant trace metals from all buffers. Recombinant Aβ42 was expressed in *Escherichia coli* [BL21 (DE3) pLysS, Novagen] and purified as described (Walsh et al., 2009). To obtain the monomeric form, about 3 mg of Aβ42 was dissolved in 7 M guanidine hydrochloride (Sigma, MO, USA) and eluted in a Superdex S75 (GE Healthcare, IL, USA) with 50 mM HEPES [4-(2-hydroxyethyl)-1-piperazineethanesulfonic acid, NZYtech, Lisbon, Portugal] pH7.4. Monomeric Aβ42 concentration was estimated by UV spectroscopy (SPECTROstar Nano BMG LabTech, Ortenberg, Germany) at 280 nm using the theoretical extinction coefficient value of $\varepsilon_{280\ nm}$ = 1,424 $M^{-1}cm^{-1}$. Pre-formed fibrils (seeds) were prepared by incubating freshly isolated monomeric Aβ42 diluted in 50 mM HEPES pH7.4 for at least 24 h at 37°C. Fibril concentration was defined as monomer equivalents. Low-binding tubes (Axygen Scientific, Corning, NY, USA) were used in all manipulations of Aβ42. Human dimeric and tetrameric S100B were also expressed in *E. coli* [BL21 (DE3) E. Cline Express, Lucigen] and purified to homogeneity as described (Ostendorp et al., 2005; Botelho et al., 2012). S100B concentrations were estimated as homodimer equivalents using by UV spectroscopy at 280 nm using the theoretical extinction coefficient value of $\varepsilon_{280\ nm}$ = 2,980 $M^{-1}cm^{-1}$. Biochemical characterization and oligomeric state validation of S100B dimer and tetramer preparations was performed by size-exclusion chromatography and electrophoresis analysis as described (**Supplementary Figure 5**; Figueira et al., 2022).

Aggregation kinetics

Aβ42 aggregation kinetics were performed by recording ThT (440 nm excitation filter/480 nm emission filter) or X-34 (370 nm excitation filter/480 nm emission filter) fluorescence intensity as a function of time in a plate reader (FLUOstar Optima, BMG Labtech, Ortenberg, Germany). The fluorescence was measured using bottom optics in half-area 96-well polyethylene glycol-coated black polystyrene plates with a clear bottom (Corning, 3881, NY, USA). The microplates were sealed with foil to avoid evaporation. Monomeric Aβ42 was diluted in 50 mM HEPES pH7.4 supplemented with 1.1 mM $CaCl_2$ (Sigma) or 1.1 mM EDTA (ethylenedinitrilotetraacetic acid, Sigma, MO, USA) and the specified concentrations of dimeric/tetrameric S100B and pre-formed fibrils (seeds). ThT (*Twofold* Aβ42 monomer excess, Sigma, MO, USA) or X-34 (2 μM, Sigma, MO, USA in 100% dimethyl sulfoxide) was added to each condition. Appropriate controls in the absence of Aβ42 were performed to rule out the formation of ThT and X-34 positive species by S100B alone under identical experimental conditions (**Supplementary Figure 6**). All assays were performed in triplicates at 37°C, under quiescent conditions and fluorescence measurements taken every 400 s. Sample-size and descriptive statistical methods (mean ± standard deviation) were determined based on previous studies employing analogous *in vitro* Aβ42 aggregation assays (Cohen et al., 2013, 2015; Cristóvão et al., 2018).

Transmission electron microscopy

For the analysis of structure and morphology of samples at different Aβ42 aggregation time-points, 5 μL aliquots directly removed from the aggregation plate were adsorbed into carbon-coated collodion film supported on 300-mesh copper grids (Electron Microscopy Sciences, PA, USA) and negatively stained twice with 1% (m/v) uranyl acetate (Electron Microscopy Sciences, PA, USA). Grids were visualized with a JEOL (Tokyo, Japan) JEM-1400 transmission electron microscope equipped with an Orious (CA, USA) Sc1000 digital camera, and exhaustively observed.

Mechanistic analysis and simulations

Fitting of aggregation kinetics and rate constant estimation were performed on the AmyloFit (Meisl et al., 2016) online platform. ThT-monitored Aβ42 fibrillation kinetics in the absence or presence of S100B dimer/tetramer were globally fitted to the secondary nucleation dominated model which can by mathematically defined by the following set of differential equations (Eq. 1 and 2), expressing the time evolution of fibril number concentration $[P(t)]$ and fibril mass concentration $[M(t)]$ (Meisl et al., 2016).

$$\frac{dP(t)}{dt} = k_n m(t)^{n_c} + k_2 m(t)^{n_2} M(t) \quad (1)$$

$$\frac{dM(t)}{dt} = 2k_+ m(t) P(t) \quad (2)$$

Where k_n, k_2 and k_+ denote, respectively, the individual rate constants associated with primary nucleation, fibril catalyzed secondary nucleation and fibril elongation, n_c and n_2 the reaction orders for primary and secondary nucleation (for Aβ42, $n_c = n_2 = 2$) (Arosio et al., 2015) and $m(t)$ the monomer concentration. Such equations can be solved in order to obtain the integrated rate law expressing the time progression of fibril mass $[M(t)]$, as in Meisl et al. (2016).

The relative values of k_+ in the absence and presence of S100B were determined from the linear fit of high-seeded (20%) kinetics at initial time-points. Under such conditions, Aβ42 aggregation is completely dominated by the elongation of pre-existing fibrils, exhibiting a pseudo-1st order hyperbolic kinetic whose initial slope is directly proportional to k_+ (Meisl et al., 2014), according to the relation $v_0 = 2k_+ m(0) P(0)$. To constrain the number concentration of employed seeds $[P(0)]$, the same fibril

veil was used in all tested conditions. Aβ42 reactive flux toward oligomers [$r(t)$] were calculated in PLAS (Power Law Analysis and Simulation) (Voit, 2000) using the relative individual rate constants calculated in AmyloFit and taking in account the generation of new aggregates by primary and fibril-catalyzed secondary nucleation (Eq. 3). The total amounts of AβO/nucleation units were evaluated by integrating $r(t)$ in respect to time.

$$r(t) = k_n m\,(t)^{n_c} + k_2 m\,(t)^{n_2}\,M(t) \quad (3)$$

Aβ42 oligomers normalized kinetic profile [$O(t)$] estimated from ThT-monitored aggregation rate constants was also computed in PLAS according to the reaction network and system of ODE (ordinary differential equations) depicted in **Supplementary Figure 3**.

Data availability statement

The original contributions presented in this study are included in the article/**Supplementary material**, further inquiries can be directed to the corresponding author.

Author contributions

CG conceived, designed, and supervised the study, analyzed the data, and wrote the manuscript with AF. AF, JS, and IC designed, conducted, and analyzed the experiments. All authors revised and approved the manuscript.

Funding

This study was funded by the Fundação para a Ciência e Tecnologia (Portugal) through research PTDC/MEDPAT/0959/2021 (to IC), Ph.D. fellowship BD/06393/2021 (to AF), fellowship BID/FCT_Proj2020/i3S/231107 12/2021 (to JS), center grants UID/MULTI/04046/2020 (to BioISI), and Norte-01-0145-FEDER-000008 (to IBMC/I3S). This study was also funded by the European Union (TWIN2PIPSA–Twinning for excellence in biophysics of protein interactions and self-assembly, GA 101079147).

Acknowledgments

We are grateful for funding from LabCollector Scientific Award 2021 (Agilebio, France) (to CG). We thank the support of the i3S Histology and Electron Microscopy Scientific Platform.

Conflict of interest

The authors declare that the research was conducted in the absence of any commercial or financial relationships that could be construed as a potential conflict of interest.

Publisher's note

All claims expressed in this article are solely those of the authors and do not necessarily represent those of their affiliated organizations, or those of the publisher, the editors and the reviewers. Any product that may be evaluated in this article, or claim that may be made by its manufacturer, is not guaranteed or endorsed by the publisher.

Author disclaimer

The views and opinions expressed are, however, those of the author(s) only and do not necessarily reflect those of the European Union or the European Research Executive Agency (REA). Neither the European Union nor the granting authority can be held responsible for them.

Supplementary material

The Supplementary Material for this article can be found online at: https://www.frontiersin.org/articles/10.3389/fnins.2023.1162741/full#supplementary-material

References

Aprile Francesco, A., Sormanni, P., Podpolny, M., Chhangur, S., Needham, L.-M., Ruggeri Francesco, S., et al. (2020). Rational design of a conformation-specific antibody for the quantification of Aβ oligomers. *Proc. Natl. Acad. Sci. U.S.A.* 117, 13509–13518. doi: 10.1073/pnas.1919464117

Arosio, P., Knowles, T. P., and Linse, S. (2015). On the lag phase in amyloid fibril formation. *Phys. Chem. Chem. Phys.* 17, 7606–7618.

Arosio, P., Michaels, T. C., Linse, S., Mansson, C., Emanuelsson, C., Presto, J., et al. (2016). Kinetic analysis reveals the diversity of microscopic mechanisms through which molecular chaperones suppress amyloid formation. *Nat. Commun.* 7:10948. doi: 10.1038/ncomms10948

Barton, J., Arias, D. S., Niyangoda, C., Borjas, G., Le, N., Mohamed, S., et al. (2019). Kinetic transition in amyloid assembly as a screening assay for oligomer-selective dyes. *Biomolecules* 9:539. doi: 10.3390/biom9100539

Benilova, I., Karran, E., and De Strooper, B. (2012). The toxic Aβ oligomer and Alzheimer's disease: An emperor in need of clothes. *Nat. Neurosci.* 15, 349–357. doi: 10.1038/nn.3028

Biancalana, M., and Koide, S. (2010). Molecular mechanism of Thioflavin-T binding to amyloid fibrils. *Biochim. Biophys. Acta* 1804, 1405–1412.

Botelho, H. M., Fritz, G., and Gomes, C. M. (2012). Analysis of S100 oligomers and amyloids. *Methods Mol. Biol.* 849, 373–386.

Chen, G., Andrade-Talavera, Y., Tambaro, S., Leppert, A., Nilsson, H. E., Zhong, X., et al. (2020). Augmentation of Bri2 molecular chaperone activity against amyloid-β reduces neurotoxicity in mouse hippocampus in vitro. *Commun. Biol.* 3:32. doi: 10.1038/s42003-020-0757-z

Chia, S., Habchi, J., Michaels, T. C. T., Cohen, S. I. A., Linse, S., Dobson, C. M., et al. (2018). SAR by kinetics for drug discovery in protein misfolding diseases. *Proc. Natl. Acad. Sci. U.S.A.* 115, 10245–10250. doi: 10.1073/pnas.1807884115

Cline, E. N., Bicca, M. A., Viola, K. L., and Klein, W. L. (2018). The amyloid-beta oligomer hypothesis: Beginning of the third decade. *J. Alzheimers Dis.* 64, S567–S610. doi: 10.3233/JAD-179941

Cohen, S. I., Linse, S., Luheshi, L. M., Hellstrand, E., White, D. A., Rajah, L., et al. (2013). Proliferation of amyloid-beta42 aggregates occurs through a secondary nucleation mechanism. *Proc. Natl. Acad. Sci. U.S.A.* 110, 9758–9763. doi: 10.1073/pnas.1218402110

Cohen, S. I. A., Arosio, P., Presto, J., Kurudenkandy, F. R., Biverstal, H., Dolfe, L., et al. (2015). A molecular chaperone breaks the catalytic cycle that generates toxic Abeta oligomers. *Nat. Struct. Mol. Biol.* 22, 207–213. doi: 10.1038/nsmb.2971

Cristóvão, J. S., Figueira, A. J., Carapeto, A. P., Rodrigues, M. S., Cardoso, I., and Gomes, C. M. (2020). The S100B alarmin is a dual-function chaperone suppressing amyloid-beta oligomerization through combined zinc chelation and inhibition of protein aggregation. *ACS Chem. Neurosci.* 11, 2753–2760. doi: 10.1021/acschemneuro.0c00392

Cristóvão, J. S., Morris, V. K., Cardoso, I., Leal, S. S., Martínez, J., Botelho, H. M., et al. (2018). The neuronal S100B protein is a calcium-tuned suppressor of amyloid-β aggregation. *Sci. Adv.* 4:eaaq1702. doi: 10.1126/sciadv.aaq1702

Cristóvão, J. S., Romão, M. A., Gallardo, R., Schymkowitz, J., Rousseau, F., and Gomes, C. M. (2021). Targeting S100B with peptides encoding intrinsic aggregation-prone sequence segments. *Molecules* 26:440. doi: 10.3390/molecules26020440

Cristóvão, J. S., Santos, R., and Gomes, C. M. (2016). Metals and neuronal metal binding proteins implicated in Alzheimer's disease. *Oxid. Med. Cell. Longev.* 2016:9812178.

Cuello, A. C. (2017). Early and late CNS inflammation in Alzheimer's disease: Two extremes of a continuum? *Trends Pharmacol. Sci.* 38, 956–966. doi: 10.1016/j.tips.2017.07.005

De Felice, F. G., Velasco, P. T., Lambert, M. P., Viola, K., Fernandez, S. J., Ferreira, S. T., et al. (2007). Abeta oligomers induce neuronal oxidative stress through an N-methyl-D-aspartate receptor-dependent mechanism that is blocked by the Alzheimer drug memantine. *J. Biol. Chem.* 282, 11590–11601. doi: 10.1074/jbc.M607483200

Decker, H., Lo, K. Y., Unger, S. M., Ferreira, S. T., and Silverman, M. A. (2010). Amyloid-beta peptide oligomers disrupt axonal transport through an NMDA receptor-dependent mechanism that is mediated by glycogen synthase kinase 3beta in primary cultured hippocampal neurons. *J. Neurosci.* 30, 9166–9171. doi: 10.1523/JNEUROSCI.1074-10.2010

Donato, R., Sorci, G., Riuzzi, F., Arcuri, C., Bianchi, R., Brozzi, F., et al. (2009). S100B's double life: Intracellular regulator and extracellular signal. *Biochim. Biophys. Acta* 1793, 1008–1022. doi: 10.1016/j.bbamcr.2008.11.009

Figueira, A. J., Moreira, G. G., Saavedra, J., Cardoso, I., and Gomes, C. M. (2022). Tetramerization of the S100B chaperone spawns a Ca2+ independent regulatory surface that enhances anti-aggregation activity and client specificity. *J. Mol. Biol.* 434:167791. doi: 10.1016/j.jmb.2022.167791

Forloni, G., and Balducci, C. (2018). Alzheimer's disease, oligomers, and inflammation. *J. Alzheimers Dis.* 62, 1261–1276.

Gade Malmos, K., Blancas-Mejia, L. M., Weber, B., Buchner, J., Ramirez-Alvarado, M., Naiki, H., et al. (2017). ThT 101: A primer on the use of thioflavin T to investigate amyloid formation. *Amyloid* 24, 1–16. doi: 10.1080/13506129.2017.1304905

Hagmeyer, S., Romão, M. A., Cristóvão, J. S., Vilella, A., Zoli, M., Gomes, C. M., et al. (2019). Distribution and relative abundance of S100 proteins in the brain of the APP23 Alzheimer's disease model mice. *Front. Neurosci.* 13:640. doi: 10.3389/fnins.2019.00640

Hardy, J. A., and Higgins, G. A. (1992). Alzheimer's disease: The amyloid cascade hypothesis. *Science* 256, 184–185.

Heneka, M. T., Carson, M. J., El Khoury, J., Landreth, G. E., Brosseron, F., Feinstein, D. L., et al. (2015). Neuroinflammation in Alzheimer's disease. *Lancet Neurol.* 14, 388–405.

Holtzman, D. M., Morris, J. C., and Goate, A. M. (2011). Alzheimer's disease: The challenge of the second century. *Sci. Transl. Med.* 3, 77sr1.

Kato, S., Gondo, T., Hoshii, Y., Takahashi, M., Yamada, M., and Ishihara, T. (1998). Confocal observation of senile plaques in Alzheimer's disease: Senile plaque morphology and relationship between senile plaques and astrocytes. *Pathol. Int.* 48, 332–340. doi: 10.1111/j.1440-1827.1998.tb03915.x

Kayed, R., Head, E., Sarsoza, F., Saing, T., Cotman, C. W., Necula, M., et al. (2007). Fibril specific, conformation dependent antibodies recognize a generic epitope common to amyloid fibrils and fibrillar oligomers that is absent in prefibrillar oligomers. *Mol. Neurodegener.* 2:18. doi: 10.1186/1750-1326-2-18

Klingstedt, T., Aslund, A., Simon, R. A., Johansson, L. B., Mason, J. J., Nystrom, S., et al. (2011). Synthesis of a library of oligothiophenes and their utilization as fluorescent ligands for spectral assignment of protein aggregates. *Org. Biomol. Chem.* 9, 8356–8370. doi: 10.1039/c1ob05637a

Knowles, T. P., Vendruscolo, M., and Dobson, C. M. (2014). The amyloid state and its association with protein misfolding diseases. *Nat. Rev. Mol. Cell Biol.* 15, 384–396.

Lacor, P. N., Buniel, M. C., Furlow, P. W., Sanz Clemente, A., Velasco, P. T., Wood, M., et al. (2007). Aβ oligomer-induced aberrations in synapse composition, shape, and density provide a molecular basis for loss of connectivity in Alzheimer's disease. *J. Neurosci.* 27, 796–807. doi: 10.1523/JNEUROSCI.3501-06.2007

Lazzari, C., Kipanyula, M. J., Agostini, M., Pozzan, T., and Fasolato, C. (2015). Aβ42 oligomers selectively disrupt neuronal calcium release. *Neurobiol. Aging* 36, 877–885. doi: 10.1016/j.neurobiolaging.2014.10.020

Li, C., Zhao, R., Gao, K., Wei, Z., Yin, M. Y., Lau, L. T., et al. (2011). Astrocytes: Implications for neuroinflammatory pathogenesis of Alzheimer's disease. *Curr. Alzheimer Res.* 8, 67–80.

Limbocker, R., Chia, S., Ruggeri, F. S., Perni, M., Cascella, R., Heller, G. T., et al. (2019). Trodusquemine enhances Abeta42 aggregation but suppresses its toxicity by displacing oligomers from cell membranes. *Nat. Commun.* 10:225. doi: 10.1038/s41467-018-07699-5

Linse, S., Scheidt, T., Bernfur, K., Vendruscolo, M., Dobson, C. M., Cohen, S. I. A., et al. (2020). Kinetic fingerprints differentiate the mechanisms of action of anti-Aβ antibodies. *Nat. Struct. Mol. Biol.* 27, 1125–1133. doi: 10.1038/s41594-020-0505-6

Ma, Q. L., Yang, F., Rosario, E. R., Ubeda, O. J., Beech, W., Gant, D. J., et al. (2009). Beta-amyloid oligomers induce phosphorylation of tau and inactivation of insulin receptor substrate via c-Jun N-terminal kinase signaling: Suppression by omega-3 fatty acids and curcumin. *J. Neurosci.* 29, 9078–9089.

Mannini, B., and Chiti, F. (2017). Chaperones as suppressors of protein misfolded oligomer toxicity. *Front. Mol. Neurosci.* 10:98. doi: 10.3389/fnmol.2017.00098

Marshak, D. R., Pesce, S. A., Stanley, L. C., and Griffin, W. S. T. (1992). Increased S100β neurotrophic activity in Alzheimer's disease temporal lobe. *Neurobiol. Aging* 13, 1–7.

Meisl, G., Kirkegaard, J. B., Arosio, P., Michaels, T. C., Vendruscolo, M., Dobson, C. M., et al. (2016). Molecular mechanisms of protein aggregation from global fitting of kinetic models. *Nat. Protoc.* 11, 252–272.

Meisl, G., Yang, X., Hellstrand, E., Frohm, B., Kirkegaard, J. B., Cohen, S. I., et al. (2014). Differences in nucleation behavior underlie the contrasting aggregation kinetics of the Aβ40 and Aβ42 peptides. *Proc. Natl. Acad. Sci. U.S.A.* 111, 9384–9389. doi: 10.1073/pnas.1401564111

Michaels, T. C. T., Saric, A., Curk, S., Bernfur, K., Arosio, P., Meisl, G., et al. (2020). Dynamics of oligomer populations formed during the aggregation of Alzheimer's Abeta42 peptide. *Nat. Chem.* 12, 445–451.

Michaels, T. C. T., Saric, A., Habchi, J., Chia, S., Meisl, G., Vendruscolo, M., et al. (2018). Chemical kinetics for bridging molecular mechanisms and macroscopic measurements of amyloid fibril formation. *Annu. Rev. Phys. Chem.* 69, 273–298. doi: 10.1146/annurev-physchem-050317-021322

Moreira, G. G., Cantrelle, F.-X., Quezada, A., Carvalho, F. S., Cristóvão, J. S., Sengupta, U., et al. (2021). Dynamic interactions and Ca2+-binding modulate the holdase-type chaperone activity of S100B preventing tau aggregation and seeding. *Nat. Commun.* 12:6292. doi: 10.1038/s41467-021-26584-2

Mrak, R. E., and Griffinbc, W. S. (2001). The role of activated astrocytes and of the neurotrophic cytokine S100B in the pathogenesis of Alzheimer's disease. *Neurobiol. Aging* 22, 915–922. doi: 10.1016/s0197-4580(01)00293-7

Nagarajan, S., and Lapidus, L. J. (2017). Fluorescent probe DCVJ shows high sensitivity for characterization of amyloid β-peptide early in the lag phase. *Chembiochem* 18, 2205–2211.

Needham, L.-M., Weber, J., Varela, J. A., Fyfe, J. W. B., Do, D. T., Xu, C. K., et al. (2020). ThX – a next-generation probe for the early detection of amyloid aggregates. *Chem. Sci.* 11, 4578–4583. doi: 10.1039/c9sc04730a

Ostendorp, T., Heizmann, C. W., Kroneck, P. M. H., and Fritz, G. (2005). Purification, crystallization and preliminary X-ray diffraction studies on human Ca2+-binding protein S100B. *Acta Crystallogr. Sect. F Struct. Biol. Cryst. Commun.* 61(Pt 7), 673–675. doi: 10.1107/S1744309105018014

Ostendorp, T., Leclerc, E., Galichet, A., Koch, M., Demling, N., Weigle, B., et al. (2007). Structural and functional insights into RAGE activation by multimeric S100B. *EMBO J.* 26, 3868–3878. doi: 10.1038/sj.emboj.7601805

Poska, H., Leppert, A., Tigro, H., Zhong, X., Kaldmäe, M., Nilsson, H. E., et al. (2020). Recombinant Bri3 BRICHOS domain is a molecular chaperone with effect against amyloid formation and non-fibrillar protein aggregation. *Sci. Rep.* 10:9817. doi: 10.1038/s41598-020-66718-y

Rodrigues, F. E. P., Figueira, A. J., Gomes, C. M., and Machuqueiro, M. (2021). Computational analysis of the interactions between the S100B extracellular chaperone and its amyloid β peptide client. *Int. J. Mol. Sci.* 22:3629. doi: 10.3390/ijms22073629

Rodriguez Camargo, D. C., Sileikis, E., Chia, S., Axell, E., Bernfur, K., Cataldi, R. L., et al. (2021). Proliferation of tau 304–380 fragment aggregates through autocatalytic secondary nucleation. *ACS Chem. Neurosci.* 12, 4406–4415. doi: 10.1021/acschemneuro.1c00454

Schützmann, M. P., Hasecke, F., Bachmann, S., Zielinski, M., Hänsch, S., Schröder, G. F., et al. (2021). Endo-lysosomal Aβ concentration and pH trigger formation of Aβ oligomers that potently induce Tau missorting. *Nat. Commun.* 12:4634. doi: 10.1038/s41467-021-24900-4

Selkoe, D. J., and Hardy, J. (2016). The amyloid hypothesis of Alzheimer's disease at 25 years. *EMBO Mol. Med.* 8, 595–608. doi: 10.15252/emmm.201606210

Staats, R., Michaels, T. C. T., Flagmeier, P., Chia, S., Horne, R. I., Habchi, J., et al. (2020). Screening of small molecules using the inhibition of oligomer formation in α-synuclein aggregation as a selection parameter. *Commun. Chem.* 3:191. doi: 10.1038/s42004-020-00412-y

Tornquist, M., Michaels, T. C. T., Sanagavarapu, K., Yang, X., Meisl, G., Cohen, S. I. A., et al. (2018). Secondary nucleation in amyloid formation. *Chem. Commun.* 54, 8667–8684.

Voit, E. O. (2000). *Computational analysis of biochemical systems: A practical guide for biochemists and molecular biologists*. Cambridge: Cambridge University Press.

Walsh, D. M., Thulin, E., Minogue, A. M., Gustavsson, N., Pang, E., Teplow, D. B., et al. (2009). A facile method for expression and purification of the Alzheimer's disease-associated amyloid beta-peptide. *FEBS J.* 276, 1266–1281. doi: 10.1111/j.1742-4658.2008.06862.x

Wang, X., Wang, W., Li, L., Perry, G., Lee, H.-G., and Zhu, X. (2014). Oxidative stress and mitochondrial dysfunction in Alzheimer's disease. *Biochim. Biophys. Acta* 1842, 1240–1247.

Williams, T. L., Johnson, B. R., Urbanc, B., Jenkins, A. T., Connell, S. D., and Serpell, L. C. (2011). Aβ42 oligomers, but not fibrils, simultaneously bind to and cause damage to ganglioside-containing lipid membranes. *Biochem. J.* 439, 67–77. doi: 10.1042/BJ20110750

frontiers | Frontiers in Neuroscience

TYPE Review
PUBLISHED 22 March 2023
DOI 10.3389/fnins.2023.1132670

OPEN ACCESS

EDITED BY
Jinghui Luo,
Paul Scherrer Institut (PSI), Switzerland

REVIEWED BY
Sean Chia,
Bioprocessing Technology Institute (A*STAR), Singapore
Joongoo Lee,
Pohang University of Science and Technology, Republic of Korea

*CORRESPONDENCE
Louise C. Serpell
✉ L.C.Serpell@sussex.ac.uk

SPECIALTY SECTION
This article was submitted to Neurodegeneration, a section of the journal Frontiers in Neuroscience

RECEIVED 27 December 2022
ACCEPTED 01 March 2023
PUBLISHED 22 March 2023

CITATION
Maina MB, Al-Hilaly YK and Serpell LC (2023) Dityrosine cross-linking and its potential roles in Alzheimer's disease.
Front. Neurosci. 17:1132670.
doi: 10.3389/fnins.2023.1132670

Dityrosine cross-linking and its potential roles in Alzheimer's disease

Mahmoud B. Maina[1,2], Youssra K. Al-Hilaly[1,3] and Louise C. Serpell[1]*

[1]Sussex Neuroscience, School of Life Sciences, University of Sussex, Falmer, United Kingdom, [2]Biomedical Science Research and Training Centre, College of Medical Sciences, Yobe State University, Damaturu, Nigeria, [3]Department of Chemistry, College of Science, Mustansiriyah University, Baghdad, Iraq

Oxidative stress is a significant source of damage that accumulates during aging and contributes to Alzheimer's disease (AD) pathogenesis. Oxidation of proteins can give rise to covalent links between adjacent tyrosines known as dityrosine (DiY) cross-linking, amongst other modifications, and this observation suggests that DiY could serve as a biomarker of accumulated oxidative stress over the lifespan. Many studies have focused on understanding the contribution of DiY to AD pathogenesis and have revealed that DiY crosslinks can be found in both Aβ and tau deposits – the two key proteins involved in the formation of amyloid plaques and tau tangles, respectively. However, there is no consensus yet in the field on the impact of DiY on Aβ and tau function, aggregation, and toxicity. Here we review the current understanding of the role of DiY on Aβ and tau gathered over the last 20 years since the first observation, and discuss the effect of this modification for Aβ and tau aggregation, and its potential as a biomarker for AD.

KEYWORDS

Alzheimer's disease, amyloid-beta, tau, oxidative, dityrosine

Introduction

Dityrosine (DiY) is a covalent cross-link formed by ortho-ortho coupling between two tyrosine residues between carbons in the phenol ring (**Figure 1**). The general mechanism of its formation begins with the generation of a tyrosyl radical generated due to the removal of the hydrogen atom from the hydroxyl group on the phenoxy ring (Atwood et al., 2004; DiMarco and Giulivi, 2007). The two tyrosyl radicals then undergo radical isomerization followed by diradical coupling, and finally enolization resulting in DiY (Correia et al., 2012). The tyrosyl radical also has the capacity to react with another tyrosine to form tri-tyrosine and other high-order structures (Partlow et al., 2016).

Dityrosine was initially recognized by Gross and Sizer (1959) generated by peroxidase oxidation of tyrosine in the presence of H_2O_2. Previous work had established that peroxidase enzymes could catalyze the oxidation of phenols and aromatic amines by hydrogen peroxide (Elliott, 1932). Later, it was revealed that the diphenyl formation mechanism involved free

radical generation as intermediates (Waters, 1952). Based on these observations, Gross and Sizer (1959) suggested that DiY formation was achieved through the generation of tyrosyl radical as an intermediate. Several studies revealed a native role of DiY in natural elastic materials and invertebrate tissues. DiY has been identified within resilin, the rubber-like protein found in arthropods (Andersen, 1964). This was the first documentation of the natural occurrence of this cross-linker in proteins and it was suggested to stabilize resilin through the formation of a stable three-dimensional network (Andersen, 1964). It was subsequently reported that DiY cross-links occur naturally in several elastic and structural proteins, including elastin, fibroin, keratin, cuticlin, and collagen (LaBella et al., 1967; Raven et al., 1971; Fujimoto, 1975; Waykole and Heidemann, 1976). In these proteins, DiY cross-links can contribute to increased mechanical strength and insolubility (Skaff et al., 2005).

Dityrosine has been shown to play a protective or stabilizing role in many proteins (Bailey, 1991; Kanwar and Balasubramanian, 1999). DiY has been found in fungal cell wall proteins (Smail et al., 1995) and in the fertilization envelope of the sea urchin egg where it may regulate the production of a hard fertilization membrane that blocks the entry of additional sperm (Foerder and Shapiro, 1977). In the large roundworm of the pig (*Ascaris suum*) it forms part of the structural components of the cuticle (Fetterer et al., 1993), and is involved in hardening of the mosquito egg chorion (Li et al., 1996). DiY has been suggested to contribute to spores' resistance to lytic enzymes (Briza et al., 1990) and has been suggested to be involved in the biosynthesis of thyroxine and melanin (Bayse et al., 1972). For a detailed review of DiY in natural materials and mammalian tissues, the reader is referred to Partlow et al. (2016).

Oxidative environments can lead to the cross-linking of other amino acids as well as tyrosine and have been suggested to be associated with biological dysfunction. These include cross-links that form between Cys and Tyr, Trp, Lys, Ser, Phe; between Tyr and Gly, His, Trp and between His and His, Arg, Lys, and finally Trp-Trp. The most commonly reported cross-link in proteins is DiY (see Fuentes-Lemus et al., 2021 for extensive review of detailed chemical mechanisms). In this review, we focus on the literature relating to DiY formation in Alzheimer's disease (AD) proteins Amyloid-β and Tau.

Alzheimer's disease, Parkinson's disease (PD), and other neurodegenerative diseases are classified as misfolding diseases reflecting the characteristic amyloid fibril pathology. Each disease is characterized by one or more proteins that form amyloid fibrils and in the case of Alzheimer's disease, Aβ and Tau fibrils accumulate extracellularly and intracellularly, respectively. DiY cross-links in proteins have also been implicated in many diseases, including AD and PD (Souza et al., 2000; Atwood et al., 2004; Al-Hilaly et al., 2013, 2016, 2019), cystic fibrosis (Van Der Vliet et al., 2000), atherosclerosis (Leeuwenburgh et al., 1996), cataracts in the eye lens (Bodaness and Zigler, 1983; Wells-Knecht et al., 1993)„ and acute myocardial infarction (Mayer et al., 2014). For example, DiY can be generated *in vitro* in samples of Aβ (Galeazzi et al., 1999; Atwood et al., 2004; Al-Hilaly et al., 2013; Maina et al., 2020b), α-synuclein (Souza et al., 2000; Al-Hilaly et al., 2016), and Tau (Reynolds et al., 2005; Maina et al., 2021, 2022b). However, there remains more to learn about the specific role played by this modification in these aggregation-prone proteins. Here, we review the studies that have explored the potential roles of DiY on Aβ, and Tau in the pathogenesis of AD.

Amyloid beta

In his 1907 article describing the disease, Alzheimer's post-mortem analysis of Auguste Deter, revealed intracellular neurofibrillary tangles and "minute miliary foci" deposited extracellularly as amyloid plaques (Alzheimer et al., 1995). This finding triggered a strong interest in understanding the biochemistry of these plaques and tangles, leading to the discovery that the plaques are predominantly made up of an amino acid peptide of about 40–42 residues and 4.2 kDa, now called Aβ (Glenner and Wong, 1984). The tangles were shown to be comprised of a hyperphosphorylated form of the microtubule-associated protein tau (Grundke-Iqbal et al., 1986a; Wood et al., 1986). Aβ peptide is synthesized from the processing of a single-pass integral membrane protein called amyloid precursor protein (APP) encoded by a gene located on chromosome 21, which has 18 exons, of which, exon 16 and 17 encode the Aβ peptide (Yoshikai et al., 1990). The processing of APP by β secretase 1 or β-site APP cleaving enzyme 1 (BACE 1) and γ-secretase (comprised of a complex including presenilin 1 and 2) leads to the generation of species of Aβ peptide (**Figure 2**).

The important role played by Aβ in AD pathogenesis led to the amyloid cascade hypothesis (Hardy and Higgins, 1992), based on the observation that early onset, familial forms of AD are associated with mutations in APP or presenilin 1 or 2 and that all appear to be associated with Aβ generation, deposition, or aggregation propensity (Levy et al., 1990; Van Broeckhoven et al., 1990; Chartier-Harlin et al., 1991; Goate et al., 1991; Hardy, 1991). The updated amyloid cascade hypothesis suggests that aggregation of Aβ from monomers to dimers, oligomers, fibrils, and eventually to plaques subsequently drives downstream changes, such as tau phosphorylation, cell loss, and dementia (Selkoe and Hardy, 2016). The amyloid cascade hypothesis has been supported by biomarker studies which show that changes in CSF levels of Aβ and its deposition into plaques appear decades before the onset of dementia (Jack et al., 2013).

Many pieces of evidence have subsequently shown that the oligomeric form of Aβ is the most toxic species, not fibrils, even though a consensus is lacking about the exact structure and composition of these soluble species (Benilova et al., 2012). Accumulated evidence shows that Aβ oligomers disrupt cellular function in cultured cells and animal models (Lambert et al., 1998; Lacor et al., 2007; Reddy and Beal, 2008; Wu et al., 2010; Li et al., 2011; Soura et al., 2012; Zhang et al., 2014; Fuchsberger et al., 2016; Marshall et al., 2016, 2020; Selkoe and Hardy, 2016; Biasetti et al., 2023). In the double-transgenic APP^{swe}-Tau mouse, neuronal loss and activated astrocytes in the entorhinal cortex and the CA1 hippocampal subfield were found to correlate with the burden of Aβ oligomers (DaRocha-Souto et al., 2011). In human AD, soluble Aβ also correlates positively with the severity of dementia (McLean et al., 1999; Walsh and Selkoe, 2007). With the onset of the accumulation of Aβ oligomers, the novel AD mouse model—PS1V97L-Tg expressing the human PS gene with the V97L mutation, show synaptic alteration, tau hyperphosphorylation, and

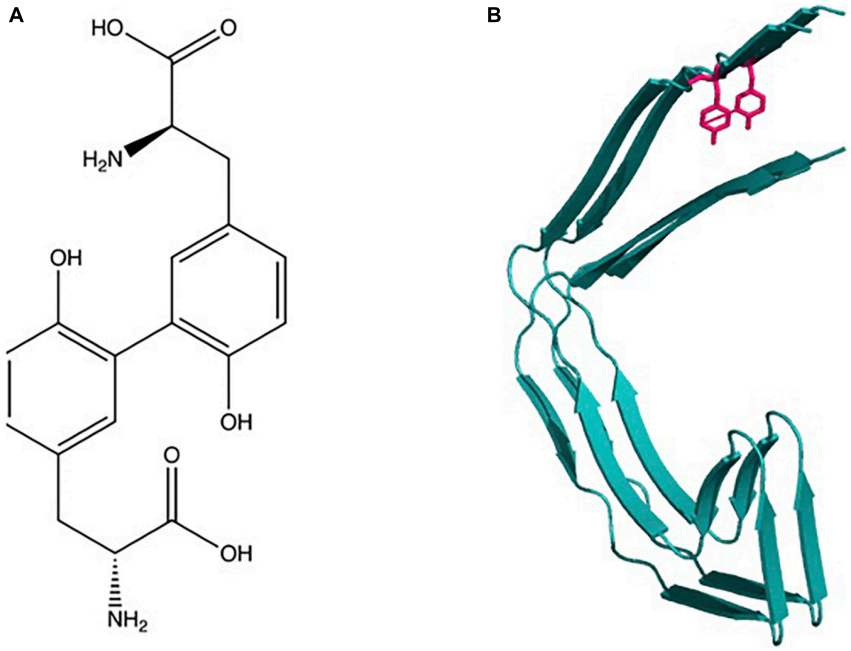

FIGURE 1
Dityrosine: **(A)** Chemical structure and molecular formula of dityrosine produced from two tyrosine amino acids. **(B)** Schematic shows depiction of crosslinking of two β-sheet rich protein molecules.

glial activation, hence supporting an early role for this Aβ species and their role in neurotoxicity (Zhang et al., 2014). Aβ oligomers alone have been shown to impair learning and memory in the pond snail *Lymnaea stagnalis* (Marshall et al., 2016; Ford et al., 2017). Collectively, these studies support the deleterious role of soluble Aβ, rather than fibrils (Zhu et al., 2011; Selkoe and Hardy, 2016). The role of the insoluble fibrils and plaques remains debated but it has been suggested that they may contain around them an equilibrium of both toxic oligomers and inert fibrils which may "spillover" to surrounding tissues to cause neuronal damage, and/or they may mediate toxicity by triggering neuroinflammation (Benilova et al., 2012).

Dityrosine cross-linking in amyloid beta

Amyloid beta is known to become increasingly stable and insoluble as it self-assembles and is deposited in amyloid plaques in brain tissue that are highly protease resistant (Kheterpal et al., 2001). Aβ oligomers and fibrils formed *in vitro* and extracted from tissue show SDS-stability and resistance to proteolytic degradation (Wang et al., 1999; Walsh and Selkoe, 2007; Rambaran and Serpell, 2008; Shankar et al., 2008; Masters and Selkoe, 2012). However, such SDS resistance could arise from a number of different modifications, and/or experimental artifacts (Jomova et al., 2010; Sitkiewicz et al., 2014). The stability of the Aβ assemblies could arise from either the formation of a strong ionic complex or the formation of covalent cross-links, which may include transglutaminase (TGase)-induced cross-linking between the glutamyl side chains and the ε-amino groups of lysine; cross-linking generated by 4-hydroxynonenal (4-HNE) and DiY cross-linking (Siegel et al., 2007; Wilhelmus et al., 2009; Roberts et al., 2012; Al-Hilaly et al., 2013; Sitkiewicz et al., 2014).

Multiple studies suggest that DiY formation through Tyrosine (Y10) of Aβ could provide the observed stability of Aβ. DiY cross-linked Aβ has been found in the AD brain (de la Torre et al., 2018), around Aβ plaques and shown to occur *in vitro* (Al-Hilaly et al., 2013). We have also demonstrated that DiY cross-linked Aβ could be internalized into cells and found around amyloid plaques in the human AD brain, suggesting it may play a role in disease pathogenesis or as a marker of the disease process (Al-Hilaly et al., 2013). To understand the specific contribution of DiY cross-linking on Aβ and its contribution to AD, several studies have studied the influence of this cross-linking on Aβ assembly. *In vitro,* DiY formation has been primarily generated via metal-catalyzed oxidation (MCO), photooxidation, and enzyme-catalyzed mechanisms (Partlow et al., 2016). To induce DiY, copper has been mostly employed for MCO, ultra-violet light (UV) for photooxidation, and peroxidase for enzyme-catalyzed reactions (Yoburn et al., 2003; Atwood et al., 2004; Maina et al., 2020b). Early work from Galeazzi et al. (1999) showed that *in vitro* oxidation using H_2O_2/peroxidase induces DiY cross-linking on Aβ42 and suggested that this would promote Aβ aggregation in AD. This was the first evidence to suggest that DiY formation may play a role in stabilizing Aβ assemblies in AD.

Among the many processes that could lead to the formation of DiY, transition metal catalysis is particularly very relevant in the context of AD (Yoburn et al., 2003; Atwood et al., 2004). About 400 μM copper, 100 μM zinc, and 100 μM iron have been found around amyloid plaques, suggesting increased concentrations of these metals could be implicated in the pathogenesis of AD

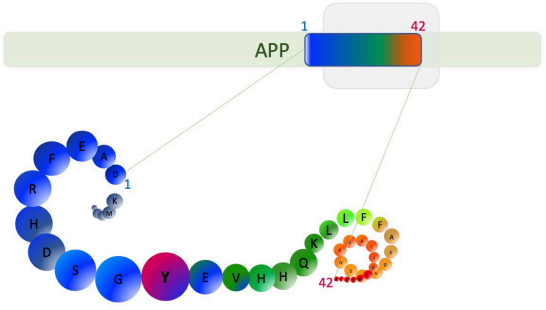

FIGURE 2
Aβ1–42 generation from amyloid precursor protein (APP). β-secretase cleavage beside aspartic acid and cleavage by γ-secretase can generate Aβ1–42 as well as other alternative length Aβ peptides. Amino acids are depicted as circles. Tyrosine (Y10) is able to form dityrosine cross-links and is highlighted in pink.

(Lovell et al., 1998; Suh et al., 2000; Bush, 2003). Many studies have demonstrated that copper Cu^{2+} ions coordinate Aβ via the three histidine residues; His6, His13, His14, and Tyr10 (Curtain et al., 2001; Atwood et al., 2004; Tickler et al., 2005). Coordination of Cu^{2+} ions to Aβ at these residues places Y10 in close proximity to the redox-active copper ion (Sarell et al., 2009; Viles, 2012; Gu et al., 2018). The Y10 has been shown to play a critical role in facilitating Aβ/Cu mediated H_2O_2 production (Barnham et al., 2004). Thus, it has been suggested that copper interactions with Aβ could be responsible for causing DiY cross-linking. This would be facilitated by the presence of H_2O_2 in the milieu which can be produced through Aβ's ability to reduce Cu^{2+} (Yoburn et al., 2003; Atwood et al., 2004; Barnham et al., 2004). Indeed, Barnham et al. (2004) revealed that Aβ peptide coordinates Cu^{2+} to form an Aβ-Cu^{2+} complex, which in turn leads to the production of H_2O_2 catalytically in the presence of a reducing substrate such as ascorbate and through this process, tyrosine radicals are generated that are later coupled and result in Aβ aggregation. Atwood et al. (2004) showed that the incubation of Aβ with Cu^{2+} at a concentration lower than that in amyloid plaques led to the formation DiY cross-links on Aβ and the appearance of SDS-resistance Aβ oligomers, which is a characteristic feature of the neurotoxic Aβ extracted from the AD brain (Walsh and Selkoe, 2007). The authors also revealed that the addition of H_2O_2 to the reaction significantly promoted DiY formation compared to incubation with Cu^{2+} only, indicating that DiY formation becomes more favorable in an increased oxidative environment (Atwood et al., 2004). Smith et al. (2006) also demonstrated that the generation of the Aβ toxic species is modulated by both the Cu^{2+} concentration and the ability to form intermolecular histidine bridges.

There is an extensive literature on the impact of DiY cross-linking on Aβ assembly (Urbanc, 2021). Most of the early studies link DiY formation with Aβ aggregation (Galeazzi et al., 1999; Yoburn et al., 2003; Atwood et al., 2004; Zhang et al., 2017) or serves as a seed that promotes further aggregation (Ono et al., 2009). However, in the early *in vitro* studies in which DiY formation on Aβ was established, the aggregation of Aβ was not followed over time, especially using techniques like Thioflavine T(Th-T) fluorescence assay, to study the typical aggregation kinetics of Aβ. Collectively, recent literature suggests that DiY formation significantly stabilizes Aβ assemblies (Williams et al., 2016; Maina et al., 2020b), slows Aβ aggregation to fibrils (Al-Hilaly et al., 2013; Kok et al., 2013; O'Malley et al., 2014, 2016), or inhibits assembly into fibrils (Gu et al., 2018; Vázquez et al., 2019; Maina et al., 2020b). Some studies have linked DiY cross-linked Aβ with toxicity (Barnham et al., 2004; O'Malley et al., 2014; Williams et al., 2016) and others have shown that DiY inhibits self-assembly, and as a result, reduces or prevents Aβ toxicity (Maina et al., 2020b). To fully understand the exact roles of DiY on Aβ, it is thus important to consider the preparation method, buffer and temperature conditions, and Aβ sequence carefully since environmental conditions will have a significant effect on the eventual structures and the formation of any intermediate species (**Table 1**).

Based on these studies (**Table 1**), it is difficult to compare the levels of DiY produced by the different conditions reported in the literature. This may partly be responsible for the difference in the outcome of DiY cross-linking from the different studies. It is also likely that the dosage of DiY formed per condition would be critical for the assembly of Aβ. This may explain why in some studies, the DiY cross-linked Aβ assembled to fibrils, albeit in a significantly slower fashion (Kok et al., 2013; O'Malley et al., 2014). While in other studies, DiY cross-linking completely inhibited the formation of such higher assemblies (Gu et al., 2018; Maina et al., 2020b).

Moreover, the cross-linking timing may be another factor that would impact the assembly of Aβ. Indeed, it was suggested that DiY cross-linking inhibits primary nucleation and subsequently retards fibril elongation and fibril–fibril interactions (O'Malley et al., 2014). We also showed that DiY cross-linking before the onset of aggregation leads to the rapid self-association of the random-coil rich monomeric assemblies of Aβ into stable amorphous-like structures that never assemble into amyloid fibrils (Maina et al., 2020b). Cross-linking after the onset of aggregation also significantly inhibited Aβ elongations into fibrils and stabilized the intermediate Aβ species (Maina et al., 2020b). Based on our work, it appears like the self-association of Aβ assemblies caused by the DiY cross-linking depletes the pool of available monomers that are needed for the primary and secondary nucleation.

The available data in the literature is yet to clearly define whether DiY cross-linking on Aβ leads to a deleterious effect. This is specifically reflected in the data on toxicity experiments with DiY cross-linked Aβ (**Table 1**). Some of the studies that suggested that DiY cross-linked Aβ42 dimers and oligomers were toxic did not fully characterize the self-assembly property of the Aβ (Barnham et al., 2004; Davis et al., 2011). Other studies have shown that dimers, trimers, and tetramers stabilized by Aβ oxidation using photo-induced cross-linking of unmodified proteins (PICUP) are toxic to cultured cells (Ono et al., 2009; Jana et al., 2016; Cline et al., 2019). Work from the Walsh group suggested that the toxicity of the DiY cross-linked assemblies was not due to the dimers but the higher assemblies formed by the dimers (O'Malley et al., 2014). Our recent series of work has made a strong case for self-assembly process as a critical driver of Aβ toxicity (Marshall et al., 2016, 2020; Vadukul et al., 2017, 2020; Maina et al., 2020b). The DiY cross-linked dimers reported by O'Malley et al. (2014, 2016) retained their self-assembly properties, albeit at a slow rate. These DiY cross-linked dimers were reported to self-associate to form larger structures and generate aggregates that potently block LTP (O'Malley et al., 2014). In another study, it was shown that

TABLE 1 Different oxidation conditions used in producing dityrosine in Aβ .

Aβ form and concentration	Method of DiY cross-linking	Results of oxidation	References
Aβ42 (25 μM)	Aβ in PBS pH 7 mixed with horseradish peroxidase (HRP) (30 μM)/0.3% H_2O_2 at 37°C for 6 h	Formation of Aβ42 dimers. DiY cross-linked Aβ42 remained soluble. Aggregation not reported	Galeazzi et al., 1999
Freshly prepared Aβ40 (100 μM) Fibrillar Aβ40 (100 μM) obtained after 4.5 days stirring of freshly prepared Aβ at RT	1. Aβ in PBS pH 7.4 mixed with $CuSO_4$ (6.25 μg)/H_2O_2 (0.28 μl of a 30% stock solution) at 37°C for 2 h 2. Aβ in PBS pH 7.4 mixed with $CuCl_2$ (38 μg)/ascorbic acid (240 μg) at RT for 2 h 3. Aβ in water irradiated with UV bulb in a glass tube for 24 h 4. Aβ in $Na_2B_4O_7$ pH 9 mixed with HRP (12.5 μg)/H_2O_2 (1.5 μl of a 1% stock solution) at 37°C for 2 h	Formation of high molecular weight DiY cross-linked assemblies DiY formed in higher quantity in fibrils than in soluble species $CuSO_4$-H_2O_2 and HRP- H_2O_2 systems more efficient in inducing DiY	Yoburn et al., 2003
Aβ28 (10 μM), Aβ40 (5 μM), and Aβ42 (5 μM)	Aβ in PBS pH 7.4 mixed with $CuCl_2$ (25 μM)/H_2O_2 (250 μM) for 0–3 days at 37°C	DiY cross-linked Aβ peptides aggregated to dimers and oligomers. The level of DiY cross-linking increased when $CuCl_2$ was mixed with H_2O_2. DiY cross-linked Aβ were SDS-resistant	Atwood et al., 2004
Aβ42 (10 μM)	Aβ in PBS pH 7.4 mixed with $CuCl_2$ (25 μM)/H2O2 (250 μM) with stirring for 22 h at 37°C	Formation of toxic DiY cross-linked dimers and oligomers. Non-toxic dimers and oligomers also formed on Aβ42 with Y to A substitution	Barnham et al., 2004
Aβ28 (3 μM)	Aβ in ammonium acetate buffer pH 7.4 mixed with CuCl (31 μM) or $CuCl_2$ (31 μM)/H_2O_2 (30 μM) with or without methionine for 24 h at 37°C	Methionine oxidation promotes Y10 oxidation	Ali et al., 2005
Aβ40 (0.4 mg/ml), Aβ28 (0.2 mg/ml)	Aβ in acetate buffer pH 7.4 mixed with Horseradish peroxidase (0.4 mg/ml)/H_2O_2 (30 μM) for 6 h at 37°C	Formation of DiY cross-linked dimers and oligomers	Ali et al., 2006
Aβ42 (10 μM)	Aβ in PBS pH 7.4 mixed with $CuCl_2$ (10 μM)/H_2O_2 (250 μM) with stirring at 200 RPM for 2 or 24 h at 37°C	Aβ42–copper complex formed via a histidine-bridged dimer and DiY cross-linking of Aβ42 show toxicity to cells	Smith et al., 2006
Aβ42 (10 μM)	Aβ in Sodium Phosphate buffer pH 7.4 mixed with $CuCl_2$ (10–100 μM)/H_2O_2 (250 μM) with stirring at 200 RPM for 24 h at 37°C	High copper-Aβ42 ratio results in a higher level of DiY cross-links and the formation of non-amyloidogenic aggregates. DiY cross-linking forms after the onset of aggregation, not before	Smith et al., 2007b
Aβ42 (5 μM)	Aβ in PBS pH 7.4 mixed with $CuCl_2$ (25 μM)/H_2O_2 (250 μM) for 5 days	DiY cross-linked Aβ significantly induce cofilin-actin rods in dissociated neuronal culture	Davis et al., 2011
Aβ40 (no concentration given)	Chemical synthesis of DiY-linked Aβ dimers	Cross-linked Aβ showed significantly reduced aggregation kinetics, leading to the formation of long-lived, soluble oligomeric aggregates that reduce cell viability in neuroblastoma cells	Kok et al., 2013
Aβ42 (20 μM)	Aβ in PBS pH 7.4 mixed with $CuCl_2$ (20 μM)/H_2O_2 (0.5 mM) for 3 days at 37°C with agitation	Cross-linking stabilize Aβ42 assemblies but also appears to slow assembly. Externally administered Aβ42 become oxidized and cross-linked during incubation in neuroblastoma cells, and can be internalized into lysosomes. DiY cross-linked Aβ fibrils are resistant to formic acid digestion	Al-Hilaly et al., 2013
Aβ40 (40 μM)	Aβ40 in ammonium bicarbonate buffer pH 8.5 mixed with horseradish peroxidase (2.2 μM)/H_2O_2 (250 μM) overnight at 37°C. Toxicity experiments in SEC isolated Aβ in phosphate buffer pH 8	DiY cross-linked Aβ40 does not aggregate even at 96 h, unless agitated. When agitated, its aggregation rate is ∼15-fold lower than that of non-crosslinked Aβ40. Aggregated DiY cross-linked Aβ40, not monomer/dimer precursors, inhibit LTP similar to aggregated Aβ40. 25 mM ammonium bicarbonate buffer at pH 8.0 and low temperature (4 C) reduces the aggregation of DiY cross-linked and uncross-linked peptides	O'Malley et al., 2014
Aβ40 (30 μM)	Horseradish peroxidase (45 μg/ml)/H_2O_2 (20 μM) for 20–30 min	DiY cross-linking stabilize compact dimeric and trimeric Aβ species thus leading to a decrease in the population of more extended species	Sitkiewicz et al., 2014

(Continued)

TABLE 1 (Continued)

Aβ form and concentration	Method of DiY cross-linking	Results of oxidation	References
Aβ42 (40 μM)	Aβ in ammonium bicarbonate buffer, pH 8.5 mixed with Horseradish peroxidase (2.2 μM)/H_2O_2 (250 μM) for 14 h at 37°C	DiY cross-linking slows aggregation lag phase and growth phase and forms smaller soluble aggregates than non-oxidized Aβ42	O'Malley et al., 2016
Aβ42 (20 μM), Aβ40 (20 μM)	1. For copper and h202 induced crosslinking of unmodified pro teins (CHICUP), Aβ in phosphate buffer pH 7 mixed with $CuCl_2$ (20 μM)/H_2O_2 (0.5 mM) for 10 min at 37°C with agitation 2. For PICUP, Aβ in phosphate buffer pH 7 mixed with 1 mM $[Ru(bpy)_3]^{2+}$ and 20 mM ammonium persulfate (APS) in sodium phosphate buffer pH 7.4, then irradiated using a XGY-II (B) cold halogen light source for 1 s at a distance of 10 cm	DiY cross-linking with lower Cu^{2+}/H_2O_2 concentrations leads to efficient dimer/oligomer formation and cross-linking with higher Cu^{2+}/H_2O_2 concentrations result in a decrease in Aβ oligomers Both CHICUP and PICUP DiY cross-linking appear to stabilize Aβ40 and Aβ42 early assemblies (oligomers) and inhibits their conversion into fibrils. The DiY cross-linked peptide disrupts membrane integrity	Williams et al., 2016
Aβ40 (10 μM)	1. Aβ mixed with $CuCl_2$ (5 μM)/H_2O_2 (50 μM–1.6 mM) in a solution with 100 μM HEPES buffer and 160 mM NaCl for 0–400 h 2. $CuCl_2$ (5 μM)/Ascorbate (50–500 μM) in a solution with 100 μM HEPES buffer and 160 mM NaCl for 0–400 h	DiY cross-linking inhibits assembly and causes fiber fragmentation. Inhibition of assembly is more pronounced in a highly oxidative reaction	Gu et al., 2018
Aβ40 (30 and 50 μM)	1. 30 μM Aβ in HEPES pH 7.4 mixed with 30 μM $CuCl_2$, 30 μM and 600 μM H_2O_2 at 37°C 2. 50 μM Aβ n HEPES pH 7.4 mixed with 50 μM $CuCl_2$, and 1 mM H_2O_2 at 37°C with agitation a 700 RPM	DiY cross-linking completely inhibited aggregation revealed by Th-T assay	Vázquez et al., 2019
Aβ42, variant Aβ42 (vAβ42) (50 μM)	1. Aβ or vAβ in phosphate buffer pH 7.4 mixed with 400 μM $CuCl_2$ or 400 μM $CuCl_2$ and 2.5 mM H_2O_2 at 37°C 2. Aβ or v Aβ in phosphate buffer pH 7.4 irradiated with ultra-violet-C (UV-C) in the dark with samples kept on ice	DiY cross-linking with $CuCl_2$ or UV-C led to Aβ or vAβ stabilization at the time of oxidation. For example, oxidation on oligomers led to oligomer stabilization Seeding experiments revealed that oxidized Aβ are unable to seed further assembly DiY-stabilized Aβ assemblies lost the ability to cause toxicity to neuroblastoma cells	Maina et al., 2020b

toxic DiY cross-linked Aβ assemblies retain their self-assembling property, but at a significantly reduced speed that results in the formation of long-lived, soluble oligomeric aggregates (Kok et al., 2013). This has led to the assumption that DiY cross-linking may stabilize toxic oligomers and prolong their toxicity (Kok et al., 2013; O'Malley et al., 2016; Williams et al., 2016). However, our recent work revealed that DiY cross-linking trapping of Aβ oligomers, a mixture of oligomers and protofibrils and fibrils in a non-assembling conformation renders these assemblies non-toxic to differentiated neuroblastoma cells (Maina et al., 2020b). While non-oxidized Aβ was more toxic during its self-assembling (oligomeric) state compared to when the assembly plateaus (Maina et al., 2020b). We have previously designed a variant form of Aβ that lacks the propensity to aggregate due to F19S and G37D substitutions in Aβ42 (Marshall et al., 2016). Interestingly, the DiY cross-linked non-assembling variant Aβ showed no toxicity to cells (Maina et al., 2020b). Our work suggested that the self-assembly process, not individual Aβ assemblies or DiY cross-linking was responsible for the Aβ toxicity. If DiY Aβ is genuinely toxic, then it may depend on the DiY dose. However, none of the previous studies that evaluated DiY Aβ toxicity except (Maina et al., 2020b) quantified the level of DiY formed on Aβ. As a result, discrepancies may also arise from the differences in the amount of Aβ DiY cross-links used in toxicity assays.

At this stage, it is difficult to conclude the exact role of DiY cross-linking on Aβ aggregation or toxicity in a physiological environment and clearly more studies are needed. This raises the need for maintaining a closely similar method of preparations for Aβ experiments, as the method of peptide preparation, peptide concentration, time and aggregation, and model system used may play a huge role in determining the role of DiY on Aβ toxicity (Cecchi et al., 2008; Krishtal et al., 2015; Jana et al., 2016; Kaniyappan et al., 2017).

On the other hand, DiY cross-linking on existing fibrils might stabilize and help to maintain insoluble Aβ species found in plaques in the AD brain (Wang et al., 1999; Rambaran and Serpell, 2008; Masters and Selkoe, 2012). We have shown previously that DiY antibody colocalizes with Aβ fibrils in human AD plaques (Al-Hilaly et al., 2013). Overall, more work is needed to fully understand the role of DiY on Aβ species *in vitro* and *in vivo*. However, it is also worth noting that many modifications may occur on Aβ e.g., oxidation of histidine, lysine, and methionine35 of Aβ (Palmblad et al., 2002; Kowalik-Jankowska et al., 2004; Ali et al., 2005), which may also affect the Aβ differently (Smith et al., 2007a).

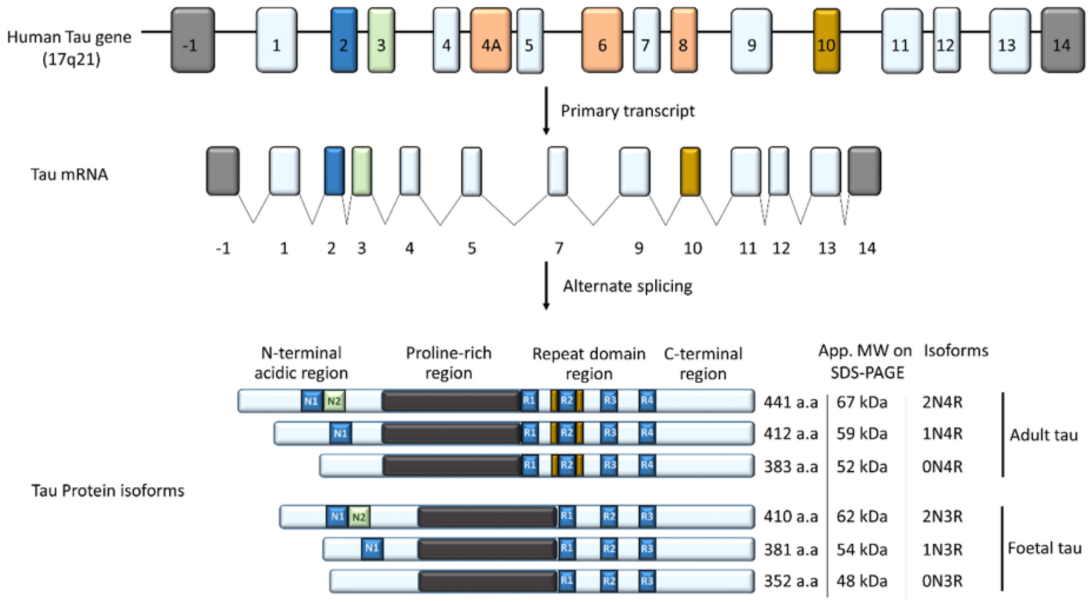

FIGURE 3
The tau gene has 16 exons; exon 1, 4, 5, 7, 9, 11, 12, and 13 (light blue) are constitutively transcribed in the CNS (Martin et al., 2011). Exon 4A, 6, and 8 (orange) are rarely expressed in the brain but included in mRNA of most peripheral tissues, while exon 14 forms part of the 3′ untranslated region of the tau mRNA (Andreadis, 2005; Connell et al., 2005). Alternate splicing of exon 2 (blue), 3 (Green), and 10 (Yellow) in the CNS generates the widely known six isoforms of tau; 352–441 amino acids in length and 48–67 kDa on SDS-PAGE (Martin et al., 2011). Depending on the inclusion and/or exclusion of exon 2, 3, and 10, tau has zero, one or two (0/1/2) N-terminal inserts and three or four (3R/4R) microtubule binding repeats, leading to the six isoforms of tau in the CNS. Structurally, tau is subdivided into an N-terminal acidic region; proline-rich region/domain (PRD), repeat domain region, and a C-terminal region.

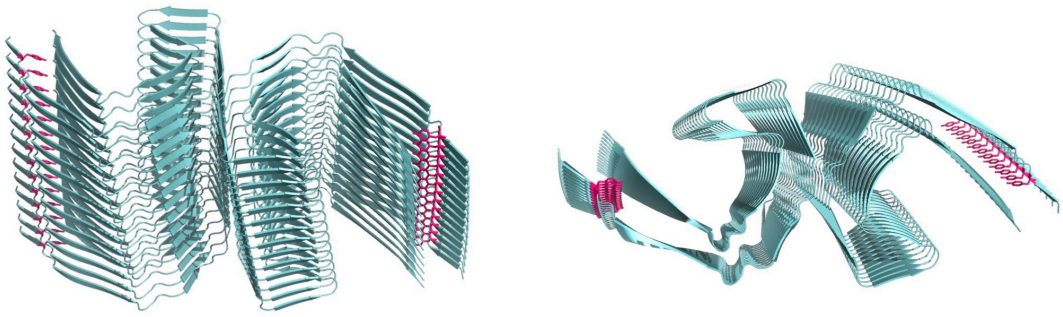

FIGURE 4
Cryo-electron microscopy structure of paired helical filaments (Fitzpatrick et al., 2017) 5O3L.ENT showing position of tyrosine10 in magenta. Left side view, right panel top view.

Ultimately, studies that define these different modifications and specifically isolate the contribution of DiY would provide the much-needed data to support the interpretation of the studies generated thus far in the literature.

Tau protein

Tau is a small molecular weight protein with the capacity to promote microtubule assembly *in vitro* (Weingarten et al., 1975). It is found in both neuronal and non-neuronal eukaryotic cells, but predominantly in neurons (Loomis et al., 1990; Stoothoff and Johnson, 2005; Rossi et al., 2008; Martin et al., 2011). Tau is well-known for its role in stabilizing the microtubules through their nucleation and elongation (Cleveland et al., 1977). However, recent evidence suggest that tau is a multifunctional protein, playing a role in many cellular compartments, including the synapse and nucleus (Buée et al., 2000; Dixit et al., 2008; Ittner et al., 2010; Martin et al., 2011; Bukar Maina et al., 2016; Maina et al., 2018a,b). Tau is a product of the microtubule-associated protein gene, located on chromosome 17q21.1 (Neve et al., 1986; Andreadis et al., 1992; Andreadis, 2005; **Figure 3**). A complex post-transcriptional processing of the tau transcript results in a less abundant 2kb tau transcript which encodes for a tau mainly targeted to the nucleus (Wang et al., 1993); 6kb transcript which tau predominantly directed to the soma/axons in the central nervous system (CNS) (Andreadis, 2005; Liu and Götz, 2013); and 8/9 kb transcript producing a tau preferentially expressed

in the retina and peripheral nervous system (PNS) and with an apparent molecular weight of about 110–120 kDa, often called high molecular weight tau (Georgieff et al., 1993; Nunez and Fischer, 1997).

The alternate splicing of exon 2, 3, and 10 of the Tau gene generates the six major isoforms of tau in the CNS with three (3R) or four (4R) microtubule-binding repeats on its C-terminal (3R) (**Figure 3**; Buée et al., 2000; Martin et al., 2011). Structurally, tau is subdivided into four regions; an N-terminal acidic region, a proline-rich domain (PRD), microtubule-binding repeat domain region (MBD), and a C-terminal region, and the epitopes across these areas vary depending on the tau isoform (Buée et al., 2000; Martin et al., 2011; **Figure 3**).

Physiologically, Tau is a monomeric protein that exists in solution in a random-coil conformation (Schweers et al., 1994). Thus, its aggregation is believed to be a sign of pathology thought to be driven by changes in its conformational state, moving from a random coil to the amyloid cross-β structure (von Bergen et al., 2005). This pathological folding of Tau is evident in a group of diseases collectively called tauopathies, which include AD, Pick's disease, Huntington's disease, and Fronto-Temporal Dementia with Parkinsonism linked to Chromosome 17 with MAPT mutations (FTDP-17T) (Oakley et al., 2020). For example, in AD, tau misfolds into paired helical filaments (PHFs) and straight filaments (SFs) and these filaments accumulate in the cell bodies of neurons as neurofibrillary tangles (NFT) (Grundke-Iqbal et al., 1986b; Wischik et al., 1988b). NFT burden correlates with the extent of AD pathology (Arriagada et al., 1992) and provides a reliable staging of the disease process (Braak and Braak, 1991). The precise mechanism involved in tau filament formation is still not fully understood. However, it involves the aggregation of Tau monomers to dimers, oligomers, some of which convert to fibrils, and eventually to PHFs and SFs (Cowan and Mudher, 2013). Many post-translational modifications have been proposed as key molecular events in the abnormal tau aggregation leading to the formation of PHFs. Tau can undergo glycosylation, glycation, prolyl-isomerization, polyamination, nitration, oxidation, ubiquitination, sumoylation phosphorylation (Martin et al., 2011; Guo et al., 2017), and truncation (Wischik et al., 1988b; Wang et al., 2007).

Dityrosine cross-linking on Tau

Interest in understanding Tau physiology and pathology has resulted in the development of many *in vitro* models over the past decades. These models include the full-length Tau (T40, 2N4R), dGAE (Wischik et al., 1988b), K18, and K19 (Mukrasch et al., 2005; Oakley et al., 2020). The T40 tau which has 441 amino acid residues contains five tyrosine residues, located at positions 18, 29, 197, 310, and 394. However, the model peptides, dGAE, K18, and K19 contain only the tyrosine residue at position 310. Y310 is part of the aggregation prone hexapeptide ^{306}VQIVYK^{311} which is thought to be important for Tau assembly *in vitro* (von Bergen et al., 2000; Ganguly et al., 2015). Unlike Aβ, there is a significant lack of research on the role of DiY formation on tau and its contribution to tau pathology. This raises the question as to whether the conclusions drawn from research using Aβ also apply to Tau. Few of the early studies in this area were from the Binder's laboratory on T40 tau, which represents the full-length tau carrying five tyrosine residues. Specifically, this showed that peroxynitrite oxidation results in the oligomerization of soluble T40 tau via the cross-linking of the tyrosine residues independent of disulfide bonds (Reynolds et al., 2005). However, it was not clear whether DiY formed on tau filaments and the consequence on its aggregation or stability. Tau filaments are usually induced *in vitro* with the help of heparin, arachidonic acid, or other polyanionic molecules (Goedert et al., 1996; Kampers et al., 1996; Pérez et al., 1996; Wilson and Binder, 1997; Friedhoff et al., 1998). Thus, the same group further showed that oxidative stress induced by peroxynitrite on arachidonic acid-induced filaments of T40 tau results in the formation of DiY on the tau filaments. Their work showed that the DiY cross-linking is associated with the stabilization of the pre-formed tau filaments (Reynolds et al., 2006). Although these studies provided the initial evidence that DiY forms in tau, it remained unclear how DiY cross-linking influences tau oligomer formation and aggregation into filaments and NFTs, especially in the absence of additives.

We recently established a truncated tau fragment corresponding to residues Ile297–Glu391, called dGAE, as an excellent model of studying tau assembly *in vitro* (Al-Hilaly et al., 2017, 2020). This tau fragment was first isolated from the proteolytically stable core of paired-helical filaments (PHFs) (Wischik et al., 1988b) and more recently was found to overlap with the region identified in the PHF and SF core by cryogenic electron microscopy (CryoEM) (Fitzpatrick et al., 2017; **Figure 4**). Our work showed that without the addition of exogenous additives dGAE can self-assemble to form filaments *in vitro* that structurally resemble PHF (Al-Hilaly et al., 2017, 2020; Lutter et al., 2022) and more recently, CryoEM structure determination showed the capacity for tau297–391 to form a filament structure identical to those derived from AD brain (Lövestam et al., 2022). Recently, we used MCO and UV oxidation to induce DiY cross-linking in dGAE, showing that oxidation facilitates the assembly of soluble dGAE into T22 antibody-positive tau oligomers which do not elongate into fibrils (Maina et al., 2020a). Different preparations of tau oligomers produced *in vitro* have been described to possess a β-sheet conformation and to induce toxicity in culture (Chen et al., 2009; Lasagna-Reeves et al., 2010; Flach et al., 2012; Tian et al., 2013). Interestingly, we found that the DiY cross-linked tau oligomers formed by dGAE lacked β-sheet structure, instead remained in a random-coil conformation, and were not acutely toxic to differentiated neuroblastoma cells after 3 days of culture (Maina et al., 2020a). This supports the work from the Binder's group on T40 tau (Reynolds et al., 2005), in showing that DiY cross-linking promotes the formation of tau oligomers. Our work specifically suggests that the oligomers are incapable of further elongation into fibrils and are non-toxic.

Furthermore, we showed that dGAE fibrils formed DiY to a lower extent than the oligomers and other smaller assemblies (Maina et al., 2022a). The reduced ability for these fibrils to form DiY could be due to the reduced accessibility to the tyrosine residue in dGAE (Y310) in the fibrils, unlike in prefibrillar assemblies. Y310 is buried in one of the eight β-sheets of the tau molecule that run along the length of the protofilament, adopting a C-shaped architecture in AD and other tauopathies (Shi et al., 2021; Lövestam et al., 2022; **Figure 4**). Given the DiY's ability to enhance protein

stability, DiY cross-linked oligomers and fibrils would be expected to have enhanced stability and increased insolubility, similar to tau assemblies extracted from AD brain that show increased insolubility and resistance to proteolytic degradation (Wischik et al., 1988a,b). PHFs are specifically highly insoluble in SDS and sarcosyl (Kondo et al., 1988; Greenberg and Davies, 1990; Lee et al., 1991; Miao et al., 2019). Previous work from the Binder's group showed that DiY cross-linked full length tau fibrils have increased SDS stability (Reynolds et al., 2006). We also recently showed that DiY cross-linked dGAE oligomers and especially fibrils, display a significantly reduced SDS and heat solubility (Maina et al., 2022a). The fibrils are particularly difficult to resuspend in solution, are heat and SDS-insoluble and transmission electron microscopy show that they maintain strong lateral association (Maina et al., 2022a). These studies suggest that indeed, DiY could promote the stabilization of tau assemblies *in vivo*. This begs the question as to whether DiY forms on tau assemblies *in vivo*? It is known that exposure to reactive oxygen species (ROS), aging, nitrogen dioxide, and lipid hydroperoxides can result in DiY formation (Giulivi and Davies, 1993, 1994; Kato et al., 1994). Oxidative stress is believed to accumulate early on in AD, increasing with the disease pathology (Nunomura et al., 2001; Butterfield and Halliwell, 2019). Thus, such oxidative environment that occurs *in vivo* in AD would favor DiY formation. Indeed, we recently showed that tau oligomers and fibrils extracted from the AD brain are DiY cross-linked (Maina et al., 2022a). However, whether DiY cross-linked tau oligomers also fail to elongate to fibrils *in vivo* is a question of future research. Nonetheless, available data suggests that the DiY cross-linking will promote the characteristic insoluble feature of AD fibrils. There is a significant lack of research on the role of DiY on tau and its implications. More research is needed to fully understand its relevance to AD.

Could dityrosine cross-linking serve as a biomarker in Alzheimer's disease?

The chemical stability of DiY could serve as a suitable biomarker for oxidative stress. DiY remains unchanged by exposure to oxygen and low or high pH (DiMarco and Giulivi, 2007). Furthermore, it is highly resistant to acid hydrolysis and proteases (Amado et al., 1984; Giulivi and Davies, 1994). DiY is also not incorporated into *de novo* synthesis of proteins (Eiserich et al., 1999), indicating that the level of DiY will reflect the oxidative damage to endogenous proteins (DiMarco and Giulivi, 2007). In this regard, there has been a strong interest since the 1990s on the possibility of using DiY as a marker of oxidative stress in different diseases. In 1993, DiY was considered an index of organismal oxidative stress (Giulivi and Davies, 1993). In this work, DiY production was shown in red blood cells challenged with the continuous flux of hydrogen peroxide. In the same year, Heinecke et al. (1993a) also showed that DiY could be formed via myeloperoxidase–hydrogen peroxide reaction in human neutrophils and macrophages. For this reason, they suggested that DiY could serve as a suitable marker of radical damage in phagocyte-rich inflammatory lesions *in vivo* (Heinecke et al., 1993b).

In the context of aging, it was found that DiY cross-linked proteins of mouse cardiac and skeletal muscle increased with age (Leeuwenburgh et al., 1997). Leeuwenburgh et al. (1999b) similarly showed that an increase in DiY could be detected through urine assays in aging rats. Such an increase was mirrored by a similar rise in rat skeletal muscle (Leeuwenburgh et al., 1999b). The authors suggested that urine assays of DiY could be used as a non-invasive method of estimating oxidative stress *in vivo* (Leeuwenburgh et al., 1999a,b). Kato et al. (1998) used immunohistochemistry in the human brain tissue to reveal the presence of DiY in lipofuscin pigments from aged human brains. Their work showed a significant elevation of DiY cross-links with age, suggesting a role for it in aging and lipofuscin accumulation (Kato et al., 1998). High levels of DiY was seen in lipofuscin pigments in AD human brains (Al-Hilaly et al., 2019).

In the context of neurodegenerative diseases, increased levels of DiY has been shown in the PD mouse model of 1-methyl-4-phenyl-1,2,3,6-tetrahydropyridine (MPTP) injection (Pennathur et al., 1999). In this model, DiY and nitrotyrosine were specifically increased in the striatum and midbrain, but not in brain regions resistant to MPTP. The authors suggested that oxidative species, including hydroxyl radicals, tyrosyl radicals or peroxynitrite might mediate the damage caused by MPTP to dopaminergic neurons (Pennathur et al., 1999). Similarly, Hensley et al. (1998) measured DiY and nitrotyrosine level in the AD brain regions compared to controls. They revealed that DiY and nitrotyrosine are significantly increased in the hippocampus and neocortical regions of the AD brain and ventricular cerebrospinal fluid compared to levels in controls (Hensley et al., 1998). Their work provided evidence of the suitability of DiY as a biomarker for AD although the sensitivity and reproducibility of the method they utilized—HPLC with electrochemical array detection (HPLC-ECD), has been questioned by others (Duncan, 2003). However, another report using HPLC with fluorescence detection in 63 confirmed AD patient plasma samples revealed that DiY levels were significantly increased compared to controls (Polidori et al., 2004). A similar increase, albeit not significant compared to controls, was observed in the plasma samples from vascular dementia patients (Polidori et al., 2004). DiY cross-linking can result in Aβ dimer formation (Galeazzi et al., 1999; Yoburn et al., 2003; Al-Hilaly et al., 2013). Interestingly, an increase in the plasma level of Aβ dimers was recently shown in AD, serving as a potential biomarker (Villemagne et al., 2010). This further suggests a potential role DiY cross-linking that could help in AD biomarker discovery.

Using immunogold labeling, we have previously shown an increased co-localization of DiY antibody and Aβ antibody in Aβ plaques (Al-Hilaly et al., 2013). Using the same method, we showed an increase in DiY labeling in the CSF samples from AD patients compared to age-matched controls (Al-Hilaly et al., 2013). Although more studies are needed to establish DiY as a biomarker for AD, these studies suggest its utility as a potential biomarker. It would be interesting if future studies investigate whether an increase in DiY shows a disease-dependent rise in the CSF from AD patients. Given the recent promise in plasma-based markers for AD (Karikari et al., 2020a,b; Rodriguez et al., 2020; Suárez-Calvet et al., 2020; Thijssen et al., 2020; O'Connor et al., 2021), it would be useful to expand previous studies on DiY detection in plasma from AD patients (Polidori et al., 2004), to examine whether DiY levels could predict disease progression. This could especially be promising,

giving that DiY is a general marker of protein oxidation, which is established to substantially increase in AD (Conrad et al., 2000; Butterfield and Kanski, 2001; Nunomura et al., 2001; Castegna et al., 2003; Polidori et al., 2004; Butterfield and Halliwell, 2019). As such, the DiY could be on multiple proteins, not just Aβ and Tau, which would increase its detection with disease progression.

Discussion

There are many unanswered questions about the role of DiY on Aβ and Tau which would only become clearer in the future. One of the burning questions is whether DiY cross-linking is good or bad in AD? Given the well-established role of DiY in tissue stability, it may serve to strengthen proteins or tissue following injury in AD. What is DiY's *in vivo* impact on Aβ and Tau for disease development or progression? Multiple groups have tried to address some of these questions, but the results have been variable, partly due to the differences in the peptide model used, methods of peptide preparation, peptide concentration and aggregation, and experiment duration. Importantly, many oxidative modifications can co-occur on both Aβ and Tau which may also affect them differently. Ultimately, studies that define these different modifications and specifically isolate the contribution of DiY would provide the much-needed data to support the interpretation of the studies generated thus far in the literature. Together, this will be essential for understanding the specific role of DiY on Aβ and tau in AD and its utility for bio-marker or drug discovery.

Author contributions

All authors listed have made a substantial, direct, and intellectual contribution to the work, and approved it for publication.

Funding

This work was funded by Alzheimer's Society UK (AS-PG-16b-010).

Conflict of interest

The authors declare that the research was conducted in the absence of any commercial or financial relationships that could be construed as a potential conflict of interest.

Publisher's note

References

Al-Hilaly, Y. K., Foster, B., Biasetti, L., Lutter, L., Pollack, S., Rickard, J., et al. (2020). Tau (297-391) forms filaments that structurally mimic the core of paired helical filaments in Alzheimer's disease brain. *FEBS Lett.* 594, 944–950. doi: 10.1002/1873-3468.13675

Al-Hilaly, Y. K., Mohammed, A. H., Thorpe, J. R., and Serpell, L. C. (2019). The involvement of dityrosine crosslinks in lipofuscin accumulation in Alzheimer's disease. *J. Phys. Conf. Ser.* 1294:062107.

Al-Hilaly, Y., Biasetti, L., Blakeman, B., Pollack, S., Zibaee, S., Abdul-Sada, A., et al. (2016). The involvement of dityrosine crosslinking in α-synuclein assembly and deposition in Lewy Bodies in Parkinson's disease. *Sci. Rep.* 6:39171. doi: 10.1038/srep39171

Al-Hilaly, Y., Pollack, S., Vadukul, D., Citossi, F., Rickard, J., Simpson, M., et al. (2017). Alzheimer's disease-like paired helical filament assembly from truncated tau protein is independent of disulfide crosslinking. *J. Mol. Biol.* 429, 3650–3665. doi: 10.1016/j.jmb.2017.09.007

Al-Hilaly, Y., Williams, T., Stewart-Parker, M., Ford, L., Skaria, E., Cole, M., et al. (2013). A central role for dityrosine crosslinking of Amyloid-β in Alzheimer's disease. *Acta Neuropathol. Commun.* 1:83. doi: 10.1186/2051-5960-1-83

Ali, F., Leung, A., Cherny, R., Mavros, C., Barnham, K., Separovic, F., et al. (2006). Dimerisation of N-acetyl-L-tyrosine ethyl ester and Abeta peptides via formation of dityrosine. *Free Radic. Res.* 40, 1–9. doi: 10.1080/10715760500329721

Ali, F., Separovic, F., Barrow, C., Cherny, R., Fraser, F., Bush, A., et al. (2005). Methionine regulates copper/hydrogen peroxide oxidation products of Abeta. *J. Pept. Sci.* 11, 353–360. doi: 10.1002/psc.626

Alzheimer, A., Stelzmann, R., Schnitzlein, H., and Murtagh, F. (1995). An English translation of Alzheimer's 1907 paper, "uber eine eigenartige erkankung der hirnrinde". *Clin. Anat.* 8, 429–431. doi: 10.1002/ca.980080612

Amado, R., Aeschbach, R., and Neukom, H. (1984). Dityrosine – Invitro production and characterization. *Methods Enzymol.* 107, 377–388.

Andersen, S. (1964). The cross-links in resilin identified as dityrosine and trityrosine. *Biochim. Biophys. Acta* 93, 213–215. doi: 10.1016/0304-4165(64)90289-2

Andreadis, A. (2005). Tau gene alternative splicing: Expression patterns, regulation and modulation of function in normal brain and neurodegenerative diseases. *Biochim. Biophys. Acta* 1739, 91–103. doi: 10.1016/j.bbadis.2004.08.010

Andreadis, A., Brown, W., and Kosik, K. (1992). Structure and novel exons of the human tau gene. *Biochemistry* 31, 10626–10633. doi: 10.1021/bi00158a027

Arriagada, P., Growdon, J., Hedley-Whyte, E., and Hyman, B. (1992). Neurofibrillary tangles but not senile plaques parallel duration and severity of Alzheimer's disease. *Neurology* 42, 631–639. doi: 10.1212/wnl.42.3.631

Atwood, C., Perry, G., Zeng, H., Kato, Y., Jones, W., Ling, K., et al. (2004). Copper mediates dityrosine cross-linking of Alzheimer's amyloid-beta. *Biochemistry* 43, 560–568. doi: 10.1021/bi0358824

Bailey, A. (1991). The chemistry of natural enzyme-induced cross-links of proteins. *Amino Acids* 1, 293–306. doi: 10.1007/BF00813999

Barnham, K., Haeffner, F., Ciccotosto, G., Curtain, C., Tew, D., Mavros, C., et al. (2004). Tyrosine gated electron transfer is key to the toxic mechanism of Alzheimer's disease beta-amyloid. *FASEB J.* 18, 1427–1429. doi: 10.1096/fj.04-1890fje

Bayse, G. S., Michaels, A. W., and Morrison, M. (1972). The peroxidase-catalyzed oxidation of tyrosine. *Biochim. Biophys. Acta* 284, 34–42.

Benilova, I., Karran, E., and De Strooper, B. (2012). The toxic Abeta oligomer and Alzheimer's disease: An emperor in need of clothes. *Nat. Neurosci.* 15, 349–357. doi: 10.1038/nn.3028

Biasetti, L., Rey, S., Fowler, M., Ratnayaka, A., Fennell, K., Smith, C., et al. (2023). Elevated amyloid beta disrupts the nanoscale organization and function of synaptic vesicle pools in hippocampal neurons. *Cereb. Cortex* 33, 1263–1276. doi: 10.1093/cercor/bhac134

Bodaness, R. S., and Zigler, J. S. Jr. (1983). The rapid H2O2-mediated nonphotodynamic crosslinking of lens crystallins generated by the heme-undecapeptide from cytochrome C: Potential implications for cataractogenesis in man. *Biochem. Biophys. Res. Commun.* 113, 592–597. doi: 10.1016/0006-291x(83)91767-9

Braak, H., and Braak, E. (1991). Neuropathological stageing of Alzheimer-related changes. *Acta Neuropathol.* 82, 239–259. doi: 10.1007/BF00308809

Briza, P., Ellinger, A., Winkler, G., and Breitenbach, M. (1990). Characterization of a Dl-dityrosine-containing macromolecule from yeast ascospore walls. *J. Biol. Chem.* 265, 15118–15123.

Buée, L., Bussière, T., Buée-Scherrer, V., Delacourte, A., and Hof, P. (2000). Tau protein isoforms, phosphorylation and role in neurodegenerative disorders. *Brain Res. Brain Res. Rev.* 33, 95–130. doi: 10.1016/s0165-0173(00)00019-9

Bukar Maina, M., Al-Hilaly, Y., and Serpell, L. (2016). Nuclear tau and its potential role in Alzheimer's disease. *Biomolecules* 6:9. doi: 10.3390/biom6010009

Bush, A. (2003). Copper, zinc, and the metallobiology of Alzheimer disease. *Alzheimer Dis. Assoc. Disord.* 17, 147–150. doi: 10.1097/00002093-200307000-00005

Butterfield, D. A., and Halliwell, B. (2019). Oxidative stress, dysfunctional glucose metabolism and Alzheimer disease. *Nat. Rev. Neurosci.* 20, 148–160.

Butterfield, D. A., and Kanski, J. (2001). Brain protein oxidation in age-related neurodegenerative disorders that are associated with aggregated proteins. *Mech. Ageing Dev.* 122, 945–962.

Castegna, A., Thongboonkerd, V., Klein, J., Lynn, B., Markesbery, W., and Butterfield, D. (2003). Proteomic identification of nitrated proteins in Alzheimer's disease brain. *J. Neurochem.* 85, 1394–1401. doi: 10.1046/j.1471-4159.2003.01786.x

Cecchi, C., Pensalfini, A., Liguri, G., Baglioni, S., Fiorillo, C., Guadagna, S., et al. (2008). Differentiation increases the resistance of neuronal cells to amyloid toxicity. *Neurochem. Res.* 33, 2516–2531. doi: 10.1007/s11064-008-9627-7

Chartier-Harlin, M., Crawford, F., Houlden, H., Warren, A., Hughes, D., Fidani, L., et al. (1991). Early-onset Alzheimer's disease caused by mutations at codon 717 of the beta-amyloid precursor protein gene. *Nature* 353, 844–846. doi: 10.1038/353844a0

Chen, L., Wei, Y., Wang, X., and He, R. D. - (2009). Ribosylated Tau forms globular aggregates with high cytotoxicity. *Cell. Mol. Life Sci.* 66, 2559–2571. doi: 10.1007/s00018-009-0058-7

Cleveland, D. W., Hwo, S. Y., and Kirschner, M. W. (1977). Purification of tau, a microtubule-associated protein that induces assembly of microtubules from purified tubulin. *J. Mol. Biol.* 116, 207–225. doi: 10.1016/0022-2836(77)90213-3

Cline, E., Das, A., Bicca, M., Mohammad, S., Schachner, L., Kamel, J., et al. (2019). A novel crosslinking protocol stabilizes amyloid β oligomers capable of inducing Alzheimer's-associated pathologies. *J. Neurochem.* 148, 822–836. doi: 10.1111/jnc.14647

Connell, J., Rodriguez-Martin, T., Gibb, G., Kahn, N., Grierson, A., Hanger, D., et al. (2005). Quantitative analysis of tau isoform transcripts in sporadic tauopathies. *Brain Res. Mol. Brain Res.* 137, 104–109. doi: 10.1016/j.molbrainres.2005.02.014

Conrad, C., Marshall, P., Talent, J., Malakowsky, C., Choi, J., and Gracy, R. (2000). Oxidized proteins in Alzheimer's plasma. *Biochem. Biophys. Res. Commun.* 275, 678–681. doi: 10.1006/bbrc.2000.3356

Correia, M., Neves-Petersen, M., Jeppesen, P., Gregersen, S., and Petersen, S. B. (2012). UV-light exposure of insulin: Pharmaceutical implications upon covalent insulin dityrosine dimerization and disulphide bond photolysis. *PLoS One* 7:e50733. doi: 10.1371/journal.pone.0050733

Cowan, C. M., and Mudher, A. (2013). Are tau aggregates toxic or protective in tauopathies? *Front. Neurol.* 4:114. doi: 10.3389/fneur.2013.00114

Curtain, C., Ali, F., Volitakis, I., Cherny, R., Norton, R., Beyreuther, K., et al. (2001). Alzheimer's disease amyloid-beta binds copper and zinc to generate an allosterically ordered membrane-penetrating structure containing superoxide dismutase-like subunits. *J. Biol. Chem.* 276, 20466–20473. doi: 10.1074/jbc.M100175200

DaRocha-Souto, B., Scotton, T., Coma, M., Serrano-Pozo, A., Hashimoto, T., Serenó, L., et al. (2011). Brain oligomeric β-amyloid but not total amyloid plaque burden correlates with neuronal loss and astrocyte inflammatory response in amyloid precursor protein/tau transgenic mice. *J. Neuropathol. Exp. Neurol.* 70, 360–376. doi: 10.1097/NEN.0b013e318217a118

Davis, R., Marsden, I., Maloney, M., Minamide, L., Podlisny, M., Selkoe, D., et al. (2011). Amyloid beta dimers/trimers potently induce cofilin-actin rods that are inhibited by maintaining cofilin-phosphorylation. *Mol. Neurodegener.* 6:10. doi: 10.1186/1750-1326-6-10

de la Torre, A. V., Gay, M., Vilaprinyó-Pascual, S., Mazzucato, R., Serra-Batiste, M., Vilaseca, M., et al. (2018). Direct evidence of the presence of cross-linked Aβ dimers in the brains of Alzheimer's disease patients. *Anal. Chem.* 90, 4552–4560. doi: 10.1021/acs.analchem.7b04936

DiMarco, T., and Giulivi, C. (2007). Current analytical methods for the detection of dityrosine, a biomarker of oxidative stress, in biological samples. *Mass Spectrom. Rev.* 26, 108–120. doi: 10.1002/mas.20109

Dixit, R., Ross, J., Goldman, Y., and Holzbaur, E. (2008). Differential regulation of dynein and kinesin motor proteins by tau. *Science* 319, 1086–1089. doi: 10.1126/science.1152993

Duncan, M. (2003). A review of approaches to the analysis of 3-nitrotyrosine. *Amino Acids* 25, 351–361. doi: 10.1007/s00726-003-0022-z

Eiserich, J. P., Estevez, A. G., Bamberg, T. V., Ye, Y. Z., Chumley, P. H., Beckman, J. S., et al. (1999). Microtubule dysfunction by posttranslational nitrotyrosination of alpha-tubulin: A nitric oxide-dependent mechanism of cellular injury. *Proc. Natl. Acad. Sci. U.S.A.* 96: 6365–6370. doi: 10.1073/pnas.96.11.6365

Elliott, K. (1932). Milk peroxidase: Its preparation, properties, and action with H(2)O(2) on metabolites. With a method for determining small amounts of H(2)O(2) in complex mixtures. *Biochem. J.* 26, 10–24. doi: 10.1042/bj0260010

Fetterer, R. H., Rhoads, M. L., and Urban, J. F. Jr. (1993). Synthesis of tyrosine-derived cross-links in Ascaris suum cuticular proteins. *J. Parasitol.* 79, 160–166.

Fitzpatrick, A., Falcon, B., He, S., Murzin, A., Murshudov, G., Garringer, H., et al. (2017). Cryo-EM structures of tau filaments from Alzheimer's disease. *Nature* 547, 185–190. doi: 10.1038/nature23002

Flach, K., Hilbrich, I., Schiffmann, A., Gärtner, U., Krüger, M., Leonhardt, M., et al. (2012). Tau oligomers impair artificial membrane integrity and cellular viability. *J. Biol. Chem.* 287, 43223–43233. doi: 10.1074/jbc.M112.396176

Foerder, C. A., and Shapiro, B. M. (1977). Release of ovoperoxidase from sea urchin eggs hardens the fertilization membrane with tyrosine crosslinks. *Proc. Natl. Acad. Sci. U.S.A.* 74, 4214–4218. doi: 10.1073/pnas.74.10.4214

Ford, L., Crossley, M., Vadukul, D., Kemenes, G., and Serpell, L. (2017). Structure-dependent effects of amyloid-β on long-term memory in Lymnaea stagnalis. *FEBS Lett.* 591, 1236–1246. doi: 10.1002/1873-3468.12633

Friedhoff, P., Schneider, A., Mandelkow, E., and Mandelkow, E. (1998). Rapid assembly of Alzheimer-like paired helical filaments from microtubule-associated protein tau monitored by fluorescence in solution. *Biochemistry* 37, 10223–10230. doi: 10.1021/bi980537d

Fuchsberger, T., Martínez-Bellver, S., Giraldo, E., Teruel-Martí, V., Lloret, A., and Viña, J. (2016). Aβ induces excitotoxicity mediated by APC/C-Cdh1 depletion that can be prevented by glutaminase inhibition promoting neuronal survival. *Sci. Rep.* 6:31158. doi: 10.1038/srep31158

Fuentes-Lemus, E., Hägglund, P., López-Alarcón, C., and Davies, M. (2021). Oxidative crosslinking of peptides and proteins: Mechanisms of formation, detection, characterization and quantification. *Molecules* 27:15. doi: 10.3390/molecules27010015

Fujimoto, D. (1975). Occurrence of dityrosine in cuticlin, a structural protein from ascaris cuticle. *Compar. Biochem. Physiol. B Biochem. Mol. Biol.* 51, 205–207.

Galeazzi, L., Ronchi, P., Franceschi, C., and Giunta, S. (1999). In vitro peroxidase oxidation induces stable dimers of β-amyloid (1-42) through dityrosine bridge formation. *Amyloid* 6, 7–13. doi: 10.3109/13506129908993282

Ganguly, P., Do, T., Larini, L., LaPointe, N., Sercel, A., Shade, M., et al. (2015). Tau assembly: The dominant role of PHF6 (VQIVYK) in microtubule binding region repeat R3. *J. Phys. Chem. B* 119, 4582–4593. doi: 10.1021/acs.jpcb.5b00175

Georgieff, I. S., Liem, R. K., Couchie, D., Mavilia, C., Nunez, J., and Shelanski, M. L. (1993). Expression of high molecular weight tau in the central and peripheral nervous systems. *J. Cell Sci.* 105, 729–737.

Giulivi, C., and Davies, K. J. (1993). Dityrosine and tyrosine oxidation products are endogenous markers for the selective proteolysis of oxidatively modified red blood cell hemoglobin by (the 19 S) proteasome. *J. Biol. Chem.* 268, 8752–8759.

Giulivi, C., and Davies, K. J. (1994). Dityrosine: A marker for oxidatively modified proteins and selective proteolysis. *Methods Enzymol.* 233, 363–371.

Glenner, G. G., and Wong, C. W. (1984). Alzheimer's disease: Initial report of the purification and characterization of a novel cerebrovascular amyloid protein. *Biochem. Biophys. Res. Commun.* 120, 885–890.

Goate, A., Chartier-Harlin, M., Mullan, M., Brown, J., Crawford, F., Fidani, L., et al. (1991). Segregation of a missense mutation in the amyloid precursor protein gene with familial Alzheimer's disease. *Nature* 349, 704–706. doi: 10.1038/349704a0

Goedert, M., Jakes, R., Spillantini, M. G., Hasegawa, M., Smith, M. J., and Crowther, R. A. (1996). Assembly of microtubule-associated protein tau into Alzheimer-like filaments induced by sulphated glycosaminoglycans. *Nature* 383, 550–553.

Greenberg, S. G., and Davies, P. (1990). A preparation of Alzheimer paired helical filaments that displays distinct tau proteins by polyacrylamide gel electrophoresis. *Proc. Natl. Acad. Sci. U.S.A.* 87, 5827–5831. doi: 10.1073/pnas.87.15.5827

Gross, A. J., and Sizer, I. W. (1959). The oxidation of tyramine, tyrosine, and related compounds by peroxidase. *J. Biol. Chem.* 234, 1611–1614. doi: 10.1016/S0021-9258(18)70059-8

Grundke-Iqbal, I., Iqbal, K., Quinlan, M., Tung, Y., Zaidi, M., and Wisniewski, H. (1986a). Microtubule-associated protein tau. A component of Alzheimer paired helical filaments. *J. Biol. Chem.* 261, 6084–6089.

Grundke-Iqbal, I., Iqbal, K., Tung, Y. C., Quinlan, M., Wisniewski, H. M., and Binder, L. I. (1986b). Abnormal phosphorylation of the microtubule-associated protein tau (tau) in Alzheimer cytoskeletal pathology. *Proc. Natl. Acad. Sci. U.S.A.* 83, 4913–4917.

Gu, M., Bode, D., and Viles, J. (2018). Copper redox cycling inhibits Aβ fibre formation and promotes fibre fragmentation, while generating a dityrosine Aβ dimer. *Sci. Rep.* 8:16190. doi: 10.1038/s41598-018-33935-5

Guo, T., Noble, W., and Hanger, D. P. (2017). Roles of tau protein in health and disease. *Acta Neuropathol.* 133, 665–704.

Hardy, J. E. A. (1991). Molecular classification of Alzheimer's disease. *Lancet* 337, 1342–1343.

Hardy, J., and Higgins, G. (1992). Alzheimer's disease: The amyloid cascade hypothesis. *Science* 256, 184–185.

Heinecke, J., Li, W., Daehnke, H., and Goldstein, J. (1993a). Dityrosine, a specific marker of oxidation, is synthesized by the myeloperoxidase-hydrogen peroxide system of human neutrophils and macrophages. *J. Biol. Chem.* 268, 4069–4077.

Heinecke, J., Li, W., Francis, G., and Goldstein, J. (1993b). Tyrosyl radical generated by myeloperoxidase catalyzes the oxidative cross-linking of proteins. *J. Clin. Invest.* 91, 2866–2872. doi: 10.1172/JCI116531

Hensley, K., Maidt, M., Yu, Z., Sang, H., Markesbery, W., and Floyd, R. (1998). Electrochemical analysis of protein nitrotyrosine and dityrosine in the Alzheimer brain indicates region-specific accumulation. *J. Neurosci.* 18, 8126–8132. doi: 10.1523/JNEUROSCI.18-20-08126.1998

Ittner, L., Ke, Y., Delerue, F., Bi, M., Gladbach, A., van Eersel, J., et al. (2010). Dendritic function of tau mediates amyloid-beta toxicity in Alzheimer's disease mouse models. *Cell* 142, 387–397. doi: 10.1016/j.cell.2010.06.036

Jack, C., Knopman, D., Jagust, W., Petersen, R., Weiner, M., Aisen, P., et al. (2013). Tracking pathophysiological processes in Alzheimer's disease: An updated hypothetical model of dynamic biomarkers. *Lancet Neurol.* 12, 207–216. doi: 10.1016/S1474-4422(12)70291-0

Jana, M., Cappai, R., Pham, C., and Ciccotosto, G. (2016). Membrane-bound tetramer and trimer Aβ oligomeric species correlate with toxicity towards cultured neurons. *J. Neurochem.* 136, 594–608. doi: 10.1111/jnc.13443

Jomova, K., Vondrakova, D., Lawson, M., and Valko, M. (2010). Metals, oxidative stress and neurodegenerative disorders. *Mol. Cell. Biochem.* 345, 91–104. doi: 10.1007/s11010-010-0563-x

Kampers, T., Friedhoff, P., Biernat, J., Mandelkow, E., and Mandelkow, E. (1996). RNA stimulates aggregation of microtubule-associated protein tau into Alzheimer-like paired helical filaments. *FEBS Lett.* 399, 344–349. doi: 10.1016/s0014-5793(96)01386-5

Kaniyappan, S., Chandupatla, R. R., Mandelkow, E. M., and Mandelkow, E. (2017). Extracellular low-n oligomers of tau cause selective synaptotoxicity without affecting cell viability. *Alzheimers Dement.* 13, 1270–1291. doi: 10.1016/j.jalz.2017.04.002

Kanwar, R., and Balasubramanian, D. (1999). Structure and stability of the dityrosine-linked dimer of gamma B-crystallin. *Exp. Eye Res.* 68, 773–784. doi: 10.1006/exer.1999.0669

Karikari, T., Benedet, A., Ashton, N., Lantero Rodriguez, J., Snellman, A., Suárez-Calvet, M., et al. (2020a). Diagnostic performance and prediction of clinical progression of plasma phospho-tau181 in the Alzheimer's disease neuroimaging initiative. *Mol. Psychiatry* 26, 429–442. doi: 10.1038/s41380-020-00923-z

Karikari, T., Pascoal, T., Ashton, N., Janelidze, S., Benedet, A., Rodriguez, J., et al. (2020b). Blood phosphorylated tau 181 as a biomarker for Alzheimer's disease: A diagnostic performance and prediction modelling study using data from four prospective cohorts. *Lancet Neurol.* 19, 422–433. doi: 10.1016/S1474-4422(20)30071-5

Kato, Y., Maruyama, W., Naoi, M., Hashizume, Y., and Osawa, T. (1998). Immunohistochemical detection of dityrosine in lipofuscin pigments in the aged human brain. *Febs Lett.* 439, 231–234. doi: 10.1016/s0014-5793(98)01372-6

Kato, Y., Uchida, K., and Kawakishi, S. (1994). Aggregation of collagen exposed to UVA in the presence of riboflavin: A plausible role of tyrosine modification. *Photochem. Photobiol.* 59, 343–349. doi: 10.1111/j.1751-1097.1994.tb05045.x

Kheterpal, I., Williams, A., Murphy, C., Bledsoe, B., and Wetzel, R. (2001). Structural features of the Abeta amyloid fibril elucidated by limited proteolysis. *Biochemistry* 40, 11757–11767. doi: 10.1021/bi010805z

Kok, W. M., Cottam, J. M., Ciccotosto, G. D., Miles, L. A., Karas, J. A., Scanlon, D. B., et al. (2013). Synthetic dityrosine-linked β-amyloid dimers form stable, soluble, neurotoxic oligomers. *Chem. Sci.* 4, 4449–4454.

Kondo, J., Honda, T., Mori, H., Hamada, Y., Miura, R., Ogawara, M., et al. (1988). The carboxyl third of tau is tightly bound to paired helical filaments. *Neuron* 1, 827–834. doi: 10.1016/0896-6273(88)90130-4

Kowalik-Jankowska, T., Ruta, M., Wiśniewska, K., Łankiewicz, L., and Dyba, M. (2004). Products of Cu(Ii)-catalyzed oxidation in the presence of hydrogen peroxide of the 1-10, 1-16 fragments of human and mouse beta-amyloid peptide. *J. Inorg. Biochem.* 98, 940–950. doi: 10.1016/j.jinorgbio.2004.03.001

Krishtal, J., Bragina, O., Metsla, K., Palumaa, P., and Tõugu, V. (2015). Toxicity of amyloid beta 1-40 and 1-42 on Sh-Sy5Y cell line. *Springerplus* 4:19.

LaBella, F., Keeley, F., Vivian, S., and Thornhill, D. (1967). Evidence for dityrosine in elastin. *Biochem. Biophys. Res. Commun.* 26, 748–753. doi: 10.1016/s0006-291x(67)80137-2

Lacor, P., Buniel, M., Furlow, P., Clemente, A., Velasco, P., Wood, M., et al. (2007). Abeta oligomer-induced aberrations in synapse composition, shape, and density provide a molecular basis for loss of connectivity in Alzheimer's disease. *J. Neurosci.* 27, 796–807. doi: 10.1523/JNEUROSCI.3501-06.2007

Lambert, M., Barlow, A., Chromy, B., Edwards, C., Freed, R., Liosatos, M., et al. (1998). Diffusible, nonfibrillar ligands derived from Abeta1-42 are potent central nervous system neurotoxins. *Proc. Natl. Acad. Sci. U.S.A.* 95, 6448–6453. doi: 10.1073/pnas.95.11.6448

Lasagna-Reeves, C., Castillo-Carranza, D., Guerrero-Muoz, M., Jackson, G., and Kayed, R. (2010). Preparation and characterization of neurotoxic tau oligomers. *Biochemistry* 49, 10039–10041. doi: 10.1021/bi1016233

Lee, V., Balin, B., Otvos, L., and Trojanowski, J. (1991). A68: A major subunit of paired helical filaments and derivatized forms of normal Tau. *Science* 251, 675–678. doi: 10.1126/science.1899488

Leeuwenburgh, C., Hansen, P. A., Holloszy, J. O., and Heinecke, J. W. (1999b). Oxidized amino acids in the urine of aging rats: Potential markers for assessing oxidative stress in vivo. *Am. J. Physiol.* 276, R128–R135. doi: 10.1152/ajpregu.1999.276.1.R128

Leeuwenburgh, C., Hansen, P. A., Holloszy, J. O., and Heinecke, J. W. (1999a). Hydroxyl radical generation during exercise increases mitochondrial protein oxidation and levels of urinary dityrosine. *Free Radic. Biol. Med.* 27, 186–192. doi: 10.1016/s0891-5849(99)00071-4

Leeuwenburgh, C., Hazen, S. L., Pennathur, S., and Heinecke, J. W. (1996). Massive increase in protein-bound dityrosine in Ldl isolated from human atherosclerotic aorta: Implications for the role of tyrosyl radical in atherogenesis. *Circulation* 94, 2332–2332.

Leeuwenburgh, C., Wagner, P., Holloszy, J., Sohal, R., and Heinecke, J. (1997). Caloric restriction attenuates dityrosine cross-linking of cardiac and skeletal muscle proteins in aging mice. *Arch. Biochem. Biophys.* 346, 74–80. doi: 10.1006/abbi.1997.0297

Levy, E., Carman, M., Fernandez-Madrid, I., Power, M., Lieberburg, I., van Duinen, S., et al. (1990). Mutation of the Alzheimer's disease amyloid gene in hereditary cerebral hemorrhage, Dutch type. *Science* 248, 1124–1126. doi: 10.1126/science.2111584

Li, J., Hodgeman, B., and Christensen, B. (1996). Involvement of peroxidase in chorion hardening in Aedes aegypti. *Insect. Biochem. Mol. Biol.* 26, 309–317. doi: 10.1016/0965-1748(95)00099-2

Li, S., Jin, M., Koeglsperger, T., Shepardson, N. E., Shankar, G. M., and Selkoe, D. J. (2011). Soluble Abeta oligomers inhibit long-term potentiation through a mechanism involving excessive activation of extrasynaptic Nr2B-containing Nmda receptors. *J. Neurosci.* 31, 6627–6638.

Liu, C., and Götz, J. (2013). Profiling murine Tau with 0N, 1N and 2N isoform-specific antibodies in brain and peripheral organs reveals distinct subcellular localization, with the 1N isoform being enriched in the nucleus. *PLoS One* 8:e84849. doi: 10.1371/journal.pone.0084849

Loomis, P., Howard, T., Castleberry, R., and Binder, L. (1990). Identification of nuclear tau isoforms in human neuroblastoma cells. *Proc. Natl. Acad. Sci. U.S.A.* 87, 8422–8426. doi: 10.1073/pnas.87.21.8422

Lovell, M., Robertson, J., Teesdale, W., Campbell, J., and Markesbery, W. (1998). Copper, iron and zinc in Alzheimer's disease senile plaques. *J. Neurol. Sci.* 158, 47–52. doi: 10.1016/s0022-510x(98)00092-6

Lövestam, S., Koh, F., van Knippenberg, B., Kotecha, A., Murzin, A., Goedert, M., et al. (2022). Assembly of recombinant tau into filaments identical to those of Alzheimer's disease and chronic traumatic encephalopathy. *Elife* 11:e76494. doi: 10.7554/eLife.76494

Lutter, L., Al-Hilaly, Y., Serpell, C., Tuite, M., Wischik, C., Serpell, L., et al. (2022). Structural identification of individual helical amyloid filaments by integration of cryo-electron microscopy-derived maps in comparative morphometric atomic force microscopy image analysis. *J. Mol. Biol.* 434:167466. doi: 10.1016/j.jmb.2022.167466

Maina, M. B., Bailey, L. J., Doherty, A. J., and Serpell, L. C. (2018a). The involvement of Aβ42 and tau in nucleolar and protein synthesis machinery dysfunction. *Front. Cell. Neurosci.* 12:220. doi: 10.3389/fncel.2018.00220

Maina, M. B., Bailey, L., Wagih, S., Biasetti, L., Pollack, S., Quinn, J., et al. (2018b). The involvement of tau in nucleolar transcription and the stress response. *Acta Neuropathol. Commun.* 6:70. doi: 10.1186/s40478-018-0565-6

Maina, M., Burra, G., Al-Hilaly, Y., Mengham, K., Fennell, K., and Serpell, L. (2020b). Metal- and UV- catalyzed oxidation results in trapped Amyloid-β intermediates revealing that self-assembly is required for Aβ-induced cytotoxicity. *iScience* 23:101537. doi: 10.1016/j.isci.2020.101537

Maina, M., Al-Hilaly, Y., Burra, G., Rickard, J., Harrington, C., Wischik, C., et al. (2020a). Oxidative stress conditions result in trapping of PHF-core tau (297-391) intermediates. *bioRxiv* [Preprint]. bioRxiv: 2020.12.07.414532. doi: 10.3390/cells10030703

Maina, M., Al-Hilaly, Y., Burra, G., Rickard, J., Harrington, C., Wischik, C., et al. (2021). Oxidative stress conditions result in trapping of PHF-core tau (297-391) intermediates. *Cells* 10:703.

Maina, M., Al-Hilaly, Y., Oakley, S., Burra, G., Khanom, T., Biasetti, L., et al. (2022b). Dityrosine cross-links are present in Alzheimer's disease-derived tau oligomers and paired helical filaments (PHF) which promotes the stability of the PHF-core tau (297-391) in vitro. *bioRxiv* [Preprint]. bioRxiv: 2022.05.28.493839. doi: 10.1016/j.jmb.2022.167785

Maina, M., Al-Hilaly, Y., Oakley, S., Burra, G., Khanom, T., Biasetti, L., et al. (2022a). Dityrosine cross-links are present in Alzheimer's disease-derived tau oligomers and paired helical filaments (PHF) which promotes the stability of the PHF-core tau (297-391) in vitro. *J. Mol. Biol.* 434:167785.

Marshall, K. E., Vadukul, D. M., Staras, K., and Serpell, L. C. (2020). Misfolded amyloid-beta-42 impairs the endosomal-lysosomal pathway. *Cell. Mol. Life Sci.* 77, 5031–5043. doi: 10.1007/s00018-020-03464-4

Marshall, K., Vadukul, D., Dahal, L., Theisen, A., Fowler, M., Al-Hilaly, Y., et al. (2016). A critical role for the self-assembly of Amyloid-β1-42 in neurodegeneration. *Sci. Rep.* 6:30182. doi: 10.1038/srep30182

Martin, L., Latypova, X., and Terro, F. (2011). Post-translational modifications of tau protein: Implications for Alzheimer's disease. *Neurochem. Int.* 58, 458–471.

Masters, C. L., and Selkoe, D. J. (2012). Biochemistry of amyloid β-protein and amyloid deposits in Alzheimer disease. *Cold Spring Harb. Perspect. Med.* 2:a006262.

Mayer, F., Pröpper, S., and Ritz-Timme, S. (2014). Dityrosine, a protein product of oxidative stress, as a possible marker of acute myocardial infarctions. *Int. J. Legal Med.* 128, 787–794. doi: 10.1007/s00414-014-1015-z

McLean, C., Cherny, R., Fraser, F., Fuller, S., Smith, M., Beyreuther, K., et al. (1999). Soluble pool of Abeta amyloid as a determinant of severity of neurodegeneration in Alzheimer's disease. *Ann. Neurol.* 46, 860–866.

Miao, J., Shi, R., Li, L., Chen, F., Zhou, Y., Tung, Y., et al. (2019). Pathological tau from Alzheimer's brain induces site-specific hyperphosphorylation and SDS- and reducing agent-resistant aggregation of tau in vivo. *Front. Aging Neurosci.* 11:34. doi: 10.3389/fnagi.2019.00034

Mukrasch, M. D., Biernat, J., Von Bergen, M., Griesinger, C., Mandelkow, E., and Zweckstetter, M. (2005). Sites of tau important for aggregation populate {beta}-structure and bind to microtubules and polyanions. *J. Biol. Chem.* 280, 24978–24986. doi: 10.1074/jbc.M501565200

Neve, R., Harris, P., Kosik, K., Kurnit, D., and Donlon, T. (1986). Identification of cDNA clones for the human microtubule-associated protein tau and chromosomal localization of the genes for tau and microtubule-associated protein 2. *Brain Res.* 387, 271–280. doi: 10.1016/0169-328x(86)90033-1

Nunez, J., and Fischer, I. (1997). Microtubule-associated proteins (Maps) in the peripheral nervous system during development and regeneration. *J. Mol. Neurosci.* 8, 207–222.

Nunomura, A., Perry, G., Aliev, G., Hirai, K., Takeda, A., Balraj, E., et al. (2001). Oxidative damage is the earliest event in Alzheimer disease. *J. Neuropathol. Exp. Neurol.* 60, 759–767. doi: 10.1093/jnen/60.8.759

O'Connor, A., Karikari, T., Poole, T., Ashton, N., Lantero Rodriguez, J., Khatun, A., et al. (2021). Plasma phospho-tau181 in presymptomatic and symptomatic familial Alzheimer's disease: A longitudinal cohort study. *Mol. Psychiatry* 26, 5967–5976. doi: 10.1038/s41380-020-0838-x

O'Malley, T., Oktaviani, N., Zhang, D., Lomakin, A., O'Nuallain, B., Linse, S., et al. (2014). Aβ dimers differ from monomers in structural propensity, aggregation paths and population of synaptotoxic assemblies. *Biochem. J.* 461, 413–426. doi: 10.1042/BJ20140219

O'Malley, T., Witbold, W., Linse, S., and Walsh, D. (2016). The aggregation paths and products of Aβ42 dimers are distinct from those of the Aβ42 monomer. *Biochemistry* 55, 6150–6161. doi: 10.1021/acs.biochem.6b00453

Oakley, S., Maina, M., Marshall, K., Al-Hilaly, Y., Harrington, C., Wischik, C., et al. (2020). Tau filament self-assembly and structure: Tau as a therapeutic target. *Front. Neurol.* 11:590754. doi: 10.3389/fneur.2020.590754

Ono, K., Condron, M. M., and Teplow, D. B. (2009). Structure-neurotoxicity relationships of amyloid beta-protein oligomers. *Proc. Natl. Acad. Sci. U.S.A.* 106, 14745–14750. doi: 10.1073/pnas.0905127106

Palmblad, M., Westlind-Danielsson, A., and Bergquist, J. (2002). Oxidation of methionine 35 attenuates formation of amyloid beta -peptide 1-40 oligomers. *J. Biol. Chem.* 277, 19506–19510. doi: 10.1074/jbc.M11221 8200

Partlow, B. P., Applegate, M. B., Omenetto, F. G., and Kaplan, D. L. (2016). Dityrosine cross-linking in designing biomaterials. *ACS Biomater. Sci. Eng.* 2, 2108–2121.

Pennathur, S., Jackson-Lewisu, V., Przedborskiu, S., and Heinecke, J. (1999). Marked elevations of 3-nitrotyrosine and dityrosine in mice with Mptp-induced Parkinson's disease. *Free Radic. Biol. Med.* 27, S141–S141.

Pérez, M., Valpuesta, J., Medina, M., Montejo de Garcini, E., and Avila, J. (1996). Polymerization of tau into filaments in the presence of heparin: The minimal sequence required for tau-tau interaction. *J. Neurochem.* 67, 1183–1190. doi: 10.1046/j.1471-4159.1996.67031183.x

Polidori, M., Mattioli, P., Aldred, S., Cecchetti, R., Stahl, W., Griffiths, H., et al. (2004). Plasma antioxidant status, immunoglobulin g oxidation and lipid peroxidation in demented patients: Relevance to Alzheimer disease and vascular dementia. *Dement. Geriatr. Cogn. Disord.* 18, 265–270. doi: 10.1159/000080027

Rambaran, R. N., and Serpell, L. C. (2008). Amyloid fibrils: Abnormal protein assembly. *Prion* 2, 112–117.

Raven, D. J., Earland, C., and Little, M. (1971). Occurrence of dityrosine in tussah silk fibroin and keratin. *Biochim. Biophys. Acta* 251:96. doi: 10.1016/0005-2795(71)90065-1

Reddy, P. H., and Beal, M. F. (2008). Amyloid beta, mitochondrial dysfunction and synaptic damage: Implications for cognitive decline in aging and Alzheimer's disease. *Trends Mol. Med.* 14, 45–53.

Reynolds, M. R., Berry, R. W., and Binder, L. I. (2005). Site-specific nitration and oxidative dityrosine bridging of the tau protein by peroxynitrite: Implications for Alzheimer's disease. *Biochemistry* 44, 1690–1700. doi: 10.1021/bi047982v

Reynolds, M., Lukas, T., Berry, R., and Binder, L. (2006). Peroxynitrite-mediated tau modifications stabilize preformed filaments and destabilize microtubules through distinct mechanisms. *Biochemistry* 45, 4314–4326. doi: 10.1021/bi052142h

Roberts, B. R., Ryan, T. M., Bush, A. I., Masters, C. L., and Duce, J. A. (2012). The role of metallobiology and amyloid-beta peptides in Alzheimer's disease. *J. Neurochem.* 120, 149–166.

Rodriguez, J. L., Karikari, T., Suárez-Calvet, M., Troakes, C., King, A., Emersic, A., et al. (2020). Plasma p-tau181 accurately predicts Alzheimer's disease pathology at least 8 years prior to post-mortem and improves the clinical characterisation of cognitive decline. *Acta Neuropathol.* 140, 267–278. doi: 10.1007/s00401-020-02195-x

Rossi, G., Dalprà, L., Crosti, F., Lissoni, S., Sciacca, F., Catania, M., et al. (2008). A new function of microtubule-associated protein tau: Involvement in chromosome stability. *Cell Cycle* 7, 1788–1794. doi: 10.4161/cc.7.12.6012

Sarell, C., Syme, C., Rigby, S., and Viles, J. (2009). Copper(II) binding to amyloid-beta fibrils of Alzheimer's disease reveals a picomolar affinity: Stoichiometry and coordination geometry are independent of Abeta oligomeric form. *Biochemistry* 48, 4388–4402. doi: 10.1021/bi900254n

Schweers, O., Schönbrunn-Hanebeck, E., Marx, A., and Mandelkow, E. (1994). Structural studies of tau protein and Alzheimer paired helical filaments show no evidence for beta-structure. *J. Biol. Chem.* 269, 24290–24297.

Selkoe, D. J., and Hardy, J. (2016). The amyloid hypothesis of Alzheimer's disease at 25 years. *EMBO Mol. Med.* 8, 595–608.

Shankar, G., Li, S., Mehta, T., Garcia-Munoz, A., Shepardson, N., Smith, I., et al. (2008). Amyloid-beta protein dimers isolated directly from Alzheimer's brains impair synaptic plasticity and memory. *Nat. Med.* 14, 837–842. doi: 10.1038/nm1782

Shi, Y., Zhang, W., Yang, Y., Murzin, A., Falcon, B., Kotecha, A., et al. (2021). Structure-based classification of tauopathies. *bioRxiv* [Preprint]. bioRxiv: 2021.05.28.446130.

Siegel, S., Bieschke, J., Powers, E., and Kelly, J. (2007). The oxidative stress metabolite 4-hydroxynonenal promotes Alzheimer protofibril formation. *Biochemistry* 46, 1503–1510. doi: 10.1021/bi061853s

Sitkiewicz, E., Olędzki, J., Poznański, J., and Dadlez, M. (2014). Di-tyrosine cross-link decreases the collisional cross-section of aβ peptide dimers and trimers in the gas phase: An ion mobility study. *PLoS One* 9:e100200. doi: 10.1371/journal.pone.0100200

Skaff, O., Jolliffe, K., and Hutton, C. (2005). Synthesis of the side chain cross-linked tyrosine oligomers dityrosine, trityrosine, and pulcherosine. *J. Org. Chem.* 70, 7353–7363. doi: 10.1021/jo051076m

Smail, E., Briza, P., Panagos, A., and Berenfeld, L. (1995). Candida albicans cell walls contain the fluorescent cross-linking amino acid dityrosine. *Infect. Immun.* 63, 4078–4083. doi: 10.1128/iai.63.10.4078-4083.1995

Smith, D. G., Ciccotosto, G., Tew, D., Fodero-Tavoletti, M., Johanssen, T., Masters, C., et al. (2007b). Concentration dependent Cu2+ induced aggregation and dityrosine formation of the Alzheimer's disease amyloid-beta peptide. *Biochemistry* 46, 2881–2891. doi: 10.1021/bi0620961

Smith, D. G., Cappai, R., and Barnham, K. J. (2007a). The redox chemistry of the Alzheimer's disease amyloid β peptide. *Biochim. Biophys. Acta* 1768, 1976–1990.

Smith, D., Smith, D., Curtain, C., Boas, J., Pilbrow, J., Ciccotosto, G., et al. (2006). Copper-mediated amyloid-beta toxicity is associated with an intermolecular histidine bridge. *J. Biol. Chem.* 281, 15145–15154. doi: 10.1074/jbc.M600417200

Soura, V., Stewart-Parker, M., Williams, T., Ratnayaka, A., Atherton, J., Gorringe, K., et al. (2012). Visualization of co-localization in Aβ42-administered neuroblastoma cells reveals lysosome damage and autophagosome accumulation related to cell death. *Biochem. J.* 441, 579–590. doi: 10.1042/BJ20110749

Souza, J. M., Giasson, B. I., Chen, Q., Lee, V. M., and Ischiropoulos, H. (2000). Dityrosine cross-linking promotes formation of stable alpha -synuclein polymers. Implication of nitrative and oxidative stress in the pathogenesis of neurodegenerative synucleinopathies. *J. Biol. Chem.* 275, 18344–18349. doi: 10.1074/jbc.M000206200

Stoothoff, W. H., and Johnson, G. V. W. (2005). Tau phosphorylation: Physiological and pathological consequences. *Biochim. Biophys. Acta* 1739, 280–297.

Suárez-Calvet, M., Karikari, T. K., Ashton, N. J., Lantero Rodríguez, J., Milà-Alomà, M., Gispert, J. D., et al. (2020). Novel tau biomarkers phosphorylated at T181, T217 or T231 rise in the initial stages of the preclinical Alzheimer's continuum when only subtle changes in Aβ pathology are detected. *EMBO Mol. Med.* 12:e12921.

Suh, S., Jensen, K., Jensen, M., Silva, D., Kesslak, P., Danscher, G., et al. (2000). Histochemically-reactive zinc in amyloid plaques, angiopathy, and degenerating neurons of Alzheimer's diseased brains. *Brain Res.* 852, 274–278. doi: 10.1016/s0006-8993(99)02096-x

Thijssen, E., La Joie, R., Wolf, A., Strom, A., Wang, P., Iaccarino, L., et al. (2020). Diagnostic value of plasma phosphorylated tau181 in Alzheimer's disease and

frontotemporal lobar degeneration. *Nat. Med.* 26, 387–397. doi: 10.1038/s41591-020-0762-2

Tian, H., Davidowitz, E., Lopez, P., Emadi, S., Moe, J., and Sierks, M. (2013). Trimeric tau is toxic to human neuronal cells at low nanomolar concentrations. *Int. J. Cell Biol.* 2013:260787. doi: 10.1155/2013/260787

Tickler, A., Smith, D., Ciccotosto, G., Tew, D., Curtain, C., Carrington, D., et al. (2005). Methylation of the imidazole side chains of the Alzheimer disease amyloid-beta peptide results in abolition of superoxide dismutase-like structures and inhibition of neurotoxicity. *J. Biol. Chem.* 280, 13355–13363. doi: 10.1074/jbc.M414178200

Urbanc, B. (2021). Cross-linked amyloid β-protein oligomers: A missing link in Alzheimer's disease pathology? *J. Phys. Chem. B.* 125, 1307–1316. doi: 10.1021/acs.jpcb.0c07716

Vadukul, D., Gbajumo, O., Marshall, K., and Serpell, L. (2017). Amyloidogenicity and toxicity of the reverse and scrambled variants of amyloid-β 1-42. *FEBS Lett.* 591, 822–830. doi: 10.1002/1873-3468.12590

Vadukul, D., Maina, M., Franklin, H., Nardecchia, A., Serpell, L., and Marshall, K. (2020). Internalisation and toxicity of amyloid-β 1-42 are influenced by its conformation and assembly state rather than size. *FEBS Lett.* 594, 3490–3503. doi: 10.1002/1873-3468.13919

Van Broeckhoven, C., Haan, J., Bakker, E., Hardy, J., Van Hul, W., Wehnert, A., et al. (1990). Amyloid beta protein precursor gene and hereditary cerebral hemorrhage with amyloidosis (Dutch). *Science* 248, 1120–1122. doi: 10.1126/science.1971458

Van Der Vliet, A., Nguyen, M., Shigenaga, M., Eiserich, J., Marelich, G., and Cross, C. (2000). Myeloperoxidase and protein oxidation in cystic fibrosis. *Am. J. Physiol. Lung Cell Mol. Physiol.* 279, L537–L546. doi: 10.1152/ajplung.2000.279.3.L537

Vázquez, G., Caballero, A., Kokinda, J., Hijano, A., Sabaté, R., and Gamez, P. (2019). Copper, dityrosine cross-links and amyloid-β aggregation. *J. Biol. Inorg. Chem.* 24, 1217–1229. doi: 10.1007/s00775-019-01734-6

Viles, J. H. (2012). Metal ions and amyloid fiber formation in neurodegenerative diseases. Copper, zinc and iron in Alzheimer's, Parkinson's, and prion diseases. *Coord. Chem. Rev.* 256, 2271–2284.

Villemagne, V., Perez, K., Pike, K., Kok, W., Rowe, C., White, A., et al. (2010). Blood-borne amyloid-beta dimer correlates with clinical markers of Alzheimer's disease. *J. Neurosci.* 30, 6315–6322. doi: 10.1523/JNEUROSCI.5180-09.2010

von Bergen, M., Barghorn, S., Biernat, J., Mandelkow, E. M., and Mandelkow, E. (2005). Tau aggregation is driven by a transition from random coil to beta sheet structure. Biochim. Biophys. *Acta Mol. Basis Dis.* 1739, 158–166. doi: 10.1016/j.bbadis.2004.09.010

von Bergen, M., Friedhoff, P., Biernat, J., Heberle, J., Mandelkow, E., and Mandelkow, E. (2000). Assembly of tau protein into Alzheimer paired helical filaments depends on a local sequence motif ((306)VQIVYK(311)) forming beta structure. *Proc. Natl. Acad. Sci. U.S.A.* 97, 5129–5134. doi: 10.1073/pnas.97.10.5129

Walsh, D. M., and Selkoe, D. J. (2007). A beta oligomers – A decade of discovery. *J. Neurochem.* 101, 1172–1184.

Wang, J., Dickson, D. W., Trojanowski, J. Q., and Lee, V. M. (1999). The levels of soluble versus insoluble brain Abeta distinguish Alzheimer's disease from normal and pathologic aging. *Exp. Neurol.* 158, 328–337. doi: 10.1006/exnr.1999.7085

Wang, Y. P., Biernat, J., Pickhardt, M., Mandelkow, E., and Mandelkow, E. M. (2007). Stepwise proteolysis liberates tau fragments that nucleate the Alzheimer-like aggregation of full-length tau in a neuronal cell model. *Proc. Natl. Acad. Sci. U.S.A.* 104, 10252–10257. doi: 10.1073/pnas.0703676104

Wang, Y., Loomis, P., Zinkowski, R., and Binder, L. (1993). A novel tau transcript in cultured human neuroblastoma cells expressing nuclear tau. *J. Cell Biol.* 121, 257–267. doi: 10.1083/jcb.121.2.257

Waters, W. A. (1952). *Organic chemsitry H. Gilman*. New York, NY: John Wiley and Sons, Inc.

Waykole, P., and Heidemann, E. (1976). Dityrosine in collagen. *Connect. Tissue Res.* 4, 219–222.

Weingarten, M., Lockwood, A., Hwo, S., and Kirschner, M. (1975). A protein factor essential for microtubule assembly. *Proc. Natl. Acad. Sci. U.S.A.* 72, 1858–1862. doi: 10.1073/pnas.72.5.1858

Wells-Knecht, M., Huggins, T., Dyer, D., Thorpe, S., and Baynes, J. (1993). Oxidized amino acids in lens protein with age. Measurement of o-tyrosine and dityrosine in the aging human lens. *J. Biol. Chem.* 268, 12348–12352.

Wilhelmus, M., Grunberg, S., Bol, J., van Dam, A., Hoozemans, J., Rozemuller, A., et al. (2009). Transglutaminases and transglutaminase-catalyzed cross-links colocalize with the pathological lesions in Alzheimer's disease brain. *Brain Pathol.* 19, 612–622. doi: 10.1111/j.1750-3639.2008.00197.x

Williams, T. L., Serpell, L. C., and Urbanc, B. (2016). Stabilization of native amyloid β-protein oligomers by copper and hydrogen peroxide induced cross-linking of unmodified proteins (Chicup). *Biochim. Biophys. Acta* 1864, 249–259. doi: 10.1016/j.bbapap.2015.12.001

Wilson, D. M., and Binder, L. I. (1997). Free fatty acids stimulate the polymerization of tau and amyloid beta peptides. In vitro evidence for a common effector of pathogenesis in Alzheimer's disease. *Am. J. Pathol.* 150, 2181–2195.

Wischik, C., Novak, M., Thøgersen, H., Edwards, P., Runswick, M., Jakes, R., et al. (1988b). Isolation of a fragment of tau derived from the core of the paired helical filament of Alzheimer disease. *Proc. Natl. Acad. Sci. U.S.A.* 85, 4506–4510. doi: 10.1073/pnas.85.12.4506

Wischik, C., Novak, M., Edwards, P., Klug, A., Tichelaar, W., and Crowther, R. (1988a). Structural characterization of the core of the paired helical filament of Alzheimer disease. *Proc. Natl. Acad. Sci. U.S.A.* 85, 4884–4888. doi: 10.1073/pnas.85.13.4884

Wood, J. G., Suzanne, S. M., Nancy, J. P., and Binder, L. I. (1986). Microtubule-associated protein tau (tau) is a major antigenic component of paired helical filaments in Alzheimer disease. *Proc. Natl. Acad. Sci. U.S.A.* 83, 4044–4048. doi: 10.1073/pnas.83.11.4044

Wu, H., Hudry, E., Hashimoto, T., Kuchibhotla, K., Rozkalne, A., Fan, Z., et al. (2010). Amyloid beta induces the morphological neurodegenerative triad of spine loss, dendritic simplification, and neuritic dystrophies through calcineurin activation. *J. Neurosci.* 30, 2636–2649. doi: 10.1523/JNEUROSCI.4456-09.2010

Yoburn, J., Tian, W., Brower, J., Nowick, J., Glabe, C., and Van Vranken, D. (2003). Dityrosine cross-linked Abeta peptides: Fibrillar beta-structure in Abeta(1-40) is conducive to formation of dityrosine cross-links but a dityrosine cross-link in Abeta(8-14) does not induce beta-structure. *Chem. Res. Toxicol.* 16, 531–535. doi: 10.1021/tx025666g

Yoshikai, S., Sasaki, H., Doh-Ura, K., Furuya, H., and Sakaki, Y. (1990). Genomic organization of the human amyloid beta-protein precursor gene. *Gene* 87, 257–263.

Zhang, S., Fox, D. M., and Urbanc, B. (2017). Insights into formation and structure of Aβ oligomers cross-linked via tyrosines. *J. Phys. Chem. B* 121, 5523–5535. doi: 10.1021/acs.jpcb.7b02495

Zhang, Y., Lu, L., Jia, J., Jia, L., Geula, C., Pei, J., et al. (2014). A lifespan observation of a novel mouse model: In vivo evidence supports aβ oligomer hypothesis. *PLoS One* 9:e85885. doi: 10.1371/journal.pone.0085885

Zhu, Q., Pao, G., Huynh, A., Suh, H., Tonnu, N., Nederlof, P., et al. (2011). BRCA1 tumour suppression occurs via heterochromatin-mediated silencing. *Nature* 477, 179–184. doi: 10.1038/nature10371

frontiers | Frontiers in Neuroscience

TYPE Review
PUBLISHED 11 April 2023
DOI 10.3389/fnins.2023.1081938

OPEN ACCESS

EDITED BY
Jinghui Luo,
Paul Scherrer Institut (PSI),
Switzerland

REVIEWED BY
Shivam Gupta,
Novartis Institutes for BioMedical Research,
United States
Selvakumar Govindhasamy Pushpavathi,
The University of Iowa,
United States

*CORRESPONDENCE
Musa O. Iliyasu
✉ iliyasu.mo@ksu.edu.ng;
✉ moiliyasu@gmail.com

SPECIALTY SECTION
This article was submitted to Neurodegeneration, a section of the journal Frontiers in Neuroscience

RECEIVED 27 October 2022
ACCEPTED 13 March 2023
PUBLISHED 11 April 2023

CITATION
Iliyasu MO, Musa SA, Oladele SB and Iliya AI (2023) Amyloid-beta aggregation implicates multiple pathways in Alzheimer's disease: Understanding the mechanisms. *Front. Neurosci.* 17:1081938. doi: 10.3389/fnins.2023.1081938

Amyloid-beta aggregation implicates multiple pathways in Alzheimer's disease: Understanding the mechanisms

Musa O. Iliyasu[1]*, Sunday A. Musa[2], Sunday B. Oladele[3] and Abdullahi I. Iliya[4]

[1]Department of Anatomy, Kogi State University, Anyigba, Nigeria, [2]Department of Human Anatomy, Ahmadu Bello University, Zaria, Nigeria, [3]Department of Veterinary Pathology, Ahmadu Bello University, Zaria, Nigeria, [4]Department of Human Anatomy, Federal University Dutse, Dutse, Nigeria

Alzheimer's disease (AD) is a progressive neurodegenerative condition characterized by tau pathology and accumulations of neurofibrillary tangles (NFTs) along with amyloid-beta (Aβ). It has been associated with neuronal damage, synaptic dysfunction, and cognitive deficits. The current review explained the molecular mechanisms behind the implications of Aβ aggregation in AD *via* multiple events. Beta (β) and gamma (γ) secretases hydrolyzed amyloid precursor protein (APP) to produce Aβ, which then clumps together to form Aβ fibrils. The fibrils increase oxidative stress, inflammatory cascade, and caspase activation to cause hyperphosphorylation of tau protein into neurofibrillary tangles (NFTs), which ultimately lead to neuronal damage. Acetylcholine (Ach) degradation is accelerated by upstream regulation of the acetylcholinesterase (AChE) enzyme, which leads to a deficiency in neurotransmitters and cognitive impairment. There are presently no efficient or disease-modifying medications for AD. It is necessary to advance AD research to suggest novel compounds for treatment and prevention. Prospectively, it might be reasonable to conduct clinical trials with unclean medicines that have a range of effects, including anti-amyloid and anti-tau, neurotransmitter modulation, anti-neuroinflammatory, neuroprotective, and cognitive enhancement.

KEYWORDS

Alzheimer's disease, amyloid-beta, tau protein, oxidative stress, neuroinflammation, acetylcholine, mechanisms

Introduction

The deposition of aggregated amyloid-beta (Aβ) peptide is the hallmark of Alzheimer's disease (AD), a neurodegenerative disorder that progresses over time (Riyaz Basha et al., 2005). Due to changes in the brain and the formation of plaques and tangles, it has been linked to neuronal damage and death (Kehoe et al., 2009). AD is the most prevalent type of dementia, accounting for 60% to 70% of dementia cases among older people (Burns and Iliffe, 2009; Zhang et al., 2018).

AD symptoms include short-term memory loss, as well as a progressive decline in the patient's capacity for thought, judgment, problem-solving, communication, and self-care (Mount and Downton, 2006; Prasansuklab and Tencomnao, 2013). The daily life of an AD patient is also impacted by symptoms including confusion, impatience, aggression, mood swings, personality

and behavior changes, issues with attention and spatial orientation, and loss of long-term memory (Prasansuklab and Tencomnao, 2013).

The fifth-leading cause of death in persons over 65 years is AD (Winston, 2020). Over 26.6 million individuals worldwide suffer from it, and its prevalence is significantly increasing yearly (Prince et al., 2014; Olajide and Sarker, 2020). More than 106 million AD patients are anticipated to exist worldwide by 2050. The disease will affect 1 in 85 people, according to estimates (Brookmeyer et al., 2007), as the population ages and environmental factors take effect (Prince et al., 2014).

AD is a leading cause of disability and life reliance among elderly adults worldwide (Nichols et al., 2019), and has a profound influence on individuals, their families, and societies at large (Winston, 2020). The estimated cost of dementia in 2015 was $818 billion, or 1.1% of the GDP (Youssef et al., 2019). In 2020, it was anticipated that treating AD would cost $305 billion in total, and as the population ages, the amount is expected to rise to more than $1 trillion (Winston, 2020). The expense of dementia globally is predicted to reach $2 trillion by 2030 (Wimo et al., 2017). There are currently no effective or disease-modifying medications for AD (Fu et al., 2019). Many of the clinical trials failed in recent years, however, quite a number of the trials are under evaluation. It is essential to advance AD research to suggest new compounds for treatment and prevention. The objective of the current review is to describe the mechanisms behind the implications of Aβ aggregation in AD using multiple pathways. The literature data published between the years 1993 and 2020 were collected using PubMed and Scopus.

Amyloid-beta

The intracellular cleavage of the amyloid precursor protein (APP) by the proteolytic enzymes beta-(β-) secretase and gamma-(γ-) secretase produces the short peptide known as Aβ, which has 40–42 amino acids (Prasansuklab and Tencomnao, 2013). The APP is localized at neuronal synapses and is abundantly expressed in the brain (Thinakaran and Koo, 2008; O'brien and Wong, 2011). It has been linked to synaptic plasticity, cell–cell or cell-matrix interactions, neuroprotection, and regulation of neuronal cell development (Storey and Cappai, 1999).

However, aggregation of Aβ, produced from the cleavage of the amyloidogenic pathway causes neurotoxicity. Most of the body's cells, including vascular endothelial cells, thyroid epithelial cells, and neuronal and nonneuronal cultured cells, produce Aβ monomers (Schmitt et al., 1995; Fukumoto et al., 1999; Hayes et al., 2002; Kitazume et al., 2010). Although compared to other cell types, neuronal cells appear to produce more Aβ (Fukumoto et al., 1999), demonstrating the possibility that the Aβ-peptide is crucial for maintaining proper CNS physiology. According to the increased long-term potentiation (LTP) mediated by Aβ40, there is a theory that Aβ may play a crucial role in synaptic structural-functional plasticity that underlies learning and memory (Koudinov and Koudinova, 2005).

The amyloid hypothesis

According to the amyloid hypothesis, which explains why synaptic dysfunction and neurodegeneration are brought on by the aggregation of the Aβ-peptide (Van Dyck, 2018). The main contributing factor to AD is errors in the mechanisms directing Aβ formation, accumulation, or elimination. Aβ aggregation stages impair cell-to-cell communication and stimulate the immune system, which then causes inflammation and eventually kills brain cells.

Formation of amyloid-beta

The APP is processed in two distinct pathways as shown in Figure 1. Nonamyloidogenic pathway: The α-secretase enzyme first cleaves APP within the Aβ domain, and then γ-secretase cleaves at the C-terminus. Amyloidogenic pathway: Instead of α-secretase, β-secretase (BACE1) cleaves APP first at the N-terminus of the Aβ domain, and γ-secretase then cleaves it at the C-terminus. The Aβ amylogenic peptides are produced by this chain of events, which then assemble into oligomers to create extracellular neurotoxic plaques in the brain. A similar APP intracellular C-terminal domain (AICD) is released from both pathways (Thinakaran and Koo, 2008). When compared to other fragments, Aβ is chemically "stickier" than those formed by APP proteolytic processes. Small clusters (oligomers) are formed by the fragments initially, followed by chains of clusters (fibrils), and finally "mats" of fibrils (beta-sheets). The final stage is the forming of plaques which contain clusters of beta-sheets and other chemicals (Jung et al., 2010). The amyloid cascade hypothesis (ACH) explains AD pathogenesis from the outcome of two significant facts: (i) Identification of Aβ as a key component of senile plaques (SPs). (ii) Mutations of APP genes and the presenilin 1 and 2 genes (PSEN1 and PSEN2) which are typically detected at the early stage of AD. As a result, it is believed that the emergence of Aβ within SPs is caused by these mutations, which also cause dementia and neuronal cell death (Reitz, 2012).

Formation of neurofibrillary tangles

The aggregation of Aβ causes the formation of neurofibrillary tangles (NFTs) from hyperphosphorylation of tau and its accumulation into tangles is another pathological cause of AD (McGleenon et al., 2009). In normal conditions, tau supports neuronal structures and functions in the brain (Kolarova et al., 2012). However, under pathological circumstances, tau became excessively hyperphosphorylated and aggregated into fibrils known as neurofibrillary tangles. The accumulation of abnormal tau and tangles in neurons leads to neurotoxicity and neuronal degeneration (Gómez-Isla et al., 1997). In addition to the formation of NFTs, Tau phosphorylation impairs tau's ability to bind microtubules, which impacts neuronal activities such as axonal transport and mitochondrial respiration (Ittner and Götz, 2011). Microtubule depolymerization, self-aggregation, and detachment caused by tau hyperphosphorylation result in neuronal cell death (Suganthy et al., 2016).

Mechanisms of Alzheimer disease

AD pathogenesis starts from the deposition of Aβ which trigger SPs formation, followed by the death of neurons due to NFTs formation (Armstrong, 2011). Neurotoxic mechanisms in the

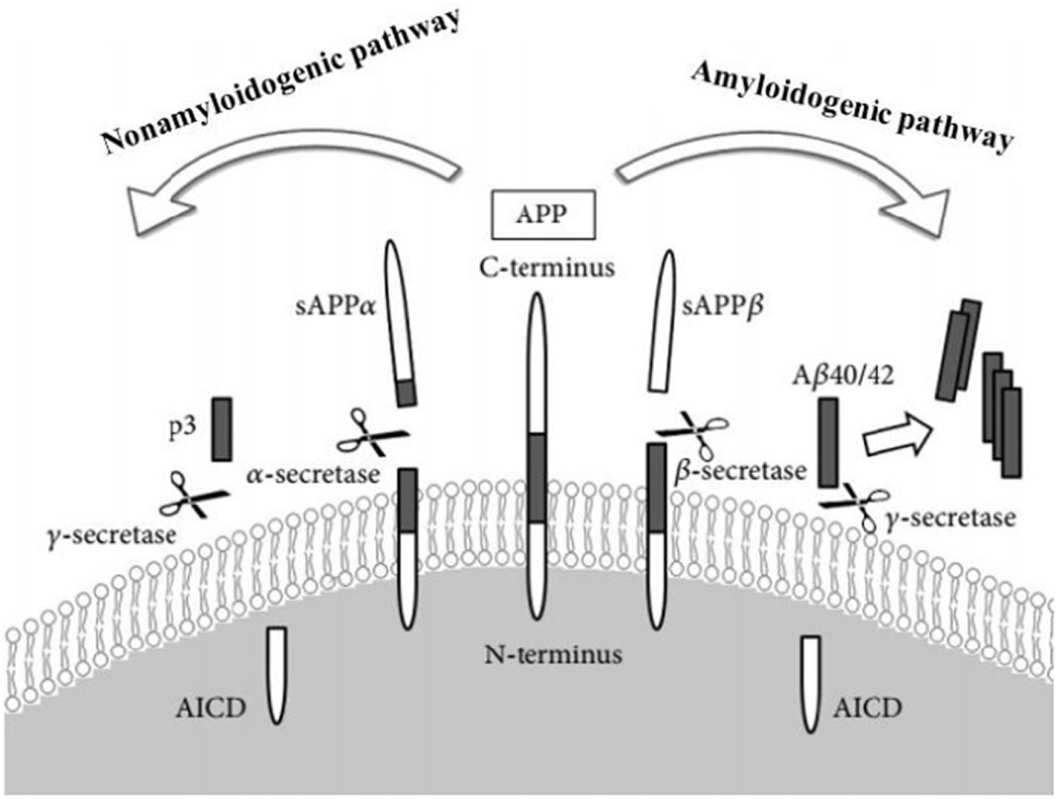

FIGURE 1
Beta-amyloid formation from the proteolytic digestion of the APP. AICD: APP intracellular C-terminal domain (Thinakaran and Koo, 2008).

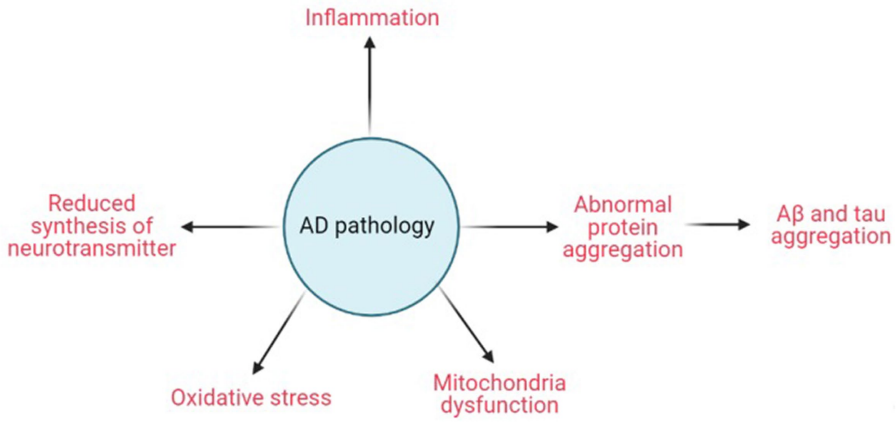

FIGURE 2
Schematic diagram of AD pathology. Created with BioRender.com.

pathology of AD include aberrant protein aggregation, dysfunction of mitochondrial, decreased neurotransmitter production, inflammation, and oxidative stress (Figure 2). However, the buildup of Aβ and the aggregation of tau are the two most prevalent etiologic models of Alzheimer's pathogenesis (Bloom, 2014).

The neuropathological events in AD patients are the result of the toxicity of amyloid oligomers and fibrils, which are from the aggregated forms of Aβ. The bodies regulate the amyloid level *via* a variety of methods as Aβ accumulates. The concentration of Aβ-peptide is controlled in healthy brain tissue by its production from APP; the influx across the blood–brain barrier (BBB) *via* its interaction with the receptor for advanced glycation end products (RAGE; Deane et al., 2003, 2009); and its clearance *via* the low-density lipoprotein receptor-related protein-1 (LRP1) from the brain and enzymatic breakdown in the brain (Selkoe, 2001; Deane et al., 2003, 2009). Additionally, the levels of Aβ affect how RAGE is expressed. RAGE is

upregulated when there is excessive Aβ synthesis, and this leads to neurotoxicity (Prasansuklab and Tencomnao, 2013) as shown in Figure 3. Thus, impairments in these regulatory processes may cause excessive Aβ-peptide to build up and deposit in the brains of AD patients. By binding to $A\beta_{12\text{-}28}$ residues, apolipoprotein E (ApoE) regulates Aβ's accumulation and lessens its clearance (Prasansuklab and Tencomnao, 2013; Zhang et al., 2018) from the brain (Sagare et al., 2007). Three isoforms of ApoE such as ApoE4 (E4), ApoE3 (E3), and ApoE2 (E2; Liu et al., 2013), regulate cholesterol levels in various ways to influence γ-secretase activity and Aβ synthesis (Osenkowski et al., 2008). According to Bales et al. (2009) and Castellano et al. (2011), the brain Aβ levels and amyloid plaque loading rely on the ApoE isoforms, demonstrating the modulatory involvement of ApoE in Aβ metabolism, aggregation, and deposition (Liu et al., 2013). The differential lipidation status exhibited by ApoE isoforms affects Aβ clearance. The ApoE particles may seize Aβ and stimulate cellular uptake and degradation of ApoE-Aβ complexes (Kim et al., 2009). Aβ clearance at the blood–brain barrier is inhibited by ApoE in an isoform-dependent manner (E4 > E3 and E2). According to studies, E4 is less effective than E3 and E2 at mediating the clearance of Aβ (Deane et al., 2008; Jiang et al., 2008).

Effects of metal ions on Aβ and tau aggregation

Strong neurotoxic candidates that alter Aβ and tau aggregation include metal dyshomeostasis (Figure 4). Metal ions' effects on the aggregation of Aβ and tau have been elucidated. Metals like Zn^{2+}, Cu^{2+}, Fe^{3+}, Mn^{2+}, Pb^{2+}, Cd^{2+}, Hg^{2+}, and Al^{3+} stimulate amyloidogenic pathways and Aβ aggregation. [red arrow] (O'brien and Wong, 2011). The neurotoxic Aβ-peptide produced by the cleavage of the APP by β- and γ-secretase is secreted into the extracellular space where it spontaneously changes into amyloid plaques. On the other hand, as seen in Figure 4A, the presence of Mg^{2+}, Fe^{2+}, and Li^{2+} inhibits the production of Aβ [blue arrow] (O'brien and Wong, 2011).

Tau hyperphosphorylation and aggregation are promoted by metal ions like Zn^{2+}, Cu^{2+}, Fe^{3+}, Mg^{2+}, Mn^{2+}, Pb^{2+}, Cd^{2+}, Hg^{2+}, and Al^{3+} [red arrow]. Numerous kinases, including glycogen synthase kinase-3 beta (GSK-3β; Rankin et al., 2007), cyclin-dependent kinase 5 (CDK-5), and others, strongly phosphorylate tau (Kimura et al., 2014). If protein phosphatase 2A (PP2A) is not activated, the hyperphosphorylation of tau may persist (Goedert, 1993). Tau that has been hyperphosphorylated forms NFTs. As depicted in Figure 4B, metal ions like Fe^{2+}, and Li^{2+}, however, lessen tau hyperphosphorylation [blue arrow].

Induction of oxidative stress by Aβ in AD

The polymeric forms of Aβ cause alterations in biochemical components and brain cell activities that lead to neuropathology associated with AD symptoms. According to reports, one of the earliest clinical manifestations of AD is increased oxidative stress. Hydrogen peroxide (H_2O_2) created due to the reduction of metal ions by Aβ-peptides served as a mediator of the oxidative stress as shown in Figure 5 (Huang et al., 1999; Atwood et al., 2003). Aβ-peptides act as powerful oxidation catalysts and can capture transition metal ions like Cu, Fe, and Zn (Miura et al., 2000). In addition, it was shown that Aβ was toxic to neuronal cultures, and Cu^{2+} ions made it more toxic

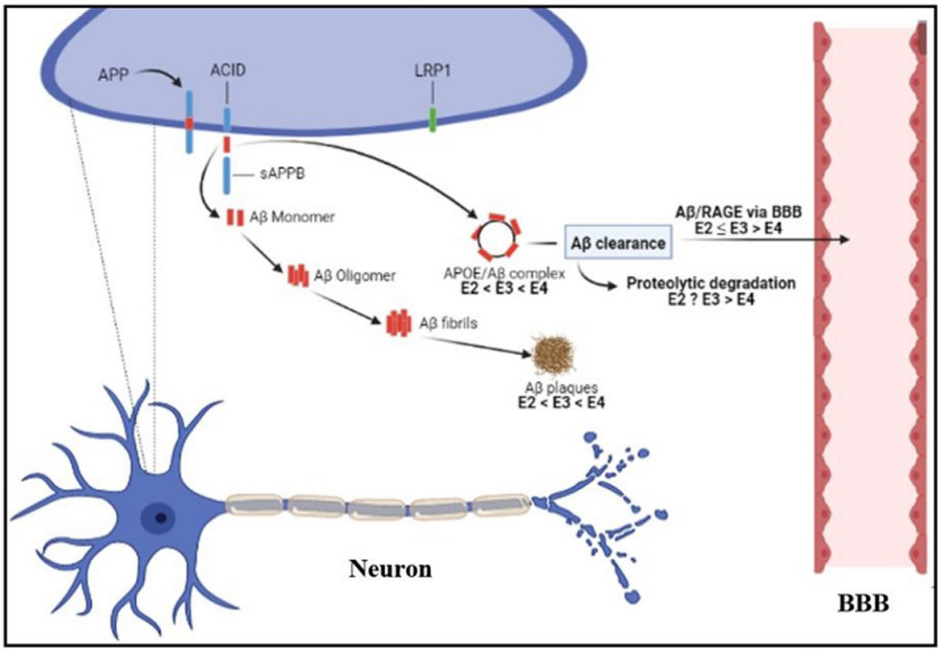

FIGURE 3
Diagrammatic representation of the regulatory systems for Aβ in an AD patient's brain. Aβ, amyloid-beta; BBB, Blood–brain barrier; RAGE, Receptor for advanced glycation end products; AICD, APP intracellular C-terminal domain; APP, Amyloid precursor protein; ApoE, apolipoprotein E; E4, ApoE; E3, ApoE3; E2, ApoE2. Created with BioRender.com.

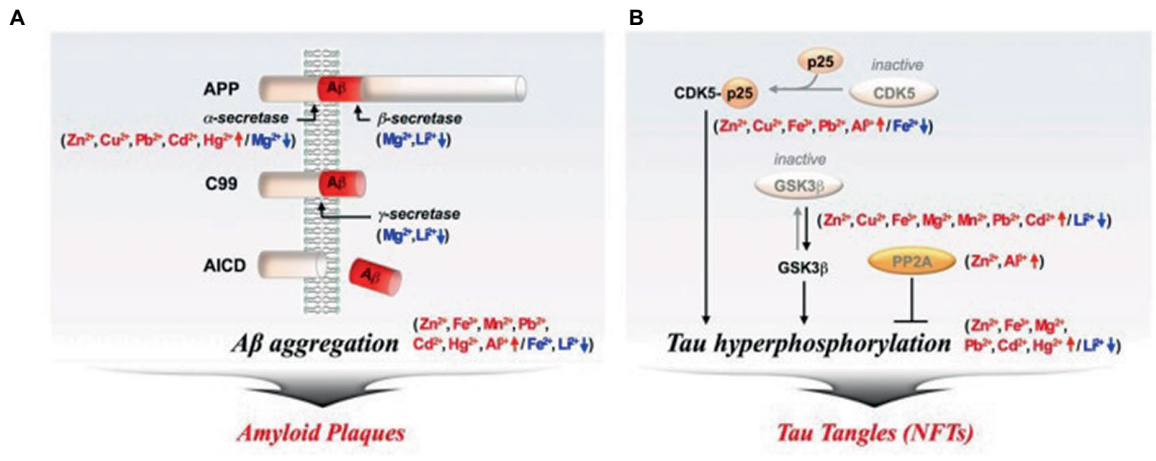

FIGURE 4
Metal ions' effects on the aggregation of Aβ and tau. **(A)** Amyloid Plaques, **(B)** Tau tangle. Aβ, amyloid-beta; CDK5, Cyclin-dependent kinase; GSK-3β, Glycogen synthase kinase-3beta; NFTs, Neurofibrillary tangles; PP2A, protein phosphatase 2A (O'brien and Wong, 2011).

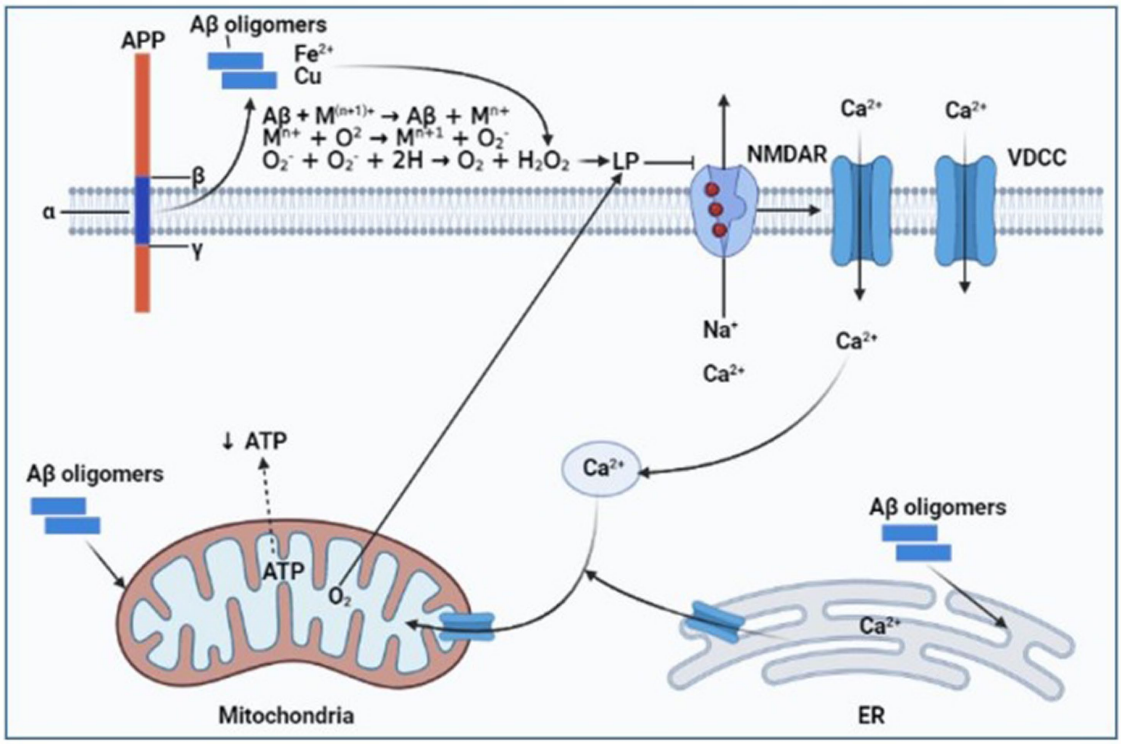

FIGURE 5
Diagram showing how Aβ and metal ions combine to cause oxidative stress in AD. Aβ, amyloid-beta; LP, Lipid peroxidation; NMDAR, N-methyl-D-aspartate receptor; VDCC, Voltage-dependent calcium channel; ER, endoplasmic reticulum; APP, Amyloid precursor protein; ATP, Adenosine triphosphate. Created with BioRender.com.

(Cuajungco et al., 2000). Reactive oxygen species can be produced by the Aβ/Cu(Fe) complexes as a toxin mediator (Huang et al., 1999). Furthermore, AD brains have an extracellular and intracellular accumulation of metal ions with high concentrations of Aβ plaques (Lovell et al., 1998; Religa et al., 2006), which produced free radicals. Because of lipid peroxidation and oxidative protein modification, several biomolecules in the AD brain experience conformational and structural changes that impair their ability to function, which, in turn, affects a variety of cellular processes (Qi et al., 2005). By upregulating the expression of the BACE1 gene, increasing oxidative stress enhances APP processing and ultimately increases Aβ generation (Tong et al., 2005; Coma et al., 2008; Quiroz-Baez et al.,

2009). This causes oxidative stress and endoplasmic reticulum (ER) stress by increasing ROS and the accompanying rise in abnormal APP and phosphorylated tau. The ER function can be severely damaged by long-term ER stress, which also causes apoptotic signaling (Ogata et al., 2006; Kouroku et al., 2007). Aβ promotes Ca^{2+} release from neurons' ER Ca^{2+} pools, increasing intracellular free Ca^{2+} (Zhou et al., 2020). Increased expression of the NR2B subunit of NMDAR causes a rise in Ca^{2+} ion concentration in extrasynaptic regions (Jusko et al., 2008), which, then increases the level of intracellular endoplasmic reticulum Ca^{2+} production (Yin et al., 1994). Studies revealed that Ca^{2+} overload could increase ER stress and facilitate mitochondrial Ca^{2+} uptake by suppressing the expression of the anti-apoptotic protein B-cell lymphoma 2 (Bcl2) and increasing the phosphorylation of extracellular regulated protein kinases (Erk) protein, which would ultimately lead to cytotoxicity and cellular apoptosis (Hajnóczky et al., 2003; Zieg et al., 2008; Zhang et al., 2018).

Induction of neuroinflammation by Aβ in AD

The expression of pro-inflammatory cytokines was increased in response to neuropathological insults induced by Aβ and its interaction with vascular RAGE (Deane et al., 2008). Microglia enhance the clearance of Aβ, but a constant generation of Aβ causes the microglia to become chronically activated, which promotes more amyloid deposition (Hickman et al., 2018). According to Kim and Choi (2015), exposure to Aβ results in microglial activation, which, in turn, causes the generation of reactive oxygen species and neurotoxic pro-inflammatory cytokines. Tau hyperphosphorylation is a result of ROS-activating p38 mitogen-activated protein kinases (p38 MAPK; Giraldo et al., 2014). p38 MAPK has been linked to neuroinflammation and AD due to its ability to activate nuclear factor-B (NF-κB; Kheiri et al., 2018), a master regulator of neuroinflammation gene transcription in the brains of AD patients (Chen et al., 2012; Liao et al., 2016; Olajide and Sarker, 2020). But data indicate that nuclear factor E2-related factor 2 (Nrf2) is negatively regulated by NF-κB (Liu et al., 2008; Kim and Vaziri, 2010; Yu et al., 2011). Substantial evidence connects the activation of the Nrf2 protection mechanism to NF-κB-mediated inflammatory actions (Nair et al., 2008; Sandberg et al., 2014). To uphold the aforementioned finding, Rojo et al. (2010) showed that cyclooxygenase-2 (COX-2), inducible nitric oxide synthases (iNOS), IL-6, and TNF-α levels are elevated when microglia are activated in Nrf2-deficient rats. Ramsey et al. (2007) first noticed this, reporting that the hippocampus of AD patients' brains had lower amounts of Nrf2 than normal. According to Lee and Kim (2017), through the activation of p38 MAPK, Aβ plaques cause neuronal impairments such as mitochondrial dysfunction, apoptosis, tau phosphorylation, and synaptic dysfunction; the primary cause of neuroinflammation in AD is increased microglial p38 MAPK signaling brought on by Aβ, which results in the production of pro-inflammatory mediators such interleukin-1β (IL-1β), tumor necrosis factor-α (TNF-α), cyclooxygenase-2 (COX-2), and inducible nitric oxide synthase (iNOS); the pathophysiology of the AD brain is worsened by the production of IL-1β from microglia, which increases p38 MAPK activation in neurons and astrocytes; Aβ plaques and IL-1β generated an increase in P38 MAPK activation in astrocytes. By releasing iNOS, COX-2, and TNF-α, this activation accelerates neuroinflammation (Figure 6).

Effects of Aβ on acetylcholine in AD

As a neurotransmitter, acetylcholine (Ach) aids in the communication between nerve cells and is essential for memory and learning processes (Kihara and Shimohama, 2004; Francis, 2005). A report revealed that Alzheimer's patients have reduced amounts of Ach in their brains (Kihara and Shimohama, 2004). Ach is decreased because oxidative stress is induced and inflammatory cytokines are produced by Aβ (Esposito et al., 2006). Free radicals produced due to amyloid peptides have been shown to lower the concentration of Ach by causing cholinergic neurons in the hippocampus to degenerate (Vinod et al., 2009). Additionally, acetylcholinesterase (AChE) activity increases and deactivates acetylcholine in synaptic clefts in the vicinity of amyloid plaques (Mordn et al., 1993; Sberna et al., 1997). According to another study, the amyloid peptide inhibits the production of acetylcholine (ACh) by causing choline to seep through cell membranes (Ehrenstein et al., 1997). Ach deficiency caused cognitive impairment and ultimately AD (Parent et al., 2013; Deture and Dickson, 2019) as shown in Figure 7.

Current state of AD treatment

According to Yiannopoulou and Papageorgiou (2013), the formation of amyloid oligomers, which mediates the amyloid cascade, is primarily responsible for neurotoxicity. The main pathophysiologic pillars are oxidation, inflammation, excessive glutamate, and tau hyperphosphorylation. Anti-amyloid disease-modifying treatments (DMTs) have therefore concentrated on three main mechanisms of action (MOAs), including reducing the formation of $A\beta_{42}$, reducing the burden of Aβ-plaque, and promoting Aβ clearance (Yiannopoulou and Papageorgiou, 2020). Hence, inhibiting the formation of Aβ-peptide accumulation and tau hyperphosphorylation may be part of the treatment for AD (Mendiola-Precoma et al., 2016). Physical exercise, a healthy diet, and mental stimulation are further AD prevention strategies (Nelson and Tabet, 2015).

Compounds used in clinical trials for the treatment of AD

Acetylcholinesterase inhibitors (AChEIs), such as rivastigmine, donepezil, and galantamine, are clinically effective in increasing the availability of acetylcholine at synapses and thereby inhibiting cognitive decline in AD (Andrieu et al., 2015; Hampel et al., 2018; Cummings et al., 2019). Nevertheless, diarrhea, nausea, and vomiting are some of the typical negative effects of AChEIs on the digestive system (Yiannopoulou and Papageorgiou, 2020). Memantine, which was approved in 2003, selectively binds to open calcium channels that are controlled by NMDA receptors, inhibiting NMDA-mediated ion flux and reducing pathologically excessive glutamate levels (Yiannopoulou and Papageorgiou, 2013; Matsunaga et al., 2015; Cummings et al., 2019). Memantine also reduces the activity of glycogen synthase kinase 3β (GSK-3β), which, in turn, reduces tau phosphorylation (Prentice et al., 2015; Folch et al., 2016).

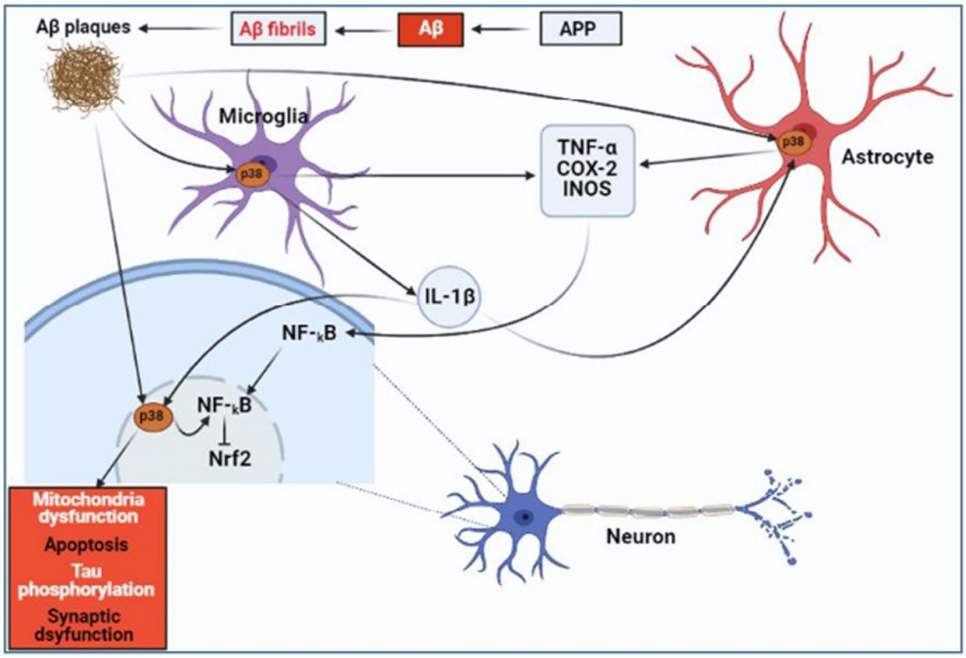

FIGURE 6
Diagrammatic representation of how Aβ causes neuroinflammation in AD. Aβ, amyloid-beta; NF-κB, Nuclear factor-κB; p38 MAPK, p38 Mitogen-activated protein kinases; Nrf2, Nuclear factor E2-related factor 2; IL-1β, Interleukin-1β; TNF-α, Tumor necrosis factor-α; COX-2, Cyclooxygenase-2; and iNOS, Inducible nitric oxide synthase (Schnöder et al., 2016; Lee and Kim, 2017). Created with BioRender.com.

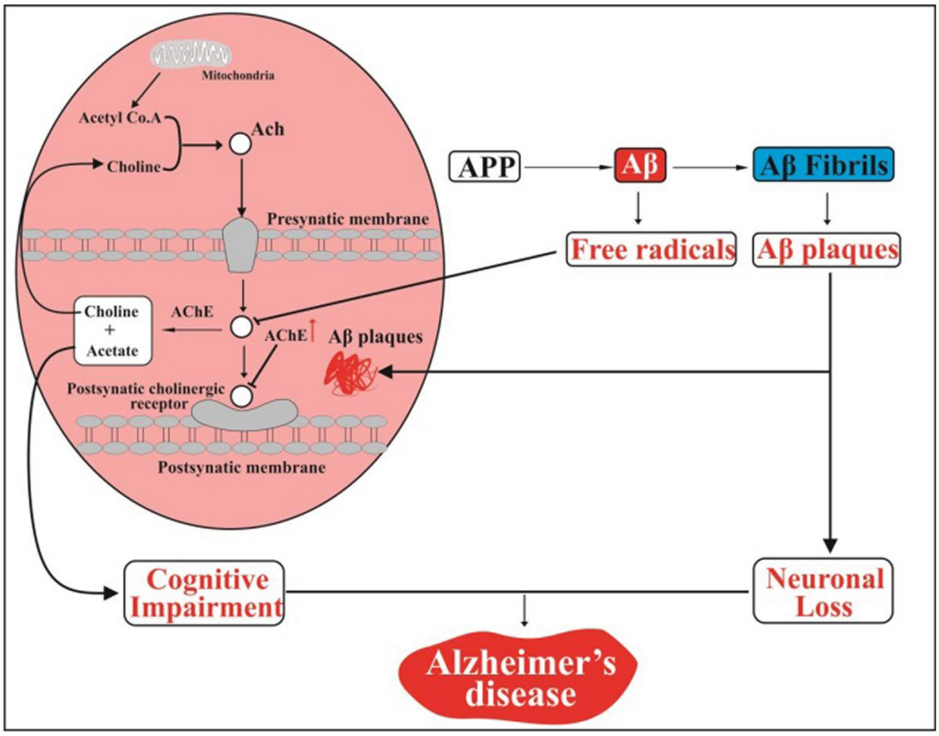

FIGURE 7
Aβ and acetylcholine interactions in an AD schematic diagram. APP, Amyloid precursor protein; Aβ, Amyloid-beta; Ach, acetylcholine; AChE, acetylcholinesterase (DeTure and Dickson, 2019). Created with BioRender.com.

Despite extensive and expensive trials, the Food and Drug Administration (FDA) has not approved any DMTs or new medications for AD since 2003 (Anderson et al., 2017; Hukins et al., 2019). The β-secretase (BACE) inhibitors, lanabecestat (Burki, 2018), verubecestat (Egan et al., 2019), and atabecestat (Henley et al., 2019), as well as the anti-amyloid agents such as semagacestat (Doody et al., 2013), bapineuzumab (Vandenberghe et al., 2016), and solanezumab (Neurology, 2016), failed in recent phase 3 clinical trials. The acknowledged explanations for the numerous failures include inadequate understanding of the pathophysiology, inappropriate drug doses, late therapies in disease progression, and wrong therapeutic targets (Gauthier et al., 2016).

Conclusion

The current review explained the molecular mechanisms of Aβ mediating AD *via* multiple events, including Aβ production and accumulation, tau hyperphosphorylation, metal dyshomeostasis, oxidative stress, neuroinflammation, and inhibition of acetylcholine production. There are presently no efficient or disease-modifying medications for AD. Some of the clinical trials targeting the above events failed in recent years, however, quite a number of the trials are under evaluation. It is necessary to advance AD research to suggest novel compounds for treatment and prevention. Prospectively, it might be reasonable to conduct clinical trials with unclean medicines that have a range of effects, including anti-amyloid, anti-tau, neurotransmitter modulation, anti-neuroinflammatory, neuroprotective, and cognitive enhancement.

Author contributions

MI wrote the manuscript. SM, SO, and AI edited, approved, and concluded the manuscript. All authors contributed to the article and approved the submitted version.

Acknowledgments

We acknowledge Musa Mustapha's advice. Biorender (https://biorender.com) was used to create some of the manuscript's figures. Additionally, we give credit to the creators of some of the figures included in this manuscript.

Conflict of interest

The authors declare that the research was conducted in the absence of any commercial or financial relationships that could be construed as a potential conflict of interest.

Publisher's note

References

Anderson, R. M., Hadjichrysanthou, C., Evans, S., and Wong, M. M. (2017). Why do so many clinical trials of therapies for Alzheimer's disease fail? *Lancet* 390, 2327–2329. doi: 10.1016/S0140-6736(17)32399-1

Andrieu, S., Coley, N., Lovestone, S., Aisen, P. S., and Vellas, B. (2015). Prevention of sporadic Alzheimer's disease: lessons learned from clinical trials and future directions. *Lancet Neurol.* 14, 926–944. doi: 10.1016/S1474-4422(15)00153-2

Armstrong, R. A. (2011). The pathogenesis of alzheimer's disease: A reevaluation of the "amyloid cascade hypothesis". *Int. J. Alzheimers Dis.* 2011, 1–6. doi: 10.4061/2011/630865

Atwood, C. S., Obrenovich, M. E., Liu, T., Chan, H., Perry, G., Smith, M. A., et al. (2003). Amyloid-β: A chameleon walking in two worlds: A review of the trophic and toxic properties of amyloid-β. *Brain Res. Rev.* 43, 1–16. doi: 10.1016/S0165-0173(03)00174-7

Bales, K. R., Liu, F., Wu, S., Lin, S., Koger, D., DeLong, C., et al. (2009). Human APOE isoform-dependent effects on brain β-amyloid levels in PDAPP transgenic mice. *J. Neurosci.* 29, 6771–6779. doi: 10.1523/JNEUROSCI.0887-09.2009

Bloom, G. S. (2014). Amyloid-β and tau: the trigger and bullet in Alzheimer's disease pathogenesis. *JAMA Neurol.* 71, 505–508. doi: 10.1001/jamaneurol.2013.5847

Brookmeyer, R., Johnson, E., Ziegler-Graham, K., and Arrighi, H. M. (2007). Forecasting the global burden of Alzheimer's disease. *Alzheimers Dement.* 3, 186–191. doi: 10.1016/j.jalz.2007.04.381

Burki, T. (2018). Alzheimer's disease research: the future of BACE inhibitors. *Lancet* 391:2486. doi: 10.1016/S0140-6736(18)31425-9

Burns, A., and Iliffe, S. (2009). Alzheimer's disease. *BMJ* 338, 467–471. doi: 10.1136/bmj.b158

Castellano, J. M., Kim, J., Stewart, F. R., Jiang, H., DeMattos, R. B., Patterson, B. W., et al. (2011). Human apoE isoforms differentially regulate brain amyloid-β peptide clearance. *Sci. Transl. Med.* 3:89ra57. doi: 10.1126/scitranslmed.3002156

Chen, C. H., Zhou, W., Liu, S., Deng, Y., Cai, F., Tone, M., et al. (2012). Increased NF-κB signalling up-regulates BACE1 expression and its therapeutic potential in Alzheimer's disease. *Int. J. Neuropsychopharmacol.* 15, 77–90. doi: 10.1017/S1461145711000149

Coma, M., Guix, F. X., Ill-Raga, G., Uribesalgo, I., Alameda, F., Valverde, M. A., et al. (2008). Oxidative stress triggers the amyloidogenic pathway in human vascular smooth muscle cells. *Neurobiol. Aging* 29, 969–980. doi: 10.1016/j.neurobiolaging.2007.01.009

Cuajungco, M. P., Goldstein, L. E., Nunomura, A., Smith, M. A., Lim, J. T., Atwood, C. S., et al. (2000). Evidence that the β-amyloid plaques of Alzheimer's disease represent the redox-silencing and entombment of Aβ by zinc. *J. Biol. Chem.* 275, 19439–19442. doi: 10.1074/jbc.C000165200

Cummings, J., Lee, G., Ritter, A., Sabbagh, M., and Zhong, K. (2019). Alzheimer' s disease drug development pipeline: 2019. *Alzheimers Dement.* 5, 272–293. doi: 10.1016/j.trci.2019.05.008

Deane, R., Bell, R. D., Sagare, A., and Zlokovic, B. V. (2009). Clearance of amyloid-β peptide across the blood-brain barrier: implication for therapies in Alzheimer's disease. *CNS Neurol. Disord. Drug Targets* 8, 16–30. doi: 10.2174/187152709787601867

Deane, R., du Yan, S., Submamaryan, R. K., LaRue, B., Jovanovic, S., Hogg, E., et al. (2003). RAGE mediates amyloid-β peptide transport across the blood-brain barrier and accumulation in brain. *Nat. Med.* 9, 907–913. doi: 10.1038/nm890

Deane, R., Sagare, A., Hamm, K., Parisi, M., Lane, S., Finn, M. B., et al. (2008). apoE isoform-specific disruption of amyloid β peptide clearance from mouse brain. *J. Clin. Investig.* 118, 4002–4013. doi: 10.1172/JCI36663

Deture, M. A., and Dickson, D. W. (2019). The neuropathological diagnosis of Alzheimer's disease. *Mol. Neurodegener.* 14, 32–18. doi: 10.1186/s13024-019-0333-5

Doody, R. S., Raman, R., Farlow, M., Iwatsubo, T., Vellas, B., Joffe, S., et al. (2013). A phase 3 trial of Semagacestat for treatment of Alzheimer's disease. *N. Engl. J. Med.* 369, 341–350. doi: 10.1056/nejmoa1210951

Egan, M. F., Kost, J., Tiffini Voss, M. D., Yuki Mukai, M. D., Paul, S., Aisen, M. D., et al. (2019). Randomized trial of Verubecestat for prodromal Alzheimer's disease. *N. Engl. J. Med.* 380, 1408–1420. doi: 10.1056/NEJMoa1812840.Randomized

Ehrenstein, G., Galdzicki, Z., and Lange, G. D. (1997). The choline-leakage hypothesis for the loss of acetylcholine in Alzheimer's disease. *Biophys. J.* 73, 1276–1280. doi: 10.1016/S0006-3495(97)78160-8

Esposito, L., Raber, J., Kekonius, L., Yan, F., Yu, G. Q., Bien-Ly, N., et al. (2006). Reduction in mitochondrial superoxide dismutase modulates Alzheimer's disease-like pathology and accelerates the onset of behavioral changes in human amyloid precursor protein transgenic mice. *J. Neurosci.* 26, 5167–5179. doi: 10.1523/JNEUROSCI.0482-06.2006

Folch, J., Petrov, D., Ettcheto, M., Abad, S., Sánchez-López, E., García, M. L., et al. (2016). Current research therapeutic strategies for Alzheimer's disease treatment. *Neural Plast.* 63, 390–401. doi: 10.1016/0012-1606(78)90143-4

Francis, P. T. (2005). The interplay of neurotransmitters in Alzheimer's disease. *CNS Spectr.* 10, 6–9. doi: 10.1017/s1092852900014164

Fu, W. Y., Wang, X., and Ip, N. Y. (2019). Targeting neuroinflammation as a therapeutic strategy for Alzheimer's disease: mechanisms, drug candidates, and new opportunities. *ACS Chem. Nerosci.* 10, 872–879. doi: 10.1021/acschemneuro.8b00402

Fukumoto, H., Tomita, T., Matsunaga, H., Ishibashi, Y., Saido, T. C., and Iwatsubo, T. (1999). Primary cultures of neuronal and non-neuronal rat brain cells secrete similar proportions of amyloid β peptides ending at Aβ40 and Aβ42. *Neuroreport* 10, 2965–2969. doi: 10.1097/00001756-199909290-00017

Gauthier, S., Albert, M., Fox, N., Goedert, M., Kivipelto, M., Mestre-Ferrandiz, J., et al. (2016). Why has therapy development for dementia failed in the last two decades? *Alzheimers Dement.* 12, 60–64. doi: 10.1016/j.jalz.2015.12.003

Giraldo, E., Lloret, A., Fuchsberger, T., and Viña, J. (2014). Aβ and tau toxicities in Alzheimer's are linked via oxidative stress-induced p38 activation: protective role of vitamin E. *Redox Biol.* 2, 873–877. doi: 10.1016/j.redox.2014.03.002

Goedert, M. (1993). Tau protein and the neurofibrillary pathology of Alzheimer's disease. *Trends Neurosci.* 16, 460–465. doi: 10.1016/0166-2236(93)90078-Z

Gómez-Isla, T., Hollister, R., West, H., Mui, S., Growdon, J. H., Petersen, R. C., et al. (1997). Neuronal loss correlates with but exceeds neurofibrillary tangles in Alzheimer's disease. *Ann. Neurol.* 41, 17–24. doi: 10.1002/ana.410410106

Hajnóczky, G., Davies, E., and Madesh, M. (2003). Calcium signaling and apoptosis. *Biochem. Biophys. Res. Commun.* 304, 445–454. doi: 10.1016/S0006-291X(03)00616-8

Hampel, H., Mesulam, M., Cuello, A. C., Farlow, M. R., Giacobini, E., Grossberg, G. T., et al. (2018). The cholinergic system in the pathophysiology and treatment of Alzheimer's disease. *Brain* 141, 1917–1933. doi: 10.1093/brain/awy132

Hayes, G. M., Howlett, D. R., and Griffin, G. E. (2002). Production of β-amyloid by primary human Foetal mixed brain cell cultures and its modulation by exogenous soluble β-amyloid. *Neuroscience* 113, 641–646. doi: 10.1016/S0306-4522(02)00191-4

Henley, D., Raghavan, N., Sperling, R., Aisen, P., Raman, R., and Romano, G. (2019). Preliminary results of a trial of Atabecestat in preclinical Alzheimer's disease. *N. Engl. J. Med.* 380, 1483–1485. doi: 10.1056/NEJMc1813435

Hickman, S., Izzy, S., Sen, P., Morsett, L., and El Khoury, J. (2018). Microglia in neurodegeneration. *Nat. Neurosci.* 21, 1359–1369. doi: 10.1038/s41593-018-0242-x

Huang, X., Cuajungco, M. P., Atwood, C. S., Hartshorn, M. A., Tyndall, J. D. A., Hanson, G. R., et al. (1999). Cu(II) potentiation of Alzheimer aβ neurotoxicity. Correlation with cell-free hydrogen peroxide production and metal reduction. *J. Biol. Chem.* 274, 37111–37116. doi: 10.1074/jbc.274.52.37111

Hukins, D., Macleod, U., and Boland, J. W. (2019). Identifying potentially inappropriate prescribing in older people with dementia: a systematic review. *Eur. J. Clin. Pharmacol.* 75, 467–481. doi: 10.1007/s00228-018-02612-x

Ittner, L. M., and Götz, J. (2011). Amyloid-β and tau—A toxic pas de deux in Alzheimer's disease. *Nat. Rev. Neurosci.* 12, 67–72. doi: 10.1038/nrn2967

Jiang, Q., Lee, C. Y. D., Mandrekar, S., Wilkinson, B., Cramer, P., Zelcer, N., et al. (2008). ApoE promotes the proteolytic degradation of Aβ. *Neuron* 58, 681–693. doi: 10.1016/j.neuron.2008.04.010

Jung, S. H., Murphy, E. A., McClellan, J. L., Carmichael, M. D., and Davis, J. M. (2010). The dietary flavonoid quercetin decreases neuroinflammation in a mouse model of Alzheimer's disease. *FASEB J.* 24:604.17. doi: 10.1096/FASEBJ.24.1_SUPPLEMENT.604.17

Jusko, T. A., Henderson, C. R., Lanphear, B. P., Cory-Slechta, D. A., Parsons, P. J., and Canfield, R. L. (2008). Blood lead concentration <10 μg/dL and child intelligence at 6 years of age. *Environ. Health Perspect.* 116, 243–248. doi: 10.1289/ehp.10424

Kehoe, P. G., Miners, S., and Love, S. (2009). Angiotensins in Alzheimer's disease—friend or foe? *Trends Neurosci.* 32, 619–628. doi: 10.1016/j.tins.2009.07.006

Kheiri, G., Dolatshahi, M., Rahmani, F., and Rezaei, N. (2018). Role of p38/MAPKs in Alzheimer's disease: implications for amyloid beta toxicity targeted therapy. *Rev. Neurosci.* 30, 9–30. doi: 10.1515/REVNEURO-2018-0008

Kihara, T., and Shimohama, S. (2004). Alzheimer's disease and acetylcholine receptors. *Acta Neurobiol. Exp.* 64, 99–105.

Kim, J., Basak, J. M., and Holtzman, D. M. (2009). The role of Apolipoprotein E in Alzheimer's disease. *Neuron* 63, 287–303. doi: 10.1016/j.neuron.2009.06.026

Kim, E. K., and Choi, E. J. (2015). Compromised MAPK signaling in human diseases: an update. *Arch. Toxicol.* 89, 867–882. doi: 10.1007/S00204-015-1472-2

Kim, H. J., and Vaziri, N. D. (2010). Contribution of impaired Nrf2-Keap1 pathway to oxidative stress and inflammation in chronic renal failure. *Am. J. Physiol. Renal Physiol.* 298, F662–F671. doi: 10.1152/ajprenal.00421.2009

Kimura, T., Whitcomb, D. J., Jo, J., Regan, P., Piers, T., Heo, S., et al. (2014). Microtubule-associated protein tau is essential for long-term depression in the hippocampus. *Philosoph Transac R Soc B Biol Sci* 369:20130144. doi: 10.1098/rstb.2013.0144

Kitazume, S., Tachida, Y., Kato, M., Yamaguchi, Y., Honda, T., Hashimoto, Y., et al. (2010). Brain endothelial cells produce amyloid β from amyloid precursor protein 770 and preferentially secrete the O-glycosylated form. *J. Biol. Chem.* 285, 40097–40103. doi: 10.1074/jbc.M110.144626

Kolarova, M., García-Sierra, F., Bartos, A., Ricny, J., and Ripova, D. (2012). Structure and pathology of tau protein in Alzheimer's disease. *Int. J. Alzheimers Dis.* 2012, 1–13. doi: 10.1155/2012/731526

Koudinov, A. R., and Koudinova, N. V. (2005). Cholesterol homeostasis failure as a unifying cause of synaptic degeneration. *J. Neurol. Sci.* 229-230, 233–240. doi: 10.1016/j.jns.2004.11.036

Kouroku, Y., Fujita, E., Tanida, I., Ueno, T., Isoai, A., Kumagai, H., et al. (2007). ER stress (PERK/eIF2α phosphorylation) mediates the polyglutamine-induced LC3 conversion, an essential step for autophagy formation. *Cell Death Differ.* 14, 230–239. doi: 10.1038/sj.cdd.4401984

Lee, J. K., and Kim, N. J. (2017). Recent advances in the inhibition of p38 MAPK as a potential strategy for the treatment of Alzheimer's disease. *Molecules* 22, 1–23. doi: 10.3390/molecules22081287

Liao, Y., Qi, X.-L., Cao, Y., Yu, W.-F., Ravid, R., Winblad, B., et al. (2016). Elevations in the levels of NF-κB and inflammatory chemotactic factors in the brains with Alzheimer's disease—one mechanism may involve α3 nicotinic acetylcholine receptor. *Curr. Alzheimer Res.* 13, 1290–1301. doi: 10.2174/1567205013666160703174254

Liu, C. C., Kanekiyo, T., Xu, H., and Bu, G. (2013). Apolipoprotein E and Alzheimer disease: risk, mechanisms and therapy. *Nat. Rev. Neurol.* 9, 106–118. doi: 10.1038/nrneurol.2012.263

Liu, F., Nguyen, J. L., Hulleman, J. D., Li, L., and Rochet, J. C. (2008). Mechanisms of DJ-1 neuroprotection in a cellular model of Parkinson's disease. *J. Neurochem.* 105, 2435–2453. doi: 10.1111/j.1471-4159.2008.05333.x

Lovell, M. A., Robertson, J. D., Teesdale, W. J., Campbell, J. L., and Markesbery, W. R. (1998). Copper, iron and zinc in Alzheimer's disease senile plaques. *Int. J. Surg. Pathol.* 15, 252–257. doi: 10.1177/1066896907302118

Matsunaga, S., Kishi, T., and Iwata, N. (2015). Memantine monotherapy for Alzheimer's disease:A systematic review and meta-analysis. *PLoS One* 10, 1–16. doi: 10.1371/journal.pone.0123289

McGleenon, B. M., Dynan, K. B., and Passmore, A. P. (2009). Acetylcholinesterase inhibitors and alzheimer's disease. *Encycloped Neurosci* 2, 9–13. doi: 10.1016/B978-008045046-9.01129-3

Mendiola-Precoma, J., Berumen, L. C., Padilla, K., and Garcia-Alcocer, G. (2016). Therapies for prevention and treatment of Alzheimer's disease. *Biomed. Res. Int.* 2016, 1–17. doi: 10.1155/2016/2589276

Miura, T., Suzuki, K., Kohata, N., and Takeuchi, H. (2000). Metal binding modes of Alzheimer's amyloid β-peptide in insoluble aggregates and soluble complexes. *Biochemistry* 39, 7024–7031. doi: 10.1021/bi0002479

Mordn, M. A., Mufson, E. J., G6mez-Ramos, P., and Morcillo, A. (1993). Acta Neuropathologlca regular papers Colocalization of cholinesterases with 5 amyloid protein in aged and Alzheimer's brains*. *Acta Neuropathol.* 85, 362–369. doi: 10.1007/BF00334445

Mount, C., and Downton, C. (2006). Alzheimer: progress o profit. *Nat. Med.* 12, 780–784. doi: 10.1038/nm0706-780

Nair, S., Doh, S. T., Chan, J. Y., Kong, A. N., and Cai, L. (2008). Regulatory potential for concerted modulation of Nrf2- and Nfkb1-mediated gene expression in inflammation and carcinogenesis. *Br. J. Cancer* 99, 2070–2082. doi: 10.1038/SJ.BJC.6604703

Nelson, L., and Tabet, N. (2015). Slowing the progression of Alzheimer's disease; what works? *Ageing Res. Review.* 23, 193–209. doi: 10.1016/j.arr.2015.07.002

Neurology, T. L. (2016). Solanezumab: too late in mild Alzheimer' s disease? *Lancet Neurol.* 16:97. doi: 10.1016/S1474-4422(16)30395-7

Nichols, E., Szoeke, C. E. I., Vollset, S. E., Abbasi, N., Abd-Allah, F., Abdela, J., et al. (2019). Global, regional, and national burden of Alzheimer's disease and other dementias, 1990–2016: a systematic analysis for the global burden of disease study 2016. *Lancet Neurol.* 18, 88–106. doi: 10.1016/S1474-4422(18)30403-4

O'brien, R. J., and Wong, P. C. (2011). Amyloid precursor protein processing and Alzheimer's disease. *Annu Rev Sci.* 34, 185–204. doi: 10.1146/annurev-neuro-061010-113613

Ogata, M., Hino, S., Saito, A., Morikawa, K., Kondo, S., Kanemoto, S., et al. (2006). Autophagy is activated for cell survival after endoplasmic reticulum stress. *Mol. Cell. Biol.* 26, 9220–9231. doi: 10.1128/mcb.01453-06

Olajide, O. A., and Sarker, S. D. (2020). Alzheimer's disease: natural products as inhibitors of neuroinflammation. *Inflammopharmacology* 28, 1439–1455. doi: 10.1007/s10787-020-00751-1

Osenkowski, P., Ye, W., Wang, R., Wolfe, M. S., and Selkoe, D. J. (2008). Direct and potent regulation of γ-secretase by its lipid microenvironment. *J. Biol. Chem.* 283, 22529–22540. doi: 10.1074/jbc.M801925200

Parent, M. J., Bedard, M.-A., Aliaga, A., Minuzzi, L., Mechawar, N., Soucy, J.-P., et al. (2013). Cholinergic depletion in Alzheimer's disease shown by [18F]FEOBV autoradiography. *Int J Mol Imaging* 2013, 1–6. doi: 10.1155/2013/205045

Prasansuklab, A., and Tencomnao, T. (2013). Amyloidosis in Alzheimer's disease: the toxicity of amyloid Beta (Aβ), mechanisms of its accumulation and implications of medicinal plants for therapy. *Evid. Based Complement. Alternat. Med.* 2013, 1–10. doi: 10.1155/2013/413808

Prentice, H., Modi, J. P., and Wu, J. Y. (2015). Mechanisms of neuronal protection against Excitotoxicity, endoplasmic reticulum stress, and mitochondrial dysfunction in stroke and neurodegenerative diseases. *Oxid. Med. Cell. Longev.* 2015, 1–7. doi: 10.1155/2015/964518

Prince, M., Albanese, E., Guerchet, M., and Prina, M. (2014). *World Alzheimer report 2014: Dementia and risk reduction. An Analysis of Protective and Modifiable Factors*. Alzheimers Disease International. London.

Qi, X. L., Xiu, J., Shan, K. R., Xiao, Y., Gu, R., Liu, R. Y., et al. (2005). Oxidative stress induced by beta-amyloid peptide1-42 is involved in the altered composition of cellular membrane lipids and the decreased expression of nicotinic receptors in human SH-SY5Y neuroblastoma cells. *Neurochem. Int.* 46, 613–621. doi: 10.1016/j.neuint.2005.02.007

Quiroz-Baez, R., Rojas, E., and Arias, C. (2009). Oxidative stress promotes JNK-dependent amyloidogenic processing of normally expressed human APP by differential modification of α-, β- and γ-secretase expression. *Neurochem. Int.* 55, 662–670. doi: 10.1016/j.neuint.2009.06.012

Ramsey, C. P., Glass, C. A., Montgomery, M. B., Lindl, K. A., Ritson, G. P., Chia, L. A., et al. (2007). Expression of Nrf2 in neurodegenerative diseases. *J. Neuropathol. Exp. Neurol.* 66, 75–85. doi: 10.1097/nen.0b013e31802d6da9

Rankin, C. A., Sun, Q., and Gamblin, T. C. (2007). Tau phosphorylation by GSK-3ß promotes tangle-like filament morphology. *Mol. Neurodegener.* 2, 1–14. doi: 10.1186/1750-1326-2-12

Reitz, C. (2012). Alzheimer's disease and the amyloid cascade hypothesis: A critical review. *Int. J. Alzheimers Dis.* 2012:369808. doi: 10.1155/2012/369808

Religa, D., Strozyk, D., Cherny, R. A., Volitakis, I., Haroutunian, V., Winblad, B., et al. (2006). Elevated cortical zinc in Alzheimer disease. *Neurology* 67, 69–75. doi: 10.1212/01.wnl.0000223644.08653.b5

Riyaz Basha, M., Wei, W., Bakheet, S. A., Benitez, N., Siddiqi, H. K., Ge, Y.-W., et al. (2005). The fetal basis of Amyloidogenesis: exposure to Lead and latent overexpression of amyloid precursor protein and-amyloid in the aging brain. *J. Neurosci.* 25, 823–829. doi: 10.1523/JNEUROSCI.4335-04.2005

Rojo, A. I., Innamorato, N. G., Martín-Moreno, A. M., De Ceballos, M. L., Yamamoto, M., and Cuadrado, A. (2010). Nrf2 regulates microglial dynamics and neuroinflammation in experimental Parkinson's disease. *Glia* 58, 588–598. doi: 10.1002/GLIA.20947

Sagare, A., Deane, R., Bell, R. D., Johnson, B., Hamm, K., Pendu, R., et al. (2007). Clearance of amyloid-β by circulating lipoprotein receptors. *Nat. Med.* 13, 1029–1031. doi: 10.1038/nm1635

Sandberg, M., Patil, J., D'Angelo, B., Weber A, S. G., and Mallard, C. (2014). NRF2-regulation in brain health and disease: implication of cerebral inflammation. *Neuropharmacology* 79, 298–306. doi: 10.1016/j.neuropharm.2013.11.004.NRF2-regulation

Sberna, G., Sáez-Valero, J., Beyreuther, K., Masters, C. L., and Small, D. H. (1997). The amyloid β-protein of Alzheimer's disease increases acetylcholinesterase expression by increasing intracellular calcium in embryonal carcinoma P19 cells. *J. Neurochem.* 69, 1177–1184. doi: 10.1046/j.1471-4159.1997.69031177.x

Schmitt, T. L., Steiner, E., Klingler, P., Lassmann, H., and Grubeck-Loebenstein, B. (1995). Thyroid epithelial cells produce large amounts of the Alzheimer β-amyloid precursor protein (APP) and generate potentially amyloidogenic APP fragments. *J. Clin. Endocrinol. Metab.* 8, 3513–3519.

Schnöder, L., Hao, W., Qin, Y., Liu, S., Tomic, I., Liu, X., et al. (2016). Deficiency of neuronal p38α MAPK attenuates amyloid pathology in Alzheimer disease mouse and cell models through facilitating lysosomal degradation of BACE1. *J. Biol. Chem.* 291, 2067–2079. doi: 10.1074/jbc.M115.695916

Selkoe, D. J. (2001). Clearing the brain's amyloid cobwebs. *Neuron* 32, 177–180. doi: 10.1016/S0896-6273(01)00475-5

Storey, E., and Cappai, R. (1999). The amyloid precursor protein of Alzheimer's disease and the Aβ peptide. *Neuropathol. Appl. Neurobiol.* 25, 81–97. doi: 10.1046/j.1365-2990.1999.00164.x

Suganthy, N., Devi, K. P., Nabavi, S. F., Braidy, N., and Nabavi, S. M. (2016). Bioactive effects of quercetin in the central nervous system: focusing on the mechanisms of actions. *Biomed. Pharmacother.* 84, 892–908. doi: 10.1016/j.biopha.2016.10.011

Thinakaran, G., and Koo, E. H. (2008). Amyloid precursor protein trafficking, processing, and function. *J. Biol. Chem.* 283, 29615–29619. doi: 10.1074/JBC.R800019200

Tong, Y., Zhou, W., Fung, V., Christensen, M. A., Qing, H., Sun, X., et al. (2005). Oxidative stress potentiates BACE1 gene expression and Aβ generation. *J. Neural Transm.* 112, 455–469. doi: 10.1007/s00702-004-0255-3

Van Dyck, C. H. (2018). Anti-amyloid-β monoclonal antibodies for Alzheimer's disease: pitfalls and promise. *Physiol. Behav.* 83, 311–319. doi: 10.1016/j.biopsych.2017.08.010.Anti-Amyloid-

Vandenberghe, R., Rinne, J. O., Boada, M., Katayama, S., Scheltens, P., Vellas, B., et al. (2016). Bapineuzumab for mild to moderate Alzheimer's disease in two global, randomized, phase 3 trials. *Alzheimers Res. Ther.* 8:18. doi: 10.1186/s13195-016-0189-7

Vinod, T., Kuhad, A., Bishnoi, M., and Chopra, K. (2009). Chronic treatment with tocotrienol, an isoform of vitamin E, prevents intracerebroventricular streptozotocin-induced cognitive impairment and oxidative-nitrosative stress in rats. *Pharmacol. Biochem. Behav.* 93, 183–189. doi: 10.1016/j.pbb.2009.05.009

Wimo, A., Elenn Guerchet, M., Ali, G.-C., Wu, Y.-T., Prina, A. M., Winblad, B., et al. (2017). The worldwide costs of dementia 2015 and comparisons with 2010. *Alzheimers Dement.* 13, 1–7. doi: 10.1016/j.jalz.2016.07.150

Winston, W. (2020). Economic burden of Alzheimer disease and managed care considerations. *Am. J. Manag. Care* 26, S177–S183. doi: 10.37765/AJMC.2020.88482

Yiannopoulou, K. G., and Papageorgiou, S. G. (2013). Current and future treatments for Alzheimer's disease. *Ther. Adv. Neurol. Disord.* 6, 19–33. doi: 10.1177/1756285612461679

Yiannopoulou, K. G., and Papageorgiou, S. (2020). Current and future treatments in Alzheimer disease: an update. *J. Central Nervous Syst Dis* 12, 117957352090739–117957352090712. doi: 10.1177/1179573520907397

Yin, J. C. P., Wallach, J. S., Del Vecchio, M., Wilder, E. L., Zhou, H., Quinn, W. G., et al. (1994). Induction of a dominant negative CREB transgene specifically blocks long-term memory in drosophila. *Cells* 79, 49–58. doi: 10.1016/0092-8674(94)90399-9

Youssef, E.-H. H., Wiley, R. E., Khoury, C. P., Daya, R. P., Ballard, C., Evans, A. R., et al. (2019). Tip of the iceberg: assessing the global socioeconomic costs of Alzheimer's disease and related dementias and strategic implications for stakeholders. *J. Alzheimers Dis.* 70, 323–341. doi: 10.3233/JAD-190426

Yu, M., Li, H., Liu, Q., Liu, F., Tang, L., Li, C., et al. (2011). Nuclear factor p65 interacts with Keap1 to repress the Nrf2-ARE pathway. *Cell. Signal.* 23, 883–892. doi: 10.1016/J.CELLSIG.2011.01.014

Zhang, X., Fu, Z., Meng, L., He, M., and Zhang, Z. (2018). The early events that initiate β-amyloid aggregation in Alzheimer's disease. *Front. Aging Neurosci.* 10, 1–13. doi: 10.3389/fnagi.2018.00359

Zhou, F., Du, G., Xie, J., Gu, J., Jia, Q., Fan, Y., et al. (2020). RyRs mediate lead-induced neurodegenerative disorders through calcium signaling pathways. *Sci. Total Environ.* 701:134901. doi: 10.1016/j.scitotenv.2019.134901

Zieg, J., Greer, P. L., and Greenberg, M. E. (2008). SnapShot: Ca2+-dependent transcription in neurons. *Cells* 134, 1080–1080.e2. doi: 10.1016/j.cell.2008.09.010

frontiers | Frontiers in Chemistry

TYPE Original Research
PUBLISHED 02 May 2023
DOI 10.3389/fchem.2023.1167766

OPEN ACCESS

EDITED BY
Wolfgang Hoyer,
Heinrich Heine University of Düsseldorf, Germany

REVIEWED BY
Giovanni La Penna,
National Research Council (CNR), Italy
Elias Akoury,
Lebanese American University, Lebanon

*CORRESPONDENCE
Alfonso De Simone,
alfonso.desimone@unina.it
Giuliana Fusco,
Gf203@cam.ac.uk

RECEIVED 16 February 2023
ACCEPTED 07 April 2023
PUBLISHED 02 May 2023

CITATION
Gonzalez-Garcia M, Fusco G and De Simone A (2023), Metal interactions of α-synuclein probed by NMR amide-proton exchange.
Front. Chem. 11:1167766.
doi: 10.3389/fchem.2023.1167766

Metal interactions of α-synuclein probed by NMR amide-proton exchange

Mario Gonzalez-Garcia[1], Giuliana Fusco[2]* and Alfonso De Simone[1,3]*

[1]Department of Life Sciences, Imperial College London, London, United Kingdom, [2]Centre for Misfolding Diseases, Department of Chemistry, University of Cambridge, Cambridge, United Kingdom, [3]Department of Pharmacy, University of Naples "Federico II", Naples, Italy

The aberrant aggregation of α-synuclein (αS), a disordered protein primarily expressed in neuronal cells, is strongly associated with the underlying mechanisms of Parkinson's disease. It is now established that αS has a weak affinity for metal ions and that these interactions alter its conformational properties by generally promoting self-assembly into amyloids. Here, we characterised the nature of the conformational changes associated with metal binding by αS using nuclear magnetic resonance (NMR) to measure the exchange of the backbone amide protons at a residue specific resolution. We complemented these experiments with ^{15}N relaxation and chemical shift perturbations to obtain a comprehensive map of the interaction between αS and divalent (Ca^{2+}, Cu^{2+}, Mn^{2+}, and Zn^{2+}) and monovalent (Cu^{+}) metal ions. The data identified specific effects that the individual cations exert on the conformational properties of αS. In particular, binding to calcium and zinc generated a reduction of the protection factors in the C-terminal region of the protein, whereas both Cu(II) and Cu(I) did not alter the amide proton exchange along the αS sequence. Changes in the R_2/R_1 ratios from ^{15}N relaxation experiments were, however, detected as a result of the interaction between αS and Cu^{+} or Zn^{2+}, indicating that binding to these metals induces conformational perturbations in distinctive regions of the protein. Collectively our data suggest that multiple mechanisms of enhanced αS aggregation are associated with the binding of the analysed metals.

KEYWORDS

α-synuclein, NMR, amide exchange, aggregation, metal interaction

1 Introduction

α-synuclein (αS) is an intrinsically disordered protein (IDP) that is primarily expressed in neuronal cells and whose aggregation is strongly associated with debilitating neurodegenerative diseases collectively known as synucleinopathies, which include Parkinson's disease (PD), dementia with Lewy bodies and multiple system amyotrophy (Spillantini et al., 1997; Uversky and Eliezer, 2009; Luk et al., 2012; Lashuel et al., 2013; Chiti and Dobson, 2017; Fusco et al., 2017; Newberry et al., 2020). Amyloid fibrils of αS are indeed the major constituents of aberrant inclusions, designated as Lewy bodies, forming in neurons of patients affected by PD (Lashuel et al., 2013; Lee and Masliah, 2015). There are also genetic links between synucleinopathies and αS, with a number of missense mutations, duplications and triplications of the gene encoding αS being identified in association with familial forms

of early onset PD (Singleton et al., 2003; Chartier-Harlin et al., 2004; Roberts and Brown, 2015).

In its physiological form, αS is predominantly localized at the presynaptic terminals of neurons, where it has been associated with the regulation of the homeostasis of synaptic vesicles (Auluck et al., 2010; Fusco et al., 2018), however, its exact function remains debated. It is generally believed that the biological activity of αS is inextricably linked to its ability to bind biological membranes (Snead and Eliezer, 2014). This interaction is recursively involved in the major putative neuronal roles of αS (Burre, 2015), and has been shown to promote αS aggregation (Auluck et al., 2010) and the mechanisms of neurotoxicity induced by its aggregates (Fusco et al., 2017).

A fundamental interaction of αS involves metal ions, including divalent cations such as Cu^{2+}, Mn^{2+}, Zn^{2+}, as well as Ca^{2+}. The latter divalent cation, a key messenger in neurotransmission, was also shown to alter the conformations and membrane interactions of αS (Lautenschlager et al., 2018). There is a crucial interest on the role of metals in PD as their dishomeostasis is increasingly recognised to play a critical role in the development of this disease. In addition, numerous evidences indicate that metal interactions promote aberrant aggregation of αS (Fink, 2006; Binolfi et al., 2008; Binolfi et al., 2010; Deas et al., 2016), including Ca^{2+} (Stephens et al., 2020), Mn^{2+} (Uversky et al., 2001; Verina et al., 2013), Zn^{2+} (Sato et al., 2013) and Cu^{2+} (Montes et al., 2014). αS has also been shown to interact with Cu^{+}, a binding implicated in the formation of reactive oxygen species inducing toxicity in dopaminergic neurons (Wang et al., 2010). The modes of metal binding by αS are variegated. Generally, the significant presence of negatively charged residues in the C-terminal region of αS promotes electrostatic interactions with cations, whereas His 50 and Met residues in the N-terminal region provide additional interaction loci for some metal cations (Supplementary Figure S1).

In order to understand the role of metal binding in the pathophysiology of αS it is therefore critical to characterise the subtle conformational alterations of αS associated with these interactions. It is indeed currently generally acknowledged that long-range interactions between the negatively charged C-terminus and the positively charged N-terminal region of αS promote an aggregation-resistant conformational ensemble whereby the amyloidogenic NAC region is partially protected from engaging in dangerous self-assembly and aggregation (Dedmon et al., 2005). Alterations of this conformational ensemble, such as, for example, those induced by Ca^{2+} binding at the C-terminal region, have been shown to modify the properties of αS in such a way to increase the exposure of the NAC, ultimately leading to its aggregation (Stephens et al., 2020).

The metal interaction by αS has been extensively studied using nuclear magnetic resonance (NMR) (Rasia et al., 2005; Binolfi et al., 2006; Binolfi et al., 2008; Binolfi et al., 2010; Binolfi et al., 2011; Miotto et al., 2014; Miotto et al., 2015; Villar-Pique et al., 2017; Lautenschlager et al., 2018; Gonzalez et al., 2019; Pontoriero et al., 2020), and here we applied NMR to probe the backbone protection factors of αS upon interaction with divalent (Ca^{2+}, Cu^{2+}, Mn^{2+}, and Zn^{2+}) and monovalent (Cu^{+}) metal ions. In particular, we used phase-modulated CLEAN chemical exchange (CLEANEX) to directly monitor the H-H exchange of amide protons with the solvent, as previously employed for the isolated αS (Okazaki et al., 2013), and complemented these experiments with ^{15}N relaxation to collectively probe conformational dynamics on various of timescales. The data collectively mapped the effects that individual metal ions exert on the conformational properties of αS upon binding, thereby suggesting the nature of the structural perturbations by which these metals trigger αS aggregation.

2 Materials and methods

2.1 αS expression and purification

αS was expressed in BL21 *Escherichia coli* using plasmid pT7-7 and purified as previously described following an established protocol (Fusco et al., 2016; Fusco et al., 2017). N-terminal acetylation of αS was obtained by co-expression with a plasmid encoding the components of the NatB complex (Maltsev et al., 2012). ^{15}N and/or ^{13}C-labelled αS was expressed in M9 minimal media containing 1 g/L of ^{15}N ammonium chloride and 3 g/L of ^{13}C-glucose. To enhance the N-terminal acetylation of αS, 1 g of ISOGRO® ^{15}N-^{13}C was added. The bacterial culture was supplemented with 100 μg/mL ampicillin, together with 100 μg/mL chloramphenicol for cultures coexpressing both plasmids where N-terminal acetylation was desired, and incubated at 37°C under constant shaking at 200 rpm to an OD600 of 0.6–1.0. Expression was induced through the addition of 1 mM isopropyl β-D-1-thiogalactopyranoside (IPTG) and overnight incubation under constant shaking at 28°C.

The cells were then harvested by centrifugation at 6,200 x g for 20 min at 4°C (Beckman Coulter Brea, United States), the cell pellets were resuspended in 1 M PBS and centrifuged again at 24 500 x g for 1 h at 4°C. Each pellet was then resuspended in lysis buffer (10 mM Tris-HCl pH 7.7, 1 mM EDTA and ½ of an EDTA-free complete™ protease inhibitor cocktail tablet) and lysed by sonication on ice (2 s on, 4 s off, total time 8 min). The sonicated samples where then centrifuged at 24 500 x g for 30 min at 4°C to remove the cell debris as pellets. The supernatant was then heated for 20 min at 94°C to precipitate heat-sensitive proteins. A further centrifugation step at 24 500 x g for 30 min at 4°C followed to remove the precipitated protein fraction. Subsequently, the supernatant was treated with 10 mg/mL of streptomycin sulfate to induce DNA precipitation. The solution was stirred for 15 min at 4°C and centrifuged again at 24 500 x g for 30 min at 4°C. In order to precipitate and recover αS, ammonium sulfate was slowly added to a concentration of 361 mg/mL and stirred for 30 min at 4°C. A final centrifugation step at 24 500 x g for 30 min at 4°C recovered the precipitated protein, which was then resuspended in 25 mM Tris-HCl, pH 7.7 and dialysed in the same buffer overnight at 4°C.

The dialysed solution was then loaded onto an anion exchange column (Q Sepharose HP HiScale 26/20, 6–7 cm, Cytiva) and eluted with a 0–1.5 M NaCl step gradient. The eluted fractions containing αS were concentrated using Vivaspin filter concentrators (Sartorius Stedim Biotech, Göttingen, Germany) and filtered through a 0.22 μm filter to remove any precipitates. The protein was then further purified by loading onto a size exclusion column (HiLoad 16/60 Superdex 75 pg, GE Healthcare, Little Chalfont, United Kingdom). The pooled fractions were concentrated and dialysed in 25 mM Tris-HCl, pH 7.0. Stored αS samples that had previously been dissolved in buffers containing metal ions were

dialysed three times to remove any traces of those metals. The purity of the fractions was monitored after every major purification step by SDS-PAGE and the concentration of monomeric αS determined by the absorbance at 280 nm using a molar extinction coefficient of 5960 M^{-1} cm^{-1} with a Nanodrop.

2.2 NMR setup

All NMR measurements in this study were carried out using a Bruker 800 MHz spectrometer equipped with a triple resonance HCN cryo-probe (Bruker, Coventry, United Kingdom). Residue assignment of NMR resonances was obtained from previous studies (Fusco et al., 2016; Fusco et al., 2017). ^{1}H-^{15}N spectra, including HSQC and CLEANEX, were performed using a data matrix consisting of 2048 (t2, ^{1}H) × 220 (t1, ^{15}N) complex points and 64 scans. NMR spectra were acquired using Topspin 3.6.0 (Bruker, AXS GmBH, DE) and processed with CCPNmr v2.0. In order to assess if during the NMR measurements the monomer concentration is reduced as a result of protein aggregation, ^{1}H-^{15}N-HSQC spectra were measured at the start and end of the dataset collection, showing no significant changes in the peak intensities and frequencies (Supplementary Figure S2). All the NMR spectra were recorded at 10°C using 25 mM Tris-HCl at pH 7.0.

2.3 Phase-modulated CLEAN chemical exchange NMR experiments

CLEANEX probes the chemical exchange between fast exchangeable hydrogen atoms with water (Hwang et al., 1998). This phenomenon can directly probe the solvent accessibility of specific groups of proteins (De Simone et al., 2011; Fusco et al., 2022). Measurements were recorded at 283K, a condition that allows for excellent signal to noise for the ^{1}H-^{15}N resonances in HSQC spectra of αS. CLEANEX experiments were measured using N-terminally acetylated or non-acetylated αS (415 μM) incubated with the different monovalent and divalent cations considered in this study. This NMR technique allows an estimation of the exchange rates from the slope of the linear interpolation of the intensities of amide peaks from spectra recorded at different mixing times τ_m (5, 10, 15, 20, and 25 ms). In particular, the volumes V_i of the peaks were normalized relative to those of the corresponding ^{1}H-^{15}N-HSQC peaks V_0. By plotting V_i/V_0 as a function of τ_m, k_{ex} can be defined from the slopes of the linear interpolation. The k_{ex} values were normalised with theoretical values calculated from the sequence (Connelly et al., 1993) and assuming that the peptide chain is in a random coil conformation (k_{int}) to obtain the protection factor logP from the logarithm of k_{int}/k_{ex}. This data analysis is formally applied under the EX2 regime of amide exchange, which was previously demonstrated in CLEANEX experiments of isolated αS at pH 7.0 (Okazaki et al., 2013). Calculated error bars in our data analysis represent the fitting error in the calculation of the k_{ex} for each residue.

2.4 Chemical shift perturbations (CSP) in ^{1}H-^{15}N-HSQC

^{1}H-^{15}N-HSQC spectra were measured at 283K using αS samples dissolved in 25 mM Tris-HCl, pH 7.70 and/or in combination with the monovalent and divalent cations discussed in this study. Mean weighted chemical shift (MWCS) profiles were calculated as $\sqrt{[(\Delta\delta^{1}H)^2 + (\Delta\delta^{15}N/10)^2]}$. For the intensity ($I/I_0$) and MWCS analyses, only well-resolved and unambiguously assigned HSQC peaks were utilised. Data were processed and analysed using the CCPNmr Analysis software. Resonance assignments were done as with CLEANEX measurements.

2.5 Transverse and longitudinal relaxation NMR experiments

Transverse (T2) and longitudinal (T1) ^{15}N relaxation experiments were acquired using standard pulse sequences (Farrow et al., 1994), including the watergate sequence (Piotto et al., 1992) to enhance water suppression. R_1 and R_2 values were obtained by fitting the data to an exponential decay function with single relaxation delays (τ delays: 4, 30, 70, 120, 200, 300, 400, 500, 700, 1,000 ms; τ delays: 0, 20, 40, 50, 60, 80, 100, 120, 140, 160, 170, and 200 ms). Experiments were recorded as data matrices consisting of 2048 (t_2, ^{1}H) × 220 (t_1, ^{15}N) complex points. Relaxation was measured at 283K on samples of N-terminally acetylated αS (400 μM) incubated with monovalent and divalent cations considered in this research, using a Bruker spectrometer operating at a ^{1}H frequency of 800 MHz equipped with a triple resonance HCN cryo-probe (Bruker, Coventry, United Kingdom). Resonance assignments were done as with CLEANEX measurements. Calculated error bars represent the fitting error in the calculation of the *Kex* for each residue.

2.6 Experimental procedure to obtain Cu^{+}

Copper was reduced by pre-incubation using an excess of 10 mM sodium ascorbate. Considering the concentration of 85 μM of copper used in this study, the molar ratio of copper: ascorbate was set to 1:120. The reduced copper solution, mixed with sodium ascorbate, was then added to the αS sample. A thin layer of mineral oil was added on top of the sample to prevent changes in the resonances of methionine residues arising from air oxidation effects.

3 Results

In order to investigate the subtle perturbations that metal ions exert on the conformational properties of αS, we employed biomolecular NMR to elucidate the nature of the weak binding with Ca^{2+}, Zn^{2+}, Cu^{+}, Cu^{2+}, and Mn^{2+}. Our approach was based on a comprehensive analysis of the metal interactions by αS, including the map of the transient protein-metal contacts, through chemical shift perturbations (CSP) in the ^{1}H-^{15}N-HSQC spectra, and the effects of the binding on slow (millisecond timescale) and fast (nanosecond timescale) protein dynamics, respectively probed using CLEANEX-PM and ^{15}N relaxation spectra. The results indicate that the modes of binding between these metals and αS can be markedly different, including the protein regions involved in the interactions and the consequent perturbations in the conformational ensemble of αS.

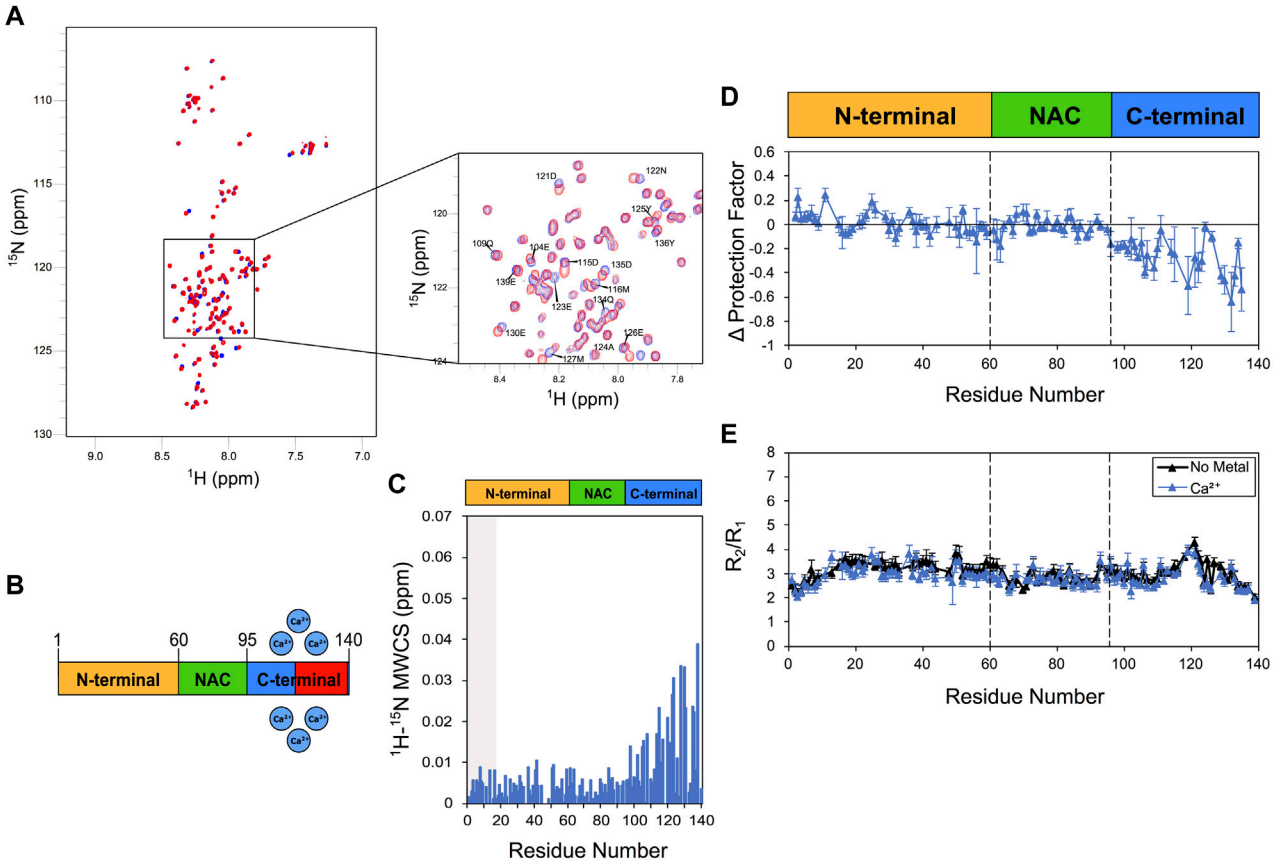

FIGURE 1
NMR analysis of Ca^{2+} binding to αS. Experiments were performed at 10°C in 25 mM Tris buffer and a pH of 7.0, and using concentrations of αS and Ca^{2+} of 415 μM and 10 mM, respectively. **(A)** ^{1}H-^{15}N HSQC spectra of αS in the presence (blue) and absence (red) of calcium. **(B)** Schematic depicting Ca^{2+} binding by αS. Red regions in the scheme indicate major CSP along the αS sequence upon metal binding. **(C)** Mean weighted CSP (^{1}H-^{15}N MWCS) of αS as a result of the calcium binding. The grey box denotes the first 15 residues of the protein. **(D)** Alteration in the LogP values of αS as a result of Ca^{2+} binding as measured in CLEANEX experiments (Supplementary Figures S5, S6). These values are calculated for each αS residue as the logP of the metal bound state minus the logP of the isolated protein state. **(E)** R_2/R_1 values from ^{15}N relaxation data of αS in the presence (blue) and absence (black) of calcium (raw data in Supplementary Figure S7). Error bars are calculated from the fitting errors in R_1 and R_2 measurements. Dotted lines delineate the different regions (N-terminal, NAC and C-terminal) along the sequence of αS.

3.1 Calcium interaction

We first employed the combination of CSP, CLEANEX-PM and ^{15}N relaxation to analyse the calcium binding by αS (Figure 1). In agreement with previous studies (Lautenschlager et al., 2018; Stephens et al., 2020), Ca^{2+} was found to induce CSP in the acidic C-terminus of αS under the present experimental conditions (Figure 1). This binding is mediated by Asp and Glu residues that are abundant in the region 110–140 (Supplementary Figure S1). In order to sample slow protein motions, we measured amide exchange protection factors through CLEANEX NMR. These experiments revealed high LogP values in correspondence of the C-terminal region of the isolated αS (Supplementary Figure S3), an observation that is in line with previous NMR studies (Okazaki et al., 2013) as well as orthogonal measurements of mass spec (Stephens et al., 2020). This pattern of C-terminal protection, which is conserved in both N-terminally acetylated and non-acetylated forms of αS (Supplementary Figure S3), has been ascribed to the local concentration of negative charges in the αS sequence (Okazaki et al., 2013). In the presence of calcium, CLEANEX revealed alterations of the protection factors of αS, primarily in correspondence of the C-terminal region of the protein where reductions up to 0.6 in LogP values were observed. These data are in apparent contrast with previous mass spec analyses (Stephens et al., 2020; Seetaloo et al., 2022), likely due to differences in the timescales of the exchange process probed by the two techniques. Both experiments, however, provide converging indication that calcium binding disrupts the electrostatically driven transient interactions between the N-terminal and C-terminal regions of αS, which were observed using NMR paramagnetic relaxation enhancement (Dedmon et al., 2005).

To further study the Ca^{2+} interaction by αS, we then employed ^{15}N-relaxation. The data showed no significant alterations in the R_2/R_1 values upon calcium binding, including residues of the C-terminal region (Figure 1E), suggesting that the metal interaction induces no specific conformational exchange in the intermediate NMR timescale. We noted a slight increase in the longitudinal relaxation rates (R_1) in correspondence of the C-terminal region of αS (residues 105–140), which is consistent with the region showing the strongest CSP and LogP

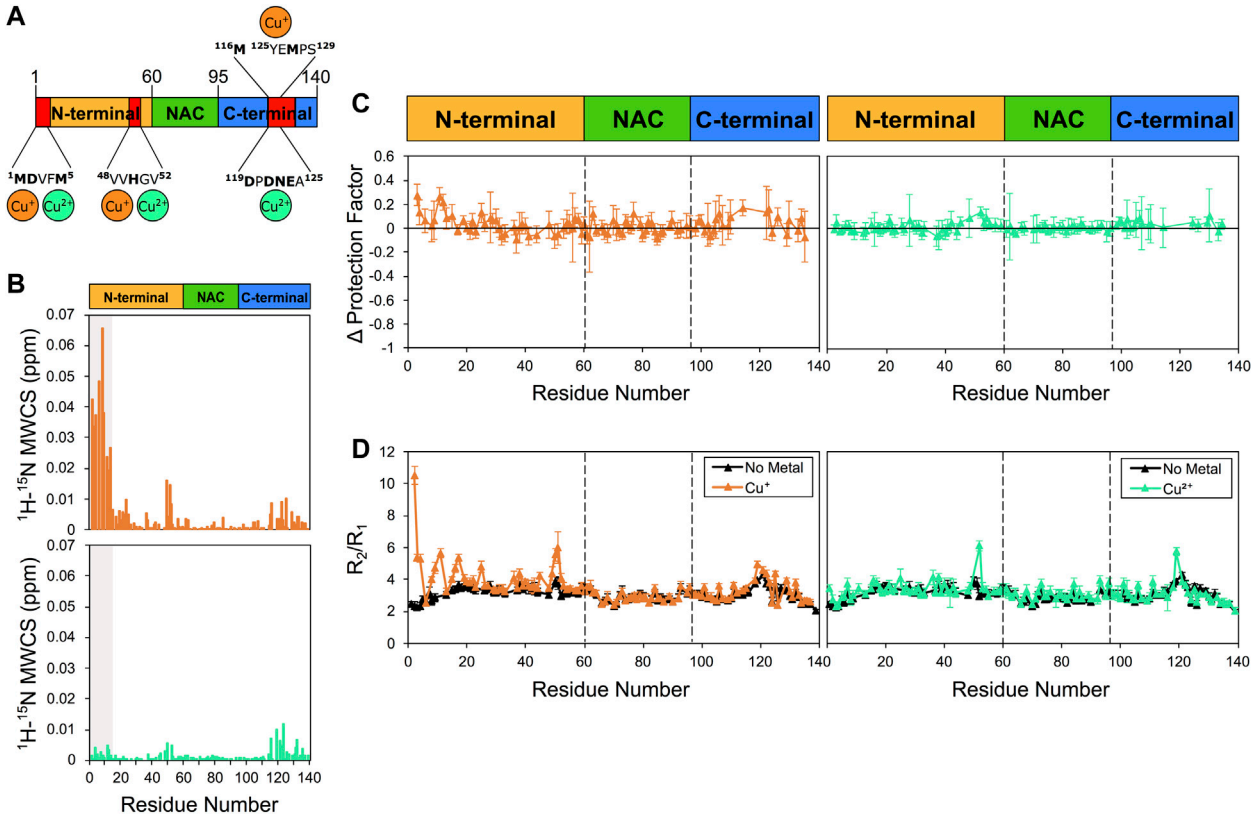

FIGURE 2
NMR analysis of copper binding to αS. Experiments were performed at 10°C in 25 mM Tris buffer and a pH of 7.0, and using concentrations of αS and Cu^{+} (or Cu^{2+}) of 415 μM and 85 μM, respectively. **(A)** Schematic depicting Cu^{+} and Cu^{2+} binding by αS. Red regions in the scheme indicate major CSP along the αS sequence upon metal binding. **(B)** Mean weighted CSP (^{1}H-^{15}N MWCS) of αS as a result of the copper binding. Top and bottom panels for Cu^{+} and Cu^{2+} binding, respectively. The grey boxes denote the first 15 residues of the protein. **(C)** Alteration in the LogP values of αS as a result of copper binding. Left and right panels for Cu^{+} and Cu^{2+} binding, respectively. These values are calculated for each αS residue as the logP of the metal bound state minus the logP of the isolated protein state. **(D)** R_2/R_1 values from ^{15}N relaxation data of αS in the presence of Cu^{+} (orange, left panel), Cu^{2+} (green, right panel) and in the isolated protein (black) (raw data in Supplementary Figure S7). Error bars are calculated from the fitting errors in R_1 and R_2 measurements. Dotted lines delineate the different regions (N-terminal, NAC, and C-terminal) along the sequence of αS.

reductions upon calcium interaction. Taken together these data indicate that calcium binding perturbs the conformational ensemble of αS by reducing LogP values in the C-terminal region, a result that is compatible with a destabilization of the transient interaction between N- and C- terminal regions of αS.

3.2 Copper binding

We then studied the αS/copper binding, a relevant interaction in the context of synucleionpathies (Rasia et al., 2005; Sung et al., 2006; Miotto et al., 2015). For these experiments, in order to reduce broadening of the NMR resonances due to paramagnetic effects, we employed a 1:5 ratio of copper:αS (85 μM: 415 μM), and maintained this ratio for both Cu^{+} and Cu^{2+} analyses. In the case of Cu^{+}, in order to ensure the optimal oxidation state of copper, we used an excess of sodium ascorbate (see Section 2). The latter was found to induce no conformational changes in αS, as the ^{1}H-^{15}N HSQC of the protein resulted unperturbed in the presence of the reducing agent. By contrast, the presence of Cu^{+} and Cu^{2+} was found to induce considerable CSP to the ^{1}H-^{15}N HSQC spectrum of αS, particularly in three regions of the protein sequence that include the N-terminus, the residues flanking His50, and the C-terminus (Figure 2). The strongest effects were observed in the case of Cu^{+}, and particularly in correspondence of the N-terminal 13 residues of αS. Despite the considerable levels of CSP, no significant alterations of the protection factors of αS were detected upon copper interaction (Figure 2C). More specifically, only a slight increase in the protection factors at the N-terminus of αS upon Cu^{+} binding was observed up to a value of +0.3 in LogP, whereas binding of Cu^{2+} did not induce any significant change in the measured protection factors of the protein. While monomer depletion was not observed during the present measurements (Supplementary Figure S2), indicating that no significant aggregation occurred during the data acquisition, it is possible that dimerization events induced by Cu^{+} (Abeyawardhane et al., 2018) may have contributed to the changes in the measured protection factors.

When analysing the ^{15}N relaxation of αS upon the interaction with copper, we observed a strong increase in R_2/R_1 values in some protein regions in the presence of Cu^{+} (Figure 2D). These changes in R_2/R_1 values, which resulted particularly evident in correspondence of the

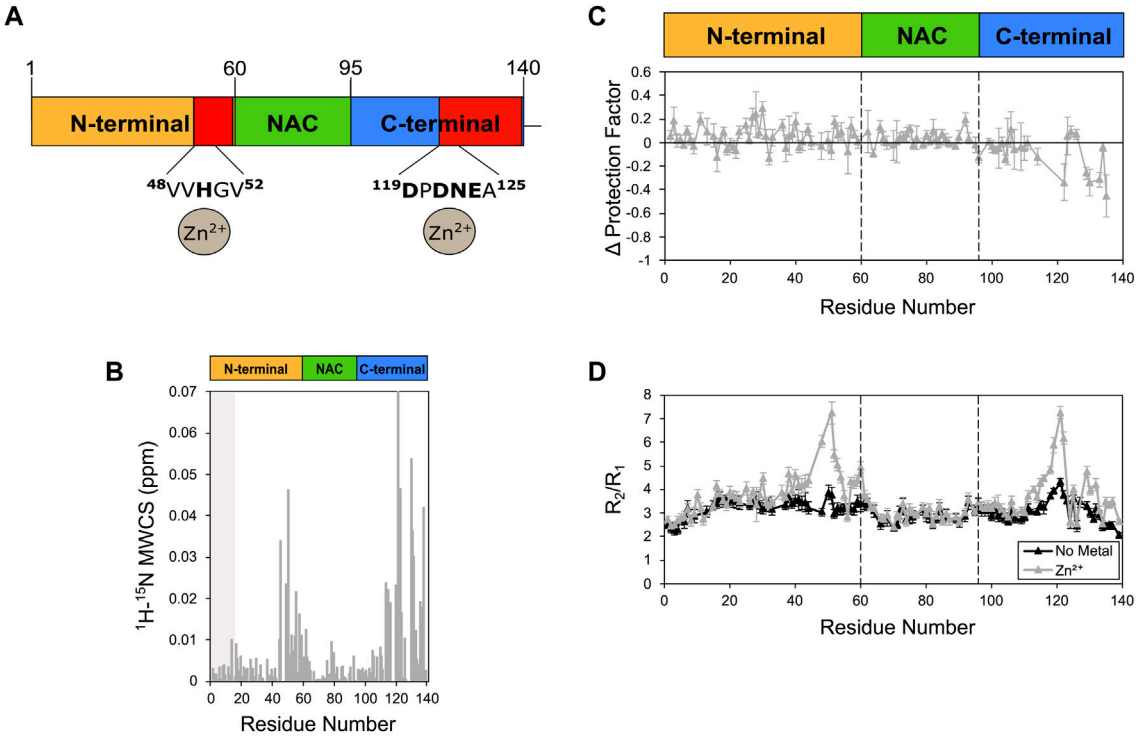

FIGURE 3
NMR analysis of Zn^{2+} binding to αS. **(A)** Schematic depicting Zn^{2+} binding by αS. Red regions in the scheme indicate major CSP along the αS sequence upon metal binding. **(B)** Mean weighted CSP (^{1}H-^{15}N MWCS) of αS as a result of the zinc binding. The grey box denotes the first 15 residues of the protein. **(C)** Alteration in the LogP values of αS as a result of Zn^{2+} binding. These values are calculated for each αS residue as the logP of the metal bound state minus the logP of the isolated protein state. **(D)** R_2/R1 values from ^{15}N relaxation data of αS in the presence (gray) and absence (black) of zinc (raw data in Supplementary Figure S8). Error bars are calculated from the fitting errors in R_1 and R_2 measurements. Dotted lines delineate the different regions (N-terminal, NAC, and C-terminal) along the sequence of αS. Experiments were performed at 10°C in 25 mM Tris buffer and a pH of 7.0, and using concentrations of αS and Zn^{2+} of 415 μM and 2.1 mM, respectively.

N-terminal region and in proximity of His50, indicate that the interaction with Cu^{+} induces conformational exchange in the intermediate NMR timescale. We also noted that Cu^{+} induces a mild reduction in R_1 values, which is significant primarily in the N-terminal region of αS, whereas binding of Cu^{2+} did not induce significant changes in R_2/R_1 values, except in proximity of His50 and Asp121.

3.3 Zinc and manganese interaction

When we probed the interaction between αS and Zn^{2+}. The experiments indicated strong perturbations of the ^{1}H-^{15}N-HSQC spectrum of αS (Figure 3), with major CSP found in proximity of His50 and Asp121 (Figure 3B). Zinc interaction was found also to induce alterations of the protection factors of αS, with significant reductions of the LogP values of the C-terminal region of the protein (Figure 3C). In addition, Zn^{2+} binding strongly perturbed the relaxation properties of αS, with significant alterations in R_2/R_1 values in proximity of His 50 and Asp121 (Figure 3D). Collectively these NMR data indicate specific zinc binding in two regions of αS resulting in conformational exchange in the intermediate timescale in the regions flanking residues 50 and 121 as well as enhanced solvent exchange in the C-terminal region of the protein.

Finally, the incubation of Mn^{2+} generated very minor CSP primarily localised in the C-terminal region of αS (Supplementary Figure S4). Because of broadening effects upon manganese binding, in the C-terminal region of αS protection factors could be obtained only for very few residues (Supplementary Figure S4C), indicating generally no perturbation in the local solvent exchange. By contrast, enhanced R_2/R_1 values were observed in correspondence in the N-terminal and C-terminal regions of the protein (residues M1, G25, A27, G36, G51, Q99, L100, G101, K102, N103, E104, E105, A107, E110, G111, and I112). It is worth noting that Mn^{2+} can induce enhanced transverse relaxation in NMR resonances, thereby possibly altering R_2/R_1 values as a result of the paramagnetic effect. In this case, changes in R_2/R_1 may not exclusively reflect alterations in the conformational ensemble of αS.

4 Discussion

A number of evidences exist about the role of metal ions in the underlying mechanisms at the onset and development of PD (Carboni and Lingor, 2015; Bjorklund et al., 2018; Vellingiri et al., 2022). Alterations in copper homeostasis in neuronal cells, for example, have been associated with processes of neurodegeneration, including oxidative stress, dopamine oxidation, mitochondrial impairment (Bisaglia and Bubacco, 2020). Long-term exposure to manganese, copper and other metals is also known to enhance the risk of developing PD (Caudle, 2017), and it is now clear

that different metal ions can act synergistically in inducing pathogenic processes in PD (Bjorklund et al., 2018). Despite these evidences, however, the role of metal dishomeostasis in PD is not fully understood and remains strongly debated. It has been extensively shown that metals can enhance the aggregation of αS by inducing the misfolding of αS into amyloid-prone species promoting fibrillization (Binolfi et al., 2006; Fink, 2006; Binolfi et al., 2008; Binolfi et al., 2010; Deas et al., 2016). The enhancement of αS aggregation has been observed in conjunction with numerous cations such as Ca^{2+} (Stephens et al., 2020), Mn^{2+} (Uversky et al., 2001; Verina et al., 2013), Zn^{2+} (Sato et al., 2013), Cu^{2+} (Montes et al., 2014) and Cu^{+} (Wang et al., 2010). We here focussed on these specific metals to aim at a detailed characterisation of their binding modes with αS. In order to generate new understanding of the effects of these interactions on the conformational properties of αS, using NMR CLEANEX we probed how the metals affect the amide protection factors of the protein. These experiments are specifically tailored to probe H/H exchange in solvent exposed regions of protein molecules (De Simone et al., 2011; Fusco et al., 2022) and IDPs (Hwang et al., 1998; Okazaki et al., 2013). Other NMR measurements of proton exchange of αS have shown that the cellular environment does not alter the rates of exchange (Smith et al., 2015), making this technique a fine probe of the conformational properties of αS in the crowded cellular environment. Backbone amide exchange is indeed specifically sensitive to slow backbone dynamics in proteins and perturbations of this process provide evidence of key conformational changes in IDPs, such as, for example, the formation of local hydrogen bonds.

Our data indicate that the individual metal ions have distinctive modes of binding with αS and induce specific perturbations of its amide protection factors. The binding signatures of each metal are even more unique when considering CSP and ^{15}N relaxation data in addition to LogP. In particular, strong effects on the protection factors were observed in the presence of Ca^{2+} and Zn^{2+}, with both cases associated with a reduction of LogP values of the C-terminal region of αS. In the presence of calcium, CSP were observed primarily in the C-terminal region of αS, suggesting only a local involvement in the metal binding, whereas upon zinc interaction CSP were observed also in the region proximal to His50. Moreover, calcium binding did not induce significant perturbations in ^{15}N relaxation of αS while zinc was found to strongly enhance R_2/R_1 values in proximity of residue His50 and the C-terminal region of αS. These data indicate that the conformational changes that zinc induces on αS are different from those induced by calcium, with the first affecting the local conformations in two spots of the protein and the second influencing primarily the properties of the C-terminal region. In addition to zinc and calcium binding, we also found that copper-αS interactions have unique signatures. Copper binding indeed generates CSPs in three regions of the protein, including the N-terminus, the region in proximity of residue His 50 and the C-terminus, with perturbations induced by Cu^{+} found to be significantly stronger than those associated with Cu^{2+}. The incubation with both types of copper cations did not affect significantly the protection factors of αS, whereas conformational changes probed by ^{15}N relaxation indicated rearrangements of the N-terminal region upon Cu^{+} as revealed by R_2/R_1 values.

Taken together our results indicate that, although all the metal ions here studied accelerate αS aggregation, they attain different binding modes with the protein suggesting that multiple mechanisms of enhanced aggregation may occur as a result of these interactions. Understanding the nature of these mechanisms is therefore critical if we are to reveal the connection between metal dis-homeostasis and αS aggregation in the context of PD. A key challenge in this research area will be the characterization of synergic effects of the metal ions in their multiple interactions with αS, and how these are related with the various phases of the normal and pathological neuronal activity.

Data availability statement

The original contributions presented in the study are included in the article/Supplementary Material, further inquiries can be directed to the corresponding authors.

Author contributions

AD and GF conceived the work. MG-G performed the NMR measurements and data analysis. All authors analysed and discussed the results. MG-G and AD wrote the manuscript with input from all authors.

Funding

This research is supported by the European Research Council (ERC) Consolidator Grant (CoG) "BioDisOrder" (819644), the UK Biotechnology and Biological Sciences Research Council (BB/M011178/1) and Alzheimer's Research UK (ARUK-PG2018B-013).

Acknowledgments

We thank Frank Sobott (University of Leeds, United Kingdom) and Jonathan J. Phillips (University of Exeter, United Kingdom) for discussions about this work.

Conflict of interest

The authors declare that the research was conducted in the absence of any commercial or financial relationships that could be construed as a potential conflict of interest.

Publisher's note

Supplementary material

The Supplementary Material for this article can be found online at: https://www.frontiersin.org/articles/10.3389/fchem.2023.1167766/full#supplementary-material

References

Abeyawardhane, D. L., Fernández, R. D., Heitger, D. R., Crozier, M. K., Wolver, J. C., and Lucas, H. R. (2018). Copper induced radical dimerization of α-synuclein requires histidine. *J. Am. Chem. Soc.* 140, 17086–17094. doi:10.1021/jacs.8b08947

Auluck, P. K., Caraveo, G., and Lindquist, S. (2010). α-Synuclein: Membrane interactions and toxicity in Parkinson's disease. *Annu. Rev. Cell Dev. Biol.* 26, 211–233. doi:10.1146/annurev.cellbio.042308.113313

Binolfi, A., Lamberto, G. R., Duran, R., Quintanar, L., Bertoncini, C. W., Souza, J. M., et al. (2008). Site-specific interactions of Cu(II) with alpha and beta-synuclein: Bridging the molecular gap between metal binding and aggregation. *J. Am. Chem. Soc.* 130, 11801–11812. doi:10.1021/ja803494v

Binolfi, A., Rasia, R. M., Bertoncini, C. W., Ceolin, M., Zweckstetter, M., Griesinger, C., et al. (2006). Interaction of alpha-synuclein with divalent metal ions reveals key differences: A link between structure, binding specificity and fibrillation enhancement. *J. Am. Chem. Soc.* 128, 9893–9901. doi:10.1021/ja0618649

Binolfi, A., Rodriguez, E. E., Valensin, D., D'Amelio, N., Ippoliti, E., Obal, G., et al. (2010). Bioinorganic chemistry of Parkinson's disease: Structural determinants for the copper-mediated amyloid formation of alpha-synuclein. *Inorg. Chem.* 49, 10668–10679. doi:10.1021/ic1016752

Binolfi, A., Valiente-Gabioud, A. A., Duran, R., Zweckstetter, M., Griesinger, C., and Fernandez, C. O. (2011). Exploring the structural details of Cu(I) binding to alpha-synuclein by NMR spectroscopy. *J. Am. Chem. Soc.* 133, 194–196. doi:10.1021/ja107842f

Bisaglia, M., and Bubacco, L. (2020). Copper ions and Parkinson's disease: Why is homeostasis so relevant? *Biomolecules* 10, 195. doi:10.3390/biom10020195

Bjorklund, G., Stejskal, V., Urbina, M. A., Dadar, M., Chirumbolo, S., and Mutter, J. (2018). Metals and Parkinson's disease: Mechanisms and biochemical processes. *Curr. Med. Chem.* 25, 2198–2214. doi:10.2174/0929867325666171129124616

Burre, J. (2015). The synaptic function of alpha-synuclein. *J. Park. Dis.* 5, 699–713. doi:10.3233/JPD-150642

Carboni, E., and Lingor, P. (2015). Insights on the interaction of alpha-synuclein and metals in the pathophysiology of Parkinson's disease. *Metallomics* 7, 395–404. doi:10.1039/c4mt00339j

Caudle, W. M. (2017). Occupational metal exposure and parkinsonism. *Adv. Neurobiol.* 18, 143–158. doi:10.1007/978-3-319-60189-2_7

Chartier-Harlin, M. C., Kachergus, J., Roumier, C., Mouroux, V., Douay, X., Lincoln, S., et al. (2004). α-synuclein locus duplication as a cause of familial Parkinson's disease. *Lancet* 364, 1167–1169. doi:10.1016/S0140-6736(04)17103-1

Chiti, F., and Dobson, C. M. (2017). Protein misfolding, amyloid formation, and human disease: A summary of progress over the last decade. *Annu. Rev. Biochem.* 86, 27–68. doi:10.1146/annurev-biochem-061516-045115

Connelly, G. P., Bai, Y., Jeng, M. F., and Englander, S. W. (1993). Isotope effects in peptide group hydrogen exchange. *Proteins* 17, 87–92. doi:10.1002/prot.340170111

De Simone, A., Dhulesia, A., Soldi, G., Vendruscolo, M., Hsu, S. T., Chiti, F., et al. (2011). Experimental free energy surfaces reveal the mechanisms of maintenance of protein solubility. *Proc. Natl. Acad. Sci. U. S. A.* 108, 21057–21062. doi:10.1073/pnas.1112197108

Deas, E., Cremades, N., Angelova, P. R., Ludtmann, M. H., Yao, Z., Chen, S., et al. (2016). Alpha-synuclein oligomers interact with metal ions to induce oxidative stress and neuronal death in Parkinson's disease. *Antioxid. Redox Signal* 24, 376–391. doi:10.1089/ars.2015.6343

Dedmon, M. M., Lindorff-Larsen, K., Christodoulou, J., Vendruscolo, M., and Dobson, C. M. (2005). Mapping long-range interactions in alpha-synuclein using spin-label NMR and ensemble molecular dynamics simulations. *J. Am. Chem. Soc.* 127, 476–477. doi:10.1021/ja044834j

Farrow, N. A., Muhandiram, R., Singer, A. U., Pascal, S. M., Kay, C. M., Gish, G., et al. (1994). Backbone dynamics of a free and a phosphopeptide-complexed src homology 2 domain studied by 15N NMR relaxation. *Biochemistry* 33, 5984–6003. doi:10.1021/bi00185a040

Fink, A. L. (2006). The aggregation and fibrillation of alpha-synuclein. *Acc. Chem. Res.* 39, 628–634. doi:10.1021/ar050073t

Fusco, G., Bemporad, F., Chiti, F., Dobson, C. M., and De Simone, A. (2022). The role of structural dynamics in the thermal adaptation of hyperthermophilic enzymes. *Front. Mol. Biosci.* 9, 981312. doi:10.3389/fmolb.2022.981312

Fusco, G., Chen, S. W., Williamson, P. T. F., Cascella, R., Perni, M., Jarvis, J. A., et al. (2017). Structural basis of membrane disruption and cellular toxicity by alpha-synuclein oligomers. *Science* 358, 1440–1443. doi:10.1126/science.aan6160

Fusco, G., Pape, T., Stephens, A. D., Mahou, P., Costa, A. R., Kaminski, C. F., et al. (2016). Structural basis of synaptic vesicle assembly promoted by α-synuclein. *Nat. Commun.* 4, 12563. doi:10.1038/ncomms12563

Fusco, G., Sanz-Hernandez, M., and De Simone, A. (2018). Order and disorder in the physiological membrane binding of alpha-synuclein. *Curr. Opin. Struct. Biol.* 48, 49–57. doi:10.1016/j.sbi.2017.09.004

Gonzalez, N., Arcos-Lopez, T., Konig, A., Quintanar, L., Menacho Marquez, M., Outeiro, T. F., et al. (2019). Effects of alpha-synuclein post-translational modifications on metal binding. *J. Neurochem.* 150, 507–521. doi:10.1111/jnc.14721

Hwang, T. L., van Zijl, P. C., and Mori, S. (1998). Accurate quantitation of water-amide proton exchange rates using the phase-modulated CLEAN chemical EXchange (CLEANEX-PM) approach with a Fast-HSQC (FHSQC) detection scheme. *J. Biomol. NMR* 11, 221–226. doi:10.1023/a:1008276004875

Lashuel, H. A., Overk, C. R., Oueslati, A., and Masliah, E. (2013). The many faces of alpha-synuclein: From structure and toxicity to therapeutic target. *Nat. Rev. Neurosci.* 14, 38–48. doi:10.1038/nrn3406

Lautenschlager, J., Stephens, A. D., Fusco, G., Strohl, F., Curry, N., Zacharopoulou, M., et al. (2018). C-terminal calcium binding of alpha-synuclein modulates synaptic vesicle interaction. *Nat. Commun.* 9, 712. doi:10.1038/s41467-018-03111-4

Lee, S. J., and Masliah, E. (2015). Neurodegeneration: Aggregates feel the strain. *Nature* 522, 296–297. doi:10.1038/nature14526

Luk, K. C., Kehm, V., Carroll, J., Zhang, B., O'Brien, P., Trojanowski, J. Q., et al. (2012). Pathological alpha-synuclein transmission initiates Parkinson-like neurodegeneration in nontransgenic mice. *Science* 338, 949–953. doi:10.1126/science.1227157

Maltsev, A. S., Ying, J., and Bax, A. (2012). Impact of N-terminal acetylation of alpha-synuclein on its random coil and lipid binding properties. *Biochemistry* 51, 5004–5013. doi:10.1021/bi300642h

Miotto, M. C., Binolfi, A., Zweckstetter, M., Griesinger, C., and Fernandez, C. O. (2014). Bioinorganic chemistry of synucleinopathies: Deciphering the binding features of Met motifs and his-50 in AS-Cu(I) interactions. *J. Inorg. Biochem.* 141, 208–211. doi:10.1016/j.jinorgbio.2014.08.012

Miotto, M. C., Valiente-Gabioud, A. A., Rossetti, G., Zweckstetter, M., Carloni, P., Selenko, P., et al. (2015). Copper binding to the N-terminally acetylated, naturally occurring form of alpha-synuclein induces local helical folding. *J. Am. Chem. Soc.* 137, 6444–6447. doi:10.1021/jacs.5b01911

Montes, S., Rivera-Mancia, S., Diaz-Ruiz, A., Tristan-Lopez, L., and Rios, C. (2014) Copper and copper proteins in Parkinson's disease. *Oxid. Med. Cell Longev.* 2014, 147251–147315. doi:10.1155/2014/147251

Newberry, R. W., Leong, J. T., Chow, E. D., Kampmann, M., and DeGrado, W. F. (2020). Deep mutational scanning reveals the structural basis for alpha-synuclein activity. *Nat. Chem. Biol.* 16, 653–659. doi:10.1038/s41589-020-0480-6

Okazaki, H., Ohori, Y., Komoto, M., Lee, Y. H., Goto, Y., Tochio, N., et al. (2013). Remaining structures at the N- and C-terminal regions of alpha-synuclein accurately elucidated by amide-proton exchange NMR with fitting. *FEBS Lett.* 587, 3709–3714. doi:10.1016/j.febslet.2013.09.039

Piotto, M., Saudek, V., and Sklenar, V. (1992). Gradient-tailored excitation for single-quantum NMR spectroscopy of aqueous solutions. *J. Biomol. NMR* 2, 661–665. doi:10.1007/BF02192855

Pontoriero, L., Schiavina, M., Murrali, M. G., Pierattelli, R., and Felli, I. C. (2020). Monitoring the interaction of α-Synuclein with calcium ions through exclusively heteronuclear nuclear magnetic resonance experiments. *Angew. Chem. Int. Ed. Engl.* 59, 18537–18545. doi:10.1002/anie.202008079

Rasia, R. M., Bertoncini, C. W., Marsh, D., Hoyer, W., Cherny, D., and Zweckstetter, M. (2005). Structural characterization of copper(II) binding to alpha-synuclein: Insights into the bioinorganic chemistry of Parkinson's disease. *Proc. Natl. Acad. Sci. U. S. A.* 102, 4294–4299. doi:10.1007/bf02192855

Roberts, H. L., and Brown, D. R. (2015). Seeking a mechanism for the toxicity of oligomeric alpha-synuclein. *Biomolecules* 5, 282–305. doi:10.3390/biom5020282

Sato, H., Kato, T., and Arawaka, S. (2013). The role of Ser129 phosphorylation of alpha-synuclein in neurodegeneration of Parkinson's disease: A review of *in vivo* models. *Rev. Neurosci.* 24, 115–123. doi:10.1515/revneuro-2012-0071

Seetaloo, N., Zacharopoulou, M., Stephens, A. D., Kaminski Schierle, G. S., and Phillips, J. J. (2022). Millisecond hydrogen/deuterium-exchange mass spectrometry approach to correlate local structure and aggregation in α-synuclein. *Anal. Chem.* 94, 16711–16719. doi:10.1021/acs.analchem.2c03183

Singleton, A. B., Farrer, M., Johnson, J., Singleton, A., Hague, S., Kachergus, J., et al. (2003). α-Synuclein locus triplication causes Parkinson's disease. *Science* 302, 841. doi:10.1126/science.1090278

Smith, A. E., Zhou, L. Z., and Pielak, G. J. (2015). Hydrogen exchange of disordered proteins in *Escherichia coli*. *Protein Sci.* 24, 706–713. doi:10.1002/pro.2643

Snead, D., and Eliezer, D. (2014). Alpha-synuclein function and dysfunction on cellular membranes. *Exp. Neurobiol.* 23, 292–313. doi:10.5607/en.2014.23.4.292

Spillantini, M. G., Schmidt, M. L., Lee, V. M., Trojanowski, J. Q., Jakes, R., and Goedert, M. (1997). α-Synuclein in Lewy bodies. *Nature* 388, 839–840. doi:10.1038/42166

Stephens, A. D., Zacharopoulou, M., Moons, R., Fusco, G., Seetaloo, N., Chiki, A., et al. (2020). Extent of N-terminus exposure of monomeric alpha-synuclein determines its aggregation propensity. *Nat. Commun.* 11, 2820. doi:10.1038/s41467-020-16564-3

Sung, Y. H., Rospigliosi, C., and Eliezer, D. (2006). NMR mapping of copper binding sites in alpha-synuclein. *Biochim. Biophys. Acta* 1764, 5–12. doi:10.1016/j.bbapap.2005.11.003

Uversky, V. N., and Eliezer, D. (2009). Biophysics of Parkinsons disease: Structure and aggregation of - synuclein. *Curr. Protein. Pept. Sci.* 10, 483–499. doi:10.2174/138920309789351921

Uversky, V. N., Li, J., and Fink, A. L. (2001). Metal-triggered structural transformations, aggregation, and fibrillation of human alpha-synuclein. A possible molecular NK between Parkinson's disease and heavy metal exposure. *J. Biol. Chem.* 276, 44284–44296. doi:10.1074/jbc.M105343200

Vellingiri, B., Suriyanarayanan, A., Abraham, K. S., Venkatesan, D., Iyer, M., Raj, N., et al. (2022). Influence of heavy metals in Parkinson's disease: An overview. *J. Neurol.* 269, 5798–5811. doi:10.1007/s00415-022-11282-w

Verina, T., Schneider, J. S., and Guilarte, T. R. (2013). Manganese exposure induces alpha-synuclein aggregation in the frontal cortex of non-human primates. *Toxicol. Lett.* 217, 177–183. doi:10.1016/j.toxlet.2012.12.006

Villar-Pique, A., Rossetti, G., Ventura, S., Carloni, P., Fernandez, C. O., and Outeiro, T. F. (2017). Copper(II) and the pathological H50Q alpha-synuclein mutant: Environment meets genetics. *Commun. Integr. Biol.* 10, e1270484. doi:10.1080/19420889.2016.1270484

Wang, C., Liu, L., Zhang, L., Peng, Y., and Zhou, F. (2010). Redox reactions of the α-synuclein–Cu^{2+} complex and their effects on neuronal cell viability. *Biochemistry* 49, 8134–8142. doi:10.1021/bi1010909

Frontiers in Neuroscience

Provides a holistic understanding of brain function from genes to behavior

Part of the most cited neuroscience journal series which explores the brain - from the new eras of causation and anatomical neurosciences to neuroeconomics and neuroenergetics.

Discover the latest Research Topics

See more →

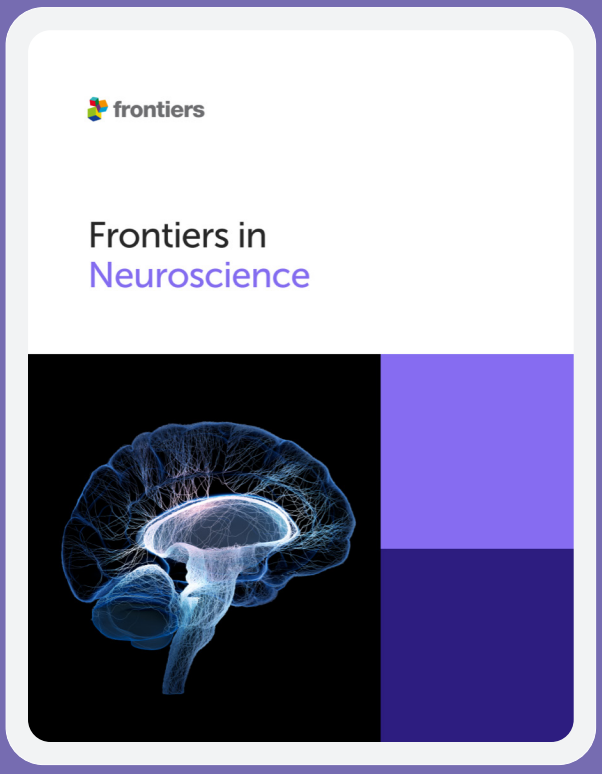

Frontiers

Avenue du Tribunal-Fédéral 34
1005 Lausanne, Switzerland
frontiersin.org

Contact us

+41 (0)21 510 17 00
frontiersin.org/about/contact